PERFORMANCE OF MULTICELL, AXIAL-ENTRY CYCLONES FOR INDUSTRIAL GAS CLEANING

BY

PARVIZ BEHROUZI

B.Sc (Eng), M.Sc (Eng)

Thesis submitted for the degree of
Doctor of Philosophy
in the Faculty of Engineering of the University of London
and for the
Diploma of Membership of the Imperial College

November 1988

Department of Mechanical Engineering
Imperial College of Science, Technology & Medicine
London SW7 2BX

ABSTRACT

Inertial dust separators in common use for removing particulates from the flue gases of industrial coal-fired boilers are barely able to meet current clean air regulations, especially with fluidised-bed combustion. More efficient devices (scrubbers, electrostatic precipitators, fabric filters) have operational disadvantages and unacceptable cost. The objectives of this project are:

(i) to investigate the causes of performance deficiencies in multicell cyclone dust separators (compared with a single, isolated cell of the same type);

(ii) to propose and test measures which could enhance their efficiency enough to comply cheaply with future emissions regulations, with acceptable pressure loss.

(iii) To develop a prediction method for single-cell performance, test it against the experimental data from (i) and attempt to predict the effects of some of the phenomena identified in (i) or of the remedial measures suggested in (ii).

The thesis begins with a review of the present status of dust separation technology in general and cyclones in particular.

An experimental programme, including design of rigs, is then described, based on cold, small-scale modelling of a representative segment of a typical multicell cyclone. Test dusts and air flows were chosen to match the Stokes numbers (controlling particle motion, to a first approximation); some departure from Reynolds number matching was justified by experiment and computation. The design and development of dust feeding and sampling systems and flow visualization techniques are outlined.

Measurements include overall mass efficiencies, grade efficiencies (using laser diffraction sizing of samples dispersed in air), gas flow rates through each cell and visualization of flows in the multicell cyclone's common dust hopper and inlet and outlet manifolds. A single axial-entry cyclone identical to those in the multicell unit

was also tested as a reference case. Laser Doppler measurements of the three-dimensional flow field in the single-cell cyclone were made to identify phenomena relevant to dust collection performance and to provide input data for a numerical model.

Results are reported on the influence of inlet flow distribution, dust type, and modifications aimed at eliminating gas circulation in the dust hopper or stabilizing the cell vortex flows. A potential for halving solids emission has been demonstrated, if multicell cyclone performance could be optimized to the levels measured for an isolated cell. Improved gas distribution between cells did not always lead to higher dust collection efficiency. It was concluded that none of the "flow management" devices investigated was likely to achieve the desired result, and that gas removal from the hopper to a secondary filter is necessary (as already implemented commercially but poorly quantified and not optimized); proposals are made for further research in that area.

An existing finite-difference code combining gas flow and particle trajectory modelling has been modified and rewritten to compute the grade efficiency of axial-entry reverse-flow cyclones. Gas flow field predictions showed significantly better agreement with the laser Doppler measurements than those of the existing program. Runs have been made for comparison of dust collection efficiency with the reference-case measurements, with encouraging agreement. Further runs were made for prediction of the effects of gas interchange between cells and the common dust hopper, as observed in the experiments, and to assess the benefits of gas extraction through the dust exit.

ACKNOWLEDGMENTS

It gives me great pleasure to express my gratitude to my supervisor, Dr. R. I. Crane for his guidance, kind advice and constructive criticism throughout my work. His encouragement and continuous interest in the project led me to the completion of this thesis.

My thanks are due to the chief technicians Mr W. Lamburn and C. Hall and all the section's technical staff whose assistance was vital to my research program; Messrs. S. Joseph, R. D. Bloxham, R. West, T. Robinson and D. Grant were particularly helpful in the experimental part of the work.

I wish to thank to Dr. J. Sabzvari who introduced me to practical laser doppler anemometry and assisted me with photography.

Finally my thanks to the Coal Research Establishment, British Coal, which supplied experimental equipment and also Prof. J. Swithenbank and Dr. F. Boysan for giving a copy of SPRINT-4.

To my wife, Mitra

CONTENTS

LIST OF TABLES

LIST OF FIGURES

NOMENCLATURE

Note: This nomenclature contains the main symbols frequently used in this thesis. Some symbols which are less frequently used are clearly defined in the text and have been omitted from this list.

Roman Characters

A	surface area in general
a	Inlet duct height (tangential cyclone, Fig. 2.4); Coefficient of finite difference equation
B	Dust exit diameter (Fig. 2.4)
b	Inlet duct width (tangential type cyclone, Fig. 2.4)
C,c	Constant factor
C_1,C_2	Coefficients of the turbulence model
C_μ	Coefficient of the turbulence model
C_D	Coefficient of the turbulence model; drag coefficient
D	Cyclone diameter (Fig. 2.4)
D_c	Vortex core diameter
D_e	Diameter of cyclone exit throat (Fig. 2.4)
d	Diameter in general
$d_{m,0.5}$	Mass median diameter
d_{rr}	Rosin-Rammler mean diameter
E	Voltage
F	Force in general
f	Lens focal length
f_D	Doppler frequency
G	Turbulence generation term
g	Gravitational acceleration
H	Cyclone total length (Fig. 2.4); pressure head
h	Cyclone cylindrical section length (Fig. 2.4)
k	Turbulence kinetic energy
m	Mass in general

m_1	Feeding mass
m_2	Total sampling mass before cyclone
m_3	Sediment mass inside upstream ducting
m_4	Hopper mass
m_5	Total sampling mass after cyclone
m_9, m_{10}	Sediment mass inside cyclone inlet and outlet manifold
N	Number in general
N_I	Number of grid line (z or x) direction
N_J	Number of grid line (r or y) direction
n	Vortex exponent; Rosin-Rammler spread parameter (Sec. 4.5.1)
P,p	Pressure in general; total turbulence energy production
Pe	Peclet number
Q,q	Flux in general
Q_{CA}	Particle dispersal air flow rate
Q_R	Rig flow rate
Q_{S1}	Sampling system flow rate (before cyclone)
Q_{S2}	Sampling system flow rate (after cyclone)
Re	Reynolds number
r	Radius of curvature in general; radial coordinate
S	Gas exit tube (vortex finder) length below vane trailing edge (Fig. 2.4)
S_p,S_u	Linearization of source term
St	Stokes number
S_ϕ	Source term in the partial differential and finite difference equations
T	Temperature; combined convection and diffusion terms (Eq. 5.18)
t	Time
U	Velocity in general
u	Axial mean velocity component
u^+	Local mean velocity/ friction velocity
u'	Velocity fluctuating of axial velocity
V	Velocity in general; volume

$\hat{V}_r$,$\hat{V}_\theta$,$\hat{V}_z$	Instantaneous velocity (r,θ,z direction)
v	Radial mean velocity component
w	Tangential (Swirl) mean velocity component
x	Coordinate in the cartesian system
y	Coordinate in the cartesian system
y+	Dimensionless distance
z	Axial coordinate

Greek Characters

γ	Ratio of specific heats
Δ	Increment
δ_{ij}	Kroneker delta (=1 for i=j, =0 for i≠j)
ε	Turbulence energy dissipation rate
η	Efficiency in general
ζ	Euler number; normally distributed random number (eq. 5.36)
θ	Angular coordinate; angular position in general
χ	Von Karman constant
λ	Light wavelength
μ	Dynamic (molecular) viscosity
μ_{eff}	Effective viscosity (=$\mu+\mu_t$)
μ_t	Turbulent viscosity
υ	Kinematic viscosity
ρ	Density
σ_k, σ_ε	Constants in the turbulence model
$\sigma_{\phi,t}$	Turbulent Prandtl / Schmidt number
τ	Characteristics time scale; shear stress
τ_w	Wall shear stress
Φ	Scalar property
ϕ	A dependent variable; half angle between LDA beams; local mean scalar property
ψ	Pressure-strain term (Eq. 5.18)
ω	Angular velocity

Subscripts

a	Of air
E,N,P,S,W	At grid nodes E,N,P,S,W (Fig. 5.6)
e,n,s,w	At cell faces e,n,s,w (Fig. 5.6)
f	Of fluid
g	Of gas
i	At inlet; the ith location
i,j,k	Cartesian tensor notation
max	Maximum
min	Minimum
O	At outlet
P,p	Of particle; central node of a discretization cell
S	Of sampling system
T	Total
W	At wall; wire

Superscripts

$\bar{}$	Time or ensemble averaged
'	Correction value; fluctuating component
^	Instantaneous value
+	Dimensionless (in the 'wall functions')
*	Estimated value

CHAPTER 1

INTRODUCTION

1.1 INTRODUCTORY REMARKS

For removal of solids from the flue gases of industrial coal-fired boilers, two factors are now seriously affecting the viability of conventional cyclones. First is the growth of fluidised-bed (f.b.) firing, which imposes a greater demand on the gas cleaning system because a greater fraction of the coal ash, in finer particle sizes, is elutriated from the bed with the combustion gases, together with quantities of bed material (typically sand) and unburnt carbon.

The second factor is the imminent introduction of new, more stringent emissions regulations. Current U.K. regulations (1971) allow solids emission up to a certain fraction of the weight of coal fired, the fraction being about 1% for boiler outputs below about 1.5 MW, decreasing to about 0.5% for large boilers (over 30 MW). With conventional firing, solids concentration and size distribution in the combustion products are such as to allow the use of simple, cheap, well-established cleaning devices, usually cyclones. Illustrative calculations presented in Table 1.1 show that overall collection efficiencies (on mass basis) around 85-90%, usually attainable by cyclones, are sufficient to meet the current regulations for chain-grate or stoker fired boilers.It is likely that the new regulations (under discussion at the time of this investigation) will be based on a prescribed maximum dust concentration, and may be applied down to quite low boiler ratings. Assuming that this concentration were set at 70 mg/Nm^3* (where Nm^3 denotes 1 m^3 of flue gas at normal, i.e. 15 ^{o}C, 1 bar, conditions), the required overall efficiency of dust collection in the example of Table 1.1 becomes almost 99%; probable ranges of efficiency for various types of firing under such an emissions limit are listed in Table 1.2 (data on pre-cleaning dust concentration from Bogucki, 1986).

Progress in pressurised fluidised bed gasifier, combined cycle power generating

---

* = 58 ppm

systems is also highlighting deficiencies in cyclone performance. Here the high temperature (1,000 ^{o}C), high pressure (20 bar) gas must be cleaned down to about 5 μm particle size prior to being fired in a gas turbine, which is beyond the current capability of cyclone devices (Biffin et al, 1981 and Boysan et al, 1982).

Therefore recently there is a renewed interest in the design of this type of collector, even at the expense of high pressure drop in certain applications. The present work arose from a demand from the Coal Research Establishment (CRE) of British Coal (formerly National Coal Board) for improving the performance of multicell cyclones (Crane, 1985).

1.2 EMISSION REGULATIONS AND THE REQUIREMENT FOR GAS CLEANING

Air pollution, arising to a large extent from energy conversion and use, is a source of increasing public and government concern in many countries. A major part of this air pollution is caused by emissions of air pollutants from energy facilities such as power plants and industrial boilers. These air pollutants consist principally of particulates (dust), sulphur and nitrogen oxides. They are implicated in such phenomena as acid rain and photochemical smog, and their effects on human health, vegetation, water, and man-made materials (Stern, 1986).

The response of governments to these problems often takes the form of emission standards, whether guidelines or strict limits. Some countries set standards which force the development of higher efficiency control technologies; others specify the means by which control is to be achieved; and in other cases reliance is placed on the ability of industry to achieve acceptable emission standards by whatever means are economically feasible (U.N., 1987 and Weidner,1987).In many respects the level of legislation and particularly its specificity reflect the level of industrialisation and/or the extent of pollution problems within the country. Transboundary pollution problems may, in the future, have an increasing influence on the stringency of air pollution control standards (Organisation for Economic Co-operation and Development (OECD), 1984).

The way in which countries express emission criteria vary widely. In general, emission limits are expressed in the form in which they appear in that country's regulations. In some cases it has been possible to standardize these units to some extent. For example standards expressed as weight of pollutant /unit of exhaust gas volume can be converted to mg/m^3. In general no globally valid conversion can be made between a standard in mg/m^3 exhaust gas volume and nanograms (ng) of pollutant/ joule of energy input (output). Such manipulations require assumptions regarding either the calorific value of the fuel in question or the exhaust gas volumes and firing rates of the plant. It is nonetheless of interest to provide a table of national emission standards or guidelines in comparable units, so some relatively simple but reasonable assumptions as to the equivalence of units have been used in compiling Table 1.3 (OECD, 1984).

On the basis of cost per unit of energy, coal is an attractive fuel for industrial steam generators, water heaters and furnaces. However, the extent to which it can penetrate the industrial boiler market is heavily dependent on capital and installation costs, which must be kept to a minimum. Gas cleaning equipment, to comply with legislation on emission of particulates to the atmosphere, forms a significant part of such costs (OECD, 1987).

There is another urgency in achieving improved gas cleaning equipment design, as current trends in methods of obtaining electrical power from fossil fuels, particularly coal, usually referred to as " advanced power technology", are requiring the treatment of gases to remove particulates for reasons of pollution control and especially for the protection of gas turbine blades (Reijnen and Brakel ,1984). In the case of combined gas/ steam cycle operation, it is desirable, for reason of overall thermodynamic efficiency, to operate the gas turbines at maximum inlet gas temperatures of>1000 ^{o}C and pressure of>10 atm (Perlsweig et al, 1981). This range of operation is commonly known as "hot gas" clean- up. Much damage will be caused to the turbine blades by even the smallest particles which evade capture. Even if they are small enough not to cause direct damage in the highly corrosive and erosive environment, they may collect on the stator blades, where given sufficient time, can block the inter-stator blade spaces completely (Biffin and Syred, 1983). It is difficult to predict the allowable size and concentration of particulates which can be

tolerated at the inlet to the gas turbine, but the current estimate for a conventional turbine is $4.6*10^{-4}$ g/m^3 with all particles greater than 6 μm removed . This specification for example is generally held to be beyond the capabilities of current cyclone technology.

1.3 REVIEW OF DUST SEPARATION TECHNOLOGY

Air pollution control regulations enacted over the past 15 years have had a profound effect on the design and cost of many industrial and energy conversion process. For example in U.S.A. new standards for coal-fired steam generators, established in 1971 and tightened in 1979, have affected the electric utility industry in particular (Rubin, 1986). Emission limits for pollutants such as total suspended particulate matter, led to the development of new combustion and post-combustion control techniques to reduce atmospheric emissions. Meanwhile, the need to dispose of new by- product wastes and to comply with stringent water pollution standards has focused attention on the many media involved in environmental control and on the importance of thinking of air, water and land as a total system.

Many types of air cleaning devices are used for arresting particles from flue gases or process, which are based on principles like gravitational, settling, inertial deposition, agglomeration, electrostatic attraction, thermal precipitation, and atomization (Stairmand 1965 &1956, Stern 1986 and Lucas 1974). The more important types of gas cleaning devices may be grouped under five main headings, according to the principle on which the separation process depends:

1- Settling chambers
2- Inertial separators, including cyclones
3- Filtration through a porous medium
4- Wet washers and scrubbers
5- Electrostatic precipitators

Brief descriptions of the various types of these devices are given here.

1.3.1 Settling Chambers

The settling chamber is the simplest form of gas cleaning device, and depends on the fact that solid or liquid particles suspended in a gas fall through the gas under the action of gravity at a speed which is dependent on the size of the particles, their density and shape, and the density and viscosity of the gas (Parker, 1978). The particles rapidly reach a constant velocity referred to as the free falling or terminal velocity, which can be calculated for smaller particles from the formula derived by Stokes, which states that

$$U_f = \frac{g\, d_p^2(\rho_P - \rho_g)}{18\mu_g} \qquad (1.1)$$

where U_f is free falling velocity. A practical form of settling chamber is shown diagramatically in Fig 1.1. For practical purposes the settling chamber is limited to the collection of dust particles in excess of 100 μm, or particles with free falling velocity in excess of 1 m/s. For smaller particles, the retention time and hence the size of the settling chamber becomes excessively large.

1.3.2 Inertial Collectors and Cyclones

There are many devices of different form falling into this category . All depend, for their increased effectiveness compared with the settling chamber, on the fact that when a dust particle is spinning in a circular path it is subject to an outward force given by $F=mv^2/r$, where m, v and r are mass of particle, velocity and radius of spinning circle. By suitable choice of values of v and r the acceleration of the particle (v^2/r) can be made many times the value of the acceleration due to gravity, g, and the force acting increases accordingly. Hence, replacing this increased acceleration for g in eqn. (1.1), the velocity of the particle relative to the gas is correspondingly increased. For instance, in a small sampling cyclone of about 3 cm diameter, designed for collecting samples of dust from flue gases from a pulverized fuel boiler, it was estimated that the radial acceleration was almost 1500 g. A 10 μm particle would have its velocity relative to the gas increased to a value greater than that of a

1000 μm particle falling under the force of gravity alone (Darby, 1978). The use of this principle extends the possibility of separating particles from the gas to 10 μm and even smaller. The simplest practical device using this principle is the inertial collector. The increased force on the particle is achieved by a sudden change in direction of gas flow, the dust particle tending to carry on for a short time in the original direction of the gas flow, passing into a dead space where it is allowed to settle, thus achieving a separation efficiency superior to the settling chamber. Fig. 1.2 shows schematically two types of these devices.

The cyclone has generally the highest possible efficiency of the inertial devices. It is the simplest and most commonly used device for removing particles from diluted gas. Uncomplicated fabrication, low capital and operating costs, and adaptability to a wide range of operating conditions are some of the factors that account for this widespread use. The most popular type of cyclone is the reverse-flow cyclone, shown diagramatically in Fig. 1.3. The dust laden gas enters the body tangentially and spirals downwards in a vortex motion. At the base of the unit the direction of axial flow reverses and the clean gas leaves the unit axially by spinning upwards in a tight, fast, central vortex. Particles, which have moved to the wall, pass down to the collection hopper where they are removed. Cyclones of this type are available with diameters in the range 0.1 to 2 m.

The smaller the cyclone diameter, the more efficient the cyclone; hence multicell cyclones (or "multicyclones" or " multiple cyclones") have been developed to take advantage of the higher collection efficiency and still handle high gas flow rates. The multicell cyclone consists of a number of small diameter cyclone cells (150 to 300 mm dia.), usually with top entry swirl vanes. The cyclones can be ' nested' close together and contained in a casing with integral inlet and outlet sections and with a single or multiple dust receiving hopper. This type of arrangement provides a compact system which can handle relatively large gas flows with a minimum of floor space and height. Fig. 3.1a shows a schematic of one type of this device. A summary of history of the cyclone design and performance is presented in Chapter 2.

Cyclone collectors have a long history in utility boiler and industrial process applications. The first application employing the cyclone principle dates back to

1886, when Morse used a cyclone for dust collection. They were among the earliest particulate controls applied to utility boilers with their primary role being protection of the induced draft fan. Under present day pollution control regulations, they are no longer acceptable as a primary collection device in most areas (Dirgo and Leith, 1985); even in those parts of the industry where a multicell cyclone is acceptable, its application is very risky (Jones, 1976). But as a pre-collector, or collector on coarse size distribution dusts, the cyclone still has a role to play (Mckee et al, 1977). Nor should their ability to withstand high temperature be overlooked and the fact that they give continuous operation with a constant resistance (Swift 1985, Leith and Mehta 1973). Atmospheric fluidized bed boilers, bark boilers, gasifiers, etc. with their need to recycle entrained material have given these venerable devices new life in the utility power plant enviroment (Bechtel et al 1985 and Greenfield 1986). Lucas (1974) agreed that multicell cyclones are still very useful but need further development. The other high value application of this technology has been in cat-cracker catalyst regeneration, particularly when applied with a down-stream expander turbine which is subject to erosion from excessive carryover (Rubin, 1986)

1.3.3 Filtration Through a Porous Medium

Filtration is the oldest method used for the removal of suspended materials in gases, on the principle of passing the dust-laden gases through porous filter media in which the dust is trapped. The filter media can broadly be considered under the following headings:

1- gravel or sand aggregate bed with or without on-line cleaning;
2- porous paper and fibrous mats, usually "fixed filters";
3- woven and felted fabric filters, usually with "on- line cleaning".

All of the filter media mentioned collect the dust by a combination of different effects, which are briefly as follows.

1- Particles are separated due to the sieving effect of the filter media; any filter medium has a particular pore size and all particles larger than this are separated
2- Particles are separated by the inertial effect. Their passage through the filter

medium is usually a very tortuous one and during the many changes of direction the dust particles are deposited on the material of the filter.

3- There is often an electrostatic charge on the dust particles and the finer particles in particular may be deposited as a result of this charge.

4- Very fine particles in the sub-micron range, which have a similar weight to the molecules of the carrier gas follow the stream lines of the gas flow and are not separated by inertial effects. Such small particles are subject to Brownian movement, and as a result of this motion are finally brought into close proximity to the filter material, where they are deposited and held by a combination of electrostatic and molecular forces.

5- Particles of size smaller than the holes through the filter are retained with high efficiency due to the accumulation of a layer of dust on and within filter material.Once the layer is established, filtration take place through the layer of deposited dust, but initially efficiency may be reduced until the layer is formed. This layer also increases the pressure loss compared with the clean filter. It is necessary to take this into account when the plant is designed, as this has a most important influence on the filter rate which can be used. The exposed area of filter is arranged so that the pressure drop across the filter bed is 10-15 cm w.g. (Darby , 1978).

Filtration methods are used for very widely varying conditions and appliances. Fabric filter is the most widely used type in this group, being capable of treating large gas volumes with the highest dust concentrations met in any process on a continuous basis, restricted only by the efficiency of the on-line cleaning system and the properties of the fabric. Table 1.4 shows properties of various fabric filters and Fig. 1.4 shows a schematic of a simple conventional baghouse with mechanical shaking. Important characteristics of the fabric filter are:

1- Efficiency is always high (99 percent, even for 0.01 μm particles) for felted materials

2- Efficiency is not greatly affected by dust concentration or by filter rate

3- The filter rate, that is the volume flow per unit area of cloth, is usually designed to give a pressure loss of 6-12 cm w.g., depending on whether the cloth is in a clean state or has a layer of dust deposited on it.

4- Pressure loss increases as filter rate. This characteristic largely determines the

economic filter rate and hence the filtering area needed.

Successful application of the fabric filter depends on two major considerations. First is the ability to remove accumulated dust from the filter, otherwise the pressure drop will increase until either the filter fails due to pressure on the material, or the flow rate through the filter cloth falls to an unacceptable level. Second is a reasonably long life, preferably several years for the filter material. In the past eight or ten years, fabric filters have been widely employed for fly-ash collection in electric utilities as well. This has been true especially of those that burn low-sulphur coals, in which high fly-ash resistivity requires the use of very large and expensive electrostatic precipitators. More recently, as efficiency requirements have grown in an attempt to capture more of the fine respirable particles, and as precipitators have got larger in size as a hedge against fuel changes, fabric filters have become competitive with precipitators for higher-sulphur coals (Rubin 1986 and Bechtel et al , 1985). This trend is expected to continue despite improvements that are enabling precipitators to cope with resistivity.

Recent operating experiences indicate that fabric filters can easily meet air pollution standards. The main variables to consider are pressure drop and bag life. Since most fabric filters depend on the captured cake to provide filtration efficiency, and since pressure drop is directly affected by the thickness and permeability of the cake, efficiency is traded for pressure drop in manner analogous to the sacrifice of efficiency for corona power in a precipitator.

1.3.4 Wet Washers and Scrubbers

Wet washers and scrubbers are devices using mixed phases of gas and liquid, the object of the scrubber or washing device being to transfer suspended particulate matter in the gas to the scrubbing liquid which can be readily removed from the gas cleaning device, leaving the clean gas to pass onwards to the process for which it is being used, or alternatively to be discharged to the atmosphere. The action of the wet washers and scrubbers is dependent on collision between the dust particles and liquid droplets in suspension in the gas. Collision and the resultant coalescence can be caused by one or more of the following:

1- Inertial effects and effect of gravity. It is apparent that the probability of collision between droplets of scrubbing liquids and suspended particles in the gas increases as the velocities of these two relative to each other also increases.
2- Electrostatic effect. Many dust particles carry an electrostatic charge, and this causes attraction between the liquid droplet and the particle, since the liquid droplet is usually at earth potential.
3- Diffusion phenomena. Very small particles in the fine fume range are subject to Brownian movement. This means that the particles are in random motion, which increases the probability of collision with liquid droplets of large diameter, which are not subject to this effect.
4- In many scrubbing processes the gases are initially at a relatively high temperature, consequently the effect of the scrubbing action is to cool the gas, saturate it, then cool below the saturation tempreture. The net effect is that the dust particles behave as condensation nuclei on which condensing vapour selectively deposits, so increasing the mass.

Gravity spray towers, cyclone spray towers, impingement scrubbers, venturi scrubbers, etc. are different types of scrubbers and Fig. 1.5 shows a schematic of some designs of these devices. The important characteristics of scrubbers and wet washers are as follows:

1-There is no limit on temperature, but high temperatures increase water consumption, since gas is discharged at higher temperature in a saturated condition. This leads to steam plume formation which can create secondary pollution problems.
2- Capital cost of the actual scrubber is moderate but, dependent on cost of water treatment plant, the overall capital cost can be high.
3- Pressure drop to give the required gas cleanliness increases with increasing cleanliness, and with decreasing particle size.
4- For the same pressure drop, scrubber efficiency increases with water quantity.
5- Although efficiencies are quoted for scrubbers, it is found that the dust concentration in the gas following the scrubber varies comparatively little for large variations in inlet concentrations (Darby, 1978).

One of the most popular wet scrubbers is the venturi scrubber which is used

primarily in industrial processes that require collection of both particulates and gases. Although venturi scrubbers require high pressure drops to capture an acceptable level of particulates, they can often be used when the particulate is sticky, corrosive, or combustible, or when mixing the particulate in a process liquid is desirable. In recent years, they have been used extensively in wood burners, as well as in such resource recovery units as rubbish incinerators. Venturi scrubbers are usually developed by equipment suppliers for a specific project or facilities (Rubin, 1986).

1.3.5 Electrostatic Precipitators

The electrostatic precipitator makes use of the fact that electrically charged particles subjected to an electrical field are attracted towards, and deposited on, the electrodes creating the field. The separation of the suspended particles from the gas requires three fundamental steps:

1- inducing an electrical charge on the suspended particles;
2- deposition of the charged particles under the influence of the electric field on the collecting electrodes;
3- transfer of the collected material from the electrodes to a storage hopper from which it may be withdrawn continually or at intervals.

Charging of the particles is achieved by passing the dust-laden gases through an electrode system designed to favour the production of corona discharge when energized by a suitable high voltage supply, which is usually unidirectional. Charging of the particles to nearly the maximum possible level takes a very short time, less than one-tenth of a second, compared with the time of several seconds during which the gas is subjected to the electric field. Once the suspended particles are charged, they pass through the electrode system and experience forces due to the electrical field. They therefore move towards and are eventually deposited on the electrodes of opposite charge to their own, which is generally that of the corona discharge. Where the material deposited in dry dust, a layer is allowed to build up which is periodically dislodged by hammering or vibrating the electrodes. From the electrodes it falls into storage hoppers below the moving gas stream, from which it is removed for disposal. Forces due to the electrical charge molecular attraction ensure

that the dislodged dust remains in agglomerated masses with high free falling velocity, sufficient to ensure that they reach the hoppers. If this did not occur the dust would be re-entrained in the gases and not caught. Fig. 1.6 shows a schematic of a simple electrostatic precipitator.

The electrostatic precipitation process has been applied industrially for well over half a century. During this period many attempts have been made to obtain a satisfactory relationship between the motion of the charged particles in the electric field, calculated from purely theoretical equations, and the actual collection efficiency of the precipitator. The electrostatic precipitator is probably the most versatile of all filtering systems. The following are some of the important features:

1- All sizes of particle down to below 0.01 μm can be removed from the gases.
2- There is a very wide range of operating temperatures but usually restricted to a maximum of 450 ^{o}C to a enable mild steel to be used in the construction.
3- Can be designed for almost any corrosive condition by a suitable choice of materials.
4- Any type of suspended material can be removed by a precipitator.
5- Any efficiency required can be obtained at the expense of cost, for example to increase efficiency from 90 to 99 percent requires the size of precipitator to be doubled. Many researchers such as Rose and Wood (1966) and Darby and Parker (1971) have given fuller information about theories, limitation, etc. of electrostatic precipitator devices.

However, despite decades of research and widespread commercial applications, many aspects of the design and operation of this system remain more an art than a science. The fruits of research in this area during the late 1970s and early 1980s are reflected in units that have begun operating in the past few years (Rubin, 1986). While sizing electrostatic precipitators for a range of fuels and operating conditions is still in large part an art, computer models that predict performance as a function of fuel, gas, and equipment design have greatly improved in recent years. Fundamental research in this area has shown the potentially detrimental effects of turbulence and secondary flows on precipitator efficiency (Bechtel et al 1985). The sizing and design of models used in specific commercial applications attempt to merge theoretical

work with statistical data based on actual operating experience. Of course, the real test of such design/ application technology is the performance in the field of newer designs. A number of novel devices have been proposed to improve electrostatic precipitator performance. Concepts recently tested at the bench or pilot scale include several types of electrode precharges, a high-intensity ionizer, bipolar ionization, an electron-beam precipitator system, and a high-temperature, high-pressure precipitator for advanced pressurized fluid-bed and coal gasification systems (Rubin, 1986).

1.4 OBJECTIVE OF PRESENT INVESTIGATION

Considering all the facts described in Section 1.2, a review of techniques for gas cleaning is urgent. Unlike developments in hot gas clean-up for pressurised f.b. combustors in future power generation systems (which can involve " high technology " in order to avoid gas turbine fouling and damage), the emphasis for cold (up to 250 ^{o}C) clean-up devices for industrial boilers is on the ability to comply with clean air regulations as cheaply as possible and with unskilled operators. Whatever the reason for gas cleaning plant being installed, the minimum standard of cleaning required must be established, as usually capital and operating costs increase as efficiency required increases. This was demonstrated by Stairmand (1969) who produced the graph shown in Fig 1.7, in which efficiency of gas cleaning is plotted against a figure based on the sum of capital and operating costs while Table 1.5 shows a summary of specification of four major types of cleaning devices (Gupta, 1981). The capital costs of bag filters and wet scrubbers are typically four to six times those of inertial systems, and of electrostatic precipitators about ten to twelve times (Crane and Behrouzi, 1988 and Sage et al, 1984). Wet scrubbers suffer from the effluent disposal problem and require skilled operating staff. The choice therefore appears to lie between developed versions of bag filters, where a size reduction is necessary to reduce costs, or of cyclones. New bag filter cloth materials have been investigated at CRE and elsewhere (Sage et al, 1984). CRE has also conducted trials on advanced single-cell cyclones developed at University College, Cardiff, and is currently testing (under cold flow conditions) a number of industrial multicell cyclones. Another study by Sage and Wright (1986) has confirmed that the efficiency of a multicell cyclone as well as single cyclone can be significantly improved by

bleeding some 10% of the gas flow through the dust exists (a "sidestream" flow); the cost of a small bag filter to clean the sidestream flow should be acceptable. However, little other work is known to be in progress to develop the commonly-used multicell cyclone.

While manufacturers of multicell cyclones frequently claim overall efficiencies up to about 95% (e.g. for dust 20% below 10 μm and pressure drop up to 100 mm w.g.), operators are generally unable to provide the ideal conditions under which such performance might be attainable. The performance of the individual reverse-flow cell is well documented in the case of tangential inlet cyclones, but much less so for the commonly used axial-entry type with swirl vanes; until very recently, theoretical treatments have been quite primitive and experimental results have been lacking in details of gas flow and solids size distribution inside the cyclone. Multicell units usually have a lower separation efficiency than an isolated cell (Stairmand 1957, Jackson 1963 and Reznik and Matsnev 1971); this is attributed to a number of effects: (a) inlet flow maldistribution; (b) gas circulation in the common dust hopper leading to re-entrainment and loss of collected dust; (c) air infiltration through gasket leaks, again re-entraining dust from the hopper; (d) plugging of dust or gas exi ts or swirl vanes. Crellin et al (1980) identify effect (b) as a consequence of the varying lengths of clean-gas outlet tubes in a design with a sloping tube-plate, as in Fig. 3.1a. Effects (a) and (b) would appear to be closely related and manifestations of the same fundamental problem; (c) should be preventable; (d) need not occur for properly-sized cells although generous sizing for sticky dusts will probably result in an efficiency penalty. There appears to have been little detailed work on this problem (in terms of gas velocity field, effects on different particle sizes, etc.). Where sidestream flows have been used, e.g. Sortor (1981), no attempts are known to have been made to optimize the numbers and locations of the gas bleeds.

The wide variety of multicell designs, reviewed by Jackson (1963), the reluctance of manufacturers to divulge details of development work leading to their favoured geometries, reports of unexpected behaviour such as an instance of failure to improve efficiency by increasing pressure drop (Lucas 1974), etc. also suggest that the problems of multicell units should be examined at a more fundamental level. Improvements in their performance will also extend their range of applicability, for

example to mineral processing.

The present work, aimed at improving the performance of multicell cyclones, was undertaken in collaboration with CRE, where a broader programme is under way (involving the testing of full-scale multicell cyclones). The objectives of the present research are:

I- To investigate the causes of performance deficiencies in multicell cyclone dust separators (compared with a single, isolated cell of the same type)

II-To propose and test measures which could enhance their efficiency enough to comply cheaply with future emission regulations, with acceptable pressure loss.

III- To develop a prediction method for single-cell performance, test it against the experimental data from (I) and attempt to predict the effects of some of the phenomena identified in (I) or of the remedial measures suggested in (II).

1.5 OUTLINE OF THE THESIS

The remainder of this thesis is divided into five parts which are outlined below.

Chapter 2 provides an extensive review of most of the relevant publications on the topics of cyclones and multicell cyclones. Different types of cyclones are shown is section 2.2. Quantification of cyclone performance is presented in section 2.3. Section 2.4 described previous theoretical and experimetal works on cyclone gas flow fields. The particle motion and cyclone efficiency theories are presented in sections 2.5 and 2.6. The prediction of cyclone pressure drop is described in section 2.7. Section 2.8 deals with reported physical phenomena inside cyclones. The last two sections (2.9 and 2.10) of this chapter describe previous modification work on cyclones, especially multicell cyclones.

Chapter 3 is concerned with the experimental rig design and apparatus, measuring instruments and experimental procedure. It includes descriptions of multicell and one-cell cyclone (water and air) rigs (sec. 3.2 to 3.4), the laser Doppler

anemometer (LDA), particle sizing (sec. 3.5) and visualization techniques (sec. 3.6), the development of data acquisition and processing equipment (sec. 3.7), and the measurement procedure, including an error analysis (sec. 3.8).

The experimental findings are presented in Chapter 4, which is divided into four main parts. The first (sec. 4.2) presents the LDA measurments. The second (sec. 4.3) presents the results of flow visualization in the multicell cyclone. The third part (sec. 4.4 and sec. 4.5) presents the mass and grade efficiency measurements of one-cell and multicell cyclones. The last part (Sec 4.6) presents the cyclone modification techniques and results for modified cyclones. Discussion follows at the end of each sub-section.

The computational investigation is presented in Chapter 5. The theory and governing equations for the continuous phase flow are shown in section 5.2, while section 5.3 contains the particle phase of the solution procedure. The present modification and alterations of the code (SPRINT-4) for axial-vane-type cyclones are shown in section 5.4 and section 5.5 presents the predictions of the new numerical model (CYCINT-1) including a study of the effect of some parameters such as gas bleed on cyclone performace. Discussion follows in section 5.6.

The final Chapter (6) contains the main conclusions and findings of the present investigation together with discussion (sec 6.1) and suggestions (sec 6.2) for the continuation of the work.

CHAPTER 2

SURVEY OF LITERATURE ON GENERAL ASPECTS OF CYCLONES

2.1 INTRODUCTION

This chapter provides a review of previous investigations which are relevant to the present work. Section 2.2 describes different designs of cyclone which are already used in industry or research work. Quantification of cyclone performance is presented in section 2.3. A summary of literature on cyclone gas flow fields is discussed in section 2.4. Section 2.5 and 2.6 are concerned with particle motion in cyclones and cyclone efficiency theories. Cyclone pressure drop theories are given in section 2.7. Some reported phenomena inside cyclones are presented in section 2.8. Finally the last two sections deal with previous research on modification of cyclones, especially multicell cyclones.

2.2 TYPES OF CYCLONE

Cyclones are relatively simple and humble dust collection devices. They have served industry well for many years. Numerous designs have been used and cyclones seem to exercise a remarkable attraction to engineers and academics. The most common classification splits cyclones into axial entry or tangential entry of which the latter are most often encountered. These two groups can also be divided into many subgroups according to the design of inlet and dust discharge arrangements; for example each group may be classified again into two sub-groups, the straight-through (or uniflow) cyclone and more common conventional or reverse-flow cyclone, and so on. The most common of cyclone designs are illustrated in Fig. 2.1. Types (a) to (c) (tangential type) have similar performance with respect to dust removal capabilities. The common cyclone has the standard tangential entry with axial dust discharge (Fig. 2.1b). However, much experimentation on tangential inlets has led to the helical (curved) (Fig. 2.1c) and wraparound (Fig. 2.1a) inlets. The helical inlet is designed to give the incoming gas downward motion to avoid interference between this gas and the gas already rotating in

the annulus. However, evidence as to whether this decreases the pressure drop is conflicting and it may lower the efficiency. Such entries are rarely used commercially. The wraparound inlet has been developed to reduce the squeezing of the incoming gas between the body wall of the cyclone and the gas already rotating inside the annulus. Its main advantage is the large capacity increase that results from this design.

Axial cyclones, type (d) and (e) , where swirling flow is produced by guide vanes, tend not to have such a good performance as other types, owing to non-optimum tangential velocity produced (i.e. forced vortex type distribution). Axial cyclones are thus used for applications requiring high air throughput at low pressure drop. Axial entry cyclones have a capacity about twice that of wraparound entry cyclones of the same diameter. The shape of the inlet vanes (Fig. 2.2) affects the pressure drop and collection characteristics. Axial cyclones cannot be used with dusts that will damage or plug the vanes. They are usually used in parallel multicell cyclone units with common hoppers. Fig. 3.1a and 2.3 show some types of multicell cyclone design which have been used by industry and Table 2.1 shows typical dimensions for a multicell cyclone (this particular unit does not have axial-entry cells, but is representative of any small multicell unit). Where collection efficiency requirements are high, it may better to use a number of smaller diameter cyclones in series to process given gas throughput, rather than risk re-entrainment from a single, larger cyclone (Leith and Mehta, 1973), but the use of cyclones in series is rare. It is more common for a cyclone to be in series with another more efficient air cleaning device.

The major research and observations have been performed on the popular standard tangential entry cyclones. A cyclone's geometry is described if each of the eight dimensions shown in Fig. 2.4 is known. However, it is often more convenient to state dimensions by expressing them in dimensionless form, as a multiple of diameter D. The dimensions of the cyclone are then specified by D and seven ratios, a/D, b/D, D_e/D, S/D, h/D , H/D and B/D. This permitted some researchers such as Leith and Mehta (1973) to do a comparison of the geometric similarity of several cyclones through a consideration of their dimension ratios without introducing absolute magnitude to the cyclone comparisons. A number of cyclone "standard designs" or sets of dimension ratios suggested in the literature were developed decades ago on the basis of practical experience and insight, but often without quantitative application of engineering

principles. Although these designs have worked well, they may not be the best possible (Dirgo and Leith, 1985). Many researchers such as Leith and Mehta (1973), Abrahamson and Allen (1986), Walton (1974), Biffin et al (1981) and Dirgo and Leith (1985) have studied and tabulated dimensions of conventional cyclone designs. For example table 2.2 shows the tabulation by Walton (1974).

Relative dimensions of cyclones differ according to the purpose for which they are required. High efficiency cyclones tend to have a smaller inlet area and a larger main body diameter (i.e. $D/D_e > 2$), Table 2.2. Inlets are usually of elongated rectangular shape, being always slightly shorter than the exhaust sleeve to ensure that a strong vortex is always formed and flow cannot pass directly into the outlet (Batel 1976, Ter Linden 1949, Walton 1974, Leith and Mehta 1973). Gas exit duct length (S/D) is less in the high efficiency designs, probably because inlet height (a/D) is less. General purpose standard designs appear to be a compromise between high efficiency and high throughput. Swift (1985) introduced three designs of long cone cyclones for high efficiency, medium efficiency and high throughput. Higher efficiency can be traded off somewhat against higher throughput according to Stairmand (1951) and Swift (1985). A high efficiency cyclone of standard design will process only about one half as much gas as a high throughput design of the same diameter and overall height, operating at the same pressure drop. For higher efficiencies, but lower throughput, the design alters to provide a vortex of smaller diameter but longer length. Fig 2.5 shows typical dimensions in terms of the diameter for the extremes of these types of cyclone (Smith et al, 1981). Cyclone design varies, then, according to the purpose for which the unit is to be put. The variability in design emphasizes that there is no single cyclone design which will perform best for all dust collection problems .

Ogawa and Seito (1986) tested seven different types of cyclone such as cone cyclones, sphere cyclones and a semi-sphere and cone combined cyclone (Fig. 2.6) and reported advantages and disadvantages of these designs. Also Ryabchikov et al. (1975) studied various novel types. Schmidt (1963) and Klein (1963) have described a different type of cyclone dust collector, called the rotary flow dust collector, which has two independently adjustable gas supplies (Fig. 2.7). Dirty gases are passed through a central duct, past a vane-type swirler for generating a forced-type vortex. Clean gas is injected at the top of the device tangentially to induce a free vortex distribution in the

outer section of the flow. Flow conditions are similar to the conventional cyclone except that the dirty gas is introduced swirling into the central region of a free vortex where centrifugal, and hence separation forces, are greatest. In contrast to the conventional cyclone dust separator, dust concentration does not directly affect the separation efficiency owing to the differing secondary flow patterns in the device. The particle size removed is an order of magnitude better than that obtained with a conventional cyclone. Nevertheless, the penalties for the enhanced performance are (a) far greater pressure drop and (b) the need for secondary air injection. Ciliberti and Lancaster (1976) investigated the performance of rotary flow cyclones and concluded that no dust below 1 μm will be captured in this equipment under normal conditions.

Several papers in the literature deal with hydrocyclones, which are essentially for centrifugal separation of liquid/gas and liquid/solid suspensions (Kelsall 1952, Rietema 1961, Bednarski and Wiechowski 1984, etc). The hydrocyclones are not so effective as gas dust cyclones because of the lower density differences between the fluids being separated .

2.3 QUANTIFICATION OF CYCLONE PERFORMANCE

A number of differing parameters have been suggested directly or indirectly to characterize cyclone performance by many researchers. Some of the most important of these parameters are described below.

Cyclone Swirl Number

Assuming a uniform exit velocity profile, the cyclone swirl number for isothermal flow was given by Gupta et al (1985) as:

$$S_n = \frac{\pi D_e D}{4 A_t} \qquad (2.1)$$

and by Yajnik and Subbaiah (1973) as :

$$S_n = \frac{\text{Angular momentum flux}}{D_e/2 \text{ Axial momentum flux}} = \frac{\int_0^{D_e/2} u\, w\, r^2\, dr}{D_e/2 \int_0^{D_e/2} u^2 r\, dr} \qquad (2.2)$$

where D_e and D are the diameters of the exit throat and main section of the cyclone chamber respectively and A_t is the area of tangential inlet. Typical swirl numbers for cyclone separators lie in the range of 2 to 4.5 which are appreciably higher than these encountered in swirl generators (Gupta et al, 1985).

Cyclone Saltation Velocity

Saltation velocity may be defined in several ways, of which two, applicable to cyclone design, are: the minimum fluid velocity necessary to prevent the settling out of particles carried in the stream; and the velocity necessary to pick up deposited particles and transport them without settling. To apply the saltation concept to cyclone design the following assumptions were made (Koch and Licht, 1977):

1- No slippage between fluid and particles
2-The cyclone inlet breadth is the effective pipe diameter for calculating saltation effects.
3-Low dust loading
4- The diameter effect on saltation velocity is proportional to the 0.4 power of the inlet width.

Defining the inlet width in terms of a dimensionless size ratio b/D, the saltation velocity can calculated by the following formulae (Koch and Licht, 1977)

$$w_s = 2.055\ \omega \left[\frac{b/D}{(1 - b/D)^{1/3}} \right] D \quad 0.067\ w_i^{2/3} \qquad (2.3)$$

where w_s, ω, w_i are saltation velocity, angular velocity and cyclone inlet swirl velocity

respectively. Thus, the saltation velocity is a fuction of particle and fluid properties as well as cyclone dimensions (Gupta et al, 1985). It was shown by Kalen and Zenz (1974) that maximum collection efficiency occurs at $w_i/w_s=1.25$ while re-entrainment of dust occurs at $w_i/w_s=1.36$. The commonly accepted inlet-velocity working range of 16-30 m/s, depending upon cyclone diameter, is consistent with these results and Koch and Licht (1977) also give correction factors for w_i/w_s ratio in terms of particle density and temperature, and they give a simple cyclone design procedure.

Cyclone Particle Cut Size

Solid particles do not follow the primary gas flow because of their inertia. The viscosity of the fluid subjects particles to viscous drag which, by itself, would cause particles to spiral into the inner vortex. Against this, the centrifugal action causes the particles to move towards the cyclone wall. In the case of larger particles, the centrifugal effect wins while with finer particles, the centrifugal effect has less influence and the particles escape into the inner vortex. For particles of a certain size, the viscous drag of the inward drift will equal the centrifugal effect and such particles will theoretically have no radial velocity. When this occurs at the surface of the inner vortex with its maximum centrifugal force, that particle size is known as the cut size of the cyclone, and is the maximum size of particle which should in theory escape from the cyclone. Those particles reaching the cyclone wall are carried to the dust exit by the downward components of the gas velocity (Swift, 1985). Using Stokes law for the displacement velocity relative to the flow resistance, and assuming a free vortex for the outer part of the flow, the following expression can be derived for the minimum particle size removed (Gupta et al, 1985).

$$d_P = \frac{1}{\Gamma}\left[\frac{36\, Q_r\, \pi\, \eta}{S(\rho_P - \rho_a)}\right]^{1/2} r_i \qquad (2.4)$$

where $\Gamma=2\,\pi\,r\,w$ and Q_r is the flow rate in radial direction. That is, the minimum particle size removed is directly proportional to the radius r_i bounding the transition from free to forced vortex flow. The corresponding equation for a forced vortex is given by

(Batel, 1976):

$$d_P = \left[\frac{9 \eta Q_r}{(\rho_P - \rho_a) \pi S} \right]^{1/2} \frac{1}{\omega r_i} \qquad (2.5)$$

where ω is the angular velocity; that is, for maximum separation of small particles the radius r_i must be maximized. Thus, in the central forced vortex region of a Rankine vortex, dust separation capability decreases in proportion to the radius. The above approach and others, given by Batel (1976), Walton (1974), Littlejohn and Smith (1978), Stairmand (1949), etc. , can indicate the dust collection performance of one cyclone relative to another, but is not a satisfactory substitute for a grade efficiency curve as obtained by Leith and Licht (1972).

Cyclone Reynolds and Stokes Number

For quantification of cyclone performance, parameters are needed to characterize the gas flow and the particle motion. Fluid flow can be characterized by the Reynolds number

$$Re = \frac{\rho_g V_i D}{\mu_g} \qquad (2.6)$$

and particle trajectories by the Stokes number (Reijnen and Brakel 1984), which represents the ratio of characteristic time scales of particle motion and gas flow:

$$St = \frac{\tau_P}{\tau_g} \quad \text{where } \tau_P = \frac{\rho_P d_P^2}{18 \mu_g} \quad \text{and } \tau_g = \frac{D}{V_i} \qquad (2.7)$$

Cyclone Euler Number

An important aspect of dust separators is the power required to operate them. With

cyclone dust separators this is determined by the pressure drop across the separator. The parameter which is adopted to characterise this feature is a dimensionless pressure drop often referred to as the Euler number ζ, given by

$$\zeta = \frac{\Delta P}{1/2\ \rho_g\ V_i^2} \tag{2.8}$$

This parameter is useful since it compares the pressure drop with the throughput of the separator (Leith and Mehta, 1973). For a given geometrical design, the Euler number remains essentially constant over a wide range of Reynolds number (Biffin and Syred, 1983).

Cyclone Sharpness Index

Fig. 2.8 prepared by Lucas (1974) shows a typical sharpness index plot. It provides a useful performance evaluation for any particle size classifier. The ordinate is C/F, the weight ratio of coarse, collected material to fine, escaping material, and the abscissa is particle diameter (μm) . C/F is related to collection efficiency by the following equation.

$$\eta = \frac{C/F}{(C/F)\ +1} \tag{2.9}$$

The cut size is the particle diameter corresponding to C/F=1. The slope of the line is called the sharpness index. A perfect classifier would yield a vertical line. Most cyclones have a sharpness index of 2 but the data usually do not follow the line throughout the size range. The data for particles larger than 10 μm fall to the right of the line of Fig. 2.8. This is evidence of the bounce-out problem (Lucas, 1974).

2.4 CYCLONE GAS FLOW FIELD

In order to visualize the flow field in a cyclone, the velocity characteristics of the gas must be studied separately from those of the particle. The gas entering a cyclone is

accelerated by the pressure differential existing across the inlet orifice. The ingressing gas is introduced in a slightly downward direction and tangentially to the walls of the cyclone (Fig. 1.3). The characteristic of the entering fluid and the geometry of the cyclone creates a strong swirling flow field. A swirling field possesses pressure gradients that accelerate the fluid in both radial and axial directions. In addition, the swirling fluid passes from a free vortex to forced vortex condition.

A free vortex is characterized by irrotational flow in which individual fluid particles do not rotate about their own axis. The tangential velocity associated with a free vortex is described by the relation w=C/r where C is constant and r=radius. A forced vortex condition results from the application of torque and produces solid body rotation. The forced vortex displays rotational flow in which each individual fluid particle rotates about its own axis. The tangential velocity for fluid in a forced vortex is given by $w=\omega.r$ where ω is the angular velocity of the forced vortex. The tangential velocity of fluid in swirling flow increases with decreasing radius across a free vortex and decreases with decreasing radius in a forced vortex. The transition zone between the free and forced vortices occurs at the point of maximum tangential velocity of the free vortex and is the shearing section of the swirling field supplying the torque to the forced vortex. Tangential gas velocity has been found by Shepherd and Lapple (1939), First (1950), Alexander (1949) and others, to be related to radial distance r from the vortex centre line raised to the power n by $w.r^n=c$. Alexander (1949) has stated that the distance the vortex extends into the cyclone depends only on gas inlet and outlet dimensions. Theoretically then, the vortex need not reach the bottom of the cyclone (Leith and Mehta, 1973).

Exhaust flows are of importance, and depending on configuration, one can alter dust removal capabilities and efficiencies considerably. Similar comments apply to the dust removal duct. The presence of a centre body is useful in preventing the highly turbulent vortex core from propagating back into the dust hopper (Batel, 1976).

The variation of velocity and pressure levels throughout a cyclone dust separator have been investigated by Ter Linden (1949) and shown in Fig. 2.9. The vortex core diameter (D_c) is between 0.4 and 0.6 D_e . The tangential velocity is of Rankine form, that is, combined free/ forced vortex, with the value of exponent n in the formula ($w.r^n=c$) varying as follows.

$n=-1$ for $D<D_c$ and $0.45<n<0.8$ for $D>D_c$

Ter Linden (1949) obtained results from a cyclone that is typical of many systems (Fig. 2.9). Tangential velocity profiles are similar to those produced in many differing types of vortex or cyclone chamber. However, Kelsall (1952) noted that under certain conditions a three-celled vortex structure was possible at high Reynolds number within a 75 mm-hydrocyclone.

Experimental studies of the whole gas flow field (or liquid flow in hydrocyclones) have used a variety of techniques. Some researchers such as Pericleous et al (1984), Bhattacharyya (1984), Bradly and Pulling (1959) employed an optical tracking method to photograph the movement of dyed particles in glass hydrocyclones and others used other visualization techniques. For example Kelsall (1952) used an ingenious technique of measuring the trajectories of suspended Alumina particles. Before the availability of reliable hot-wire anemometry or laser Doppler anemometry, Ter Linden (1949), Kelsall (1952), Ohasi and Maeda (1958), etc. have reported velocity measurement in cyclones in which the main instrument was an impact (pitot) tube. Because of the sensitivity of highly swirling flows to disturbance of streamlines caused by the tubes, Boysan et al (1982) believed that the reliability of these data can not be guaranteed. Nevertheless these data have formed the basis of many necessarily semi- empirical correlations on which current cyclone design practice is almost entirely based. Binark and Patel (1961) made tangential velocity measurements in a test cyclone using a hot-wire anemometer (but were not able to do so in the core region). Recently many researchers such as Escudier et al (1980), Ayers et al (1985), Biffin et al (1984), Colman et al (1984), Pericleous and Drake (1987), etc. used LDA systems for studying cyclone flow fields (mostly tangential type).

Also the cyclone flow pattern has been studied theoretically by Fontein and Dijksman(1953), Bloor and Ingham (1973 &1985), Yoshioka and Hotta (1955), Rietema (1961) and others. In all cases only swirl velocity has been investigated. Mathematical models of gas flow in a tangential type cyclone (and also hydrocyclone) have been developed recently by Pericleous et al (1984), Crowe and Pratt (1974), Boysan et al (1981), etc., which solve the discretised form of the Navier-Stokes equations using a well established finite-difference scheme (brief description of this

method is in Chapter 5).

2.5 PARTICLE MOTION IN CYCLONE

In a cyclone chamber, the solid particles co-existing with the gas are subjected to various aerodynamic and inertial forces associated with their trajectories and drag effects from the gas motion. The vector sum of the forces at a given time determines the acceleration of the particle . The three-dimensional velocity patterns for the particles prescribe the trajectory of a given particle. The particles entrained in the fluid are influenced by the fluid velocities and the inertia forces. Due to the drag characteristics of the fluid upon the individual particles, the fluid-flow patterns within the swirling field determine the particle trajectory. Nevertheless, the centrifugal force on the particles opposes the radial drag effects of the fluid and tends the restrain the particles from moving toward the axis of the cone. The centrifugal force is an inertia effect created by the mass of the moving particle desiring to travel in straight paths. This centrifugal force can be expressed as (Gupta et al, 1985):

$$F = C_1 d_P^3 (\rho_P - \rho_a) \frac{w^2}{r} \qquad (2.10)$$

where C_1 is a constant.The effectiveness of the cyclone depends upon the generation of high centrifugal forces. It is clear from the above equation that high centrifugal forces will result from large and dense particles at small radius with low specific gravity fluid at high tangential velocities. The radial velocity of the fluid reduces the separation effectiveness of the cyclone. This radial drag force can be given approximately by:

$$F_d = C_2 d_P \mu_g v \qquad (2.11)$$

The effectiveness of swirling separation can be enhanced by the reduction of the drag forces, both radial and axial, achieved by small particles in low viscosity fluid. The size of the particle has a greater effect (third power) in the value of the centrifugal force than in the drag force (first power), therefore, the larger the particle, the greater the separation efficiency.

Centrifugal forces can be several times that due to gravity and thus such devices of an appropriate size can serve to separate particles as small as 1 μm. The lower limit is set by turbulence and secondary flow effects. Using Stokes' law, the displacement velocity relative to the flow (Batel, 1976) can be described according to:

$$W_P = \frac{1}{18\,\mu_g} (\rho_P - \rho_a) d_P^2 . \frac{w^2}{r} \qquad (2.12)$$

for a given tangential inlet velocity it is clear that a small radius cyclone will possess higher centrifugal forces than a larger radius cyclone (Gupta et al, 1985). It is usually assumed that dust particles reaching the region of $r<0.3\ D_e$ are not separated; this is only partly valid as dust particles move outwards under the influence of the centrifugal force field. Examination of dust separation processes in cyclones shows that most of the dust separation occurs at a relatively short distance beyond the entry. Large accumulations of dust occur at the wall so that the limiting load is exceeded. The dust flows in spiral paths along the cyclone walls into the hopper; the remaining unseparated dust passes into the 'free' vortex flowfield ($r>0.3\ D_e$) (Gupta et al, 1985).

Ayers et al (1985) compared the high-efficiency cyclone design of Stairmand (1951), in terms of collection efficiency, with the results of the stochastic particle tracking techniques. Fig. 2.13 shows a typical predicted trajectory with the turbulence effect included.

2.6 CYCLONE EFFICIENCY

To design a new cyclone system, or upgrade an existing one, it is necessary to predict cyclone performance accurately. Over the years, a number of methods have been developed to predict cyclone pressure drop and efficiency. All make assumptions regarding the characteristics of gas and particle motion within the cyclone. The accuracy of the performance equations depends upon how well the assumptions made in their development reflect the actual operating conditions within the cyclone (Leith and Mehta, 1973). Experience in dealing with cyclones has shown that collection efficiency increases with:

1- Increasing particle size and density

2- Increasing speed of rotation in the cyclone vortex

3- Decreasing cyclone diameter

4- Increasing cyclone length

5- Drawing some of gas from the cyclone through the dust exit duct.

6- Wetting the cyclone's walls

Many empirical and theoretical formulae have been suggested by many researchers such as Lapple (1951), Barth (1956), Sproul (1966) and Leith and Licht (1972) to predict cyclone efficiency (mainly tangential type). For example Leith and Licht (1972) derived an equation for predicting cyclone efficiency from theoretical cosiderations. They assumed complete mixture of particles in a horizontal plane, and a deposition velocity at the wall equal to the centrifugal drift velocity which a hypothetical particle initially released near the centre of the cyclone would have obtained at the time it had descended to the level of the horizontal plane in question. Their equation is:

$$\eta = 1 - \exp\left[-2\,(C\,\Psi)^{1/(2n+2)}\right] \qquad (2.13)$$

where C is a function of the cyclone's dimension ratios only:

$$C=\frac{\pi D^2}{ab}\left[2\left[1-\left(\frac{D_e}{D}\right)^2\right]\left(\frac{S}{D}\,\frac{a}{2D}\right)+\left(\frac{S+L-h}{3D}\right)\left[1+\frac{d}{D}+\left(\frac{d}{D}\right)^2\right]+\frac{h-S}{D}\left(\frac{D_e}{D}\right)^2\frac{L}{D}\right] \qquad (2.14)$$

and where

$$\frac{L}{D} = 2.3\,\frac{D_e}{D}\left(\frac{D^2}{ab}\right)^{1/3} \qquad (2.15)$$

$$\frac{d}{D} = \frac{D-(D-B)\left[(S+L-h)/(H-h)\right]}{D} \qquad (2.16)$$

Here, L is the farthest distance the vortex extends below the gas exit duct as given by Alexander (1949), and d is the diameter of the conical section at that point. Ψ is a

modified inertia parameter, reflecting the nature of the gas/particle system to be treated:

$$\Psi = \frac{\rho_P d_P^2 v_q}{18 \mu_g D} (n+1) \qquad (2.17)$$

The value of vortex exponent n, can be calculated as:

$$n = 1 - \left[1 - \frac{(0.394\ D_c)^{0.14}}{2.5} \right] \left(\frac{T}{283} \right)^{0.3} \qquad (2.18)$$

Here, D_c is the diameter of cyclone in cm. Leith and Mehta (1973) have compared the four methods for calculating cyclone efficiency with experimental data given in the literature by Stairmand (1951) and Peterson and Whitby (1965); Fig. 2.10a and b compare computed efficiency values with experimental values, and show that at least for these data, the Leith and Licht (1972) relationship appears to work best. Subsequently Dirgo and Leith (1985) showed that the Leith and Licht theory overestimated efficiency for smaller particles and underestimated the collection of larger sizes. Recently some researchers such as Koch and Licht (1977) and Dirgo and Leith (1985) used modified versions of previous efficiency theories, but because these do not allow for physical phenomena such as electric forces and agglomeration (which was shown by Abrahamson et al (1978) to be necessary), can not be reliable for general purpose cyclone design (Reijnen and Brakel, 1984).

Particle collection efficiency is usually expressed in terms of fractional efficiency for a particle size or size range as a function of dust concentration. Particles of greater than 10 μm can easily be removed with high efficiency by conventional design; performance, however, rapidly falls-off with reducing particle size such that efficiencies of between 20-50 percent are obtained for particles of up to 3 μm. The collection is not only a function of particle size but also of dust concentration and is particularly noticeable with smaller particles (d<5 μm). Leith and Licht (1972), Van Ebbenhorst Tengbergen (1965) have shown that collection efficiency can be doubled by high concentration for particles in the size range of 0-3 μm. Several researchers such as Schneider (1960) and

Littlejohns and Smith (1978) showed that a large increase in gas flow rate can occur for a given pressure drop with dust concentration > 0.25 g/m^3 , thus indicating that fundamental changes in aerodynamic flow structure occur with high levels of dust concentration (Fig 2.11). It appears therefore that there are two mechanisms in operation that can be inferred from the following evidence:

1- The greatest change in gas flow rate for given pressure drop occurs with large particles (d>50 μm, Littlejohn and Smith, 1978)
2- Large increases in particle collection occur for small particles only (d<5 μm) as particle concentration is increased (Van Ebbenhorst Tengbergen, 1965)

Both mechanisms appear to be connected with the vortex core region due to the suspension and trapping of particles in this region for long periods (Gupta et al, 1985).

A cyclone's grade efficiency curve relates size of particles entering the cyclone to the cyclone's efficiency for particles of that size. Cyclone 'grade' or 'fractional' efficiency may be calculated according to the original Leith and Licht (1972) concept. With this theory grade efficiency may, for example, be calculated as a function of cyclone design parameters and operating conditions. An overall efficiency may then be found for a given particle distribution, via the following equation.

$$\eta_T = \sum m_i \eta_i \qquad (2.19)$$

where m_i and η_i are the mass fraction of particles in size range designated by i and grade efficiency for particle size at mid point of interval i respectively. Modern optical sizing techniques permit the calculation of more accurate grade efficiency curves and such measurements have recently been supplied by Mothes et al (1981) for a 0.19 m diameter cyclone. These have been compared (Boysan et al, 1982) with the corresponding predictions in Fig 2.12 which illustrates the results which were obtained for a range of vortex finder diameters.

2.7 CYCLONE PRESSURE DROP

A correct estimate of the pressure drop across a cyclone is necessary, in addition to collection efficiency, so that the cost effectiveness may be calculated. For cyclones, approximately 25 cm H_2O or less is a generally acceptable operating range and represents a considerable amount of energy to produce swirling flow. Correlations for pressure drop prediction have been largely empirical. Pressure drop in a cyclone will be considered as that between point 1 and point 2 in Fig. 2.4. A number of factors contribute to the pressure difference between these points, and have been identified by Shepherd and Lapple (1939) as:

1- loss due to expansion of the gas when it enters the cyclone chamber
2- loss as kinetic energy of rotation in the cyclone chamber
3- losses due to wall friction in the cyclone chamber
4- any additional frictional losses in the exit duct, resulting from the swirling flow, above and beyond those incurred by straight flow
5- any region of the secondary flow.

Most pressure drop theories consider factors 2) and 3) to the most important in determining cyclone pressure drop. Many researchers such as Shepherd and Lapple (1939), First (1950), Alexander (1949), Stairmand (1949) and Barth (1956) suggested empirical formulae for cyclone pressure drop. Leith and Mehta (1973) have compared these theories and reported that the Barth (1956), Stairmand (1949), and Shepherd and Lapple (1939) methods are the best. In general, the following type of expression is used to characterise the pressure drop through cyclones.

$$\Delta P = \frac{\zeta \rho_a U^2}{2} \qquad (2.20)$$

where U is either the inlet tangential velocity (W_{in}) or maximum tangential velocity at peak of velocity profile, W_{ti}. Values of ζ for various cyclone configurations are given by Gupta et al (1985) in Table 2.3. Koch and Licht (1977) showed that pressure drop could be correlated in terms of the geometry of the cyclone as follows:

$$\zeta_1 = \frac{\Delta H}{\rho_{H_2O}} \qquad (2.21)$$

where from Shepherd and Lapple , (1939):

$$\Delta H = K \frac{a\,b}{D_e^2} \qquad (2.22)$$

and K is constant, dependent on inlet geometry and ζ_1 has values of between 1 and 27.

2.8 PHENOMENA INSIDE CYCLONES

In spite of the simplicity of cyclone structure, some aspects of gas/particle behaviour inside this system are still unknown. Existence of some phenomena such as agglomeration, particle bouncing, precession, dust storm, dust carry over and dust re-entrainment are reported by many researchers such as Swift (1985), Abrahamson et al (1978), Leith and Mehta (1973), Reznik and Matsnev (1971), Gupta et al (1985). Because of the complexity of these phenomena, nearly all researchers eliminated them from their theoretical and empirical formulae. A brief description of the most important of these phenomena is presented here.

Agglomeration

Agglomeration is most likly to occur with very small particles, where surface forces are appreciable compared with other forces acting on them. An agglomerate has a higher terminal velocity for any given external applied force (centrifugal, gravity) than has its component particles, and hence should be collected more easily in a cyclone. In order that suspended particles be given a chance to agglomerate, they must make contact with one another, and a major obstacle to assessing the role of agglomeration has been a lack of knowledge of the frequency of collision of particles suspended in a gas (Abrahamson et al, 1978). The force acting to hold particles together in an agglomerate once they have collided may be (a) molecular Van der Waals forces, (b) electrostatic forces, and (c)

capillary liquid bridging forces. Van der Waals forces are strong for easily deformed particles and for example it was shown that a 0.3 μN force existed between a 6 μm polystyrene ball and a metal surface (Abrahamson et al, 1978). Liquid bridging forces increase with humidity. The act of dispersion of a dust can generate high electric charges of opposite sign, and agitation of polymer particles of 20 μm diameter has been found sufficient to cause electrostatic attractive forces of 0.1 to 2 μN (Abrahamson et al, 1978). When these forces are compared with a gas drag-force of the order 0.1 μN for small stationary particles held in a cyclone, it can be seen that cohesion forces can dominate over break-up forces, and the life-time of agglomerates may be significant even in the turbulence of a cyclone .

The circumstantial evidence for the influence of agglomeration in cyclone operation should be clearly stated here. (a) Smigerski (1970) collected silica particles more efficiently in a uniflow cyclone when the humidity was raised. For example, for 2 and 4 μm particles, the efficiency was increased from 20 to 80%, for a relative humidity increase from 15 to 90%. (b) Much higher efficiencies are commonly found for very fine dusts than expected from single particle behaviour. For example, Hejma (1971) found a collection efficiency of 40% for a monodisperse 1 to 2 μm dust in his 314 mm diameter cyclone, and Smigerski (1970) found increasing efficiencies with decreasing mono-disperse particle size (high humidities) below 10 μm. (c) The comprehensive survey by Stern et al (1955) shows that in general an increasing efficiency is found with increasing fine dust concentration. In general sense, therefore, the collection of a particle is more favoured by the presence of others and is not independent of them. (d) Industrial-sized cyclones classify particles by size very poorly. Stairmand and others have considered agglomeration as an aid to the normal collection mechanisms of a cyclone, while Abrahamson et al believed that it is necessary for all particles below about 50 μm in size to be agglomerated before being collected in a normal industrial cyclone. Fig 2.14a and b summarises the two different ideas about capturing particles.

Particle Bouncing on the Walls

Stairmand introduced this mechanism to explain the lower collection efficiencies he found with particles coarser than the normal operating range (2 to 100 μm). According to the classical laminar model, the larger a particle is, the easier it should be to collect in a

cyclone in contradiction to the experimental results. Carey and Stairmand (1949) supported the proposed bouncing mechanism with their reported observation of "bouncing" of particles larger than 60 to 80 μm from the walls of a cyclone after they had been 'already separated'. Jackson (1963) purposely looked for such behaviour with single round particles dropped into the cyclone flow, and he found that "this mechanism (of escape) was unusual". He stated that particles were observed to bounce at the walls but were deflected along the wall by the high velocity swirl and tended to move in a series of very low bounces. This apparent conflict with Stairmand's ideas can be reconciled by the occurrence of "saltation", and to enlarge upon this we must describe in more detail the behaviour of coarse dust in a cyclone. Fig. 2.15 shows the grade efficiency curve which was obtained by Sage and Wright (1986) for a secondary unit of a pair cyclones (1 m dia.) connected in series. This curve shows a drop of efficiency as the particle diameter increased from 20 to 45 μm. They mentioned that the reason for this phenomenon is unclear, but it could have been caused by poor internal finish of the cyclone resulting in bouncing of these relatively coarse particles back into the cleaned flow. Morii et al (1968) worked with small cyclones (0.06 to 0.24 dia.) and found that collection efficiency of sand particles became markedly lower as the particle size was increased in the range 70 to 250 μm. Thus any mechanism explaining this behaviour must become more severe as the particle size increases. Morii, et al also varied the amount of sand fed to the cyclones and found that proportion lost was inversely proportional to the calculated sand concentration. For a constant gas velocity, this indicates a constant mass-loss irrespective of the amount fed but something easily explained in terms of particle hopping and elutriation from an already-deposited surface of sand. Kalen and Zenz (1974) have extended the saltation concept to cover the smaller particles more often collected in a cyclone. They considered that cyclone operation, even with particles<40 μm, is limited by the gain/loss balance of the moving bed of particles at the wall.

Therefore particles of large size can bounce off the cyclone walls into the inner vortex. This effect is obviously most marked with cyclones of small diameter and the main problem to overcome in the design of a cyclone is dust re-entrainment caused by particle bounce (Smith et al, 1981). Therefore attention must be paid to the design of the cyclone inlet and its relationship to the vortex finder exit. Smooth walls help and any joint rings between flanges must be cut and fitted very carefully (Swift, 1985).

Dust Storm

With certain cyclone geometries, Van Tongeren (1935) found a 'double eddy' (or secondary flow) structure in the upper cylindrical section of the cyclone, Fig. 2.16 which recycles and suspends dust in this region. Once a critical mass of dust has accumulated, the secondary flow can no longer support it and it falls into the main body of the cyclone, causing dust storms near the exit which transport particulates to the exhaust gases reducing the overall cyclone performance. This effect is especially prevalent in lightly loaded cyclones. As the dust loading is increased, a steady state condition is reached where the build-up of dust matches the rate of escape. This accounts for the reported phenomena of increased separation performance of cyclones at high dust loading (Syred et al, 1985). Cherrett (1962) has mentioned seeing a distinct "dust storm" in his cyclones, which moved away from the gas outlet towards the hopper on lengthening the cone (with a rise in efficiency). By increasing the diameter of the cyclone, one might also remove the "dust storm " towards the wall if other dimensions are held constant. Indeed, Ter Linden(1949) shows an increase in efficiency when this was done with a large cyclone. Gupta et al (1985) pointed out that there is little or no advantage in increasing inlet velocities beyond 20 to 30 m/s for improving performance of the cyclone; the reason for this being that it increases kinetic energy of turbulence which, in turn, increases back mixing and effects such as apex dust storms.

Dust Re-entrainment

It is also probable that some collected particles, primarily in the smaller size range, will be re-entrained from the cyclone wall and hopper, before being discharged through the dust exit duct. Smaller particles may be more susceptible to re-entrainment as they are only collected with difficulty in the first place. It has been noted by Stairmand (1951) that cyclone efficiency increases if the cyclone walls are wetted, as wetting presumably hinders particle bounce and re-entrainment. Boysan, et al (1982) believed that the apparent over-prediction for the larger particles may be due to the occurence of turbulent bursts in the wall boundary layer which may cause parcels of particles to shoot in the radial direction towards the axis of the cyclone, and to re-entrainment of dust from hopper, which according to Stairmand may be as much as 28%.

At the base of the cyclone cone, the walls are nearest to the inner vortex and hence the downward flowing centrifuged dust. Swift (1985) believed that this gives rise to considerable re-entrainment of dust particles into the inner vortex. This is probably the greatest cause of cyclone inefficiency. Abrahamson et al (1978) investigated flow inside a number of cyclone hoppers and they showed that particles collected at the wall of a cyclone, or even particles entering the hopper are not necessarily finally captured by the cyclone. Because of high circulation inside the hopper and stretching of the inner vortex into the hopper, dust re-entrainment from hopper appeared to be unavoidable (for relatively low cyclone entry velocity of 12 m/s, the tangential velocities found by Abrahamson et al (1978) in the hoppers ranged from 12 m/s near the centre of the smaller hoppers to 2 m/s near the wall).

Other Phenomena

The top of a tangential-type cyclone body presents a surface area against the flow of gas and so causes an added frictional effect. This leads to "precession" currents (Fig. 2.17), and increases the inwards drift. This effect is particularly detrimental to mist cyclones or those with water irrigation (Swift 1985 and Sutton 1972).

Leakage of air into a cyclone hopper often brings about a dramatic loss of efficiency (Crellin et al, 1980). For example, Van Ebbenhorst Tengbergen (1965) noticed a 30% increase in dust emission when allowing a 5% (of total flow) leakage into the hopper, and Hurley (1951) found a drop of efficiency from 85% to 40% with a "slight" leak. This can be attributed directly to the leakage flow picking up dust in the hopper and transporting it into the cyclone exit tube.

With fine dusts it is often observed that particles collected near the wall move down the wall in well-defined "ropes" of dust, as reported by Ter Linden (1949), Morii et al (1968) and also observed during the present study. The ropes themselves are aligned with the gas flow and, being dependent on small particle/ particle forces, offer some protection for the dust moving within them to the elutriating action of the gas. The ropes become more dominant at higher dust concentrations, and then will provide more protection to more dust in moving past the gas exit region (Abrahamson et al, 1978).

A dust carry over mechanism from the cells of a multicell cyclone was reported by Reznik and Matsnev (1971) and also observed in the present investigation. When the dust accumulates inside cyclone inlet manifold or vanes or cyclone body, aerodynamic forces tend to break up the deposits and some fraction is likely to pass into the clean gas exit when such deposits fall intermittently into the cells.

The probability of chokage in cyclones depends upon the nature of the adhesive forces between the particles, a subject about which little is known, and also probably upon the number of contacts per unit volume of powder (Sutton, 1972). The adhesion of particles in bulk is thus greatly increased by the presence of fines smaller than 5 μm because in this range the forces of adhesion, even with sand, appear to exceed the weights of the particles. . Chokage in tangential-entry cyclones is chiefly observed in the inlet duct and near the apex of the cone (Sutton, 1972).

2.9 MODIFICATIONS TO CYCLONES

Cyclone separators were first conceived and utilized in plant more than 100 years ago. Despite scientific advancement during much of this period, many cyclones being installed on plant today have changed very little in the basic design. It is widely accepted that mechanical separators such as the cyclone are capable of meeting more stringent performance requirements than are presently being achieved (Boysan et al, 1982, and Koch and Licht, 1977). In practice, most commercial cyclones do not provide ideal aerodynamics partly because the designs seek an optimum between throughput and acceptable efficiency (Smith et al, 1981). There have been many attempts to improve cyclone performance by modifying boundary conditions, introducing auxiliary injection via vanes or stationary propellers, incorporating vortex stabilising baffles and recirculating devices.

As listed by Gupta et al (1985), cyclones have the following main characteristic features of interest

(a) Residence times are long, particularly with long-bodied cyclones.
(b) Solids particles can be separated or suspended for very long periods by the centrifugal force field generated by the swirling motion of the fluid.

(c) Recirculation zones and moderate levels of turbulence intensity (~ 30%) can be generated internally by shear between differing fluids. It is possible to alter drastically the shape, location and extent of such zones.
(d) Large radial and axial boundary layer flows can develop close to the end walls due to the reduced centrifugal force field in this region.
(e) In the exhaust region, large toroidal recirculation zones, high levels of turbulence intensity and a precessing vortex core are usually formed.

Depending on application, any one of the above factors can be emphasised by good design. For example it is possible to alter radically the distribution of axial and radial velocity by small changes in design and position of the tangential inlet (Schneider, 1960). Dirgo and Leith (1985) showed that by increasing the gas inlet velocity, or by decreasing cyclone inlet area, cyclone collection efficiency was increased but this also caused higher pressure drop. Because of trade-offs between efficiency and pressure drop, an unconstrained optimum cyclone design is not possible, and the design objective must be restated.

Experiments were conducted by Dabir and Petty (1984) in order to investigate the effect of the vortex finder geometry of a 75mm hydrocyclone on the mean velocity field. A comparison of the axial velocity for different vortex finder configurations (Fig. 2.18) showed that the vortex finder design influences the core region but not the outer region. Depending on the specific design and operating parameters, a three-celled, a two-celled, or a single-celled vortex flow occurs. Also Escudier et al. (1980) studied confined turbulent vortex flows by using LDA and a flow visualisation technique. They showed that the size of the exit hole affects the location and magnitude of the swirl velocity and, thereby, the number of flow reversals possible. Bradly and Pulling (1959) studied the flow pattern inside a 75 mm-hydrocyclone using a flow visualization technique for different size vortex finders and cone angles. They observed a stagnant zone surrounding the core indicating a region of negligible axial and radial velocities. Such a region, which has been observed by many researchers, is commonly referred to as the "mantle". Bradly and Pulling observed that the " mantle" is basically unaffected by changes in the vortex finder dimensions, provided the vortex finder diameter is smaller than the "mantle" diameter. However the "mantle" diameter increases as the cone angle increases.

A computer program was developed by Dirgo and Leith (1985) to use some empirical cyclone pressure drop and efficiency theories to predict dimensional changes that would improve cyclone efficiency without increasing pressure drop. Four new cyclones were designed with the program; they were tested under experimental conditions identical to those used to evaluate the standard design. The new cyclones did not perform as efficiently as predicted and only one of the cyclones performed better than the standard design. Dirgo and Leith indicated that although cyclone theories may work for some designs under some operating conditions, they are not developed to a sufficient extent to allow design optimization. In fact despite the cyclone's apparent simplicity, the fluid dynamics of cyclones is complex (Boysan et al, 1982) and there is no really fundamental understanding of the separation process, so optimization using empirical theories could easily produce such unsatisfactory results.

One way of increasing the collection efficiency of cyclones is to induce a downward flow of gas from the main body of cyclone into the hopper or dust disengagement chamber below so as to minimize the re-entrainment of particles. This is usually achieved by bleeding off a small fraction of the gas stream from a point in the disengagement chamber and discharging it via the stack to atmosphere after cleaning using a high efficiency device such as a bagfilter (Fig. 2.19). Analysis by Stairmand (1951) has indicated that a purge flow of 10% of the total gas flow may decrease dust emission from a relatively efficient cyclone by 20 to 28%. The effects of gas bleed and bleed position on cyclone performance have been measured by Sage and Wright (1986) for a laboratory-scale high-efficiency cyclone at ambient temperature. Fig 2.20a shows the effects of gas bleed and positions on overall cyclone collection efficiency. It can be seen that the bottom bleed position is the most effective, a 15% bleed reducing emissions by some 40%. Results for cyclone grade efficiencies with and without gas bleed are shown in Fig. 2.20b.

Biffin and Syred (1983) introduced a novel design of cyclone which combines conventional cyclone and vortex valve technology (Fig. 2.21). The swirl chamber, although only partly optimized, removed up to 60% of the particles entering the separator. Comparing the particles collected in the central and outer region of the separator, it was observed that the coarser particles were collected in the outer chamber. This enables the centre region to handle fine particles without any fear of choking or

large particles 'bouncing' out of the separator. They reported 97% efficiency for their design which is 2% more a than similar high efficiency Stairmand cyclone. Also Syred et al. (1985) reported a new dust collection device termed Vortex Collector Pocket (VCP). Particles are centrifuged into one or more VCPs, where swirling motion is driven by the swirl in the main cyclone body. By appropriate placement it is possible to create multi-stage dust separation systems with the pressure drop of a single unit (Fig. 2.22). The long central cone can also be eliminated.

Experimental results have clearly shown that substantial head recoveries, resulting either in saving in energy cost or increased throughputs, could be achieved by the use of some special outlet configurations with both gas and hydro cyclones (Arato 1984). Browne and Strauss (1978) show how a 22% reduction in pressure drop can be achieved by first deswirling the exit flow without loss of static pressure and then diffusing the resulting axially dominated flow to recover velocity energy as pressure energy. This was accomplished by placing a cascade blade into the outlet duct some two exit diameters downstream. Schneider (1960) has conducted a detailed series of tests on the reduction of pressure drop attainable by the use of various types of outlet geometry. He showed that a diffuser so located as to recieve the exhausting swirling flow from the cyclone with minimum separation losses (Fig. 2.23a) could give pressure recoveries of up to 49% compared with the situation where the exhaust flow passed directly into an elbow of the same diameter as the exhaust duct; he also shows how substantial reduction in inlet pressure loss can be achieved (up to 60%) by angling the tangential inlet duct toward the base of the cyclone (Fig. 2.23b).

2-10 MULTICELL CYCLONES AND MODIFICATION ATTEMPTS

It is known that cyclones attain a better particle separation efficiency with a small main barrel diameter, due to the increased centrifugal force on a particle. For a given tangential velocity distribution in a cyclone, maximum centrifugal forces are obtained with smaller values of r. There is an obvious limit to the extent to which r can be reduced; the cyclone becomes susceptible to particle cake build up which is then periodically passed directly into the exhaust gas duct as the device saturates. This is especially true with larger sized particles. Very small cyclones can, in principle, be

constructed to separate very fine particles of d<3 μm, but they soon get choked with particles of larger size (Brookman et al 1963 and Hochstrasser, 1976).

Thus, when dealing with a large volume flow of particle-laden gas, cyclones are generally connected in parallel but additional problems have arisen due to plugging, erosion and difficulties of flow distribution and particle removal (Fig. 2.24). Efficiencies of these cyclones can vary according to the cell geometry and particularly the inlet vane design of axial-entry cells (Fig. 2.2). Vanes which are constructed in such a manner as to induce the solid particles to flow quickly to the wall of the cyclone, can enhance the cyclone efficiency (Greenfield, 1986). Theoretically the smaller the cell diameter the better will be the efficiency but in practice this is offset by the problems of much higher wear rates from solids erosion and increased risk of recirculation between cells causing re-entrainment. Doerchlag and Miczek (1980) mentioned that if the gas pressure at the cyclone outlet is not identical for each cell, secondary circulation will develop through the dust hopper from one cell to another. Those cyclones that take in gas through their dust outlet perform at lower collection efficiency and may cease to collect any dust at all.

Efficiencies of multicell cyclone collectors on spreader stoker boilers approach 95%; with pulverized fuel fired boilers, the efficiency drops to 90%. Putting units in series only improves collection efficiency by a fraction (Jones, 1976). In other applications, multicell cyclones are used as pre-cleaners for a scrubber or baghouse to reduce the dust loading to the primary unit (Fig. 2.25). The dust loadings from coal-fired boilers are not generally high enough to warrant pre cleaning prior to going into a baghouse or scrubber (Jones, 1976).

Gerrard and Liddle (1976) have described two alternative methods for selection of the cyclone diameter and the number of units to be used in parallel for a given duty; both methods are based on the optimization of the operating costs and fixed charges per unit time. They assumed that a particle cut-size has been fixed at an appropriate value so that the major part of the dust loading may be removed. Clearly, the optimum thus obtained is dependent on good mechanical design to obviate the danger of maldistribution of gas and dust loading between the cyclones.

Three different types of cell which are used in multicell cyclones in the USSR are shown in Fig. 2.26 (Reznik and Matsnev 1971). The main type of dust collector for boilers up to 320 t/h in capacity is a multicell cyclone assembled of cells 254 mm in diameter, Fig 2.26a. Dust-laden gases are swirled at the inlet of the element by eight vanes, which smoothly turn the flow through 65^{o} with respect to the initial direction of the flow along the axis of the cell. To remove dust from the drying agent in the case of drying coal by flue gases, use is made of cyclones with cells 231mm in diameter, which have a semiscroll swirler (Fig. 2.26b). In an ash removal system with extraction and recirculation of some gas from the hopper multicell cyclones are used with cells having a scroll-type swirler (Fig. 2.26c). Advantages of one type over another were shown by some authors (Reznik and Matsnev, 1971), however, no comparative tests on multicell cyclone with different cell types have been carried out under the same conditions and the region of their employment has been determined without sufficient experimental backing. Of three cells tested with respect to aerodynamic characteristics of the flow, the best performance was achieved with a vaned swirler (Fig. 2.26a).

In 1974, a refinery in the USA initiated a study to find alternatives for control of particulate emissions from its fluid coker stack. This study identified a multicell cyclone as having potential for bringing the particulate mass emission rate into compliance with anticipated, tightening state air pollution regulations. Although multicell cyclones had been used widely (primarily in Europe) for control of flyash from oil-fired boilers used for power generation, there was no known application of the device to particulate matter of the type emitted from this plant (Byers and Gage, 1981). A pilot plant (Fig. 2.27a) was built to demonstrate the performance capabilities of the multicell cyclone in such service. The pilot multicell cyclone consisted of a bank of 12 axial cyclones, 25.4 cm in diameter, operating in parallel, while the full scale unit (Fig. 2.27b) was a three stage cleaning device. At the primary collector with 0.75 kPa pressure drop, an overall collection efficiency 84-86% was obtained. The particulate mass emission rates for the tests ranged from 1.8-5 g/s, well within the regulatory requirement of 8.2 to 10.7 g/s.

It is possible to enhance the efficiency of a cyclone system by using a small amount of continuous underflow from the cyclone hopper dust outlet, and if properly designed this can be used to transport the dust pneumatically to a disposal ash hopper (Fig. 2.28), thus avoiding the use of a separate transport system (Greenfield, 1986).

A multicell cyclone unit comprising 12 cells with barrel and outlet tube dia. of 250 and 150 mm respectively was tested by Sage and Wright (1986). This device was equipped with a fan assisted mechanical secondary cleaning system whereby up to about 20% of the inlet gas flow could be drawn off from below the tubeplate and passed through a high efficiency cyclone (Fig. 2.29) (They tried to simulate a `sidestream separator'). The results showed a reduction in emissions of dust over 30% from 4.8 to 3.3 kg/h for a bleed rate of 10%. The developement and successful application of the sidestream separator, also known as hopper ventilation, or the fractionating system, to existing high efficiency centrifugal collectors on spreader stoker fired boilers burning bituminous coal was described by Sortor (1981) and Henry et al (1982). The aim was to reduce particulate emissions from three boilers in order to achieve compliance with increasingly restrictive emission regulations. The sidestream-separator system (Fig. 2.30) was found to consistently reduce the emissions from properly operated and maintained high efficiency multicell cyclones on spreader stoker fired boilers by 35%-50%. This emission reduction is partially due to the fact that the sidestream flow is passed through an almost absolute high efficiency collector (filter or scrubber, Sortor, 1981).

Crellin et al (1980) reported some modification works on multicell cyclones. They mentioned that air infiltration, hopper circulation and plugging are weaknesses of multicell cyclones (Fig. 2.24). They reported that the use of dust hopper fractionation (a sidestream flow, or bottom bleed, Fig. 2.30) on brown coal fired boilers has proved to be a most effective method of improving the collecting efficiencies of the multicell cyclone dust collector.

CHAPTER 3

EXPERIMENTAL RIGS DESIGN, APPARATUS AND PROCEDURES

3.1 INTRODUCTION

In this chapter, the experimental rig design and apparatus, measuring instruments and experimental procedure will be presented. The multicell cyclone rig and one cell rigs (water and air) are described in sections 3.2 to 3.4. Section 3.5 explains the use of measuring instruments:, laser Doppler anemometer (LDA), Malvern particle sizing system and flow measurement devices. Visualization and photography techniques, using a smoke-wire system and smoke generator are described in section 3.6 . The computerised data acqusition and processing equipment is dealt with in section 3.7. Finally the measurement procedure as well as error analysis of the experimental results are dealt with section 3.8 .

3.2 MULTICELL CYCLONE RIG DESIGN

3.2.1 Preliminary Remarks

A representative full-scale multicell cyclone had been taken to be a 35-cell unit designed for a total gas flow of 10.4 m^3/s (22000 acfm) at 200 ^oC and approximately atmospheric pressure. Each cell had gas inlet diameter D of 254 mm (10 inch) and gas outlet diameter D_e of 152 mm (6 inch). The type of multicell cyclone had been chosen (Crane 1985) as horizontal, in line (but offset) inlet and outlet ducts, vertical-axis cells, and stepped exhaust tube plate, which separates the inlet from exhuast gas (Fig. 3.1). This design is loosely based on a Western Precipitation (division of Joy Mfg. Co,U.S.A., and Leatherhead, U.K.) design, formerly made under licence in the U.K. by Steetley Engineering Ltd.

Scaling of the model and choice of the number of cells was dependent on the

available laboratory space and air flow capacity, as well as the need to model adequately the gas flow field, determined largely by the Reynolds number Re and the particle inertial behaviour, determined to a first approximaion by the Stokes number St. (High St implies high collection efficiency, and vice versa).

It was agreed that a minimum acceptable segment of the complete unit, for experimental purposes, would be a 3*3 cell array. Air supply (using an existing centrifugal blower) and the space required for large-bore ducting for flow settling and particle sampling then dictated a roughly half-scale model.The experimental multicell cyclone (Fig. 3.1b) consists of nine axial-inlet, reverse-flow cyclones at 150 mm pitching. Each cell has eight equi-spaced swirl vanes, with 60^{o} turning angle and 36 mm chord in the axial direction and 3 mm thickness. The cell inlet diameter (D) was selected as 100 mm (nominal) in order to use standard size tubing for cell construction; similarly, 50 mm internal dia., 60 mm external tubing was chosen for the clean-gas outlet tubes.The common hopper, with bottom blanking plate and observation window, was mounted over a removable section of laboratory floor, for ease of access.Two pipes had been considered for sampling purposes (before and after cyclone), with bag filters and blower at the end of rig. Acrylic tubes or sheets had been used only for manufacturing those parts of the rig needed for visualization purposes. Other parts of the rig were manufactured from steel or wood to minimize static charge effects on particle motion. Fig. 3.2 and 3.3 shows the multicell cyclone arrangement and the preliminary arrangement of the complete rig (Crane 1985).

It was desired to match the gas flow field and the particle inertial behaviour between full-scale and model. For matching the gas flow field, the Reynolds number needed to be modelled. For the representative full-scale cyclone, Reynolds number had been calculated at 67400; this required V_i=10.1 m/s (at 20^{o}c), hence a total (9-cell) flow rate of 0.458 m^3/s. Pressure drop ΔP, expressed as a number of inlet velocity heads (Euler No.), should then also be similar to the full-scale value. Because of the limited choice of the particle sizes and physical properties, it was not possible to match the full-scale Re and St simultaneousely. It was therefore accepted that dust collection efficiency measurements would have to be made at a reduced flow rate in order to match St , provided that the gas flow characteristics were not substantially altered. For matching Stokes number, cell flow rate had been calculated at 0.0128 m^3/s and the Reynolds

number had been calculated as approximately one quarter the full-scale value, assuming that the particle specification (ρ_p=2000 kg/m^3,$d_{m,0.5}$=10 μm) to be used in the rig would be similar to that of solids emitted from fluidized-bed boilers. Table 3.1 shows a summary of preliminary design data for model multicell cyclone and full-scale (Crane 1985). It will be seen later that the final choice of test dusts allowed closer Reynolds number matching than envisaged in the preliminary design.

3.2.2 Air Circuit Design

When the main components of the rig, such as the multicell cyclone, had been manufactured, commisioning of the rig was begun. This was the beginning of the author's research. During commisioning, the following development work was done.

Fan Performance Improvement

The type of fan available had backward-curved blades (580 mm dia.) and was driven by a 400 V D.C. motor. From preliminary tests it was found that the fan was not adequate for the proposed aerodynamic tests at full-scale Reynolds number. Fan performance curves were found by experiment (Fig. 3.4a). According to this curve, for 0.458 m^3/s (aerodynamic matching) flow rate, the maximum suction pressure is 1.45 kPa below atmosphere, which is smaller than the system pressure drop for aerodynamic tests, estimated as 4.3 kPa. For fan modification or decreasing the system pressure drop, many alternatives were investigated. using 0.15 m pipe diameter for the sampling sections improved system pressure drop by about 2 kPa. Use of a fan bypass system and taking advantage of the venturi effect at the outlet end of the cyclone's downstream sampling pipe, also improved suction pressure by about 0.9 kPa. Fig 3.4b shows the principle of this system. Results of tests on the fully-modified system indicated that the air flow rate was sufficient for aerodynamic tests.

Bag Filter House

For controlling air pollution in the laboratory and as an alternative clean-stream solids measurement system originally recommended by CRE, a bag filter house had been designed to capture all remaining particles in the cleaned gas (Fig. 3.3), using 16 bags

with a face velocity of about 1 m/min.The bag filter was set up and then commisioned. Measurements showed that the bag filter pressure drop was not acceptable with the rig as it was then configured. Because of shortage of laboratory space and filter total face area (10.6 m^2), bag filter house modification was not possible. Also the laboratory had a suitable underfloor air extraction system which could be adapted to extract remaining particles, so the bag filter house was deleted from the experimental rig.

Rig Duct and Piping Optimization

Because of shortage of laboratory space and the length of the multicell rig, a bend followed by a diffuser before the cyclone entrance had been unavoidable. Fig. 3.6a shows this part of the rig. Air mean velocity profiles at the cyclone entrance for 45, 90 and 135 mm heights from the duct bottom (Fig. 3.6a) have been measured and are shows in Fig. 3.7a. These graphs and observations of the unsteadiness in velocity show that flow entering the cyclone inlet manifold separated intermittently from one diverging wall of the transition duct; this "bistable" behaviour is commonly seen in diffusers and suggests an unsatisfactory transition duct design in the British Standard (B.S.-2831,1971) on which this part of the rig was based.

For more investigation, a smoke system plus photography was used. Transistory stall and flow unsteadiness were observed at the cyclone entrance, as shown in Fig. 3.8.Two more tests were done to prove that the bend and diffuser, not the cyclone, mainly caused the bad inlet flow pattern at cyclone entrance. First the cyclone was replaced by a parallel duct which connected inlet and outlet ducts together; results of tests showed that the flow pattern was still distorted and unsteady. For the second test, the diffuser and upstream duct and piping system were replaced by a parallel-sided duct with bell mouth entrance. Fig. 3.6b and 3.7b show the new configuration and measured air velocity profiles at cyclone entrance for this case. As Fig. 3.7b shows, the air profiles at cyclone entrance were ideally flat and also absolutely steady, and no transistory stall was observed. These investigations showed that the cyclone upstream duct needed to be redesigned.

Diffusers in most engineering application have area ratios of less than three and they are designed for maximum pressure recovery in a given length. At the outlet from these

diffusers the core flow is virtually unaffected by energy dissipation within the diffuser, with the result that the core's total pressure remains virtually constant. It can be concluded that insufficient diffusion, rather than energy dissipation, is the main cause of poor diffuser performance. If the divergence of a diffuser is too rapid (Fig. 3.9a), large scale separation or stall occurs. Re-attachment following separation does not take place unless the divergence is reduced. Pressure recovery in a diffuser with extensive stall is low and the outlet flow is very distorted with areas of reverse flow. Space restrictions frequently dictate that diffusers operate with areas of stall. The amount of flow separation ranges from numerous, very local areas of stall, which are continually being formed and swe pt out of the diffusers, to large cells of separation that slowly build up causing extensive areas of revese flow, which are then suddenly swe pt out. The cycle of growth and swe p-out is called "transistory stall". Large changes in pressure recovery and outlet velocity distribution occur when diffusers operate with transistory stall. When a constant-area section is added to a diffuser's outlet (Fig. 3.9b) part of the excess velocity pressure is converted to static pressure by large scale mixing. A diffuser's performance also depends upon the energy distribution at its inlet. Pressure recoveries approaching the ideal are only possible if the inlet profile is nearly uniform. Therefore when the air profile is biased to one side and secondary flows are strong at diffuser inlet (as in the present study), rapid diffusion certainly causes flow unsteadiness and strong transistory stall inside and at diffuser outlet (Miller 1978). Fig. 3.9c shows a bend followed by a diffuser which steepens the inner wall adverse gradient and makes separation inevitable.

Flow regimes in plane-wall two-dimensional subsonic diffusers (Kline et al, 1959) are shown in Fig 3.10. According to this graph the present diffuser was working in the region of large transistory stall.Many modifications such as using honey comb, egg box, baffles inside diffuser, etc (Fig. 3.6c to f) were tested and none of them had a significant effect on diffuser maloperation. Fig. 3.7c shows some measured profiles from these investigations. For having a uniform velocity profile at diffuser inlet, a new bend according to Miller's (1978) recommendation was designed and manufactured. Fig. 3.5 shows details of this new mitre bend with turning vanes. At bend exit a movable fin was installed to optimize the cyclone entrance air flow pattern. Diffuser performance was restored to a reasonable level by using an internal wall along the diffuser centre line (diffuser angle improvement) and also adding two parallel duct sections between diffuser

and cyclone entrance (increasing mixing zone). Fig. 3.6g shows the final arrangement of this part of the rig and Fig. 3.7d shows the final cyclone entrance air velocity profile which is reasonably symmetric and without back flow or transistory stall phenomena.

Flow Circuit Description

The flow system of the multicell cyclone test rig was of the open circuit type, consisting of particle feeding system, multicell cyclone, fan , two sampling sections and sediment dispersal jet system. Fig. 3.11 shows the final layout of the rig.The particle feeding system, described in section 3.2.6, injected dust into the rig's bell-mouth entrance. The particles mixed with air inside a 0.15 m dia. steel pipe of 1.5 m length upstream of the sampling section. The isokinetic sampling from dirty gas was performed in the first sampling section (0.15 m dia., 2.2 m length). The bend (with turning vanes), diffuser (150 mm dia. to 450*180 mm with a central internal wall) and two parallel sided duct sections connected the sampling section to the multicell cyclone entrance flange. A suitable purging system which used compressed air (see sec. 3.2.6), removed dust sediment from the duct floor. An aerofoil-shaped fin after the bend was used for optimization of the velocity profile at the cyclone entrance. The multicell cyclone captured a portion of the particles and collected them inside the hopper. The clean air passed through the cyclone outlet duct and a contraction which connected the cyclone outlet flange to the second (152 mm dia. ,2.4 m length) sampling section, which was identical in terms of component spacing to the dirty gas sampling section. At the downstream end of the rig the centrifugal blower (plus bypass system) gave enough suction for flows up to 0.45 m^3/s. The blower exhausted via plywood ducting to the laboratory underfloor space, where an existing extraction system disposed of dust not collected by the cyclones.The rig flow rate was measured by the traversing pitot static tube in the clean gas sampling section. Many tappings and access holes for probes were put in different parts of the rig (hopper, ducts, pipes,etc) for pressure/ velocity measurement (using pitot tube) or visualization purposes (using smoke-wire probe, smoke distributor, etc). Fig 3.12 shows a photograph of the complete multicell cyclone rig.

3.2.3 Selection of Test Dusts

Choice of the principal test dust was based on consideration of (Crane and Behrouzi 1987):

(a) Stokes number matching, as a first approximation to correct modelling of the inertial behaviour of typical boiler flue gas solids;
(b) avoiding the possibility of explosive mixtures with air;
(c) non toxicity;
(d) continued availability in the required quantities at moderate cost.

Size distributions of atmospheric fluidized bed boiler solids(ash, bed sand, unburnt carbon) suggested (Sage et al., 1984, Bogucki 1986) a typical mass median diameter $d_{m,0.5}$ of around 45 μm. The preliminary calculation lead to an ideal $d_{m,0.5}$ around 37 μm for the model experiments (the Stokes number matching procedure assumed the test dust to have similar particle material density to boiler flue gas solids, and used the minimum recommended velocity (9 m/s) for satisfactory sampling in the 150 mm pipe).

Pozzolan (processed pulverized fuel ash, Pozzolanic Lytag Ltd.), Fuller's earth (Laporte Earths Ltd.," Surrey Powder" grade), Syenex-40 (nepheline syenite, Nornef Minerals Ltd.), etc, were sufficiently cheap and available in appropriate quantities for using as test dusts. Fig. 3.14 shows size distributions of these dusts measured on-line in the jet from the dust feeding system by a Malvern 2600 instrument. A grade of fuller's earth was obtained which appeared to satisfy all the requirements (a) to (d) above, with some remaining uncertainty over the relative densities of atmospheric fluidized bed solids and fuller's earth. However, the first dust collection measurements with this material showed very high overall efficiencies, around 96% in the multicell model and 99% in the single cell, for Re=36000 and St=0.21 (based on $d_{m,0.5}$). These values were likely to make it difficult or impossible to discern the effect of any modifications made with a view to improving the efficiency. A finer test dust was clearly required, since a reduction in V_i to reduce St was no longer an option.

Coal-derived dusts were considered, with $d_{m,0.5}$ in the region of 10 μm, including Pozzolan, meeting requirements (a),(c) and (d) but of questionable safety in the present

circumstances. Due to explosion risk, the carbon-containing Pozzolan was ruled out after discussion with the Fire Research Station, Borehamwood. A fine, inorganic powder, Syenex-40, was then located, which in its chemical make-up closely resembled the fly ash from fluidized-bed combustion of colliery tailings described by Seville et al (1984). By weight, 57% consists of S_iO_2 and 24% of Al_2O_3, compared with 53% and 27% respectively for the fly ash repoted by Seville et al. Syenex-40 (see table 3.2) is a grade of pure nepheline syenite with nodular particle shape, having a material density of 2445 kg/m^3 and $d_{m,0.5}$ around 10 μm (both measured by the author and corresponding well with the manufacturer's figures). This dust provided Stokes number matching (based on $d_{m,0.5}$) at a total rig flow rate of 0.216 m^3/s or 0.024 m^3/s per cell, giving Re=32600 (i.e. about half the value required for strict gas flow similarity). Details of the calculated parameters are given in table 3.3, where the full-scale dust is now taken to have an average material density equal to that measured by the author for a sample of atmospheric fluidized bed boiler solids collected by bag filtration at Marden, a boiler described by Fisher et al (1980), and a mass median size equal to the lowest value in the range of Fig. 3.15 (Sage et al, 1984). The relevance of Stokes number matching need not be stressed because trials with Syenex-40 yielded multicell cyclone overall efficiencies near 85%, itself a satisfactory reason for using Syenex-40 as the principal test dust. (It is also likely that properties such as the tendency to agglomerate, adhesion to cell walls etc. are as important in determining overall efficiency as inertial behaviour while gas-borne.)

Results presented in the thesis are for Syenex-40, with brief mention of the small number of tests carried out with fuller's earth and Pozzolan on the single-cell cyclone ("clean" gas heavily diluted before entering the fan, hence less risk).

3-2-4 Sampling Systems

Before and after the multicell cyclone, isokinetic sampling systems were chosen for efficiency tests. According to Stairmand's recommendation (1951), the sampling section consisted of mixing baffle, nozzle, probe tube, filter, rotameter, control valves, exhauster and pitot tube. Fig. 3.16 illustrates diagrammatically the sampling system. Fig. 3.13 also shows a picture of the sampling system after the cyclone.The following is a summary of sampling system components design.

Design of Nozzle

The size of sampling nozzle diameter is dependent on particle mass concentration, sampling time and air velocity. Also the following conditions were considered for sampling nozzle design (Stairmand 1951, B.S.-893, 1978).

1- Duct velocity should preferably be in the range of 9-16 m/s for sampling nozzle
2-Nozzle diameter should not be less than 10 mm or greater than 30mm,and to prevent choking it was not recommended that a nozzle smaller than 9.5 mm be used.
3-The nozzle should be sharp-edged, self compensating and null-point. Fig.3.17 shows the limit of some important sizes for a typical sampling nozzle.

For Stokes number matching, cell inlet bulk velocity and rig flow rate were calculated respectively as 5.13 m/s and 0.024 m^3/s. Therefore the mean air velocity inside sampling section was calculated as 12.32 m/s which is inside the range of Stairmand's (1951) recommendations. Dust concentration for typical fluidized bed combustion was taken as 10 g/m^3 (Bogucki 1986). This figure need not be exactly replicated in the rig and so the rig dust concentration was chosen as 12 g/m^3.The test duration time was chosen as 10 minutes (Dorman 1974) mainly because of limitations on cyclone hopper space, sampling system capacity and pollution.The sampling mass should not be less than 2-3 g for reliable size distributions (Stairmand 1951, Pillai and Wood,1980), therefore for catching at least 10 g particles in the sampling system before the multicell cyclone, nozzle diameter was calculated at 14 mm.

The multicell cyclone efficiency was assumed for design purposes to be 90%, so the dust concentration in the sampling system after the multicell cyclone was calculated at 1.2 g/m^3. To have enough sampling mass,the nozzle diameter was chosen as 28 mm (near the recommended upper limit). The sampling section after the cyclone would catch nearly 5 g of particles which is more than the minimum limit and acceptable. Ofcourse, for weighing purposes, the balance would need to have an accuracy of about 0.05 g (Reznik and Matsnev, 1971) or be capable of weighing to within 0.1% of the minimum weight of dust on the filter (B.S.-1701,1970).

Mixing Baffle

A disc-shaped mixing baffle was used before the sampling nozzle and its use enables a representative sample to be extracted from a single point on the axis of the main sampling pipe. The area of the baffle was chosen as about half the pipe area (Stairmand 1951, Pillai and Wood,1980), the disc diameter being 106 mm.

Sampling Probe

10 mm inside-diameter copper tube was used, with a screw connection to the nozzle. The radius of the probe bend was chosen as 3.5 D and this figure is more than the minimum limit,1.5 D (B.S.-893,1978).

Filters

The filter was used in the sampling system to catch particles for two reasons, first for determining particle concentration and second for size analysis. Filters can be divided into categories of fibre filters, membrane filters and electrostatic filters. Suitable filters depend on the kind of particles and fluid, filter pressure drop, kinds of tests on particles, filter throughput, cost,etc. Where the only purpose of a test is determining the weight of particles, the choice of the filter is relatively easy and the best choice may be slag-wool or composite filter types (Stairmand 1951, Hawksley et al 1961) and where the purpose of sampling is size analysis, the best choice may be porous metal (Bogucki 1986).

After many tests, glass fibre medium (Gelman Sciences Ltd.) was choosen because of low pressure drop, weight and cost. This filter could catch all particles greater than 0.3 μm. A 150 mm diameter disc of glass fibre medium clamped in lightweight double-funnel-shaped holders was designed for both sampling systems.

Exhauster

Vacuum pumps, ejectors and vacuum cleaners have previously been used as exhausters to extract the gas sample against the sampling system resistance. Cost, system pressure drop and simplicity of usage, determined a suitable system. Ejectors are

more popular (Stairmand 1951) and were chosen for the present sampling system on grounds of cost. Ejectors were designed and manufactured by the author, as sketched in Fig. 3.18. This ejector works with compressed air at 40 psi and creates enough suction to pass 5 l/s through the sampling system. The required sampling rates before and after the multicell cyclone were calculated as 1.9 l/s and 7.58 l/s (nozzle area multiplied by duct velocity) respectively; one ejector was chosen for sampling system before the cyclone and two ejectors for the sampling system after the cyclone.

Rotameter

For measuring the sampling flow rate, cone-and-float flowmeters ("rotameter") were used. Rotameters usually have an accuracy of from 0.5% to 2% of the full scale readings (Murphy 1984) which is suitable for sampling flow rate measurment (Reznik and Matsnev, 1971). Rotameters of capacity 200 l/min and 500 l/min were chosen for the sampling systems before and after the multicell cyclone respectively.

Pitot Tube

After each nozzle in the sampling sections, a pitot tube was used to measure duct velocity. The measured velocity was compared with the velocity at nozzle entrance (calculated from rotameter data) to check isokinetic sampling. The pitot tube was designed and manufactured according to the recommendation of B.S.-893 (1978) and B.S.-1042 (1983). Fig. 3.11 shows the location of mixing baffle, sampling nozzle and pitot tube inside the sampling sections (Stairmand 1951 and B.S.- 893, 1978).

3.2.5 Particle Feeding System

Many mechanisms, such as screw-feeder and vibrator (Perry et al 1984) are used for this purpose. Because of cost, unchanging particle size distribution and also recommendations in B.S.-1701,1970 and B.S.-2831,1971, a vibrating feeder was chosen.The size of vibrator required to promote flow of particles depends on a great many elements, such as size, shape, construction and condition of material (wet/ dry).

Previous calculation showed that the dust concentration should be about 12 g/m^3.

This figure should remain constant during 10 minutes, with the efficiency-test flow rate of 0.218 m^3/s; therefore the minimum dust feeding rate should be 9.4 kg/h. A "Minor-E/M disperser with C/W CVC9 controller" was chosen and bought from Coote Vibratory Co. This system is powered by a type 9 electro-magnetic vibrator with an input of 0.25 amp. at 240 volt. The principle of operation is the opposition of a moving mass to a fixed unit, coupled together by a tuned spring system. The moving mass is magnetically attracted to the fixed unit and returned by the spring system. This cycle of events takes place nearly 100 times each second. The maximum and minimum delivery were claimed to be respectively 50 kg/h and 0.6 kg/h . Particle feed rate was controlled by varying the vibration amplitude.The dust injector unit was designed and manufactured according to B.S.-2831 (1971). Fig. 3.19 and 3.20 show a sketch of this system and a general arrangement of particle feeding system respectively.

3.2.6 Sediment Dispersal System

As already mentioned, a bend, a diffuser and two parallel ducts were used to connect the 0.15 m dia. mixing and dirty gas sampling pipe to the cyclone entrance flange (0.18*0.45 m). This configuration was suitable for aerodynamic tests but it had weaknesses for efficiency tests in view of the opportunities for particle sedimentation.The outlet/inlet area ratio of this transition duct system was 4.58 and the bulk air velocity fell to nearly 2.7 m/s inside the diffuser; gravitational deposition occured in this low-speed region ahead of the cyclone, causing a change in particle size distribution and a non-uniform dust concentration at the cyclone entrance.

A compressed air system was designed and constructed for dispersing particles from the duct floor during the efficiency tests. Unfortunately this caused diffuser instability and much effort was put into re-optimizing this system in order to restore a reasonable flow pattern at the cyclone entrance.Two air distributors (tubes with multiple perforations) plus two single air jets achieved the desired effect. Fig. 3.21a shows this system which worked with 0.011 m^3/s (about half the flow rate for one cell) of compressed air at 40 psi. The first and second distributor had 18 (2mm dia, 15 mm pitch) and 25 (2mm dia, 15 mm pitch) holes respectively and were installed 5 mm above the duct floor. Fig. 3.21b shows the velocity profile at cyclone entrance when the dispersal system was in operation.

3.3 ONE CELL WATER RIG DESIGN

3.3.1 Preliminary Remarks

Without any information about the performance of one isolated cell, analysis of multicell cyclone results would have been much less valuable. A separate single-cell test section was therefore designed and constructed from perspex, with the aim of visualizing the flow and making velocity measurements in the absence of any influence from other cells. Such observations and measurements provided a "reference case" to aid in isolating effects due to cell-cell , cell-manifold and cell-hopper interactions in the multicell rig; this was especially important in view of the very sparse information in the literature on the behaviour of axial-entry (swirl-vane) reverse-flow cyclones, in sharp contrast with the abundant information on tangential-entry cyclones. A more specific objective was to provide laser Doppler measurements of the velocity field for verification of the numerical model which has been developed for this type of cyclone.

3.3.2 Cyclone Design

All cyclone dimensions were chosen to equal those of a multicell cyclone cell, and Fig. 3.22 shows the necessary dimension of this cyclone. A suitable hopper and inlet duct were designed.Sufficient length was chosen for the entry duct to have a uniform entry flow parallel with the cyclone axis.Also at the middle of this duct a sheet of perspex, drilled with equispaced holes 5 mm dia., 10 mm pitch was placed to provide a nearly uniform velocity profile upstream of the swirl vanes as an idealization of the inlet geometry of a multicell cyclone cell. The cross-section of this entry duct was square, with side equal to the multicell cyclone cell spacing. The system was able to be changed if necessary to a " worst entry" case, i.e. stream lines nearly perpendicular with the cyclone axial direction.To provide circumferential traversing across one or more pitches, the cyclone portion of the test section rotated within a stationary, square-section , water-filled, outer tank, whose function was to minimise refraction effects on the laser beam crossing location and angle.

3.3.3 Water Circuit Design

Tests needed to be performed at Reynolds number equal to 67400, for hydrodynamic matching between one-cell rig and full-scale conditions. Therefore the inlet bulk velocity and rig flow rate were calculated at 0.69 m/s and 200 l/min respectively. Cyclone pressure drop could not be predicted easily, but was estimated as about 4 kPa, by using a combination of "equivalent components" (Kay and Nedderman 1974). 50 mm dia. pipes were chosen for conections. An open header tank of volume 0.1 m^3 was positioned before the cyclone to damp any pump vibration or similar flow unsteadiness. The specification of an available pump met rig flow rate and pressure drop requirements. This was a constant-speed radial pump with 3-phase motor; to control flow rate, a bypass loop and control valve were added.

The flow system of the one-cell rig was of the closed circuit type. Flow rate was measured with a rotameter (Rotameter Manufacturing Co. Ltd.) with a maximum capacity of 250 l/min and $\pm$ 0.5 l/min accuracy. A heat exchanger was also incorporated in the system to keep the water temperature constant (20^0 C). A Copper/Copper-Nickel thermocouple with $\pm$ 0.1 ^{0}C accuracy was used for this purpose. A schematic diagram of the circuit is shown in Fig. 3.23.The pump supplied water to the open header tank; water then flowed by gravity (70 cm above cyclone inlet) to enter the cyclone inlet duct. For controlling temperature, make up and drainage, further control valves were employed.

With careful attention paid to joint sealing and to the fitting of baffles in the open header tank, it was possible to reduce air entrainment in to the water to a level low enough for adequate laser Doppler signal-to noise ratio (light scattering from air bubbles can completely swamp the signal, which arises from contaminant particles of order 1 μm in size). The water rig was successfully commisioned at a flow rate of 200 l/min, providing correct Reynolds number modelling.

3.4 ONE-CELL AIR RIG DESIGN

3.4.1 Preliminary Remarks

As already mentioned, for a better aerodynamic study of the multicell cyclone, the one-cell water rig was designed and constructed. Unfortunately it was not possible to use this rig for dust collection efficiency tests, mainly because it was closed-circuit and designed for water (no control on particle size and mass at cyclone entrance). A separate single-cell air rig was designed and constructed from perspex, with the aim of performing mass and grade efficiency tests in the absence of any influence from other cells. Such measurement provided a "reference case" which is important for checking multicell cyclone efficiency results. Others objectives were to provide mass and grade efficiency data (experimentally) to compare with results of the numerical model which has been developed for this kind of cyclone; also this rig could be used as a guide for certain multicell cyclone performance improvement devices,with obvious advantages in first testing them on one cell rather than nine.

3.4.2 Cyclone Design

All cyclone dimensions were chosen to equal those of a multicell cyclone cell; Fig. 3.24 shows major dimensions of this cyclone. The hopper was a cylinder of diameter 200 mm and depth 300 mm. The cross section of the entry duct was square with side equal to the multicell spacing, and to minimize particle sediment inside the inlet duct a funnel-shaped transition piece was made from cardboard and fitted inside the inlet duct. Silicone rubber was used to seal all gaps and connections. a suitable frame was constructed to support the cyclone inlet duct. An adjustable table was used as a support underneath the cyclone hopper to facilitate emptying and cleaning.

3.4.3 Air Circuit Design

For matching between the one-cell air rig and full-scale conditions, efficiency tests needed to be performed at a Stokes number equal to 0.043. Therefore the rig flow rates were calculated at 0.024, 0.044 and 0.0054 m^3/s for matching with Syenex 40, Pozzolan and Fuller's earth respectively. Because of system pressure drop and shortage

of space, 100 mm dia. and 50 mm dia. pipe were chosen for the piping system before and after the cyclone respectively. Also a 75 mm dia., 800 mm length pipe was chosen for the sampling section after the cyclone. For running the one-cell rig, many fans were examined and finally the multicell cyclone fan was found suitable and was chosen.

The flow system of the one-cell air rig was of the open-circuit type, shown in Fig. 3.25. The same variable speed fan (as for the multicell rig) was used at the end of rig to suck air through the rig at up to 0.05 m^3/s. An orifice plate (d=41.3 mm) according to B.S.-1042 (1983) plus micromanometer were used to measure rig flow rate. Before and after the cyclone, static tappings were drilled for cyclone pressure drop measurement.

Air velocity was calculated at 5.3 m/s inside the sampling pipe, which was less than the minimum recommendation (9 m/s, Stairmand 1951) and could have caused heavier particles to deposit on, or bounce along, the bottom of a horizontal pipe. Therefore a vertical position was chosen for the sampling section.Dust concentration, as for the multicell cyclone, was chosen as 12 g/m^3. Preliminary tests had showed a higher efficiency for the one-cell cyclone than the multicell cyclone. Therefore for sampling system design, cyclone efficiency was assumed to be around 96%. A suitable test duration time was considered to be 30 minutes.With these assumptions the total emitted mass from the cyclone during one complete test was calculated as 20 g . For acceptable accuracy and for size distribution purposes at least a 5 g sampling mass was needed after the cyclone (a quarter of the emitted mass). Therefore the nozzle diameter was calculated at 40 mm which was more than maximum recommended value of 30 mm (Stairmand 1951) for isokinetic sampling.

A systematic error arises if sampling is not isokinetic. A difference between the velocity of suction into the sampling nozzle and the velocity of the gases at the sampling point (Fig. 3.26) results in a difference between the weight of solids actually entering the nozzle and the weight flowing through the sample area defined by the nozzle. When the two velocities are equal the flowlines are undisturbed and the solids do not deviate from their paths. If the suction velocity is too high, solids that would not have passed through the sample area are drawn into the nozzle, whilst if the suction velocity is too low, some solids that should enter the nozzle will fail to do so. Therefore the accuracy of isokinetic sampling is dependent on sampling nozzle diameter mainly because of the air velocity

profile over the nozzle entrance, causing difficulties in controlling the nozzle suction velocity.

The nozzle position was 600 mm after a bend (equal to eight pipe diameters). Air velocity profile at the nozzle position was measured (at efficiency test flow rate, 0.024 m^3/s for Syenex-40) and Fig. 3.27 shows this profile. The profile was nearly flat and so the 40 mm nozzle diameter for sampling should be acceptable and was chosen. The multicell cyclone downstream sampling system (filter, valve, rotameter and ejectors) was used also for one-cell cyclone efficiency tests.

Unfortunately it was not possible to use the multicell cyclone particle feeding system mainly because of the dust sediment problem inside the upstream piping (air velocity inside this pipe was 3 m/s and was not suitable for carrying dust). Therefore a funnel was inserted near the cyclone entrance to receive dust from the vibratory feeder (described in section 3.2.5), relying on the highly turbulent flow in the square-section entry duct to achieve adequate dust-gas mixing.

3.5 MEASURING INSTRUMENTS

3.5.1 Introductory Remarks

A laser Doppler anemometer, laser diffraction particle sizing system and pitot tubes were used to carry out the experimental part of the project. The laser Doppler anemometer was used for flow velocity measurements inside the one-cell cyclone (water rig), and a Malvern particle sizing system plus Malvern particle feeding system was used off-line for size distribution measurement of dust samples (hopper sample, clean air sample, feed sample, etc.), which previously had been collected during efficiency tests. Many pitot tubes which were designed and constructed especially for the multicell cyclone rig, were used to measure cell flow rate, rig flow rate and velocity profiles in different parts of the rig such as the cyclone entrance.

3.5.2 The Laser Doppler Anemometer (General)

Laser Doppler anemometer (LDA) is the most suitable choice for the measurement of

separate components of both mean and fluctuating velocity. This type of measurement employs the phenomenon of Doppler shifting of light frequencies to measure the velocity of small particles (of the order of 1 micron) suspended in the fluid. For such small particles the measured particle velocity can be considerd for all practical purposes as the fluid velocity. The attraction of this method is that by being a purely optical method, it does not interfere or perturb the flow in any way since no measuring probes have to be introduced. Numerous improvements and developments have been reported on both optics and signal processing of laser Doppler systems since they first appeared in 1964 . Durst et al (1976) for example have discussed in great detail the principles, operation, capabilities and limitations of LDA systems. The basic theory and operating principles of LDA are shown in Appendix A.The most commonly used system is the single-channel forward-scatter fringe mode anemometer as used in the present investigation. The fringe type of optical system was shown to be the most suitable for water flow experiments by Wang and Snyder (1974) and Vlachos (1977), giving a better signal to noise ratio than other methods.

The optical equipment used in laser Doppler anemometery can be classified in two groups: transmitting optics and receiving optics. The transmitting optics cosists of, beside the laser itself, a beam splitter unit and a focussing lens to provide the beam intersection volume (or control volume) and the receiving optics comprises a collecting lens and a photodetector.The resulting signal may be processed by either a frequency counter or frequency tracking demodulator, depending on the nature of the experiment. Other processing instruments are occasionally preferable.

3.5.3 Present LDA Arrangement

The light source was a 5 mW He-Ne laser (Spectra Physics 120) with 632.5 nm wavelength and 0.65 mm unfocused beam diameter at the $1/e^2$ intensity level, diverging by 1.7 millisteradians.An integrated optical unit was used to provide the intersecting beams. The two beams were of equal intensity, had a fixed separation of 48.5 mm, and were symmetrical to the axis of the incoming laser beam. The focusing lens was a plano-convex lens of 100 mm diameter and 150 mm focal length, designed to avoid spherical abberation.The receiving optics consisted of a plano-convex lens of 200 mm focal length which focused the image of the measuring volume onto a pinhole (0.4 mm diameter) on

the front face of the photodetector. The lens produced an optical magnification of the control volume of around 2.5 .

The photodetector used was an EMI 9558 photomultiplier, with wavelength range 320-850 nm. The power supply was a V.G. Electronics Ltd. model M2.5K1 which delivered 100-2500 V at 5 mA according to the need specified by the flow condition and the clarity of the signal.In this investigation, a frequency tracking demodulator was used (Cambridge Consultants model CC08). The tracker output signal was also monitored on an oscilloscope (Hitachi V302) so that the signal drop-out and input gain settings could be adjusted for minimum noise. The mean and r.m.s. velocity fluctuations were visually monitored using a DISA 55D35 r.m.s unit and a DISA 55D31 mean value unit, before entering the computerised data acqusition system. They were used as a cross-reference point to the digital system any time a spurious result or reading was encountered. Fig 3.29 show photographs of the complete LDA system.

3.5.4 Mechanical-Optical Arrangement of Present LDA System

All the optical components of the laser system, from the laser on one end to the photomultiplier on the other end, were mounted on a purpose-built optical bench, shown in Fig. 3.29a. The beam splitter, the focusing lens, the collecting lens and the photomultiplier were mounted on a steel beam of triangular cross-section, and approximately 1.5 m in length, which ensured easy alignment of the optics. The laser itself was mounted on a specially-made aluminium table. This table provided the laser with movements in the x and z directions as well as with rotations about the z and y axis as shown in Fig. 3.28 . The laser table and the steel beam were fixed on a steel frame which provided enough space internally for the one cell rig, between the transmitting and recieving optics. All this structure was mounted on a milling table by means of a scissor-jack mechanism with linear roller bearings. The scissors-jack provided the vertical (z-direction) movement, while the milling table provided the horizontal x and y direction movements. The introduction of the laser table to the existing optical bench (Sabzvari 1984 and Leoutsakos 1987) reduced the time for alignment of the laser optics to a few minutes instead of hours.

3.5.5 Malvern Particle Sizing System

The measurement of the size distribution of aerosols is an important parameter in industrial technology . Before advent of commercial laser diffraction instruments in 1977, particle sizing was often a time consuming, tedious task dependent on operator skill and requiring repeated calibration. A variety of particle sizing techniques are available (Allen 1975, Weiner 1979). The measurement of particle sizes by use of the laser diffraction technique has become widespread in recent years. This is due to speed, versatility and simplicity of the method coupled with its non-intrusive nature. In most cases, powders can be poured, dry blown, or suspended in liquid and simply passed through an analyser beam to make a measurement. Complete particle size distributions can be obtained from measurement through computation to printed results in under five minutes.

The Malvern 2600 particle sizer is based on the principle of laser diffraction, described by Swithenbank et al. (1976). The basic optical experiment is shown diagrammatically in Fig. 3.30. The light from a low power Helium-Neon laser is used to form a collimated and mono-chromatic beam of light, typically 1 cm in diameter. This beam of light is known as the analyser beam and any particles present within it will scatter this laser light. The particles are introduced to the analyser beam by the particle feeding system through the measurement area. When a beam of light falls on to a particle, a diffraction pattern is formed whereby some of the light is diffracted by an amount dependent upon the size of the particle (Fig. 3.31).

The light scattered by the particles and the unscattered remainder are incident on a receiver lens, also known as the range lens. This operates as a Fourier transform lens forming the far-field diffraction pattern of the scattered light at its focal plane. A detector, in the form of a series of 31 concentric annular rings, gathers the scattered light energy over a range of solid angles of scatter.The unscattered light is brought to a focus on the detector and passes through a small aperture in the detector and out of the optical system. The total laser power passing out of the system in this way is monitored as it allows the sample volume concentration to be determined.The range lens configuration has the interesting and useful property that wherever the particle is in the analyser beam its diffraction pattern is stationary and centred on the range lens optical axis. This is shown

diagrammatically by Fig. 3.32. In practise many particles are simultaneously present in the analyser beam and the scattered light measured on the detector is the sum of all individual patterns overlaid on the central axis. Thus the system inherently measures the integral scattering from all particles present in the beam. In a typical experiment the number of particles needed in the beam simultaneously to obtain an adequate measurement of the scattering would be 100-10000 (Malvern Instruments Ltd., 1985).

As material flows through the beam, the measured light scattering is continuously changing to give the instantaneous integral of the material illuminated by the analyser beam. By making many measurements of the detector readings (a sweep) and averaging over many such sweeps of the detector it is possible to build up an average light scattering characteristic based on millions of individual particles. The over-whelming advantage of laser diffraction over particle counting techniques is that because each sweep measures many 100's or 1000's of particles it does not take long to build up acceptable measurements, typically only 5 seconds.

The detector thus provides an electronic output signal proportional to the light energy measured over 31 separate solid angles of collection. The computer reads this signal and performs the time averaging by successively reading the detector over a period of time set by the user, and summing the data. Over the size range of interest, typically 1 μm and upwards, the scattering with angle is independent of the optical properties of the material or the medium of suspension. Thus it is possible for the computer to deduce the volume size distribution that gives rise to the observed scattering characteristics. It achieves this by a process of constrained least squares fitting of theoretical scattering characteristics to the observed data. It is normal to allow the best fit result to be obtained with no assumed form of size distribution and this allows the characterisation of multi-modal distribusions with high resolution. By iterative use of an algorithm for minimizing the difference between measured and calculated (from an assumed distribution) angular distribution of scattered light energy, it produces an approximation to the distribution of projected-area particle diameter. This is known as the model-independent mode of operation, but to the author's knowledge the manufacturers have never revealed details of the computational procedure for this mode. In some instances however it is possible to constrain the analysis by asking the computer to assume the distribution has a known form, such as Rosin-Rammler or Log-Normal in volume. The results may then be compared directly

with any data from other measurement techniques, or more easily subjected to subsequent calculations.

Fig. 3.33 shows the Malvern particle sizer, comprising a small, safe laser transmitter mounted at one end of a rigid aluminium beam. At the opposite end of the beam the detector, lens and electronics are contained in a suitable housing (the reciever unit). Transmitter and receiver are typically separated by approximately 60 cm. The Malvern PS64 dry powder feeder (Malvern Instrument Ltd., 1985) mounts directly on to the optical bench. The powder sample is placed into a vibrating hopper from which it passes into the feed mechanism (Fig. 3.34). Here, large, loose aggregates are gently broken up and the feed rate is regulated as the powder is introduced into a shearing air flow. Smaller agglomerates are broken down and the fast moving powder flow is then decelerated and presented via an orifice to the analyser beam. The powder then exhausts into a vacuum cleaner. All measurement functions are automatic and results are computed in the micro-computer (in this case an Olivetti M24) and presented on the monitor display in both numerical and histogram form, together with hard copy for long-term retention of results.

3.5.6 Flow Measurement

Orifice, rotameter and traversing pitot tube were used for flow measurement. The specification of the orifice was according to B.S-1042 (1983). Many traversing pitot tubes were designed and manufactured for cell and rig flow rate measurement. For design of pitot tubes, the following restrictions were taken into consideration (B.S.-1042, 1983 and B.S.-893, 1978)

1- Bulk velocity head should be more than 10 N/m^2

2- The length of pitot tube head is generally between 15 and 25 times the pitot tube diameter

3- The ratio (d_{pitot}/D_{pipe}) of pitot tube should not exceed 0.02

4- The velocity at each measuring point was calculated from following formula (B.S.-1042, 1983)

$$V = \alpha\,(1-\varepsilon).\sqrt{\frac{2\,\Delta P}{\rho}} \qquad (3.1)$$

where α is the calibration factor of the pitot tube and

$$(1-\varepsilon) = \left[1 - \frac{1}{2\gamma}\,\frac{\Delta P}{\rho} + \frac{\gamma-1}{6\gamma^2}\left(\frac{\Delta P}{P}\right)^2\right]^{1/2} \qquad (3.2)$$

For cell flow rate, more than ten measurements (equi-interval) were made across each traverse line, and the flow out of each cell was calculated by using numerical integration as specified in B.S.-1042, but averaging the four data values at each radial co-ordinate. For this method, the boundary coefficient (as defined in B.S.-1042) was calculated from experimental data.

A suitable traversing pitot tube system which was able to measure stagnation pressure at three different horizontal planes in the 450*180 mm inlet duct was designed and manufactured. Also corresponding static pressure was averaged from 8 tappings round the walls of the multicell unit inlet duct, 10 mm from the multicell test section flange. A digital micromanometer and microcomputer-based data processing system was adapted for this study and Fig. 3.35 shows a schematic of this system.

3.6 FLOW VISUALIZATION

3.6.1 Smoke Technique

Flow visualization is one of the important methods in experimental fluid mechanics for providing an initial understanding of the physics of a flow problem. The popular method for air flow visualization is smoke (Merzkirch 1982 and Asanuma 1977). This technique was used for inlet and outlet ducts visualization. Fig. 3.36 shows this system which consists of a blowing fan, control valve, evaporator, mixing chamber, paraffin tank, etc. Ordinary paraffin was used for generating smoke. Many kinds of smoke distributor were designed and manufactured. The intensity of smoke was regulated by

the control valve. This system is able to generate sufficient white smoke for about two hours testing.

3.6.2 Smoke-Wire Technique

The smoke generator was not suitable for hopper investigation, because it affected the vacuum and flow structure in the hopper. The smoke-wire system was chosen for hopper visualization and a suitable system was designed and manufactured.The smoke wire is heated by passage of an electrical pulse through the wire, and evaporates paraffin for about 100 ms. The intensity and duration of the pulse is varied by the voltage and capacitance, so it was necessary to calculate C (capacitance) and E (voltage) of the pulse generation system.The maximum temperature of the wire is approximately given by following formula (Torii 1982).

$$(T_w - T)_{max} = \frac{2}{\pi} \cdot \frac{C}{\rho c} \cdot \frac{E^2}{Ld^2} \cdot \left[1 - \frac{\tau}{2\Delta t} \left(1 + \mathrm{Ln} \frac{2\Delta t}{\tau}\right) \right]$$

$$\approx \frac{2}{\pi} \cdot \frac{C}{\rho c} \cdot \frac{E^2}{Ld^2} \quad \text{for } \Delta t >> \tau = RC \qquad (3.3)$$

ρ, c, L, d and R represent the density, heat capacity, length, diameter and electrical resistance of the wire respectively. Nichrome wire (60% Ni, 16% Cr, 24% Fe) was chosen for this system (Yamada and Matsui,1982). The smoke-wire diameters used by Torii (1986), Yamada and Matsui (1982), etc. varied between 40 mμ and 1 mm. For the present work, this diameter was chosen as 0.125 mm. Fig. 3.37a shows a circuit diagram of the smoke-wire system which consists of variable transformer, rectifier, capacitor and switch. The capacitance of the capacitor was chosen as 1500 μF and it was possible to change the voltage in order to use different lengths of wire. For hopper visualization the length of wire was chosen as 75 mm. From equation(3.3) the system voltage was calculated as 70 V.

The special smoke-wire probe was designed and manufactured from hypodermic tube (Fig. 3.37b). The paraffin was injected (from outside the hopper, Fig. 3.37c) into the probe from a syringe and passed through the hypodermic to coat the smoke-wire for

the next smoke pulse. This system was manufactured and successfully commisioned.

3.6.3 Photography Technique

By taking photographs a permanent record of flow patterns inside the cyclone were obtained. A Minolta XG-M camera with motor drive (3.5 frame per second) and automatic flash (Vivitar auto thyristor 28.3 photoflash) were used for this purpose. Black and white Ilford HP5 ISO 400 film was used which was developed with Kodak D76 by the author. Cross sectional visualization could be observed and photographed by introducing planes of light at right angles to the top and front surface of the multicell outlet duct. The planes of light were introduced by shining a slide projector lamp onto black polystyrene sheets with appropriate slits cut in them (1.5 mm width). The arrangement for this case is shown in Fig. 3.38. The camera with motor drive was used for photography of flow patterns inside the multicell cyclone inlet duct. This method was also used for photography of smoke generated by the smoke-wire inside the hopper. The arrangement for hopper photography is shown in Fig. 3.39.

3.7 DATA ACQUISITION AND PROCESSING

3.7.1 Introduction

Data acqusition and processing was done using an Apple II+ microcomputer coupled to the LDA system or digital micromanometer, via a 12-bit fast A/D converter. Sampling at up to 4 kHz, and subsequent processing for evaluation of mean and r.m.s. and related quantities using machine code routines, provided an accurate, reliable, versatile and easy to use data acquisition system. This system had been developed by Leoutsakos (1987).

3.7.2 System Description

A schematic representation of the equipment and the data acquisition system is shown in Fig. 3.40 . The main units of the data acquisition system were as follows:

Main Microcomputer

The Apple II+ has 64K of memory, 48K being random access memory (RAM), available for program and data storage. Programming is done in Applesoft BASIC or 6502 machine code. Interfacing to peripheral devices is done through a row of light peripheral connectors (slots) at the back of the printed circuit board. A twin disk drive, a Silent type printer,a 12" monochrome monitor, an A/D converter, and an RS232 serial interface card comprised the available peripherals.

A/D Converter

This was a Tecmar Inc. AD211 model. The standard resolution was 12 bits, and the conversion rate was 30 kHz . The A/D comprised two printed circuit boards, the "mother" board and the " daughter" board. The mother board contained entirely digital logic and was plugged directly into the Apple bus. The daughter board contained all the analogue circuitry and is designed to be external to the Apple, a feature which allows the daughter board to be located nearer the source of the signals being acquired, and also away from the digital noise of the Apple bus. A 50-line ribbon cable connected the two boards.

Graphics Microcomputer

Lacking a suitable graphics facility on the Apple, a standard 32K BBC 'B' micro with a disk drive, a monitor and an Epson FX-80 printer (for screen dump) was used for on-line graphics. The reason for doing so was to save time and effort by allowing immediate repetition of measurements giving unexpected results until their validity was established. It was connected to the Apple through the RS232 serial interface card, via its own RS423 serial interface. Once the Apple evaluated the mean and r.m.s. values at a certain location, then these two values would be transmitted to BBC micro and be instantly plotted on the screen. At the end of a set of points, the graph was screen-dumped on to paper. This system had been tested and its validity, accuracy and reliability proved by Leoutsakos (1987).

3.7.3 Software Development

For each measuring system (LDA and micromanometer), new software (for Apple and BBC computers) was developed and employed. These modifications were mainly done in the BASIC parts of the programs. Here a brief description of the modifications is reported.

LDA System

The main object of using the LDA system was to measure three components of velocity at any arbitary point inside the cyclone. Therefore as already mentioned a special laser table was re-designed and constructed to move in three (x,y,z) directions with acceptable accuracy ($\pm$ 0.05 mm). Fig. 3.42 shows the exact positions of grid points which were used in the numerical model. It was decided to measure three components of velocity at these same points, to compare with numerical values. Therefore it was necessary to move and place the laser intersection volume correctly at these positions. The relationship between the positions of the laser intersection volume and the laser table movement have been incorporated in a program described in Appendix B. This gave a series of data such as laser beam crossing half-angle and laser table position for each grid point. By using these data and also other information such as rig flow rate, cyclone geometry, etc., three separate programs (for Apple) were developed for measuring u, v and w velocity components. For preventing any error in setting laser intersection volume position, after reading each point, these programs were able to calculate and display the amount of laser table movement needed for the next point. Also for data processing purposes on a main frame (CDC), some ancillary programs were written for transfering data from Apple to BBC and then to CDC computers (using the Kermit file transfer protocol).

Pitot Tube System

A Furness Controls FC012 digital micromanometer was calibrated to transfer the pressure signal to the A/D converter; new software for this purpose was developed for Apple and BBC computers.

3.8 MEASUREMENT PROCEDURE

3.8.1 Efficiency Tests Procedure in Multicell Cyclone

Many sizes of polythene bags were used for dust handling purposes. A Sartorius balance with $\pm$ 0.01 g accuracy was used for weighing empty and dust-containing bags. A Nilfisk industrial vacuum cleaner with a smooth bore hose was used for collecting sediment dust and multicell cyclone hopper dust; the nozzle hose and bag filter unit of the vacuum cleaner were cleaned before each test, and a new, weighed filter bag was loaded. When all dust appeared to have been collected by the vacuum cleaner, sediment dust inside the cleaner hose and joints was moved toward the filter bag by shaking, rapping and continued suction. Afterwards, the filter was carefully removed and put inside a previously weighed plastic bag. Before performing each efficiency test, the following conditions were established.

1- Piping system before cyclone, feeding system, cyclone hopper, sampling systems, pitot tubes, etc. were cleaned by compressed air or vacuum cleaner.
2- All connections (flanges) and unused measuring holes were blocked and sealed by silicone rubber or adhesive tape.
3- Cyclone inlet velocity profile was checked and reoptimized by adjusting the fin which helped to prevent transistory stall inside the diffuser.
4- Multicell cyclone rig was run for warming-up purposes for at least one and a half hours before each efficiency test, to establish steady conditions, especially for laboratory temperature, multicell cyclone hopper vacuum and fan performace (hence rig flow rate).
5- Laboratory humidity and air temperature were measured.
6- Rig flow rate was measured by traversing pitot static tube(that belonging to the sampling system after the cyclone) connected to the digital micromanometer and data acquisition system. Compressed air flow to the sediment dispersal system was measured by a 13 mm dia. orifice plate which used a high pressure duty mercury manometer.
7- Feeding dust was weighed and loaded into the feeder hopper.
8- Filter case and filter paper were weighed and installed. The weight of case and paper were around 150 g and 2.7 g respectively
9- Air velocity inside the sampling pipe was measured and then sampling flow rate was calculated from the following formula:

$$Q_s = C.V_c.A_n \qquad (3.4)$$

where V_c is air velocity measured by pitot tube, A_n is nozzle area and C is the new proposed correction factor (see section 4.4.1). By opening the sampling system control valves, the required sampling flow rate was fixed.

After the above preparations, the particle feeding system was run for 7-12 minutes (depending on the sampling system performance). During an efficiency test, the sampling flow rate was controlled and maintained at a fixed rate (by progressively opening the sampling system control valves to counteract the increasing filter pressure drop due to blockage. After finishing each efficiency test, the remaining feeding mass, sediment mass (inside piping and ducts before cyclone) and hopper mass were collected and weighed. Also the sampling system filter paper and case were removed and weighed. All results were recorded on test log-sheets for efficiency calculation. All samples were labeled for size distribution measurements, to be used for grade efficiency calculation.The measurement procedure was, as far as possible, the same for all efficiency tests. For minimizing the effects of air humidity and temperature on efficiency results, at least three tests were done during a single day for each multicell cyclone configuration. For operator safety, a battery-powered filtering helmet (Airstream Dustmaster Co.) was worn during efficiency tests.

3.8.2 Efficiency Tests Procedure in One-Cell Cyclone

The one-cell rig was smaller and simpler than the multicell cyclone rig, therefore a simpler procedure was used for performing efficiency tests. The conditions of the tests (such as flow stability, system leakage, cleaning, etc) were maintained as in the multicell cyclone procedure. Before each efficiency test, measurements such as air temperature and humidity, feeding mass, etc., were performed. For increasing measurement accuracy and eliminating the role of the vacuum cleaner, the cyclone hopper itself was weighed before and after each efficiency test; also the test duration was increased to 20-30 minutes. Periodically during a test, sediment mass inside the cyclone inlet duct was removed by knocking. Sampling system flow rate was maintained at 400 l/min by using the sampling system control valve. An orifice plate (41 mm dia.) plus the

micromanometer were used for rig flow measurement. The test procedure for all of efficiency tests was the same and at least three tests were done in a single day for each cyclone configuration.

3.8.3 Aerodynamic Tests Procedure in Multicell Cyclone

Smoke visualization inside the inlet and outlet manifolds, dust hopper circulation investigation, cyclone pressure drop measurement, cell flow rate measurement and cyclone inlet flow pattern investigation were the major aerodynamic tests done on the multicell cyclone rig. A brief description of test procedures is reported here:

Smoke Visualization Inside Inlet Manifold

The smoke generator was used for this purpose. A smoke distributor with 20 equi-spaced holes (2.5 mm dia.) was positioned at the cyclone inlet manifold entrance, perpendicular to the entry air flow direction. The smoke was produced in parallel lines to follow the flow streamlines. It was impossible to visualize the flow pattern at high flow rates mainly because of the low concentration and high diffusivity of smoke under these conditions, thus all visualization was done at approximately 10% of the efficiency-test flow rate (for studying the structure of complex flows, it is common to use lower Reynolds numbers but the possibility of some error in the results is mentioned by Bradshaw (1971). Using a high speed camera from the top and side of the cyclone manifold, many pictures were taken of the formation of wakes, vortex and secondary flows.

Smoke Visualization Inside Outlet Manifold

The smoke generator system was used and again the rig flow rate was about 10% of the efficiency-test flow rate. By introducing planes of light at right angles to the top and front of the multicell cyclone outlet manifold, the flow patterns at different places were observed and captured by photography. Fig. 3.38 shows the general arrangement of camera and projector and how the planes of light were generated.

Hopper Circulation Study

The smoke-wire system was used for this study. The bouyancy effect, checked in still air, was of much shorter duration than the useful viewing time of the smoke-line, and did not significantly influence the subsequent movement of the smoke. When the rig was running at the 0.218 m^3/s efficiency test flow rate, by putting the smoke-wire in different parts of the dust hopper (especially under cell exits), the direction of flows was observed and recorded.

Cyclone Pressure Drop Measurement

Cyclone pressure drop was measured for a range of rig flow rates. Static pressure was averaged from eight tappings round the walls of the multicell unit inlet and exit ducts, in each case 10 mm from the multicell test section flanges where the duct cross-section was 450*180 mm. The difference Δp between the inlet and exit averaged static pressure then represented the cyclone pressure drop, without requiring any correction for difference in dynamic pressure.

Cells Flow Rate Measurement

Because of technical problems, direct measurement of an individual cell flow rate was impossible; for example, obtaining the axial-velocity component in a strongly swirling flow inside the vortex finder tube would have been a difficult task (Lea and Price, 1974 and Shin and Hu, 1985) which proved not to be possible within the time scale of this investigation. Therefore it was necessary for estimating cell flow rates to suppress the swirl in order to use a combination of pitot tube and wall static tapping. Honeycomb flow straighteners were therefore inserted temporarily in the lower part of each outlet tube. The new roof was designed and manufactured which has nine cross-shaped slots (sealed in normal use) to allow traversing of exit (one diameter (50 mm) below its exit) from individual cells using a pitot tube. Local static pressure (from tapping) was also measured,to interpret the pitot data as velocity and hence to integrate over the outlet tube cross-section to obtain cell exit flow rate. At rig flow rate 0.218 m^3/s pitot tube traverses were made across two perpendicular diametral lines of each clean gas outlet tube. Measurement at each probe position was taken over a period of 1-2 minutes

in order to average out the effects of any low-frequency flow unsteadiness. The digital micromanometer plus data acquisition system was used during these tests.

Cyclone Inlet Flow Pattern Investigation

For many multicell cyclone upstream piping system configurations (Fig. 3.6), cyclone inlet velocity profile at heights of 45, 90 and 135 mm have been measured by traversing pitot tube.

3.8.4 Hydrodynamic Tests Procedure in Water-Rig Cyclone

Tangential, radial and axial velocity at the grid points shown in Fig. 3.42 have been measured by LDA system for rig flow rates of 70 l/min, 100 l/min (nearly same Reynolds number as for efficiency tests) and 200 l/min (Reynolds number matching). During tests, rig flow rate and water temperature (at 20 ^{o}C) were maintained constant. All tests were performed under nearly dark conditions. For strengthening the Doppler burst signals, a drop of milk was sometimes injected into the water circuit. For each point measurement, nearly 40000 samples with sampling rate 4 kHz were collected and averaged by the data acquisition system. The laser beam had to pass from air through the side walls of the cyclone into water, thus undergoing a series of refractions due to the changes in refractive indicies. A computer program (on main frame) was written to calculate the exact position of the laser intersection volume against laser table position (described in Appendix-B). The results were used for setting the intersection volume at the measuring points.

The plane of laser beams for measuring tangential and radial velocity was horizontal. For measuring axial velocity component, the beam splitter was turned through 90^{o}, which put the plane of the laser beams in a vertical position.For measurement of u, v or w, the direction of laser table movement and intersection volume fringe orientation are shown in Fig. 3.41. It is necessary to mention that because of the cyclone's cylindrical body, the laser beam refraction differed during measurments of u, v and w and this problem was accounted for in the computer program. All the above tests were done at a fixed diametral plane of measurement which passed through the middle of a passage

between two swirl vane trailing edges(described as θ=0 see also Fig. 4.3). By turning the cyclone body on its axis, thus varying θ, a series of u, v and w velocity measurements at 150 l/min were made especially for grid points near the vanes. With these tests the effect of vane wakes on the cyclone flow structure was investigated. Finally cyclone pressure drop was measured for many different rig flow rates.

3.8.5 Particle Size Distribution Tests Procedure

The principal instrument for dust sizing was a Malvern 2600 laser diffraction particle size analyzer. It was hoped to use this on-line during rig operation, but the fineness of Syenex-40 test dust required the selection of a receiver lens (63 mm focal length) which would not have allowed the entire pipe section diameter to be within its measurement range. Off-line sizing of collected samples was therefore used, the samples being re-dispersed in air by a Malvern dry powder feeder accessory which operates in almost the same way as the rig's dust feeder. This was preferred to sizing the samples in liquid dispersions, following experience of time-varying size distribution of fuller's earth in water or alcohol (Crane and Behrouzi 1987); confidence in this procedure was obtained by comparing the measured size distibution of a feed dust sample from the vibrating feeder's hopper and a dirty-gas sample collected from rig's upstream sampling nozzle (Fig. 4.55). It appears that any agglomerates formed in the sampling system are adequately broken down in the Malvern's feeding system. During each efficiency test on the multicell rig, dust was collected at five different places (feeder, inlet duct, hopper and two sampling systems). After weighing, a dust cake on the sampling filter was gently removed by brush and shaking, taking care not to contaminate the sample with any of the filter material. Enough dust from each sample was gathered and put inside sealed, labeled plastic bags. The same procedure was used for collecting dust in the one-cell rig.

The Malvern Master Sizer V.4.3 software includes a programming facility for automating the desired sequence of operations. This was used to good effect in the present work, allowing measurement of the background light intensity (for subtraction from the scattered light) and the sample scattering, saving the scattered intensity distribution, calculation of the size distribution and display of results in a continuous operation. Screen prompts were issued to indicate readiness for each stage, which was initiated simply by pressing the computer keyboard's space bar (or activating the powder

feeder); measurements could therefore be carried out in almost total darkness, the optimum condition for a light scattering technique.

15 psig compressed air and a vacuum cleaner were connected to the dust feeder. By controlling the feeder tray gate, the system was optimized and fixed to disperse enough dust (Syenex-40) for normal laser light obscuration. This optimization procedure was also done for Pozzolan and fuller's earth. The 63 mm lens and the Rosin-Rammler size distribution model were chosen and all tests were performed according to manufacturer's recommendations (Malvern Instruments Ltd. 1985). Before using a new sample, all relevant parts of the dust feeder, such as tray and nozzle were cleaned. From each sample, at least two size analysis tests were done.

3.8.6 Particle Density Measurement Procedure

A simple method was used to measure particle material density. A volume V_1 of water was poured into an empty beaker of mass M_0 using a burette; then a considerable amount of powder was mixed and stirred in, and the volume V_2 of the mixture and total weight M_2 were measured. Particle material density ρ_p was calculated as:

$$\rho_P = \frac{(M_2 - M_0) - \rho_w V_1}{V_2 - V_1} \qquad (3.5)$$

where ρ_w is the density of water. Three density tests were done for syenex-40, Pozzolan, fuller's earth dusts, etc. The average values of particle material density were calculated as 2445, 1969, 1938 and 1450 kg/m^3 for Syenex-40, Pozzolan, fuller's earth and Marden bag filter dusts respectively.

3.8.7 Error Analysis and Accuracy of Measurement

I- Flow Measurement

One-cell air rig flow rate and sediment dispersal air flow rate for the multicell cyclone were measured by orifice plates 41.3 mm dia. and 12.7 mm dia. respectively. The accuracy of flow measurement was estimated as ±2% and ±5% respectively. One-cell

water rig flow rate and sampling systems flow rate were measured by rotameter. Rotameter ranges 250, 200 and 500 l/min were used for the one-cell water rig, the sampling system before and sampling after the cyclone respectively. The accuracy of rotameter readings were ±2 l/min.

Multicell cyclone rig flow rate and cell flow rate of multicell cyclone were measured by traversing pitot tube. This method was affected by errors in positioning of pitot tube, accuracy of test section construction, data acqusition system, calculation procedure, static pressure location (for cells flow measurement), etc. The main source of error in pitot tube positioning was the uncertainty of the wall reference position. The maximum error was estimated as ±0.5 mm including errors from the traversing mechanism. The construction accuracy of slots and vortex finder tube (cells flow measurement) and sampling pipe (rig flow measurement) were within ±0.5 mm and ±1 mm respectively. The uncertainty from the digital micromanometer and data processing system has been estimated as around ±0.2 m/s. Flow calculation was the last important source of error. By dividing the pipe area into many concentric circles and then multiplying by the corresponding velocity, pipe flow rate is estimated to have been calculated to ±2%.The maximum uncertainties for pipe (or rig) flow rate from pitot tube traversing have been estimated as ±3.5%.

II- Mass Efficiency

Cyclone efficiency results were affected directly by errors in dust handling, dust collection, dust weighing, isokinetic sampling, rig flow rate, etc; and indirectly by some uncontrollable effects such as humidity (in air and feed mass), dust carry-over, dust agglomeration, dust sediment inside cyclone inlet and outlet manifolds, change in feed mass size distribution, etc. These sources of error are explained briefly here.

Uncertainties due to dust handling are estimated to be ±2 g, ±0.05 g, ±3 g and ±4 g for feed mass, sampling systems,upstream piping system and downstream piping system respectively, which in total is nearly equal to ±1% of the feed mass in to the cyclone (one cell or multicell). The vacuum cleaner was used for collecting hopper dust and sediment dust in the multicell cyclone rig. Allowing for hose cleaning before collecting new dust and after removing the bag filter, this method of collecting had an

estimated uncertainty equal to ±5 g which gave errors of ±0.5% and ±0.2% of feed mass for collected hopper mass and sediment mass respectively.The Sartorious digital balance used for weighing dust had an accuracy of ±0.01g (up to 2 kg), therefore errors in weighing feed mass, hopper mass and sediment mass were negligible but uncertainties in sampling systems mass were estimated as ±1% of sample mass. In the isokinetic sampling systems, filter pressure drop continuously increased with time (because of dust capture), so the sampling flow rate was maintained constant manually during efficiency tests. The sampling flow rate variation was ±0.1 l/min and ±2 l/min for sampling systems before and after the cyclone; these resulted in ±1% and ±0.5% uncertainties in sample mass before and after the cyclone respectively. Without allowing for other sources of error it was estimated that the above errors cause uncertainties equal to ±1% and ±2% in dust collection efficiency of one cell cyclone and multicell cyclone respectively (Kline and McClintock, 1953)

The most important source of error in cyclone efficiency which were unavoidable and uncontrollable and indirectly affecting cyclone performance were physical phenomena such as humidity (in air, compressed air used for sediment dispersal and feed mass), and agglomeration or break-up. In general agglomeration and particle break-up inside cyclone manifold and cells increase or decrease cyclone efficiency respectively. These are random and unpredictable phenomena and increase cyclone efficiency uncertainties, espicially in short-time tests (like the present tests). Because of the multicell cyclone design, using a stepped tube plate, inlet and outlet manifolds have many dead zones (corners,etc.) and surfaces suitable for settling particles. After several efficiency tests, heaps of dust (some of them up to 20 mm in height) had been formed in these areas and because of flow unsteadiness and turbulence, these heaps were broken up and dust re-entered the flow during a subsequent test (which was ignored for averaging purposes). This phenomenon (intermittent particle carry-over) also was unpredictable and uncontrollable and increased efficiency errors in the sense that the reported efficiencies are not long-term average values including many intermittent break-up events.

By experiment it was found that the uncertainty in feed mass median diameter was ±0.5 μm which indirectly increased the mass efficiency uncertainty. The laboratory air

temperature and humidity were measured during efficiency tests. In general all tests were done at air temperature 20 $^{o}C \pm 4\ ^{o}C$ and humidity of 55% ±10. Humidity is one of the most important parameters which directly affects particle behaviour in cyclone. It increase particles stickiness and van der Waals force, which may cause more agglomeration and particle sediment inside the cyclone. It is obvious that change in air humidity increases uncertainties in cyclone mass and grade efficiency. In industrial boiler cyclones, this effect would be dependent on excess air, coal moisture content etc.

The above discussion shows that because of the nature of the tests and limitation on test duration time (due to hopper space, sampling system pressure drop, etc.), the particle phase was in semi-steady condition and it was impossible to estimate the total uncertainty in cyclone efficiency. Therefore total efficiency uncertainties have been characterized experimentally by using multiple samples. Each efficiency test was repeated between three and six times in one day (to minimize humidity effects), and much care was taken to perform all tests in nearly fixed conditions. For minimizing effects of unobserved particle carry-over and other random phenomena, cyclone mass efficiency has been calculated by many methods. For example a test with high carry-over gives a high efficiency based on hopper mass and a low efficiency based on sampling system mass. Such results were monitored and allowed the test to be ignored and further repeat tests to be made. Finally, the average of the two " best" efficiency results have been chosen as a representive final result ("best" refers to a cluster of repeatable results which was almost always obtainable in addition to unrepeatable runs which may have been subject to dust carry over, etc. Sec. 4.4.1 provides further details.). The variation in mass efficiency over all valid representative tests with any one combination of cyclone configuration and test dust did not exceed ±3% and ±1.5% for multicell and one-cell cyclones respectively. In many cases, the variation was considerably less.

III- Particle Size Distribution

The accuracy and limitations of the Malvern particle size distribution analyser have been investigated by many researchers including Negus and Azzopardi (1978) and Seville et al (1984). Reports convey a mixed impression of the capability of laser diffraction instruments for sizing particulates in the range below about 3 μm, where the Fraunhofer diffraction approximation to Mie scattering theory breaks down and results

begin to depend on the refractive index and light absorbing properties of the particles. It should be pointed out that the present version of the Malvern (the model 2600) has a software correction for these effects, based on published error contours. Nevertheless, it would be unwise to rely on measurements below about 2 μm. According to Malvern Instruments Ltd. (1986), the system should have an accuracy of ±4% on volume median diameter for particle sizes between 0.5 μm and 564 μm.

IV- Velocity Measurement with LDA

The LDA measurements were affected by errors in positioning the beam intersection volume, the accuracy of the test section construction, setting the flow rate, variation in water temperature and hence water viscosity, electronic noise, incorrect optics alignment, and the broadening of the Doppler signal frequency spectrum (a result of the finite transit time of the particle through the measuring volume), the gradient in mean velocity, and the small scale turbulent fluctuations within the scattering volume. Each source of error will be taken in turn.

The main source of error in the intersection volume positioning was the uncertainty of the wall reference position. The maximum error was estimated at ±0.2 mm in the z direction and ±0.5 mm in x or y direction, including errors from the traversing mechanism. The construction accuracy of the cyclone body was within ±1 mm tolerance which is a 2% error in cyclone diameter. Therefore the maximum uncertainty for intersection volume position has been estimated about ±1.2 mm. The error in setting the desired flow was ±0.5 l/min which almost equals ±0.25% error in bulk velocity, provided that the rotameter manufacturer's specification is correct. The accuracy of the frequency tracker output is within ±1%. By combining all the errors it is deduced that the maximum errors in determining velocites are ±3%. It is considered however that the LDA measurements were of high quality and accuracy because of good optics alignment and the large number of scattering particles in the flow (by addition of milk to the water). The final source of experimental error was the variation in water temperature which in turn produced a variation in the kinematic viscosity of water. For this reason the water temperature was monitored very frequently using a digital thermocouple system (Copper/Copper-Nickel) and every effort was made to keep it constant (by the cooling system). The maximum variation in water temperature was ±0.2 C which is negligible.

The above errors with maximum ±3% uncertainty were expected for velocity measurement at all points shown in Fig. 3.42 except node points near the cyclone axis (N_j=1,2). Because of highly turbulent flow, air bubbles and the small values of the velocity components, measurement of velocities (u, v and w) at points near the axis are unavoidably subject to larger uncertainty. It is also necessary to mention that the LDA system was not capable of specifying the direction of velocity vectors, therefore axial velocity measurements have a large uncertainty inside the zone where axial velocity sharply changed its direction. For this reason two methods have been employed to assign the velocity direction. The first relies on knowing the physics of the flow and using the results of the numerical modelling. Secondly the r.m.s and mean axial velocity at each point have been measured simultaneously by the data acquisition system. In zones with change in axial velocity direction, a sharp gradient of r.m.s occured while the mean value remained nearly unchanged.

CHAPTER 4

EXPERIMENTAL RESULTS

4.1 INTRODUCTION

In this chapter the experimental results will be presented. The results of LDA measurement of three components of velocity and cyclone pressure drop are described in section 4.2. Section 4.3 explains the results of flow visualization inside the multicell cyclone inlet manifold, outlet manifold and hopper. Also inter-cell flow distribution results are explained in this section. Mass efficiency results from one-cell and multicell cyclones are dealt with in section 4.4. The results of particle size analysis and grade efficiency calculation for one-cell and multicell cyclones are presented in section 4.5. Finally cyclone modification techniques and mass and grade efficiency results for modified one-cell and multicell cyclones are described in section 4.6.

4.2 HYDRODYNAMIC RESULTS IN ONE-CELL CYCLONE WATER-RIG

4.2.1 Introductory Remarks

After commisioning the one-cell water rig, it was observed that air bubbles gathered at the cyclone axis, because of the low pressure (hydrocyclones frequently operate with an air core). This column of air, and any other region containing air bubbles, were not suitable for LDA measurement because of the lack of signal and increased noise level, hence inaccuracy of measurement. Therefore all joints and flanges were carefully sealed by silicone rubber. Also suitable baffles and honeycomb were installed inside the header tank for reducing flow flactuations and decreasing the possibility of entraining air into the system. Unfortunately because of sediment on the surface of the perspex (which decreases LDA signal quality), it was necessary to drain the water, take apart, clean, and reassemble the cyclone and re-commision the rig after each three days of testing. From experience it was found that after renewing the water, it was necessary to leave the system for at least 24 hours to get rid of nearly all

dissolved air, which was released through the header tank and vents. In general all tests were performed under steady conditions and constant temperature (20 ^{o}C) which required the rig to be run for over an hour before collecting results.

Theoretically the flow pattern inside the cyclone should be symmetric and therefore measuring the velocity profiles over a distance of one radius may be sufficient. For better understanding of complete flow pattern of vane-type cyclone and checking the symmetry, it was decided to measure a complete velocity profile across a full diameter. Fig.4.1 and 4.2 shows the on-line output from the BBC computer. The up-right triangular symbols are results relating to the half-diameter closest to the laser and transmitting optics while the inverted triangles show results of other half-diameter. It is obvious that the laser beam refraction in former half diameter is less than in the latter half (especially in vortex finder regions) and here for presentation and also comparing with theory, results from the former half-diameter were chosen. All velocity measurements were made on a fixed meridional plane which passed through the middle of a passage between two swirl vane trailing edges (described as θ=0, Fig. 4.3).

4.2.2 Cyclone Pressure Drop

Before measuring three components of velocity, cyclone pressure drop was investigated. For different rig flow rates from 10 to 210 l/min, cyclone static pressure drop was measured by water manometer with tappings located at P_1' and P_2' positions shown in Fig. 3.22.

The cyclone static pressure drop was measured as 4070 and 1050 Pa for 200 l/min ($\cong$ Re number matching) and 100 l/min respectively. Fig 4.5 shows the experimental results together with the prediction of the numerical model (CYCINT-1). Because of technical problems the location of experimental static tappings (P_1',P_2', Fig. 3.22) was different from the location used in the numerical model (P1,P2, Fig. 3.42), therefore vane pressure drop and inlet/outlet extra piping pressure drop are excluded from the numerical results. This may account for the experimental results being higher than the numerical prediction.

It is nearly impossible to measure the drop in total pressure through the cyclone. Some researchers tried to predict actual cyclone pressure drop using static pressure drop. For example measured static pressure difference were corrected by Dirgo and Leith (1985) to account for velocity pressure differences between the cyclone inlet and outlet.

$$\Delta P = \Delta P_S + V_{P_i} - V_{P_o} \tag{4.1}$$

Here Δp_s is the measure static pressure loss between inlet and outlet, V_{pi} and V_{po} are the inlet and outlet velocity pressure, and Δp is the corrected pressure drop. Therefore the difference between Δp_s and Δp is approximately calculated (using Bernoulli equation) as :

$$V_{P_i} - V_{P_o} = \frac{1}{2}\rho Q^2 \left[\frac{1}{A_i^2} - \frac{1}{A_o^2} \right] = -1.072 \times 10^8 \, Q^2 \tag{4.2}$$

With this method, for 200 l/min and 100 l/min flow rates, the difference between static and corrected cyclone pressure drop were calculated as 1191 and 297 Pa respectively. The accuracy of these measurements strongly depends on the degree of swirl inside the vortex finder tube. Fig 4.4 shows a schematic of static pressure profiles for a pipe with and without swirl. In highly swirling flow the difference between measured static pressure at the wall and average pressure is considerable, therefore to allow for the swirl effect we need another correction. Thus to indicate cyclone performance trends it seems that to rely on measured static pressure drop is more reasonable and practical than using a corrected one with low accuracy.

Although there are many empirical formulae for predicting cyclone pressure drop which are described in section 2.7, to the author's knowledge all were derived for tangential-entry cyclones and can not be adapted for vane-type cyclones (mainly because of inlet geometry) to check experimental results.

4.2.3 Axial Velocity Measurement (u)

The plane of laser beams and intersection volume fringes was alinged as in Fig. 3.41 (It is necessary to mention that observation of the secondary refractions/ reflections of the laser beam through the perspex walls was a very useful tool for this purpose). After establishing steady conditions (20 ^{o}C) at 200 l/min rig flow rate (nearly the Reynolds number matching flow rate), the laser system was aligned and optimized for receiving the best Doppler burst signal. Radial profiles of axial mean and r.m.s. velocity were measured at 12 axial stations situated at 5.8, 17.4, 29, 40.7, 52.3, 64, 76, 87.2, 98.8, 110.5, 122.1 and 133.7 mm (defined in Fig. 3.42 as grid lines 21 to 10 respectively) below the vane trailing edges, for the cylindrical body region. After some modification on the rig (because of the cyclone height problem), radial profiles of axial velocity for the conical region also were measured at three axial stations located at 219, 292 and 366 mm (defined as grid lines 7,5,3 respectively) below the vane trailing edges. All these tests were repeated for 100 l/min (the Reynolds number corresponding to the Stokes number matching flow in the air rig) and 70 l/min rig flow rate. To give a more compact presentation important results are presented in Fig. 4.6 to 4.9 (comparison with the computed results plotted in the same figures is discussed in sec. 4.2.7).

It is important to repeat that the present LDA system gave only the magnitude of mean velocity and could not specify flow direction. Therefore the measured r.m.s. velocity pattern, results from the numerical model (CYCINT-1) and the physics of swirl flow were used to predict flow direction. By studying the pattern of velocity profile and relative r.m.s., it is possible to predict the positions of changes in flow direction. For example in Fig. 4.1a, mean velocity has a uniform pattern in the region r=20 to 30 mm, but at the same place, r.m.s. velocity shows a trough which indicates a change of velocity direction in this region. Also by knowing the physics of the flow and results of the numerical model (CYCINT-1), the direction of flow in Fig. 4.1b was predicted and is shown.

Ignoring some scatter in the results (which may be caused by vane wakes), the axial velocity profiles for the region just below the vanes (Fig. 4.6 and 4.8) have a nearly flat pattern. There is a considerable change in axial velocity pattern inside the

vortex finder tube with axial direction and it seems that the uniformity is increasing with distance from the vortex finder inlet (grid lines 16 to 21). Fig. 4.7 and 4.9 show axial velocity profiles in the cyclone cylindrical part beneath the vortex finder tube. In this region axial velocity gently increases with decreasing radius until it reaches a maximum value (nearly 2 and 1 m/s for 200 and 100 l/min flow rate respectively) and then in the core region, axial velocity sharpy decreases with decreasing radius.

4.2.4 Radial Velocity Measurement (v)

The plane of laser beam and intersection volume fringe orientation was located as in Fig. 3.41 and radial profiles of radial mean and r.m.s. velocity were measured at six axial stations situated at 40.7, 52.3, 64, 76, 87.2 and 98.8 mm (defined in Fig. 3.42 as grid lines 18 to 13 respectively) below vane trailing edges. Because of negligible amount of radial velocity component for others grid lines, the scatter in the results was so great that no worthwhile comparision with theory could be made, therefore measuring radial velocity was useless and neglected. Bloor and Ingham (1985) also reported this difficulty for their measurements. All these tests were repeated for 100 l/min and 70 l/min flow rate. Results are presented in Fig. 4.10 and 4.11.

In general, only the region situated just underneath the vortex finder tube (grid lines 15 and 14, Fig. 3.42) is important in terms of radial velocity. The measured radial velocity shows a peak of 1 and 0.5 m/s for 200 and 100 m^3/s flow rate, exactly underneath the vortex finder tube wall. other grid lines near to line no. 15 show a small value for radial velocity.

4.2.5 Tangential Velocity Measurement (w)

After setting the plane of intersection volume fringe orientation as in Fig. 3.41, radial profiles of mean and r.m.s. tangential velocity on grid lines 21 to 10 (Fig. 3.42) were measured under steady conditions, for 70, 100, and 200 l/min rig flow rate. Also after some modification of the rig, profiles of mean and r.m.s. tangential velocity were measured at three axial stations located at 219, 292 and 369 mm below vane trailing edges, in the conical part. Fig 4.2 shows typical on-line results. Fortunately here only the magnitude of swirl velocity is important and there is no need to specify the direction

of velocity.

The important tangential velocity results are shown in Fig. 4.12 to 4.15. In the region just below the vanes, Fig. 4.12 and 4.14 show that there is no significant radial gradient of tangential velocity. Inside the vortex finder tube, a Rankine-type vortex structure can be observed, showing free vortex behaviour in the outer zone and forced vortex behaviour in the core zone. The maximum swirl velocity at the intersection of these two regions was nearly 2 and 1 m/s for 200 and 100 l/min flow rate respectively. Fig. 4.13 and 4.15 show profiles below the vortex finder. A twin Rankine-type vortex was established in this region. The swirl velocity increases with radius up to a maximum of nearly 3 and 1.5 m/s for 200 and 100 l/min flow rate respectively and then gently decreases with increasing radius. The diameter of core zone seems to be half of the vortex finder inner diameter or less.

4.2.6 Effect of Vanes on The Cyclone Flow Field

In theoretical models the effect of individual vanes on the cyclone flow structure can not be considered due to difficulties in inserting boundary conditions and the two-dimensionality of numerical models (cyclone flow field assumed to be axisymmetric). For this reason vanes are assumed to have an infinitesimal thickness, their only role being to create swirl at the inlet of the domain of solution. In all theoretical studies of cyclones (Bloor and Ingham 1973,Ter Linden 1949, Boysan et al. 1982, etc), to the author's knowledge, researchers neglected inlet effects, not only for vane-type cyclones but also the popular tangential type. Here an attempt was made to study experimentally the effect of vanes on axial and tangential components of velocity in the region underneath the vane trailing edges.

For five different angular positions (θ=22.5 ,11.25, 0.0 (the centre of a passage between two swirl vanes of their trailing edges, see also Fig. 4.3), -11.25 and -22.5 degrees), radial profiles of mean tangential and axial velocity component were measured, at four axial stations situated at 5.8, 17.4, 29, and 40.7 mm below the vane trailing edges. All tests were performed at a steady condition and the LDA system was optimized for the best Doppler burst signal.

The effect of change in angular position (θ variation) on the axial and tangential velocity profiles at a fixed height (corresponding to a numerical grid line) are shown in Fig. 4.16 and 4.17 respectively. Because of wakes created by the vanes, the experimental u vs r and w vs r curves are different, especially when the measuring line passes through the wake zone. For example in Fig. 4.16 and 4.17, for grid lines number 21, 19 a wake appears to have been encountered during measuring at θ=0.0 and 22.5 degrees respectively.

Also for better understanding, effect of change in axial location on axial and tangential velocity profiles at a fixed angular position (θ= constant) were plotted in Fig. 4.18 and 4.19 respectively. From these graphs it is obvious that the wakes created by vanes can be detected at a considerable distance below the vanes.

4.2.7 Discussion

The flow behaviour in a hydrocyclone is quite complex. Fluid enters through vanes and the initially linear motion is converted to angular motion. During steady operating conditions, the familiar double-vortex pattern is established, comprising an outer free vortex region and an inner forced vortex (Pericleous et al, 1984). In order to compare the experimental results with the corresponding theoretical prediction, two available mathematical models, SPRINT-4 and the new version of it (CYCINT-1 developed by the author) were used. These models need to use a staggered grid system (see Fig. 5.6), and by considering this fact and using interpolation, values of each variable at the measuring points have been calculated. The results are plotted with the experimental findings in Fig. 4.6 to 4.15.

In spite of some scatter in experimental results, mainly inside the core zone, good agreement has been obtained between experimental results and predictions, especially for the new version (CYCINT-1). It is clear that the general behaviour of the flow is accurately predicted by CYCINT-1. Considering the axial velocity profiles (Fig. 4.6 to 4.9), it is seen that a region of reverse flow is predicted on the cyclone axis, especially pronounced in the SPRINT-4 prediction. Although in a hydro cyclone this region would usually take the form of an air core (Boysan et al. 1982), this was not observed during the present experiments. The LDA results show nothing about this reverse

flow. However in the core zone the LDA results are uncertain mainly because of the existence of sharp velocity gradients compared with the size of the laser intersection volume (nearly 1.5 mm in the r-direction). Also because of uncertainties in laser alignment, the possibility of measuring a combination of all three velocity components was unavoidable near the cyclone axis. Other researchers such as Binark and Patel (1961) (using the hot-wire technique) were not able to measure correctly the components of velocity in the core zone. Biffin, et al. (1984) (using LDA) believed that periodic instability of the vortex core causes error in measurement. Boysan et al. (1982) agreed that numerical predictions of strong reverse flow in the core zone may be due to the sensitivity of the flow to the down stream boundary conditions; and Pericleous (1987) implies that it is the proximity of the conical wall in the lower part of the cone.

In highly swirling flow, correct prediction of the tangential velocity profiles is essential in order to reproduce the rest of gas flow field adequately. Fig. 4.12 to 4.15 show experimental findings and numerical predictions for tangential velocity profiles. The agreement between the measurement and predicted profiles (by CYCINT-1) is satisfactory in both magnitude and velocity pattern. The swirl increases linearly with radius up to a maximum at the boundary of the twin-vortex structure and a further increase in radius leads to a reduction in swirl to a minimum close to the wall. The maximum value of w is approximately three times the inlet tangential velocity.

Fig. 4.10 and 4.11 show the experimental data and numerical predictions for radial velocity profiles. Because of the negligible radial velocity for all grid lines except lines 14 to 16 and especially in the core zone, a comparison between computation and experiment is generally unhelpful. However for the important grid lines 15 and 16 just below the vortex finder, good agreement can be observed between experiment and the CYCINT-1 prediction. In the core zone, as with axial velocity, errors in the experimental method were considerable and unavoidable.

4.3 AERODYNAMIC RESULTS IN MULTICELL CYCLONE

4.3.1 Flow Distribution Between Cells

The only accessible location for measuring the cell flow rate in each of the nine cells was in the gas outlet (vortex finder) tubes, where the flow is axisymmetric and with negligible radial component but strong swirl. Techniques for isolating the axial velocity component in swirling flows can be complex and time-consuming (e.g. hot-wire anemometry with x-wires and two separate anenometer systems, as reported by Tutu and Chevray (1975); LDA would require less data processing but in present cyclone a large volume of air would have to be seeded and special optics might be necessary). Thus it was necessary for estimating cell flow rates to suppress the swirl in order to use a combination of pitot tube and wall static tapping. Honeycomb flow straigheners (one hexagonal cell per 1 cm^2 with 25 mm height) were therefore inserted temporarily in the lower part of each outlet tube while pitot traverses were made across two perpendicular diametral lines of each clean gas outlet tube, one diameter (50 mm) below its exit.

With maldistributed inlet flow from the unmodified bend and transition duct, as in Fig. 3.6a, the rig was run at 0.152, 0.284, 0.38 and 0.433 m^3/s flow rate and cell exit velocity profiles were measured. During tests, laboratory temperature and rig flow rate were monitored and controlled. The tests was repeated three times, to ensure repeatibility. Fig. 4.20 shows the results of cell velocity measurement at the above rig flow rates, while Fig. 4.21 explains the numbering scheme for cells and cell rows of the multicell cyclone. Asymmetric profiles were found in some cells. The cell flow rates calculated by integration of the velocities are shown in Fig. 4.23. The flow in each cell increases linearly with increasing multicell cyclone flow rate, and cells 1,2 and 3 (row 1) together, passed less flow than one third of the total (9-cells) flow rate while cells 7,8,9 passed more.The flow in the other cells (4, 5, and 6) was nearly equal to the average cell flow rate. By increasing multicell cyclone flow rate (from Stokes No. matching value to Reynolds No. matching value), the difference between cell flow rates also increased (Fig. 4.24). The maximum difference in cell flow rate (for Re No. matching) was 9% and was between cells No. 1 and 9.

The most important weakness of a multicell cyclone may be monitored with these tests. Unbalanced flow between cells may be created by bad inlet flow pattern, inlet manifold design, common hopper or unequal gas outlet tube length. For checking the effect of inlet flow pattern on cell flow distribution, the rig upstream piping was replaced by a parallel duct with bell- mouth entry to give an ideal inlet flow pattern to the multicell cyclone inlet manifold (Fig 3.6b) and the experiment was repeated for St and Re matching flows. The results are presented in Fig 4.27, plus a relative velocity pattern from previous tests. Symmetry of the velocity profiles about the cell axis was improved or unchanged in most cells by uniform multicell inlet flow; cell 8 and 9 gave less symmetric profiles, and it was not clear whether the precise positioning of the honeycomb flow straighteners influenced the symmetry. The apparent distribution of flow between cells was altered by the change of inlet ducting and this time the maximum difference decreased to 5% . Cells 4 and 8 now passed the least and greatest flow respectively. This test shows that even with an ideal inlet flow pattern, the flow still distributes unequally between cells. For the final rig configuration also, this test was repeated and the maximum difference between cells no. 3 and 9 was measured as 4.9%.

For studying the effect of the common hopper on cell flow distribution, the hopper was effectively replaced by nine isolated, equi-volume small hoppers made from polystyrene drinking cups and fixed under each cell as shown in Fig 4.22 with the rig in its final configuration (Fig. 3.6g). The maximum deviation was measured as 6.9% and was between cell no. 3 and 9. This test showed that the common hopper is partly responsible for cell maldistribution (due to gas flow through dust exits), but still inlet and outlet design seriously affect cell flow distribution. Fig. 4.25 shows a summary of cells flow distribution for all these four tests (for Stokes number matching flow rate).

Fig 4.26 shows the flow distribution between cell rows (as specified in Fig 4.21) and it is clear that there is little difference (~1%) between rows parallel with inlet flow direction, while between rows perpendicular with inlet flow direction, the difference was considerable (~6%).

4.3.2 Cyclone Inlet Manifold Flow Visualization

The smoke distributor was positioned at the entry of the inlet duct, and perpendicular with the entry air flow direction. For different smoke distributor vertical positions and under rig steady conditions, with 0.02 m^3/s rig flow rate (10% of flow for Stokes number matching), the flow patterns inside the inlet manifold were visualized and many pictures were taken. The following results were observed.

Flow Unsteadiness

The smoke lines inside the inlet duct showed strongly unsteady behaviour. Fig 4.28 shows two pictures taken a short time after each other; the local inlet flow direction has changed noticeably. It was possible to observe some long-time cyclic change in flow pattern inside the inlet manifold.

Formation of Vortex at Cell Entry

Fig 4.29 shows a schematic of a vortex which formed as the flow turned sharply to enter cells no. 2 and 5. The shape of these vortices was cylindrical and nearly oval and because of the existence of vortex finder tubes inside the inlet manifold, the shape and location of these vortices differed from cell to cell. This is possible that this non-uniform asymmetric pattern of vortices contributes to the unequal distribution of flow between cells.

Formation of Vortices Behind Vortex Finder Tube

The vortex finder tubes passed vertically through the inlet duct and so the entry air impinged on these tubes and created wakes behind them. Fig 4.30b shows a picture of the wake and other disturbances behind a vortex finder tube (cell no. 2). The air behind each vortex finder tube entered the cell in a twin-spiral pattern which is shown schematically in Fig 4.30a.

Secondary Flows in Corners

The stepped top wall of the inlet manifold is one weakness of this multicell cyclone design, creating a lot of dead zones. Fig 4.31 shows a schematic of a flow pattern which was observed during visualization. When the air impinged on the back wall, secondary flows with a lot of disturbance were formed. It is obvious that more disturbance and blockage causes energy dissipation and indirectly increases cyclone pressure drop. The corners also act as dust traps.

4.3.3 Cyclone Outlet Manifold Flow Visualization

The smoke generator system was used for cyclone outlet manifold visualization. Two rig flow rates were used, about 10% and 50% of the rate for dust measurements. By introducing planes of light at right angles to the top and side of the outlet manifold, the flow patterns at different locations were observed and recorded while the smoke was injected from the inlet duct. Because of flow unsteadiness, the smoke was distrubuted unequally between cells, especially 1 , 2 and 3 and this was helpful for visualization in the outlet duct.

Fig 4.32 shows the effect of swirling jet impingement on the top wall. The jets were flattened against the top wall and spread in the transverse direction, and created nine nearly square cells, divided by narrow cylindrical vortices. This feature supported the view that the 9-cell model was sufficiently representative of a cyclone with many more cells. Because of the outlet duct's stepped floor, jets from cell rows 1 , 2 and 3 have different blockage ratio (vortex finder diameter divided by distance between vortex finder exit and top wall), thus some cells in Fig 4.32 are more obvious than others. On lowering the horizontal plane of light, it was observed that the thickness and apparent turbulence level of boundary regions between jets (cells) were increased, which indicates the presence of highly sheared flow with considerable turbulence energy dissipation, contributing to cyclone pressure drop.

After many tests on the duct using vertical planes of light, it was seen that it is possible to distinguish four important regions inside the cyclone outlet manifold, which are shown in Fig 4.33. These regions are:

(I) region of very high turbulence, where the direction of swirl is opposite to the flow direction;
(II) region of high turbulence where the swirl and flow have the same direction;
(III) region with low turbulence, mainly under swirling jets and between rows 4, 5 and 6;
(IV) finally in corners and dead zones, steady secondary flows were observed.

Fig 4.34a and b show smoke patterns with vertical sheet illimination along lines of cell centres (1, 4, 7) and (2, 5, 8) respectively. The swirling jets expand and then impinge on each other and form many high-turbulence zones with many vortices which extend toward the cyclone outlet (Fig 4.34c). The flow structure in these regions was observed to be completly unsteady.

Fig 4.35a and b show side views with vertical sheet illumination midway between cell centres. A strong air stream was observed near manifold floors. This may be because of the jets venturi effect and jet impingement on the manifold roof; this could create a vertical pressure gradient, thus causing the air in the illuminated plane to move toward the duct floors (lower pressure zones). This could help to deposit the escaping particles inside the outlet duct.

By moving the vertical illumination through the plane of cell axes, it was observed that the flow patterns on the two sides of the jet were completely different, as expected in view of the strong shear on the side where the swirl direction is opposed to the cross flow.

4.3.4 Hopper Flow Pattern Visualization

For the hopper investigation, smoke generator and smoke-wire systems and tufts were used. Nearly all observations were made under steady conditions with rig flow rate 0.21 m^3/s (matching Stokes number). The rig configuration was mainly as in Fig 3.6g, but some tests were repeated with the ideal inlet pattern, as in Fig 3.6b. Major events observed during the hopper investigation are as follows.

Cells Underflow

Before running the rig, the hopper was filled with smoke and then the flow was started. After a few minutes, it was seen that there was a considerable amount of smoke passing through cells no. 7, 8 and 9 (back row), while there was a small amount of smoke inside cells no. 4, 5, 6. The front row (cells no. 1, 2, 3), hardly passed any smoke. This observation indicated that there was an unbalanced flow distribution between cells, especially cells in the front (1, 2, 3) and back (7, 8, 9) rows.

The above test was done under unsteady conditions (i.e. without the 1-hour "warming-up" period) and because of the importance of hopper vacuum on cyclone performance this test could not be done under steady conditions; therefore the smoke-wire system was used. The smoke-wire was placed vertically under each cell and aligned with the cell axis. At a steady condition, the smoke-wire was excited and the white smoke followed the air flow stream lines, the events being captured by high-speed camera. Fig 4.36a shows the smoke-wire below cell no. 2; smoke diffused downwards into the hopper and followed the hopper circulation. When the rig was running at a higher flow rate, the speed of diffusion also increased and the smoke was observed as mist. The same effect was seen when the experiment was repeated for cells no. 1 and 3.

When this test was repeated for cells no. 4, 5 and 6, smoke behaviour was different. Fig 4.36b shows the smoke-wire under cell no. 6; the smoke rotated around the smoke-wire axis (swirling motion), some diffusing through the hopper while some moved into the cell. The results of tests for cells no. 5 and 4 were very similar and shows a "null" behaviour for middle row (row 2) in view of cell-to-hopper flow. Finally the results of tests for the back row (row 3, cells 7, 8 and 9) showed that smoke behaved completely differently from that below the other six cells. Fig 4.36c and 4.36d show the smoke-wire under cells no 9 and 8 respectively. This time, the smoke moved completely into the cells. These observations indicated that there was an exchange of flow between cells through the common hopper; cells no. 1, 2, 3 had underflow to the hopper while cells no. 7, 8 and 9 had flow into the cells from the hopper.

The last series of tests used a tuft. A tuft of cotton was attached to the end of approximately 0.5 m of wire and was inserted into a hole 2 cm below the hopper window such that some of the wire protruded out of hole. The wire was held in position by adhesive tape which also sealed the rest of the hole. All other holes in the hopper were sealed likewise, otherwise they would have affected the flows in the hopper and the results would have been invalid. Fig. 4.37a shows a tuft under cell no. 3. There was significant turbulence with a general downward flow of air, while Fig. 4.37b shows a tuft under cell no. 9 which shows a strong tendency for the tuft to be drawn into the dust exit. This experiment was repeated for all cells and the results were in good agreement with the smoke-wire findings.

Vacuum Effect

When the cyclone was running under steady conditionds, a small amount of smoke was injected into the hopper. By altering the hopper vacuum (allowing air to leak into the hopper from one of the holes), it was observed that the hopper circulation was changed greatly. Air leakage into the hopper decreased vacuum, increased cells-to-hopper flow and finally increased circulation speed inside the hopper (hence likely to increase particle re-entrainment).

Hopper Circulation

By using smoke-wire and tuft it was found that there was a strong circulation inside the common hopper. The direction of air stream lines near hopper walls is shown in Fig 4.38a and b. These flow directions were similar to the swirl direction inside cells (clockwise looking downwards). Between cells, there was disorderly flow and the main direction of flow between front row (1) and centre row (2) was toward the hopper floor, and between back row (3) and centre row was toward the top wall. Fig 4.38c shows approximately the main direction of hopper circulation.

4.3.5 Discussion

Multicell cyclone performance (efficiency and pressure drop) is greatly affected by hopper, inlet and outlet manifold design. It is obvious that the flow structure in all parts

of the cyclone (except cells) is complex, three dimensional, unsteady and fully turbulent. To the author's knowledge there has been no quantative research on these parts of a multicell cyclone. It seems that it is impractical to optimize theoretically the multicell cyclone performance, but by experimental methods (as used here) it is possible to find out the weaknesses of design which result in poor cyclone performance. It hoped that in future some empirical rules (such as developed for single tangential cyclones) may be obtained from these findings.

Asymmetric velocity profiles were found in some cells. At both Re-matching and St-matching flow rates, the first row of cells (1-3) was estimated to be passing ~ 4% less flow to the exit manifold than the average. This is not inconsistent with a situation where all cells have nearly equal entry flow, but this first row losses ~4% to the hopper. There was little variation (~ 1%) between the flows passed by "columns" of cells (1, 4, 7), (2, 5, 8) and (3, 6, 9).

The ideal inlet manifold should distribute flow equally between cells with minimum pressure drop; but because of geometry restrictions, existence of vortex finder tubes and stepped top wall (which creates a lot of problems such as flow unsteadiness, back flow, formation of wakes, vortices, secondary flow and circulating zones inside inlet manifold), the flow distributes unequally with a considerable pressure drop. Unbalanced flow distribution between cells caused unbalanced cells pressure, hence increased cell-to-hopper flows (positive and negative) and hopper circulation.

The result of section 3.2.2 shows how the inlet velocity pattern can make disturbances (back flow, pulsation, etc) inside the inlet manifold. A conventional multicell entry configuration effectively requires a cell designed to operate with axial inlet flow to perform well when placed immediately downstream of a sharp bend containing a tube bank, and this visualization served to underline how unrealistic is this exception, regardless of any interaction between cells.

The mixing process of nine swirling flows inside the outlet manifold creates many areas of high shear stress with high turbulent energy dissipation. To the author' s knowledge, there is not any research on optimization of the mixing process of several swirling jets (to minimize pressure drop). The planes midway between rows of cells

are regions of strongly sheared flow, resulting from having the same swirl direction in all cells; this will contribute to overall pressure drop and it is suggested that alternating swirl vane settings (e.g. clockwise in odd- numbered cells, anti- clockwise in the remainder) might reduce the pressure loss.

The experiment shows the existence of high air circulation inside the hopper which could cause particle re-entrainment and prevent particle settling, and help the particles to re-enter the cells and escape from the cyclone. This effect would certainly decrease the multicell cyclone efficiency. The existence of cell-to-hopper flows and vice versa has been proved. Cells closer to the cyclone inlet flange (1, 2, 3) operated as if positive bottom bleed were induced by a secondary fan while the furthest (7, 8, 9) had the effect of negative bottom bleed. It means that cells (1, 2, 3) should have better efficiency than cells (7, 8, 9). Few direct references to this phenomenon can be found in the literature on cyclones, although instabilities in parallel tube assemblies are well known in other fields. Crellin et al. (1980) attribute the non- uniform flow distribution to the unequal lengths of vortex finder tubes in different cell rows. It was observed that air leakage into the hopper can increase back flow from hopper to cells and the speed of circulation (hence worsen performance).

These findings suggested various modifications which could prove benefical to collection efficiency and/ or pressure drop, such as baffles in the dust hopper, devices in each cone to serve as an attachment point for inner vortex, etc.

4.4 MASS EFFICIENCY RESULTS

4.4.1 Introductory Remarks

Fig 4.41 shows a mass balance diagram for multicell and one- cell cyclones. By looking at the multicell cyclone mass balance diagram with different views, the mass efficiency of the cyclone can be calculated by the following formulae, in which

m_1= Feeding mass (g)
m_2= Total sampling mass before cyclone (g)
m_3= Sediment mass inside upstream ducting (g)

m4= Hopper mass (g)

m_5= Total sampling mass after cyclone (g)

Q_R= Rig flow rate (m^3/s), measured at pitot tube position (sampling system after cyclone)

Q_{S1}= Sampling system flow rate (m^3/s) before cyclone

Q_{S2}= Sampling system flow rate (m^3/s) after cyclone

I-FHE method ; based on feed and hopper mass (transition duct sediment mass excluded from mass captured by the cyclone).

$$\eta = \frac{m_4}{m_1 - m_2 - m_3} \tag{4.3}$$

II-FHI method ; based on feed and hopper mass (transition duct sediment mass included in mass captured by the cyclone).

Mass median diameter of sediment mass was measured for a typical efficiency test and it was nearly twice the mass median diameter of the feed dust (Fig 4.42a). Normally cyclones could capture all particles above the feed mass median diameter (about 10 μm) and therefore if the sediment mass was able to enter the cyclone, then probably 99% would be captured by the cyclone. It is thus logical to use an alternative defination of efficiency, for the cyclone itself plus the inlet transition duct, as follows:

$$\eta = \frac{m_4 + m_3}{m_1 - m_2} \tag{4.4}$$

III-FSE method ; based on feed and downstream sampling mass (sediment mass excluded).

One of the popular and recommended methods for cyclone efficiency calculation is based on feed mass and down stream sampling, which has higher reliability and accuracy than other methods. Cyclone efficiency can be determined by the following

formula :

$$\eta = \frac{(m_1 - m_2 - m_3) - m_5 \cdot \dfrac{Q_R + Q_{S2}}{Q_{S2}}}{m_1 - m_2 - m_3} \qquad (4.5)$$

For example, for the experimental multicell cyclone, feed mass, hopper mass, sampling mass and efficiency are typically around 1000g, 900g, 3g and 90% respectively. If hopper and sampling mass measurements have an error of 10% then the error in efficiency can be estimated (Kline and Mcclintock, 1953) as 1% and 10% for FSE and FHE methods respectively. For the present experiments, the FSE method was used for efficiency calculation, while other methods were used for validating test condition to eliminate effects of intermittent dust carry-over, etc.

IV-FSI method ; based on feed and downstream sampling mass (sediment mass included).

$$\eta = \frac{(m_1 - m_2) - m_5 \cdot \dfrac{Q_R + Q_{S2}}{Q_{S2}}}{m_1 - m_2} \qquad (4.6)$$

V-SSE method ; based on two sampling systems (sediment mass excluded) .

$$\eta = \frac{m_2 \cdot \dfrac{Q_R - Q_{CA}}{Q_{S1}} - m_3 - m_5 \cdot \dfrac{Q_R + Q_{S2}}{Q_{S2}}}{m_2 \cdot \dfrac{Q_R - Q_{CA}}{Q_{S1}} \cdot m_3} \qquad (4.7)$$

Because of the comparative simplicity of the one-cell cyclone, its efficiency can be calculated from the following formulae.

I-FH method ; based on feed and hopper mass.

$$\eta = \frac{m_{\prime}}{m_1} \tag{4. 8}$$

II-FS method ; based on feed and downstream sampling mass.

$$\eta = \frac{m_1 - m_5 \cdot \frac{Q_R}{Q_{S2}}}{m_1} \tag{4. 9}$$

After many runs the sediment level inside the cyclone seemed to stabilize, justifying the neglect of m_9 and m_{10} in equations 4.3 to 4.9. The preliminary efficiency test was done on the multicell cyclone with rig configuration as in Fig 3.6g, and also on the one-cell rig, with fuller's earth dust. These tests were performed at nearly the Stokes no. matching flow rate (0.167 m^3/s and 0.026 m^3/s for multicell cyclone and one-cell cyclone respectively. The feeding mass, sediment mass and hopper mass for multicell cyclone test were measured as 3600.6, 1876 and 1442 g respectively. The mass efficiency was calculated as 84.8%, 92.7%, 94.6% and 97.4% by using FHE, FHI, FSE and FSI methods respectively. For the one-cell efficiency test, feed mass and hopper mass were measured as 580.7 and 570.9 respectively while sampling mass after cyclone was negligible. Cyclone efficiency was calculated as 98.3% and 99.9% by using FH and FS methods respectively. These tests were not acceptable mainly because of the high amount of sediment mass inside the upstream ducting (nearly 50%) and the high efficiency for the one-cell cyclone (99%).The high efficiencies were likely to make it difficult or impossible to discern the effect of any modification made with a view to improving the efficiency. A finer test dust was clearly required, hence Syenex-40 was chosen as described in section 3.2.3.

Sediment mass inside upstream ducting causes many problems such as inaccuracy in mass and grade efficiency, dust concentration gradient at cyclone entrance (which certainly creates imbalance in cells inlet dust concentration), dust carry-over from one

test to another, etc.For example Biffin et al. (1981) reported a large deposition of dust on tube pipe walls of his cyclone rig and typical measured collection efficiencies were 75% instead of 98%; he resolved this problem by introducing the dust directly into the inlet of the cyclone, and sizing a sample of dust separately for grade efficiency purposes (as used for the one-cell rig in the present study). Because of low air velocity inside the multicell inlet duct and technical problems such as dust injector and distributor design, this technique seemed to be impratical, so a dust dispersal system was designed (as described in section 3.2.6), to remove sediment mass and mix it with dirty air before the cyclone entrance. This method gave an opportunity of using the upstream sampling system for checking purposes. The new dust and rig configuration (Fig 3.11) was successfully tested and for a typical efficiency test, ducting sediment mass was measured as around 5% of feed mass.

Before performing dust collection efficiency tests, the particle feeding system and sampling system were calibrated. With the feeder gate at fixed positions, the relationship between feed rate and feeder control knob position was found, and the system feed rate was maintained at 2.5 g/s for efficiency tests with Syenex-40 . The air velocity profile at pitot tube and sampling nozzle positions were measured (Fig. 4.39). These profiles showed that the pipe centreline air velocity at the nozzle position was less than at the pitot tube position and so the velocity recorded by the pitot tube could not be used directly to set the isokinetic sampling rate. A correction factor was developed for sampling flow rate calculation. For the standard rig flow rate of 0.21 m^3/s, this factor was calculated from the measurements as 0.946 and 0.959 for the sampling systems before and after the multicell cyclone respectively.

4.4.2 One Cell and Multicell cyclone Mass Efficiency Results

The one-cell cyclone mass efficiency was calculated from averaged measurements of a set of tests as 93.74% $\pm$0.5 for Syenex-40 dust (where $\pm$ 0.5 represents the scatter). The rig flow rate, air temperature, humidity and cyclone inlet dust concentration were nearly 0.024 m^3/s, 20.8^oC, 50% and 11.7 g/m^3 respectively. Also the same procedure was carried out with Pozzolan powder and the mass efficiency was calculated as 89.9%$\pm$0.1. The rig flow rate, air temperature, humidity and cyclone inlet concentration were nearly 0.0197m^3/s, 20 ^oC, 45% and 14.4 g/m^3 respectively. The

test duration for these tests was between 25 and 30 minutes, the feed mass was around 0.5 kg and the clean-stream sampling mass was between 8 and 10 g per test.

Many efficiency tests were performed on the multicell cyclone rig in the configuration shown in Fig 3.11 (with Syenex-40). The mass efficiency was calculated from averaged measurements as 85.8% ±1.0. The general conditions for the tests, i.e. air temperature, humidity, feed mass, dust concentration, rig flow rate, sampling mass after cyclone, test duration time and sediment mass were around 20 ^{o}C ±1, 40% ±10, 700 g ±100, 7 g/m^3 ±2, 0.022 m^3/s ±0.005, 3.5 g±1, 7-10 minutes and 150 g ±50 respectively.

4.4.3 Discussion

For each run, the dust collected in the hopper was also weighed. Efficiencies based on hopper dust mass rather than clean stream sample are subject to large uncertainties, but the values were consistently lower than those based on sampling, reflecting dust captured on the inlet manifold and cell internal surfaces. Run-to-run variations in "hopper-based" efficiency were greater than in "sample-based" efficiency, again pointing to the essentially unsteady operation of the multicell cyclone.

Dust "ropes" in the multicell cyclone cells, during a test, are illustrated in Fig 4.43a, which also shows a side view and a view into the inlet manifold after a number of runs. Deposits on the front (and rear) of the outside of the clean gas outlet tubes reached a reasonably steady state, but the dust heaps next to the inlet manifold side walls appeared to be growing continuosly (Fig. 4.43b and c). Some, but not all, of these deposits could be removed by passing air only through the rig at maximum flow rate for some minutes. The spiral patterns are on the insides of the outlet tubes, and give an indication of the strength of the swirl.

The procedure adopted in a sequence of tests with the same cyclone configuration was to let the deposits build up, but ignore the results of any run where deposits broke up to pass extra dust "clouds" through the cells. These break-up events were detectable visually and by results which showed a marked increase in collected dust both in the hopper and in the clean stream sample.

The single cell efficiency of ~ 93.7%, indicates a potential for halving dust emission if the multicell unit could be made to perform as well as an isolated cell.

Using the same conditions as in the experiments (Stokes matching flow rate), and with Syenex-40, Pozzolan and fuller's earth properties , the overall mass efficiency predictions of the new numerical model (CYCINT-1) were 87.0%, 78.9% and 96.0% respectively. By comparing these results the corresponding experimental findings (93.7%, 89.9% and 99% respectively) it becomes obvious that the predictions of the numerical model are lower than experimental values but show the correct trend. According to Abrahamson et al. (1978), the overall efficiency of a cyclone depends on the efficiencies of two sequential processes, with each process contributing to the dust emission. The first of the processes is a migration of particles to the wall, in competition with a migration to the gas outlet. Under normal conditions of operation, this first step largely controls the cyclone collection. This process is supposed to be correctly modelled in the present numerical method. The second of the processes is an agglomeration of dust close to the wall. This second process normally has an efficiency close to one, but may be affected by gas humidity, generation of electrostatic charge, etc. For the present work, agglomeration could not considered in the numerical model, therefore the calculated efficiency by CYCINT-1 is expected to be lower than the actual cyclone efficiency. Greenfield (1986) also had unexpectedly higher experimental results than predicted by theory for a tangential type cyclone, and he commented that in practice a certain amount of agglomeration may have taken place at the "fine" end of the dust size spectrum which had improved the efficiency. On the other hand because of deposition inside cyclone manifolds, the experimental findings should be higher than actual average cell efficiency. Therefore by considering the above facts and also uncertainties in experimental and numerical methods, it may be that the above differences between efficiencies are to be expected.

4.5 GRADE EFFICIENCY RESULTS

4.5.1 Introductory Remarks

Malvern instruments were used for particle sizing measurements. Before starting main measurments, some preliminary tests were done on samples of particles to

standardize the particle sizing tests procedure. A Malvern instrument was used off-line on samples of syenex-40, fuller's earth, Pozzolan, etc. dispersed in distilled water and in ethyl alcohol; the results were difficult to interpret since repeated measurements showed the proportions of smaller particles increasing with time as illustrated in Fig 4.44 (for fuller's earth). This was attributed to break-up of agglomerates and Fig 4.45 shows this effect on a sample of Pozzolan with and without the ultrasonic stirring system in operation before the measurement.

Fig 4.46 shows a comparison of Coulter Counter instrument size distribution measurements (tests performed at CRE) with Malvern measurements, which gives different size distributions for apparently similar samples of Syenex-40. The Malvern instrument measures projected-area diameter, whereas the Coulter counter uses the electrical sensing zone technique, so there is no reason why they should agree closely. However, by relying on Malvern data only, trends should be correctly indicated.

Finally the effect of Malvern system parameters such as mathematical model, lens focal length, etc., have been studied. For example , Fig 4.47 shows results of sizing pulverized fuel ash (PFA) from Fiddlers Ferry power station (CEGB NW region, 500 MW boilers), using Rosin-Rammler, log-normal and model-independent models. The results at the large-diameter end of the distributions are distinctly different from each other. These studies confirmed that results of particle size distribution tests are strongly dependent on the definition of system parameters and lead to the choice of a standard procedure for all future particle size distribution tests to minimize uncertainties in results. Therefore particle suspension in air, 63 mm lens focal length and Rosin-Rammler model were chosen mainly because they corresponded most closely to test conditions.

The size distribution of particles may be changed by change in humidity (because of agglomeration), therefore it was important to choose a procedure to minimize this effect on grade efficiency results. Firstly it was decided to dry feed dust inside an oven (150 ^{o}C for 2 hr) before efficiency tests (this method was used only for tests performed with fuller's earth). But after some studies, it was decided to use undried dust for efficiency tests . Fig. 4.48 shows a comparison between size distributions of dried and undried fullers's earth and Pozzolan, and shows that the difference between

undried and dried is inside the experimental error and negligible. It is also obvious that during dispersal of dried dust in air, air humidity can easily affect it, and because of changes in laboratory humidity from one test to another (up to ±15%), and existence of agglomeration inside the cyclone, uncertainty in tests using dried dust will be more difficult to assess than if using undried dust which has a humidity balance with laboratory air.

The Rosin-Rammler distribution was derived originally for friable material in the latter stages of crushing and it is defined by :

$$m_i = 1 - \exp\left[-\left(\frac{d_i}{d_{rr}}\right)^n\right] \qquad (4.10)$$

where m_i is the cumulative mass under size d_i, and d_{rr} and n are Rosin-Rammler mean diameter and spread parameter respectively (see also Appendix C). For each sample, the Malvern calculated these two parameters. By using Malvern results and the following procedure, a cyclone grade efficiency curve for each efficiency test was obtained. Fig. 4.40 shows a typical Rosin-Rammler size distribution. The mass fraction between two particle diameter sizes d_i and d_{i+1} can be calculated as:

$$\Delta_{m_i} = \exp\left[-\left(\frac{d_i}{d_{rr}}\right)^n\right] - \exp\left[-\left(\frac{d_{i+1}}{d_{rr}}\right)^n\right] \qquad (4.11)$$

A stepped function may be fitted to a Rosin-Rammler distribution curve as shown in Fig 4.40. It is obvious that by increasing the number of particle sizes (especially in the sharp gradient region), the fit will be closer. For each multicell cyclone efficiency test, four Rosin-Rammler curves were obtained (for feed mass, sediment mass, hopper mass and sampling mass after cyclone). If the same particle sizes division (such as shown in Fig. 4.40) is used for all of these curves, then the mass efficiency of each band of the curve (D_1, D_2, ...,D_i) may be approximated by two different

approaches.

I-(FHE method) ; grade efficiency based on hopper mass.

$$\eta_{D_i} = \frac{m_4 \Delta H_i}{m_1 \Delta F_i - m_3 \Delta Se_i} \qquad (4.12)$$

where m_1, m_2 and m_4 are feed mass, sediment mass and hopper mass respectively and ΔF_i ,ΔH_i and ΔSe_i are mass fraction between (d_i and d_{i+1}) of Rosin-Rammler size distribution curves of feed mass, hopper mass and sediment mass respectively.

II-FSE method ; grade efficiency based on sampling system mass after cyclone.

$$\eta_{D_i} = \frac{m_1 \Delta F_i - m_3 \Delta Se_i - m_5 \Delta S_i \frac{Q_R + Q_{S2}}{Q_{S2}}}{m_1 \Delta F_i - m_3 \Delta Se_i} \qquad (4.13)$$

where m_5, Q_R, Q_{S2} and ΔS_i are respectively the sampling mass, rig flow rate, sampling flow rate and mass fraction between (d_i and d_{i+1}) of Rosin-Rammler size distribution curve of sample mass. Simpler formulae (deleting sediment terms from equation 4.12 and 4.13) were used for obtaining one-cell grade efficiency curves. These procedures were computerised to facilitate calculation.

4.5.2 One-Cell and Multicell Cyclone Grade Efficiency Results

As already mentioned, enough samples from feed mass, hopper mass and clean stream sampling mass after each one-cell efficiency test, were carefully gathered. Fig 4.49a shows size distributions of feed mass, hopper mass and clean stream sample mass for an efficiency test performed at Stokes number matching (0.02 m^3/s) flow rate, with Pozzolan. For an efficiency test with Syenex-40 (0.024 m^3/s rig flow rate) , similar results are presented in Fig 4.49b. The mass median diameter of feed mass, hopper mass and clean gas sample were measured as 7.3, 9.0 and 3.7 μm respectively for Pozzolan and 9.8, 10.2 and 3.4 μm respectively for syenex-40. Fig 4.50 shows

the comparison of size distribution of feed and clean stream sample mass from Rosin-Rammler and model-independent fits to the same scattered light intensity distribution. Fortunately the size distribution of Syenex-40 (Fig 4.50b) for both methods is nearly the same, while for Pozzolan (Fig 4.50a) it is completely different.

For better understanding of the size distributions of collected dust from different parts of the one-cell rig, histograms of results for efficiency tests with Pozzolan and Syenex-40 are presented in Fig. 4.51. From Fig. 4.51 it becomes obvious that all particles bigger than 7 and 18 μm were captured by the cyclone when working with Pozzolan and Syenex-40 respectively. The major reason for this difference will be difference in particle properties, such as shape, tendency to break-up, etc. The measured material densities of Pozzolan and Syenex-40 are such that one would expect the opposite trend, but it must be remembered that Pozzolan exhibited a range of different-density constituents, which may correlate with size.

Fig. 4.52 shows results of grade efficiency calculation (FHE and FSE efficiency methods) for one-cell cyclone test, with Syenex-40 at Stokes number matching flow rate (0.024 m^3/s). The sampling-based (FSE method) curve (Fig 4.52) shows that cyclone efficiency rapidly increased with increasing particle diameter from zero to 15 μm and then gently approached 100%. An interesting result is the hopper-based (FHE method) curve (Fig. 4.52), which gave an efficiency of 110% for particle diameter around 10 μm and nearly zero efficiency for particle diameters more than 50 μm. Agglomeration of fine particles (near the cyclone wall), large particle break-down (in regions of highly sheared flow) and particle bouncing on the cyclone wall, are some possible reasons for this unusual but interesting result. Hopper-based calculation (FHE method) therefore can indicate the existence of agglomeration or break-down processes inside the cyclone.

Fig. 4.55a shows size distributions of feed mass, sediment mass, hopper mass, dirty and clean gas sampling mass for a multicell cyclone efficiency test performed at flow rate 0.2 m^3/s with Syenex-40. Fig 4.55b shows similar results at 0.185 m^3/s rig flow rate with fuller's earth. The size distribution of feed mass and dirty gas samples are close to each other, indicating satisfactory sampling system performance. The mass median diameter of feed mass, sediment mass, hopper mass and clean gas sample were

measured as 9.1, 15.0, 9.1 and 2.5 μm respectively for Syenex-40 and also 18.5, 54.0, 24.5 and 3.8 μm respectively for fuller's earth. The histograms of these results are shown in Fig. 4.42 for fuller's earth and Syenex-40. The multicell cyclone was able to capture all particles bigger than 8 and 24 μm for fuller's earth and Syenex-40 respectively. If we compare hopper histograms of one-cell (Fig. 4.51b) and multicell cyclone (Fig. 4.42b), it is seen that the multicell cyclone could not capture any particle less than 2 μm while a considerable amount of particles below this range were captured by the one-cell cyclone. The reason for this effect may be the existence of backflow into multicell cyclone cells and high hopper circulation which are liable to promote particle re-entrainment.

4.5.3 Discussion

Each dust sample has an almost constant size distribution when two or more "sub-samples" are measured with the same instrument and procedure. However, because of many factors such as size analyser system errors, particle dispersing medium, mathematical model, method of test, chemical and physical properties of particles, etc., different size distributions are measured by different instruments or by different procedures with the same instrument. For example the mass median diameter of Syenex-40 was obtained by the Malvern 2600/3600 systems as 38 and 10 μm when the powder was dispersed in water and air respectively. Seville et al. (1984) reported that an earlier model of Malvern sizer oversized fly ash (similar to Syenex) in water by 100-250% and beleived that this was probably due to the fact that most of the particles were within the range for which the Fraunhofer approximation is not applicable (The present Malvern 2600 software incorporates an approximate correction for this). Also Fig. 4.46 shows how the predictions of Coulter Counter and Malvern systems had a 25% difference in mass median diameter of Syenex-40.

It may be that the particle physical properties, especially material density and shape, are the most important parameters contributing to these discrepancies. During density measurement of particles, it was observed, especially for Pozzolan, that the powder was a combination of particles with very different densities which would certainly give differences in particle drag force and inertial behaviour and particle-particle forces inside the domain of size measurement.

For aerosols of industrial interest, which are in general both irregular and light-absorbing (and also frequently of inhomogeneous refractive index), theoretical light scattering predictions are too complicated to be used to predict the response of a particular instrument (Seville et al, 1984); even for spherical aerosols of known refractive index, theoretical response prediction is tedious. Also depending on particle orientation inside the domain of measurement, different scattered patterns are expected, hence different size distributions. In general in spite of uncertainties, the Malvern results for one-cell and multicell cyclone which are shown in Fig 4.49 to 4.51 are reasonable; the most coarse dust is identified as sediment mass while the finest is the clean air sampling system mass.

The experimental findings were compared with numerical results of CYCINT-1 and SPRINT-4; for better presentation the investigation covers only the important particle size range of 0-15 μm . Fig. 4.56 shows comparison of one-cell grade efficiencies (Q=0.024 m^3/s and Syenex-40), calculated from experimental results (FHE and FSE efficiency method), with numerical predictions. Above 5 μm, the CYCINT-1 prediction is in good agreement with the FSE method , while below 5 μm experimental findings and theoretical predictions are far from each other. The Malvern results are not reliable below 2 μm; and in the numerical study there may be errors due to preliminary assumptions such as identical shape (spherical) and density for all particles, absence of agglomeration, etc. The CYCINT-1 prediction is closer than the SPRINT-4 prediction to the experimental findings.

The same comparison for Pozzolan and fuller's earth are shown in Fig. 4.57 and 4.58 respectively for one-cell cyclone and Stokes number matching flow rate. The results are the same as Syenex-40 results but near 4 μm, FSE method gave a minimum for efficiency . Experimental error or agglomeration may be responsible for this decreasing efficiency. Many researchers such as Stairmand reported a similar phenomenon and they explained that particle bouncing on cyclone internal walls causes this anomalous region of decreasing efficiency. Wheeldon et al. (1980) also monitored such a minimum and they concluded that an agglomeration process was resposible.

Fig. 4.59 shows experimental findings for the multicell cyclone, working with fuller's earth (Stokes number matching). Comparing with one-cell results (Fig. 4.58),

a considerable drop in efficiency (hopper based, FHE) can be seen for multicell cyclone; also greater emission of finer particles occurs for the multicell cyclone. Finally Fig. 4.53 shows grade efficiencies of one-cell and multicell cyclone (FSE method) for Syenex-40 (Stokes number matching) which are compared with results of numerical models. This graph can perhaps summarise the results of this section, which shows; higher efficiency for one-cell than multicell cyclone; the CYCINT-1 prediction closer than SPRINT-4 to experimental findings; and unreliablity of experimental results below 3 μm.

4.6 MODIFICATIONS TO CYCLONES

4.6.1 Introductory Remarks

The overall efficiencies, obtained by clean-stream sampling, demonstrated a potential for halving emissions, if the multicell cyclone performance could be restored to that of an isolated cell. Also certainly there are possibilities for increasing one-cell cyclone efficiency by doing some optimization work on cyclone design. The present investigation shows that cyclone performance suffers from design weakness in the hopper, inlet/ outlet manifold, cells arrangement, etc. Geometry of isolated cyclones (mainly tangential type) were optimized by many researchers such as Stairmand (1951), Dirgo and Leith (1985), but to the author's knowledge no research in optimization of multicell cyclone geometry has been published. Unfortunately because of cost, shortage of time, too many design parameters, etc., it was not possible in the present study to attempt optimization of inlet/ outlet manifold, cell arrangement, hopper geometry, etc. However by using some simple techniques inside the hopper and cells, experiments were carried out to improve one-cell and multicell cyclone performance. Also the effects of some modifications such as bottom bleed, change of vane angle, etc. on one-cell vane-type cyclones were theoretically studied and reported in Chapter 5.

4.6.2 Modification Techniques

The effect of some modifications on the multicell cyclone have been tested. After putting upward pointing cones in the cell dust exists (to provide an attachment point for

the vortex, as frequently used in German-designed cyclones (e.g. Gloger and Hanke, 1971) and shown in Fig. 4.54, many efficiency tests have been performed. The conditions of these tests were as far as possible the same as for the unmodified cyclone. Each cone, with 60^0 apex angle, was suspended by three fine wires from the inside of a cell, two thirds of its height being within the cell. The effect of using twin baffles inside the hopper (to suppress the circulating flow and hopefully minimize the tendency for back flow from the hopper into the rear row of cells), as also shown in Fig 4.54 has been examined. The hopper baffles were flexible curtains, inserted through the hopper window, fixed in place by a top rod and held vertical by the weight of another rod along the bottom edge. Finally many efficiency tests have been done for studying the effect of skewed inlet flow patterns on multicell cyclone performance.

The effect of several modifications on one-cell cyclone performance has also been investigated. The vortex-stabilizing cone (as on the multicell cyclone) was tested. Four devices tested only on the single-cell consisted of: a cruciform baffle in the cylindrical dust hopper, to suppress rotation and possible dust pick-up; a triple-cone extension to the clean gas outlet tube entry, modelled on a Western Precipitation (or Joy, or Steetley) design ("tricone") and claimed to increase collection efficiency; a three-vane de-swirler extension to the outlet tube, similarly based on a Western Precipitation design ("spirocone") and claimed to reduce pressure drop; a spiral-slotted extension to the outlet tube, already used by Schmidt (1986) to reduce pressure drop and increase grade efficiency for larger particle sizes. Fig 4.60 shows manufacturer's sketches and the present model versions of the de-swirler, triple cone and spiral-slotted devices. The procedure and condition of tests were maintained as much as possible the same as for those without any modification.

4.6.3 Results for Modified Cyclones

I- Cyclone Pressure Drop Results

The cyclone pressure drop test was performed for all modified one-cell cyclones. Results are presented in Fig 4.61. There were not any significant changes in one-cell cyclone pressure drop (compared with unmodified cyclone) when using the baffle in the hopper or cone stabilizers. The effect of using the three-vane de-swirler was

considerable and cyclone pressure drop was decreased by 30% at flow rate 0.024 m^3/s. Use of the triple cone and spiral slotted extensions, increased cyclone pressure drop by 15% at the same flow rate. Also modified multicell cyclones (with hopper baffles or with cone vortex stabilizing) were tested at steady condition and for different flow rates. Again, no significant changes in cyclone pressure drop were observed (compared with unmodified multicell cyclone).

II- Mass Efficiency Results

The same efficiency measurement procedures as for original one-cell and multicell cyclone were used for testing modified cyclones. The repeatibility of tests was checked and for each case many efficiency tests were performed with Syenex-40. Mass efficiency (based on FSE) of modified multicell cyclones with bad inlet flow (rig as Fig. 3.6a), baffle inside hopper and cone vortex stabilizers were measured as 89.8% ± 0.05, 88.8% ±0.02 and 85.9% ±0.2 respectively. The results of mass efficiency tests (based on FSE method) for modified one-cell cyclone with spiral slotted, de-swirler and triple cone extensions, baffle inside hopper and cone vortex stabilizers were 94.9% ±0.15, 93.4% ±0.05, 96.6% ±0.1, 94.8% ±0.02 and 94.6% ±0.1 respectively. Fig. 4.65 shows overall mass collection efficiencies of multicell and single-cell cyclones based on FSE efficiency calculation. From this figure, it can be seen that vortex-stabilizers cones at the cell dust exit had little effect on the overall efficiency of the single-cell cyclone; repeatability was better but the results were within the range found for the unmodified cell. The effect for the multicell cyclone was also insignificant, suggesting that dust scouring by vortex unsteadiness is not a major cause of poor cyclone performance for this design.

Hopper baffles in the multicell cyclone did produce a significant improvement, cutting emissions from 14% to around 11% of the dust mass entering the cyclone. Prevention of swirl in the hopper of the single-cell model by means of the cruciform baffle likewise gave a drop in emissions, from 6% to 5%.

The modification producing the greatest fractional improvement in overall efficiency was the triple cone entry to the clean gas outlet tube on the single-cell cyclone, halving the emission to 3%. The de-swirling device, intended for pressure

drop reduction, produced no change in efficiency, as expected, neither did the spiral-slotted extension. Lacking time to construct and test triple cone devices on the multicell unit, it may be assumed for the time being that they would similarly improve the multicell efficiency; however, it is difficult to envisage even a combination of hopper baffles and triple cones resulting in an efficiency greater than about 94% for the conditions of the experiments with Syenex-40.

III- Grade Efficiency Results

The Malvern system was again used for particle size analysis of samples which were collected after each efficiency test. Fig. 4.66 shows size distributions of samples of feed mass, hopper mass and clean-stream mass for modified one-cell cyclones. Also Fig. 4.55 shows some results for the modified multicell cyclone. In spite of some differences mainly because of experimental errors especially in the range 1 to 3 μm, the size distributions of emitted dust (clean-stream), are close together and it is difficult to conclude any result.

By using the FSE method, grade efficiencies of modified cyclones were calculated and plotted in Fig. 4.62 and 4.63 for one-cell and multicell cyclone respectively. As expected, modified one-cell cyclone with triple-cone and modified multicell cyclone with baffles inside the hopper have the best grade efficiency, compared with others.

4.6.4 Discussion

Dimensionless pressure drop (sometimes called Euler no.) is plotted against flow rate (Q) in Fig. 4.67; the right-hand vertical scale shows the Δp under hot-gas full-scale conditions which corresponds to the measured dimensionless value. The multicell results indicate a slightly increasing trend in Euler no. as Q increases, and also show that removal of the temporary flow straighteners in the clean gas outlet tubes and addition of the sediment dispersal jets in the transition duct together increase the pressure drop. The overall level of pressure drop, equivalent to 70-90 mm w.g. in an industrial unit, suggests that there is scope for reducing the number of cells (hence the cost) for a given duty. For example, if a doubling of ΔP were acceptable, an increase in Q per cell, hence Vi and St, by a factor of around 2 would be implied. Judging by

the general levels of dust collection efficiency quoted in sec. 3.2.3 (~85% at St=0.04, ~96% at St=0.21), the resulting improvement in dust collection might be fairly small.The unmodified single-cell cyclone shows an opposite trend in dimensionless ΔP as Q increases, perhaps implying that the multicell cyclone inlet and exit manifold contribute an increasingly significant fraction of the total multicell pressure drop as flow increases.

One important parameter likely to affect multicell cyclone performance is the flow pattern at the cyclone entrance, mainly because of the effect on flow distribution between cells. Horzella (1980) believed that ductwork design is an important element determining the final dust-collection efficiency of a cyclone. The layout of the equipment sometimes makes it impossible to furnish a straight inlet duct long enough to ensure proper gas distribution. On industrial boiler multicell cyclones, it is rare to find an inlet duct longer than about 1 m. Horzella suggested putting gas deflectors in the duct or adjustable dampers in each tube's gas entrance to permit some adjustments. Some researchers tried to optimize this part of a cyclone. For example Byers and Gage (1981), faced with a sharp right-angle turn in the ductwork immediately upstream of the multicell cyclone inlet, installed turning vanes in this duct bend to ensure a good velocity distribution at the inlet plane. Using the rig configuration as in Fig. 3.6a plus sediment dispersal system in operation, gave the worst profile pattern which is shown in Fig 4.64. Overall collection efficiency measurement (FSE method) showed surprisingly little difference (but a slight improvement) between the case of skewed and uniform velocity distributions at entry to the multicell unit (Fig. 4.65). The reason for this is unknown.

The hopper baffles reduced dust emissions from 14% to 11%; it is probable that hopper circulation occurs in all industrial multicell cyclones having cell outlet tubes of unequal length (hence unequal flow resistance), and baffles are recommended as a cheap means of obtaining a modest but worthwhile efficiency improvement. Attempts to stabilize the cell inner vortices, by providing vortex attachment points in the form of upward- pointing cones in the cell dust exits, were ineffective in improving multicell overall efficiency while in the one-cell rig a small improvement was measured. Perhaps the cones upset any interchange of gas between cell and hopper or interfere with the particle ropes, which could cause changes in cyclone efficiency.

Of the various devices tested only on the isolated cell, two were noteworthy. The three-vane de-swirler mounted at the entry to the clean gas outlet tube cut the pressure drop by about five cell inlet velocity heads but did not affect overall efficiency; triple cone in the same location halved dust emissions but with a pressure-drop penalty of around three velocity heads.

Grade efficiency curves b and d in Fig 4.68 show that multicell hopper baffles and single-cell triple cone both have their major influence at the small-diameter end of the particle size range, as might be expected from considerations of gas-borne particle behaviour. A curious result is the apparent reduction in grade efficiency above about 9 μm caused by hopper baffles, although this is exaggerated on Fig. 4.68 by the probability scale of the ordinate and could be subjected to a poorer than usual Rosin-Rammler fit by the Malvern software.

CHAPTER 5

THEORETICAL WORK

5.1 INTRODUCTION

This chapter begins with a description of the mathematical basis and the numerical solution procedure of an existing model for gas flow and particle motion in cyclones, followed by details of major modifications made by the author to improve its predictions, especially for axial-entry cyclones. Results of investigations using the new model are then presented.

The relevant laws of nature (source laws, transport laws, conservation laws) may be combined into differential equations, which may then be transformed into finite-difference form. All the finite difference equation then are solved by the line-by-line iteration method. The procedure employed in so doing is the SIMPLE algorithm. Section 5.2 explains briefly this solution for the continous phase flow. The particle phase of the solution procedure, carried out by calculating the individual trajectories of a large number of particles, is described in Section 5.3. The existing finite-difference code (SPRINT-4) has been modified and rewritten to provide (CYCINT-1) a more straightforward and computationally sounder means of modelling the gas flow field in axial-entry reverse-flow cyclones. In Section 5.4 the major steps in modifing the numerical model are reported. Results from the new numerical model are dealt with in Section 5.5, consisting of cyclone scale-up, cyclone flow field, cyclone pressure drop, efficiency and particle trajectory investigations. At the end of this section the effect of some parameters such as underflow on cyclone performance are reported. Finally the results are discussed in Section 5.6

5.2 SOLUTION FOR CONTINOUS-PHASE FLOW

5.2.1 Mathematical Description of The Flow

The equations required for the description of the flow patterns in cyclone

separators are given here in cylindrical co-ordinates (z,r,θ), best suited to the geometry.

Instantaneous Continuity Equations

The conservation of mass is given by:

$$\frac{\partial}{\partial r}(\hat{\rho}\,\hat{V}_r)+\frac{\hat{\rho}\,\hat{V}_r}{r}+\frac{1}{r}\frac{\partial}{\partial\theta}\hat{\rho}\,\hat{V}_\theta+\frac{\partial}{\partial z}(\hat{\rho}\,\hat{V}_z)=0 \qquad (5.1)$$

Instantaneous momentum equations

The conservation of momentum is given in the three co-ordinate directions (r, θ and z) by :

r-direction

$$\hat{\rho}\left(\hat{V}_r\frac{\partial\hat{V}_r}{\partial r}+\frac{\hat{V}_\theta}{r}\frac{\partial\hat{V}_r}{\partial\theta}+\hat{V}_z\frac{\partial\hat{V}_r}{\partial z}-\frac{\hat{V}_\theta^{\,2}}{r}\right)=\hat{\rho}\,g_r-\frac{\partial\hat{p}}{\partial r}$$

$$+\frac{\partial}{\partial r}\left[2\hat{\mu}\frac{\partial\hat{V}_r}{r}+\left(\tau-\frac{2}{3}\hat{\mu}\right)\operatorname{div}\vec{\hat{V}}\right]+\frac{1}{r}\frac{\partial}{\partial\theta}\left[\hat{\mu}\left(\frac{1}{r}\frac{\partial\hat{V}_r}{\partial\theta}+\frac{\partial\hat{V}_\theta}{\partial r}-\frac{\hat{V}_\theta}{r}\right)\right]$$

$$+\frac{\partial}{\partial z}\left[\hat{\mu}\left(\frac{\partial\hat{V}_r}{\partial z}+\frac{\partial\hat{V}_z}{\partial r}\right)\right]+\frac{2\hat{\mu}}{r}\left(\frac{\partial\hat{V}_r}{r}-\frac{1}{r}\frac{\partial\hat{V}_\theta}{\partial\theta}-\frac{\hat{V}_r}{\partial r}\right) \qquad (5.2)$$

θ–direction

$$\hat{\rho}\left(\hat{V}_r\frac{\partial\hat{V}_\theta}{\partial r}+\frac{\hat{V}_\theta}{r}\frac{\partial\hat{V}_\theta}{\partial\theta}+\hat{V}_z\frac{\partial\hat{V}_\theta}{\partial z}+\frac{\hat{V}_r\hat{V}_\theta}{r}\right)=\hat{\rho}\,g_\theta-\frac{1}{r}\frac{\partial\hat{P}}{\partial\theta}$$

$$+\frac{1}{r}\frac{\partial}{\partial\theta}\left[\frac{2\hat{\mu}}{r}\frac{\partial\hat{V}_\theta}{\partial\theta}+(\tau-\frac{2}{3}\hat{\mu})\,\mathrm{div}\,\hat{\vec{V}}\right]+\frac{\partial}{\partial r}\left[\hat{\mu}(\frac{1}{r}\frac{\partial\hat{V}_r}{\partial\theta}+\frac{\partial\hat{V}_\theta}{\partial r}-\frac{\hat{V}_\theta}{r})\right]$$

$$+\frac{2\hat{\mu}}{r}\left[\frac{1}{r}\frac{\partial\hat{V}_r}{\partial\theta}+\frac{\partial\hat{V}_\theta}{\partial r}-\frac{\hat{V}_\theta}{r}\right]+\frac{\partial}{\partial z}\left[\hat{\mu}(\frac{1}{r}\frac{\partial\hat{V}_z}{\partial\theta}+\frac{\partial\hat{V}_\theta}{\partial z})\right] \qquad (5.3)$$

z-direction

$$\hat{\rho}\,(\,\hat{V}_r\frac{\partial\hat{V}_z}{\partial r}+\frac{\hat{V}_\theta}{r}\frac{\partial\hat{V}_z}{\partial\theta}+\hat{V}_z\frac{\partial\hat{V}_z}{\partial z}\,)=\hat{\rho}g_z-\frac{\partial\hat{P}}{\partial z}$$

$$+\frac{\partial}{\partial z}\left[2\hat{\mu}\frac{\partial\hat{V}_z}{\partial z}+(\tau-\frac{2}{3}\hat{\mu})\,\mathrm{div}\,\hat{\vec{V}}\right]+\frac{1}{r}\frac{\partial}{\partial r}\left[\hat{\mu}r(\frac{\partial\hat{V}_r}{\partial z}+\frac{\partial\hat{V}_z}{\partial r})\right]$$

$$+\frac{1}{r}\frac{\partial}{\partial\theta}\left[\hat{\mu}\,(\frac{1}{r}\frac{\partial\hat{V}_z}{\partial\theta}+\frac{\partial\hat{V}_\theta}{\partial z})\right] \qquad (5.4)$$

$$\text{where}\quad \mathrm{div}\,\vec{V}\equiv\frac{1}{r}\frac{\partial}{\partial r}(\,r\,\hat{V}_r)+\frac{1}{r}\frac{\partial\hat{V}_\theta}{\partial\theta}+\frac{\partial\hat{V}_z}{\partial z} \qquad (5.5)$$

Conservation Equation for a General Scalar Property, $\hat{\Phi}$

The general equation of any scalar $\hat{\Phi}$,such as k,ε can be represented in a form:

$$\hat{\rho}(\hat{V}_r\frac{\partial\hat{\Phi}}{\partial r}+\frac{\hat{V}_\theta}{r}\frac{\partial\hat{\Phi}}{\partial\theta}+\hat{V}_z\frac{\partial\hat{\Phi}}{\partial z})=\hat{\rho}\,D\left[\frac{1}{r}\frac{\partial\hat{\Phi}}{\partial r}+\frac{1}{r^2}\frac{\partial^2\hat{\Phi}}{\partial\theta^2}+\frac{\partial^2\hat{\Phi}}{\partial z^2}+\frac{\partial^2\hat{\Phi}}{\partial r^2}\right]+\hat{S}_\Phi \qquad (5.6)$$

Where D is the diffusion coefficient, and $\hat{S}_\Phi$ is a source or sink term.

Time-Averaged Equations

The instantaneous flow equations given above are exact equations and are

applicable to laminar flow. They apply equally to a turbulent motion, where many important properties of turbulence are small-scale in character. Fortunately for most engineering purposes, it is not required to consider the details of turbulence, since we are usually concerned only with its time-averaged effects, even when the flow is unsteady. The time-averaged equations can be derived from the instantaneous equations by writing an instantaneous value as a sum of its mean value (represented by an overbar, (-) on the variable but neglected here) and a fluctuating part (represented by ') and then time averaging the whole equation.

In view of the experimental evidence that the flow in axial type cyclones loses its three-dimensional character at a short distance from the inlet (below the vanes) and becomes axially symmetric, all the derivatives with respect to the tangential direction have been neglected. So for steady flow the above equations are simplified as follows:

Continuity

$$\frac{\partial u}{\partial z} + \frac{1}{r}\frac{\partial}{\partial r}(rv) = 0 \qquad (5.7)$$

z-momentum

$$u\frac{\partial u}{\partial z} + v\frac{\partial u}{\partial r} = \frac{1}{\rho}\frac{\partial P}{\partial z} - \frac{\partial}{\partial z}\overline{u'^2} - \frac{1}{r}\frac{\partial}{\partial r}r\,\overline{u'v'} \qquad (5.8)$$

r-momentum

$$v\frac{\partial v}{\partial r} + u\frac{\partial v}{\partial z} - \frac{w^2}{r} = \frac{1}{\rho}\frac{\partial P}{\partial r} - \frac{\partial}{\partial z}\overline{u'v'} - \frac{1}{r}\frac{\partial}{\partial r}r\,\overline{v'^2} + \frac{\overline{w'^2}}{r} \qquad (5.9)$$

θ-momentum

$$u\frac{\partial w}{\partial z} + v\frac{\partial w}{\partial r} + \frac{vw}{r} = \frac{\partial}{\partial z}\overline{u'w'} - \frac{1}{r}\frac{\partial}{\partial r}r\,\overline{v'w'} - \frac{\overline{v'w'}}{r} \qquad (5.10)$$

5.2.2 Turbulence Model

Methods for specifying the stresses represented by the velocity correlations $\overline{u'v'}$,$\overline{u'^2}$, etc. are referred to in general as turbulence models. As disscussed by Launder and Spalding (1974), the requirements of a turbulence model are **(i)** width of applicability, **(ii)** accuracy, **(iii)** economy of computer time and **(iv)** simpilicity. Many turbulence models have been proposed; their validity varies according to the problem under consideration. Turbulence models are sometimes classified by number of differential equations they incorporate. The zero, one and two equation models employ Boussinesq's eddy viscosity concept to relate the Reynolds stresses in the mean momentum equations to the mean velocity gradient, eg. $\tau \approx -\overline{\rho u'v'}$ is replaced by $\mu_t.\partial u/\partial y$ for the case of a two-dimensional boundary layer flow where μ_t is termed the turbulent viscosity. If the attention is shifted from the turbulent viscosity to the transport of stresses themselves, it leads to solution of more than two differential equations. These are known as 'multi-equation' model, Reynolds stress model or algebraic stress model.

The k-ε Turbulence Model

By using the gradient transport hypothesis (Hinze 1959), where the fluxes are expressed as coefficients times gradients, following expression can be achived (Launder and Spalding 1974).

$$-\rho\overline{u'v'} = \mu_t \left(\frac{\partial u}{\partial r} + \frac{\partial v}{\partial z}\right) \tag{5.11}$$

$$-\rho\overline{v'\,\Phi} = \frac{\mu_t}{\sigma_{\Phi,t}}\frac{\partial \Phi}{\partial r} \tag{5.12}$$

where μ_t= turbulent viscosirty and $\sigma_{\phi,t}$= effective Prandtl /Schmidt number. It is then necessary to seek a way of determining the turbulent (or eddy) viscosity, μ_t. There are various methods of determining μ_t, and the k-ε model was recommended for this calculation (Launder and Spalding 1974). $\sigma_{\phi,t}$ is often assumed known, and from dimensional analysis, μ_t turns out to be a function of the turbulence

energy ($k=0.5(u'^2+v'^2+w'^2)$) and its dissippation rate ε:

$$\mu_t = C_\mu \rho \frac{k^2}{\varepsilon} \tag{5.13}$$

k and ε are derived from their own transport equations (Gosman and Ideriah 1976). The turbulence energy equation and energy dissipation equation may be obtained from the transport equation (5.6).

Turbulence Energy k

$$\frac{1}{r}\left[\frac{\partial}{\partial z}(r\rho uk) + \frac{\partial}{\partial r}(r\rho vk)\right] = \frac{1}{r}\left[\frac{\partial}{\partial z}\left(r\frac{\mu_{eff}}{\sigma_k}\frac{\partial k}{\partial z}\right) + \frac{\partial}{\partial r}\left(r\frac{\mu_{eff}}{\sigma_k}\frac{\partial k}{\partial r}\right)\right] + \underbrace{G - C_D\rho\varepsilon}_{S_K} \tag{5.14}$$

Energy Dissipation Rate ε

$$\frac{1}{r}\left[\frac{\partial}{\partial z}(r\rho u\varepsilon) + \frac{\partial}{\partial r}(r\rho v\varepsilon)\right] = \frac{1}{r}\left[\frac{\partial}{\partial z}\left(r\frac{\mu_{eff}}{\sigma_\varepsilon}\frac{\partial \varepsilon}{\partial z}\right) + \frac{\partial}{\partial r}\left(r\frac{\mu_{eff}}{\sigma_\varepsilon}\frac{\partial \varepsilon}{\partial r}\right)\right]$$

$$\underbrace{+C_1\frac{\varepsilon}{k}G - C_2\rho\frac{\varepsilon^2}{k}}_{S_\varepsilon} \tag{5.15}$$

where

$$G = \mu_t\left[2\left[\left(\frac{\partial u}{\partial z}\right)^2 + \left(\frac{\partial v}{\partial r}\right)^2 + \left(\frac{v}{r}\right)^2\right] + \left(\frac{\partial u}{\partial r} + \frac{\partial v}{\partial z}\right)^2\right] + S_G \tag{5.16}$$

$$S_G = -\frac{2}{3}\mu_t\left[\frac{1}{r}\frac{\partial}{\partial r}(rv) + \frac{\partial u}{\partial z}\right]^2 \tag{5.17}$$

G represents generation of k from the mean flow by turbulent shear stress and ε is the rate of viscous dissipation of k to heat by the smallest turbulent eddies. The c's and σ's are generally empirical functions, but they turn out to be constant for high

Reynolds number flows (Gosman and Ideriah 1976). The value for C's and σ's were recommended as follows (Launder and Spalding 1974)

$C_\mu = 0.09$ $C_1=1.44$ $\sigma_k=1.0$
$C_D= 1.0$ $C_2=1.92$ $\sigma_\varepsilon=1.3$

Effective viscosity models have led to satisfactory prediction of many two-dimensional thin-shear-layer flows (Launder and Spalding 1974); their use in three-dimensional flows and other flows with more than a single significant component of mean velocity gradient has achieved at best moderate success. Two-equation models are not universally applicable. Even a seemingly simple flow such as an axisymmetric round jet can not be predicted accurately with the set of constants which serves for plane free shear flows. Attention is therefore shifted from the turbulent viscosity to the Reynolds stresses themselves and this generally leads to solution of more than two differential equations.

Algebraic Reynolds Stress Turbulent Model

The theoretical analysis of confined vortex flows on the other hand is extremely difficult and little progress in this area has so far been achieved. Apart from the fact that the governing equations are non-linear and strongly coupled, the structure of turbulence is non-homogeneous and anisotropic. Despite these difficulties, most of the existing turbulence models assume that the turbulence is isotropic and although more complex Reynolds stress models are being developed, these have not so far led to successful predictions of strongly swirling flows. In order to successfully apply finite difference modelling to these classes of flows it has therefore been found necessary to adapt a more fundamental approach to turbulence modelling (Boysan et al. 1981). The equations 5.7 to 5.10 can be solved only when the terms containing the fluctuating components can be evaluated. By introducing the fluctuating components of velocity more unknown quantities have been generated than there are equations, so that some form of closure hypothesis is required which relates the Reynolds stresses to the time averaged quantities. It is possible to derive the exact differential equations for the transport of Reynolds stress components from the Navier- Stokes equations. In tensor form these can be written as (Ayers et al. 1985):

$$T_{ij} = P_{ij} - \frac{2}{3}\varepsilon\,\delta_{ij} + \psi_{ij} \qquad (5.18)$$

where T_{ij} represents the combined convection and diffusion terms, P_{ij} is production, ε is dissipation and Ψ_{ij} is the pressure-strain term. These equations can be incorporated into the numerical solution procedure provided the latter is appropriately modelled. In order to reduce the computational effort required for their solution they are reduced to an algebraic form where possible. The pressure-strain term model proposed by Erdogan et al (1980) was used and the transport terms were replaced (Boysan et al 1981) by the following approximation which is due to Rodi (1976):

$$T_{ij} = \frac{\overline{u_i' u_j'}}{k}\,(P-\varepsilon) \qquad (5.19)$$

Hence the following algebraic relations were obtained by Boysan et al. (1981) for the six Reynolds stresses.

$$\overline{u_i' u_j'} = \alpha\frac{k}{P}\left(P_{ij} - \frac{2}{3}\delta_{ij}P\right) + \beta\frac{k}{P}\left(D_{ij} - \frac{2}{3}\delta_{ij}P\right) + \gamma\frac{k^2}{P}\left(\frac{\partial u_i}{\partial X_j} + \frac{\partial u_j}{\partial X_i}\right) \qquad (5.20)$$

where

$$P_{ij} = -\left[\overline{u_i' u_k'}\,\frac{\partial u_j}{\partial X_k} + \overline{u_j' u_k'}\,\frac{\partial u_i}{\partial X_k}\right] \qquad (5.21)$$

$$D_{ij} = -\left[\overline{u_i' u_k'}\,\frac{\partial u_k}{\partial X_j} + \overline{u_j' u_k'}\,\frac{\partial u_k}{\partial X_i}\right] \qquad (5.22)$$

$$P = -\overline{u_i' u_j'}\,\frac{\partial u_i}{\partial X_k} \qquad (5.23)$$

α, β, γ are functions of P/ε which are independent of one another. These variable coefficients can be expressed as (Boysan and Swithenbank 1981) :

$$\alpha=\frac{0.26P/\varepsilon}{0.443+P/\varepsilon} \quad \beta=\frac{-0.176(P/\varepsilon)^3}{2.92+(P/\varepsilon)^3} \quad \gamma=\frac{-0.135(P/\varepsilon)^3}{0.927+(P/\varepsilon)^3} \qquad (5.24)$$

In addition to the above set of algebraic relations it is necessary to solve the equations for the transport of the kinetic energy of turbulence and its dissipation rate (5.14 and 5.15) to complete the model.

5.2.3 Wall Function

Near the wall the equation of mean flow is simplified and with assumptions like one-dimensional, constant shear, the momentum equation may be written as :

$$\frac{\tau}{\tau_w}=\left(1+\frac{\mu_t}{\mu}\right)\frac{du^+}{dy^+} \qquad (5.25)$$

Near a wall, the local Re becomes very small and the turbulence model, which is designed for high Re, becomes inadequate. Both this fact and the steep variation of properties near walls necessitate special alteration for grid nodes close to walls (Gosman and Ideriah, 1976).

The wall region is made up of three zones (Hinze 1959 ,Fig. 5.1). These are the viscous sublayer ($0.0< y^+<5$) where viscous effects dominate, the inertial sublayer ($30<y^+<400$) where the flow is assumed to be completly turbulent but $\tau \cong \tau_w$, and the transition (or ' buffer') zone ($5<y^+<30$) of vigorous turbulence dynamics where the flow is neither completely dominated by viscous effects nor completely turbulent.

The wall treatment needed to be simplified and a well-known procedure (Spalding 1972) was used. The approach, is to dispose of the 'buffer' layer by defining a point $y^+=11.63$ (where the linear velocity profile in the viscous sublayer meets the logarithmic velocity profile in the inertial sublayer) below which the flow is assumed to be purely viscous and above which it is purely turbulent.

$$\text{For } y^+ \leq 11.63 \ , \ \frac{\mu_t}{\mu} << 1 \ , \ \tau \approx \tau_w \ , \ \text{thus } U^+ = y^+$$

$$\text{For } y^+ > 11.63 \ , \ \frac{\mu_t}{\mu} >> 1 \ , \ \tau \approx \tau_w \ , \ \nu_t = \chi \, y \, u_t$$

$$\text{thus } U^+ = \frac{1}{\chi} \log_e (E \, y^+) \text{ where } y^+ = \frac{U_t \, y}{\nu} \ , \ U^+ = \frac{U}{U_t} \ , \ U_t = \sqrt{\frac{\tau_w}{\rho}} \ ,$$

χ (Von Karman Constant) = 0.4187 and E= 9.793

The basis of the wall treatment for k and ε equations is :

k- Equation

$$\text{Production} \approx \text{Dissipation} \Longrightarrow -\overline{uv}\frac{du}{dy} = \varepsilon$$

$$k = \frac{\tau_l}{\rho} / C_\mu^{0.5} \qquad \tau_l = \text{shear stress in inertial sublayer}$$

ε-Equation

$$\varepsilon = c_\mu^{0.75} \, k^{1.5} / \chi y \tag{5.26}$$

The approach adopted is strictly valid only for the inertial sublayer where the flow is assumed to be completely turbulent. The final form of wall shear is:

$$\tau_w = \rho \, C_\mu^{0.25} \, K^{0.5} \, \chi \, u \, / \left[\log_e (E \, y^+) \right] \tag{5.27}$$

$$y^+ = y \sqrt{\frac{\tau_w}{\rho}} / \nu \approx y \, \rho \, C_\mu^{0.25} \, K^{0.5} / \mu \tag{5.28}$$

The transformation of the governing equation into finite difference form can be done by various methods, including Taylor series expansion, Polynominal fitting,

integral method and control volume approach. The control volume approach has been employed with a hybrid scheme (combination of upwind and central differencing) for the evaluation of the fluxes. All the f.d.e's are solved by the line-by-line iteration method which employs the tri-diagonal matrix algorithm (TDMA). A consequence of using 'primitive' variables (u,v,w,p) is the need to obtain the pressure field by some special method. The procedure employed in so doing is the SIMPLE algorithm. At the boundaries of the calculation domain, the general f.d.e's are not applicable, hence special measures are required for the cells next to the boundaries. Appendix D gives more information about the solution procedures.

5.3 SOLUTION FOR PARTICLE PHASE

The particle phase of the solution procedure is carried out by calculating the individual trajectories of a large number of particles, rather than by solving a continuum equation. The gas phase solution is carried out in an Eulerian frame of reference and the solids phase in a Lagrangian frame. This is thought to be most appropriate model of fluid-particle interactions because it closely corresponds to the physical process being modelled.

5.3.1 Particle Trajectories

The determination of the paths that the particles follow in a given gas flow field is of paramount importance in cyclones for the estimation of efficiency of collection. The slip velocity between the particles and gas is likely to be small in cyclones (Boysan et al. 1982) and if the solid phase is sufficiently dilute, then it can be assumed that interactions between the particles are absent and that the influence of the particles on gas-phase momentum is negligible (i.e. gas-particle momentum coupling is one-way only). When all external effects except drag are neglected the equations of motion of a particle can be written as (Williams 1965):

$$\frac{du_P}{dt} = -F\,(u_P - u_\infty) \tag{5.29}$$

$$\frac{dv_P}{dt} = \frac{w_P^2}{r_P} - F\,(v_P - v_\infty) \tag{5.30}$$

$$\frac{dw_P}{dt} = -\frac{v_P w_P}{r_P} - F(w_P - w_\infty) \tag{5.31}$$

and the equations of the trajectory are:

$$\frac{dX}{dt} = u_P \qquad \frac{dr}{dt} = v_P \qquad r\frac{d\theta}{dt} = w_P \tag{5.32}$$

Here the subscript p refers to the particle and ∞ to the mean gas flow. The gas velocities vary throughout the flow field, and the values used are those prevailing in the finite difference cell which the particle occupies at any given moment. The term F in the above equations can be written as:

$$F = \frac{18\,\mu_g}{\rho_P\, d_P^2} \cdot \frac{C_D\, Re}{24} \tag{5.33}$$

Re stands here for relative Reynolds number, which is defined as:

$$Re = \frac{\rho_g\, d_P\, |\, u_P - u_\infty |}{\mu_g} \tag{5.34}$$

The drag coefficient C_D is expressed as a function of the relative Reynolds number with general form :

$$C_D = a_1 + \frac{a_2}{Re} + \frac{a_3}{Re^2} \tag{5.35}$$

where the a's are given for several ranges of Reynolds number by Morsi and Alexander (1972) so that the Stokes regime is obeyed for Re < 0.1, and for 0.1 < Re < 1 the a's take the values, a_1=3.69 , a_2=22.73 and a_3= 0.0903 respectively.

A stochastic particle tracking method is applied which involves the inclusion of the instantaneous values of the fluctuating components in the gas flow velocities appearing in the equations of motion. The values of u', v' and w', which prevail during the lifetime of a fluid eddy that the particle is traversing, are sampled by assuming that these obey a Gaussian probability distribution, so that (Boysan et al. 1982):

$$u' = \zeta\sqrt{\overline{u'^2}} \qquad v' = \zeta\sqrt{\overline{v'^2}} \qquad w' = \zeta\sqrt{\overline{w'^2}} \tag{5.36}$$

where ζ is a normally distributed random number, and the remainder of the right-hand side is the local r.m.s value of the velocity fluctuations, which is calculated during the solution of the gas flow field. The value of the random number chosen is applied for the characteristic life-time of the eddy, defined as:

$$\tau = \frac{C_\mu^{0.75}}{\sqrt{2}} \frac{k}{\varepsilon} \tag{5.37}$$

after which a new value of ζ is chosen. The values of u, v, w, $(u'^2)^{0.5}$, $(v'^2)^{0.5}$and $(w'^2)^{0.5}$ are updated whenever migration into a neighbouring cell occurs. When these two time constraints are combined a time interval is obtained during which the gas flow velocity remains constant. This permits the direct integration of the equation of motion in the z-direction to obtain a local closed-form solution. The other two equations in the r and θ directions can also be solved analytically provided that it is assumed that the body force remains constant over a given time interval. Clearly the time interval in question must be sufficiently small for this assumption to hold. These integrated expressions for u_p, v_p and w_p thus obtained can be written

$$u_p = u+u'+ (u_{p,0} - u - u') \exp\left[-F(t-t_o)\right] \tag{5.38}$$

$$v_p = v+v'+ \frac{w_p^2}{F\, r_{p,0}} + \left[v_{p,0} - v - v' - \frac{w_p^2}{F\, r_{p,0}} \right] \exp\left[-F(t-t_0) \right] \tag{5.39}$$

$$w_P = w + w' - \frac{w_{P,0}\, v_{P,0}}{F\, r_{P,0}} + \left[w_{P,0} - w - w' + \frac{v_{P,0}\, w_{P,0}}{F\, r_{P,0}} \right] \exp\left[-F(t-t_0) \right] \qquad (5.40)$$

Here the subscript "0" refers to the conditions at the beginning of the time interval. When a particle migrates into a cell corresponding to the boundaries of the domain of integration, or an internal wall, etc, one of several contingencies may arise, and these can be summarised as follows (Boysan et al, 1982):

Reflection : The particle bounces off the boundary in question as if it had a coefficient of restitution of unity. This is assumed to occur at the inlet zone boundaries and the vortex finder

Saltation : In order to prevent time consuming "trickling" of a particle down a wall, in some cases the particle is replaced in the gas field a small distance from the wall as though it was "leaping" back into the flow.

Collection : this condition is applied when the particle reaches the entrance to the hopper or reaches a boundary where this outcome is considered inevitable such as on the conical wall (it is necessary to mention that in SPRINT-4 this condition applies when the particle reaches any part of the cyclone wall).

Escape : The particle is lost when it passes through the vortex finder exit

The last two of these conditions effectively terminate the particle tracking process.

5.4 NUMERICAL INVESTIGATION

5.4.1 Introduction

SPRINT-4 is a computer program developed at Sheffield University which simulates the fluid flow and particle motion in axially-symmetric confined turbulent

flows with special emphasis on cyclone separators. The mathematical modelling techniques have been described in Sec.5.2 and 5.3 and some results for tangential-entry reverse-flow cyclones are described by Boysan et al (1982). There is an option for axial-entry cyclones (having swirl vanes), in which the tangential velocities produced by the vanes must be of either free-vortex or forced-vortex type (Boysan,1983). It is an interactive program in FORTRAN IV, claimed to be machine independent except for a random number subroutine and the graphics system. However, because of its interactive nature, its usage of characters and file handling systems are not necessarily portable to other computer systems and may need some adaption. This section outlines a modification of SPRINT-4, which includes some major changes in the logic of the gas flow solution as well as those necessitated by the change of computer.

Firstly this program was modified to use FORTRAN 77 compilers without changing its logic, then it was adapted to run on CDC Cyber and Amdahl mainframe computers, because of the superior debugging facilities (CDC) and the availability of the GHOST 80 plotting routines included in SPRINT4 (Amdahl).

Secondly because of some problems with specifying boundary conditions such as vortex finder wall thickness, inlet velocity profile, vane angle, etc. the logic of the program was changed. In so doing, it was noticed that certain features of the gas flow solution algorithm in SPRINT-4 differed from those in the Imperial College program TEACH-T (Gosman and Ideriah 1976 and Gosman et al. 1979) on which it was originally based, and did not correspond to the practices currently recommended by users and developers of similar algorithms. The opportunity was therefore taken to re-write those parts of SPRINT-4 to conform to current Imperial College usage, but leaving alone the turbulence model of SPRINT4. This resulted in the program CYCINT-1 (for axial-entry cyclones only). It must be stressed that descriptions of the detailed operation of SPRINT4 refer specifically to the version supplied to the author.

Finally, the interactive version of this program was adapted (mainly in terms of file handling) to run on an IBM PC-AT microcomputer or compatible computer with 80286/386 processor and 80287/387 maths co-processor (Behrouzi ,1987).

5.4.2 Adaption of SPRINT-4 for CDC and Amdahl Computers

The major modifications during adaption were grid system alteration, using FORTRAN 77, deleting unnecessary subroutines (graphics etc.), using random number generators from the appropriate libraries, changing the program from interactive to batch use and some optimization work for decreasing the size of the program. In all these stages, the logic of SPRINT-4 for calculating gas flow field and particle collection efficiency remained unchanged.

SPRINT-4 was written mainly for tangential-entry cyclones, but can also accept a swirl vane inlet condition. For the latter case, it appears necessary to specify a false space (for example the height of vane) above the main calculation domain. The SPRINT-4 grid system was therefore edited. The new grid system consists of two parts, first the main domain of calculation which has exactly the same geometry as required for further development into CYCINT-1, and a smaller part for the inlet zone which was necessary for SPRINT-4. Fig. 5.3 shows the grid system for SPRINT-4 and CYCINT-1.

5.4.3 Grid System Improvement

A new grid system was developed for axial-entry cyclones only, which contains no more than the required domain of calculation. Compared with SPRINT-4, it has no inlet zone (Fig. 5.3), so needs less memory space and also less execution time. Unlike SPRINT-4, CYCINT-1 considers a finite thickness for the vortex finder tube, particularly relevant for comparison with small-scale laboratory cyclones. To accomodate new boundary conditions at the vortex finder walls it is necessary to have an axial grid line which passes through the vortex finder wall. The grid system generated by CYCINT-1 is automatically adjusted if necessary to provide an additional grid line within the vortex finder wall. Fig 5.4 shows the control points of the new grid system.

5.4.4 Modification of Inlet Conditions

Axial-entry cyclone geometry is shown in Fig 5.2. New input data for the numerical model includes swirl vane exit angle. The axial velocity component at the inlet (the vane trailing edge plane) is calculated from the specified flow rate by the continuity equation and the inlet swirl velocity is calculated from the axial velocity and the vane angle.

SPRINT-4 specifies a flat profile (i.e. uniform radial distribution) for axial velocity at the inlet and the user selects a free or forced vortex profile for swirl velocity. Fig. 5.5 shows experimental results obtained by the author using laser-Doppler anemometry in the model cyclone. The swirl velocity profile leaving the vanes nearly is flat and so CYCINT-1 assumes initially flat profiles for both swirl and axial velocity components.

5.4.5 Boundary Condition Improvement

For all gas-phase equations (those solved for the three velocity components, pressure, turbulent kinetic energy and its rate of dissipation), new boundary conditions have been written. The major differences between those of CYCINT-1 and of SPRINT-4 are reported here, assuming some knowledge of the solution method (Patankar 1980, Gosman et al 1979 & 1969).

Fig. 5.4 shows the exact position of cylone walls and boundaries. Because of restrictions on the numerical method, the conical wall is assumed to be a stepped wall. This figure shows only grid points at which scalar quantities are calculated. Backward-staggered grids are used for defining the locations of vector variables (Fig. 5.6), and according to the variable the boundary cells require a variety of treatments.

I-Axial Velocity (u)

For all walls which are parallel with the axial direction, complete boundary conditions according to Gosman and Ideriah (1976) were inserted. For all these

walls, shear stresses for further usage were calculated using the "wall function" procedure (Patankar 1980). For all walls perpendicular to the axial direction, the convection and diffusion coefficient (a) is assumed to be zero. SPRINT-4 has not used wall functions for the conical wall and one side of the vortex finder tube; for the other side of the vortex finder a simple shear calculation was made, based on a specified, constant value of friction factor. For all nodes inside the vortex finder wall and outside the conical wall, the value of velocity is put to zero in CYCINT-1.

As in SPRINT-4, the continuity of gas mass flow between inlet, dust exit (if there is underflow or bottom bleed), and gas outlet is checked and the outlet velocity is adjusted to reduce the imbalance to zero. CYCINT-1 can accept underflow and for this case, a uniform axial velocity profile is assumed at the exit to the hopper; SPRINT-4 has this facility but all the underflow is considered to exit from one grid point, that nearest to the conical wall, while other nodes on the dust exit plane still have zero velocity. For all nodes at this boundary, with no underflow, the convection and diffusion coefficient is put to zero in CYCINT-1; SPRINT-4 puts the u value at these nodes to zero through the source term.

II- Radial Velocity (v)

The normal procedure (Gosman et al, 1979) is used for vortex finder walls and the conical wall; SPRINT-4 does not use wall functions for the conical wall. SPRINT-4 does some unnecessary boundary computation in the domain which does not apply to the axial-entry case; this has been deleted in CYCINT-1. For the symmetry axis boundary, the convection and diffusion coefficient is put to zero, while SPRINT-4 uses the source term method for this purpose. At the dust exit boundary, the values are put equal to those at adjacent nodes, whereas SPRINT-4 cuts the relation between hopper and cyclone by putting the convection and diffusion coefficient to zero. Values at nodes inside the vortex finder wall are put to zero.

III-Pressure (p)

The values at all nodes inside the vortex finder wall and outside the conical wall are put to zero. The vortex finder walls are isolated from the domain of solution by

putting to zero the value of the convection and diffusion coefficient at nodes next to the walls.

IV-Swirl Velocity (w)

A complete wall function procedure and related shear stress for further use were considered for all walls. SPRINT-4 only uses a conventional wall function for the parallel part of the cyclone body and a simplified wall function for the vortex finder. Some unnecessary boundaries are again handled by SPRINT-4. The convection and diffusion coefficient is put to zero for the symmetry axis boundary, as normal practice; SPRINT-4 has no boundary condition for this. The value at nodes inside the vortex finder wall is put to zero through the source term. For outlet boundaries SPRINT-4 uses the value at the nearest point to the vortex finder as the reference value (w_{ref}) and the values at other points are calculated from the forced vortex relation, $W_{ref}.(r/R_{ref})$. The convection and diffusion coefficients are put to zero by SPRINT-4 only for nodes with back flow (expected near the centre line because of high swirl). For the gas outlet boundary CYCINT-1 uses normal procedure and for all boundary nodes puts the values equal to those at adjacent nodes; i.e. a zero axial gradient boundary condition. At the dust exit, SPRINT-4 disconnects the relation between hopper and the cyclone; CYCINT-1 again has a zero axial gradient condition.

V-Turbulence Kinetic Energy (k) and Dissipation Rate (ε) and others

For turbulent kinetic energy, SPRINT-4 seems to use on the cylindrical outer wall a procedure intended only for energy dissipation boundary treatment, and again treats boundaries outside the required domain. CYCINT-1 has rectified these anomalies. As for other variables, CYCINT-1 puts the values of turbulence parameters at the dust exit boundary equal to the values at adjacent nodes whereas SPRINT-4 again isolates the cyclone from the gas below the dust exit by putting the convection and diffusion coefficient to zero. CYCINT-1 uses everywhere the correct procedure for shear stress at walls in order to calculate k.

5.4.6 Swirl Velocity Improvement

After each iteration, SPRINT-4 checks the swirl velocity at each node inside the domain of solution and if it exceeds some specified limit its value may be changed. This may have been connected with stability problems but it is not a recommended procedure (Behrouzi 1987). In CYCINT-1 this part of the program is deleted and swirl velocity is calculated directly from the solution of finite difference equation.

5.4.7 Cyclone Pressure Drop Improvement

Cyclone pressure drop is calculated in SPRINT-4 by subtracting the mean pressure over the outlet cross-section from the pressure at the nearest node to the cyclone body wall at inlet. This method may be suitable for tangential-entry cyclones, but not for vane type cyclones. CYCINT-1 therefore calculates the pressure drop from integrated values over the cross-sections at both inlet and outlet of the cyclone. In either case, the output shows the drop in static pressure between two locations where the axial mean velocity is likely to differ, and therefore needs further processing to yield the true stagnation (or total) pressure loss. The additional stagnation pressure drop through the vanes clearly cannot be calculated, but is expected to be small.

5.4.8 Improvements in Cyclone Efficiency Calculation

Three major changes have been made to this section of program. The first concerns the initial locations and velocities of the particles. The vane-entry option in SPRINT-4 does not easily allow initial placing of particles at a radius smaller than the inner side of a normal tangential inlet duct (i.e. it is difficult to avoid a particle-free zone adjacent to gas exit tube); this has been remedied in CYCINT-1, together with the method of specifying the particles' initial tangential velocity.

Second, the criterion for final capture of particles has been changed. Descriptions of SPRINT-4 in the literature explain how, originally, particles were tracked as they slowly "bounced" down the parallel and conical walls until they reached the dust exit, and how this time-consuming " saltation" procedure was replaced, without much

error, by the assumption that a particle was captured as soon as it reached the wall. Experience with CYCINT-1 has shown that with higher turbulent velocities near the top of conical part of the cyclone, particles frequently escape to the gas exit after trickling for some distance down the wall. The saltation process has therefore been retained in CYCINT-1,at the expense of execution time. For relatively coarse dust, comparision runs with both methods have shown overall mass collection efficiencies reduced by ~ 3 % when using the saltation procedure, which could have a very large effect on the amount of dust in the clean gas stream. Results are also sensitive to the way in which particles are returned to the flow after each impact with the wall; modelling this via a restitution coefficient may be considered in future, but at present the old SPRINT-4 method, of repositioning the particle at a fixed fraction (e.g. 0.995) of the local wall radius, has been retained.

The third main change is to the method of calculating overall mass collection efficiency. The version of SPRINT-4 recieved by the author simply counted captured particles and divided by total number of particles tracked, and may therefore have been intended only for monodisperse particulates; it also requested as input the parameters required to define a Rosin-Rammler size distribution (see Appendix C), but made no use of these data. CYCINT-1 now constructs a Rosin-Rammler distribution and runs through all the specified injection locations and number of tracks from each location in turn, for each size class; overall efficiency is then found as the mass of captured particles divided by the total injected mass. It is important to mention that this method is based on a fit of a stepped function to the Rosin-Rammler curve (see section 4.5.1 and also Fig. 4.40) and then using the following formula:

$$\eta = \frac{\sum \eta_{D_i} \Delta m_i}{\sum \Delta m_i} \qquad (5.41)$$

where η_{D_i} and Δm_i are efficiency and mass fraction for a particles (assumed all to have a diameter D_i between d_i and d_{i+1}, see also Fig. 4.40). The accuracy of results depends on the number of particle sizes, especially where the cumulative mass varies sharply with diameter.

Additional changes include the necessary logic to handle the now-finite thickness of the gas exit tube wall (including the possibility of particle reflection from the tube lip), replacement of the random number generator by a routine from the appropriate system library, correction of some coding in the routine which samples the fluctuating gas velocity component for the stochastic tracking procedure, and simplification by removal of features relevant only to tangential-entry cyclones.

5.5 RESULTS FROM NEW NUMERICAL MODEL

5.5.1 Introductory Remarks

CDC Cyber and Amdhal mainframe computers have been used for running CYCINT-1 (cyclone interactive modelling, version 1). For presentation of results, three graphics systems have been employed. A graphic packages using the MLOOK77 facility on the CDC has been developed for plotting contours, profiles, stream lines, etc. of the cyclone flow field. Also for plotting particle tracks, a graphics package named GHOST80 on the Amdhal was used, and for the rest of the plots, Apple and Acorn BBC microcomputers have been employed.

Since each run of CYCINT-1 is expensive (needing at least 30 ULCC units on the main frames), it was decided to use an adapted version of CYCINT-1 on an IBM PC-AT microcomputer. Therefore CYCINT-1 has been compiled on an IBM PC-AT using the Prospero PRO-FORTRAN 77 compiler with the memory model required when code-plus-data storage exceeds 64 Kbytes. Execution of the resulting machine code requires an AT having 512 Kbytes of RAM,a 20 Mbyte hard disc and a 1.2 Mbyte 5 1/4" floppy disc drive. Reasonable execution times require an 80287 maths co-processor. Fig. 5.7 shows the structure of CYCINT-1 on IBM PC-AT.

5.5.2 Cyclone Scaling Investigation

For a half century the best approach to cyclone design has been to select a "standard" or known design of cyclone defined by a set of relative geometrical proportions, and only then can a meaningful scale-up or down be carried out which leads to reasonably reliable designs (Svarovsky 1981). Stairmand (1951) recognized

that the basic physical model which he used to explain the scaling relationships was too simple. In 1977 Beeckmans and Kim have shown evidence of the influence of the cyclone Reynolds number as well as the customary Stokes number on efficiency, in some careful measurements on mono-disperse dust. Also it must be borne in mind that although many claims may be made on the basis of laboratory testing on small scale experiments, these claims may be difficult to obtain or justify on a full size practical cyclone (Greenfield 1986)

By considering the above facts, the geometrical proportions of full scale and experimental cyclone were chosen as in the laboratory multicell unit (nearly those of Stairmand high-efficiency cyclone). Also the Reynolds and Stokes number matching have been considered. Since it was impossible to test experimentaly a full-scale cyclone, the scaling effect on the axial-type cyclone was theoretically investigated and reported here.

Fig. 5.8 shows axial, radial and tangential velocity contours where flow rates are 0.297 (graph a), 0.049 (graph b) and 0.0242 m^3/s (graph c), for full scale, experimental scale (Re No. matching) and experimental scale (St. No. matching) respectively. These contours shows a considerable flow field similarity between graphs (a) and (b) which have the same Re. numbers (67400). But by reducing Re to 33470 (graph c), this similarity decreases especially for radial velocity which can be as important for collecting particles as tangential velocity, in some regions of the cyclone. However, the general flow pattern is believed to be sufficiently similar at the two Re numbers to justify the decision to carry out dust measurements at less than full-scale Re.

For better understanding of matching cyclone flow fields on the basis of Reynolds number, non-dimensional profiles (at specified grid lines, see Fig. 5.4) of axial, radial and tangential velocity have been predicted by CYCINT-1 and shown in Fig. 5.9 to 5.11 for full scale cyclone, water and air experimental cyclones respectively. The Re number for all these cases is the same, 67400.

The axial velocity profiles for all grid lines seem to have the same pattern and only the water rig prediction shows a backflow effect near the cyclone axis. The

reason for this irregularity may be related to inaccuracy of the finite difference method at the swirl center or the existance of high swirl plus high viscosity (water). Anyhow, Nuttall (1953) showed that reverse flows are also characteristic of swirling flows in circular pipes. In the important regions especially near vortex finder exit tube (grid line No. 15), the radial velocity profiles seem to have reasonably similar patterns for all cases. Some grid lines (e.g. No. 10) show a considerable difference for radial velocity profile. It seems that the values of radial velocity in these zones are too small for reliable comparison. The tangential velocity profiles seem nearly similar for all cases and grid lines. From these results it becomes apparent that Reynolds number matching of the gas flow fields of the full-scale and experimental cyclones should be satisfactory for investigating the aerodynamics, if not the dust collection performance.

The mass efficiencies of full-scale and experimental scale cyclones were predicted as 84.8±1% and 87.0 ±1% respectively for Stokes number equal to 0.044 in each case. For the range of particle size from 1 to 15 μm, the mass efficiencies were estimated as 62.6±1% and 82.4±1% for full scale and experimental cyclones respectively. SPRINT-4 predicted 75% for 1-15 μm particles in the experimental cyclone at the same Stokes number (SPRINT-4 efficiency calculation is different from CYCINT-1,see also Sec.5.4.8). At this stage it is impossible to draw firm conclusions about the method of scaling particle behaviour with Stokes number, mainly because present model excluded physical effects such as agglomeration and humidity. Svarovsky (1981) recommended using St * Re=constant, for similarity in hydro-cyclones while Beeckmans (1979) who investigated a number of functions which correlate cyclone efficiency with Re and St in gas cyclones. It is possible that these or some other relationship would produce better matching,but this has not yet been investigated using CYCINT-1.

5.5.3 Cyclone Gas Flow Field

A computer prediction of the gas flow field for the experimental cyclone at 67400 Re. number is shown in Fig. 5.12 to 5.14. The velocity vectors and streamline plots give an overall impression of the flow. CYCINT-1 predicted the surface of zero axial velocity ("mantle" see also section 2.9) to have a conical shape with side parallel

with the cyclone conical wall (Fig. 5.12b section A-A), at a distance of nearly 1/4 of the cyclone exit diameter from the conical wall.

Tangential velocity profiles are given in Fig. 5.13c and show the expected Rankine type vortex. For the outer section of flow it is nearly of free vortex type whilst for the inner section it resembles a forced vortex. There is also a sharp swirl velocity gradient near the cyclone walls. The vortex core diameter is predicted as nearly half the vortex finder exit diameter which is the same as predicted by Ter Linden (1949) and Pericleous et al (1984).

The radial velocity (Fig. 5.13b) profiles show a negligible radial velocity except near the vortex finder tube entry, where CYCINT-1 predicted a strong inward radial velocity with a peak underneath the vortex finder tube wall.

The turbulence of the cyclone flow field is presented in Fig. 5.14. The regions of highest turbulence intensity are the core zone and the region near the vortex finder entry. For all numerical outputs the turbulence intensity at the inlet was assumed to be 5%. The results from the numerical model were not very sensitive to inlet turbulence intensity, mainly because of high turbulence energy generation inside the domain of solution.

The effect of cyclone flow rate on axial, radial and tangential velocity profiles have been investigated theoretically by CYCINT-1. Fig. 5.15 to 5.20 show results of this investigation, performed for the experimental cyclone working with water (Fig. 5.15 to 5.17) and with air (Fig. 5.18 to 5.20). All the results agree well in general shape with results of other researchers such as Ter Linden (1949), Boysan et al (1982), Pericleous et al (1984) and Bloor and Ingham (1987) (all for tangential-inlet cyclones). For example Fig. 5.15 shows that by increasing rig flow rate (hence Reynolds number), a reverse flow occurs at cyclone axis. This phenomenon was reported by Ter Linden (1949), Kelsall (1952), etc. Kelsall noted that under certain conditions (high Reynolds number) a three-celled vortex structure was possible within a cyclone (normally there exists a twin-vortex structure).

5.5.4 Cyclone Pressure Drop and Mass Efficiency

Fig. 5.21a shows pressure contours predicted by CYCINT-1 for the experimental cyclone at 0.024 m^3/s flow rate. Also Fig. 5.21b shows the contours predicted by SPRINT-4. The pressure on the cyclone axis has a minimum in the vortex finder tube entry region, in the form of an elongated bubble of low pressure. The pressure increases with radius, but does not appear to change with axial location. At the vane trailing edge, the predictions of CYCINT-1 and SPRINT-4 are different and SPRINT-4 predicted a flat pressure profile at cyclone inlet zone. It seems that the CYCINT-1 prediction adheres more closely to the physics of the flow than that from SPRINT-4. It is necessary to point out that because of the different pressure reference points in CYCINT-1 and SPRINT-4, the values on the contours in Fig. 5.21a and b do not match each other.

Fig. 5.22 shows effect of flow rate on cyclone pressure drop predicted by CYCINT-1 and also measured experimentaly by the author for the one-cell water rig. The cyclone static pressure drop (sta.) is the difference between grid points P1 and P2 shown in Fig. 5.4, while the cyclone average pressure drop (ave.) is the difference between integrated values over the cyclone inlet and outlet planes. Because of technical problems, the locations of the measuring pressure tappings were outside the domain of solution. Therefore experimentally the cyclone pressure drop included a vane-zone pressure drop plus about 1m (50 mm dia.) pipe pressure loss in the vortex finder tube extension. This may account for the difference between numerical and experimental curves shown in Fig. 5.22.

For choosing cyclones, mass efficiency and pressure drop are the most important parameters. The effect of cyclone flow rate on these two parameters, as predicted by CYCINT-1, are shown in Fig. 5.23 and 5.24 for the experimental and full scale cyclones respectively. Fig. 5.25 shows similar curves for the experimental cyclone predicted by SPRINT-4. The rate of efficiency increase falls off at high flow rates where, as expected, the pressure drop is rising rapidly. This demonstrates the required trade-off between efficiency and pressure drop (hence fan power and capital and running costs) if using a single cyclone. The difference between CYCINT-1 and SPRINT-4 predictions is mainly because of the methods of solution already

described in sections 5.4.7 and 5.4.8.

5.5.5 Particle Trajectories

Fig. 5.26 and 5.27 show particle trajectories predicted by CYCINT-1 and SPRINT-4. As already mentioned, when a particle reaches the cyclone body, it is assumed captured by SPRINT-4 whereas in CYCINT-1 it starts bouncing, hence has a chance of being re-entrained. Fig. 5.26a and b show trajectories of 4 μm particles in the experimental cyclone (with Syenex-40 dust). In the first graph one of the particles has bounced, re-entered the flow and after circulation, is finally captured, while in second graph, it was able to escape through the vortex finder. Fig. 5.26c shows three trajectories predicted by SPRINT-4 for this case; after one particle strikes the wall, it is assumed to be collected. Fig 5.26d and e show trajectories of 10 μm particles and it becomes apparent that with increasing particle diameter, particles have less chance of escaping after repeated bouncing.

The difference between CYCINT-1 and SPRINT-4 particle trajectory prediction is shown clearly in Fig. 5.27a and b, in which 1 μm particles were injected from three radial locations. According to CYCINT-1, two particles which reached the wall were able to escape by bouncing while in SPRINT-4 they were assumed to be captured.

All the above trajectories were predicted with the turbulence effect included. As Fig. 5.27c and d show, identical injection locations for three 1 μm particles can result in very different paths. Finally Fig. 5.27e shows trajectories of 1 μm particles when the turbulent effect is excluded and here the paths of all particles injected from a fixed point would be exactly the same.

5.5.6 Cyclone Grade Efficiency

Effect of cyclone flow rate on grade efficiency curves has been investigated using CYCINT-1 and is illustrated in Fig. 5.28 and 5.29 for the experimental and full-scale cyclones respectively. Syenex-40 and Marden dust specifications have been used for experimental and full-scale cyclone calculations respectively. Trajectories were

computed from each of 10 radial locations at injection for each of 10 particle sizes. These figures show, as expected, that increasing flow rate causes an improvement in cyclone grade efficiency curve, but the rate of efficiency improvement for finer particles is less than for coarse ones.

Fig. 5.30 shows cyclone grade efficiency curve predictions with and without turbulence effects on the trajectories, and confirmed that consideration of this parameter is very important for particle tracking and collection efficiency for finer particles.

Finally Fig. 5.31 shows grade efficiency curves for full-scale and experimental cyclones predicted by CYCINT-1 and SPRINT-4. It seems that the grade efficiency of full-scale and experimental cyclones at mass median Stokes number equal to 0.044, are considerably different from each other. Also higher efficiencies are predicted by CYCINT-1 than by SPRINT-4 for most particle sizes in the experimental case, while the opposite is true for the full-scale case.

It is necessary to mention that because of limitations on the number of particle tracks (computing cost and memory), it is nearly impossible to establish a fixed efficiency curve for each case; each curve needs to be imagined as a curve with a thickness of ±5% tolerance. This will account for some irregularity in the presented grade efficiency curves.

5.5.7 Effect of Underflow on Cyclone Performance

One of the most important parameters which causes multicell cyclone maloperation is flow interchange between cells inside the common hopper. Therefore the effect of underflow (or bottom bleed) on the cyclone flow structure has been theoretically studied. Fig. 5.32a,b and c shows the change in gas flow pattern when the experimental cyclone (Q=0.0242 m^3/s) works with ±20% underflows (a positive value here denotes flow from the cyclone into the dust hopper space).

Fig. 5.32a shows that with +20% underflow, the axial velocity near the conical wall should be strong enough to sweep all deposited particles into the hopper. With

positive underflow (+20%) the maximum axial velocity inside the cyclone is less than half that when the cyclone works with -20% underflow. It means that near the vortex finder tube there should be less turbulence and particle escaping.

Fig. 5.32b and c give more interesting results. With positive bleed, swirl velocity is considerably stronger near the dust exit, therefore deposited particles are less likely to re-enter the flow. But with negative underflow swirl velocity is nearly destroyed in the region near the dust exit and is weak inside the conical section. Therefore particles which have been deposited have a higher chance to re-enter the flow and finally escape through the vortex finder tube.

Radial velocity pattern is nearly the same in both cases but the pattern of pressure contours is considerably changed (Fig. 5.32c). With positive underflow the pressure increase with radius is not unlike that with zero underflow and does not change much with axial location, but with negative underflow the pressure changes markedly with axial direction and the low-pressure core is a much less prominent feature (except inside the vortex finder tube).

The effect of bottom bleed on cyclone pressure drop and cyclone mass efficiency are presented in Fig. 5.33. According to the CYCINT-1 prediction, by increasing bottom bleed the cyclone pressure drop decreases while efficiency increases.

Finally the effect of underflow on cyclone grade efficiency is plotted in Fig. 5.34. The particle size collected with 50% efficiency is reduced from 5 μm to 2.5 μm as the bleed is increased from -20% to +20% of cyclone inlet flow.

5.5.8 Effect of Vane Angle and Particle Density

Vane angle is one of the most important parameters for determining swirl velocity inside the cyclone and it needs to be optimized against cyclone pressure drop and efficiency. Unfortunately it was not possible experimentally to use different vane angles for studying cyclone performance, but CYCINT-1 gave an opportunity for preliminary study of this parameter. Fig. 5.35 shows the effect of vane angle on cyclone pressure drop and mass efficiency. By increasing vane angle, the cyclone

efficiency increases nearly linearly while pressure drop increases nearly exponentially. Fig. 5.36 shows that vane angle is a very effective parameter in determining grade efficiency; the improvement is remarkable when vane angle changes from 20 ^{o} (unrealistically low) to 70^{o}. In practice, the increase of vane passage blocking as vane angle increases must also be taken into account.

Also the effect of particle density on grade efficiency has been studied and plotted in Fig. 5.37. As expected, the predicted grade efficiency curve improved by increasing particle density. It is necessary to mention that particle density is more effective on coarse dust than finer and Fig. 5.38 shows this matter.

5.6 ACCURACY AND DISCUSSION

The accuracy of the numerical model is mainly a function of convergence and the grid system. By use of an appropriate relaxation method for an iterative process, convergence may be improved and, in some instances, divergence may be avoided. Fig. 5.41 shows the effect of the number of iterations on the stability of main flow parameters (u,v,w,k,ε) with low relaxation factors 0.1 and 0.2 for (u,v,w) and (p,k,ε) respectively. As it shows, at least 250 iterations are necessary for CYCINT-1 to have stable gas flow results for grid points inside the domain of solution.

In general using a finer mesh results in higher accuracy in the finite difference method. Because of restrictions on memory, the maximum total number of grid lines in the axial and radial directions for CYCINT-1 are forty and twenty one respectively. Of course choosing a low number of grid lines will increases the speed of calculation (lower cost) but will seriousely decrease the accuracy of the results.

Other aspects of accuracy and stability of the finite difference method for gas flow have been reported by many researchers (e.g. Spalding 1972). The number of particle tracks, particle injection points, particle sizes and grid lines (used for gas flow field calculation) all affect grade and mass efficiency results. Choosing higher numbers of the above parameters will certainly improve the accuracy of results but there is again a limit due to computer running cost and memory requirement. Also the tracking method suffers from its simpilicity (for example, the particle drag coefficient

at present refers only to spherical particles) and does not include physical phenomena such as agglomeration and particle break-down. Fig. 5.39 and 5.40 show the effect of the number of tracks on mass and grade efficiency respectively. These figures show how the result is effectively constant when the number of tracks is around 3000 or more.

The results of the new numerical model which are presented in Section 5.5 have indicated that it is possible to employ a theoretical approach to the analysis of multicell cyclone cell performance and to cell design, which is based on the fundamental physical laws govering the motion of particles suspended in gas. This numerical model is capable of supplying a very large amount of detailed information about the gas and particle dynamics within axial-type reverse-flow cyclones, as well as predicting performance. In addition, this information allows better understanding of the complex and interacting processes occurring, so that a rigorous approach to cyclone separator design can be undertaken.

In summary, differences between CYCINT-1 and SPRINT-4 gas flow field predictions for the experimental cyclone (Q=0.024 m^3/s) are shown in Fig. 5.42a and b. Looking also at Fig. 4.6 to 4.15, the CYCINT-1 prediction seems to give a better velocity vectors and radial velocity pattern especially near the vortex finder tube which is an important region affecting efficiency. The axial velocity pattern has changed a lot especially in the core centre where SPRINT-4 predicted a back flow for this air flow case. Swirl velocity seems nearly the same in each case.

Hydrodynamic flow field predictions of CYCINT-1 have been validated by comparision with LDA results in water. Fig. 5.43 demonstrates that the experimental results have a good agreement with the CYCINT-1 prediction for an important grid line (number 15) near the vortex finder tube. A complete comparision between CYCINT-1 predictions (for gas flow field as well as particle behaviour) and experimental results is presented in Chapter 4.

The present investigation shows that the Reynolds number approach for scaling the gas flow field can be used successfully. But still it seems that the Stokes number approach for scaling particle behaviour inside cyclone is insuffecient, partly because

it does not account for physical phenomena such as humidity effects and agglomeration and probably also because of particle characterization problems when comparing experiment and prediction. Additionally, turbulence effects on the particles are not modelled by Stokes number matching.

The investigation also shows that CYCINT-1 is able to predict plausibly the effect of any important parameter such as underflow, vane angle, etc., on cyclone performance. For example change in cyclone underflow from -20% to +20% causes 10% increase in cyclone efficiency. Therefore CYCINT-1 can be also useful for cyclone design optimization.

Against a background of very little research on vane-type reverse-flow cyclones, the results for gas flow pattern were compared with those for tangential-type cyclones (Bloor and Ingham 1987, Pericleous et al, 1984& 1987, Boysan et al 1982, Ter Linden 1949, etc.). It has been shown that the predictions of CYCINT-1 agree well in general form with these studies (cyclone inlet zone excluded), suggesting that existing data on performance trends for tangential-inlet cyclones may often be relevant to axial-inlet cells of multicell cyclones.

CHAPTER 6

CONCLUSIONS AND RECOMMENDATIONS

6.1 CONCLUSIONS

A literature survey has been presented on the status of dust separation technology and general aspects of cyclone dust separators such as cyclone geometry, design, efficiency and pressure drop, with particular emphasis on modification of conventional types, especially on multicell cyclones.

A roughly half-scale model rig of a nine-cell segment of a multicell cyclone with axial-entry reverse-flow cells and stepped tube plate was designed and constructed. Two single cell rigs were also built, one for aerodynamic tests and the other for efficiency tests. The chosen test dust, nepheline syenite with mass-median diameter 10 μm, and cold-air flow conditions gave particle inertial behaviour representative of the finest distributions of fluidised-bed boiler elutriated material. Many measuring instruments such as a smoke-wire system for flow visualization and dust-feeding and sampling systems were designed and developed. A computerised data acqusition and processing system was developed for LDA measurement in one of the single-cell rigs.

LDA measurements, using a single-channel fringe-mode anemometer, provided profiles of mean axial, radial and tangential velocities at different planes in the cyclone, which show the development of a Rankine-type vortex structure inside the cyclone.

Visualization by smoke-wire and cell flow rate measurements by pressure probe revealed gas circulation through the common dust hopper, from the cells nearest to the multicell unit inlet to those furthest from the inlet. Cell outlet flow rates were three to four per cent greater than the nine-cell average for the furthest row and three to four per cent less than the average for the nearest row, when the duct velocity at entry to the multicell unit had an unsteady, skewed distribution as a result of upstream duct

components. Measures taken to produce a steady, more uniform inlet velocity distribution reduced cell row flow rate deviations to one per cent of the nine-cell average, but did not significantly alter the visual observations of back flow into the dust exi ts of the rear cell row. The complex, highly turbulent flows observed in the multicell inlet and exit manifold could make a significant contribution to pressure drop; it is conceivable that this could be minimized by having opposite swirl directions in adjacent cells and, where possible, arranging for a vertical exit. Gas flow measurements and supporting numerical studies showed little Reynolds number dependence, justifying the half-full- scale Reynolds number used for dust measurements.

Pressure drop was typically 25 cell inlet velocity heads. Pressure drop expressed as a number of inlet velocity heads showed a slight increase with flow rate for the multicell cyclone and an opposite trend for the single cell, suggesting an increasing contribution from multicell inlet and exit manifold flow phenomena as flow rate increased.

Overall collection efficiency measurements, based on dust entering the multicell cyclone and clean-stream samples, showed virtually no difference between the cases of skewed and uniform velocity distributions at entry to the multicell unit. However because of the apparently improved uniformity of flow among cells with the uniform inlet velocity distribution, the design of inlet ducting on industrial cyclones should not be regarded as irrelevant to performance. Comparison of the overall efficiencies of unmodified multicell and single-cell cyclone demonstrated a potential for reducing dust emissions by a factor of just over two, from 14% to 6%, if the multicell performance could be raised to the level of the isolated cell. Hopper baffles reduced dust emissions from 14% to 11%; it is probable that hopper circulations occur in all industrial multicell cyclones having cell outlet tubes of unequal length (hence unequal flow resistance), and baffles are recommended as a cheap means of obtaining a modest but worthwhile efficiency improvement. Attempts to stabilize the cell inner vortices, by providing vortex attachment points in the form of upward-pointing cones in the cell dust exi ts, were ineffective in improving overall efficiency.

Measurements of grade efficiency, from off-line air-dispersed laser-diffraction sizing of inlet dust and clean stream samples, indicated that the poorer overall efficiency of the multicell cyclone, compared with the single cell, was associated mainly with particles below 10 μm in size. The improvement with hopper baffles also appeared to be connected entirely with sub-10 μm particle behaviour.

Of various devices tested only on the isolated cell, two were noteworthy. Both modelled on commercial devices, one was a three-vane de-swirler mounted at the entry to the clean gas outlet tube, which cut the pressure drop by about five cell inlet velocity heads but did not affect overall efficiency; the other, a triple-cone entry to the clean gas exit tube, halved dust emissions but with a pressure-drop penalty of around three velocity heads.

In the computational work, a numerical finite difference code (SPRINT-4) was successfully modified to compute flow structure and particle trajectories in axial-type reverse-flow cyclones.Boundary treatment for the gas flow was corrected and improved. A version of the program has also been produced to run under MS.DOS on 80286+80287-based microcomputers, to cut the cost of further investigations with this model. Encouraging results have been obtained by comparing the prediction of the gas flow field and trends in particle collection efficiency with experimental results. Discrepancies between measured and predicted efficiency have been attributed to phenomena such as agglomeration which have not yet been incorporated in the model. In particular, the predictions of the continuous-phase flow field show significantly better agreement than those of the original SPRINT-4 with the results of 3-component velocity measurement made by LDA. The new numerical model (CYCINT-1) is able to predict the effect of any important parameter on axial-flow cell performance. A particular study showed that by increasing cyclone underflow (gas bleed from the dust exit) from -20% to +20%, cyclone efficiency changed from 77.5 % to 88 %. This is believed to be the first quantitative prediction of the detrimental effect on a cell of hopper circulation, and of the beneficial effect of gas bleed.

6.2 SUGGESTIONS FOR FURTHER WORK

The present work suggests a number of areas where further research is needed to improve multicell cyclone performance.These are as follows:

1- Experimental investigation should continue on the one-cell air rig in order to assess the optimum cyclone geometry, especially vane angle, for highest efficiency with reasonable cyclone pressure drop.

2- LDA measurement in the one-cell water rig should be performed inside the cyclone hopper, with or without baffle, to quantify the effect of the vortex extending below the dust exit. Also effect of changes in vane angle, underflow, etc. on cyclone flow field could be measured. Finally the possibility of measuring three components of velocity under unsteady conditions (such as in multicell cyclone cells) should be considered, especially for vortex finder exit and core zones.

3- In view of the part played by cell-hopper gas interchange in the present experimental investigation and the numerical prediction of significant efficiency increases from gas bleed through cell dust exits, together with the success of gas bleeds on industrial multicell cyclones, it is suggested that the present model cyclone and associated facilities be used in a follow-up project. The objective of this further work would be to investigate and compare conventional "sidestream" arrangements of gas bleed from various locations in the dust hopper (Fig. 6.1) and a separator based on the "concentrator" principle (Fig 6.2) and with uniflow-type scavenge offtakes from the clean-gas outlet tubes (Fig. 6.3). Such arrangements need not cost very much more than the conventional "sidestream" separator with bag filter, itself about only twice the cost of a simple multicell cyclone and considerably cheaper than bag filtration of the whole gas flow.

4- In the multicell cyclone rig, cell flow rates should be measured without having to suppress the exit tube swirl. This would require considerable expertise in multiple-hot-wire anemometry and associated data reduction procedures, or, if using LDA, would require a high-power laser and pose flow seeding problems.

5- It is felt that considerable improvements can be made in the design of multicell cyclone inlet and outlet manifolds. Use of baffles, or a non-stepped, inclined tube plate (as shown in Fig. 2.3b), or alternating swirl vane settings in adjacent cells, etc., are cheap techniques which are recommended. Their optimization could probably be performed mainly by smoke visualisation without a great deal of quantitative work.

6- It is suggested that further study be performed on the multicell cyclone hopper. The effect of hopper vacuum, quantity of collected dust, hopper circulation, etc, on mass and grade efficiency could be studied. A systematic study of the influence of air leakage could serve as a useful reminder to cyclone operators of the need for high maintenance standards.

7- Particular cyclone phenomena should be studied in greater depth. For example by changing air humidity or dust concentration and by using different dusts, agglomeration processes could be investigated.

8- It would be interesting to propose and test an electrostatically enhanced cyclone, based for example on the electro-cyclone described by Perlsweig et al. (1981, Fig. 6.4). Subject to acceptable cost in the industrial boiler context, tests should be performed to compare efficiency and pressure drop with other dust cleaning devices and consideration given to any problems of adapting it to multicell form.

9- Considerable improvement could be made to the numerical model, in order to improve accuracy of results. The grid system should be improved for the conical wall (using diagonal grid lines). In the particle tracking procedure, allowance should made for particle shape effects on drag coefficient, and the possibility of allowing (in a crude way) for agglomeration should be considered for particle tracking method. Particle-wall interaction could also be handled in a more sophisticated way. Finally, development of a simple model for multicell cyclone optimization purposes is suggested, making use of results obtained from CYCINT-1 for various cell design parameters.

APPENDIX A

PRINCIPLE OF LASER DOPPLER ANEMOMETER

This technique is based on the measurement of Doppler frequency shift in laser light caused by moving particles scattering the light. The equation relating the Doppler frequency shift, f_D, as a function of wavelength, direction and velocity of particles is (Fig A.1):

$$f_D = f_S - f_i = \frac{1}{\lambda} \vec{U} (\hat{e}_s - \hat{e}_i) \qquad (A.1)$$

where f_S, f_i are the frequencies of scattered and incident light respectively, $\hat{e}_S$ and $\hat{e}_i$ are the unit vectors of scattered and incident light respectively, $\vec{U}$ is the particle velocity vector and λ is the incident light wavelength. The differential Doppler mode or fringe mode is considered to be the simplest and most practical, for fluid flow measurements with moderate or low particle concentrations. This method was used in the present investigation. In this system, the original laser beam is split into two beams of equal light intensity (Fig. A.2). The intersection volume consists of a set of real interference fringes. For a correct fringe pattern with straight and not skewed bright and dark light bands, the two beams must cross at the beam waist (Fig. A.3). The Doppler frequency f_D is the difference between the two scattering frequencies f_{S1} and f_{S2} and is the independent of the direction of scattering $\hat{e}_S$. The equation relating the fluid velocity and the Doppler frequency is (Durst et al. 1976):

$$V = \frac{f_D \lambda}{2 \sin \phi} \qquad (A.2)$$

where ϕ is the half angle of intersection of the beams. The most important feature of the LDA system is the location where the two beams cross and form a set of interference fringes. The part of the intersection region viewed by the collecting

optics (typically 50-80%) form the measuring volume. Its size, shape and characteristics depend upon the transmission and collecting optics. Since the light intensity of each beam varies in a Gaussian manner, the intersecting volume is an ellipsoid (Fig. A.4). When a laser beam is focused by a single lens, the diameter of the focused beam d is given by:

$$d = \frac{4\,\lambda f}{\pi\, d_o} \tag{A.3}$$

where λ=wavelength of laser light , f= focal length of lens and d_o=diameter of Gaussian beam specified at $1/e^2$ of the peak intensity value. From simple geometry (Fig. A.4 and A.5) it can be shown that the intersection volume dimensions are :

$$2a = L_V = \frac{d}{\sin\phi}\ ,\ 2C = d_V = \frac{d}{\cos\phi}\ ,\ 2b = d \tag{A.4}$$

where ϕ is the half angle of intersection of the two beams. Also the fringe spacing d_f and number of fringes (n_f) are equal to :

$$d_f = \frac{\lambda}{2\sin\phi} \quad , \quad n_f = \frac{d_v}{d_f} \tag{A. 5}$$

where d_V is the intersection diameter.

The final link in the LDA systems is the signal processing unit which extracts the velocity information from the output signal of the photomultiplier. As shown in Fig A.6 the signal consists of :

a) a high frequency component at the fringe crossing frequency, which contains the velocity information;

b) a low frequency component related to the particle transit time across the intersection volume (the "pedestal" signal);

c) wide band noise, of optical (fluctuation of laser beam, vibration of the mecahnical-optical arrangement, imprecise alignment) and electronic (photodetector

noise) nature.

The pedestal signal may be removed using a high-pass filter. However, in certain circumstances like recirculating or highly turbulent flows, the required frequency and the pedestal signal are sometimes close together, so the high-pass filter setting is critical. In such cases, light frequency shifting can aid the separation of the pedestal signal (Durst et al. 1976), but was unneccessary in the present work.

The problem of processing the photomultiplier output signal consists of extracting the fringe crossing frequency and measuring its mean and fluctuating values. The frequency tracker (as used in the present work) is a unit which follows the Doppler signal giving an output voltage proportional to the instantaneous input frequency. This is achieved by means of a voltage-controlled oscillator in the feedback loop (Durst et al. 1976). The output signal is step-linked, and is continuous even though the input is not, so care must be taken in interpreting the signal. If E is the output voltage of the tracker and C_R a constant of proportionality, depending on the tracker range, the following relation holds.

$$f_D = C_R \cdot E \qquad \text{(A.6)}$$

APPENDIX B

OPTICAL CORRECTION FOR LDA MEASUREMENT

The equation relating Doppler frequency and velocity of the working fluid, given in Appendix A (eq. A.2), is valid only in a medium such as air with refractive index equal to unity. However, in many practical situation, where more than one medium is involved, the laser beams have to pass from air through the walls of the test section into the working fluid, thus undergoing a series of refractions due to the changes in refractive indices. The refraction of laser beams at the wall interfaces and through different media will change the wavelength and the path of the beams. Therefore it is necessary to make corrections to the half-angle between the beam and the location of the measuring intersection volume in the fluid. Moreover if the interface between the media is curved, as with the cyclone body, the beam will have further refraction. The actual velocity of the working fluid (V_f) can be determined by:

$$V_f = \frac{f_D \lambda_f}{2 \sin \phi_f} \qquad (B.1)$$

where ϕ_f is the half-angle between the beams and λ_f is the wavelength of the laser light in the working fluid. Fig. B.1 shows schematically a cross-section of the one-cell cyclone body just below the vane trailing edge position. For measuring velocity at points A, B and C by LDA, the laser beam must pass through two, three and four perspex walls respectively. Therefore the correct intersection volume position and beam half-angle needed to be specified for these arbitrary points.

By using the laws of refraction, the measuring intersection volume displacement (Δx) and change in beam half-angle ($\Delta\phi$) were obtained for straight and curved walls. For example for a single concave wall, as shown in Fig. B.2, these values were calculated from the following formulae (Sabzvari 1984).

$$\Delta\phi=(\alpha_2+\alpha_4-\alpha_1-\alpha_3) \tag{B.2}$$

$$\Delta X = R_o \frac{\sin \alpha_1}{\sin \alpha_i} - R_i \frac{\sin \alpha_2}{\sin (\alpha_i + \Delta\phi)} \tag{B.3}$$

where

$$\alpha_1 = \sin^{-1}\left[\frac{R_a}{R_o} \sin \alpha_i\right] \tag{B.4}$$

$$\alpha_2 = \sin^{-1}\left[\frac{n_w}{n_p}\frac{R_a}{R_o} \sin \alpha_i\right] \tag{B.5}$$

$$\alpha_3 = \sin^{-1}\left[\frac{n_w}{n_p}\frac{R_a}{R_i} \sin \alpha_i\right] \tag{B.6}$$

$$\alpha_4 = \sin^{-1}\left[\frac{R_a}{R_i} \sin \alpha_i\right] \tag{B.7}$$

α_i and R_a are laser half angle and intersection volume position before reflection respectively. n_w and n_p are refractive index in water and perspex respectively. Extended versions of these formulae were developed by the author to handle positions like *A*, *B* and *C* in Fig. B.1. A computer program was written for calculating the relation between laser table movement and both the final position of the measuring volume and the beam half-angle, using these expressions together with details of the grid system and cyclone geometry (Fig. 3.42).

The actual dimensions of the measuring volume vary along a traverse in the y (r) direction due to the varying crossing angle of the two beams. Table B.1 shows the specification of the measuring volume along a traverse line, as obtained from the computer program. By examining the measuring volume from the receiving optics side, the diameter d_{ph} of the measuring volume and the number of fringes n_{ph}

viewed by the pinhole of the photomultiplier are given by:

$$d_{Ph} = \frac{D_{Ph}}{M} \quad , \quad n_{Ph} = \frac{d_{Ph}}{d_f} \tag{B.8}$$

where D_{ph} is the pinhole diameter and M the collecting lens magnification. Therefore, by careful selections of the pinhole diameter D_{ph} and the magnification M, the radial extent of the measuring volume can be controlled. Experience suggests that it is best to choose the pinhole to view between 50% and 80% of the fringes. In the present work the pinhole diameter was chosen to be 0.4 mm and the intersection volume observed by the pinhole was d_{ph}=0.16 mm, with n_{ph}=80.

APPENDIX C

SPECIFICATION OF PARTICLE SIZE DISTRIBUTION

The Rosin-Rammler distribution used by CYCINT-1 is a two-parameter distribution, originally developed to represent friable material after a crushing process but probably as good as any other common distribution model for the present purpose. It is defined by :

$$m_c = 1 - \exp\left[-\left(\frac{d}{d_{rr}}\right)^n\right] \qquad (C.1)$$

where m_c is the cumulative mass undersize, d is the particle "diameter", d_{rr} is the Rosin-Rammler mean diameter and n is the Rosin-Rammler spread parameter. The distribution is specified in CYCINT-1 by entering for d_{rr} and n (either before the gas flow calculation or before the particle tracking phase, a better place to do so since changes to d_{rr} and n here will not destroy a previously calculated gas flow field). To fit values of d_{rr} and n to a measured or estimated distribution, it may be noted that :

$$\log \ln\left[\frac{1}{1-m_c}\right] = n \log (d) - n \log (d_{rr}) \qquad (C.2)$$

so a plot of $\ln[1/(1-m_c)]$ versus d on log-log paper can be approximated by a straight line of slope n; d_{rr} (which is not directly related to any other mean size) is given by the value of d for which $\ln[1/(1-m_c)]$ equals one.

APPENDIX D

SOLUTION PROCEDURE FOR THE FINITE DIFFERENCE EQUATIONS

The form of the differential equations has been introduced in Sec. 5.2 and used for the derivation of the f.d.e's . The backward-staggered grid system is employed for derivation of the f.d.e. Fig. 5.6 shows this grid system. The grid employed, viewed in the r-x (z) plane , is regular and rectangular with arbitrary spacing and is shown by solid lines. A typical cluster of u, v and scalar-cells or control volumes is shown in dotted lines. Each cell surrounds the point of location of the relevant variable. The pressure P and other scalar variables are located at the intersection of grid nodes and the velocities are located at the boundaries of the scalar cells. As the number of grid lines used tends to infinity, correctly formed finite-difference equations approach those of the differential ones.

The governing partial differential equations for the conservation of mass, momentum, turbulence energy and its dissipation rate are reduced to their finite-difference analogues by integration over the computational cell into which the domain of interest is subdivided. The detailed derivation of the finite difference equation has been given by Gosman et al. (1969). For example, the exact solution for transport equation across a "west" boundary (Fig. D1.a) gives (Spalding 1972):

$$q_w^{\circ} \approx \rho_w \, U_w \, A_w \left[f_w \, \Phi_W + (1-f_w) \, \Phi_P \right] \qquad (D.1)$$

Here

$$f_w = \exp(Pe_w) / \left[\exp(Pe_w) - 1 \right] \qquad (D.2)$$

$$Pe_w = \rho_w u_w \delta x_{Pw} / \Gamma_w \quad ; \quad A_w = r_P \, \delta r_{ns} \qquad (D.3)$$

$$\rho_w = (\rho_W + \rho_P)/2 \quad ; \quad \Gamma_w = (\Gamma_W + \Gamma_P)/2 \qquad (D.4)$$

In order to avoid expensive calculation of exponentials, a hybrid scheme based on piece-wise linear fits is adopted to approximate the exact $q_w^{\bullet} \sim Pe_W$ relation with little loss of accuracy. In this method, a central difference scheme is employed for

low Peclet number and an upwind difference scheme is used for large Peclet number(Gosman and Ideriah, 1976). The total generation can be reduced to a linearized form as:

$$-\int S_{\Phi}\, dv = S_P\, \Phi_P + S_U \qquad (D.5)$$

S_p and S_u will be functions of Φ in general. The resulting algebraic equations can be given in the following common form:

$$\Big(\sum_{i=N,S,E,W} a_i - S_P\Big)\, \Phi_P = \sum_{i=N,S,E,W} a_i\, \Phi_i + S_U \qquad (D.6)$$

where Φ represents the general dependent variable, the a's are the coefficients which contain the contribution from the convective and diffusive fluxes and S_u and S_p stand for the components of the linearised source terms (Gosman and Ideriah, 1976). While the forgoing derivation of the f.d.e's is based on scalar variables, the finite-difference momentum equations are derived in similar manner except that the central volumes are displaced because the velocities are displaced. For example the U-momentum equation is given as (see Fig. D.1b):

$$\Big(\sum_{i=N,S,E,W} a_i - S_P\Big)\, u_P = \sum_{i=N,S,E,W} a_i\, u_i + A_{ew}\,(P_W - P_P) + S_U \qquad (D.7)$$

Here

$$a_w = \rho_w\, u_w\, A_{ew}\, f_w \quad , \quad A_{ew} = r_P\, \delta r_{ns} \qquad (D.8)$$

$$f_w = f_{HD}\,(Re_w) \quad , \quad Re_w = \rho_w\, u_w\, \delta x_{PW}/\mu_w \quad , \quad \rho_w u_w = (\rho_W u_W + \rho_P u_P)/2 \qquad (D.9)$$

(Suffix HD = Hybrid difference)

The Boundary Condition

Because of the elliptic nature of the conservation equations, a complete description of the gas flow problem considered necessitates the specification of the

boundary conditions at all the boundaries of the domain of interest (Boysan et al. 1982). At the boundaries of the calculation domain , the general f.d.e is not appliciable. Hence special measures are required for the cells next to the boundaries. First the grid arrangement is such that the boundaries coincide with the cell walls (Gosman and Ideriah, 1976). A typical cell whose west wall coincides with the boundary of the calculation domain is shown in Fig. D.2a. There is no link between Φ_p and Φ_w through the general f.d.e. Hence the usual $\Phi_p \sim \Phi_w$ link is suppressed by setting the coefficient a_w to zero. If the boundary flux $\overset{\circ}{q}_B$ is prescribed, the problem is much simplified as $\overset{\circ}{q}_w = \overset{\circ}{q}_B$; hence $S_p=0.$ and $S_u=\overset{\circ}{q}_B$. If the boundary value Φ_B is prescribed, $\overset{\circ}{q}_w$ may then be reduced to the linearised form as:

$$\overset{\circ}{q}_w = a'_w \, (\Phi_B - \Phi_P) \qquad (D.10)$$

then set $a_w=0$, $S_p=-a'_w$ and $S_u=a'_w \, \Phi_B$. To fix $\Phi_P$for any internal node at Φ_{fix} set $S_p=-\gamma$ and $S_u=\gamma \, \Phi_{fix}$ where γ is a large number (10^{30}). Where a tangential velocity is prescribed at the boundary, through flux or drag laws, for example the appropriate value may be inserted by way of the usual source treatment. A tangential velocity U_p for a node next to a wall is obtained from usual momentum balance. For the configuration shown in Fig. D.2b the usual expression for a_s is no longer valid, therefore it is set to zero. The correct shear force expression is now inserted from the $u^+ \sim y^+$ relation. For P within tubulent region ($y^+>11.63$),

$$F_s = \tau_s \, \delta X_{ew} = -\rho \, C_\mu^{0.25} \, k_{PW}^{0.5} \, (U_P - U_S) \, \chi \, \delta X_{ew} \, / \log (EY^+) \qquad (D.11)$$

$$\text{Where } k_{PW} = (k_P + k_W)/2 \;, \quad y^+ = \rho \, C_\mu^{0.25} k_{PW}^{0.5} \, Y_P / \mu \qquad (D.12)$$

For P within the viscous sublayer ($y^+<11.63$),

$$F_s = \tau_s \, \delta X_{ew} = - \mu \, (U_P - U_S) \, \delta X_{ew} / Y_P \qquad (D.13)$$

For velocities normal to a wall, no special wall treatment is necessary. The

incorporation of the wall boundary condition for k required some special attention. The usual k-balance is used, but, since the turbulence energy falls to zero at a wall, there is no contributory flux from the wall, hence, a_S is set to zero without insertion of any modified form for it. The generation term G in the k-equation reduces to a much simplified form which is further modified by noting that it can be expressed in terms of the wall shear stress τ_S ($\equiv \tau_W$). For k-balance, the viscous dissipation over the entire volume is evaluated as (Fig D.2c):

$$S_K = G - C_D \rho \varepsilon \tag{D.14}$$

with calculation of G altered by noting:

$$\int_V \mu_t \left[\frac{\partial u}{\partial r} + \frac{\partial v}{\partial x} \right]^2 dv = \tau_S \left(u_P - u_S \right) \frac{\delta v}{Y_P} \tag{D.15}$$

where τ_S , u_S are averages of nearby values.

$$\int_V C_D \rho \varepsilon \, dv = -C_D \rho C_u^{0.75} \left[k_P^{0.5} - k_S^{0.75} \right] U^+ \frac{\delta v}{Y_P} \tag{D.16}$$

Where $U^+ = 1/\chi \log_e (E\, y^+)$ for $y^+ > 11.63$ and $U^+ = y^+$ for $y^+ \leq 11.63$

TMDA and SIMPLE Procedure

The general solution employed is an iterative line-by-line (LBL) method. Initial guesses of values for the flow field are made, and these are improved upon from one line to the other.For the solution of the equation for points on each line (e.g. N-S line) (Fig. D.3), values of neighbouring lines are assumed to be temporarily known. The equations for each point on the N-S line then reduce to one where only three values (Φ_N, Φ_P, Φ_S) are unknown. The set of equations for all points on the N-S line then takes a particularly simple form in which the non-zero-coefficient matrix is tri-diagonal. Equations of this type are especially easy to solve by the tri-diagonal matrix algorithm (TDMA).

The f.d.e.s for non-hydrodynamic variables (k,ε,etc) can be solved directly by the TDMA. To solve for a particular Φ, an equation where that Φ is the dominant

variable is needed. All the non-hydro-dynamic variables satisfy this requirement ; u and v also satisfy this requirement via the momentum equations. However, the pressure has no equation of its own. There is an additional equation, the continuity equation, but pressure does not appear in it. Some special measure is therefore needed to obtain the pressure. The measure employed is one where the momentum equations are solved by first estimating a pressure field, then obtaining estimates of u and v, and finally correcting the pressure field to bring the velocity field into conformity with the continuity equation. This procedure is known as SIMPLE (Semi-Implicit Method for Pressure- Linked Equations, Patankar and Spalding 1972).

The fields of all variables (u,v,p,k,ε,etc) are guessed and then the coefficients of the momentum equations are assembled, and the improved values u*, v*, etc. are then solved for by means of the LBL procedure, using prevailing pressure. More than one sweep may be made, but without updating the coefficients. The coefficients of the P'-equation are next assembled and p' solved for by the LBL method. Then u' and v' are evaluated, then new values of p,u,v are obtained from p=p*+p' etc. (Gosman and Ideriah, 1976). The major objective, therefore, is to correct the velocities and pressure so as to eliminate the mass source. The pressure -correction equation may be expressed as:

$$\left(\sum_{i=N,S,E,W} a_i - S_P\right) p'_P = \sum_{i=N,S,E,W} a_i\, p_i + S_U + M_P \qquad (D.18)$$

$$\text{where} \quad a_i = \rho_i D_i A_i \qquad (D.19)$$

$$M_P = G^*_w A_w - G^*_e A_e + G^*_S A_S - G^*_n A_n \qquad (D.20)$$

$$D_i = \frac{\partial u^*_i}{\partial (p^*_i - p^*_P)} \qquad (D.21)$$

(*= Guessed value & ′ = Correction to guessed value).

The various stages in the SIMPLE algorithm may be combined with the solution

of equations for the non-hydrodynamic variables in order to form a general, unified solution procedure(Gosman and Ideriah 1976) :

1)- Guess fields of all variables

2)- Assemble coefficients of momentum equations and solve for U* and V*, by means of LBL procedure, using prevailing pressures:

$$\text{e.g. } (a_P - S_P)U_P^* = \sum_n a_n U_n^* + A_{ew}(p_W^* - p_P^*) + S_U \qquad \text{(D.22)}$$

3)- Calculated coefficients and mass sources for P' equation , and solve for P' by LBL procedure evaluate u's , e.g : $u'_w = D_w(P'_w - P'_p)$

4)- Obtain new values of p,u,v from

$$p = p^* + p' \quad , \quad u = u^* + u' \quad , v = v^* + v' \; , \; w = w^* + w' \qquad \text{(D.23)}$$

5)- Assemble coefficients and solve equations for other variables by means of LBL procedure.

6)- Test for convergence: if not attained, use prevailing fields as new guesses and repeat from 2 .

All these equations satisfy conditions under which a successive substitution method can converge (somtimes called the Scarborough criterition), since S_p is usually<=0. In the process of the solution procedure, convergence is assessed at the end of each iteration on the basis of the 'residual-source'.

By the use of an appropriate relaxation method for an iterative process, convergence may be improved and, in some instances, divergence may be avoided. The accuracy of the solution procedure will in general be a fuction of the number of grid nodes employed. For each flow configuration, a grid-independent solution is sought by increasing the number of grid lines until no further changes are observed in the final solution.

REFERENCES:

Abrahamson, J. and Allen, R.W.K. (1986), "The efficiency of conventional return-flow cyclones at high temperatures", Inst. Chem. Engrs Symposium Series No. 99

Abrahamson, J., Martin, C.G. and Wong, K.K. (1978), "The physical mechanisms of dust collection in a cyclone", Trans. Inst. Chem. Engr., Vol. 56, p.168-177

Alexander, R.M. (1949), "Fundamental of cyclone design and operation", Proc. Australas. Inst. Min. Met.(new series), 152-3, p.203-228

Allen, T. (1975), "Particle size measurement ", 2nd edition,Chapman and Hall Ltd.

Arato, E.G. (1984), "Reducing head or pressure losses across a hydrocyclone", Filtration& Separation, Vol. 21, May/June, p.180-182

Asanuma, T. (1977), "Flow visualisation", Proceedings of the International Symposium on Flow Visualisation ,Oct. Japan

Ayers, W.H., Boysan, F., Swithenbank, J. and Ewan, B.C.R. (1985), "Theoretical modelling of cyclone performance ", Filtration & Separation , Vol. 22 ,Jan. / Feb., p.39-43

Barth, W. (1956), "Design and layout of the cyclone separator on the basis of new investigations", Brenstoff. Warme Kraft, Vol. 8, p.1-9

Batel, W.(1976), "Dust Extraction Technology, principles, methods, measurement technique", Technicopy Ltd. Glos., England.

Bechtel, T.F. et al (1985), "Annual report 1983-1984 particulate controls, ASME air pollution control division", ASME Paper No. 85-JPGC-APC-10

Bednarski, S. and Wiechowski, A. (1984), "A review of hydrocyclone performance correlation", 2nd Int. Conf. on Hydrocyclones, Bath, England, Sep.

Beeckmans, J.M. (1979), In: "Aerosol measurement, analysis of the cyclone as a size selective aerosol sampler", Ed. Lundgren, D., University of Florida Press, Gainesville, FL

Beeckmans, J.M. and Kim, C.J. (1977), "Analysis of the efficiency of reversed flow cyclone", Canadian Journal Chemical Engineering, Vol. 55, p.640-643

Behrouzi, P. (1987), "CYCINT Ver. 1 User's Manual", Imperial College, London, Mech. Eng. Dept., Rep.TPS/ 87.008

Behrouzi, P. (1987), "Numerical modelling of the performance of axial-entry reverse-flow cyclones", Imperial College, London, Mech. Eng. Dept., Rep.TPS/ 87.007

Bhattacharyya, P. (1984), " The flow field inside a conventional hydrocyclone", 2nd Int. Conf. on Hydrocyclones, Bath, England, Sep.

Biffin, M., Syred, N. and Owen, I. (1981) , "New concepts in cyclone dust separators and their application to hot clean-up ", Dept. of Mech. Eng.& Energy studies, University College, Cardiff

Biffin, M. and Syred, N. (1983), "A novel design of cyclone dust separator", Filtration& Separation, Vol. 20, May/Jun, p.189-191

Biffin, M., Claypole, T.C. and Syred, N. (1984), "Velocity measurement in a cyclone dust separator", 2nd Int. Symp. on Application of LDA to Fluid Mechanics, Lisbon

Binark, M.H. and Patel, S.P. (1961), "Inertial Impaction in cyclone separators", Trans. Inst. Chem. Engrs. Vol. 29, p.356-383

Bloor, M.I.G. and Ingham, D.B. (1973), "Theoretical investigation of the flow in a conical hydrocyclone", Trans. Instn. Chem. Engrs., Vol. 51, p.36-41

Bloor, M.I.G. and Ingham, D.B. (1987), "The flow in industrial cyclones", J. Fluid Mech., Vol. 178, p.507-519

Bogucki, R. (1986), Private communication,Coal Research Establishment, British Coal, Stoke Orchard ,Cheltenham

Boysan, F. and Swithenbank, J. (1981), "Numerical prediction of confined vortex flow", Dept. of Chemical Engineering and Fuel Technology,University of Sheffield , Report No. HIC 370

Boysan, F., Erdogan, E., Ewan, B.C.R. and Swithenbank, J. (1981), "Numerical prediction of strongly swirling confined turbulent flows with an algebraic Reynolds stress closure", Dept. of Chemical Engineering and Fuel Technology,University of Sheffield , Report No. HIC 365

Boysan, F., Ayers, W.H. and Swithenbank, J. (1982), "A fundamental mathematical modelling approach to cyclone design", Trans.Inst. Chem. Engrs., Vol. 60, p.222-230

Boysan, F. (1983), "SPRINT-4 User's Manual ", Dept. of Chemical Engineering and Fuel Technology , University of Sheffield

Bradley, D. and Pulling, D.J. (1959), "Flow patterns in hydraulic cyclone and their interpretation in terms of performance", Trans. Inst. Chem. Engrs., Vol. 37, p.34

Bradshaw, P. (1971), "An introduction to turbulence and its measurement", Pergamon Press

Breuer, H. (1967), "Investigations on the suitability of cyclones for the selective sampling of respirable fine dusts", In:"Inhaled Particles and Vapours II", Ed. Davies, C.N., Pergamon Press, Oxford

British Standards Institution (1970), "Specification for air filters ", BS-1701

British Standards Institution (1971), "Methods of test for air filters used in air conditioning and general ventilation ", BS-2831

British Standards Institution (1978), "Method for the measurement of the concentration of particulate material in ducts carrying gases ", BS-893

British Standard Institution (1983), "Measurement of fluid flow in closed condiuts", BS-1042 , Section 2.1

Brookman, R.S., Phillippi, J.F. and Naisch, C.L. (1963), "Small-diameter cyclones" Chem. Eng. Progress, Vol. 59, Nov.

Browne, J.M., Strauss, W. (1978), "Pressure drop reduction in cyclones", Atmos. Environment, Vol. 12, p.1213

Bump, R.L. (1980), "Electrostatic precipitators in industry", In: " Industrial Air Pollution Engineering", Ed. Cavaseno, V. et al, McGraw-Hill

Byers, R.L. and Gage, T.L. (1981), "Multicyclones for control of petroleum coke emission", Chem. Eng. Progress, Dec., p.45

Carey, W.F. and Stairmand, C.J. (1949), Communication on the discussion on "Free jets in fluid mixing and on cyclone dust collectors", Proc. Inst. Mech. Engrs, Vol. 160, p245

Cavaseno, V. et al (1980), "Industrial Air Pollution Engineering", McGraw-Hill

Cherrett, N. (1962), "De-dusting cyclone efficiency and pressure drop as affected by change in cyclone geometry", J. Inst. Fuel, Vol. 35, P.245

Ciliberti, D.F. and Lancaster, B.W. (1976), "Performance of rotary flow cyclones", AIChE Journal Vol. 22(2), P.394-398

Clean Air (Emission of grit and dust from furnaces) Regulations (1971), (Statutory Instrument 1971, No. 162), HMSO, London

Colman, D.A., Thew, M.T. and Lloyd, D.D. (1984), "The concept of hydrocyclones for separating light dispersions and a comparison of field data with laboratory work ", 2nd Int. Conf. on Hydrocyclones, Bath, England, Sep.

Crane, R. I. (1985), "Multicell cyclone performance (rig development)", Mech. Eng. Dept. , Imperial College , London

Crane, R.I. and Behrouzi, P. (1987), "Multicell cyclone performance optimization-interim progress report ", Imperial College, London, Mech. Eng. Dept., Rep.TPS/ 87.003

Crane, R.I. and Behrouzi, P. (1988), "Multicell cyclone performance optimization- final report", Imperial College, London, Mech. Eng. Dept., Rep.TPS/ 88.001

Crawford, M. (1976), "Air Pollution Control Theory", McGraw-Hill

Crellin, C.B., Bennellick, K.R.J. and Marshall, A.B. (1980), "Improved particulate emission control for solid fuel fired boilers", Appita, Vol. 33(5), p.345-350

Crowe, C.T. and Pratt, D.T. (1974), "Analysis of the flow field in cyclone separators", Computers and Fluids, Vol.2, p.249-260, Pergamon Press

Dabir, B. and Petty, C.A.(1984), "Laser Doppler anemometry measurements of tangential and axial velocities in a hydrocyclone operating without an air core", 2nd Int. Conf. on Hydrocyclones, Bath, England, Sep.

Darby, K. and Parker, K.R. (1971), "The electrostatic precipitator and its range of application", Symp., Filtration Society, Sep.

Darby, K. (1978), " Removal of grit and dust", In: " Industrial Air Pollution Handbook", Ed. Parker, A., McGraw-Hill

Dirgo, J. and Leith, D. (1985), "Performance of theoretically optimised cyclones", Filtration&Separation, March/April, Vol. 187, p.119-125

Doerchlag, C. and Miczek, G. (1980), "Cyclone dust collector", In: " Industrial Air Pollution Engineering", Ed. Cavaseno, V. et al,McGraw-Hill

Dorman, R.G. (1974), "Dust control and air cleaning ", International series of monographs in heating , ventilation and refrigeration , V.9, Pergamon

Durst, F., Melling, A., Whitelaw, J.H. (1976), "Principles of practice of Laser-Doppler Anemometry", Academic Press

Erdogan, M.E., Boysan, F. and Swithenbank, J.(1981), "On the calculation of Reynolds stresses", Dept. of Chemical Engineering and Fuel Technology,University of Sheffield , Report No. HIC 347

Escudier, M.P., Bornstein, J. and Zehnder, N. (1980), "Observations and LDA measurements of confined turbulent vortex flow", J. Fluid Mech., Vol. 98, p.49-63

First, M.W. (1950), "Fundamental factors in the design of cyclone dust collectors", Ph.D Thesis, Harvard University, also ASME annual general meeting paper No. 49-A-127

Fisher, M.J., Payne, R.C., Tate, P. and Willis, D.M. (1980), "Development and operating experience of coal fired industrial fluidised bed boilers", .in Fluidised Combustion:System& Application, Proc. Inst. Energy Conf., London, Nov.

Fontein, J.F. and Dijksman, C. (1953), " Recent developements in mineral dressing ", In Proc. of Symp. on Mineral Dressing, London, p.229

Gerrard, A.M. and Liddle, C.J. (1976), "The optimal choice of multiple cyclones", Powder Technology, Vol. 13, p.251-254

Gloger, J. and Hanke, S. (1971), "Der Einfluss der wiederaufwirbelung des staubes und der Grenzschichtabsaugung auf den Abscheidegrad und Druckverlust von Zyklonabscheidern ", Energietechnik Vol. 21(4) , p.158-164

Gosman, A.D., Pun, W.M., Runchal, A.K., Spalding, D.B., and Wolfshtein, M. (1969) "Heat and Mass Transfer in Recirculating Flows", Academic Press, London

Gosman, A.D., Khalil, E.E.and Whitelaw, J.H. (1979), "The calculation of two-dimensional turbulent recirculating flows", In " Turbulent shear flows I" ,Ed. Durst, F. et al, Springer-Verlag

Gosman, A.D.and Ideriah, F.J.K. (1976), "A general computer program for two-dimensional turbulent recirculating flow: TEACH-T user manual", Mech. Eng. Dept, Imperial College, London

Greenfield, R.R. (1986), "The use of cyclones for control of solids emission from fluidised bed boilers", Filtration& Separation, Vol. 23, Jan./Feb., p.38-39

Gupta, V.S. (1981), "Need for pollution control measurements and related problems", Journal Fact. Tech. Society, Vol. 14(1-2), p.52-56

Gupta, A.K., Lilley, D.G. and Syred, N. (1985), "Swirl Flows", Abacus Press

Hawksley, P.G.W., Badzioch, S. and Blackett, J.H. (1961), "Measurement of solids in flue gases ", British Coal Utilization Research Association, Leatherhead

Hejma, I.J. (1971), "Influence of turbulence on the separation process in a cyclone", Staub-Reinhaltung der Luft, Vol. 31, July, p.22-28

Henry, R.F., Podolski, W.F. and Saxena, S.C. (1982), "Gas clean-up systems for fluidised-bed coal combustors", Filtration & Separation, Vol. 19, Nov./Dec., p.502

Hinze, J.O. (1959), " Turbulence", MacGraw Hill

Hochstrasser, J.M. (1976), "The investigation and development of cyclone dust collector theories for application to miniature cyclone presamplers", Ph.D. thesis, University of Cincinnati, USA

Horzella, T.I. (1980), "Selecting, installing and maintaining cyclone dust collectors", In:"Industrial Air Pollution Engineering", Ed. Cavaseno, V. et al., McGraw-Hill

Hurley, T.F. (1951), Communication on the discussion on "The design and performance of cyclone separators", Trans. Inst. Chem. Engrs, Vol 29, p.375

Jackson, R. (1963), "Mechanical equipment for removing grit and dust from gases", BCURA, Leatherhead

Jantunen, M.J., Itkonen, A., Lihtamo, H. and Savolainen, T. (1983), "Basic pollutant emissions and their statistics of two coal fired boilers", KHM Teknisk Rapport 53, Swedish State Power Board

Jones, A.H. (1976), "Air pollution control for industrial coal-fired boilers in power generation", Ed. by Noll, K.E. and Davis, W.T., Ann Arbor Science Publishers

Kalen, B. and Zenz, F.A. (1974), "Theoritical-empirical approach to saltation velocity in cyclone design", In:"Recent Advances in Air Pollution Control", AIChemE Symp. Series No. 137, p.388-396

Kay, J.M. and Nedderman, R.M. (1974), "An Introduction to Fluid Mechanics and Heat Transfer", Cambridge University Press

Kelsall, D.F. (1952), "A study of the motion of solid particles in a hydraulic cyclone", Trans. Instn. Chem. Engrs., Vol. 30, p.87

Klein, H. (1963), "Entwicklung und leistungsgrenzen des Drehstromung-senstaubers", Staub, Vol. 23, p.501, Quoted by Gupta et al (1985)

Kline, S.J., Abbott, D.E. and Fox, R.W. (1959), "Optimum design of straight-walled diffusers", Journal of Basic Engineering (Trans. ASME), Vol. 81, p.321-330

Kline, S.J. and Mcclintock, F.A. (1953), "Describing uncertainties in single-sample experiments", Mechanical Engineering, Vol. 75(1) , p.3-8

Koch, W.H. and Licht, W. (1977), "New design approach boosts cyclone efficiency", Chem. Eng., Nov., p.80

Lapple, C.E. (1951), "Proccesses use many collector types", Chem. Engng., Vol. 58, p.144-151

Launder, B.E. and Spalding, D.B. (1974), "The numerical computation of turbulent flows", Computer Methods in Applied Mechanics and Engineering, Vol. 3, p.269-289

Lea, J.F. and Price, D.C. (1974), "Mean velocity measurements in swirling flow in a pipe", Proc. Symp. : Flow,its Measurement & Control in Science and Industry, Pittsburgh, May 1971, Vol.1, p.t1 (Publ. Inst. Soc. Amer. , Pitsburgh)

Leith, D. and Licht, W. (1972), "Collection efficiency of cyclone type particle collectors, a new theoretical approach", AIChE Symp. Series , No. 68, p.196

Leith, D. and Mehta, D. (1973), "Cyclone performance and design", Atmos. Enviroment, Vol. 7, p.527-549

Leoutsakos, G. (1987), " Boundary layer transition on concave surfaces ", Ph. D. Thesis, University of London

Littlejohn, R.F. and Smith, B. (1978), "Sampling gasborne solids: some factors effecting the characteristics of miniature cyclones", Proc. Inst. Mech. Engrs., London, Enviromental Science and Technology section, Vol. 192, No. 22, p.239

Lucas, R.L. (1974), "Gas-solids separation: state-of-the-art", Chem. Eng. Prog., Vol. 70(12), p.52-58

Malvern Instruments Ltd. (1985), "Malvern 2600 Series laser diffraction Particle sizer (User Manual)", V2.1, Spring lane , Malvern, Worcestershire, England

Malvern Instruments Ltd. (1986), "Malvern 2600 Series laser diffraction Particle sizer (Reference Manual)", V. 3, Spring lane, Malvern, W0rcestershire, England

Malvern Instruments Ltd. (1985), "PS64 Dry Powder Feeder (User Manual)", V.2 Spring lane , Malvern, Worcestershire, England

Merzkirch, W. (1982), "Flow Visualiszation II", Hemisphere , London

Mckee, D.E., Lucas, R.E. and Smith, J.E. (1977), "A review of pulse jet baghouse and dual mechanical collector performance on spreader stoker fired boilers", 70th Annual Meeting of the Air Pollution Control Association, Toronto, Canada,June

Miller, D.S. (1978), "Internal Flow Systems ", BHRA Fluid Engineering, Cranfield

Morii, Y., Suganuma, A. and Tanaka, S. (1968), "On collection efficiency of gas cyclone on coarse particle range", J. Chem. Jap., Vol.1, p.82-86 (in English)

Morse, O.M. (1886), U.S. Patent No. 39219, Knickerbocker Co., Jackson, Mississipi, Quoted by Gupta et al (1985)

Morsi, S.A. and Alexander, A.J. (1972), "An investigation of particle trajectories in two-phase flow systems", J. Fluid Mech., Vol. 55 , p.193-208

Mothes, H., Sievert, J. and Loffler,F. (1981), "Investigation of the cyclone grade efficiency curves using a light-scattering particle size analyser", I. Chem. E. Symposium Series No. 63, D2/Q1-Q13

Murphy, C.H. (1984), "Handbook of particle sampling and analysis methods", Verlag Chemic International

Negus, C. and Azzopardi, B.J. (1978), "The Malvern particle size distribution analyser : its accuracy and limitations ", AERE-R-9075 ,Engineering Sciences Division ,AERE Harwell ,Oxfordshire

Nuttall, J.B. (1953), "Axial flow in a vortex", Nature 172, p.582

OECD (1984), "Emission standards for major air pollutants", France (97 84 011) ISBN 92-64-12574-4

OECD (1987), " Energy and clean air costs and reducing emissions ", Enclair' 86 Int. Symp., Oct., Italy

Ogawa, A. and Seito, O. (1986), "Collection characteristics of the special forms of the returned flow types of the cyclone dust collectors", Bulletin of JSME, Vol. 29, No. 256, Oct.

Ohasi, H. and Maeda, S. (1958) , "Motion of water in a hydraulic cyclone", Chem. Eng. (Japan), Vol. 22, p.200 (in Japanese), Quoted by Dabir and Petty (1984)

Parker, A. (1978), "Industrial Air Pollution Handbook", McGraw-Hill (UK)

Patankar S.V. (1980), "Numerical Heat Transfer and Fluid Flow", Mc Graw-Hill

Patankar, S.V. and Spalding, D.B. (1972), "A calculation procedure for heat, mass, and momentum transfer in three-dimensional parabolic flows", Int. J. Heat Mass Transfer, Vol. 15, p.1787-1805

Pericleous, K.A., Rhodes, N. and Cutting, G.W. (1984), "A mathematical model for predicting the flow field in a hydrocyclone classifier", 2nd Int. Conf. on Hydrocyclones, Bath, England, Sep

Pericleous, K.A. and Drake, S.N. (1987), "Development and validation of a mathematical model for hydrocyclones", CHAM Ltd., Wimbledon

Perlsweig, M., Neal, J.W. and Moore, W.E. (1981), "Hot gas clean-up program for pressurized fluidized bed combustor combined cycle power generation", ASME paper 81-JPGC-GT-5

Perry, H.R., Green, D.W. and Malone, J.O. (1984), "Perry's Chemical Engineering Handbook", MacGraw Hill

Peterson, C.M. and Whitby, K.T. (1965), "Fractional efficiency characteristics of unit type collectors", ASHRAE J., Vol. 7, p.42-49

Pillai, K.K. and Wood, P. (1980), "Emission from a pressurized fluidized bed coal combustor ", J. Inst. Energy, Vol. 53, Dec., p.159-175

Reijnen, K. and Brakel, J.V. (1984), "Gas cleaning at high temperatures and high pressures: a review", Powder Technology, Vol.40., p.111

Reznik, V.A. and Matsnev, V.V. (1971), "Comparing the characteristics of the elements in batteries of cyclones", Thermal Engineering, Vol. 18, No.2, p.23-26

Rietema, K. (1961), "Performance and design of hydrocyclones", Chem. Eng. Sci., Vol. 15, p.298

Rodi, W. (1976), "A new algebraic relation for calculating the Reynolds stresses", Z. Angew Math. Mech., Vol. 56, p.219.

Rose, H.E. and Wood, A.J. (1966), "An Introduction to Electrostatic Precipitation in Theory and Practice ", Constable, London

Ross, R.D. (1972), "Air Pollution and Industry", Van Nostrand Reinhold

Rubin, E.S. (1986), "Recent advances in air pollution control technology ", Mech. Eng., Vol. 108, Nov., p.72-78

Ryabchikov, S.Y., Amerik, B.K. and Karpukhovich, D.T. (1975), "Comparison of certain types of cyclones installed within fluid-bed process vessels", Chemistry and Technol. Fuels and Oils, Russian Original Vol. 10, No. 10, p.781

Sabzvari, J. (1984), " Instability in laminar and transitional boundary layers on concave surfaces", Ph. D. Thesis , University of London

Sage, P.W., Wright, M.A. and Clark, R.K. (1984), "Particulate removal developments for industrial coal fired fluidised bed boilers ", 3rd Int. Fluidized Combustion Conf. , London , Oct.(Publ. Inst. of Energy)

Sage, P.W. and Wright, M.A. (1986), " The use of gas bleeds to enhance cyclone performance ", Filtration & Separation, Vol. 23, p.32-36

Sargent, G.D. (1980), "Gas/solid separations", In:" Industrial Air Pollution Engineering", Ed. Cavaseno, V. et al, McGraw-Hill

Schmidt, K.R. (1963), "Physikalische Grundlagen Prinzip des Drehstromungenstaubers", Staub, Vol.23, p.491 (CEGB Info. Services translation No. 3863), Quoted by Gupta et al (1985)

Schmidt, P. (1986), " New results in cyclone-design, especially for higher-pressure and temperature application ", Inst. Chem. Engrs. Symp. Series No. 99, p.67-72

Schneider, F.B. (1960), General Electric Review, U.S.A. Vol. 52, p.22, Quoted by Gupta et al (1985)

Seinfeld, J.H. (1975), " Air Pollution Physical and Chemical Fundamentals ", McGraw-Hill

Seville, J.P.K., Coury, J.R., Ghadiri, M. and Clift, R. (1984), "Comparison of techniques for measuring the size of fine non-spherical particles", 3rd European Symposium on: Particle Characterization, Nuremberg, May

Shepherd, C.B. and Lapple, C.E. (1939), "Flow pattern and pressure drop in cyclone dust collectors", Ind. Eng. Chem., Vol. 31, P.972-984

Shin, H.W. and Hu, Z.A. (1985), "Measurement of swirling flow field using the single slanted hot-wire technique ", Am. Soc. Mech. Engrs. Paper 85-IGT-76

Smigerski, H.J.(1970), "Die Feinstaubagglomeration in flieh kraftenstaubern", Fortschrittberichte der Vdi, Zeitschriften,3, No. 30, Aug., VDI-Verlag, GMBH, Dusseldorf, Quoted by Abrahamson et al (1978)

Smith, J.L. (1962), " An experimental study of the vortex in the cyclone separator", J. Basic Eng. (Trans. ASME), Vol. 84, p.602

Smith, C.R., et al. (1981), "A User Guide to Dust and Fume Control", Institution of Chemical Engineers

Sortor, C.J. (1981), "Successful application of the sidestream separator", Industrial Fuel Conf., Purdue Univ., Sep./Oct.

Spalding, D.B. (1972), "A novel finite-difference formulation for differential expression involving both first and second derivatives", Int. J. Num. Methods Eng. Vol. 4, p.551-559

Sproul, W.T. (1966), "Effect of dust concentration upon gas-flow capacity of a cyclonic collector", J. Air Pollut. Control Assn., Vol. 16, p.439

Stairmand, C.J. (1949), "Pressure drop in cyclone separators", Engineering ,16B ,Oct., p.409-411

Stairmand, C.J. (1951), "The design and performance of cyclone separators", Trans. Instn. Chem. Engrs., Vol. 29, p.356-383

Stairmand, C.J. (1951), "The sampling of dust-laden gases", Trans. Inst. Chem. Engrs., Vol. 29, p.15-44

Stairmand, C.J. (1956), "The design and performance of modern gas-cleaning equipment", J. Inst. Fuel, Vol. 29, Feb. , p.58-81

Stairmand, C.J. (1957), Smokeless Air, Vol. 103, p.51

Stairmand, C.J. (1965), "Removal of grit, dust, and fume from exhaust gases from chemical engineering processes ", Chem. Eng., Dec., p.310-326

Stairmand, C.J. (1969), "Selection of gas cleaning equipment: a study of basic concepts", Gas Cleaning Manual No.1 (HO/ENS/690007), I.C.I. Ltd.

Stern, A.C., Caplan, K.J. and Bush, P.D. (1955), "Cyclone dust collectors", Amer. Petroleum Inst., New York

Stern, A.C. (1986), "Air pollution", (3rd ed.) , Academic Press

Sutton, B.W. (1972), "The design and performance of gas cyclones" , Gas Cleaning Manual No.1 (HO/ENS/720003), I.C.I. Ltd.

Svarovsky, L. (1981), "Hydrocyclone selection and scale-up", Filtration & Separation, Nov./Dec., p.551-554

Swift, P. (1985), "An empirical approach to cyclone design and application", Filtration Society Meeting on Gas Cyclones, London, June

Swithenbank, J., Beer, J.M., Tylor, D.S., Abbot, D. and McCreath, G.C. (1976), "A laser diagnostic technique for the measurement of droplet and particle size distributions", AIAA paper No. 76-69, AIAA 14th Aerospace Science Meeting, Jan., Washington

Syred, N., Biffin, M. and Wright, M. (1985), "Vortex collector pockets to enhance dust separation in gas cyclones ", Filtration&Separation, Vol. 21(6),p.367

Ter Linden, A.J. (1949), "Investigations in cyclone dust separators", Proc. Inst. Mech. Eng., Vol. 160, p.233

Torii, K. (1982), "Flow visualization by smoke-wire technique", In :" Flow Visualization II", Ed. Merzkirch, W. ,Hemisphere , London

Tutu, N.K. and Chevray, R. (1975), "Cross-wire anemometry in high intensity turbulence", J. Fluid Mech., Vol. 71, p.785

United Nations (1987), "National strategies and policies for air pollution abatement ", Results of the 1986 major review prepared within the frame work of the convention on Long-range transboundary air pollution,ECE/EB.AIR/14

U.S. Dept. of Energy (1986), "Selection of fly-ash filters for pressurized fluidized-bed combustors", Materials&Components in Fossil Energy Application(a DoE newsletter), No. 60, Feb. 1

Van Ebbenhorst Tengbergen, H.J. (1965), "Comparative studies with cyclones", Staub, Vol. 25(11), p.44

Van Tongeren, H. (1935), "A modern dust collector- a study of the principles govering its design and operation", Mech. Eng., Vol. 57, p.753

Vlachos, N.S. (1977), "Measurements and calculation of velocity in small diameter ducts with particular application to blood flow in venules", Ph. D. Thesis, University of London

Walton, W.H. (1974), "Cyclone dust separators ", in:"Dust Control and Air Cleaning", Ed. Dorman, Pergamon Press

Wang, C.P. and Snyder, D. (1974), "Laser Doppler velocimeter:experimental study ", Appl. Opt. Vol.13, p.98

Weidner, H. (1987), "Clean air policy in Europe ", A survey of 17 countries, Research unit environmental policy, Berlin, ISSN 0256 7296

Weiner, B.B. (1979), "Particle and spray sizing using laser diffraction ", SPIE Vol. 170 Optics in quality assurance II

Wheeldon, J.M., Snow, G.C and Svarovsky, L. (1985), "The performance of a cyclone in the off-gas path of a pressurised fluidized bed combustor", Filtration Society Meeting on Gas Cyclones, London, June

Williams, F. (1965), " Combustion Theory", Addison Wesley

Yajnik, K.S. and Subbaiah, M.V. (1973), "Experiment on swirling turbulent flows, Part 1, Similarity in swirling flows", J. Fluid Mech. Vol. 60, p.665-687

Yamada, H. and Matsui, T. (1982), "Visualization of vortex interaction using smoke wire technique ", in : Flow Visualization ", Ed. Merzkirch, W.

Yoshioka, N. and Hotta, Y. (1955), "Liquid cyclone as a hydraulic classifier", Chem. Engng Japan, Vol. 12, p.632

Table 1.1 Illustration of dust removal efficiencies required to meet current and possible future U.K. emissions limits

	UK Clean Air Regulations 1971		Possible future regulations
Boiler output	5 MW	20 MW	
Dust flow rate	50.4 kg/h	201.6 kg/h	
Dust concentration			4920 mg/Nm^3
Emission limit	6.8 kg/h	21.6 kg/h	70 mg/Nm^3
Required separator overall efficiency	86.5%	89.3%	98.6%

Assumptions:

Industrial washed coal, conventional firing
Net calorific value 28.6 MJ/kg
Combustion efficiency 80%
Ash content 8% (of which 20% is furnace bottom ash)
Flue gas volume 13.0 Nm^3 per kg fuel

Table 1.2 Dust removal efficiency required to meet a 70 mg/Nm^3 emissions limit and dust particle size range, for various types of firing

Type of firing	Required separator overall efficiency for 70 mg/Nm^3 emission	Typical percentage dust mass below 10 μm particle size
Chain grate stoker	86.0 - 98.4	2
Spreader stoker (<3 MW)	86.0 - 95.3	11
Spreader stoker (3-30 MW)	94.6 - 99.3	
Pulverised fuel	98.3 - 99.5	32
Atmospheric fluidized bed	99.2 - 99.6	10-30

Table 1.3 Comparison of national emission standards for electricity generating plants (OECD, 1984)

Particulate Control

Country	Fuel	Emission Limit (2)		Comments
		mg/Nm^3	ng/J (= g/GJ)	
Australia	Solid	250	105	National Guidelines
Belgium	Solid	350	147	Regulations
Canada	All	116	43	National Guidelines
Denmark	Liquid	97	36	National Guidelines
	Solid	150	63	
Germany	Liquid	50	18	Regulations
	Solid	50	21	
	Gas	5	2	
Greece	All	150	56	Regulations
Japan	Liquid	50	18	Regulations
	Solid	100	42	
	Gas	50	15	
Netherlands	Solid	48	20	National Guidelines
New Zealand	Solid	125	52	Regulations
Sweden	Solid	36	15	Regulations
United Kingdom	Solid	115	48	
United States	Solid	31	13	Regulations

Note:

1. Considerable variation occurs among countries in both definition and conditions of application of emission standards. Comparisons should be made with caution, and readers should refer to specific country tables of this compendium for further information.

2. Underlining indicates units in which limits are normally expressed in specific countries. Conversion between mg/Nm^3 and ng/GJ is carried out using the following conversion factors: 420 m^3/GJ (solid); 370 m^3/GJ (liquid); 300 m^3/GJ (gaseous fuel); for flue gas at 1 Bar pressure and 15°C (12 per cent CO_2 content of flue gas for solid and liquid-fired boilers).

Table 1.4 Bag filters - properties of various fabrics (Parker, 1978)

Material	Maximum operating temperature (°C)	Resistance	
		Acids	Alkalies
Cotton	90	Low	High
Wool	90	High	Moderate
Nylon	110	Low	High
Orlon	120	High	Moderate
Terylene	130	High	High
Nomex	200	Moderate	High
Teflon	230	High	High
Glass fibre (Silicone coated)	270	Moderate	Moderate
Stainless steel	+400		

Table 1.5 Comparison of particulate removal systems (Gupta, 1981)

Type of equipment	Max. temperature °C	Collection efficiency %	Pressure drop cm H_2O	Remarks
Cyclones/ multicyclones	400	85 (90-95% for above 30)	5-12	Used-for high dust concentration; as pre-collectors; where very high efficiency is not a critical requirement.
Electrostatic precipitators	400	99.4 (Effective range 0.1 to 10)	1	Works on the principle of electrostatic attraction. Efficiency depends on particle charging and collection. Used-for very large volume of gases.
Fabric filters	290	99	10-20	Fabric filters are made of cotton, decron, nylon, orlon, teflon, glass fibre, etc. Used-for relatively low volume of gas; for dry collection of particles.
Scrubbers	540	99	5-88	Used-for removal of fine particles as well as gases; where the gas volume is not large; for combustible gases also. The scrubbed liquid containing particulates and dissolved gases has to handled.

The approximate average cost for per m^3 gas including utilities, maintenance, capital and insurance based on a published document around 1970 are:- Cyclones 3.5 to 5,5; electrostatic precipitators 10.5; fabric filters 7 to 10.5, scrubbers 5.5 to 28. From these figures a comparative idea of cost can be obtained.

Table 2.1 Typical conventional multicell cyclone system dimensions (Greenfield, 1986)

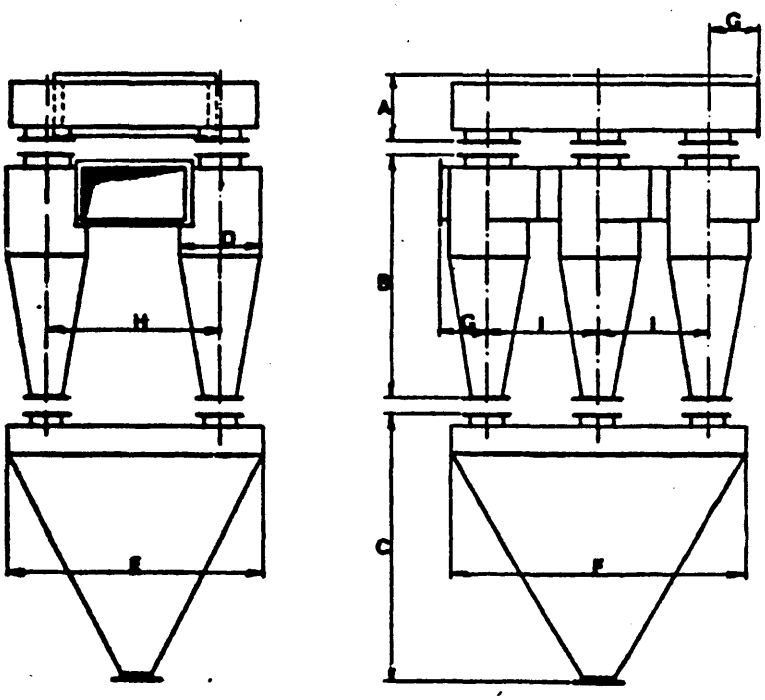

size	Dimensions in millimeters								
	A	B	C	D	E	F	G	H	I
3	290	1090	935	300	1100	1100	180	800	390
3½	325	1265	1100	350	1250	1250	210	930	450
4	360	1440	1265	400	1450	1450	240	1060	520
4½	395	1610	1430	450	1600	1600	270	1190	580
5	420	1785	1595	500	1750	1750	300	1320	650
5½	455	1960	1760	550	1950	1950	330	1450	710
6	490	2155	1925	600	2150	2150	360	1580	780
6½	525	2330	2090	650	2350	2350	390	1710	840
7	560	2505	2255	700	2550	2550	420	1840	900
8	620	2850	2550	800	2750	2750	480	2110	1010
9	680	3195	2875	900	3000	3000	540	2380	1125
10	740	3545	3200	1000	3500	3500	600	2650	1235
11	800	3895	3525	1100	4000	4000	660	2920	1350
12	860	4245	3850	1200	4500	4500	720	3190	1460

All dimensions are approximate

Table 2.2 Dimensions of conventional designs of cyclones (Walton, 1974)

	Stairmand (1951)		Breuer (1967)	Stern et al (1955)		Ter Linden (1949)
Parameter	High efficiency	H.G.R.	I, IV	Typical III	"Consensus" II	I, II
D_e	1	1	1	1	1	1
D_e	0.5	0.75	0.59	0.5	0.5	0.41
D_D	0.375	0.575	0.40	N.A.	N.A.	0.28
a	0.2	0.375	0.32	0.25	0.2	0.36
b	0.5	0.75	0.74	0.5	0.45	0.36
c	1.5	1.5	1.59	2	0.75	1
h	0.5	0.875	0.80	0.625	0.625	0.41
L	4	4	3.53	4	2	2.8
H	3	1.625	1.96	–	–	–
r_T	0.4	0.6875	0.66	0.375	0.4	0.68
Scroll	None	360°	360°	None	None	180°
Swirl No. S	3.93	2.09	1.96	3.14	4.36	2.48
A_e/A_T	1.96	1.57	1.15	1.57	2.18	1.02
$G = \frac{8K_c}{K_e^2 K_b^2}$	551.3	29.80	95.6	686	612.35	262
$N_H = \frac{16ab}{D_e^2}$	6.40	8	10.9	3.2	5.76	12.33
G/N_H	86.1	3.7	8.8	214.4	106.3	21.2

I Approximate dimensions
II Average dimensions ratios from 23 family types
III Described as a widely recommended type
IV BAT-cyclone used for dust sampling, D_1 = 34 mm.

Table 2.3 Values of Euler No. for various cyclone configurations (Gupta et al 1985)

Ratio, r_0/r_e		–	3.0	2.0	2.0	4.0
Velocity, w_{in}		(m/s)	10.7	36.6	21.0	11.2
Velocity, w_{ti}		(m/s)	20.2	18.8	14.2	15.8
Pressure drop, Δp		(N/m^2)	883.0	886.0	903.0	2060.0
Euler No. (loss factor)	$\zeta_1^1 = \frac{\Delta p_2}{\frac{\rho w_{in}^2}{2}}$	–	12.6	0.97	3.14	27.3
Euler No. (loss factor)	$\zeta_2^1 = \frac{\Delta p}{\frac{\rho w_{ti}^2}{2}}$	–	3.6	4.1	7.5	13.9

Table 3.1 Preliminary multicell cyclone design data (with unspecified dust)

Description	I	II	III
Cell inlet dia. (D_i), m	0.254	0.1	0.1
Cell exit dia. (D_e), m	0.152	0.05	0.05
Gas temperature, °C	200	20	20
Gas viscosity (μ_g), kg/m s	$2.58*10^{-5}$	$1.81*10^{-5}$	$1.81*10^{-5}$
Gas density (ρ_g), kg/m^3	0.746	1.205	1.205
Multicell flow rate, m^3/s	10.4 (35 cell)	0.115 (9 cell)	0.458 (9 cell)
One-cell flow rate, m^3/s	0.297	0.0128	0.05
Cell bulk velocity (V_i), m/s	9.16	2.54	10.12
Reynolds no. (Re)	67400	16918	67400
Particle mass median dia. (d_p), μm	10	10	-
Particle material density (ρ_p), kg/m^3	2000	2000	-
Characteristic particle time scale (τ_p), s	0.00043	0.000614	-
Characteristic gas time scale (τ_g), s	0.0277	0.03935	-
Stokes no. (St)	0.0156	0.0156	-

I - Full scale cyclone

II - Model scale cyclone (Stokes no. matching)

III- Model scale cyclone (Reynolds no. matching)

Table 3.2 Average technical data for Syenex-40

Mineralogy

SYENEX-40 is pure, dry and nodular nepheline syenite, composed of the minerals nephelin and feldspar, which are anhydrous sod ium potassium aluminium silicates. It is claimed to be totally void of free quartz.

Chemical composition		**Approximate size distribution (by mass)**	
SiO_2	57.00 %	< 44 µm	99.8%
Al_2O_3	23.80 %	< 30 µm	97.0%
Fe_2O_3	0.12 %	< 20 µm	85.0%
Na_2O	7.8 %	< 10 µm	50.0%
K_2O	9.1 %	< 5 µm	30.0%
CaO	1.1 %		
I.o.i	1.1 %		

Physical properties

Oil absorption, rub-out, ASTM D281-31 g oil/100g	17-18
Whiteness, Elrepho, Elrepho FMY/C	86
pH	10.3
Density g/ml	2.56
Specific surface BETH m^2/g	1.3
Hardness, Moh's scale	5.6
Refractive index	1.53
"Mean" particle size, µm	10.0
Tamped density g/mg	1.28
particle shape	nodular

Table 3.3 Final multicell and one cyclone design data

Description	I	II	III	IV	V
Cell inlet dia. (D_i), m	0.254	0.098	0.098	0.098	0.098
Cell exit dia. (D_e), m	0.152	0.05	0.05	0.05	0.05
Fluid temperature, °C	200	20	20	20	20
Fluid viscosity (μ_g) kg/m s	$2.58*10^{-5}$	0.001	$1.81*10^{-5}$	$1.81*10^{-5}$	$1.81*10^{-5}$
Fluid density (ρ_g) kg/m^3	0.746	1000	1.205	1.205	1.205
Multicell flow rate m^3/s	10.4 (35 cell)	- (9 cell)	0.458 (9 cell)	0.2178 (9 cell)	0.396 (9 cell)
One-cell flow rate m^3/s	0.297	0.0038	0.05	0.024	0.044
Cell bulk velocity (V_i) m/s	9.16	0.69	10.12	5.13	9.33
Reynolds no. (Re)	67400	67400	67400	32600	60871
Particle mass median dia. (d_p), μm	10	-	-	10.3	8.58
Particle material density (ρ_p), kg/m^3	1450	-	-	2445	2000
Characteristic particle time scale (τ_p), s	0.00119	-	-	0.000814	0.000452
Characteristic gas time scale (τ_g), s	0.0277	-	-	0.0191	0.0105
Stokes no. (St)	0.043	-	-	0.043	0.043

I - Full scale cyclone

II - Model scale cyclone (Reynolds no. matching, water rig)

III- Model scale cyclone (Reynolds no. matching, air rig)

IV - Model scale cyclone (Stokes no. matching, with Syenex-40)

V - Model scale cyclone (Reynolds no. matching, with Pozzolan)

Table B.1 Specification of LDA measuring volume at different positions (X is distance from cyclone body) for measuring swirl velocity

X(mm)	Φ_W	l_v	d	d_v	$d_f \times 10^{-3}$	n_f
2.64	6.904	1.546	.186	.187	1.975	94.785
5.91	6.903	1.546	.186	.187	1.975	94.762
9.17	6.901	1.547	.186	.187	1.976	94.739
12.44	6.900	1.547	.186	.187	1.976	94.716
15.70	6.898	1.547	.186	.187	1.977	94.694
17.97	6.897	1.548	.186	.187	1.977	94.678
22.24	6.895	1.548	.186	.187	1.978	94.649
26.50	6.961	1.533	.186	.187	1.959	95.571
28.78	6.953	1.535	.186	.187	1.961	95.460
32.04	6.942	1.538	.186	.187	1.964	95.302
35.31	6.931	1.540	.186	.187	1.968	95.146
38.58	6.919	1.543	.186	.187	1.971	94.992
41.84	6.908	1.545	.186	.187	1.974	94.840
45.10	6.897	1.547	.186	.187	1.977	94.688
48.37	6.887	1.550	.186	.187	1.980	94.537
51.64	6.876	1.552	.186	.187	1.983	94.387
54.91	6.865	1.555	.186	.187	1.986	94.237
58.17	6.854	1.557	.186	.187	1.989	94.087
61.44	6.843	1.560	.186	.187	1.993	93.937
64.71	6.832	1.562	.186	.187	1.996	93.787
67.98	6.822	1.565	.186	.187	1.999	93.636
71.24	6.811	1.567	.186	.187	2.002	93.485
73.50	6.803	1.569	.186	.187	2.004	93.380
77.77	6.789	1.572	.186	.187	2.009	93.179
82.04	6.699	1.593	.186	.187	2.035	91.937
84.31	6.685	1.597	.186	.187	2.040	91.741
87.57	6.664	1.601	.186	.187	2.046	91.457
90.84	6.643	1.606	.186	.187	2.052	91.169
94.11	6.623	1.611	.186	.187	2.059	90.879
97.37	6.601	1.617	.186	.187	2.065	90.586

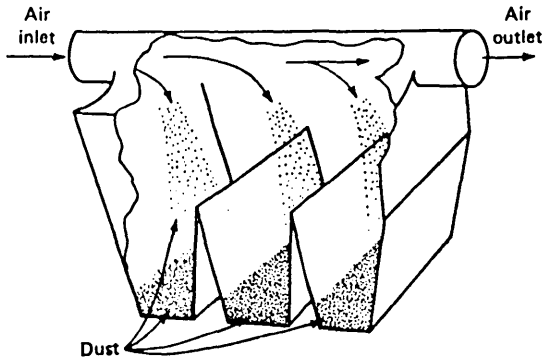

Fig. 1.1 Typical settling chamber (Seinfeld, 1975)

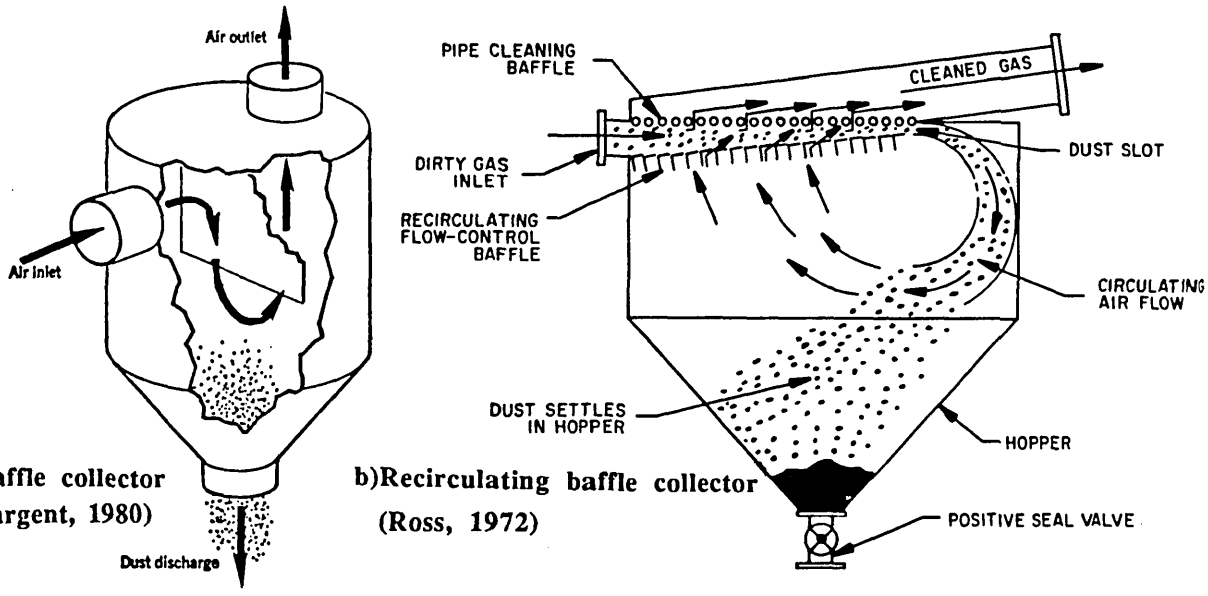

a) Baffle collector (Sargent, 1980)

b)Recirculating baffle collector (Ross, 1972)

Fig. 1.2 Schematic of two inertial dust separator devices

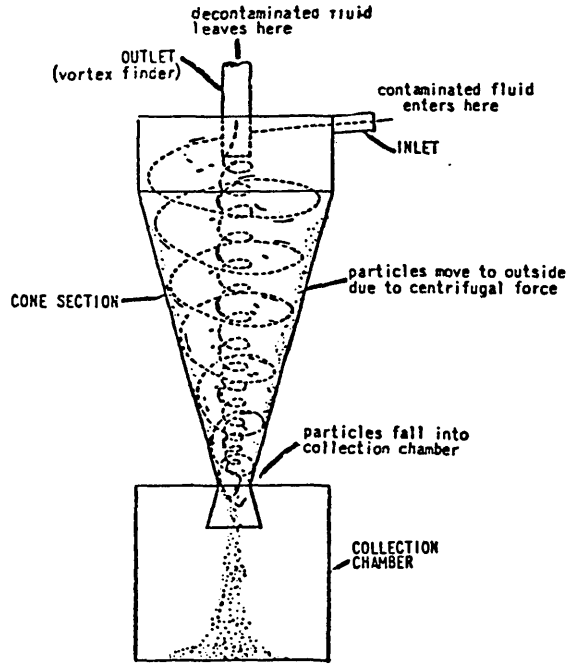

Fig. 1.3 A schematic diagram of a cyclone chamber together with the general concepts of flow and particle separation (Gupta et al. 1985)

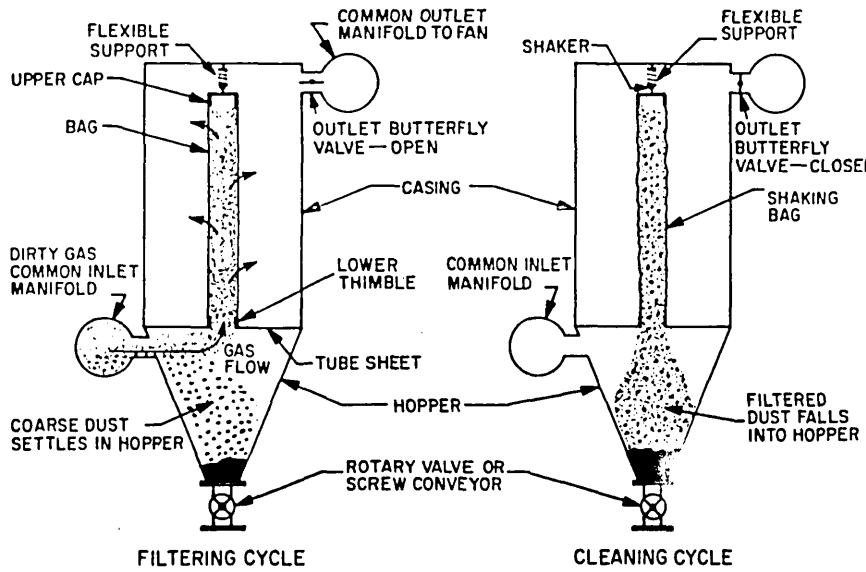

Fig. 1.4 Automatic convectional baghouse with mechanical shaking (Ross, 1972)

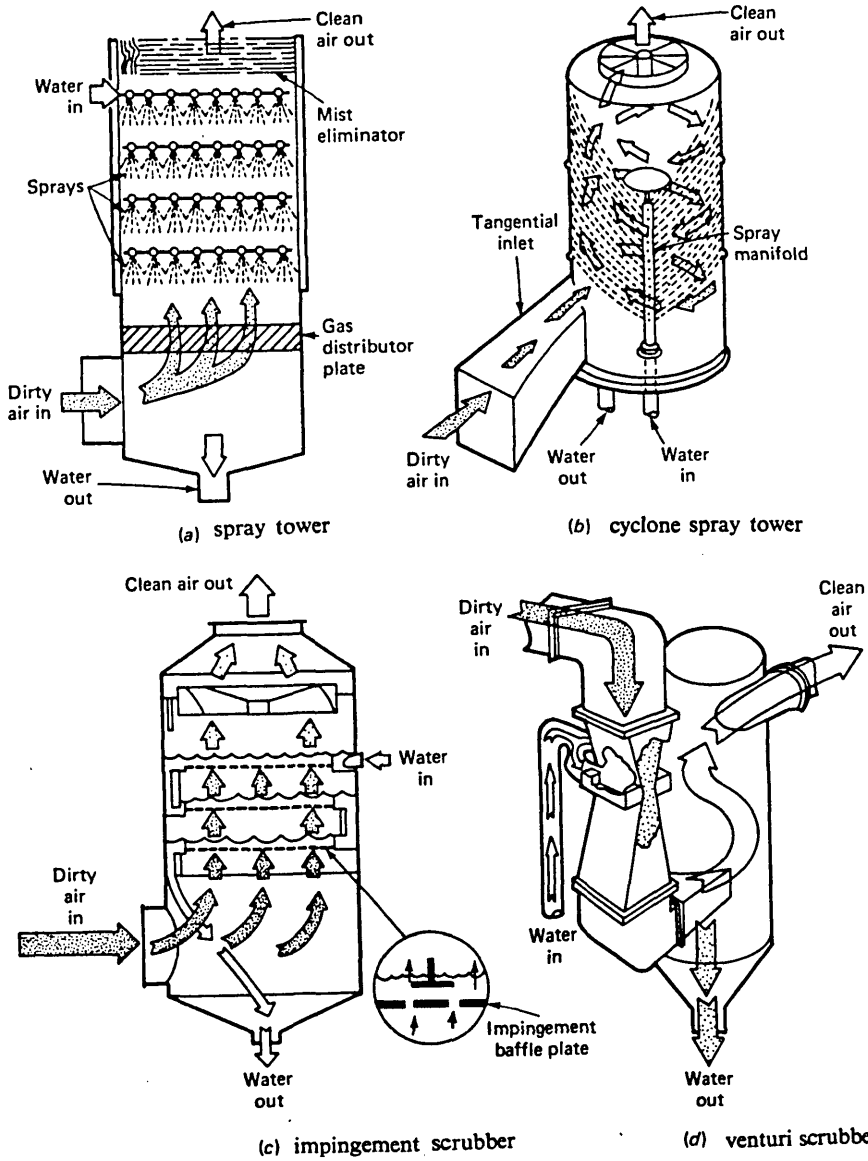

Fig. 1.5 Schematic of some types of wet scrubber (Seinfeld, 1975)

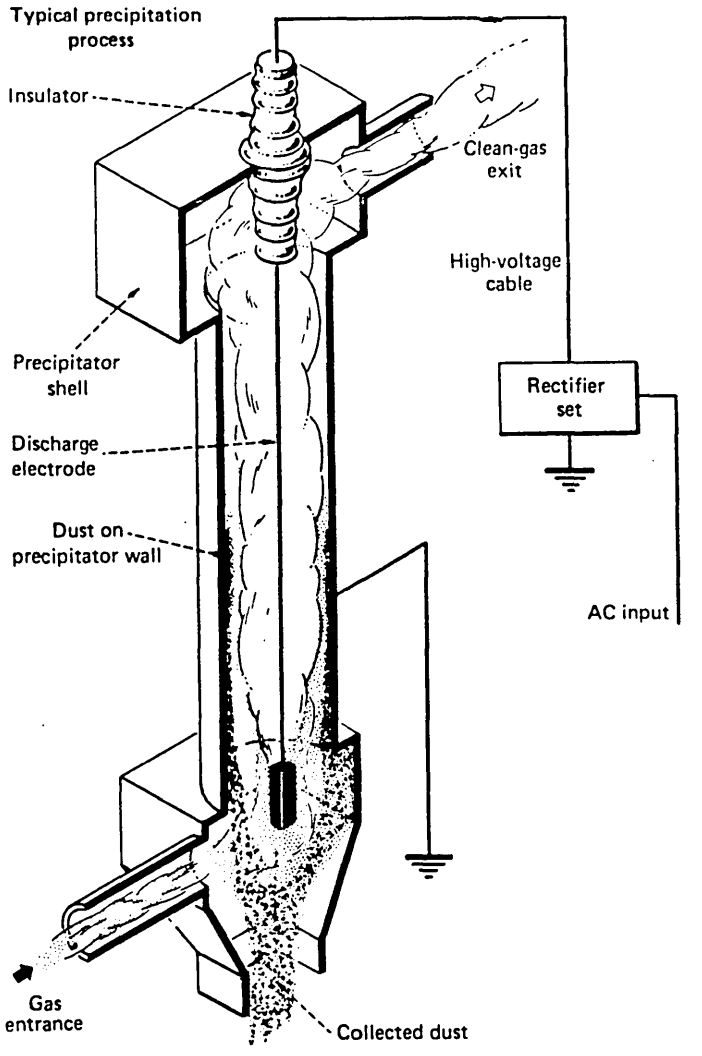

Fig. 1.6 Schematic of a simple electrostatic precipitator (Bump, 1980)

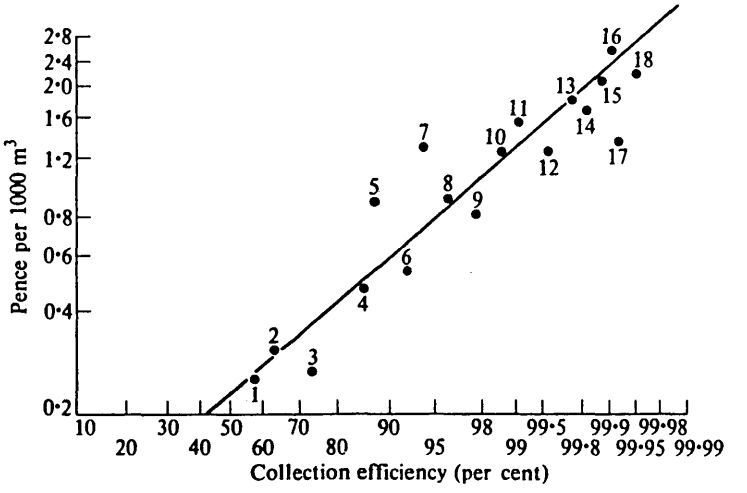

Annual capital cost taken as 10 per cent installed cost. Operating cost on basis 8000 hours per year. (1) Inertial collector; (2) medium efficiency cyclone; (3) low resistance cellular cyclones; (4) high efficiency cyclone; (5) impingement scrubber (Doyle type); (6) self-induced de-duster; (7) void spray tower; (8) fluidized bed scrubber; (9) irrigated target scrubber (Peabody type); (10) electrostatic precipitator; (11) irrigated electrostatic precipitator; (12) flooded disc scrubber, low energy; (13) flooded disc scrubber, medium energy; (14) venturi scrubber, medium energy; (15) high efficiency electrostatic precipitator; (16) venturi scrubber, high energy; (17) shaker type fabric filter; (18) reverse jet fabric filter.

Fig. 1.7 Cost of gas cleaning equipment treating fine industrial dust (Stairmand, 1969)

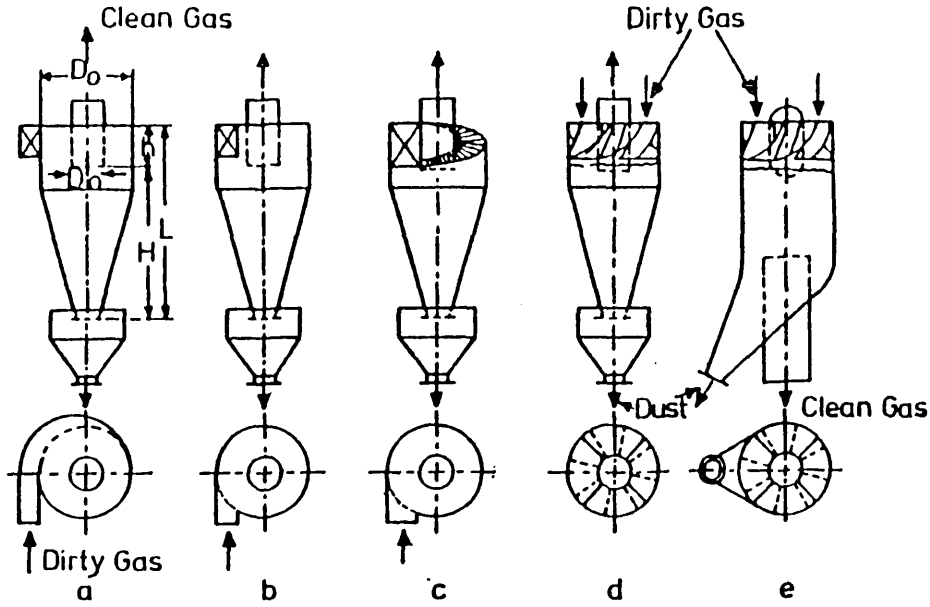

Fig. 2.1 Various type of cyclones (Biffin et al. 1981)

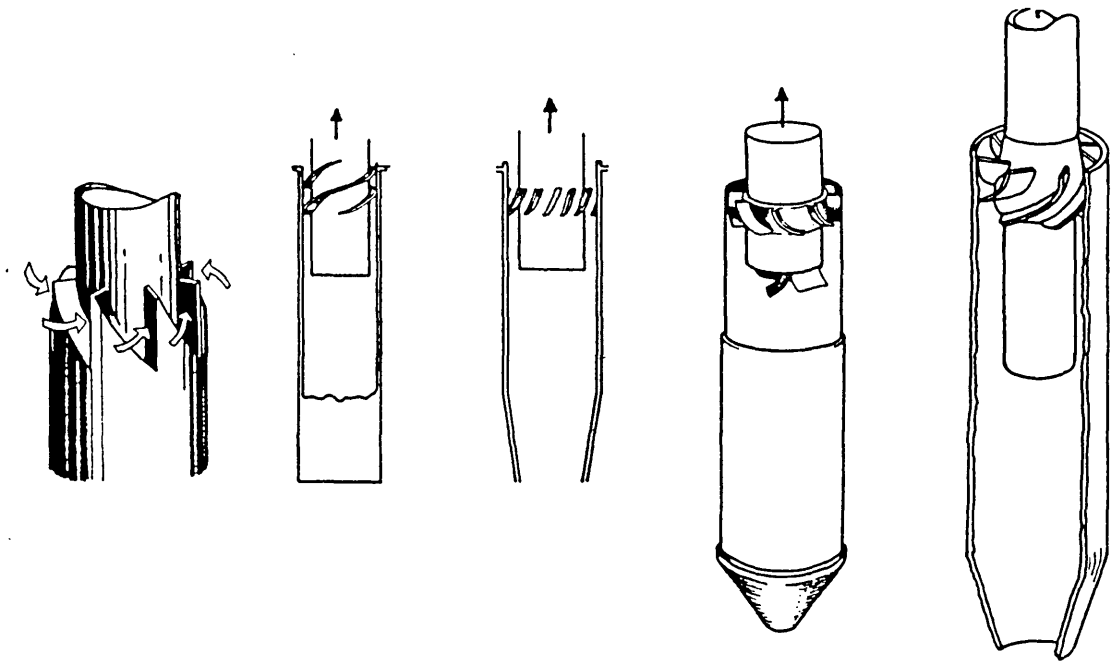

Fig. 2.2 Types of axial flow cyclones (Jackson, 1963)

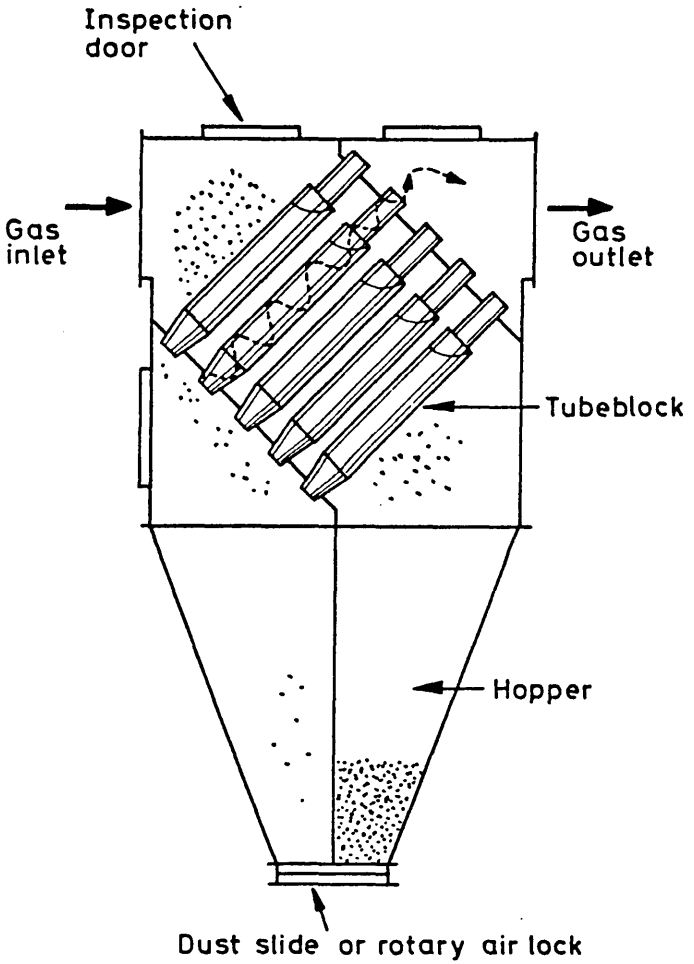

(a) " Tubix" multitubular cyclone (Smith et al. 1981)

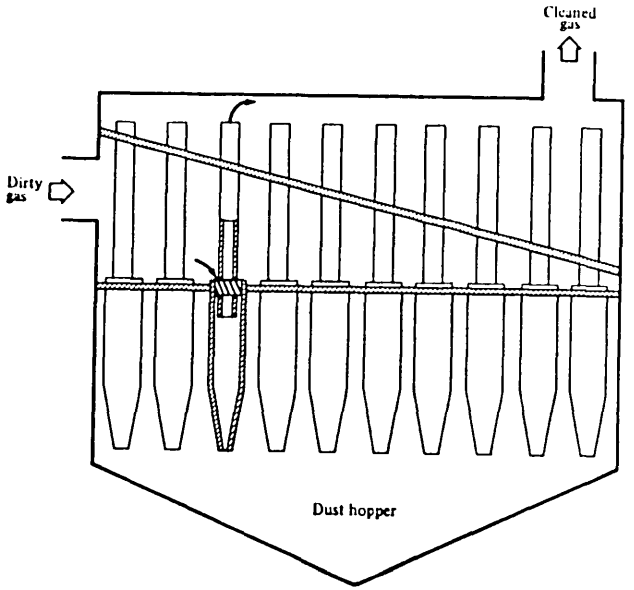

(b) Multiple reverse-flow cyclone collector (Crawford, 1976)

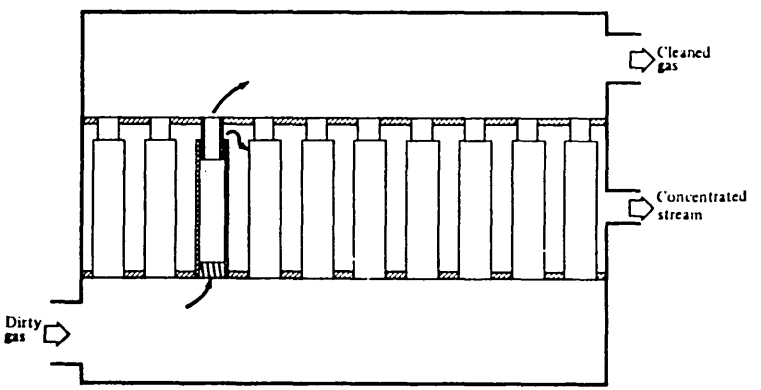

(c) Straight- through multiple cyclone concentrator (Crawford, 1976)

Fig. 2.3 Different types of multicell cyclone design

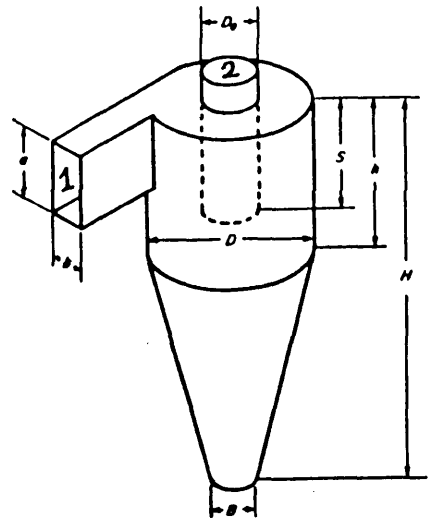

Fig. 2.4 Reverse flow cyclone with dimensions

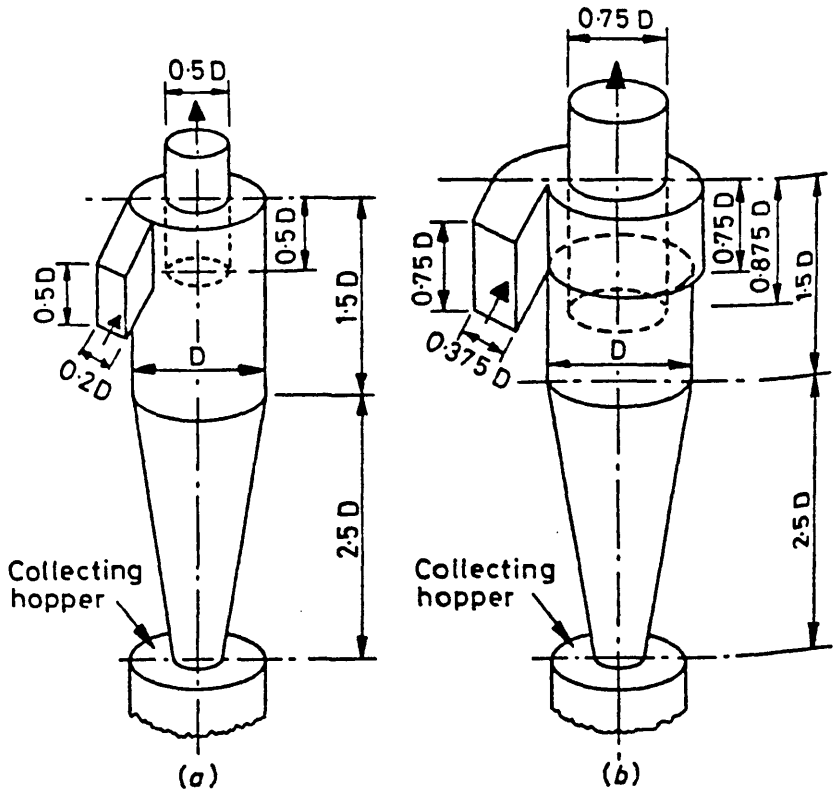

(a) high-efficiency, medium-throughput pattern: normal flow rate = 1.5 D^2 m^3/s; (b) medium-efficiency, high-throughput pattern: normal flow rate = 4.5 D^2 m^3/s. Entrance velocity at these flows is approximately 15 m^3/s in both types. *D* in the above equations = diameter (m)

Fig. 2.5 Standard cyclone designs (Stairmand 1951)

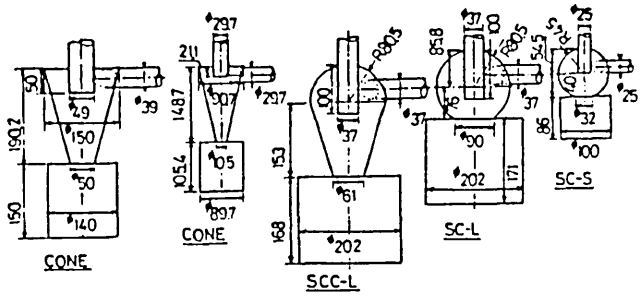

Fig. 2.6 Special forms of cyclones (Ogawa & Seito, 1986)

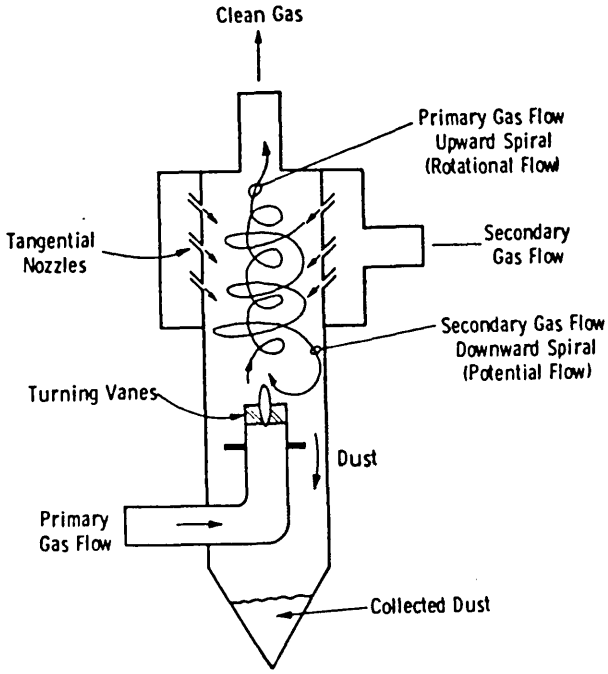

Fig. 2.7 The rotary flow dust collector (Ciliberti & Lancaster, 1976)

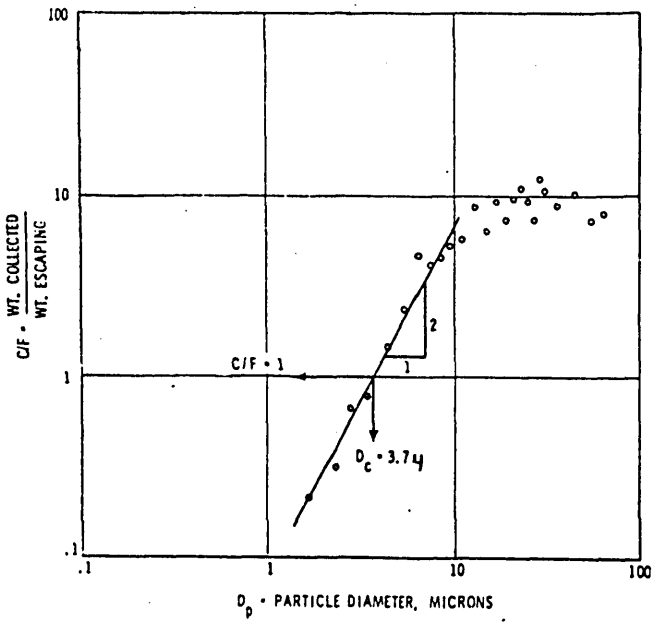

Fig. 2.8 Sharpness Index plot (Lucas, 1974)

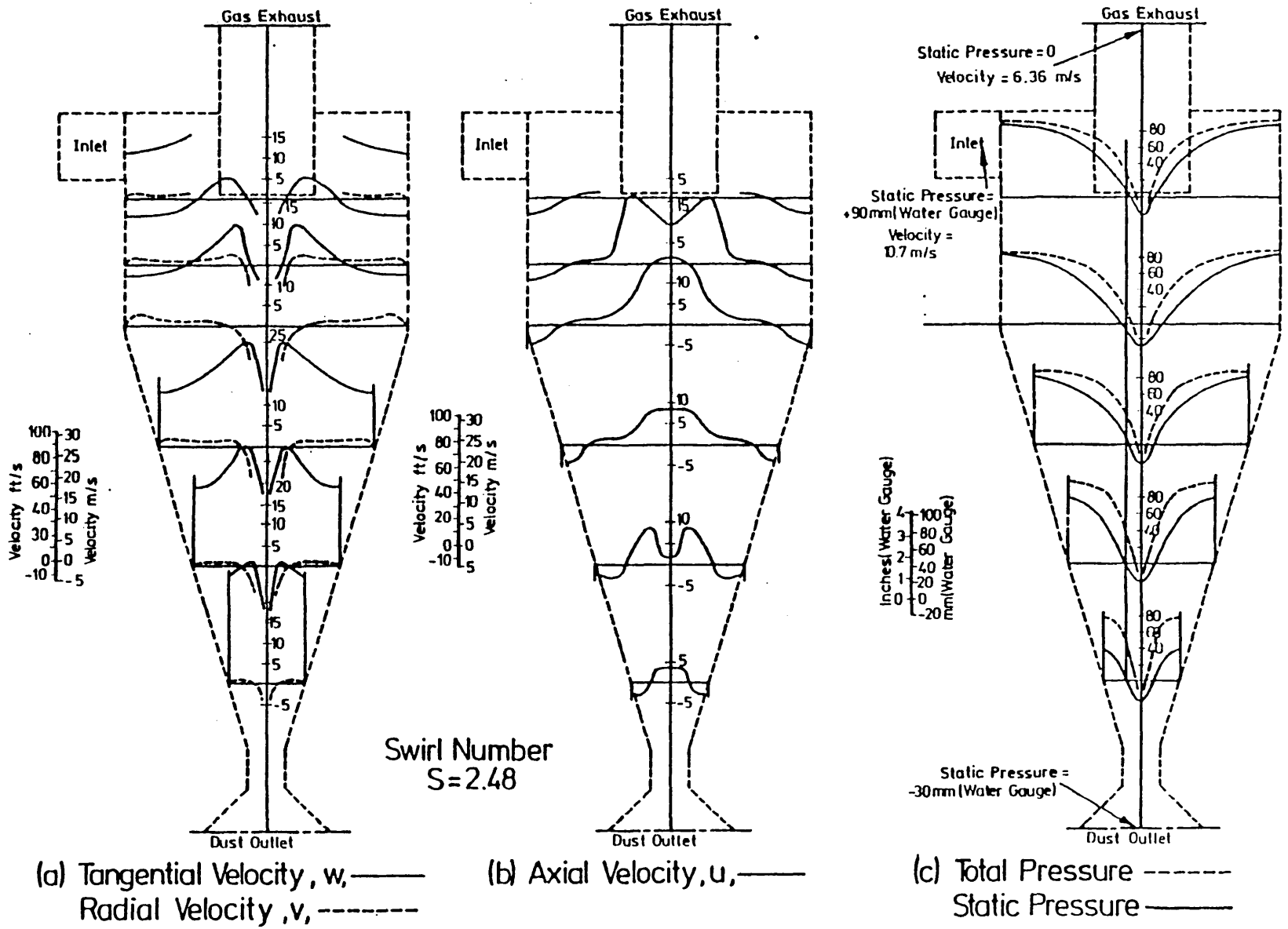

Fig. 2.9 Variation of velocity and pressure levels throughout a cyclone dust separator (Ter Linden, 1949)

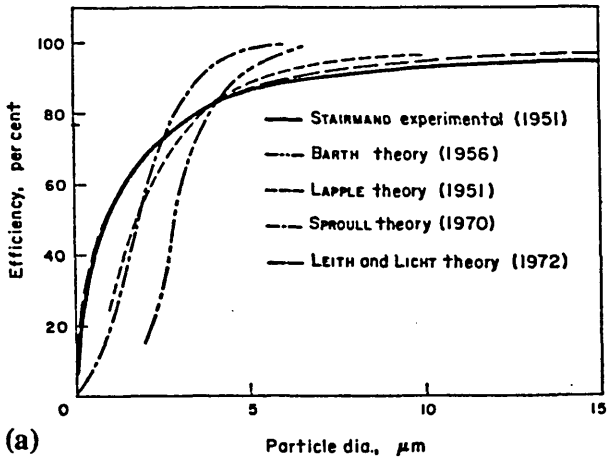

Cyclone efficiency vs particle dia., STAIRMAND (1951). Experimental results and theoretical predictions.

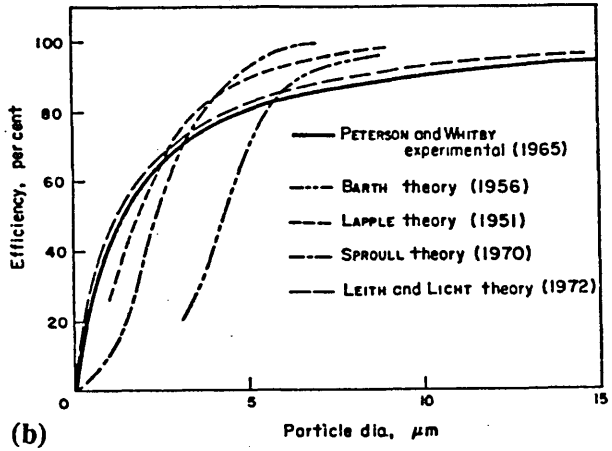

Cyclone efficiency vs particle dia., PETERSON and WHITBY (1965). Experimental results and theoretical predictions.

Fig. 2.10 Cyclone grade efficiency predictions compared with experiment (Leith & Mehta, 1973)

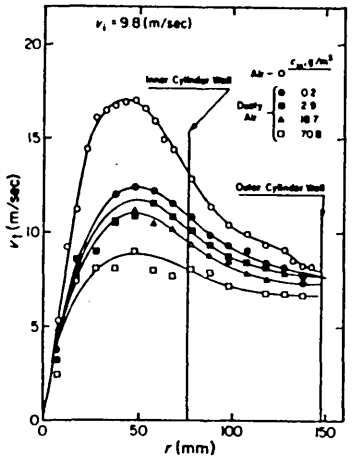

r radial distance from cyclone axis

v_t tangential gas velocity in cyclone vortex

C_{in} inlet dust concentration, Kg/m3

Fig. 2.11 Reduction in cyclone tangential gas velocity due to increasing dust concentration

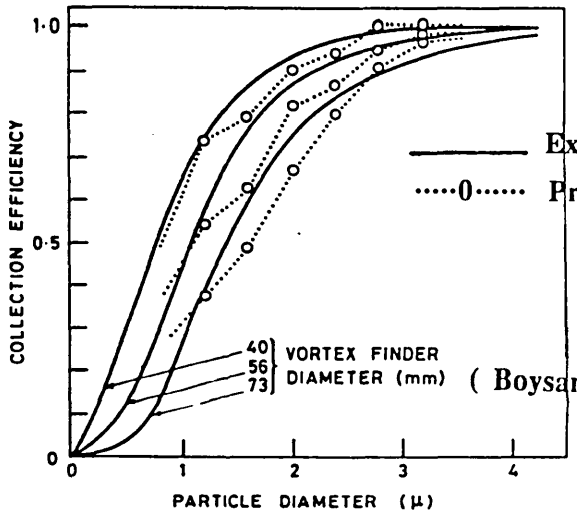

Fig. 2.12 Grade efficiency curves with varying vortex finder diameter for 0.19 m diameter cyclone

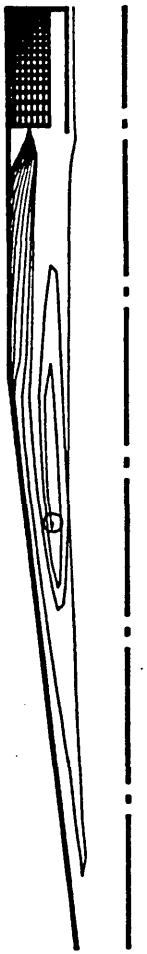

Fig. 2.13 Particle trajectories (2μm) with turbulence (Ayers et al. 1985)

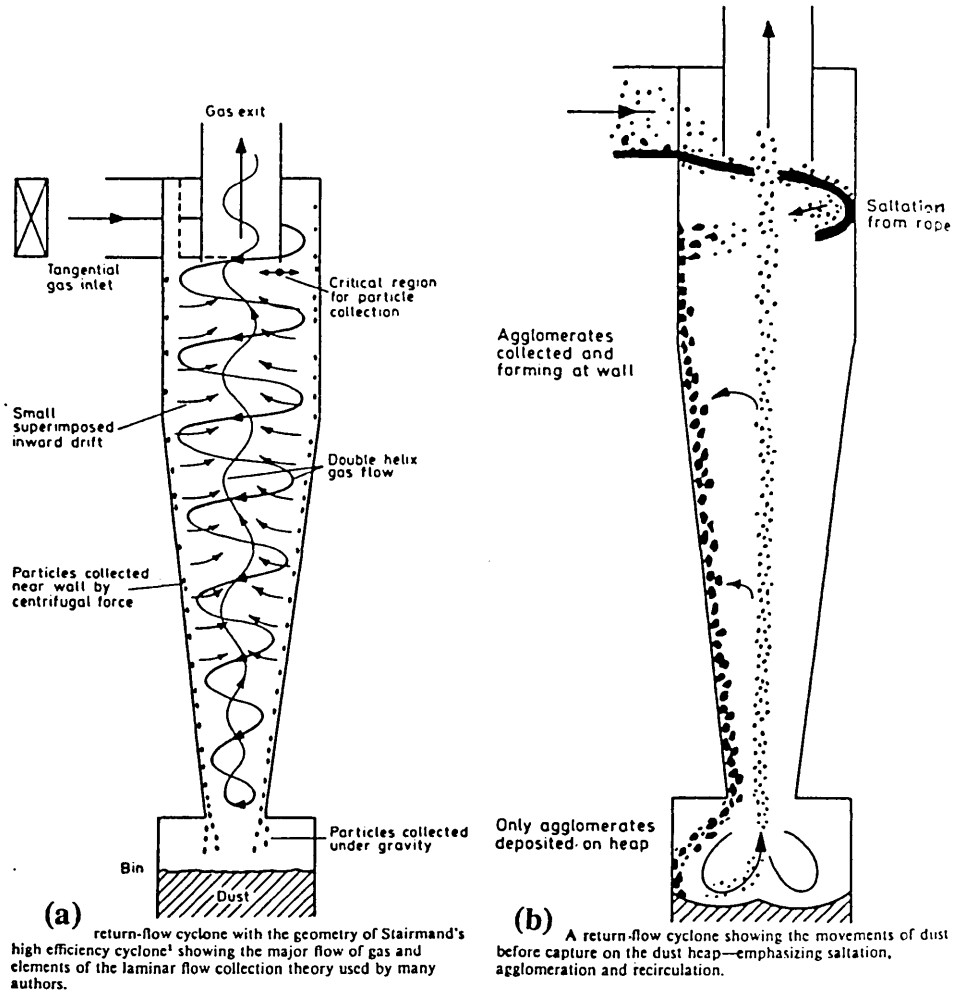

Fig. 2.14 Schematic of particle trajectories before capture from two different viewpoints (Abrahamson et al. 1978)

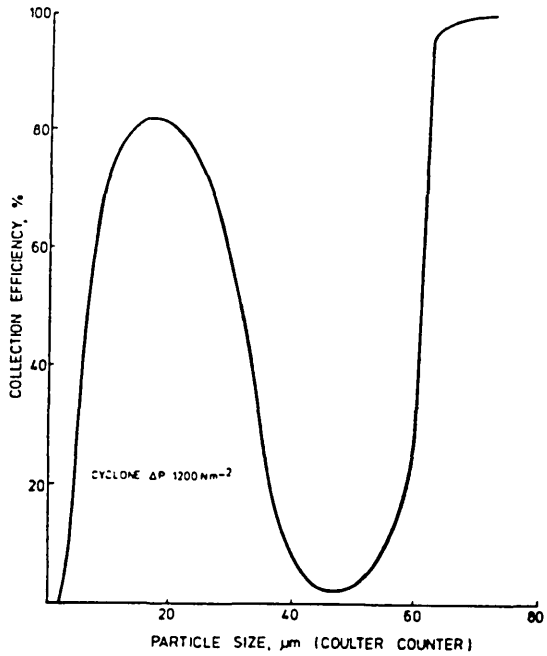

Fig. 2.15 Grade efficiency curve of secondary cyclone (Sage & Wright, 1986)

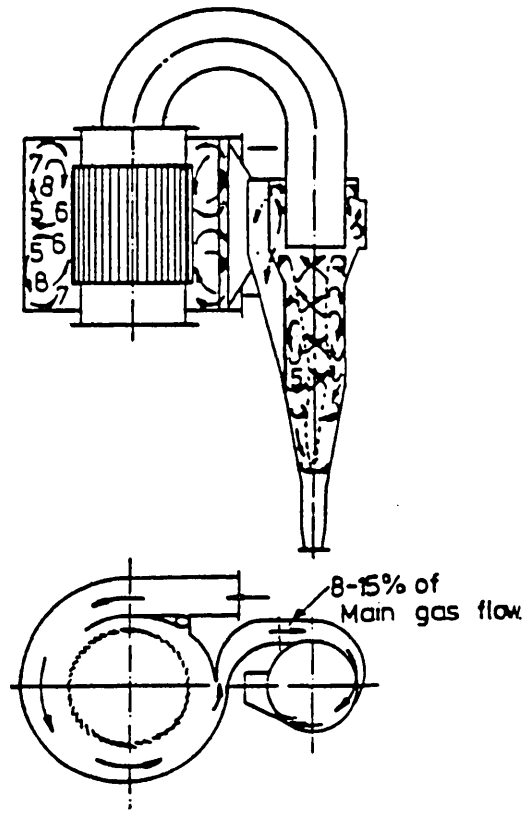

Fig. 2.16 Van Tongeren's chimney type dust collector (Van Tongeren 1965)

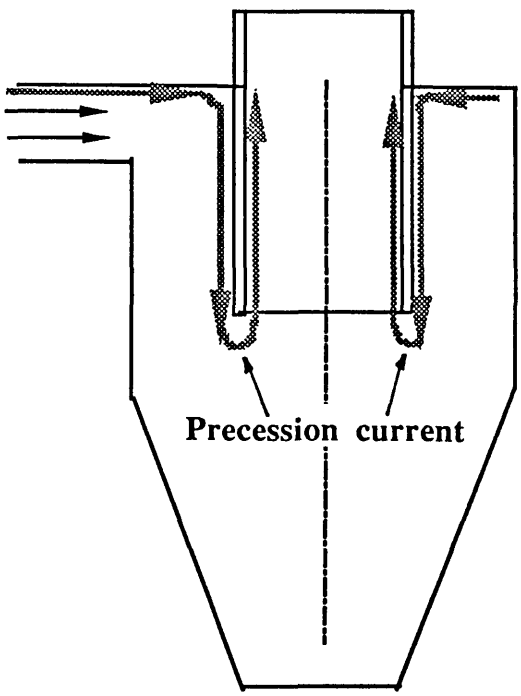

Fig. 2.17 Precession current at the top of tangential type cyclones

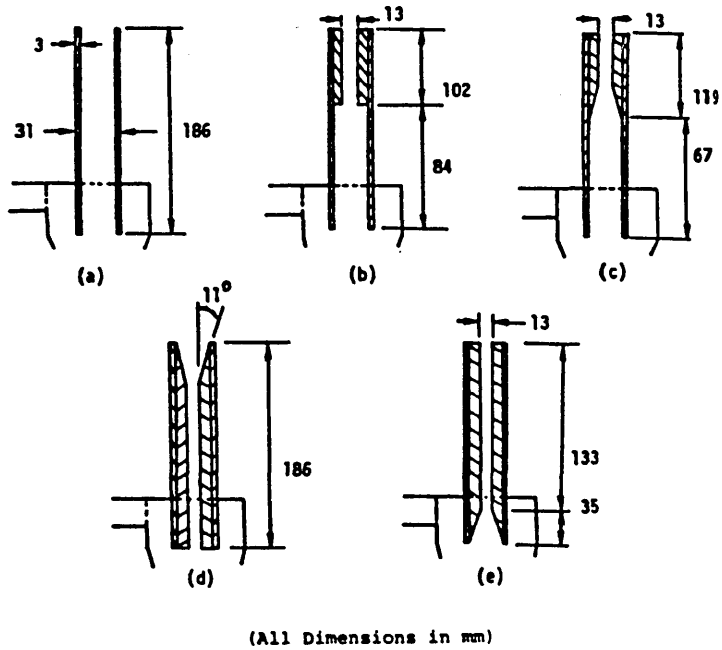

Fig. 2.18 Vortex finder configurations (Dabir & Petty, 1984)

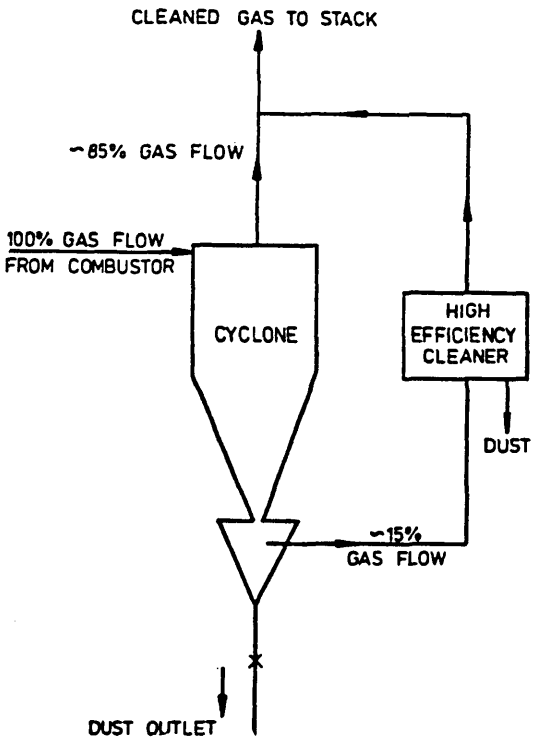

Fig. 2.19 Gas blowdown system
(Sage & Wright, 1986)

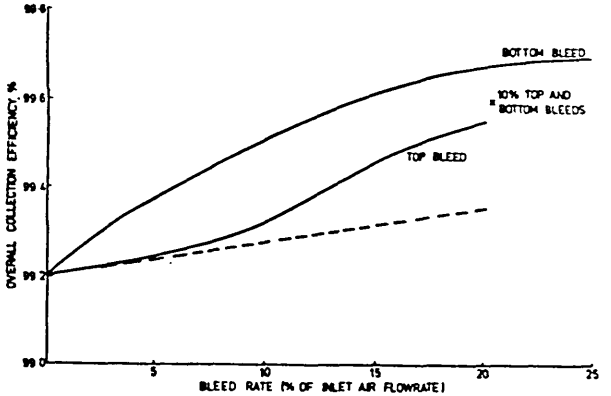

(a) Overall cyclone collection efficiencies vs. bleed rate

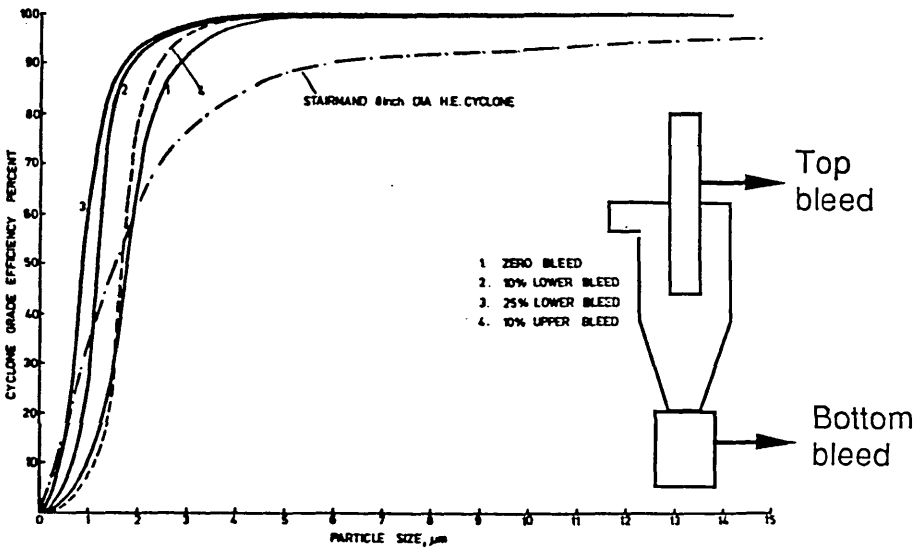

(b) Comparison of grade efficiencies

Fig. 2.20 Effect of bleed on cyclone efficiency (Sage & Wright, 1986)

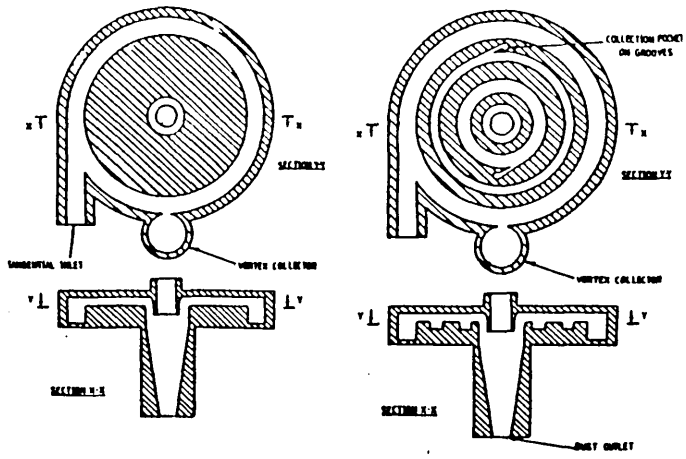

Fig. 2.21 MK.I & MK.II Cardiff cyclone separator (Biffin & Syred, 1983)

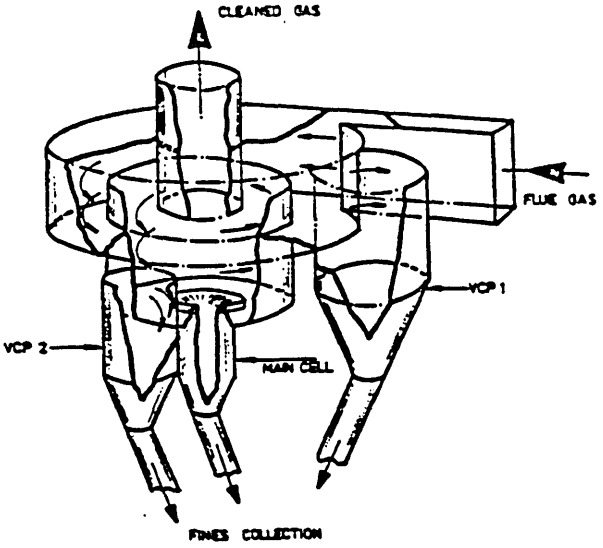

Fig. 2.22 The MK6C Cardiff cyclone dust separator (Syred et al. 1985)

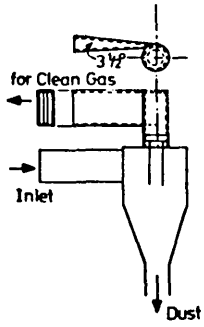

(a) Tangential facing diffuser

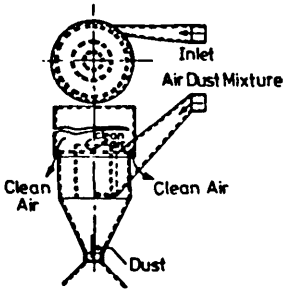

(b) with downwards inclined inlet

Fig. 2.23 Cyclone pressure drop improvement (Schneider, 1960)

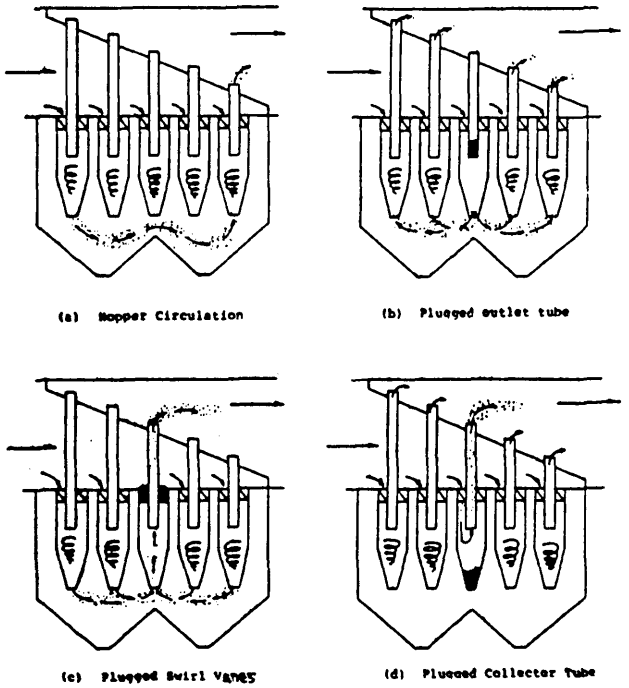

Fig. 2.24 Effect of hopper circulation and plugging (Crellin et al. 1980)

(Crellin et al. 1980)

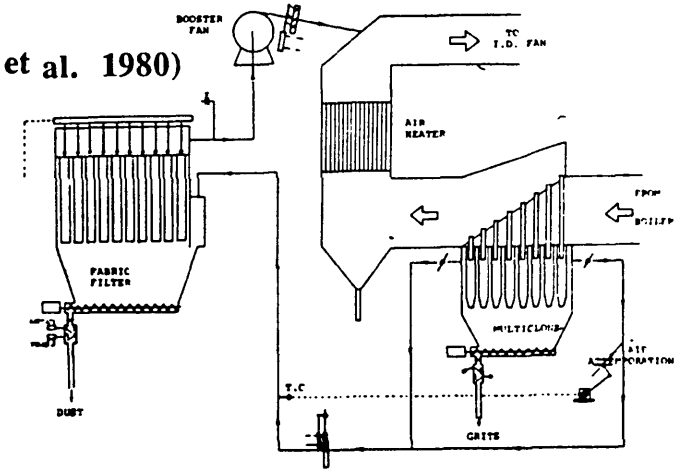

Fig. 2.25 Diagram of a typical boiler "fractionation" system

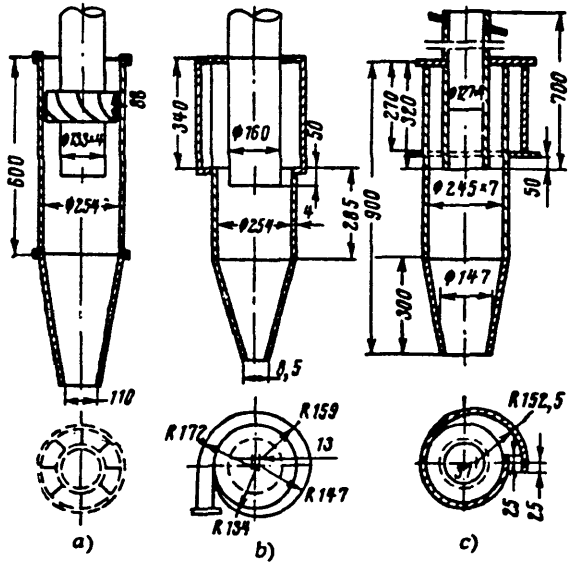

Fig. 2.26 Multicell cyclone cell types in use in USSR (Reznik & Matsnev, 1971)

(a) Multicell cyclone pilot plant

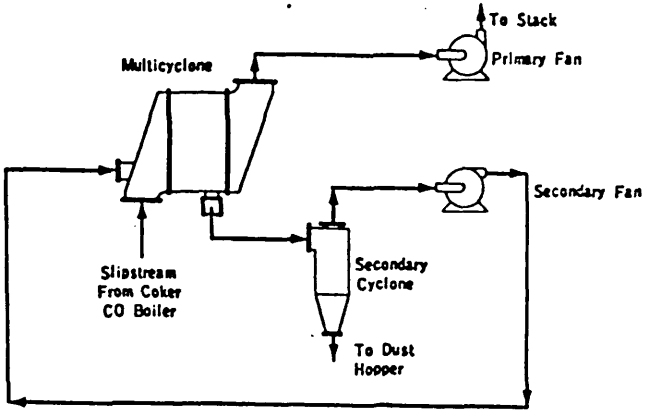

(b) Full scale flow plan

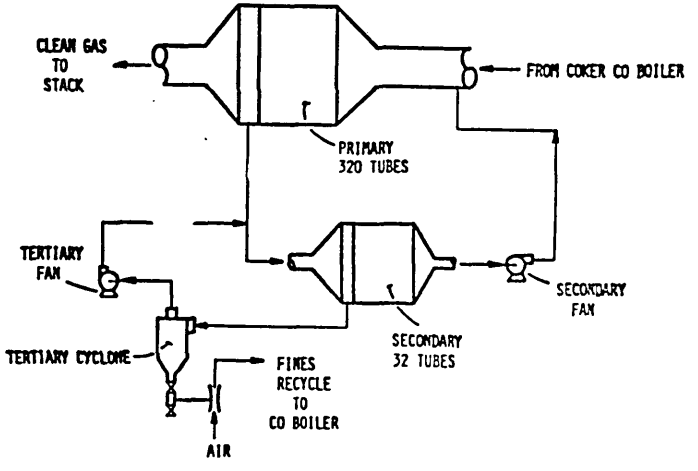

Fig. 2.27 Industrial multicyclone plant with recycling (Byers & Gage, 1981)

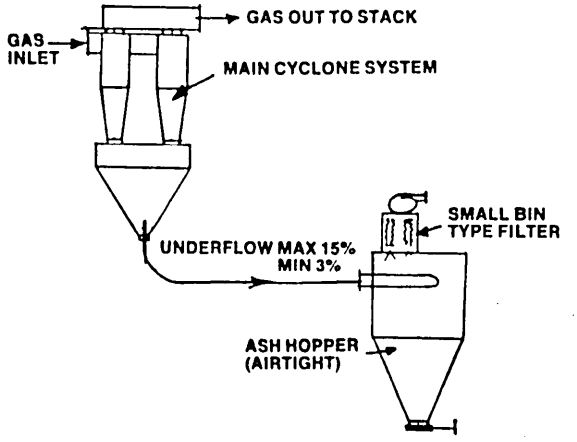

Fig. 2.28 Typical "underflow" transport system (Greenfield, 1986)

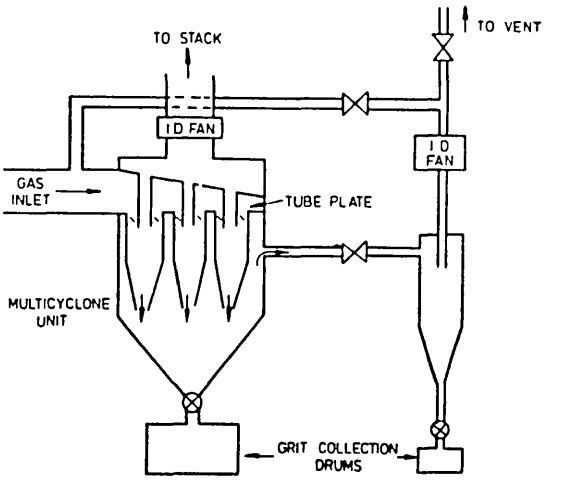

Fig. 2.29 Multicell cyclone with gas draw off (Sage & Wright, 1986)

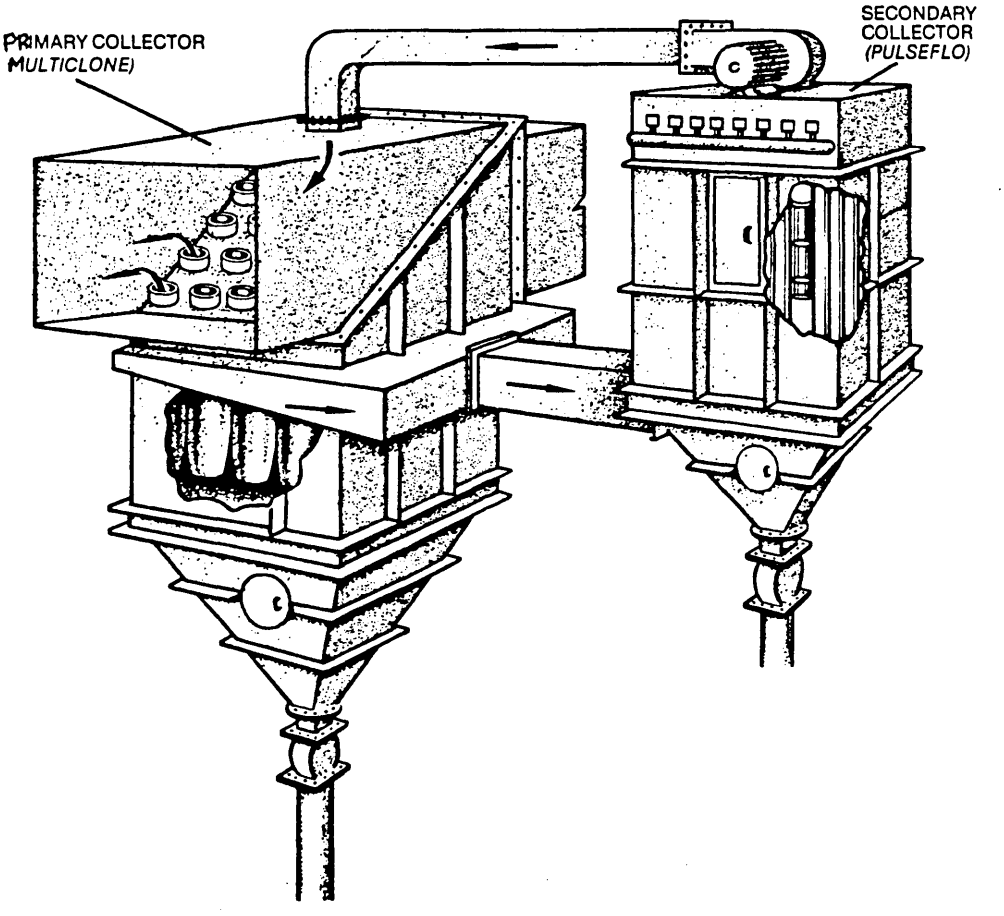

Fig. 2.30 Industrial sidestream separator (Sortor, 1981)

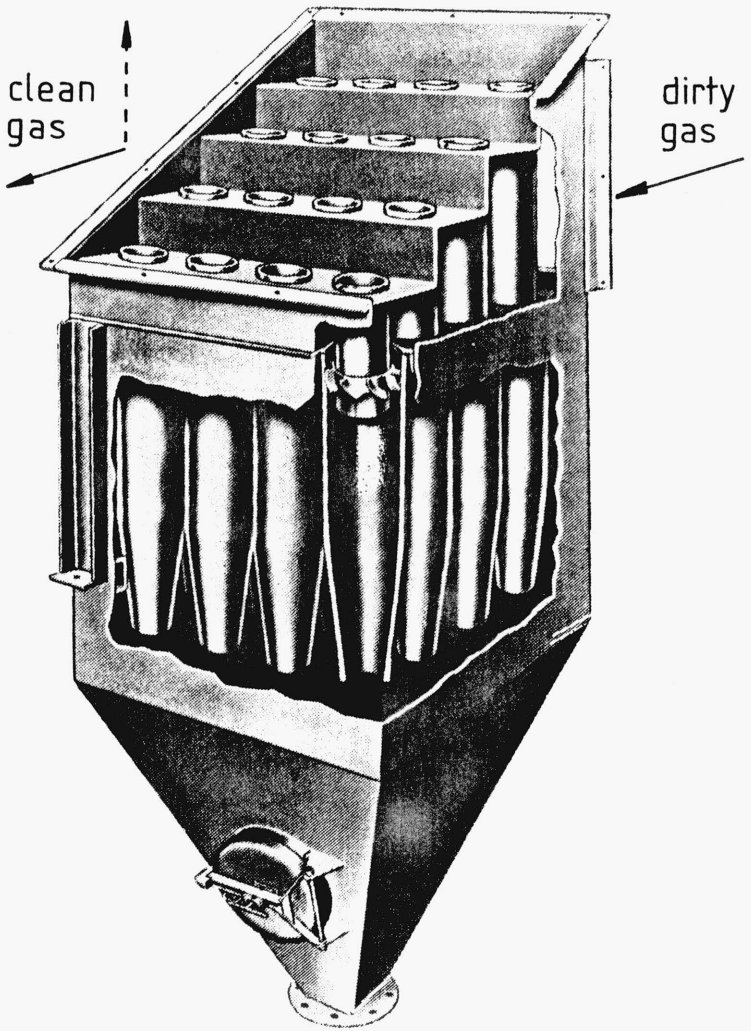

(a) Typical industrial 4 x 4 cell cyclone

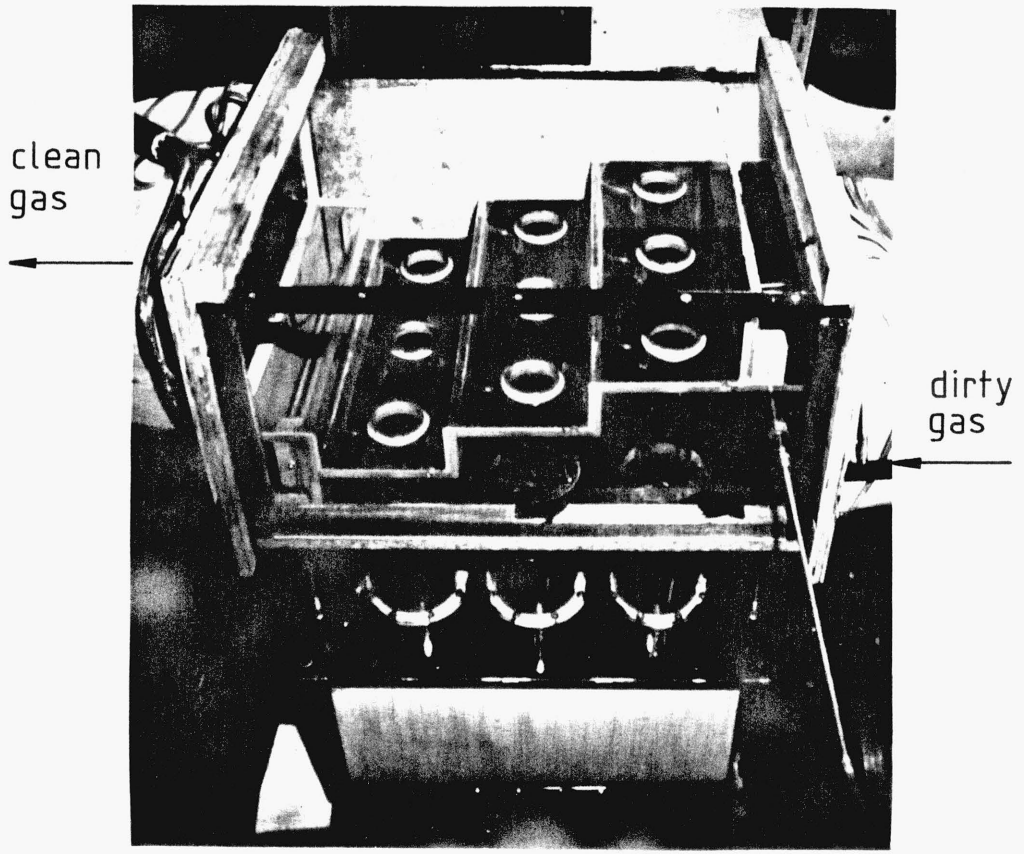

(b) Laboratory model 3 x 3 cell cyclone used in present investigation

Fig. 3.1 Mutlticell cyclone dust separators

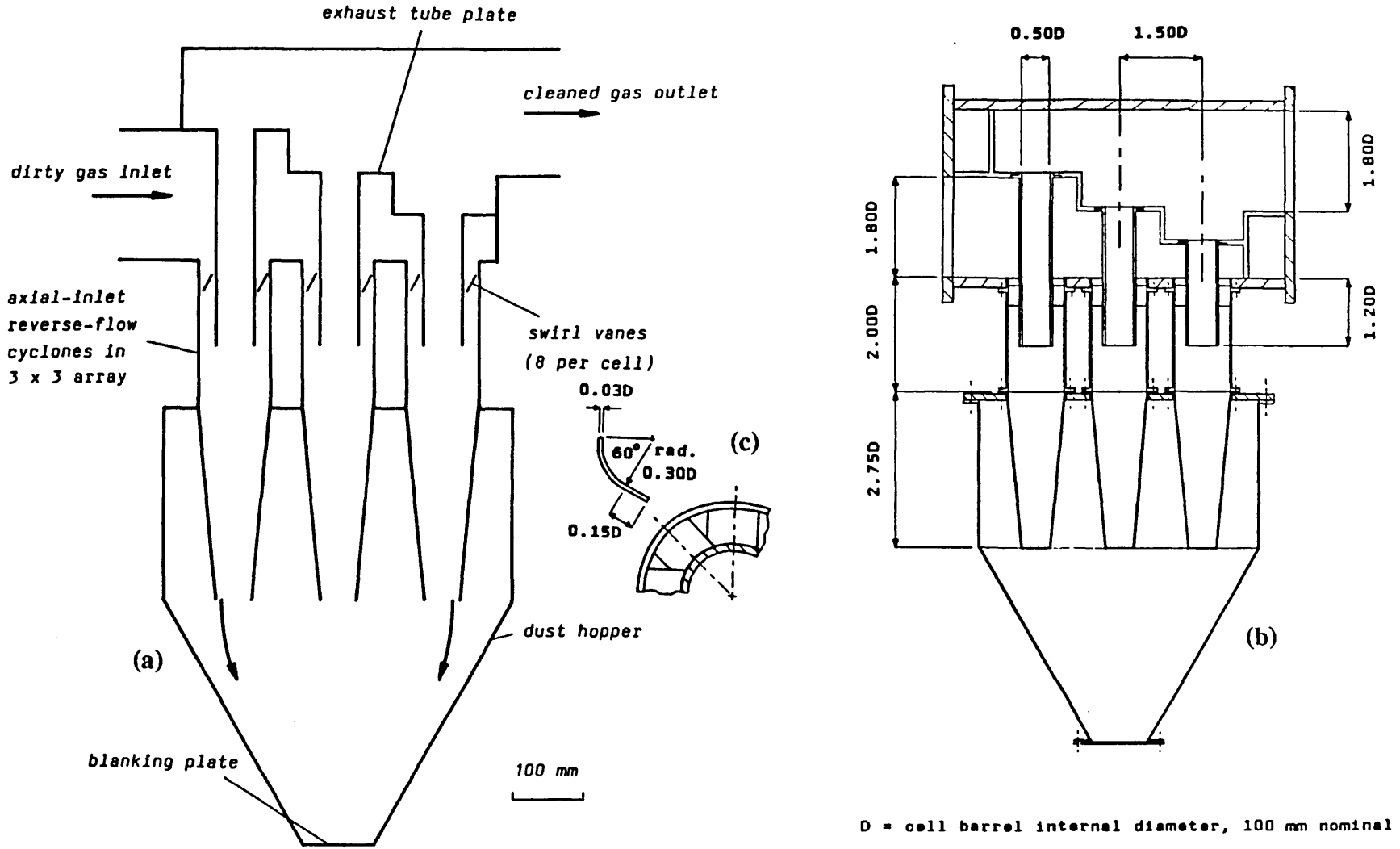

Fig. 3.2 Cross-sections of model multicell cyclone, showing (a) major features, (b) construction detail and dimensions (omitting support structure) (c) detail of swirl vanes

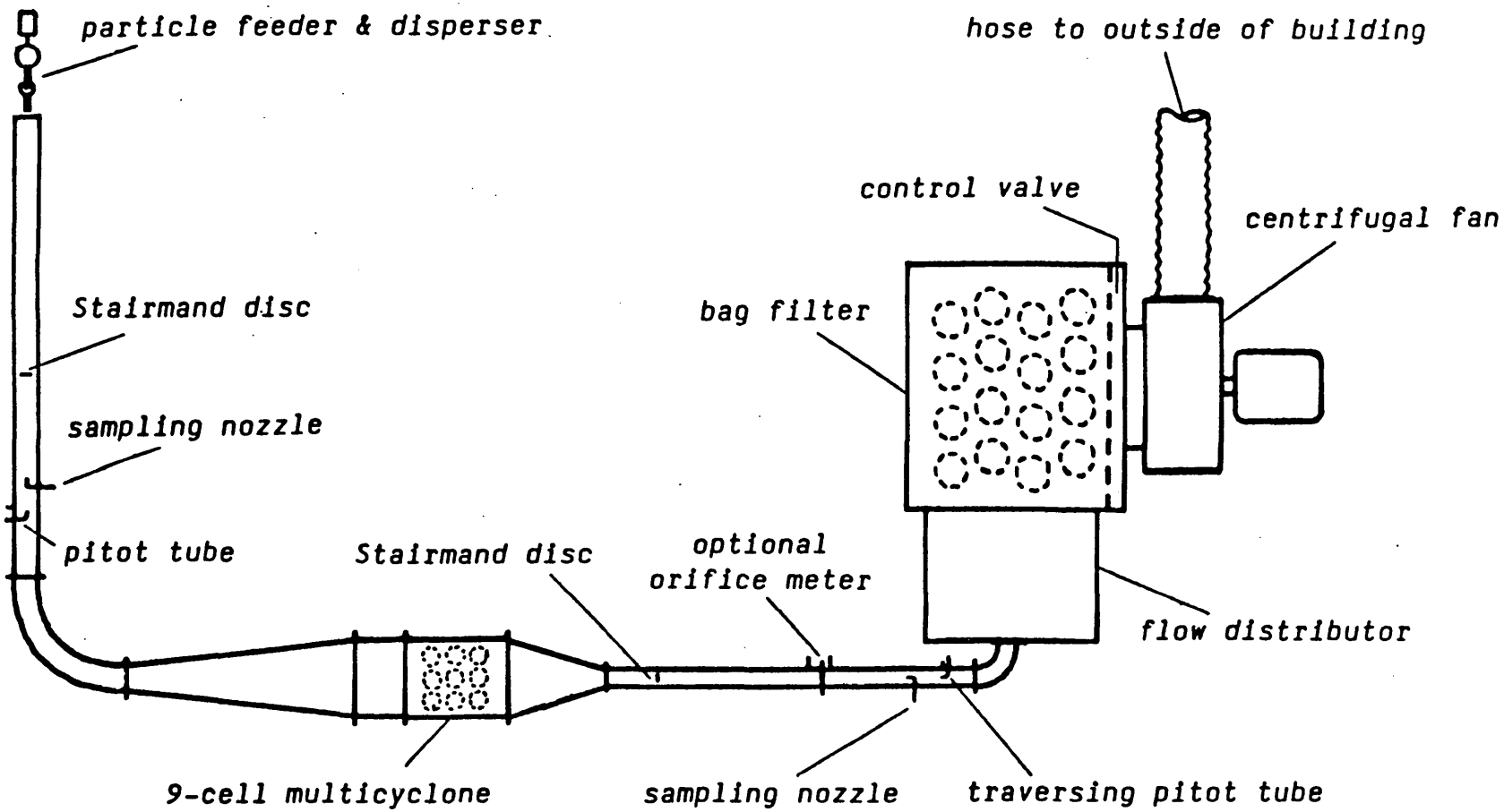

Fig. 3.3 Preliminary arrangement of complete rig

I) Fan working point without bypass system

II) Fan working point with bypass system

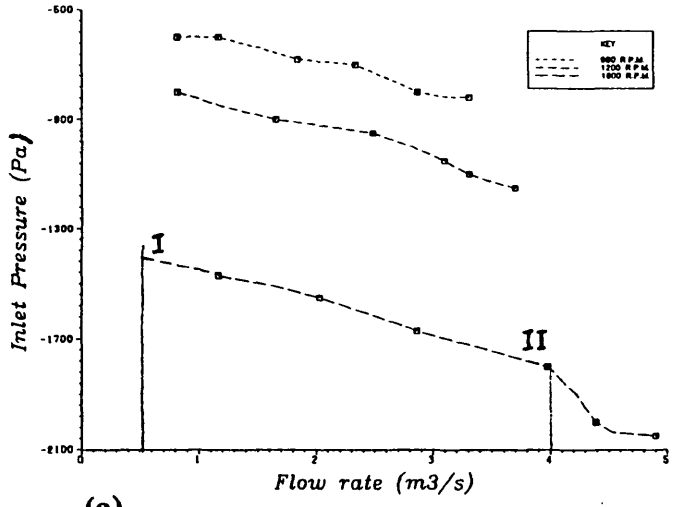

(a)

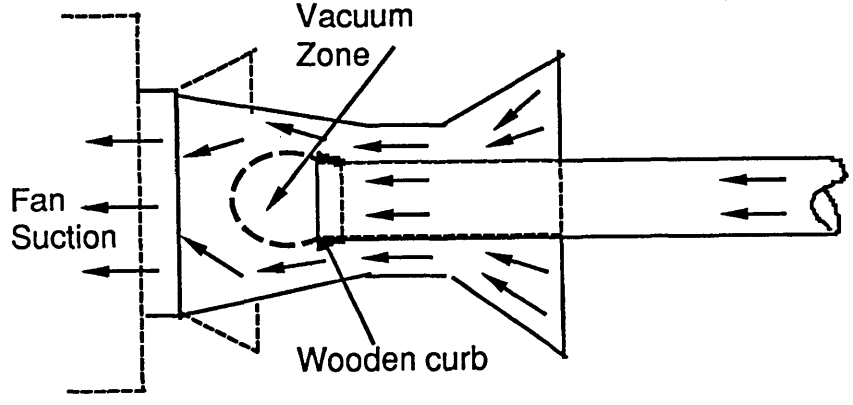

(b)

Fig. 3.4 (a) Fan performance curve; (b) fan bypass system

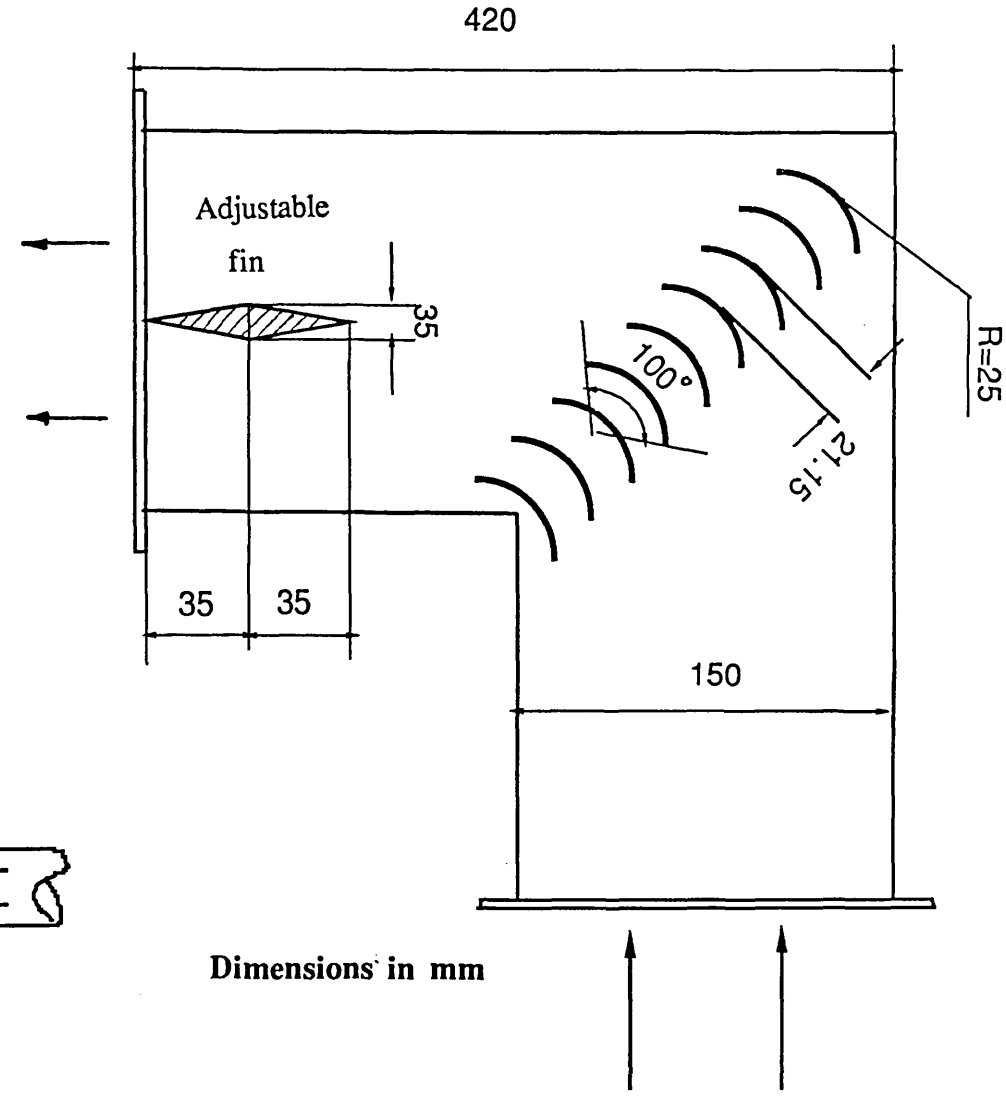

Dimensions in mm

Fig. 3.5 New bend design

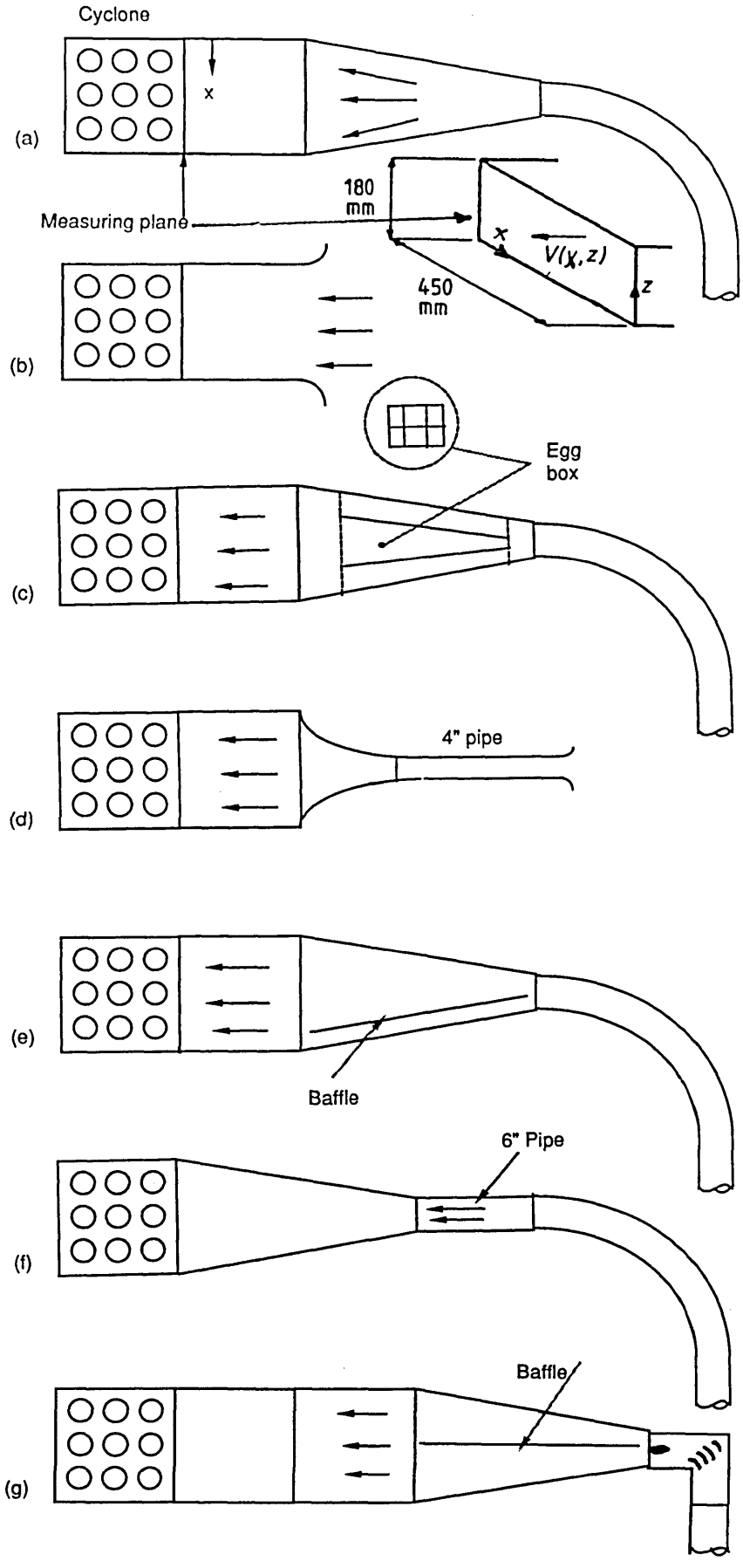

Fig. 3.6 Multicell cyclone inlet duct configurations

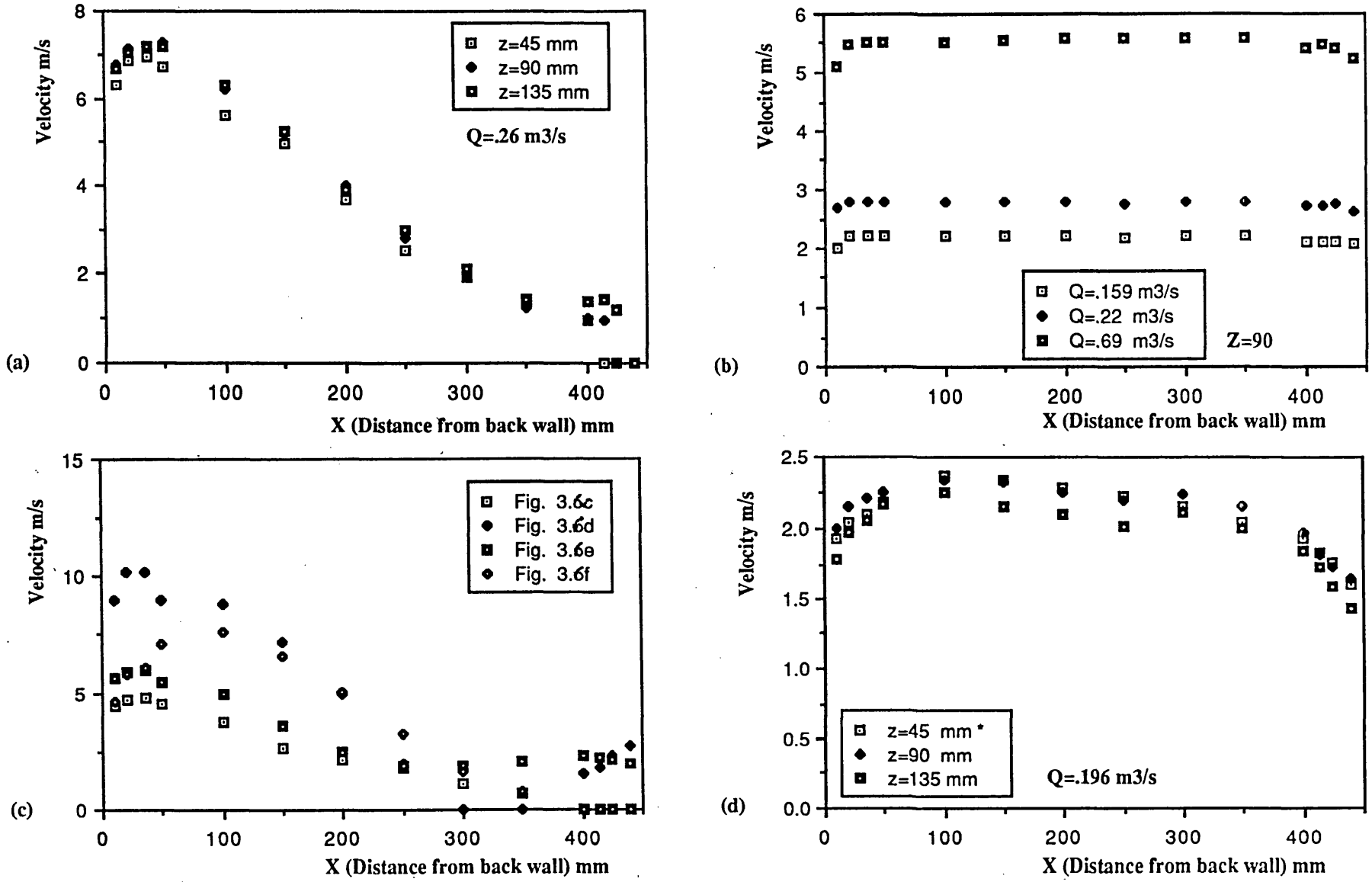

Fig. 3.7 Mean velocity profiles at cyclone entrance

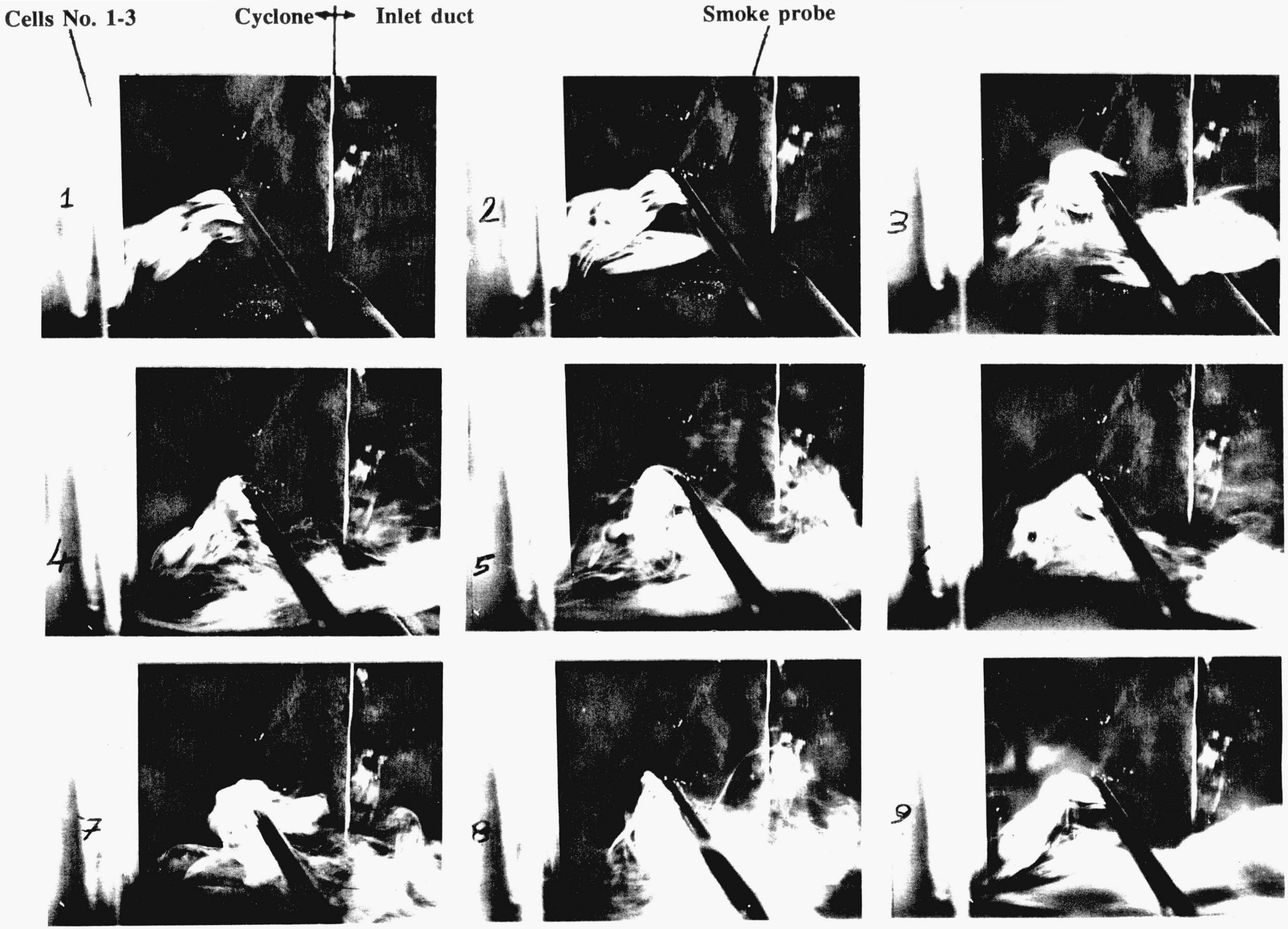

Fig. 3.8 Back flow effect inside inlet duct

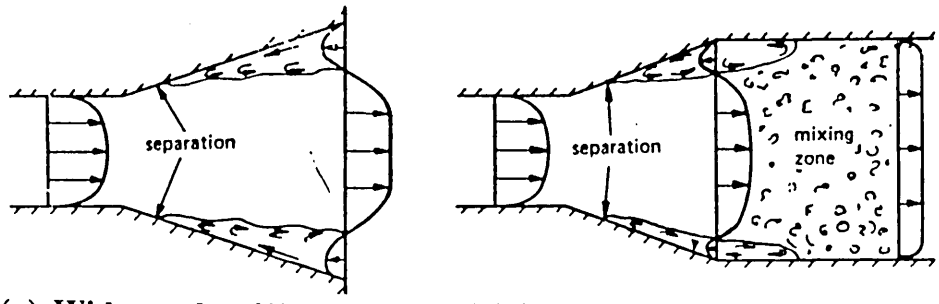

(a) Wide angle diffuser (b) Diffuser with outlet section

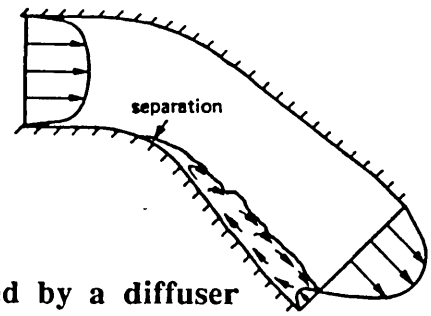

(c) Bend followed by a diffuser

Fig. 3.9 Diffuser maloperation

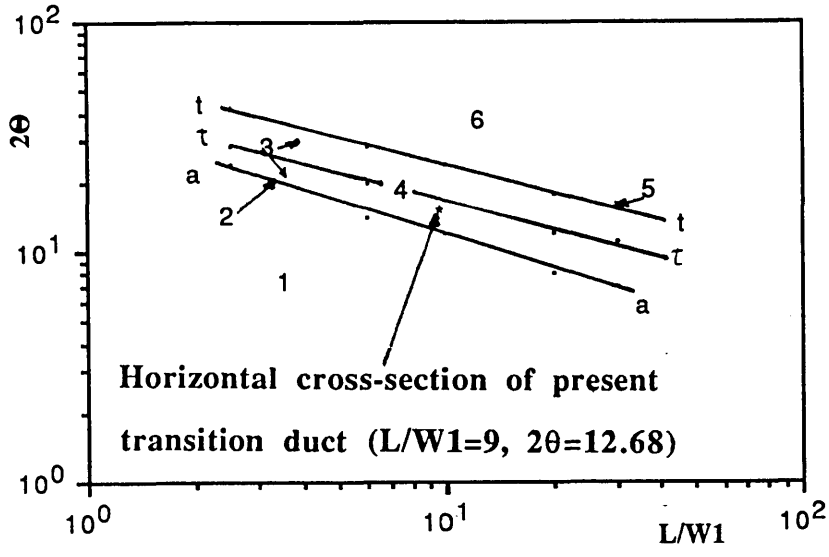

1) Region of no "appreciable" stall
2, 5) High inlet turbulence
3) Region of large transistory stall
4) Low inlet turbulence
6) Region of fully developed stall

Fig. 3.10 Flow regimes in plane-wall two-dimensional subsonic diffusers (Kline 1959)

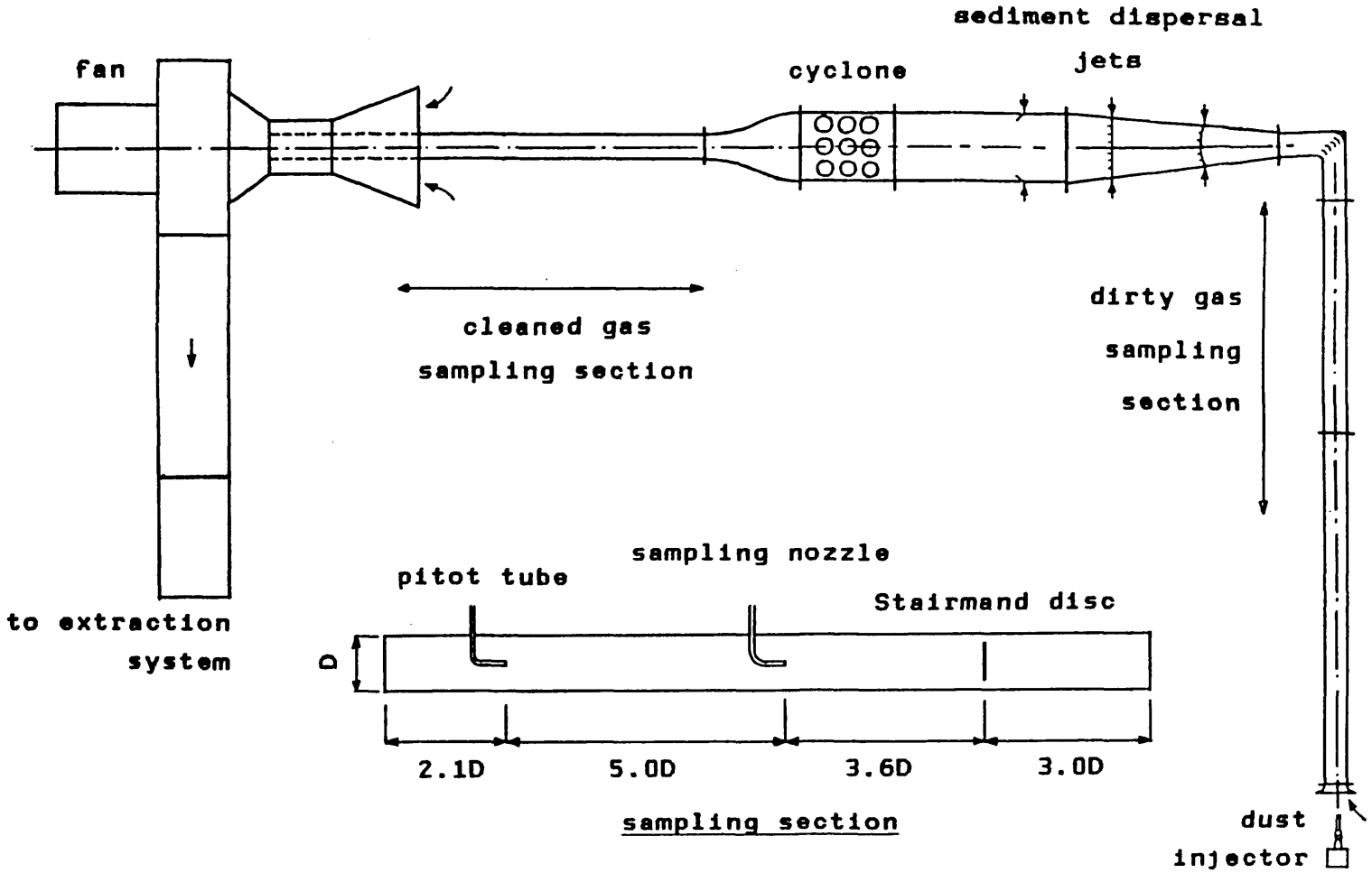

Fig. 3.11 Final configuration of flow rig for collection efficiency measurements on multicell cyclone

Fig. 3.12 Overall view of multicell rig

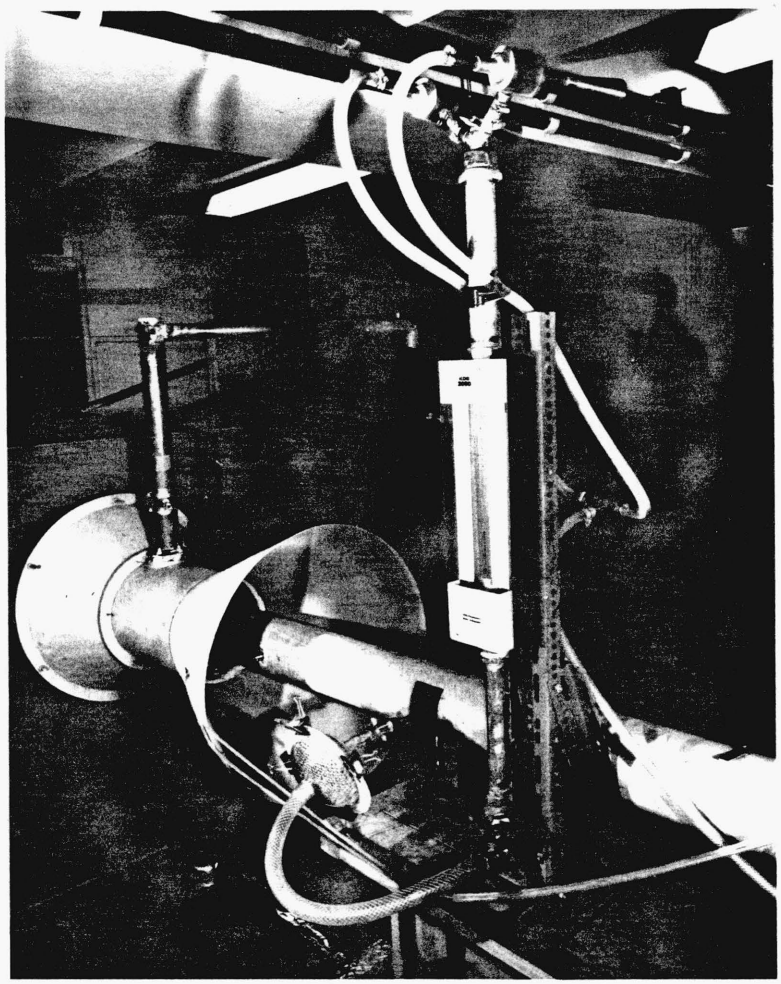

Fig. 3.13 Overall view of sampling system after cyclone

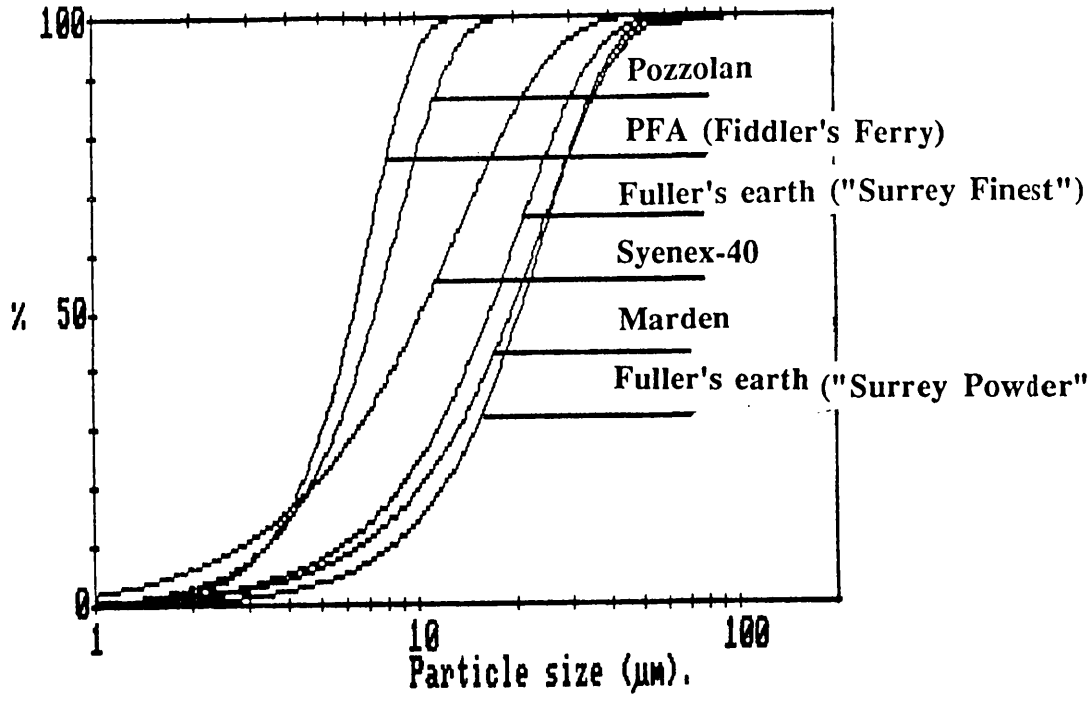

Fig. 3.14 Size distributions of some available powders

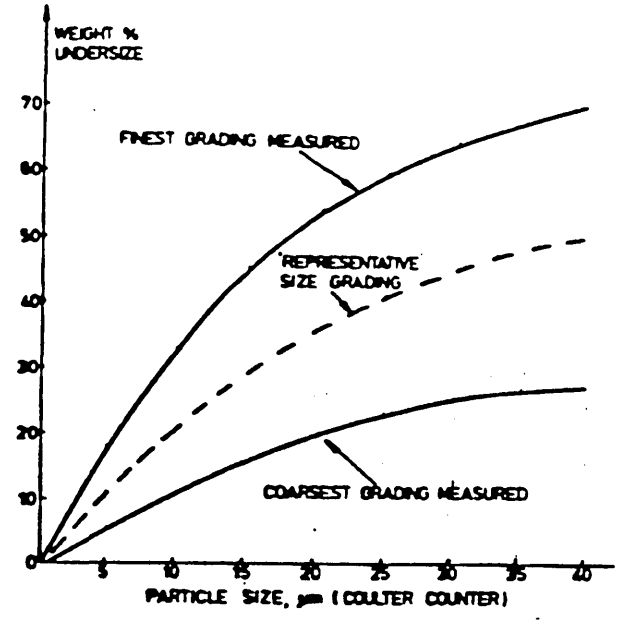

Fig. 3.15 Size distribution of solids elutriated from coal-fired fluidized bed boilers (Sage & Wright, 1984)

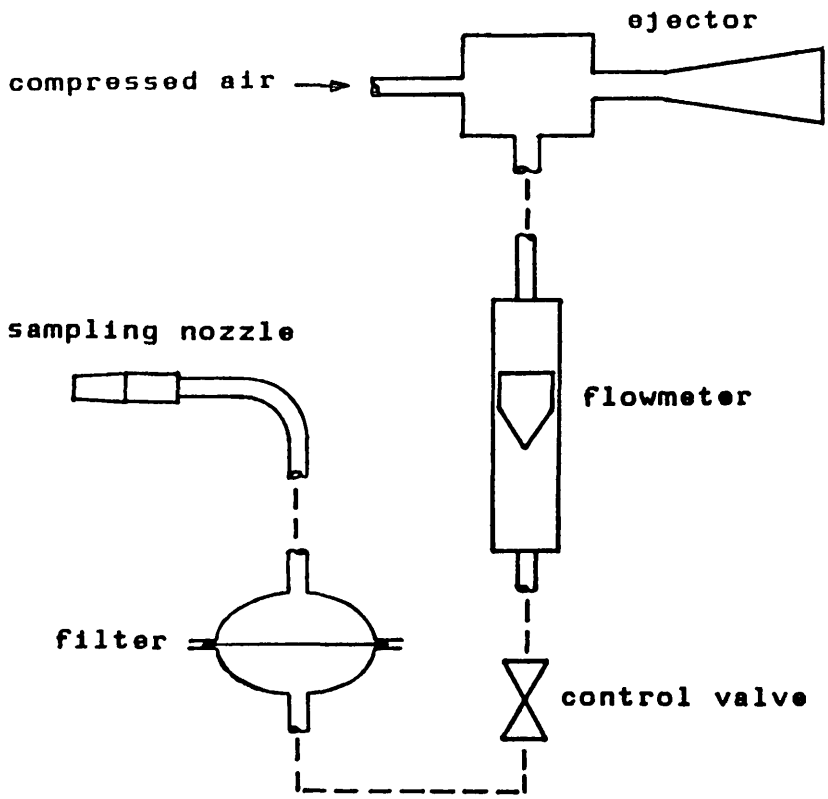

Fig. 3.16 Dust sampling system (not to scale)

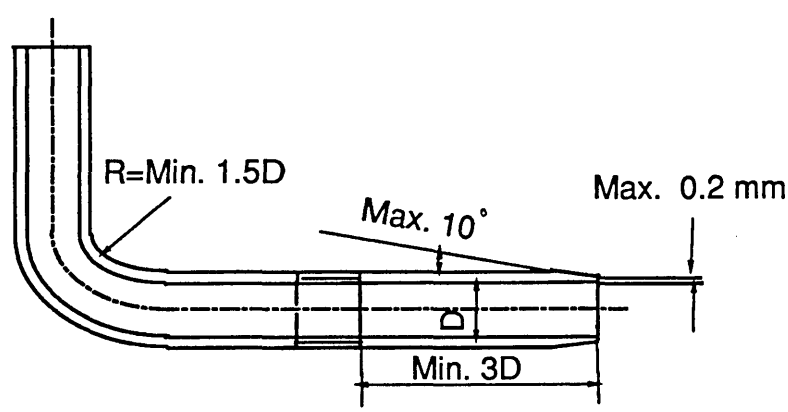

Fig. 3.17 Sampling nozzle design limitation

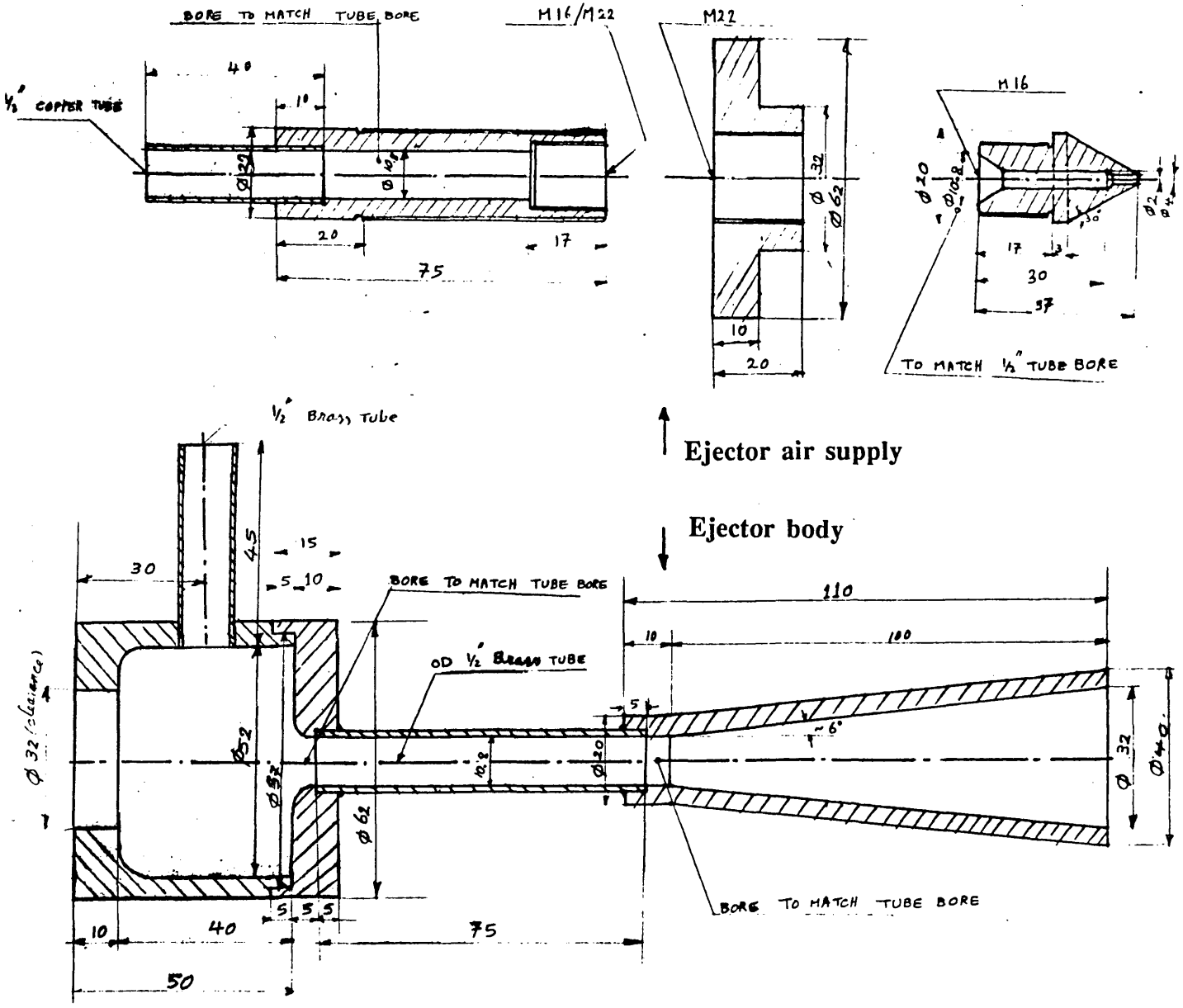

Fig. 3.18 Ejector sketch

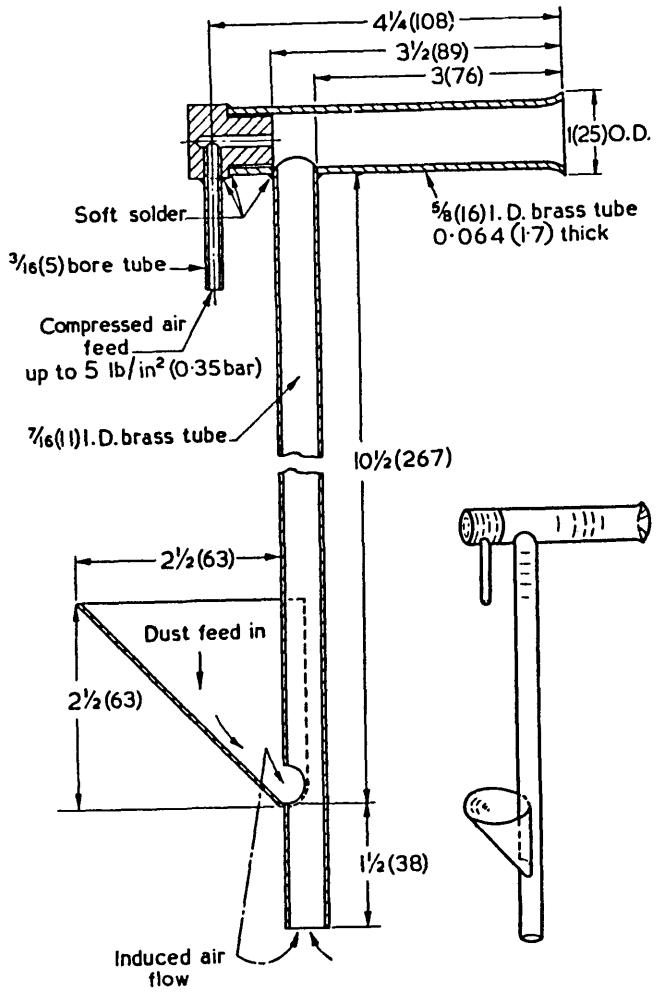

Fig. 3.19 Dust injector sketch (BS-2831)

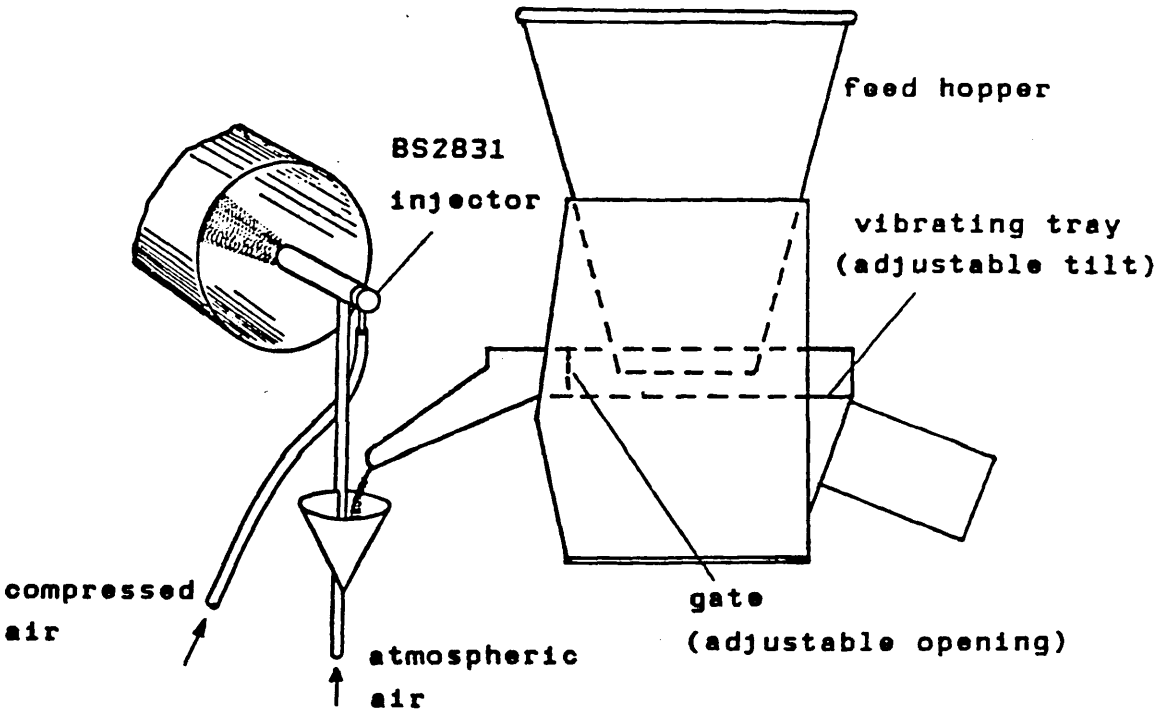

Fig. 3.20 Dust injection equipment (not to scale)

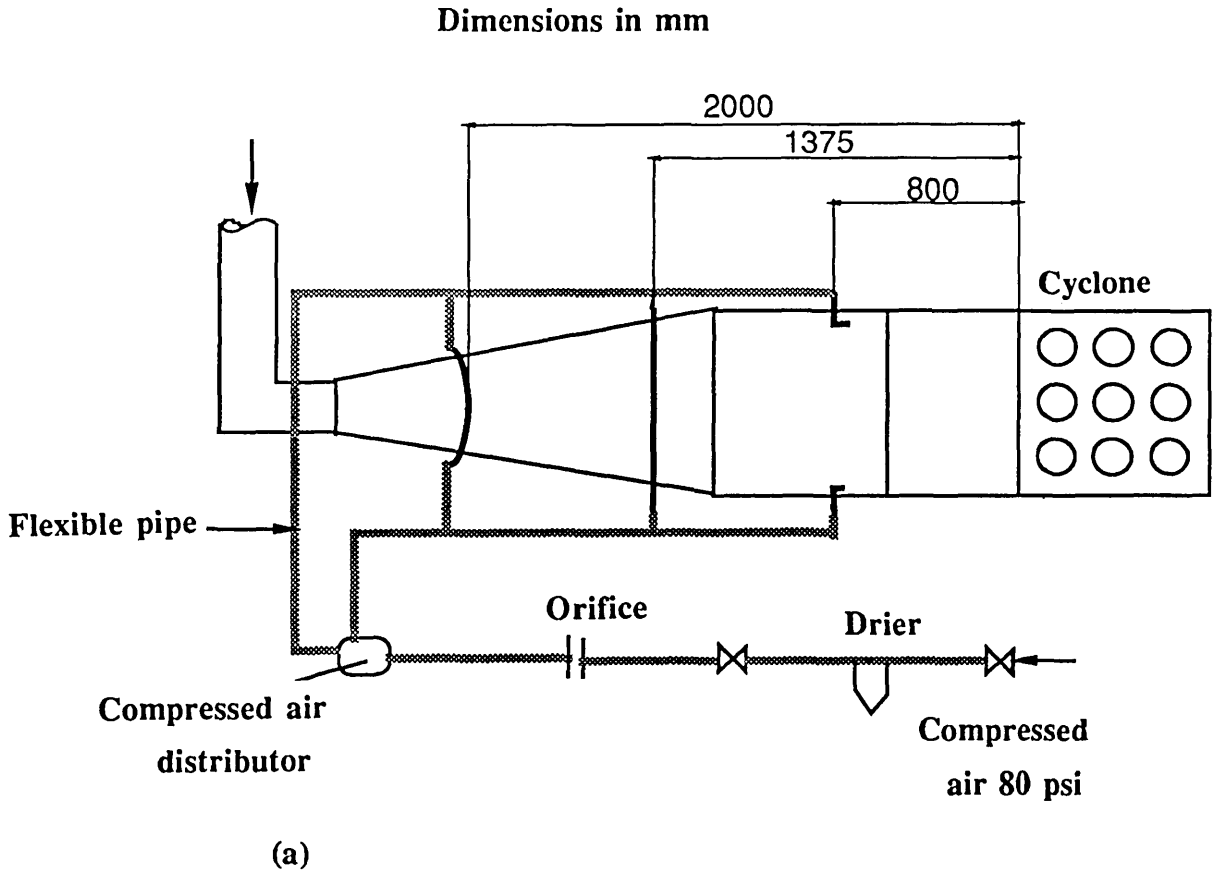

Fig. 3.21 (a) General arrangement of sediment dispersal system
(b) Flow distribution at cyclone entrance

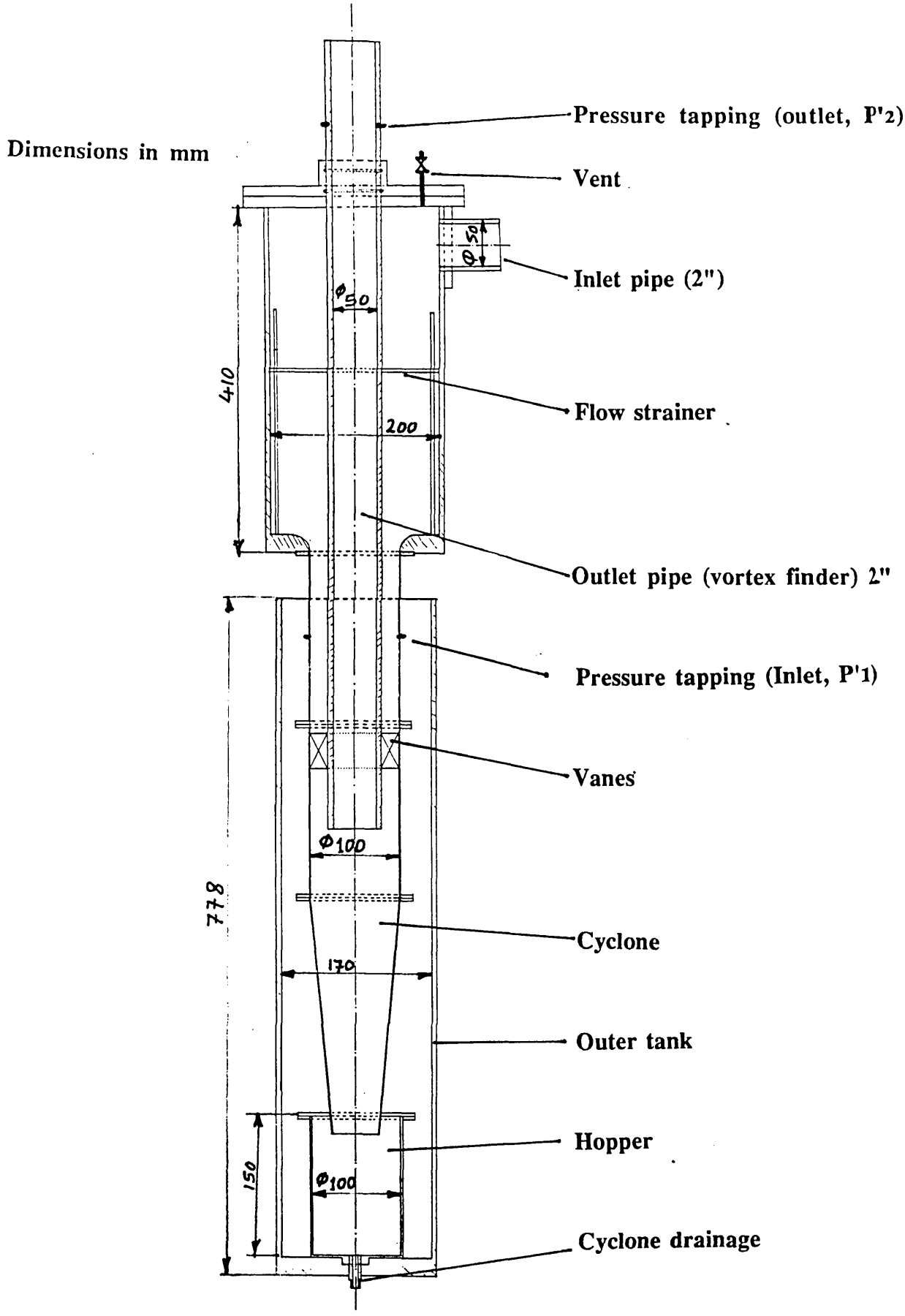

Fig. 3.22 One-cell cyclone sketch (water rig)

1- Cyclone
2- Header tank (open)
3- Rotameter
4- Pump
5- Cooler
6- Laser table
7- Laser
8- Beam splitter
9- Lens
10- Photomultiplier
11- Cyclone support
12- Flexible pipe
13- Pipe (2")
14- Valves
15- Honeycomb
16- Thermocouple monitor

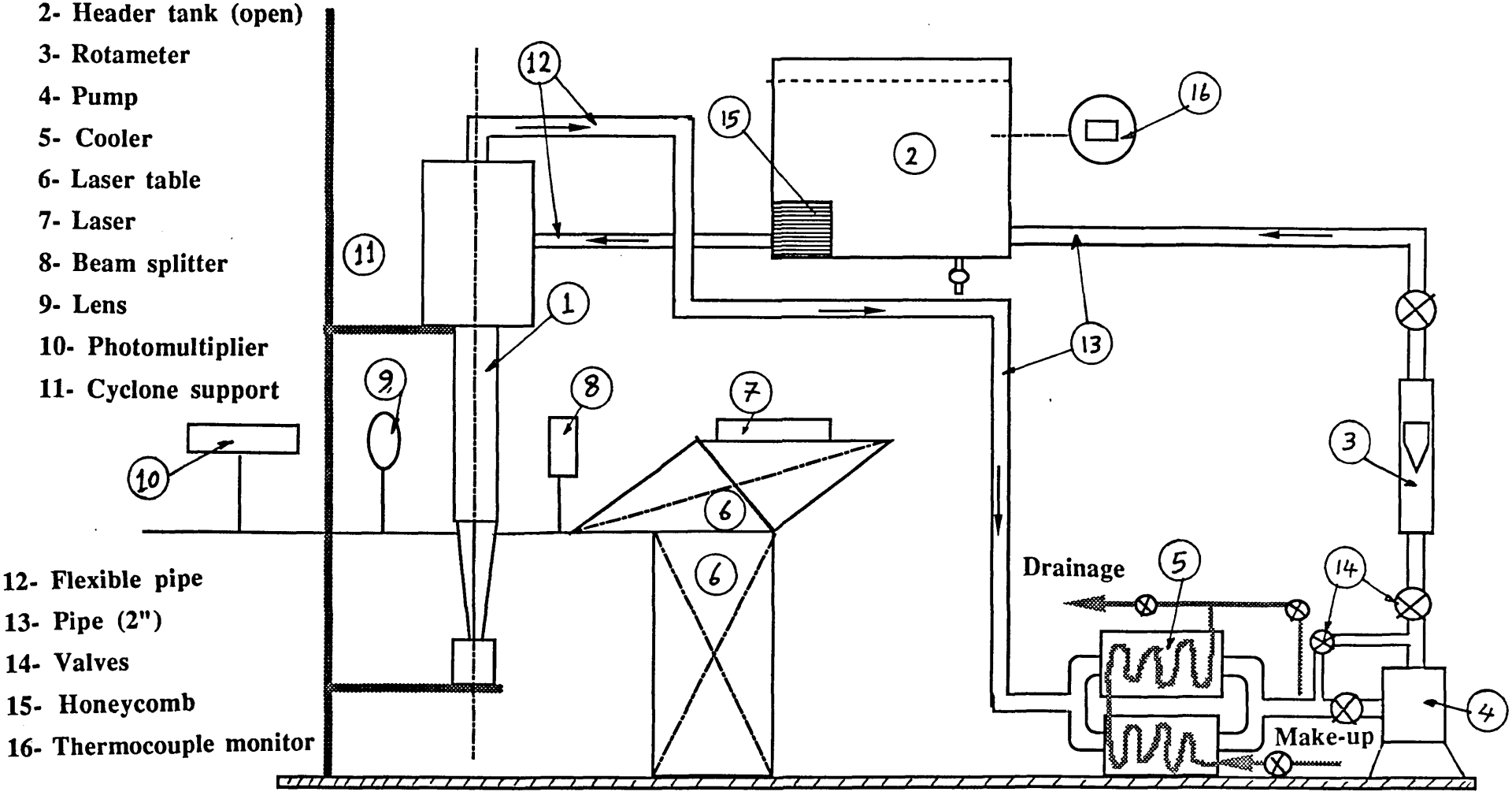

Fig. 3.23 Flow circuit diagram for one-cell cyclone in water rig

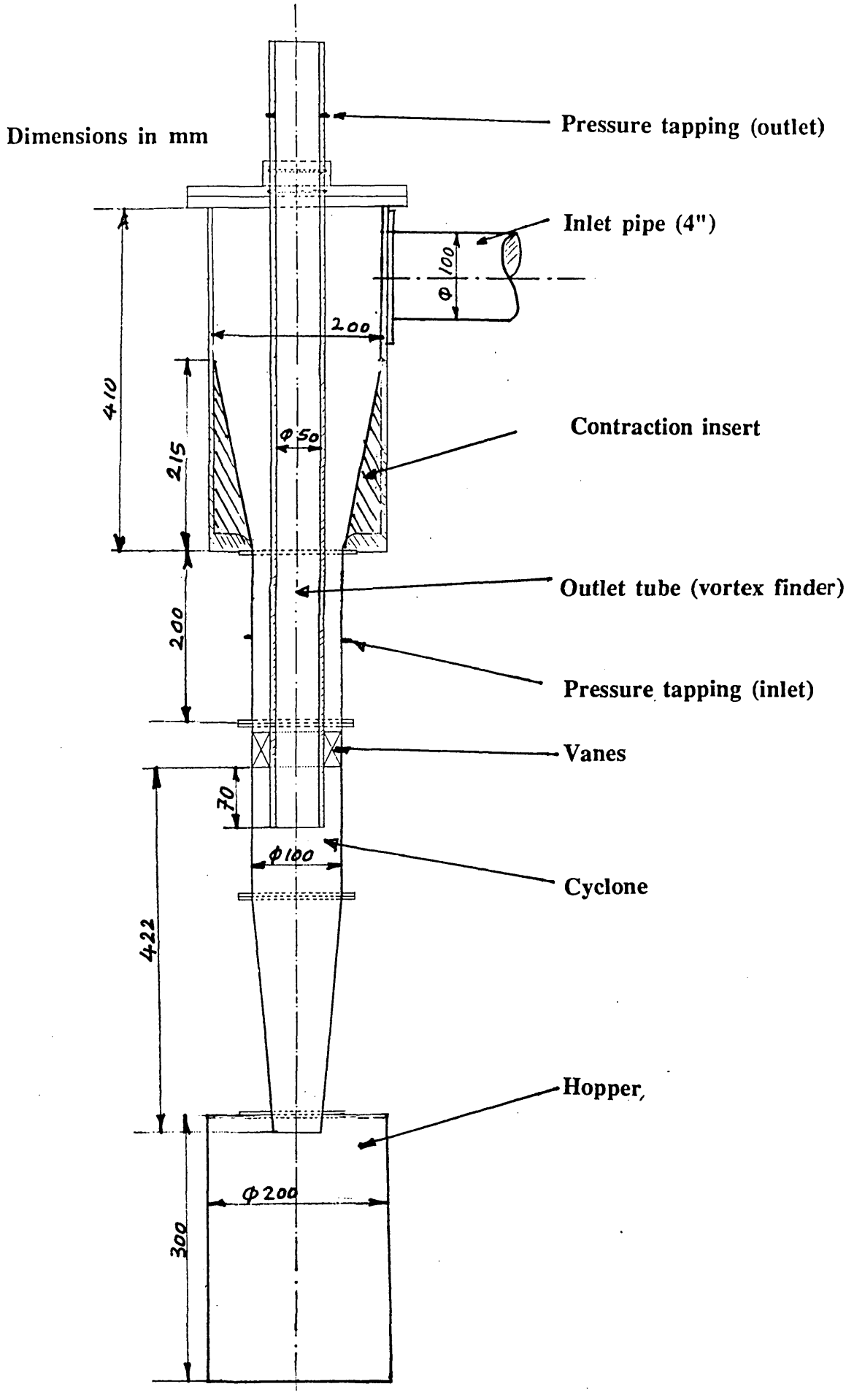

Fig. 3.24 One-cell cyclone sketch (air rig)

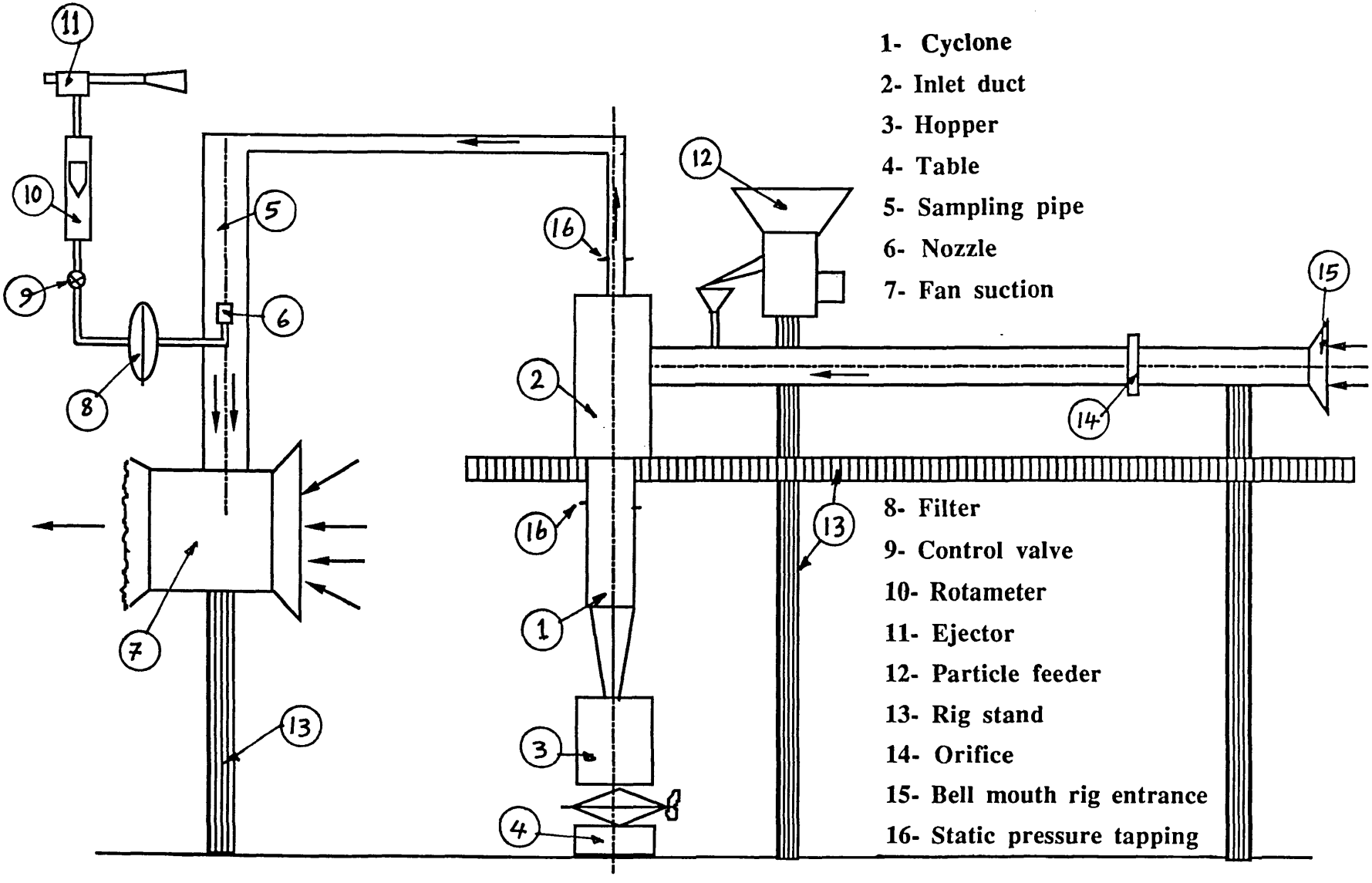

Fig. 3.25 Flow circuit digram for one-cell cyclone in air rig

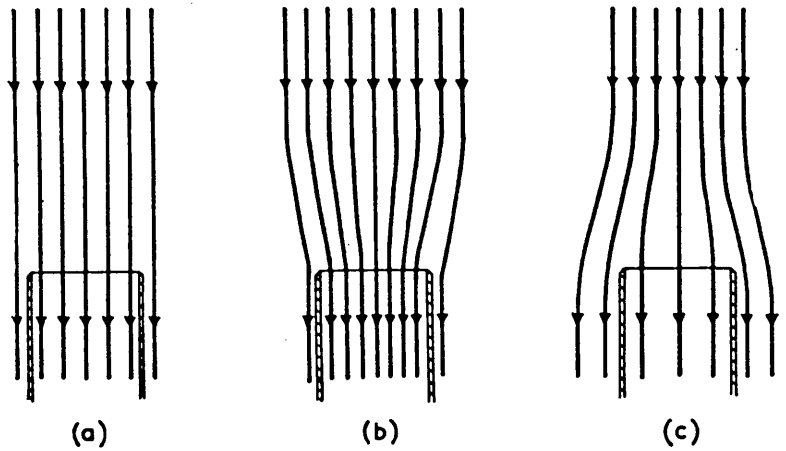

Fig. 3.26 Illustration of principle of isokinetic sampling

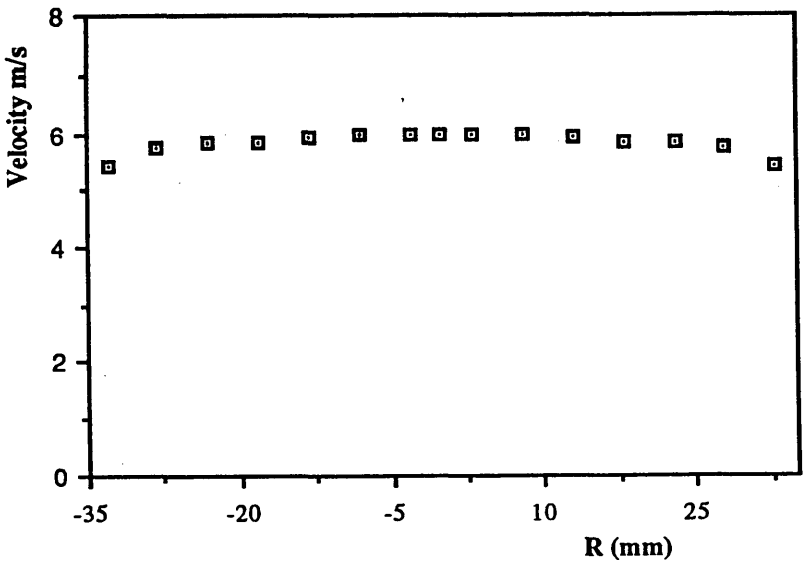

Fig. 3.27 Velocity profile at nozzle position (one-cell sampling system)

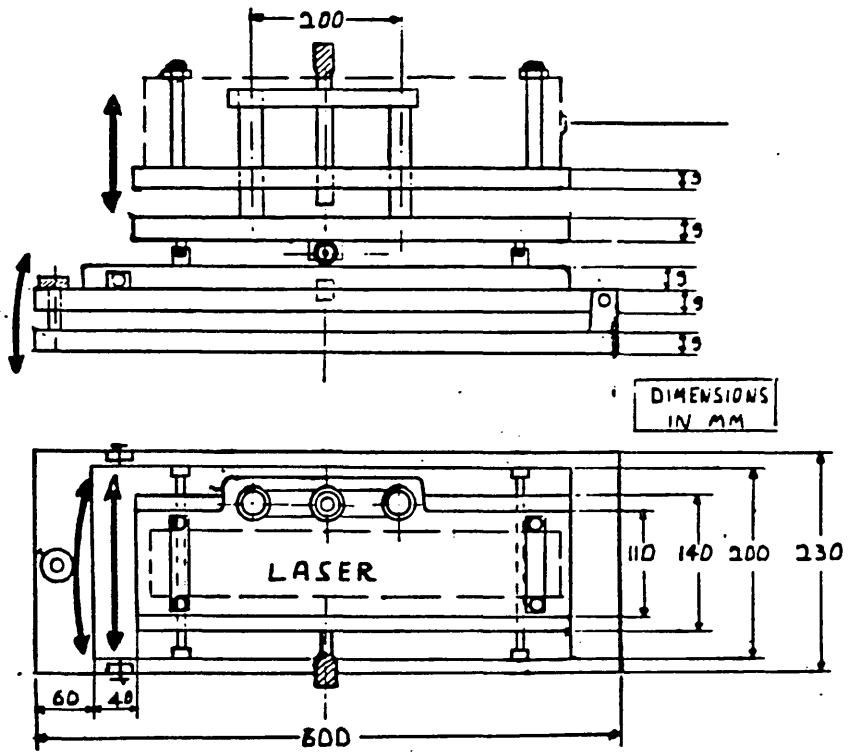

Fig. 3.28 Dimensions and movements of laser table

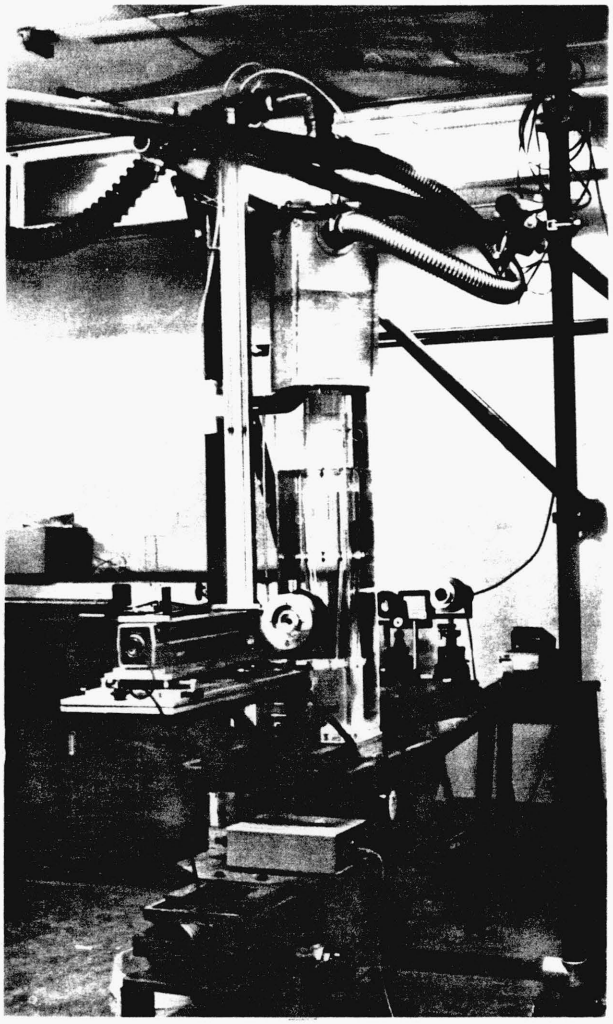

(a) LDA system with cyclone

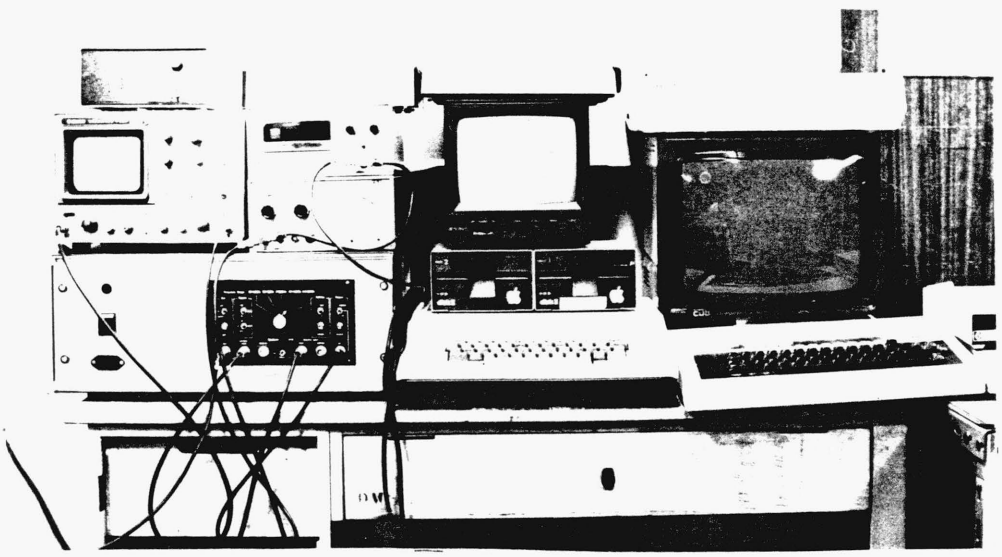

(b) LDA data processing system

Fig. 3.29 Experimental LDA system

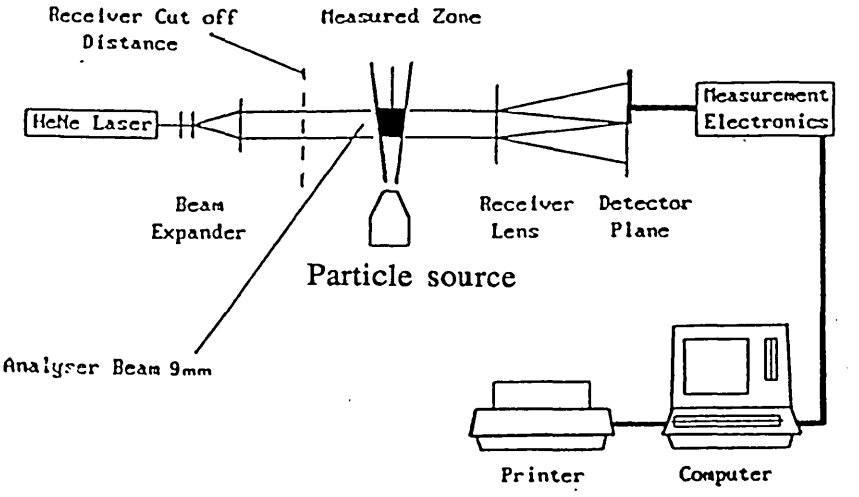

Fig. 3.30 Laser diffraction experiment

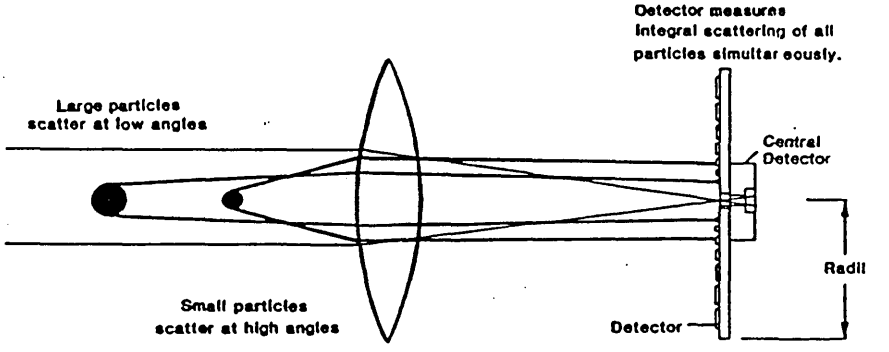

Fig. 3.31 Properties of the scattered light from particles

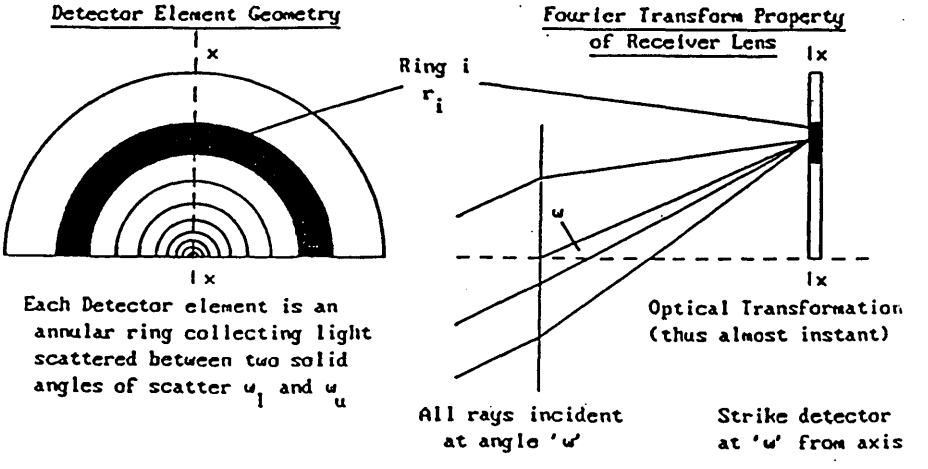

Fig. 3.32 Properties of range lens

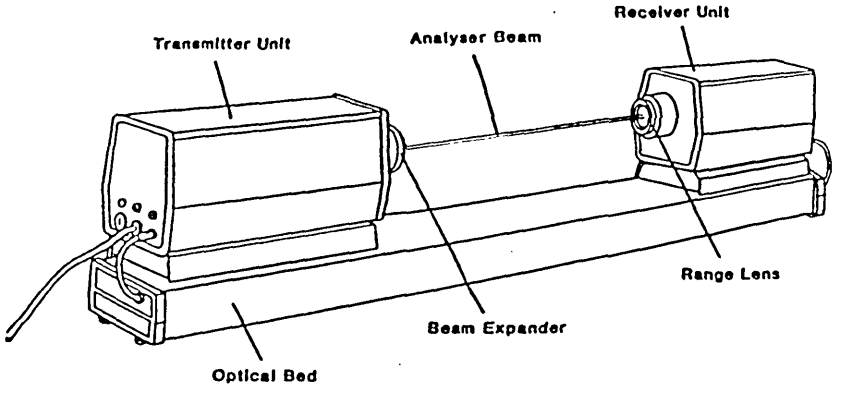

Fig. 3.33 Malvern-2600 optical unit - components & controls

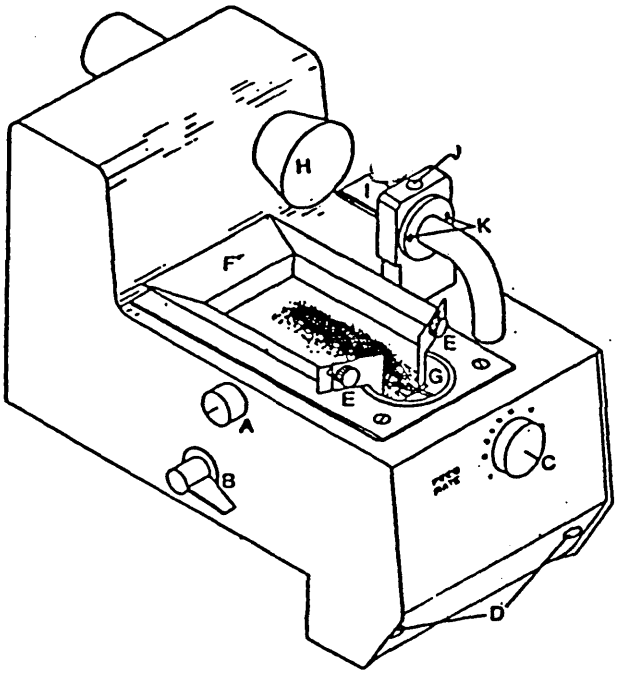

A Hopper locking screw
B Interlock switch
C Feed control
D Cross movement adjusters
E Feed gate adjusters
F Hopper
G Cone and sieve containing ball bearing
H Exhaust
I Nozzle
J Nozzle height adjusters
K Nozzle locking screws

Fig. 3.34 Malvern PS64 dry powder feeder

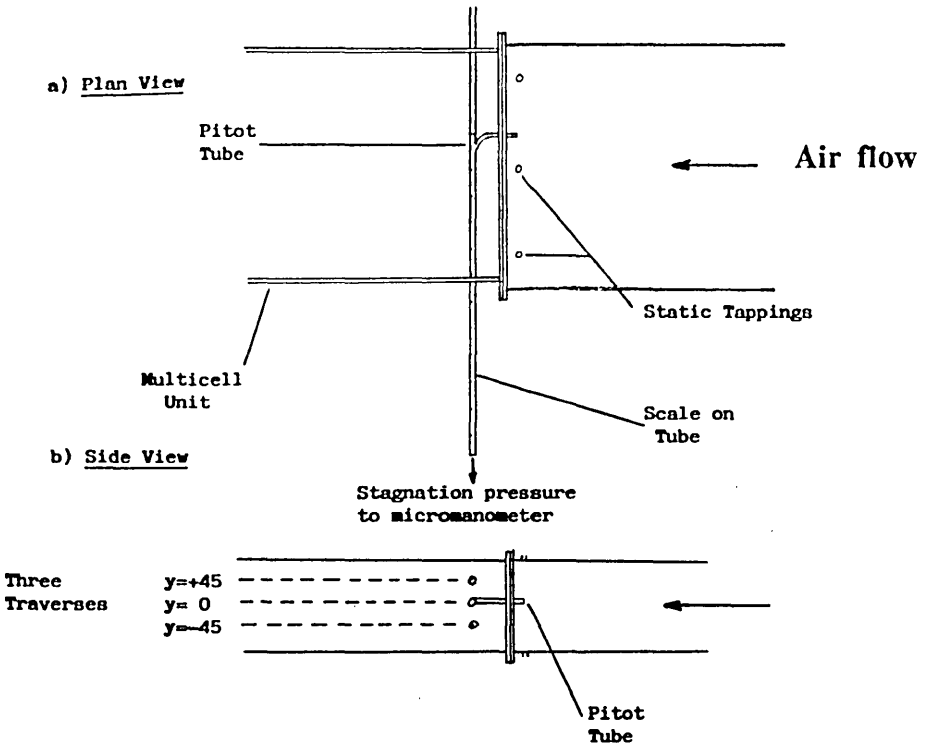

Fig. 3.35 Traversing arrangement across the inlet duct exit

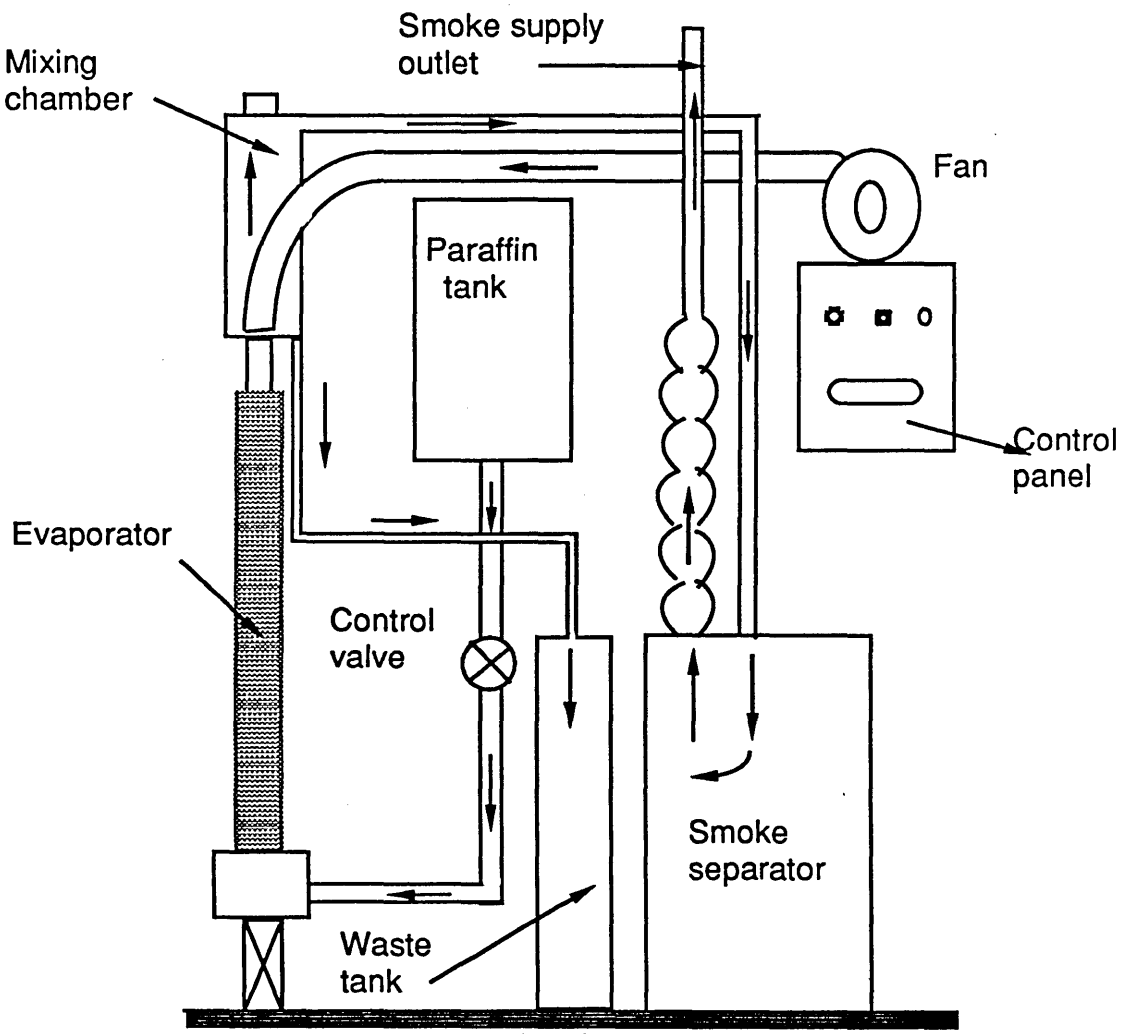

Fig. 3.36 Smoke generator

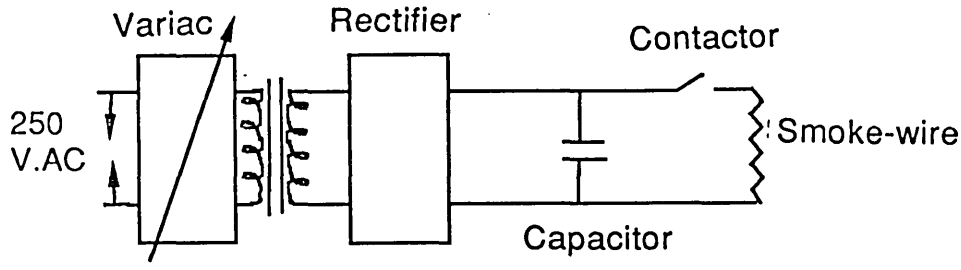

(a) Smoke-wire circuit diagram

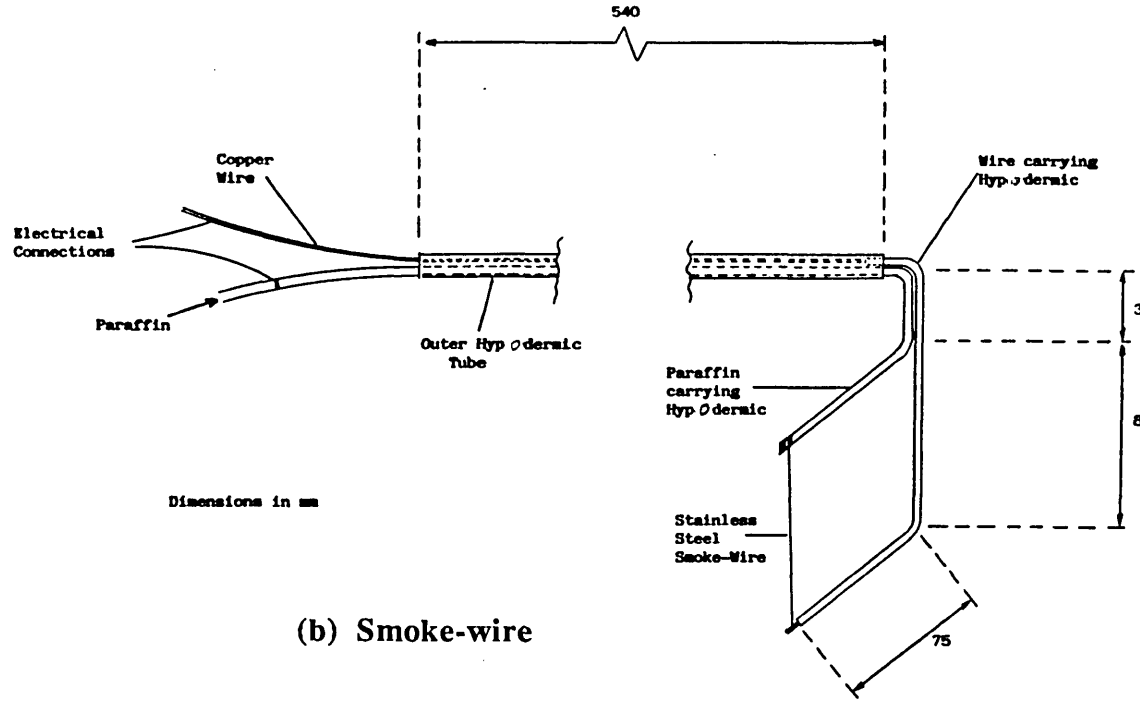

(b) Smoke-wire

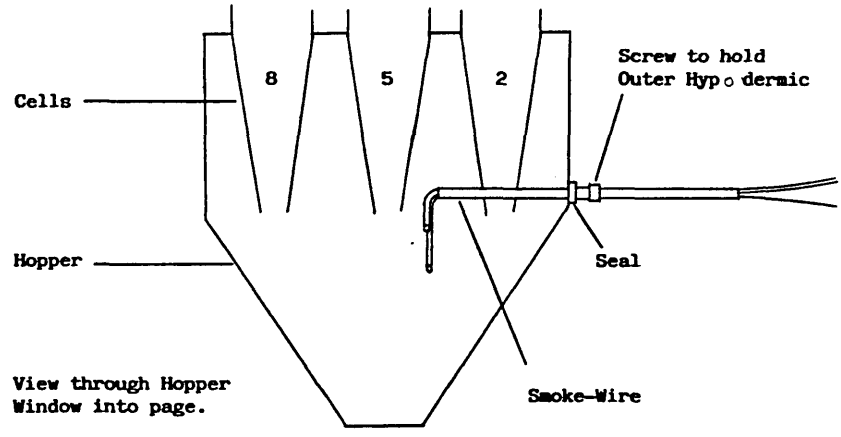

(c) Smoke-wire in the hopper

Fig. 3.37 Smoke-wire system

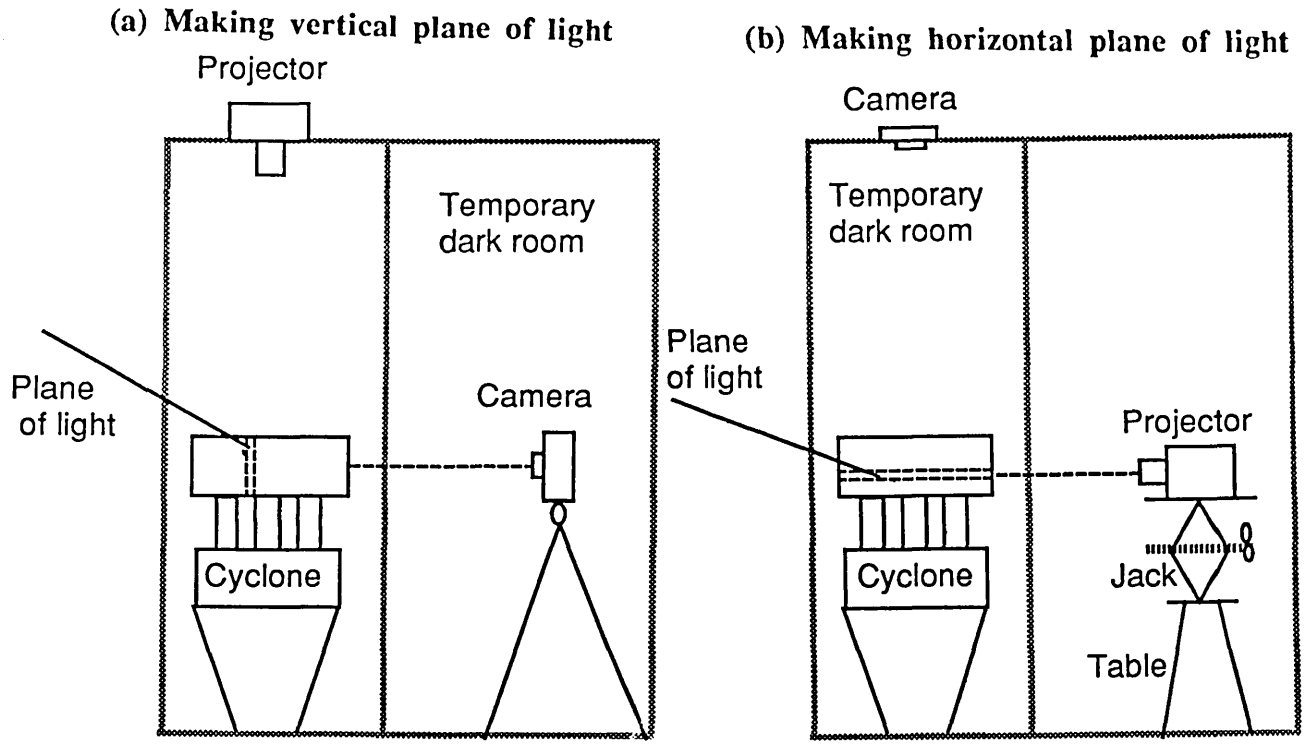

Fig. 3.38 General arrangement of outlet cyclone manifold visualization

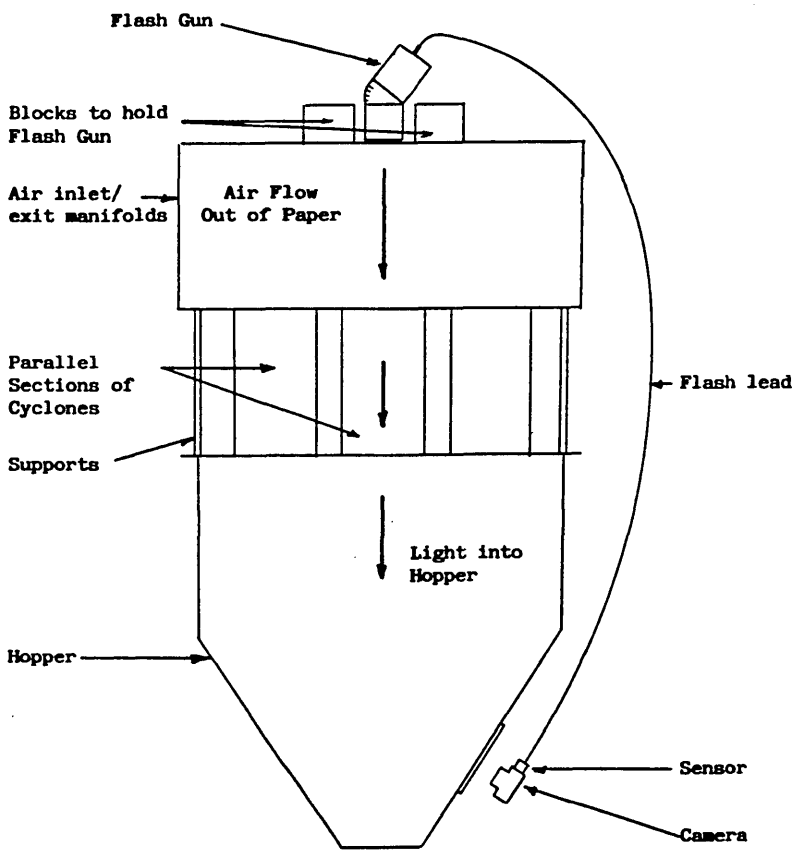

Fig. 3.39 General arrangement of hopper visualization

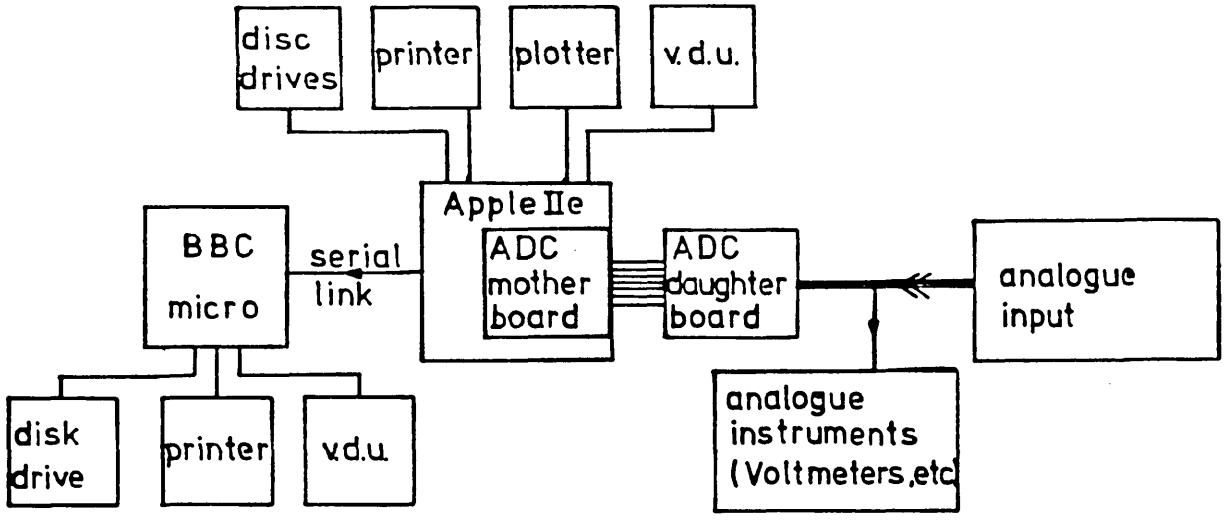

Fig. 3.40 Data acqusition system schematic representation

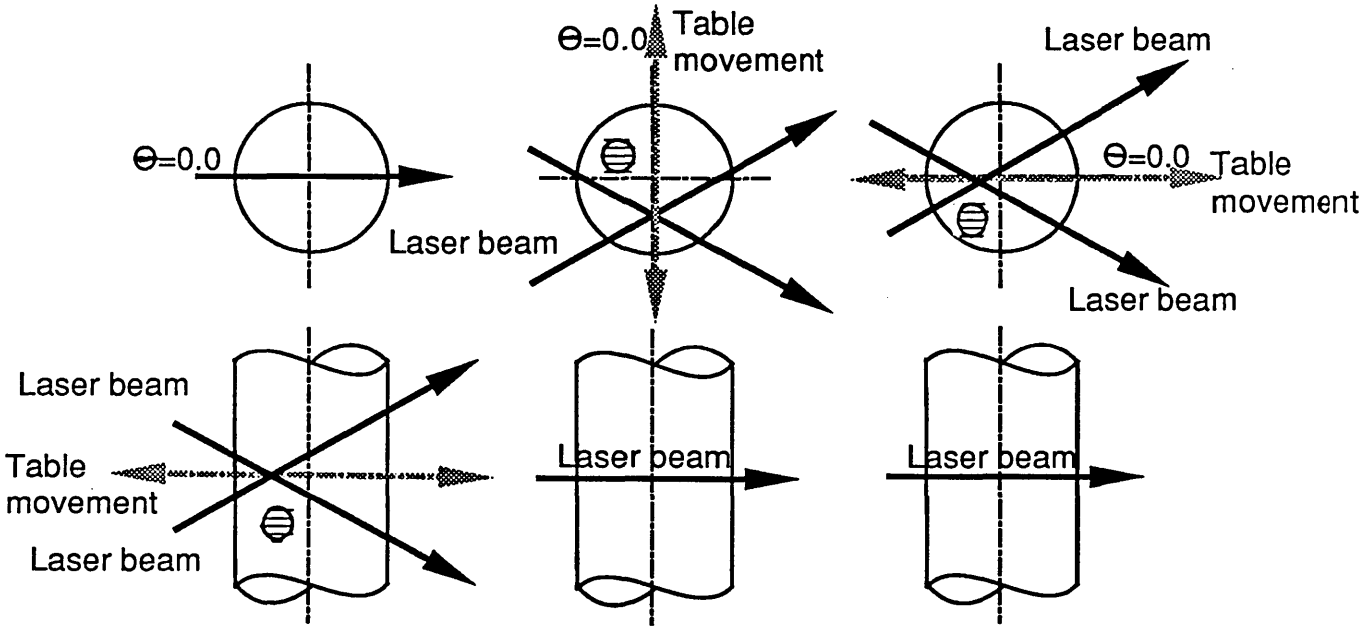

Fig. 3.41 Method of measuring three components of velocity (u, v and w) by LDA

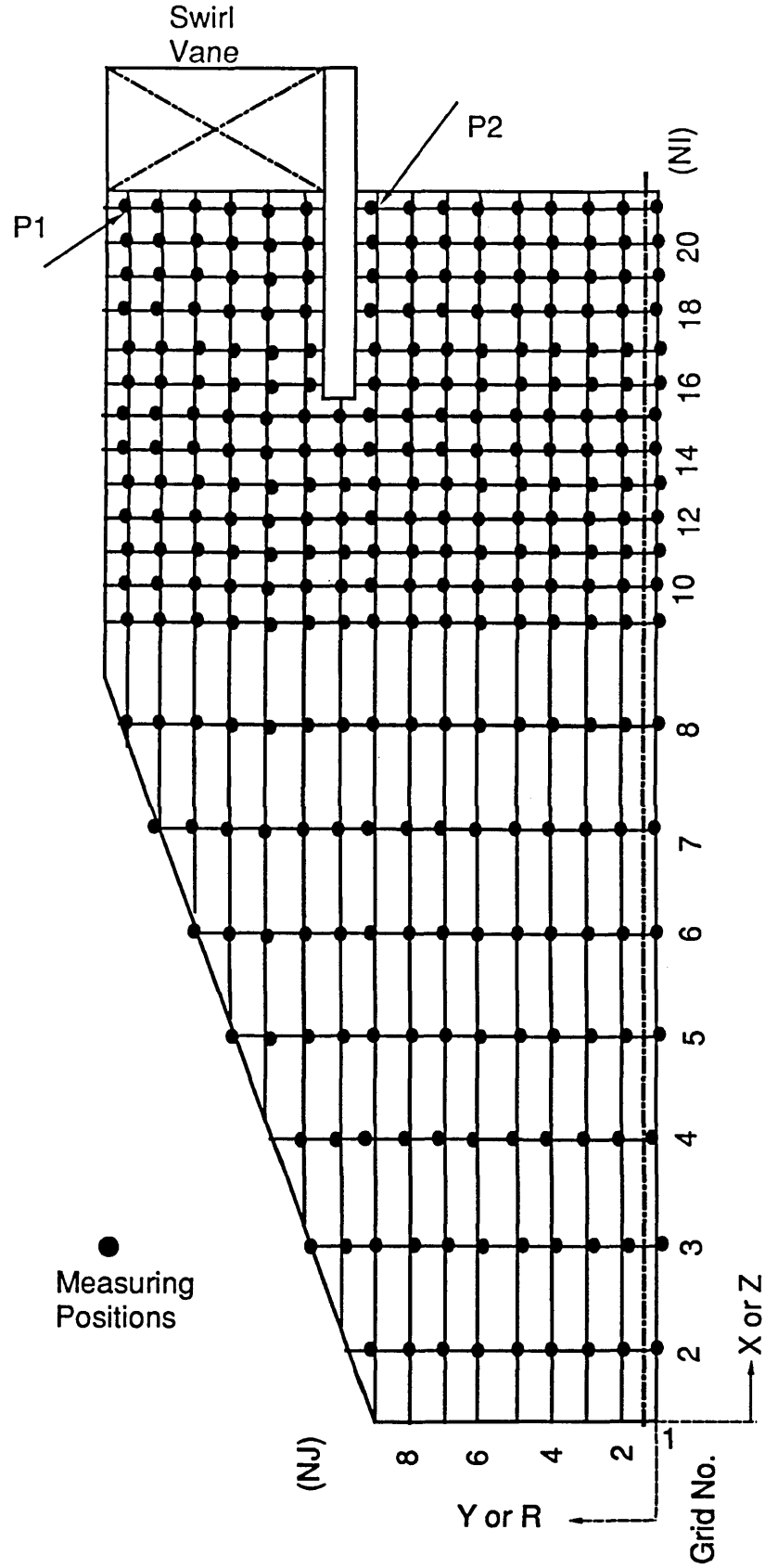

Fig. 3.42 LDA measuring points locations in one-cell water rig

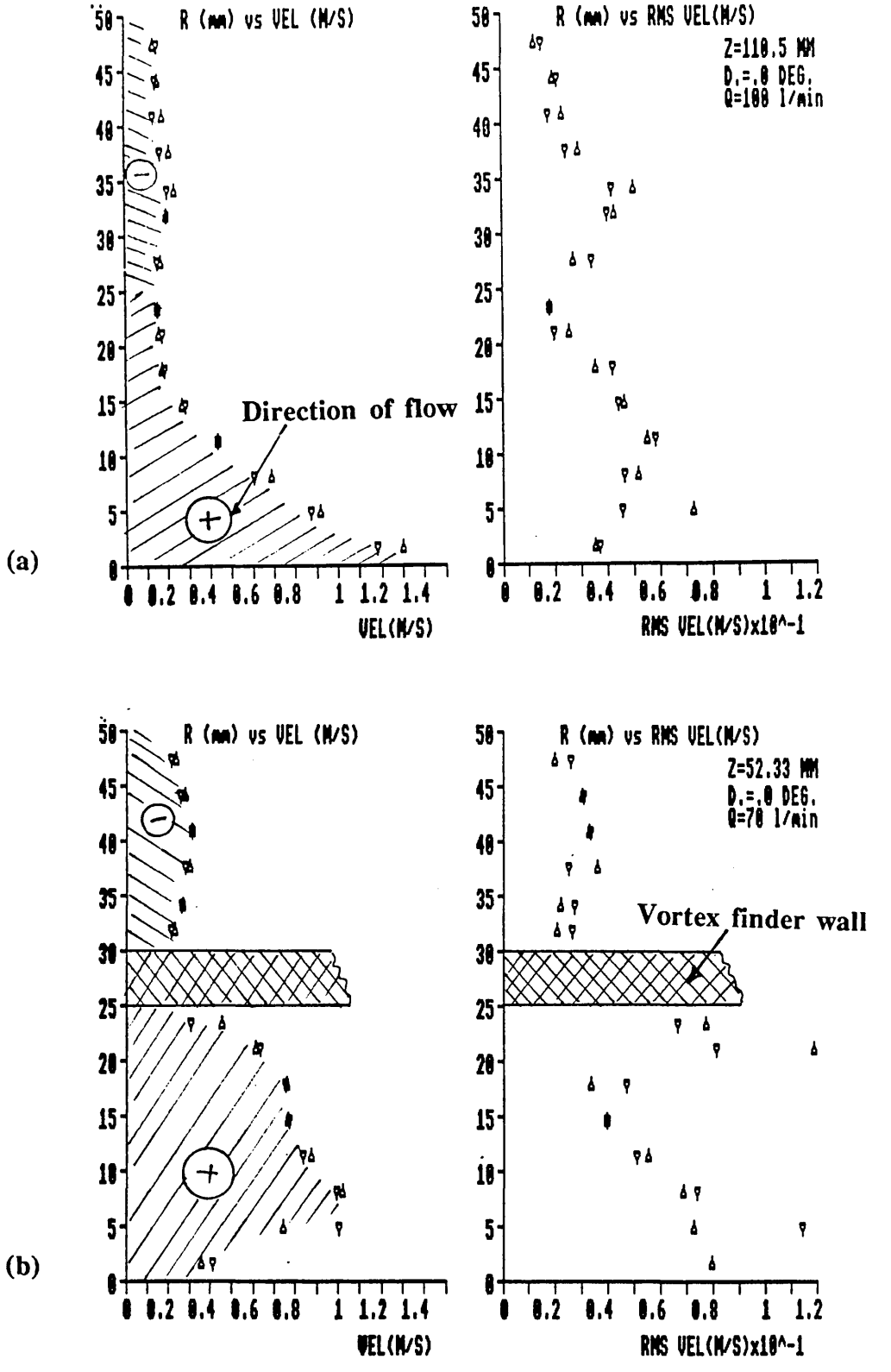

Fig. 4.1 Axial mean and r.m.s. velocity profiles measured by LDA

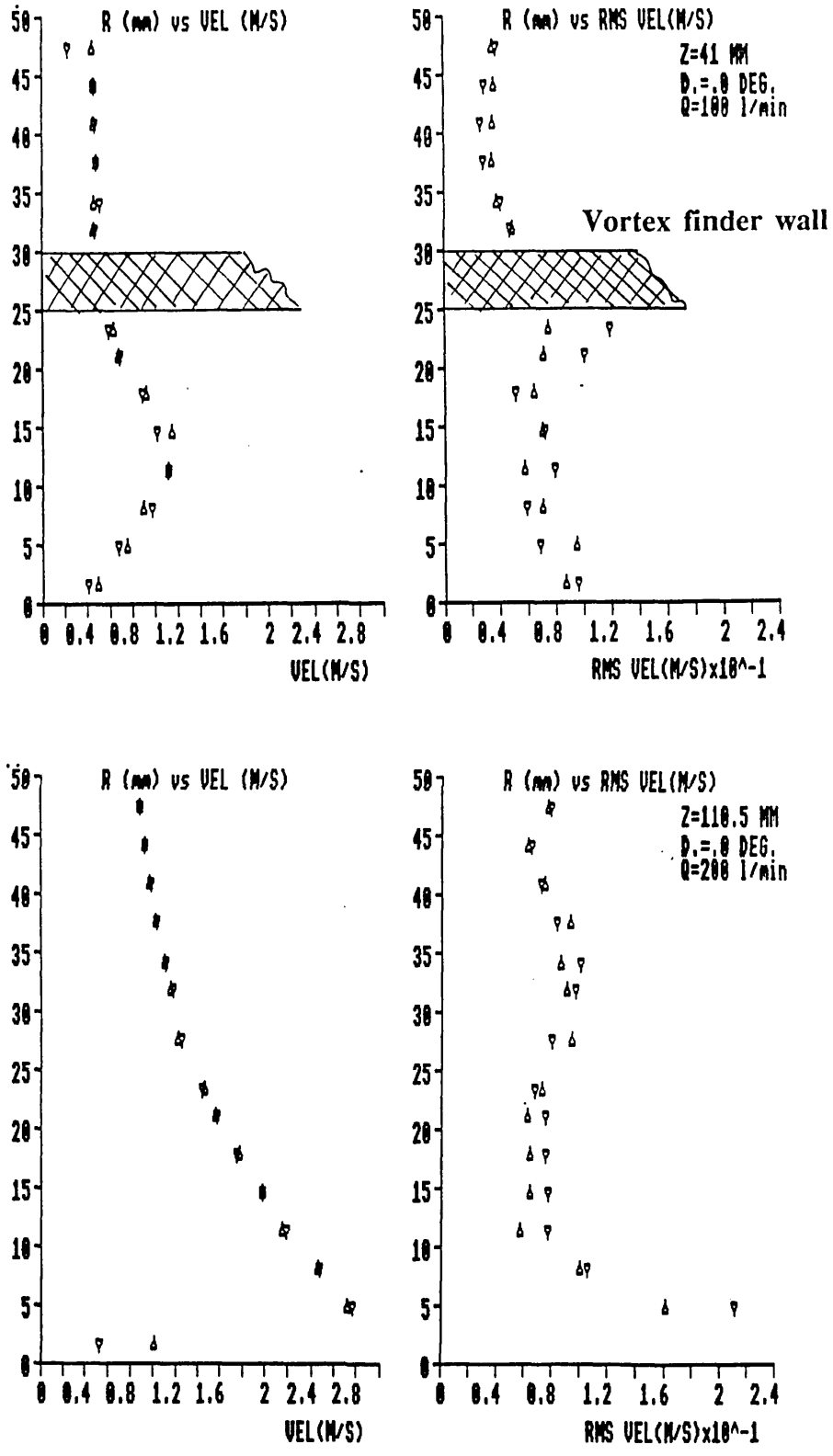

Fig. 4.2 Tangential mean and r.m.s. velocity profiles measured by LDA

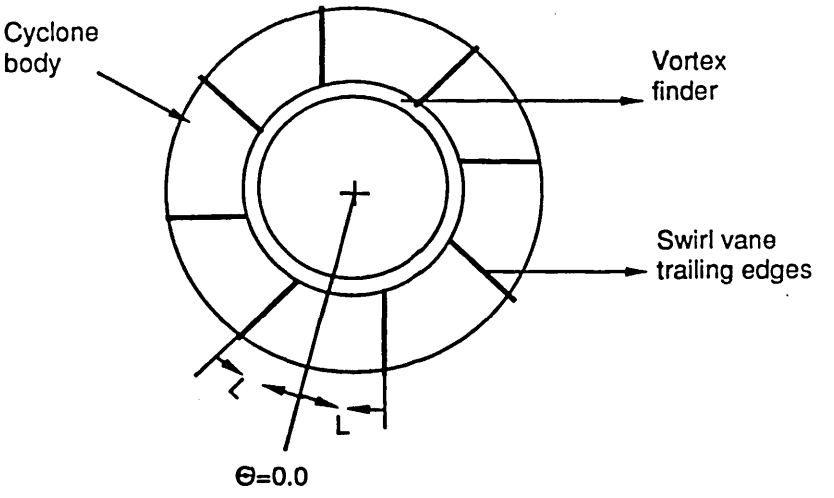

Fig. 4.3 Determination of angular reference position

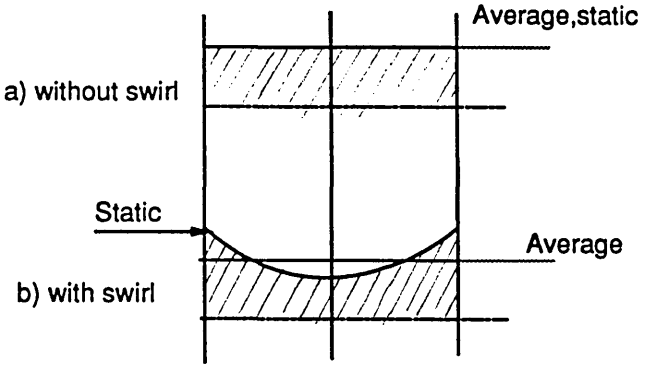

Fig. 4.4 Schematic of static pressure profiles for a pipe with and without swirl

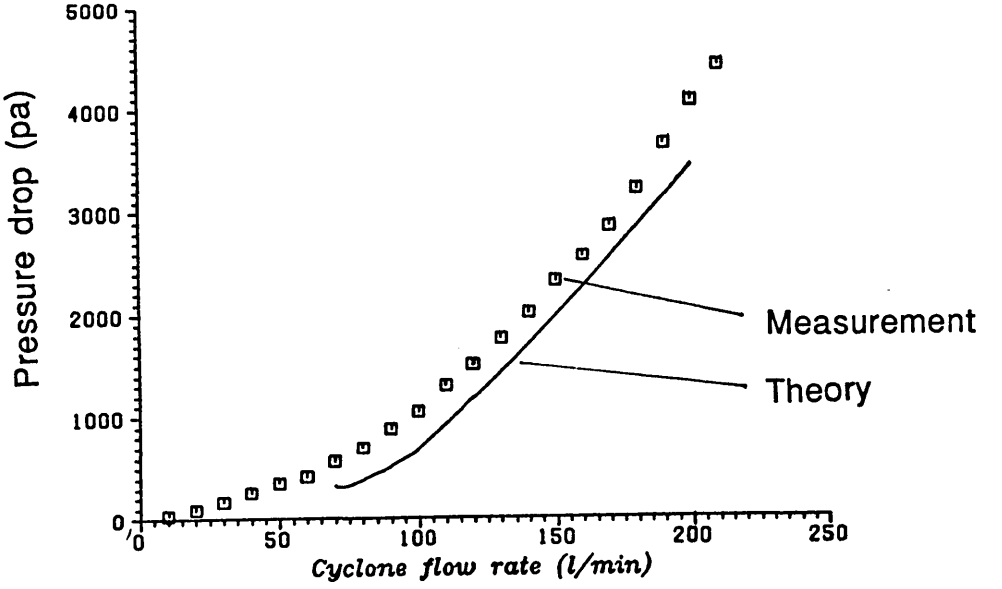

Fig. 4.5 Cyclone pressure drop versus flow rate (water rig)

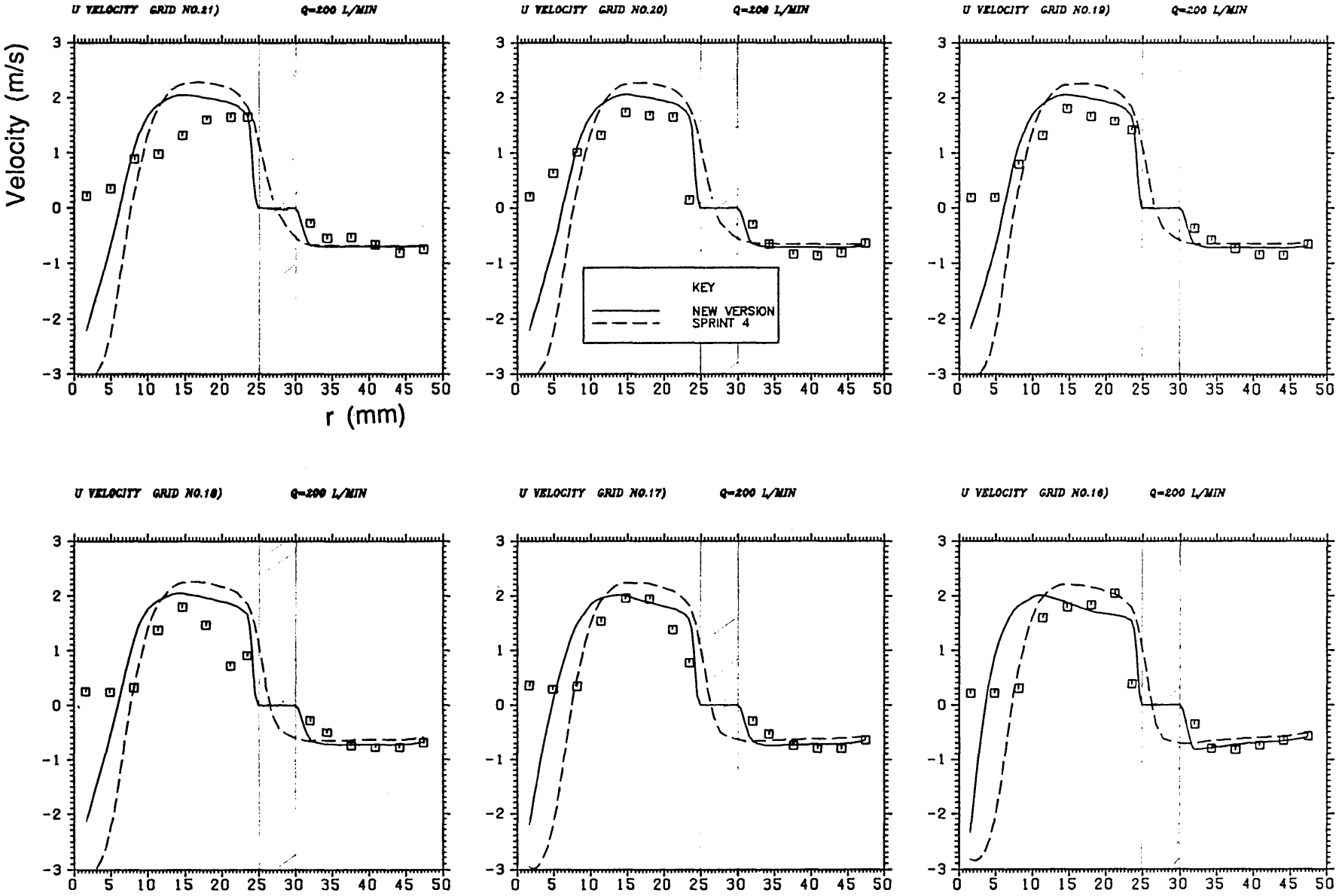

Fig. 4.6 Axial mean velocity profiles for grid lines 16-21 at 200 l/min flow rate

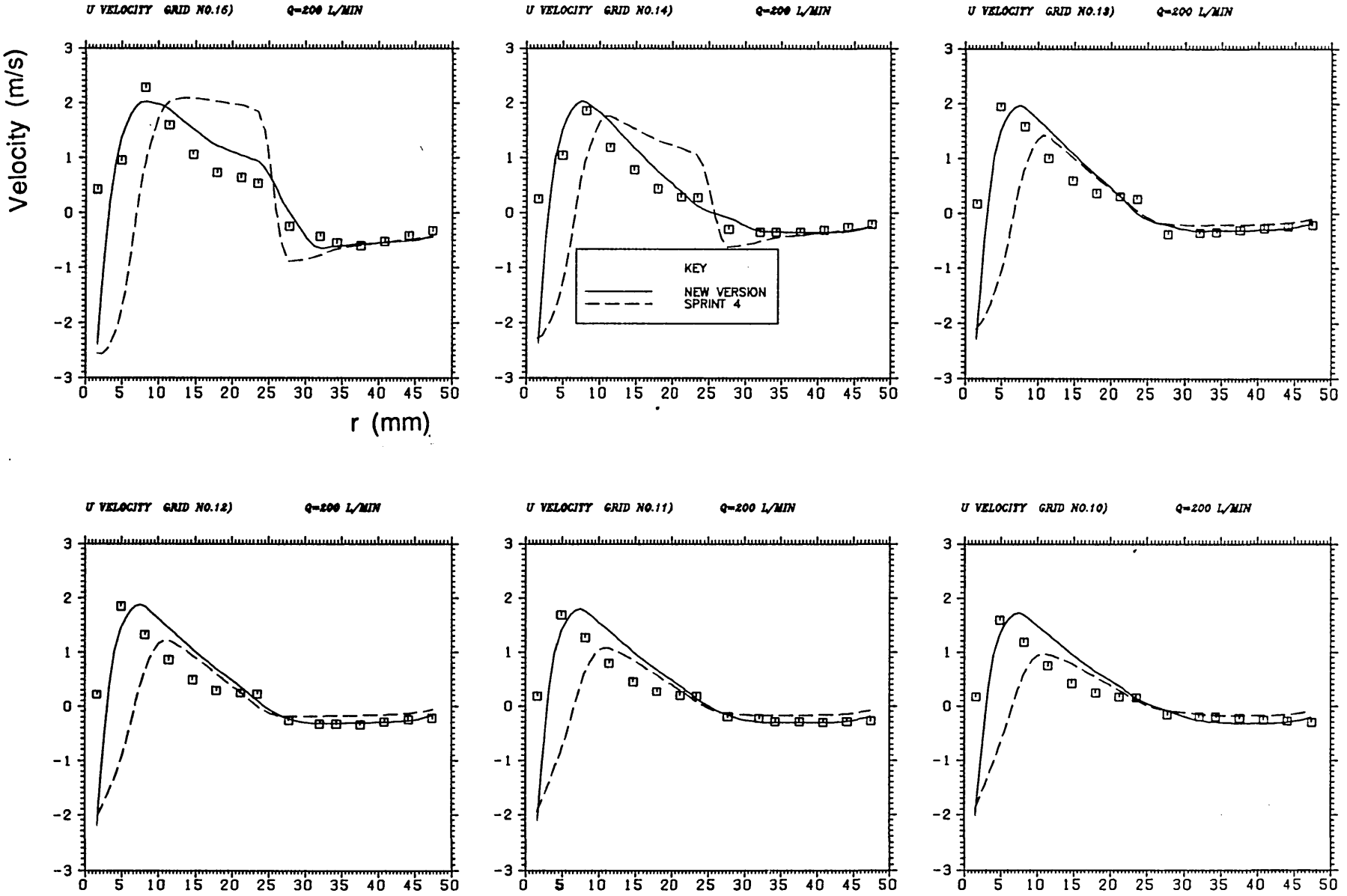

Fig. 4.7 Axial mean velocity profiles for grid lines 10-15 at 200 l/min flow rate

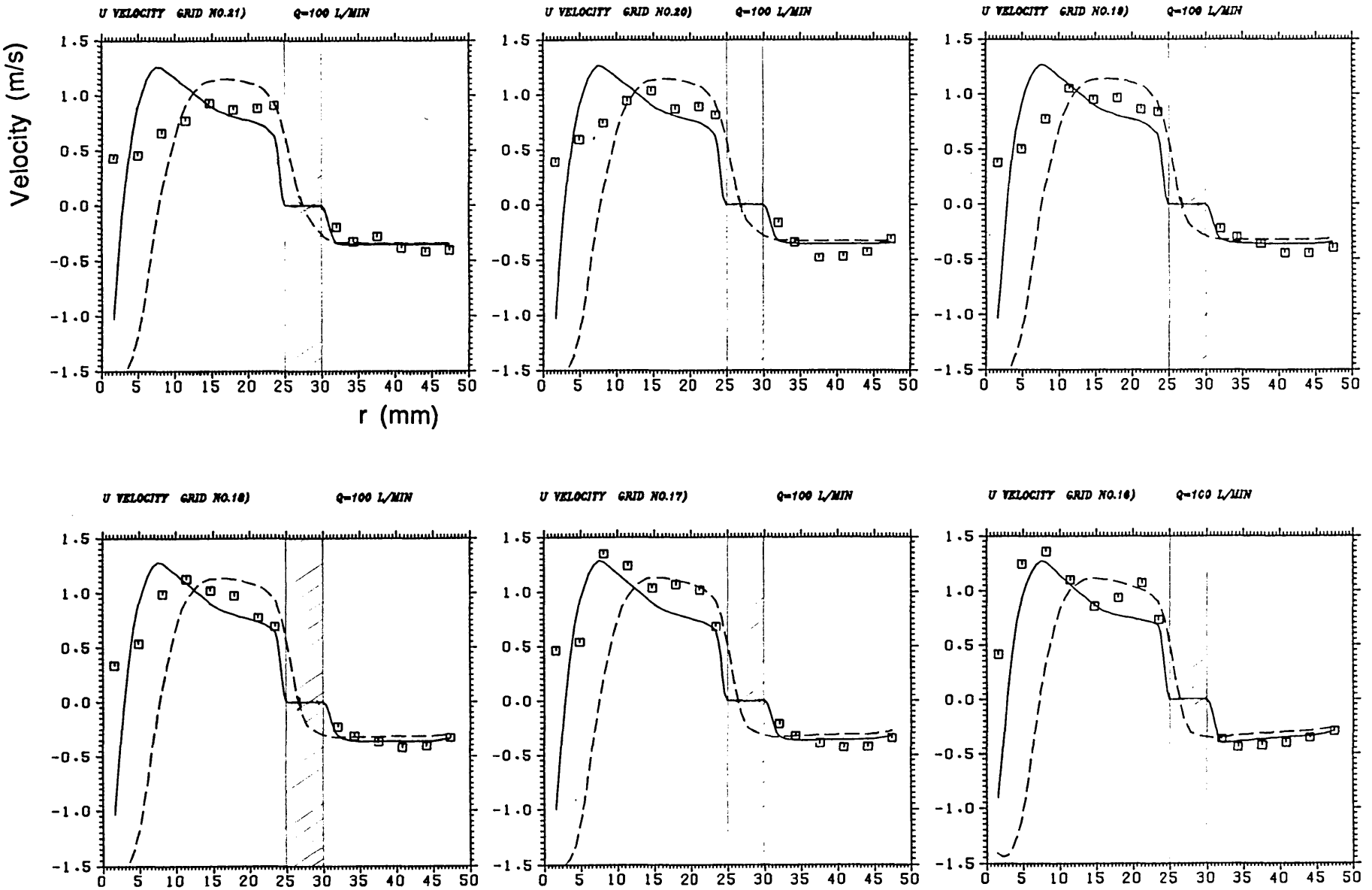

Fig. 4.8 Axial mean velocity profiles for grid lines 16-21 at 100 l/min flow rate

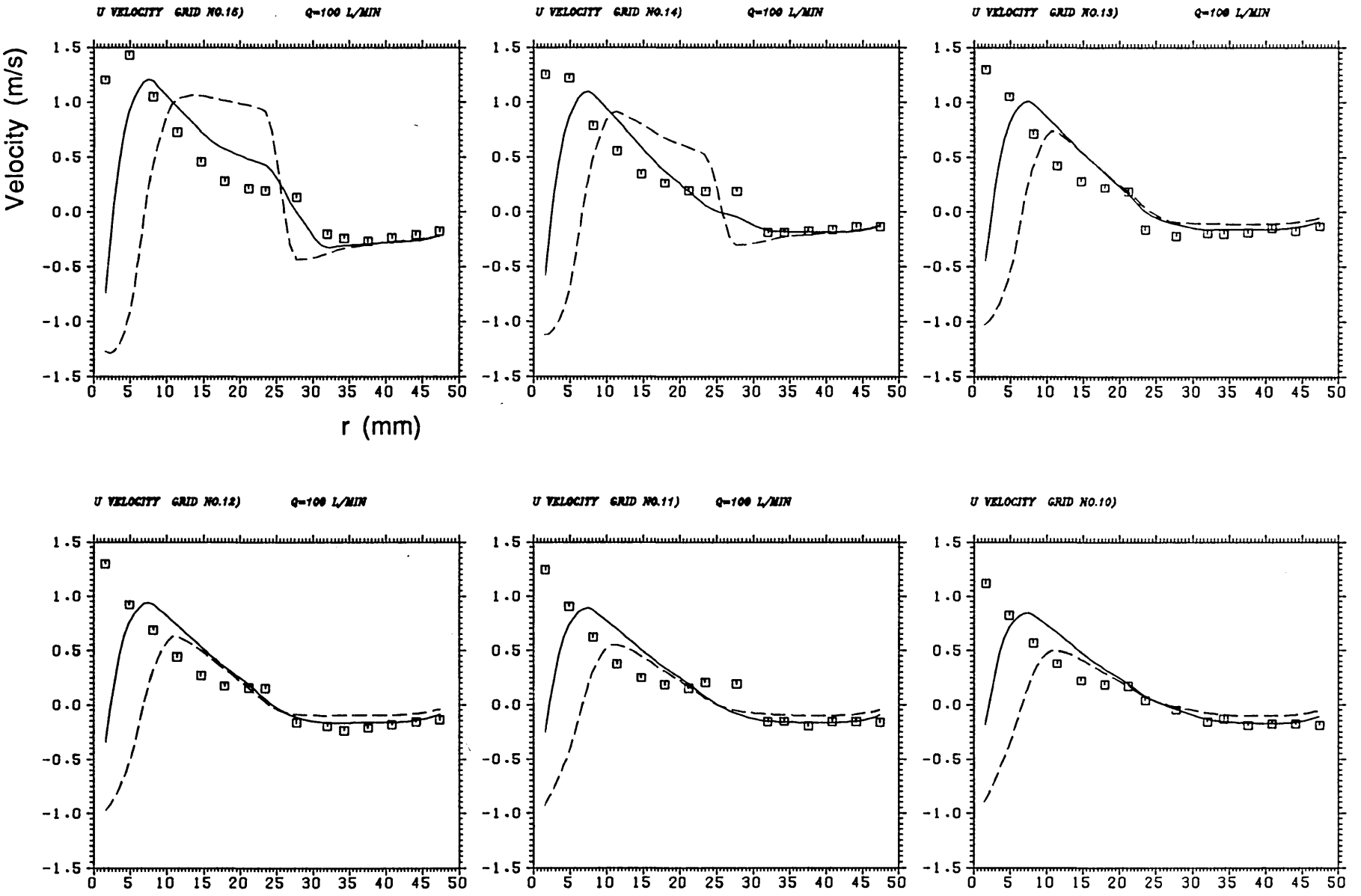

Fig. 4.9 **Axial mean velocity profiles for grid lines 10-15 at 100 l/min flow rate**

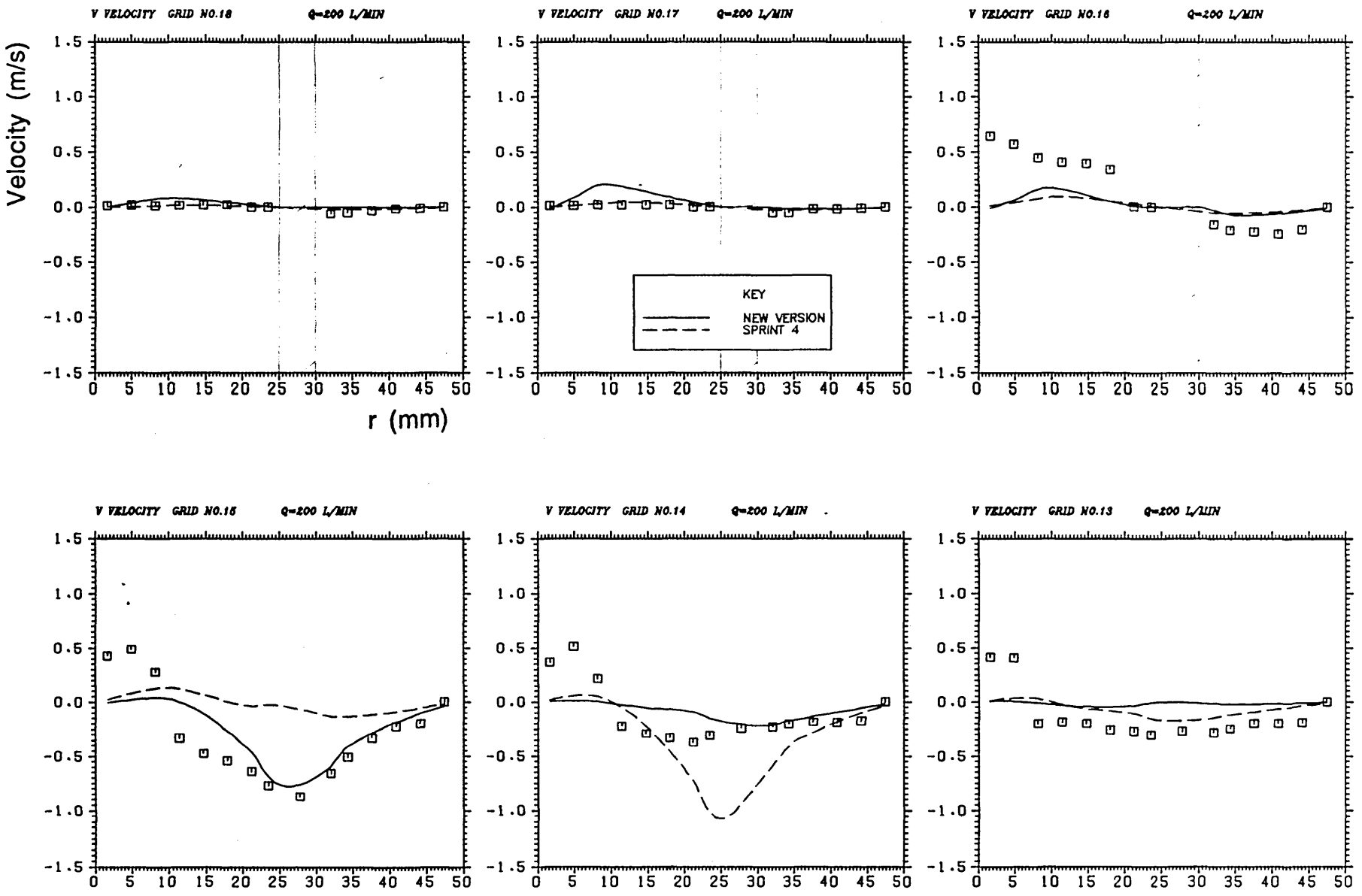

Fig. 4.10 Radial mean velocity profiles for grid lines 13-18 at 200 l/min flow rate

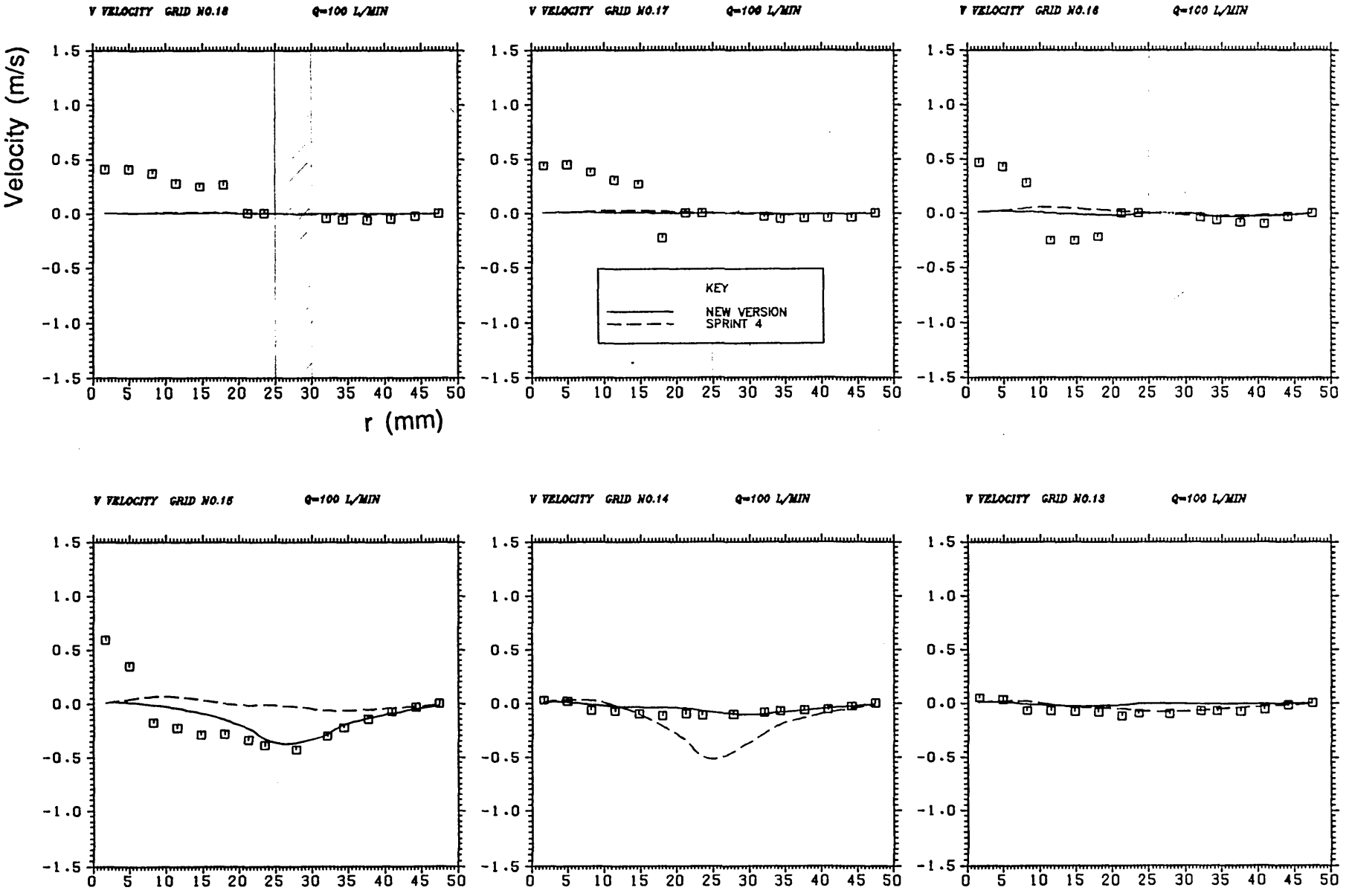

Fig. 4.11 Radial mean velocity profiles for grid lines 13-18 at 100 l/min flow rate

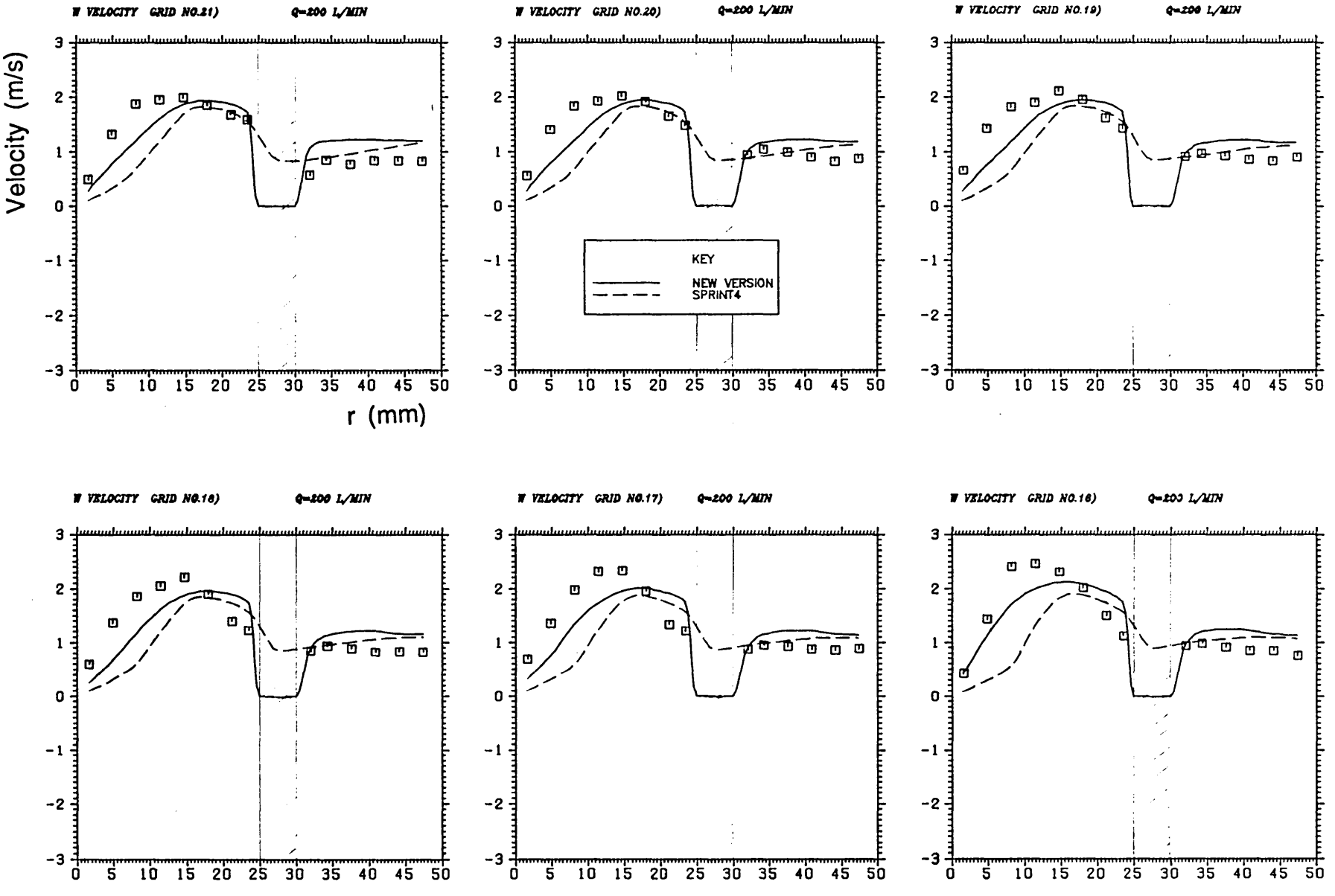

Fig. 4.12 Tangential mean velocity profiles for grid lines 16-21 at 200 l/min flow rate

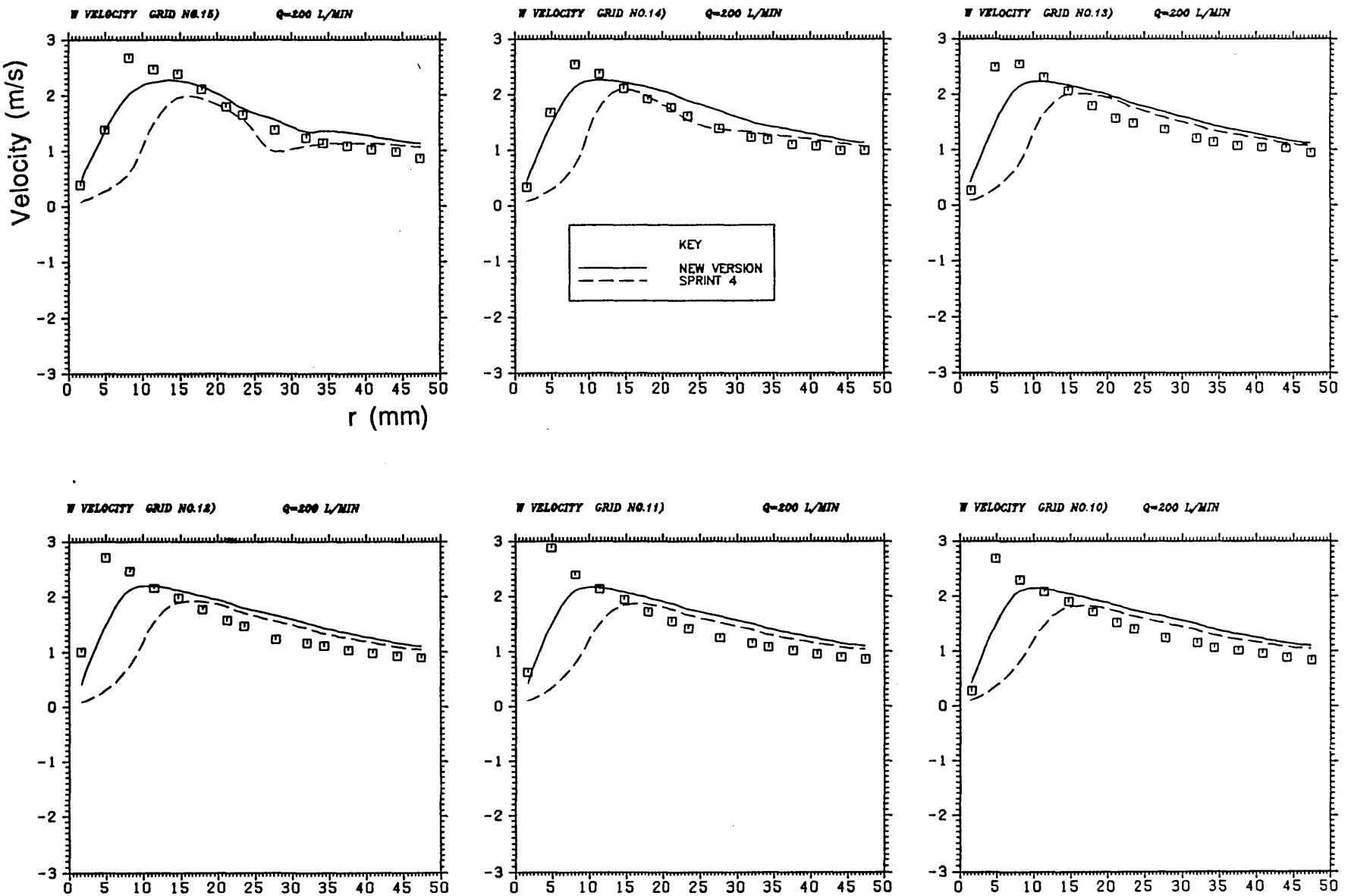

Fig. 4.13 Tangential mean velocity profiles for grid lines 10-15 at 200 l/min flow rate.

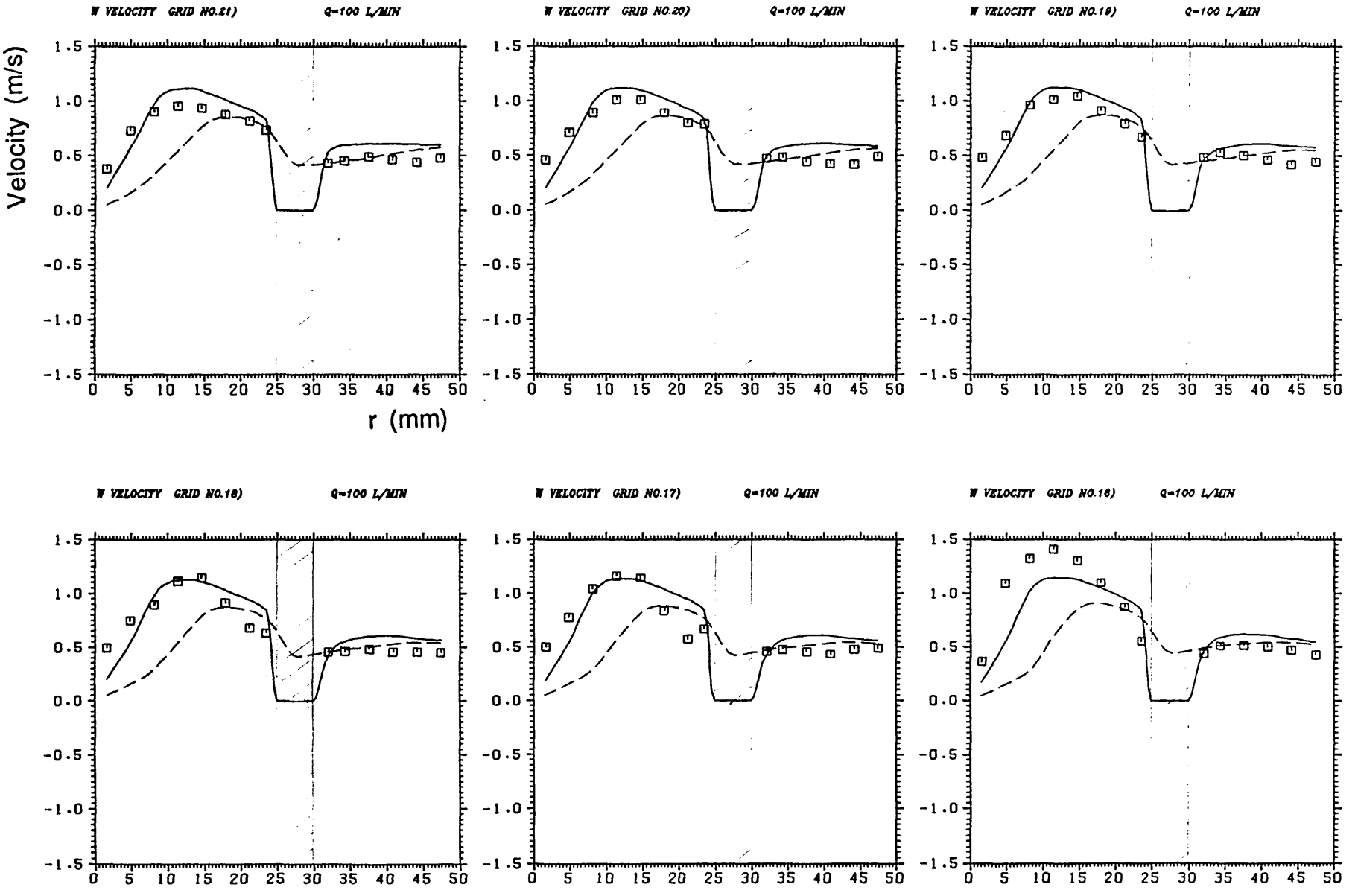

Fig. 4.14 Tangential mean velocity profiles for grid lines 16-21 at100 l/min flow rate

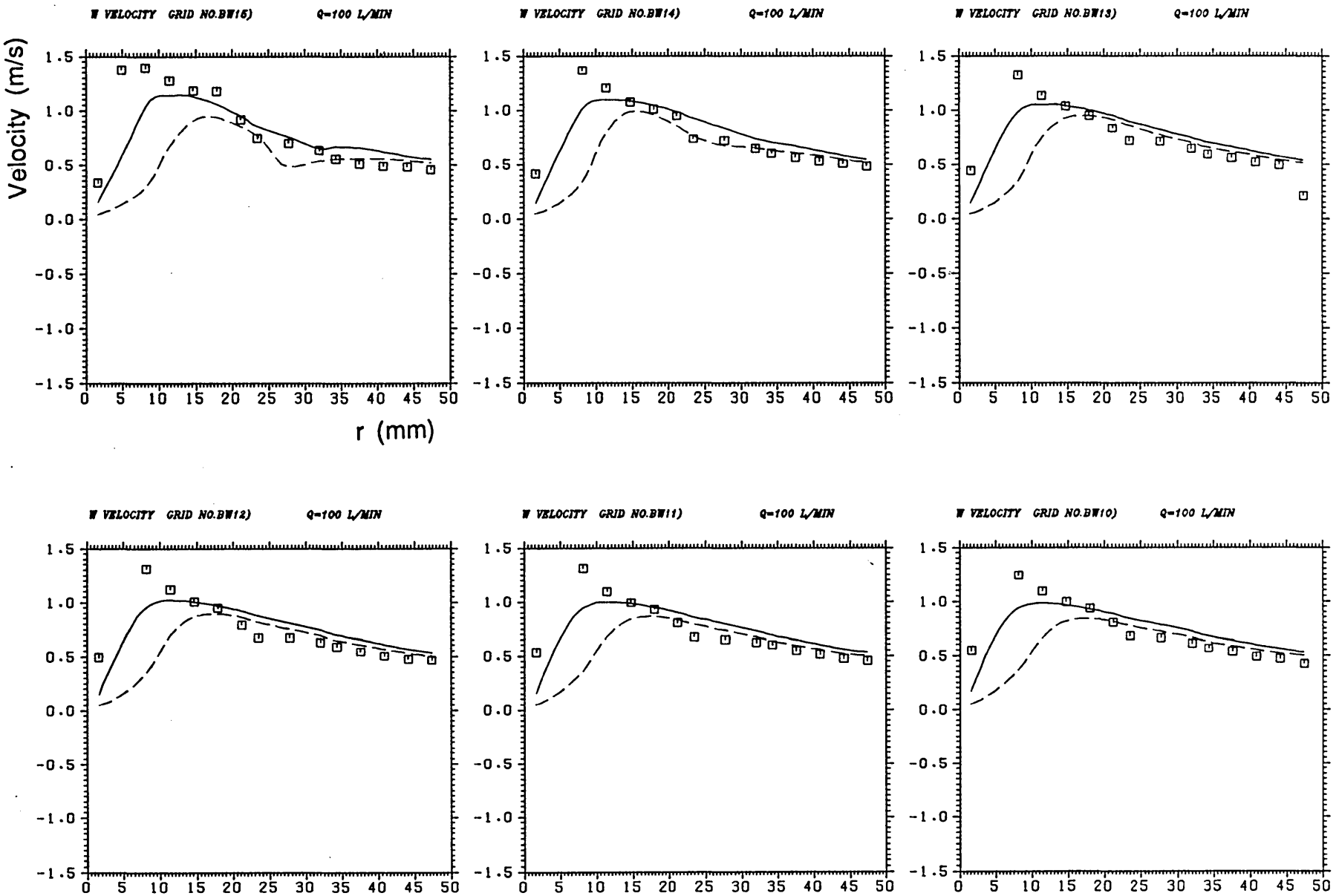

Fig. 4.15 Tangential mean velocity profiles for grid lines 10-15 at100 l/min flow rate

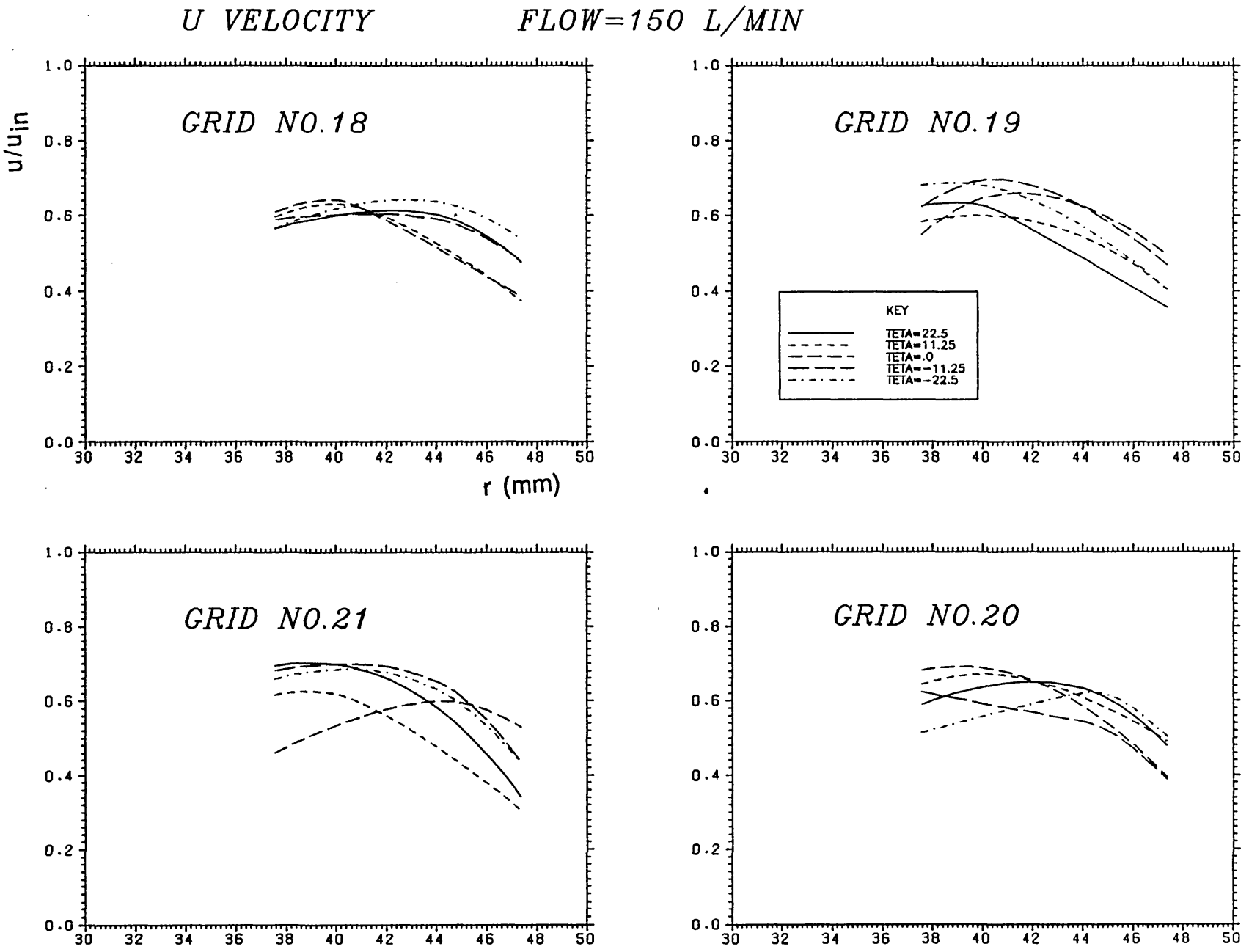

Fig. 4.16 **Effect of circumferential position on axial velocity profiles.**

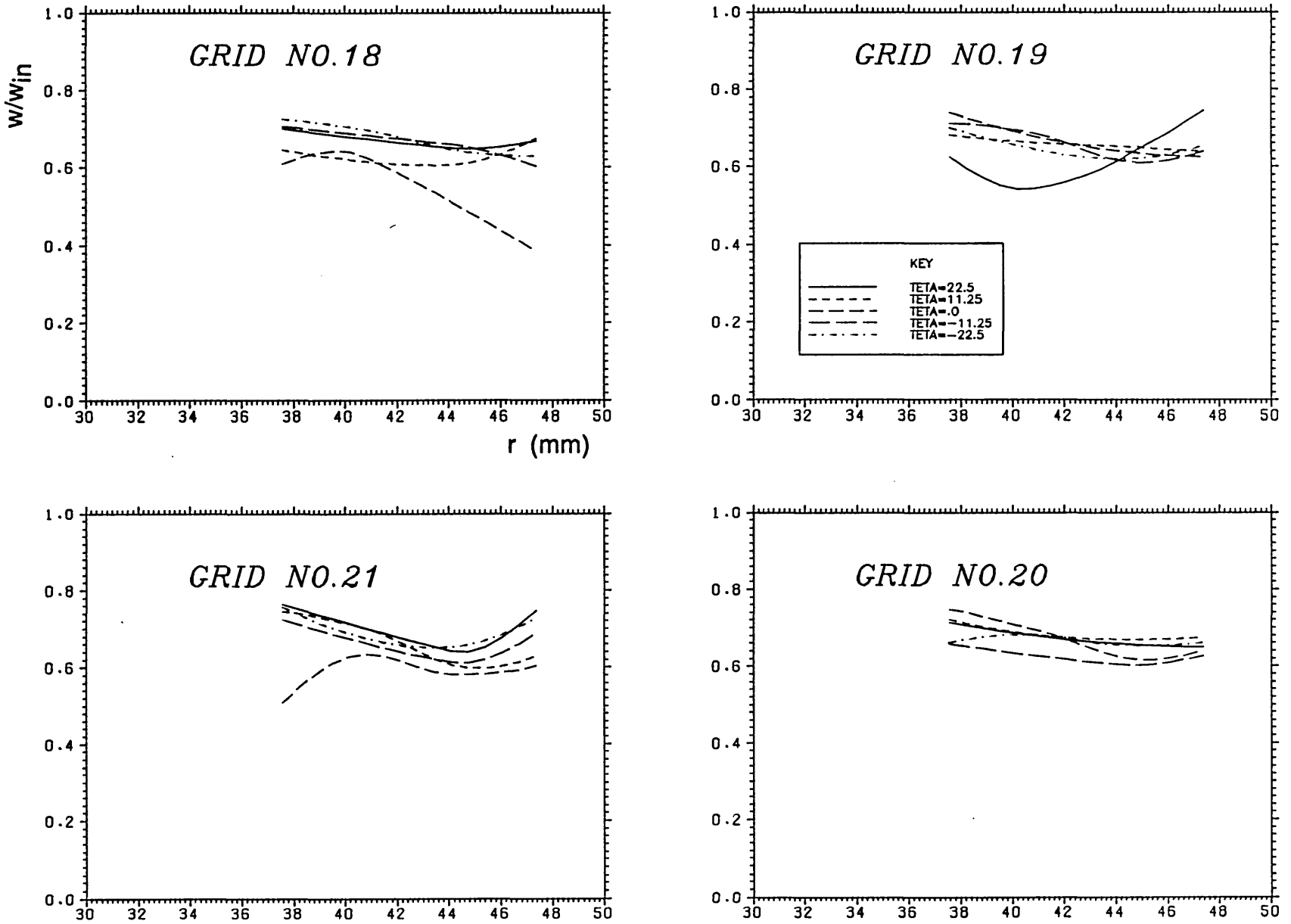

Fig. 4.17 **Effect of circumferential position on tangential velocity profiles**

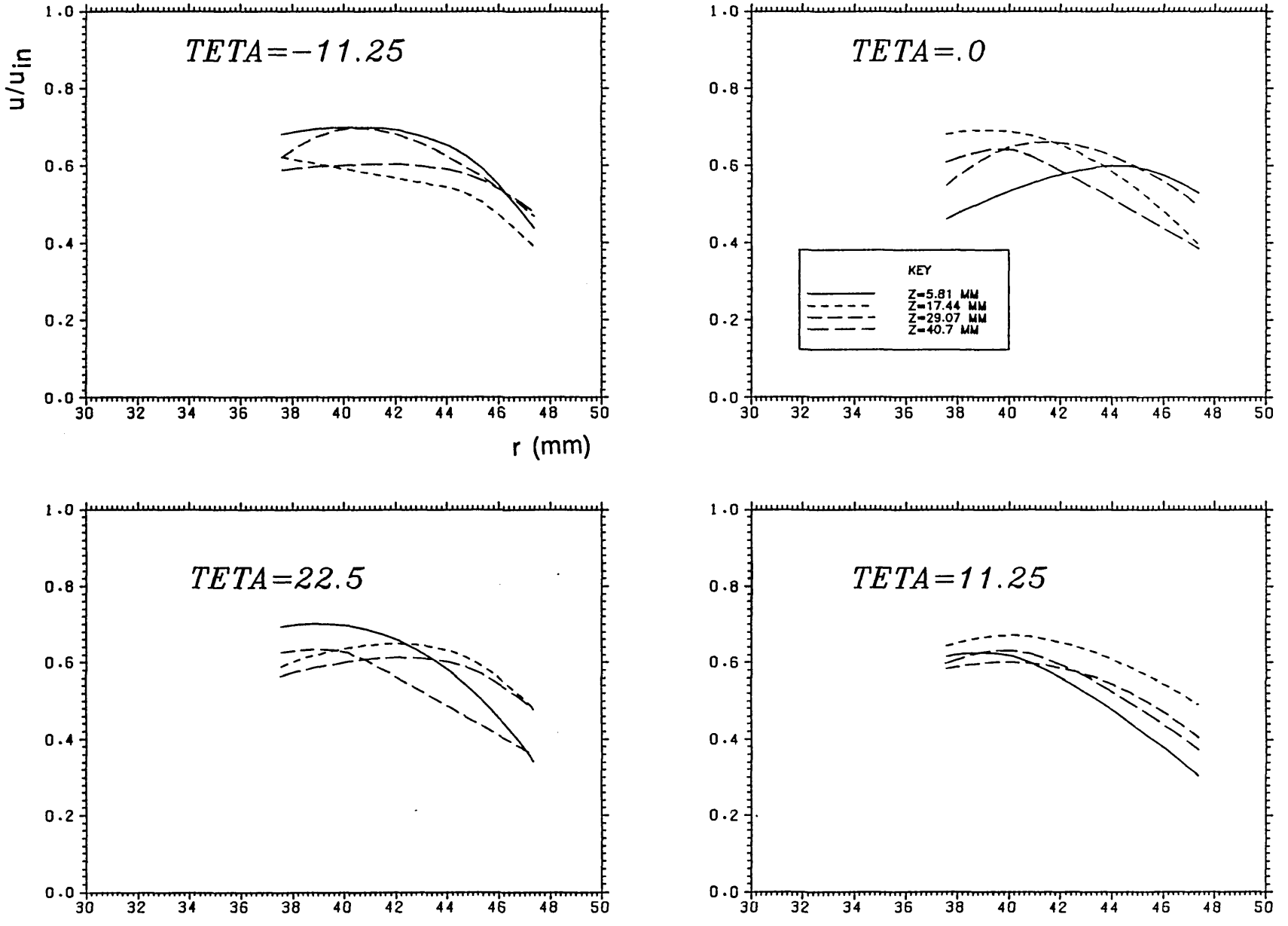

Fig. 4.18 Axial variation of axial velocity profiles at selected circumferential positions

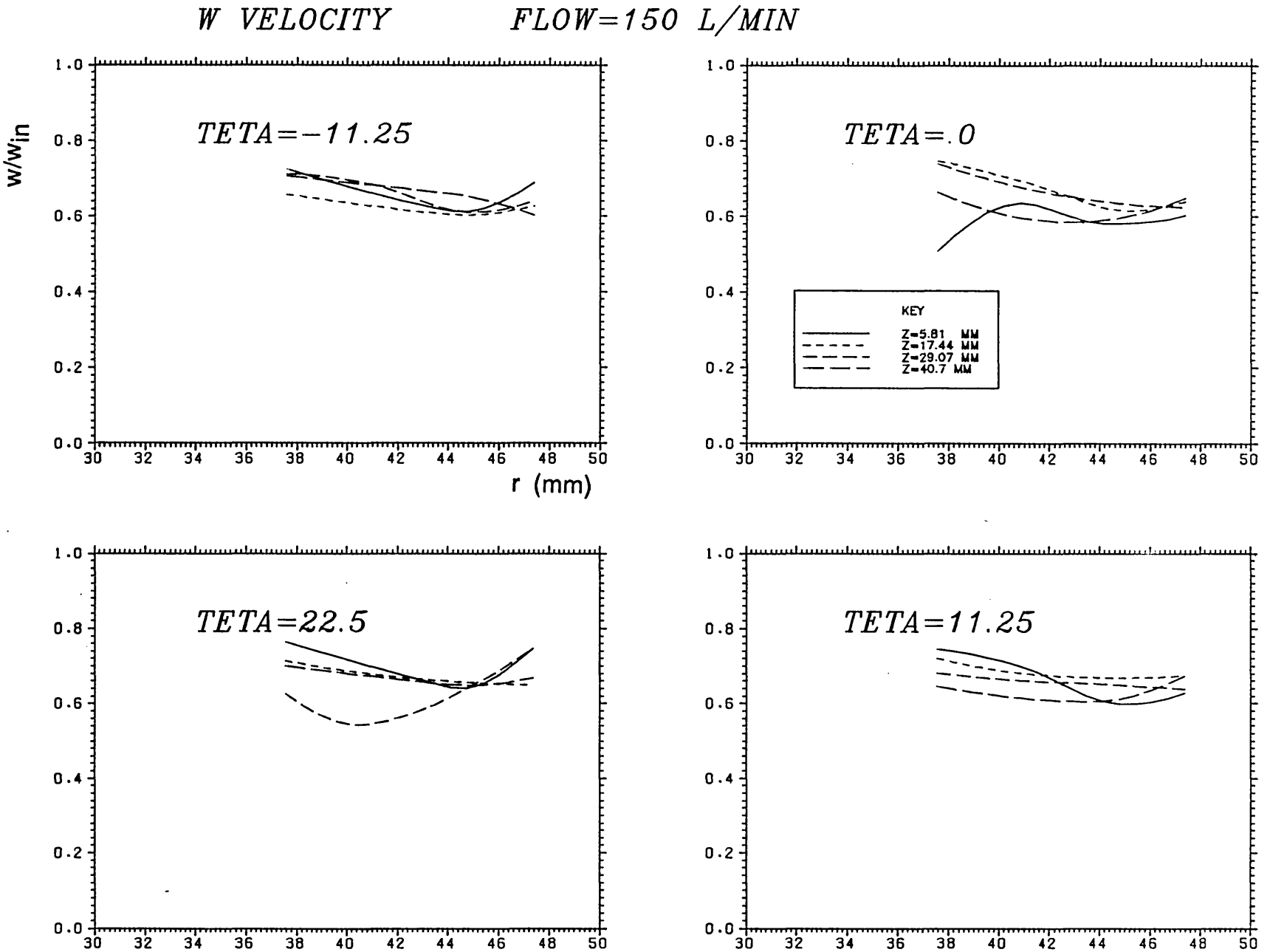

Fig. 4.19 Axial variation of tangential velocity profiles at selected circumferential positions

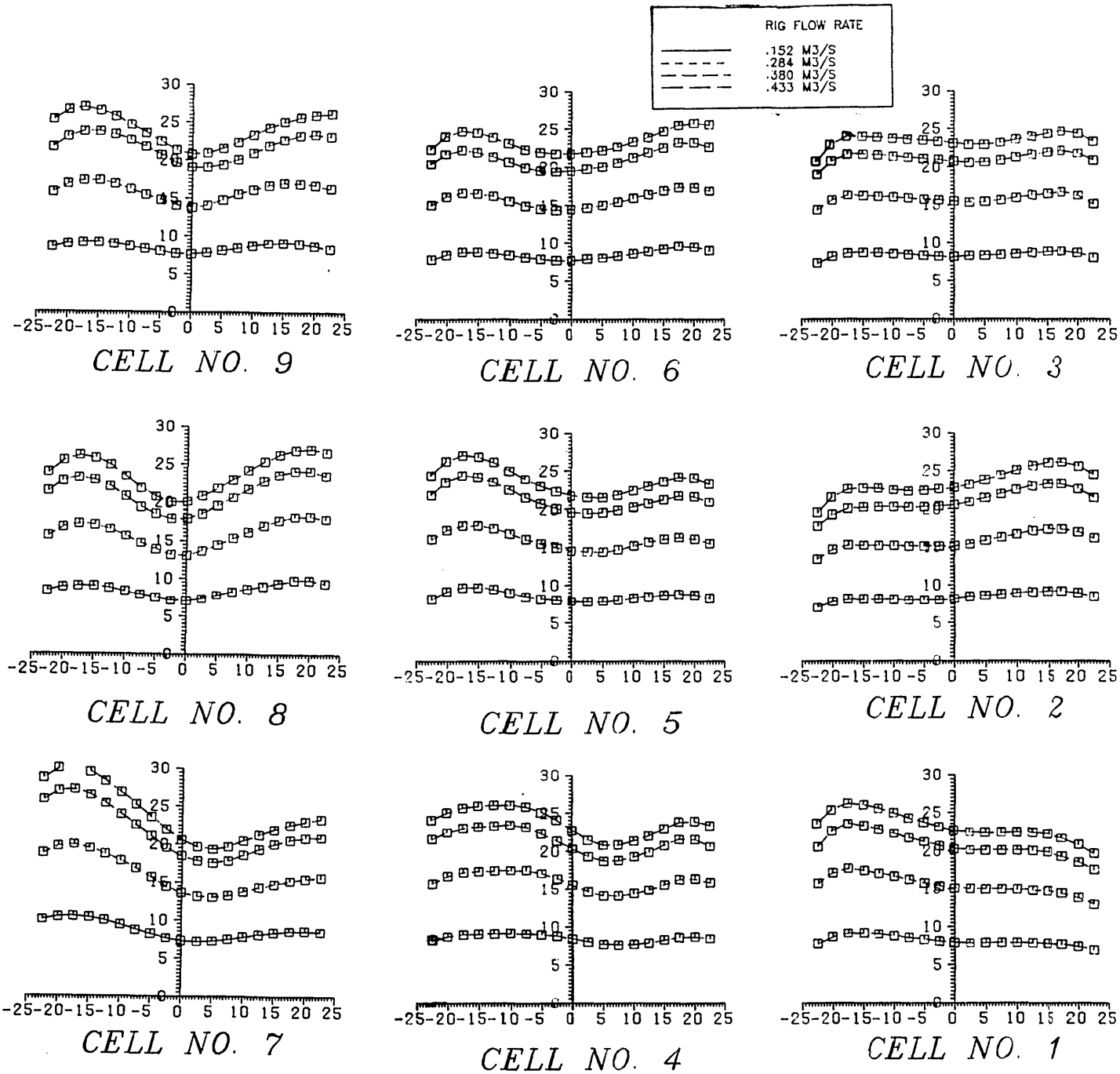

X- Axis Radial position (mm)

Y- Axis Air velocity (m/s)

Fig. 4.20 Cell velocity profiles at various flow rates

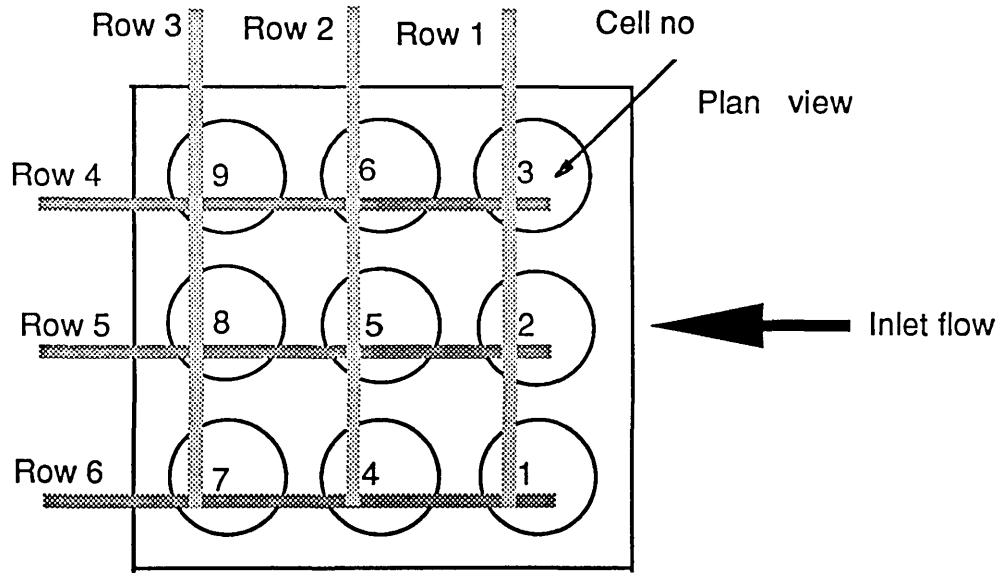

Fig. 4.21 Numbering scheme for cells and rows of multicell cyclone

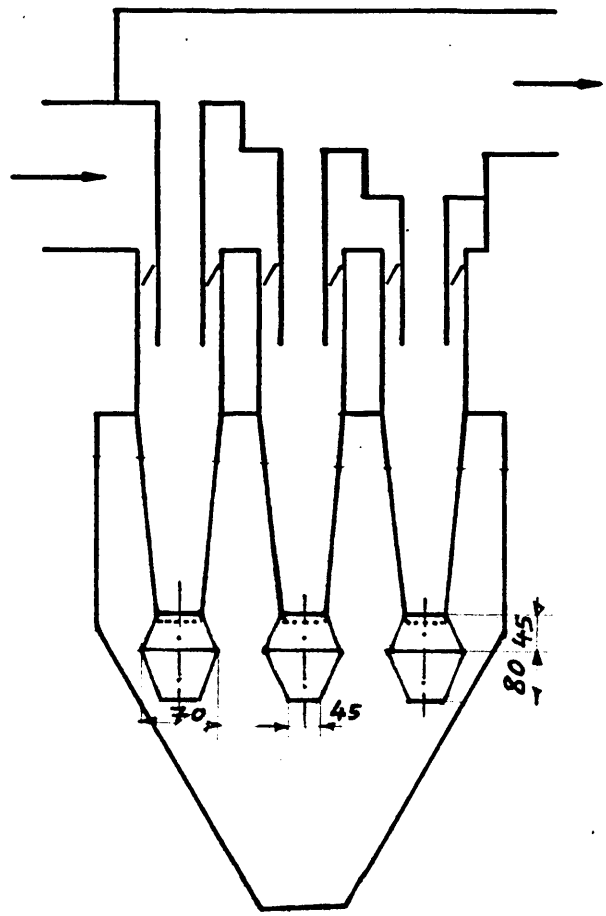

Fig. 4.22 Position and dimensions of cell sub-hoppers for cells flow distribution study

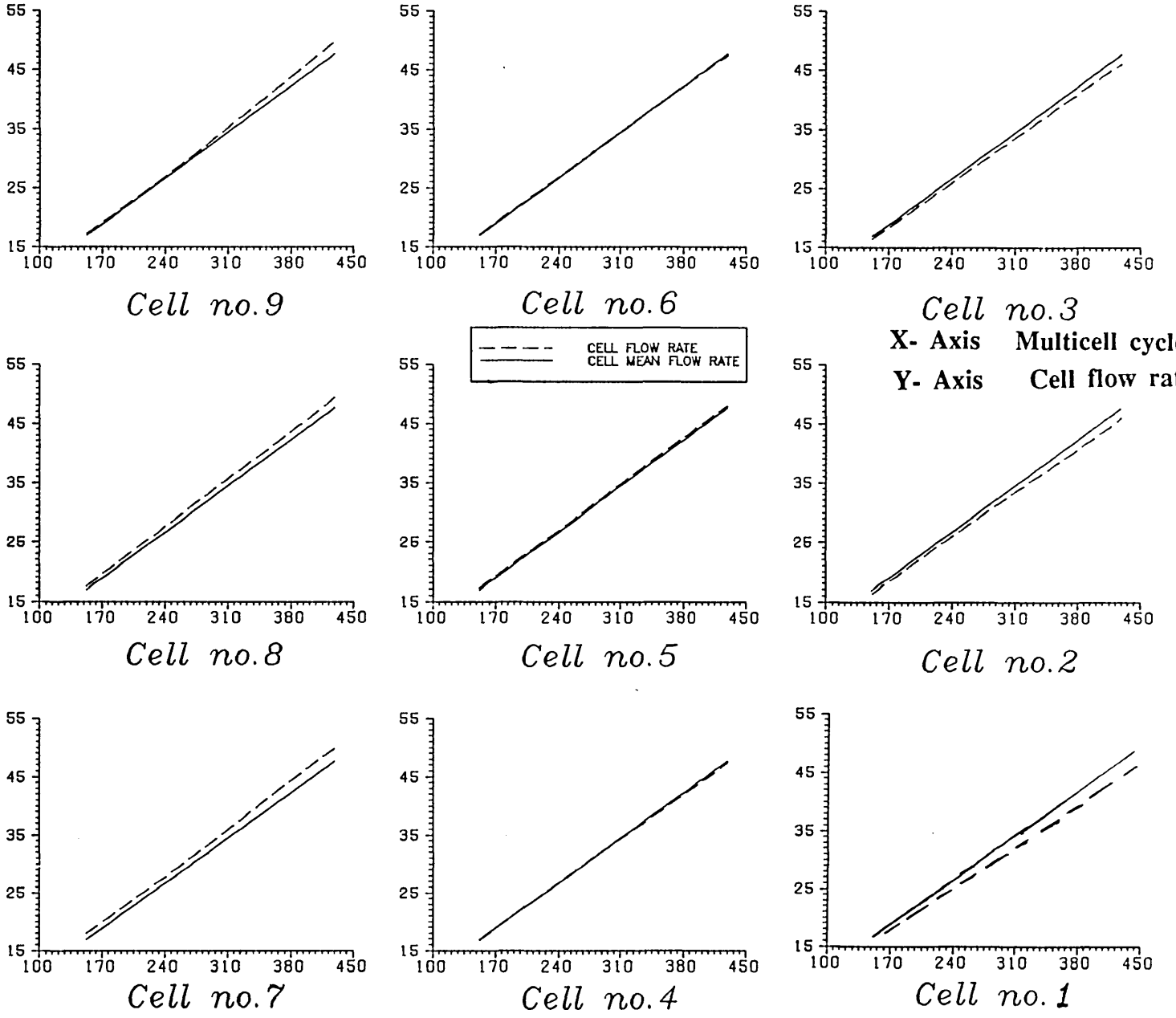

Fig. 4.23 Variation of cell flow rate with multicell cyclone flow rate

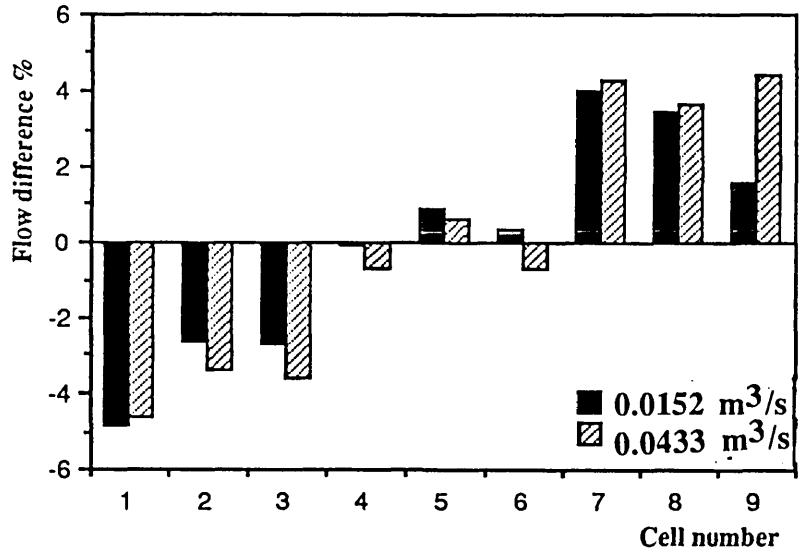

Fig. 4.24 Effect of cyclone flow rate on cell flow rate

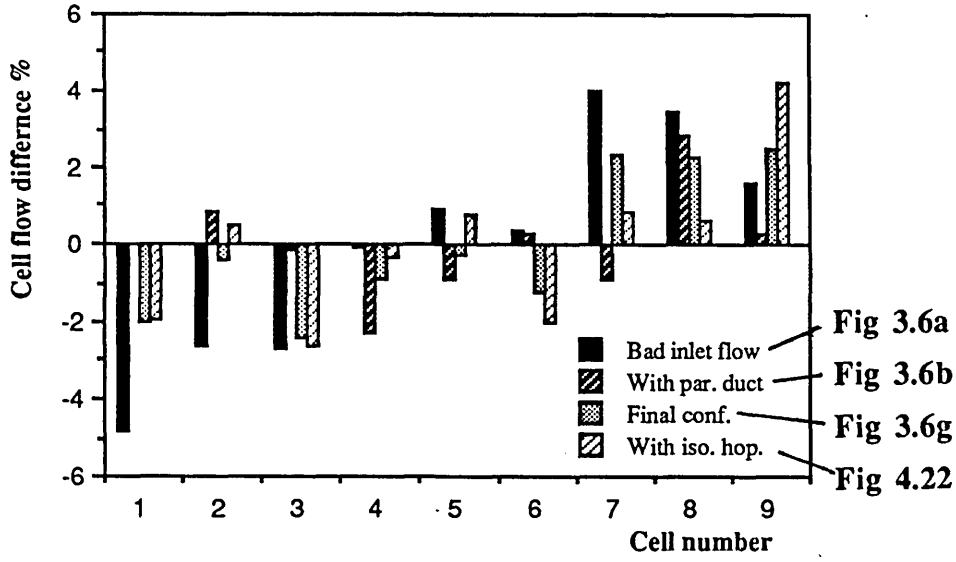

Fig. 4.25 Flow distribution between multicell cyclone's cells

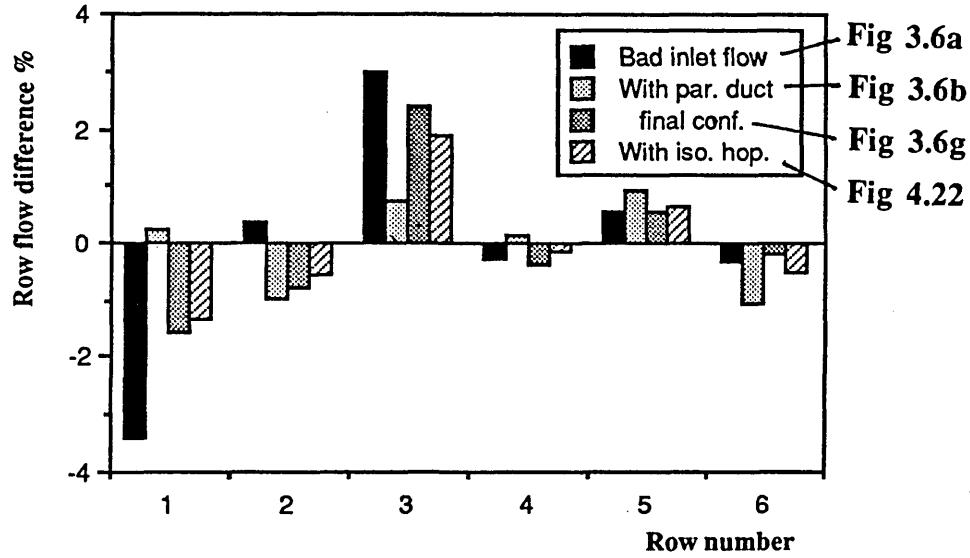

Fig. 4.26 Flow distribution between multicell cyclone's rows

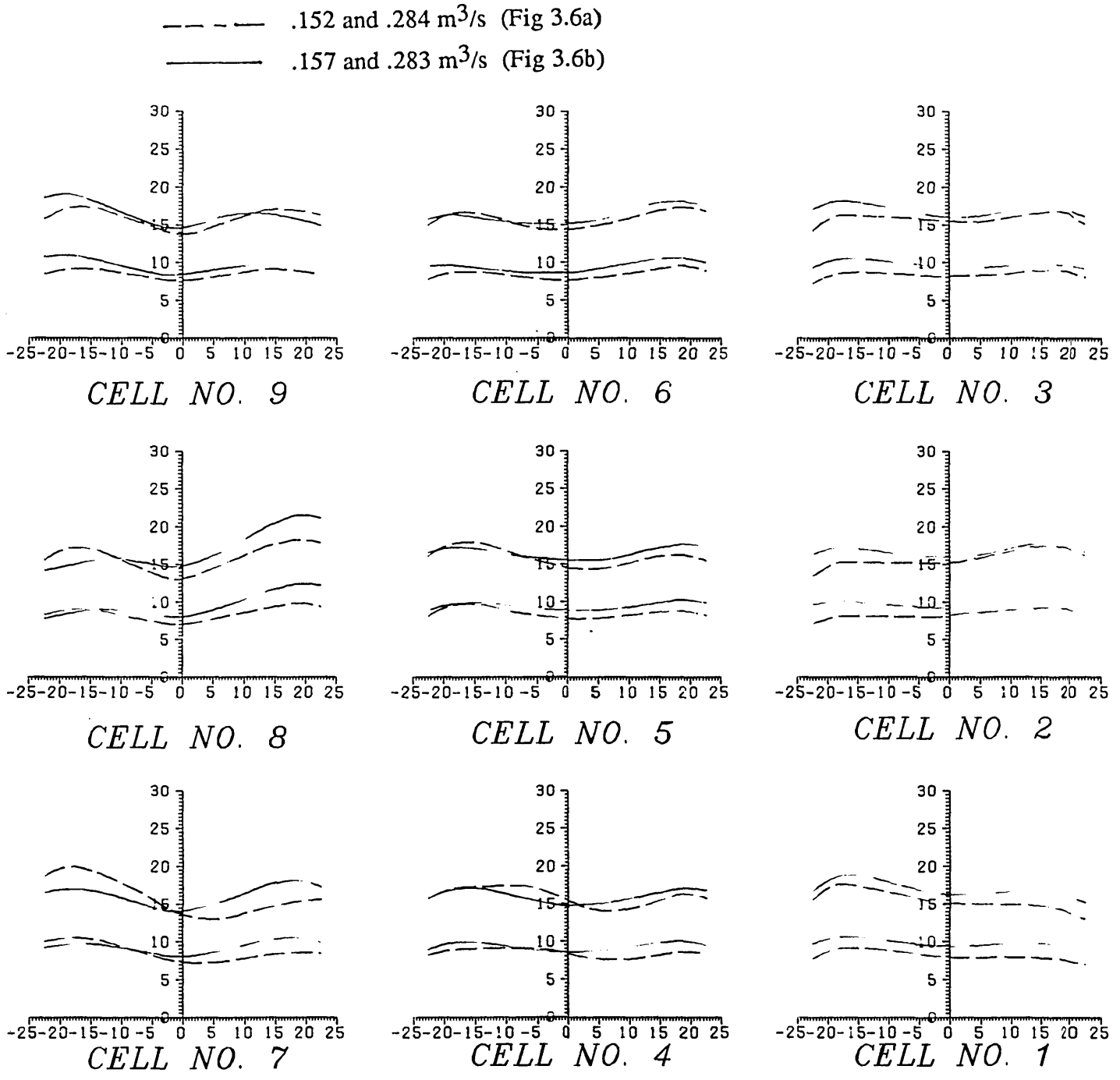

Fig. 4.27 Cell velocity profiles at various flow rates

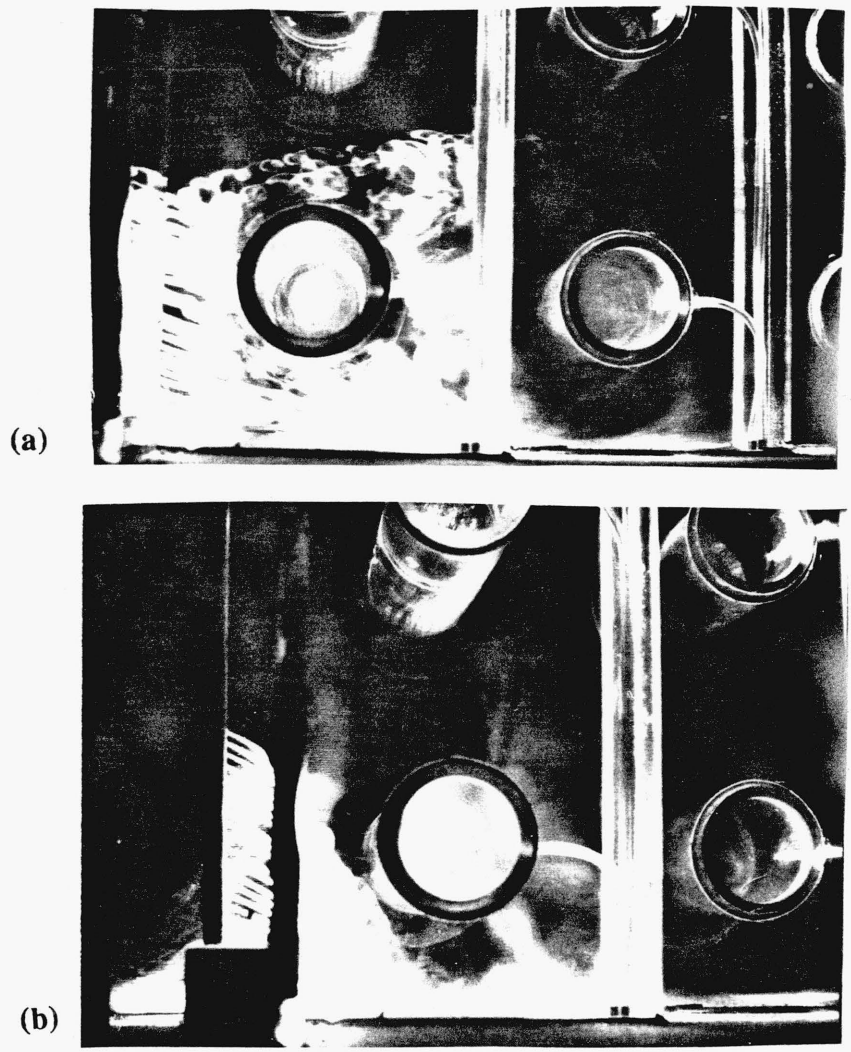

Fig. 4.28 **Unsteady behaviour of flow inside inlet manifold**

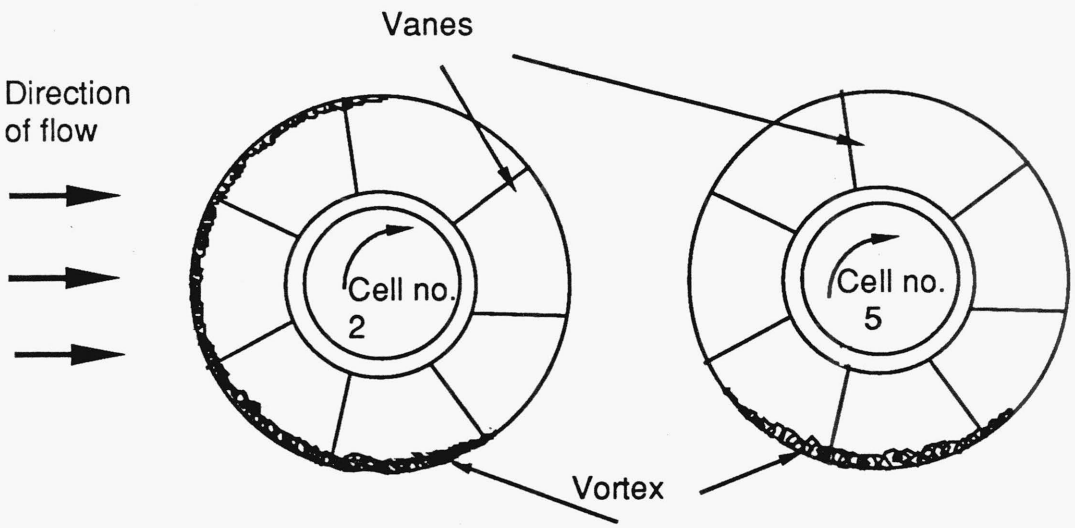

Fig. 4.29 **Formation of vortex at cell entry, above vanes**

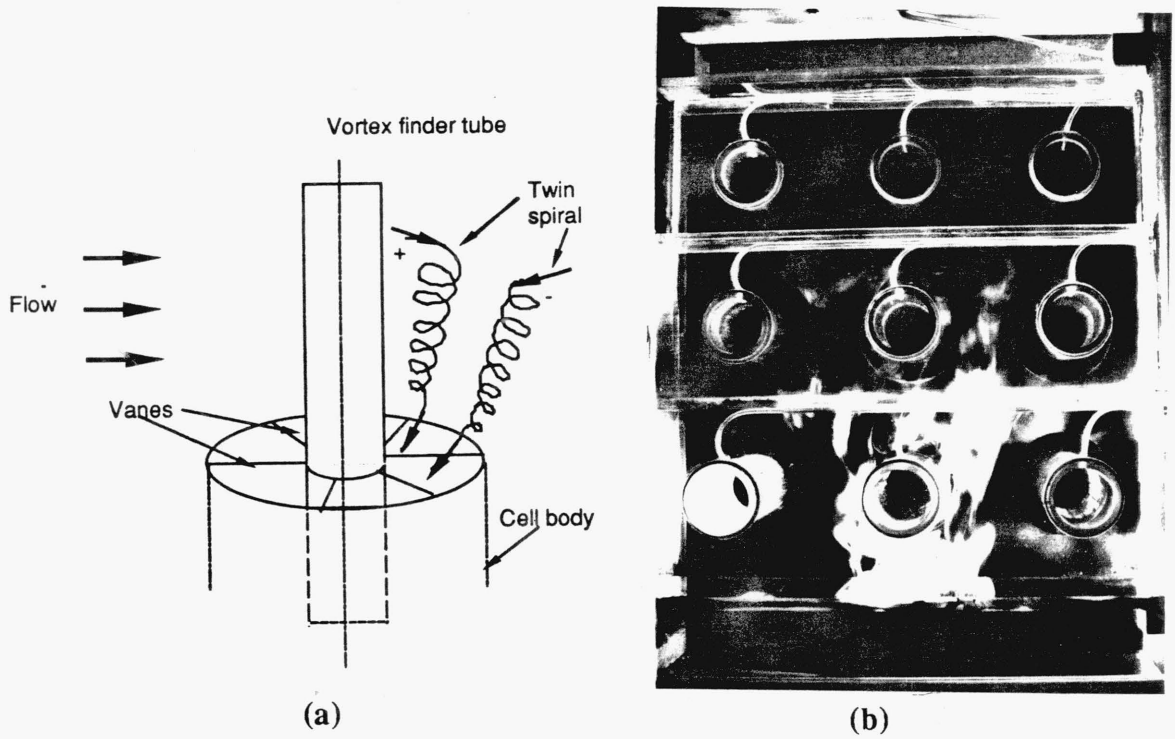

Fig. 4.30 Formation of wakes behind vortex finder tubes

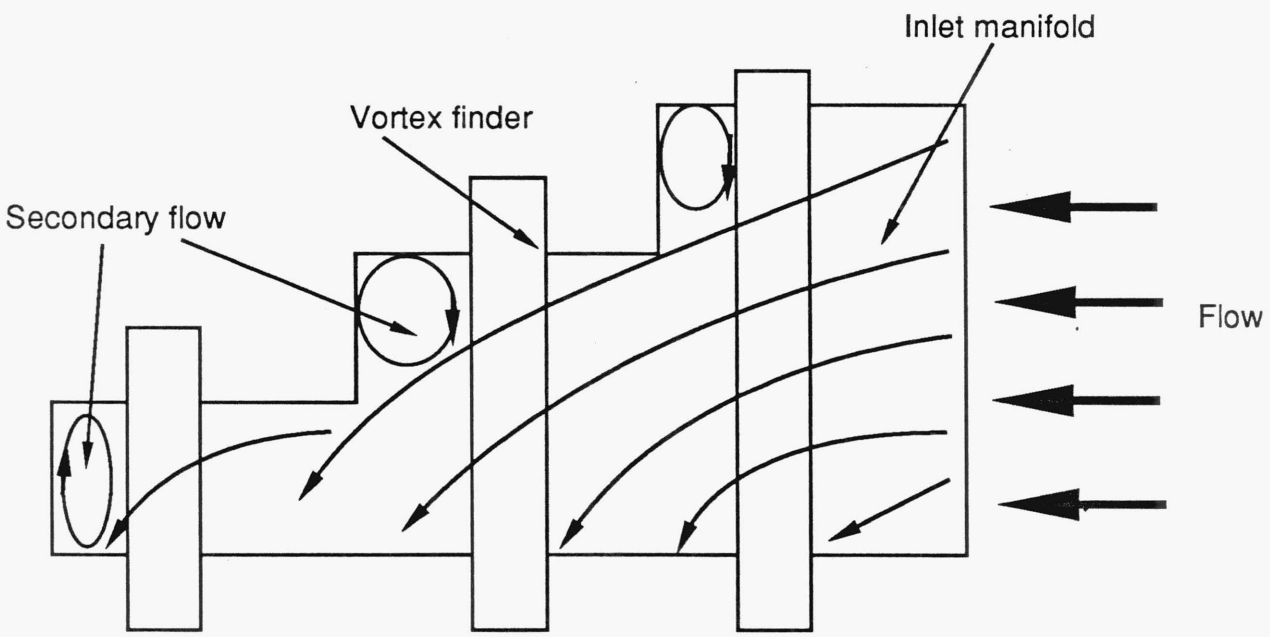

Fig. 4.31 Formation of secondary flow near stepped roof of multicell cyclone inlet manifold

Fig. 4.32 Top view of flow in outlet manifold, horizontal sheet illumination at roof level

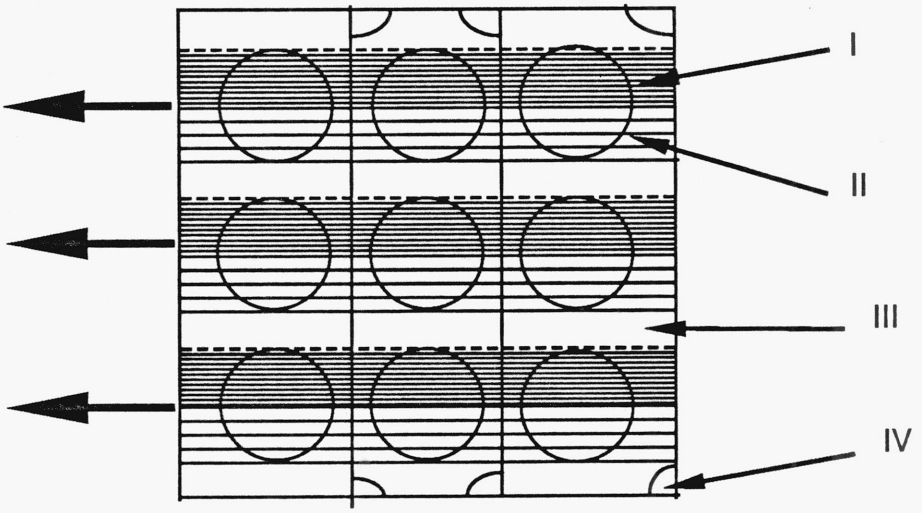

I - Region of very high turbulence (direction of swirl opposite to bulk flow)

II - Region of high turbulence (direction of swirl and bulk flow the same)

III- Region between swirl jets

IV- Secondary flow

Fig. 4.33 Cyclone outlet manifold flow characteristics

(a)

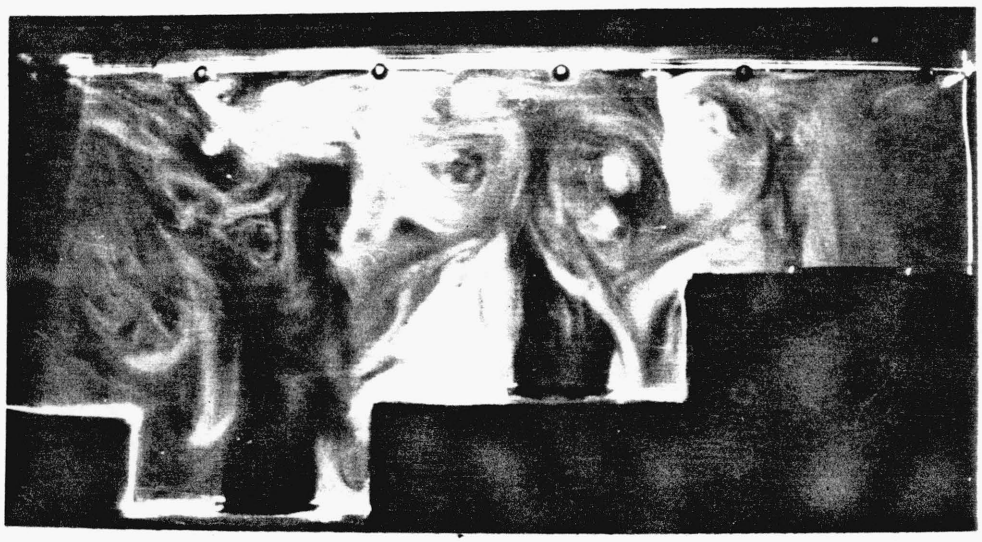

(cells No. 7, 4 and 1)

(b)

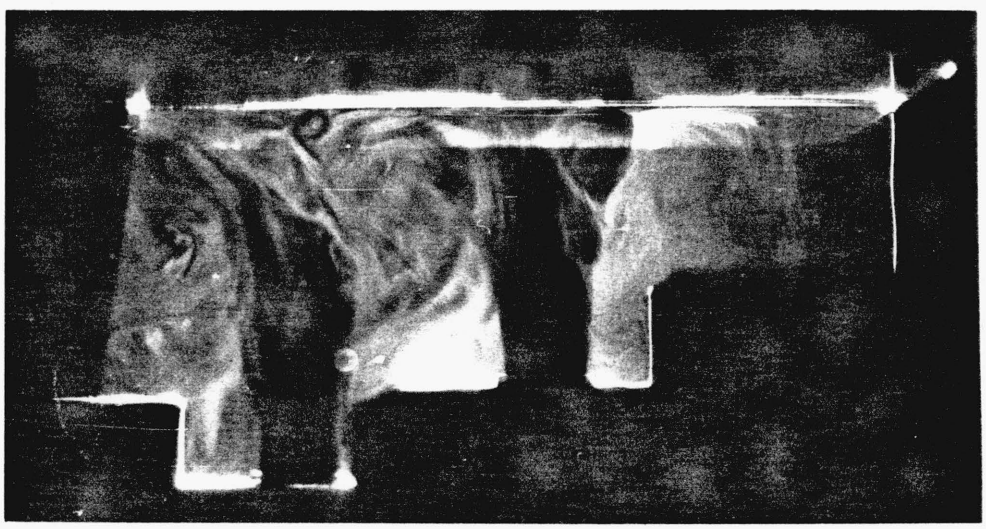

(cells No. 8, 5 and 2)

(c)

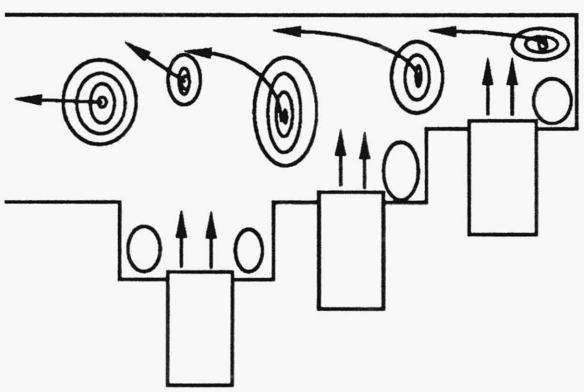

Fig. 4.34 Outlet manifold side view, vertical sheet illumination along line of cell centres

(a)

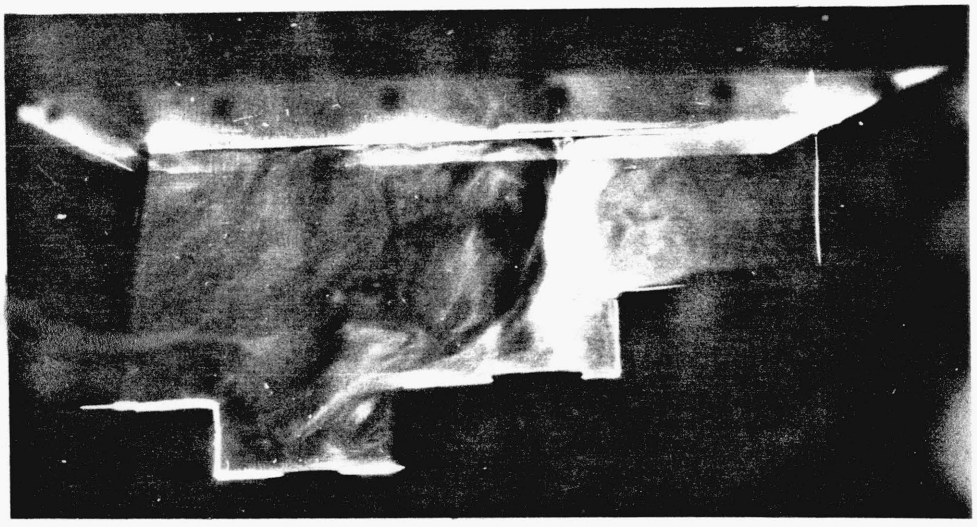

(b)

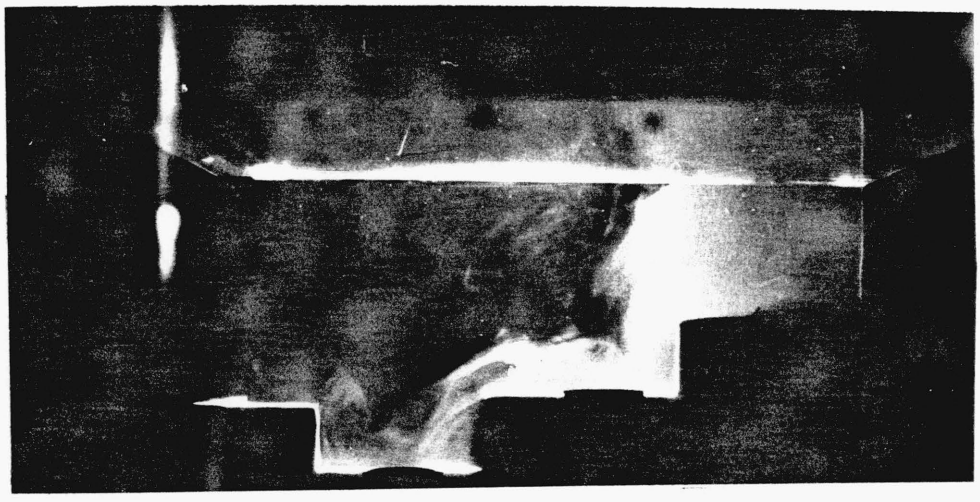

(c)

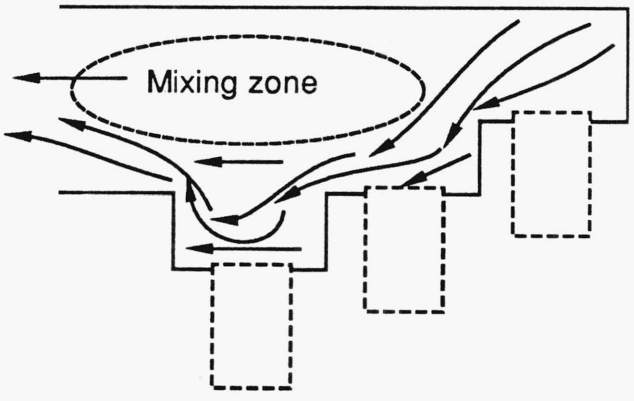

Fig. 4.35 Outlet manifold side view, vertical sheet illumination midway between cell centres

(a) Smoke-wire under cell No. 2

←

(b) Smoke-wire under cell No. 6

→

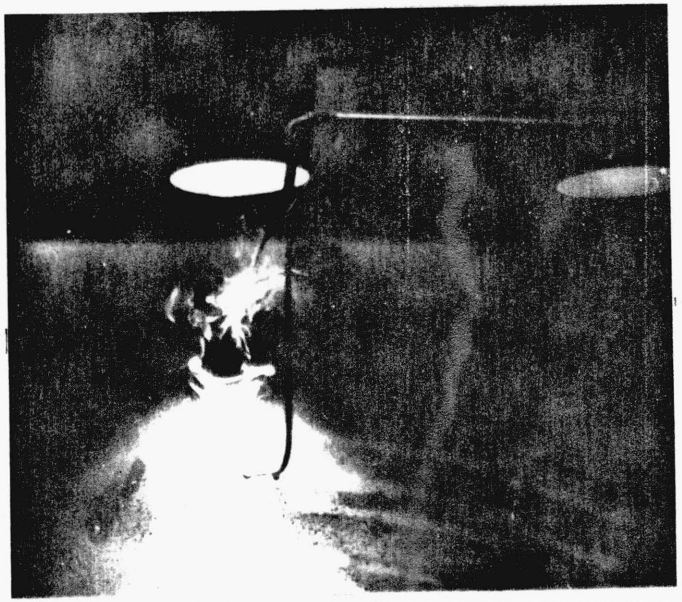

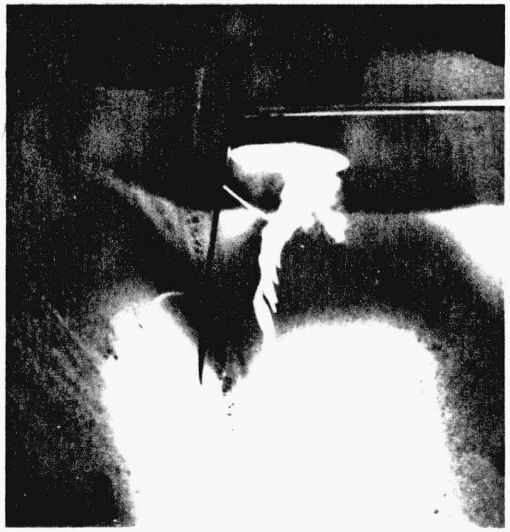

(c) Smoke-wire under cell No. 9

←

(d) Smoke-wire under cell No. 8

→

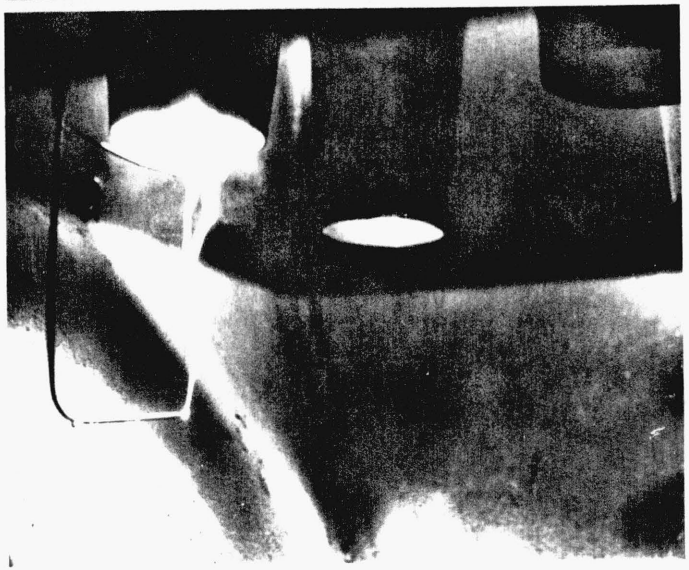

Fig. 4.36 Hopper visualization by smoke wire system

(a) Tuft under cell No. 3 (b) Tuft under cell No. 9

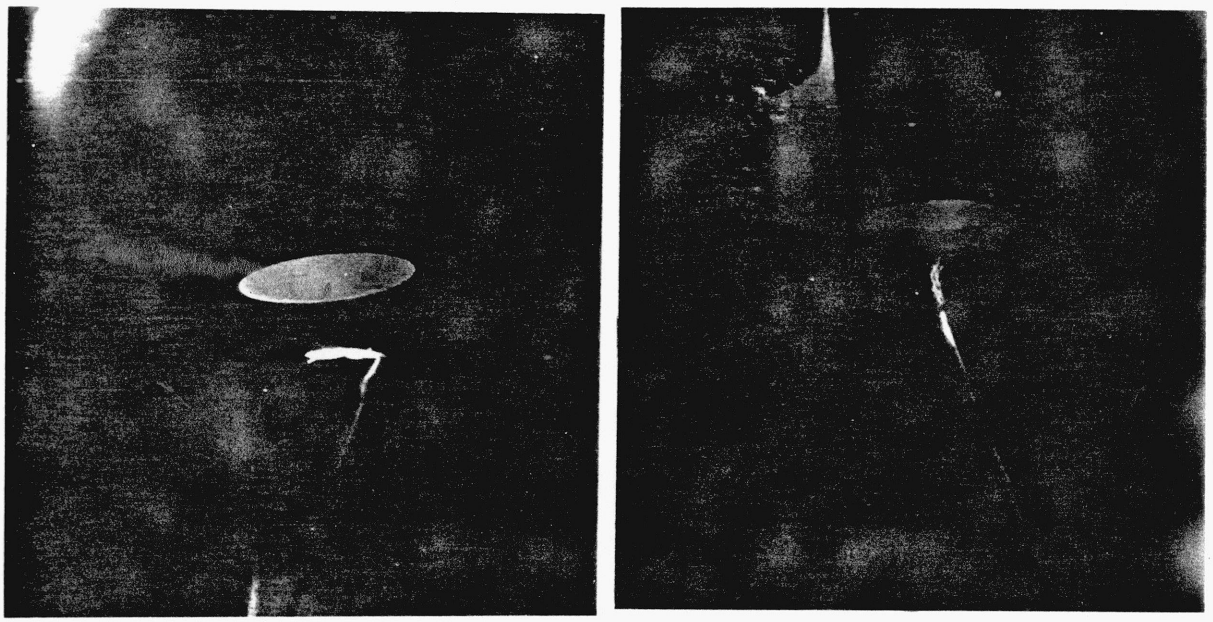

Fig. 4.37 Hopper visualization by tufts

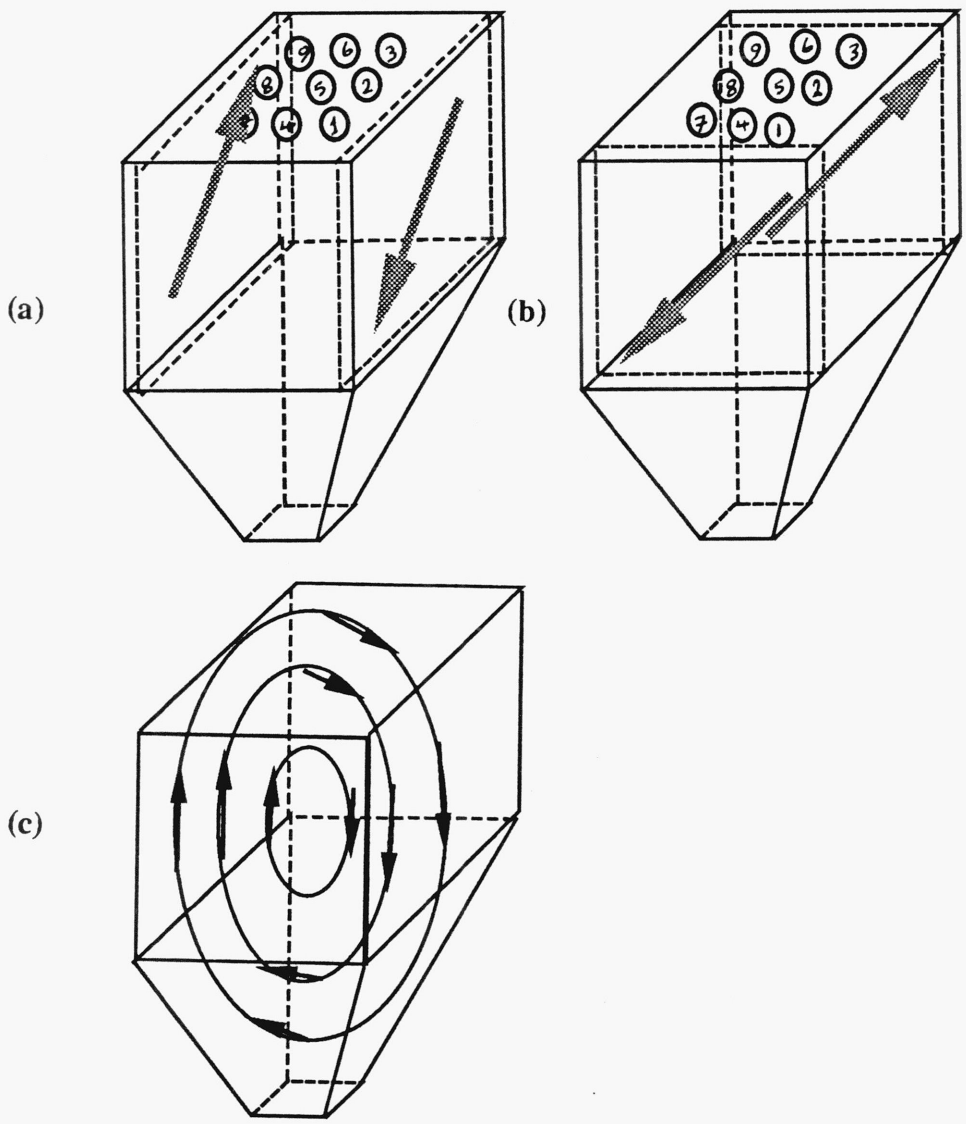

Fig. 4.38 Schematic of hopper flow circulation pattern

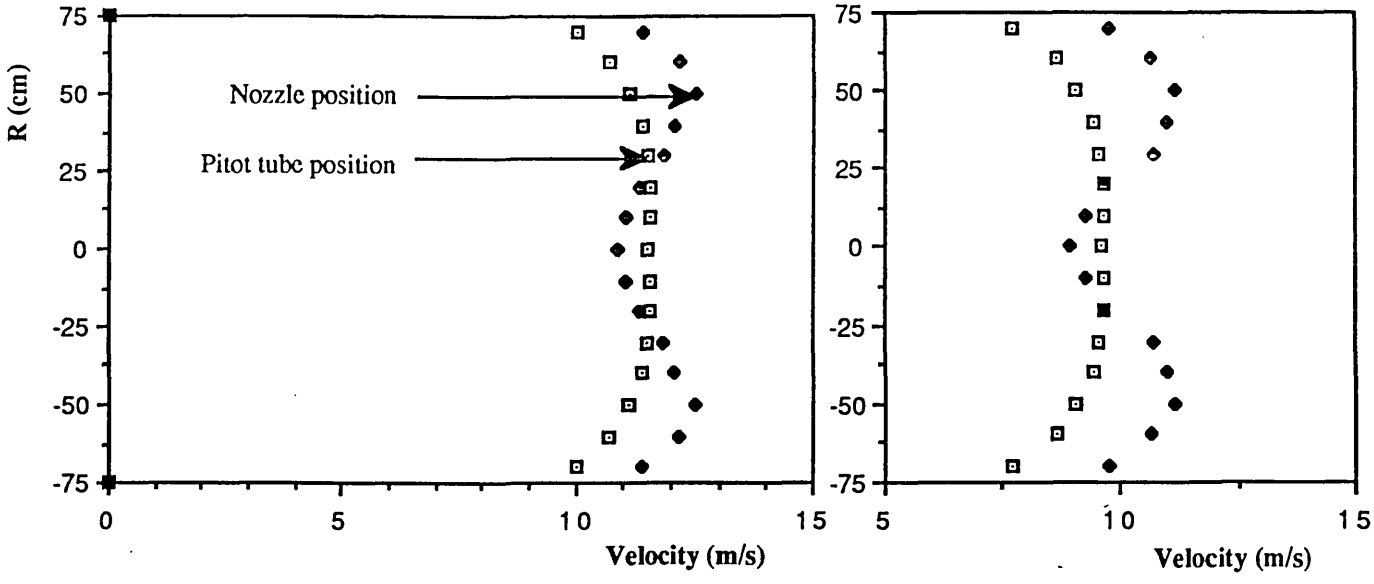

(a) For sampling system after cyclone (b) For sampling system before cyclone

Fig. 4.39 Velocity profiles at pitot tube and nozzle positions in sampling sections

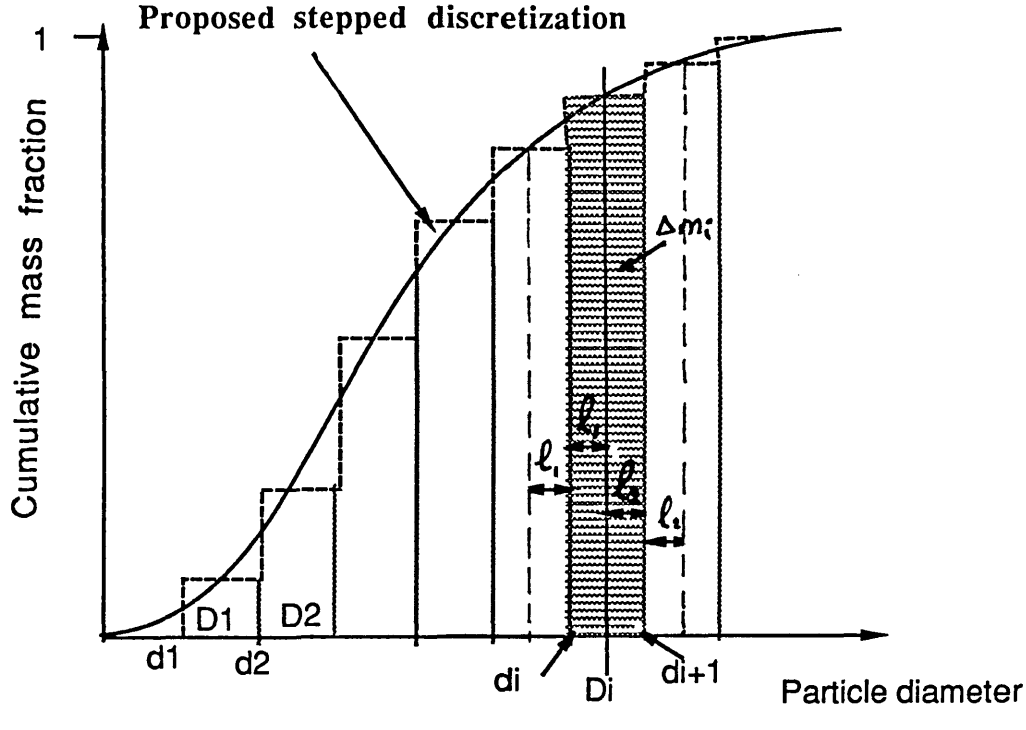

Fig. 4.40 Typical Rosin-Rammler size distribution curve and discretization

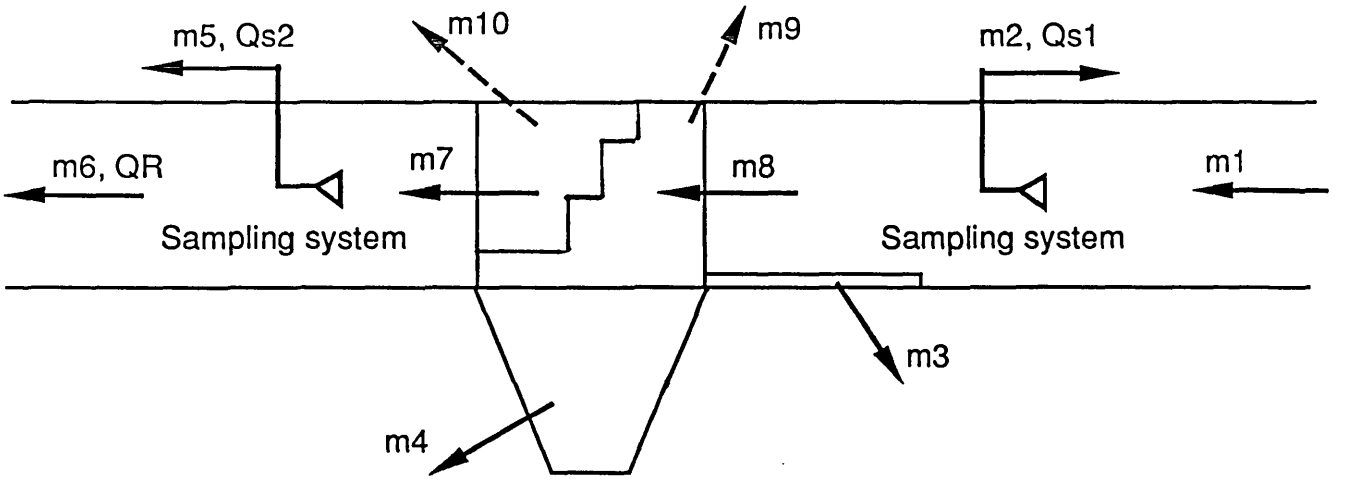

(a) Mass balance diagram of multicell cyclone

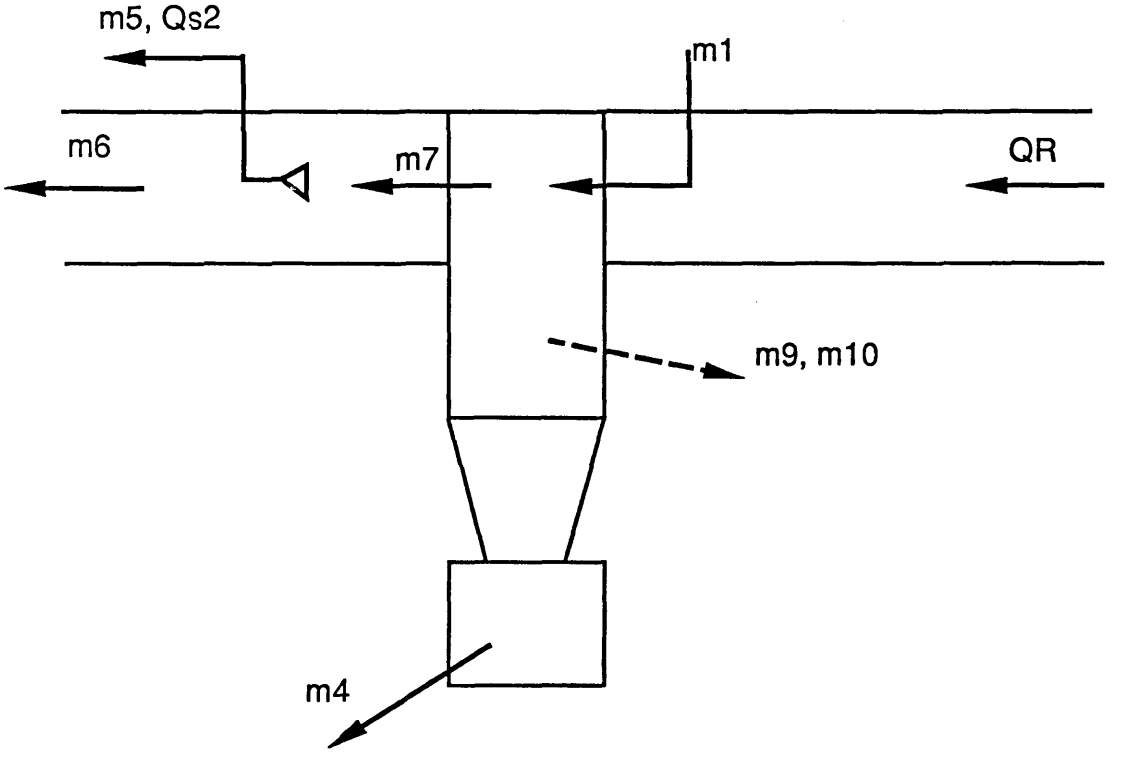

(b) Mass balance diagram of one-cell cyclone

Fig. 4.41 Cyclone mass balance diagrams

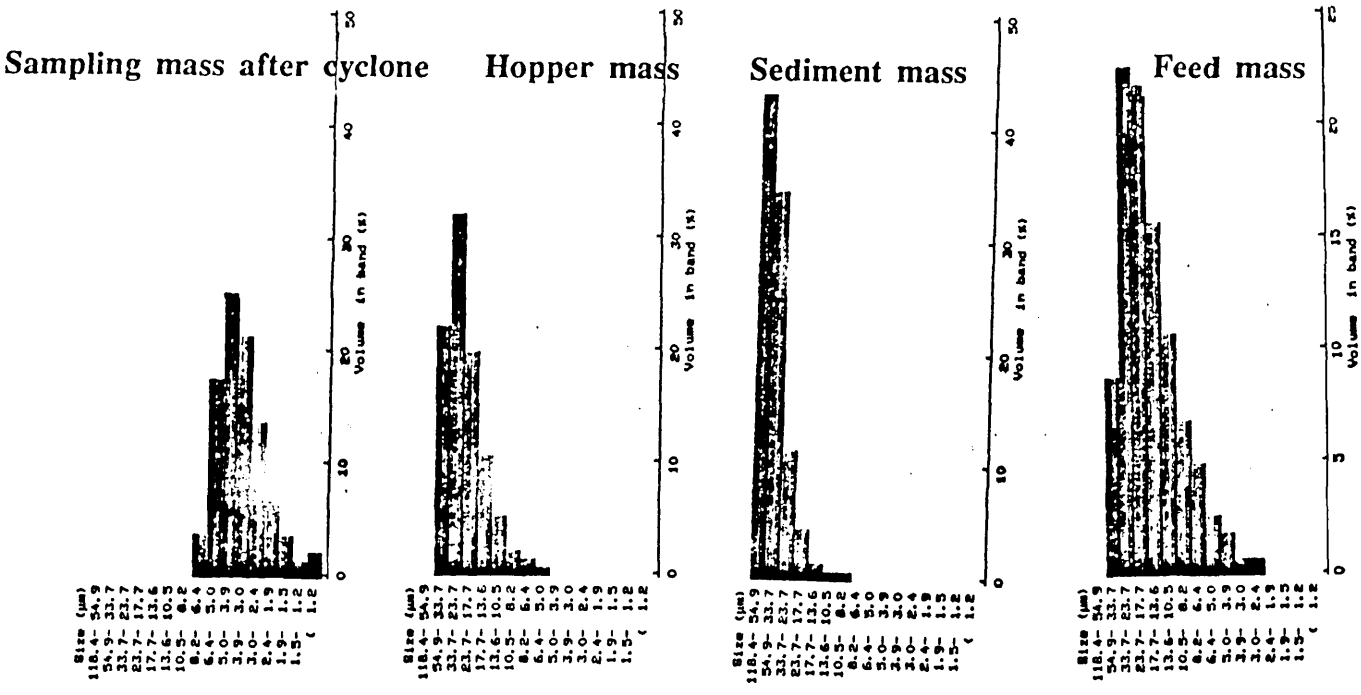

(a) Run with fuller's earth

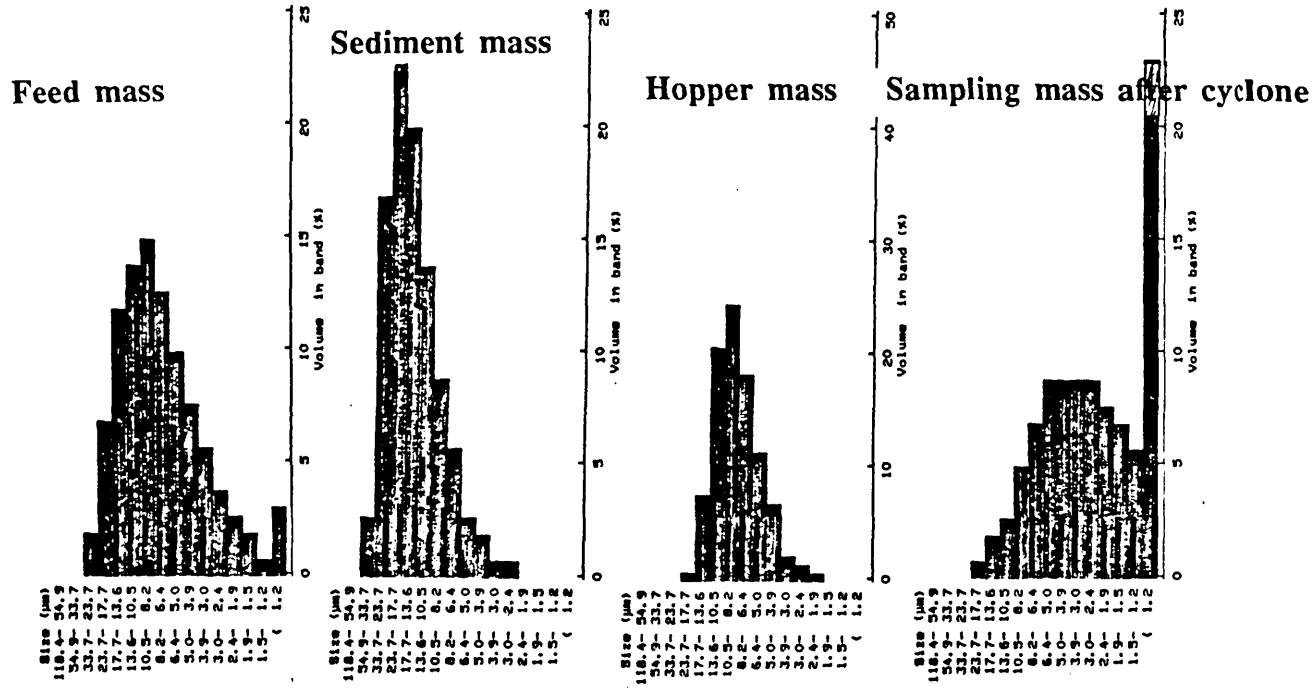

(b) Run with Syenex-40

Fig. 4.42 Histogram of size distribution of colleted samples from different parts of multicell cyclone after efficiency test

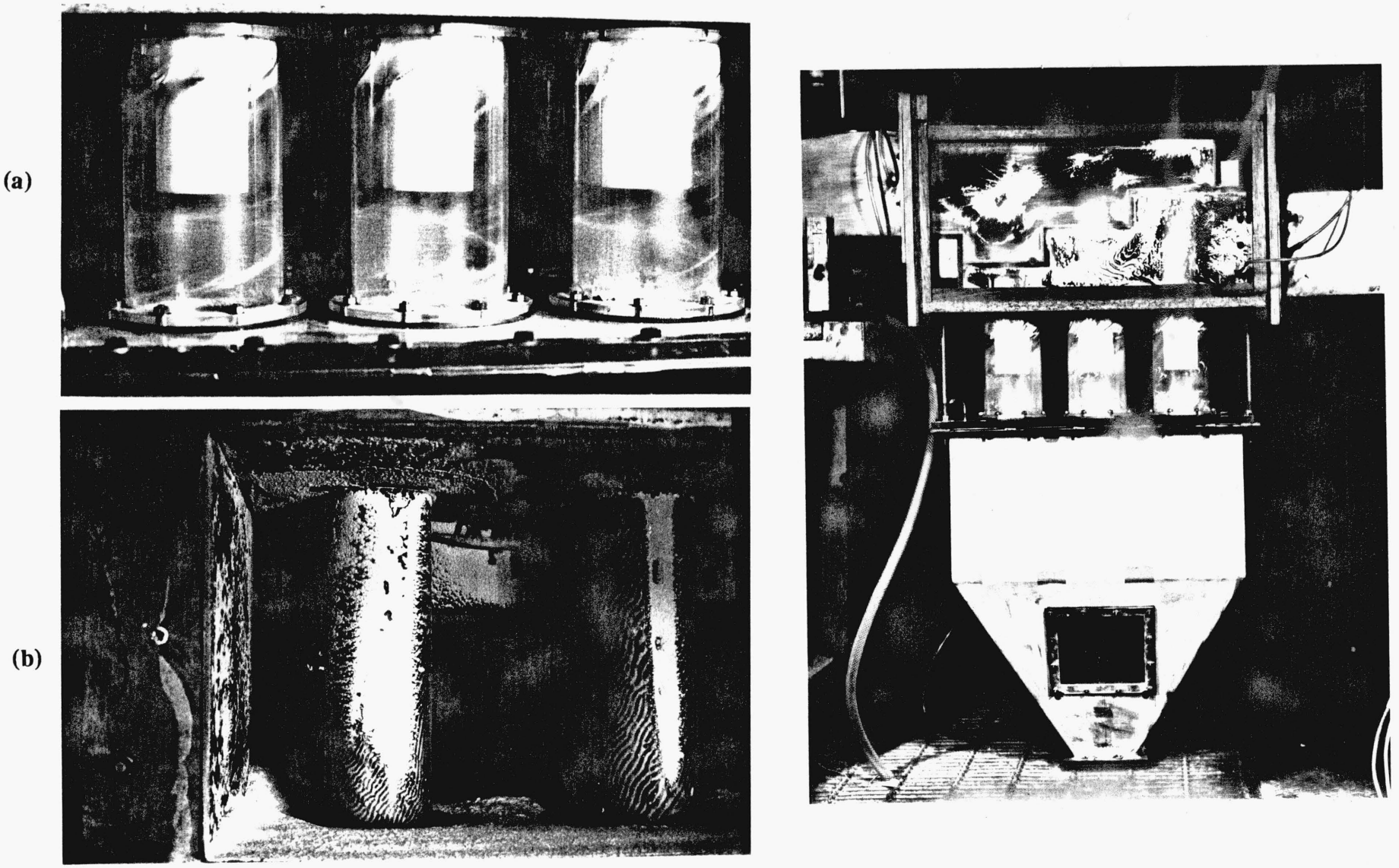

Fig. 4.43 Multicell cyclone cell dust flow patterns while running (a) and dust deposits in manifolds after several runs (b&c)

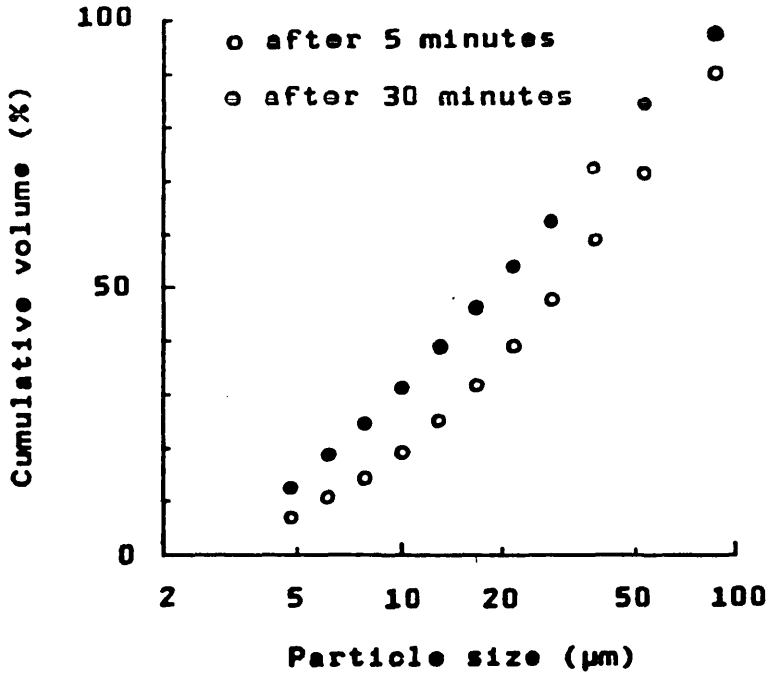

Fig. 4.44 Size distribution (Malvern 3600) of fuller's earth sample in continuously-stirred water suspension

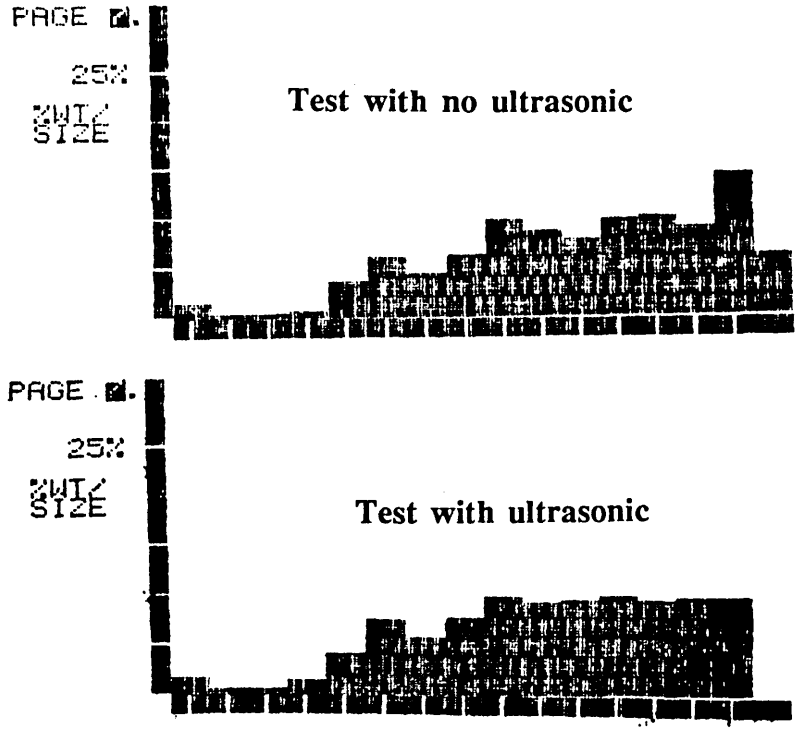

Fig. 4.45 Effect of using ultrasonic stirring system on Pozzolan size distribution (Malvern 3600, water suspension)

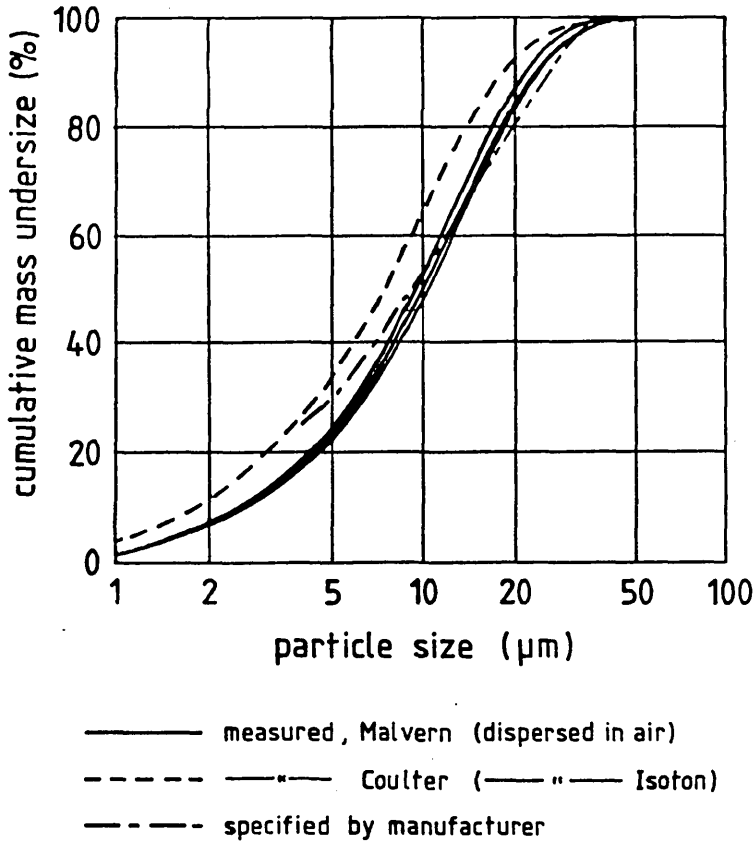

Fig. 4.46 Comparison of Malvern 2600 and Coulter size distribution measurements of samples of Syenex-40 test dust

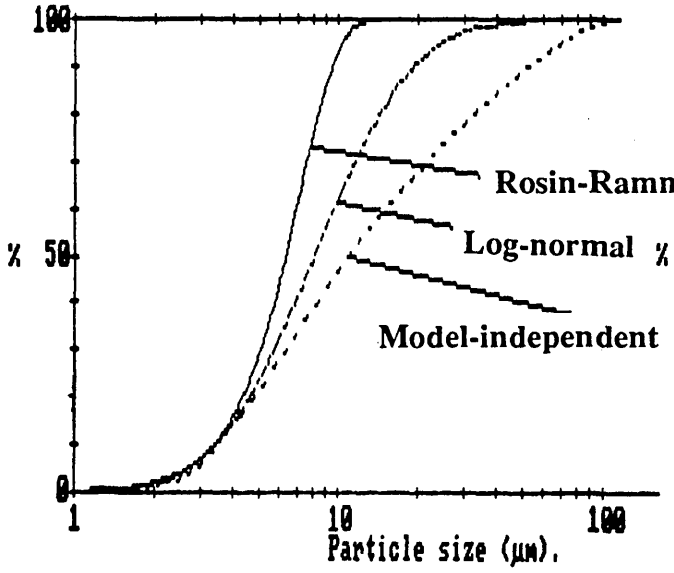

Fig. 4.47 Effect of choosing model-mode on Malvern 2600 size distribution of a pulverized fuel ash sample

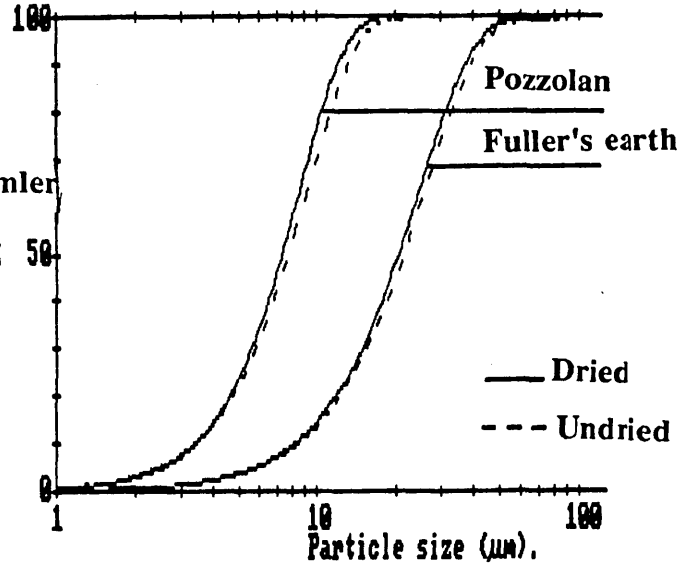

Fig. 4.48 Effect of dust humidity on size distribution of fuller's earth and Pozzolan

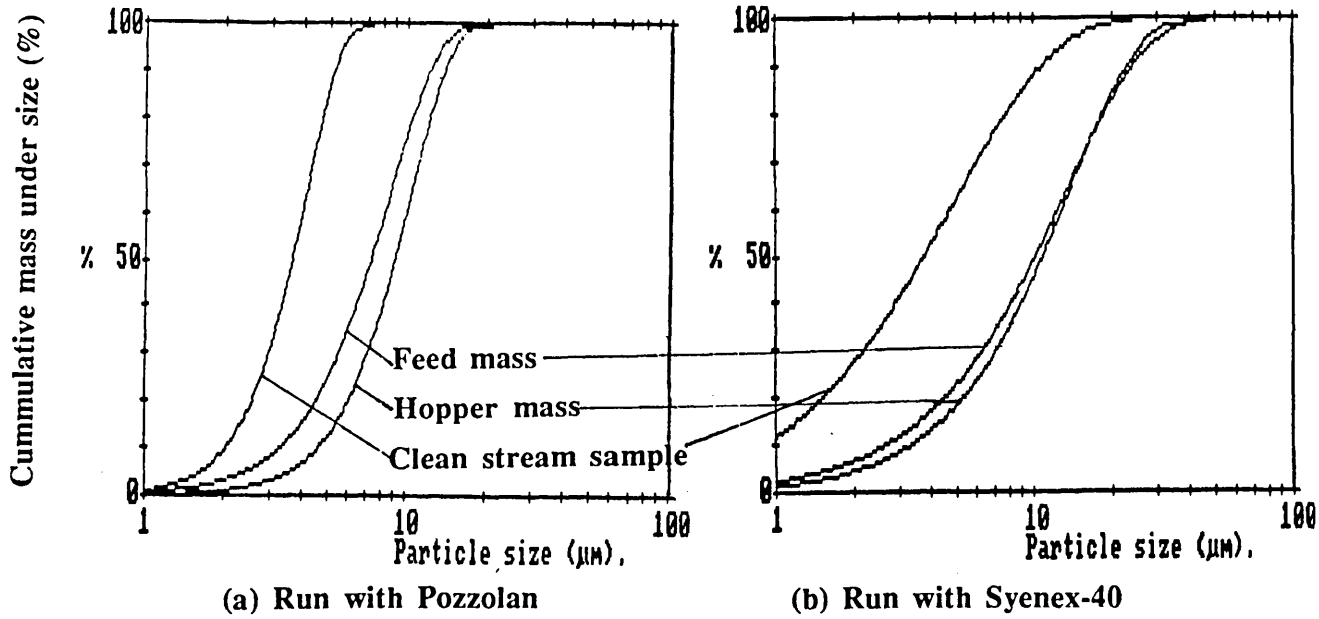

(a) Run with Pozzolan (b) Run with Syenex-40

Fig. 4.49 Size distribution of feed, hopper and clean-stream samples for one-cell cyclone

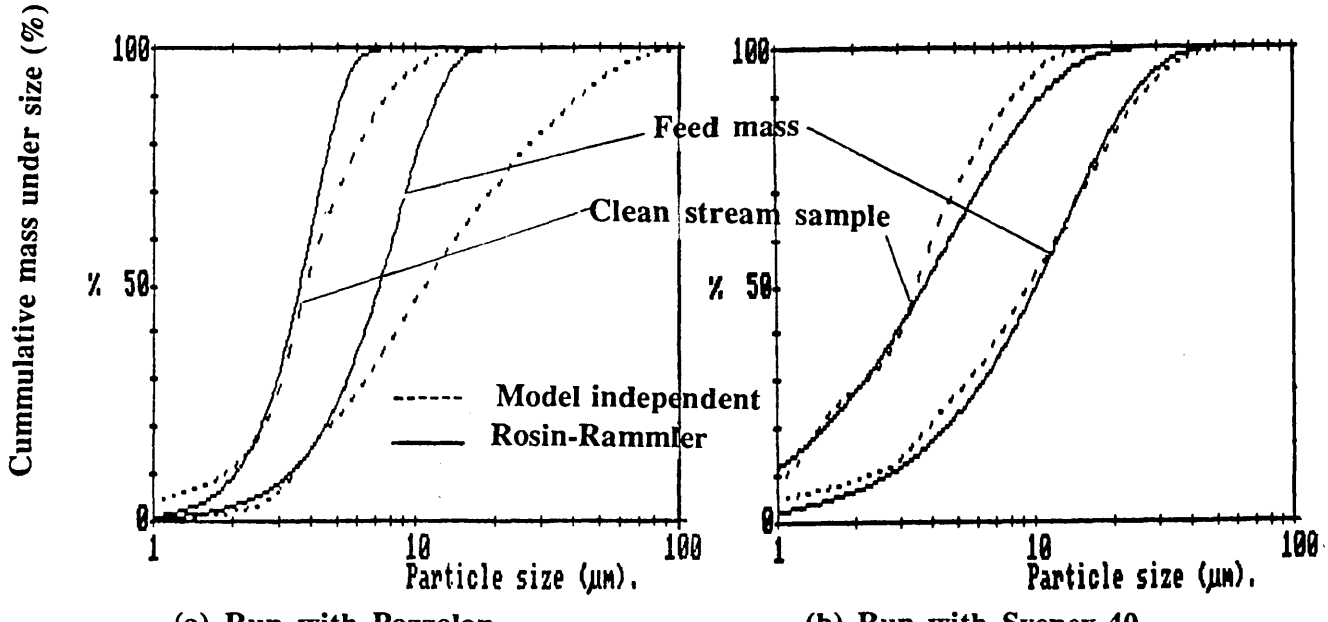

(a) Run with Pozzolan (b) Run with Syenex-40

Fig. 4.50 Comparison of size distributions of feed mass and clean-stream sample mass from Rosin-Rammler and model-independent fits to the same scattered light intensity distribution

i = Feed mass ii = Hopper mass iii= Clean stream sample

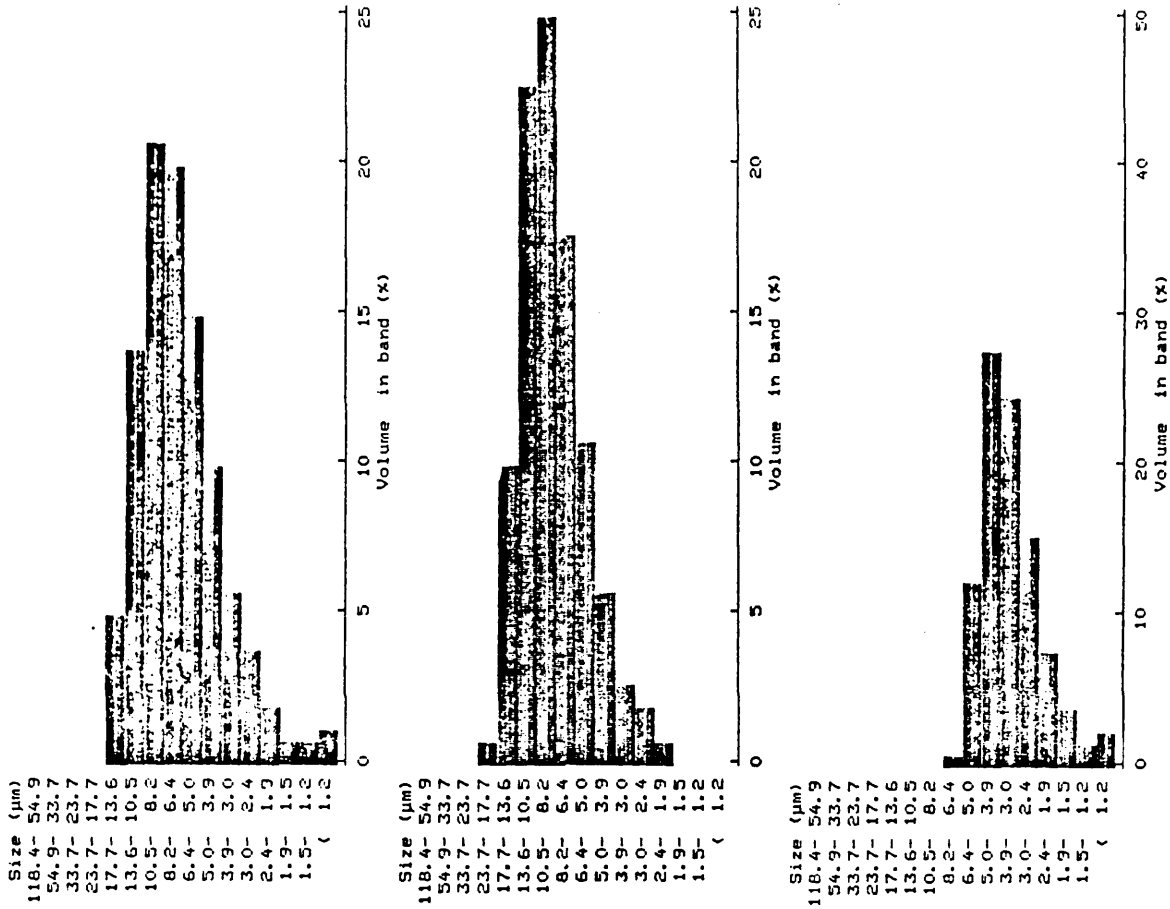

a) Run with Pozzolan

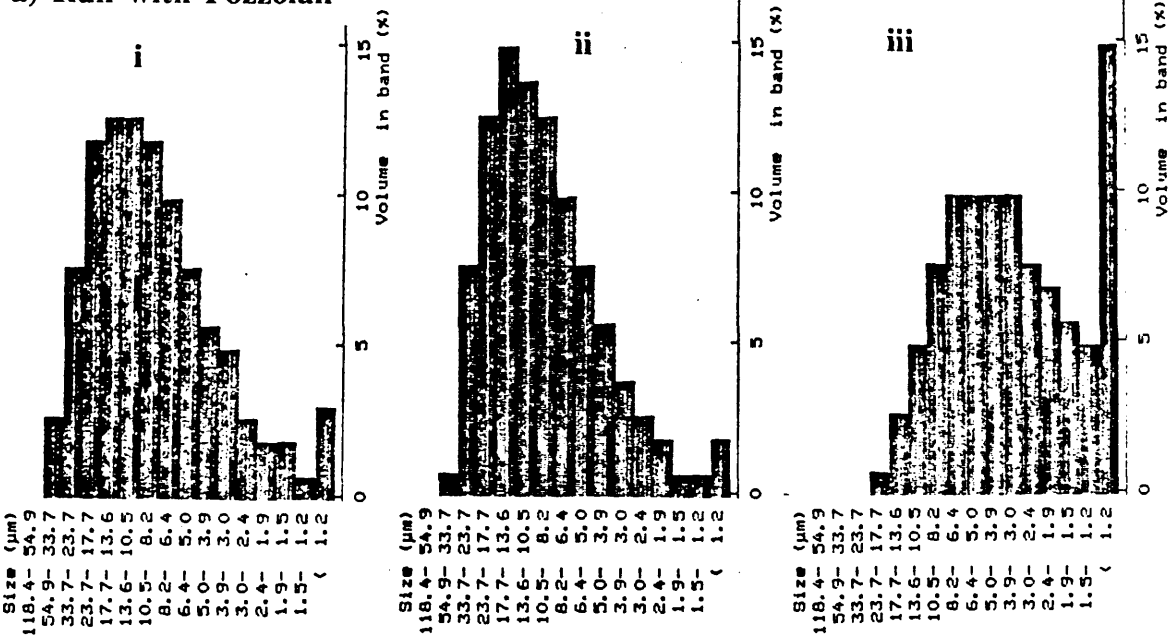

b) Run with Syenex-40

Fig. 4.51 Histogram of size distribution of collected samples from different parts of one-cell cyclone after efficiency test

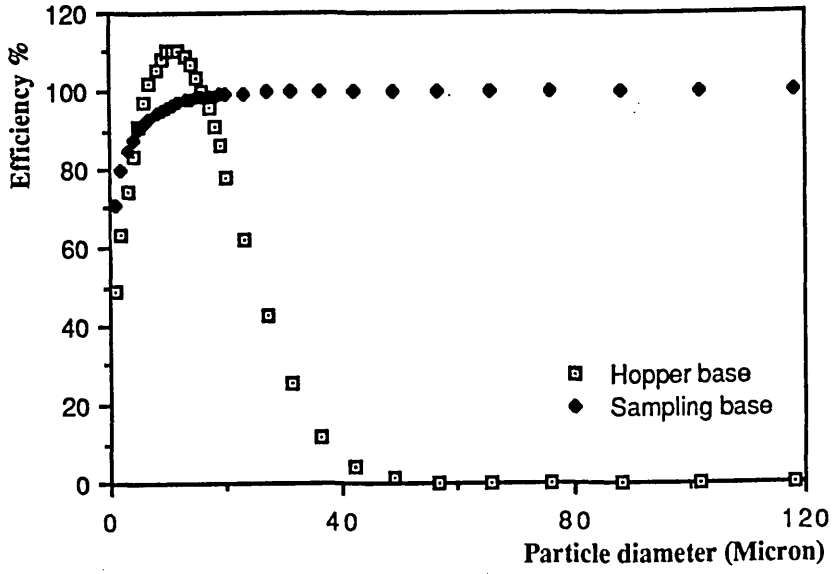

Fig. 4.52 One-cell grade efficiency curve with Syenex-40

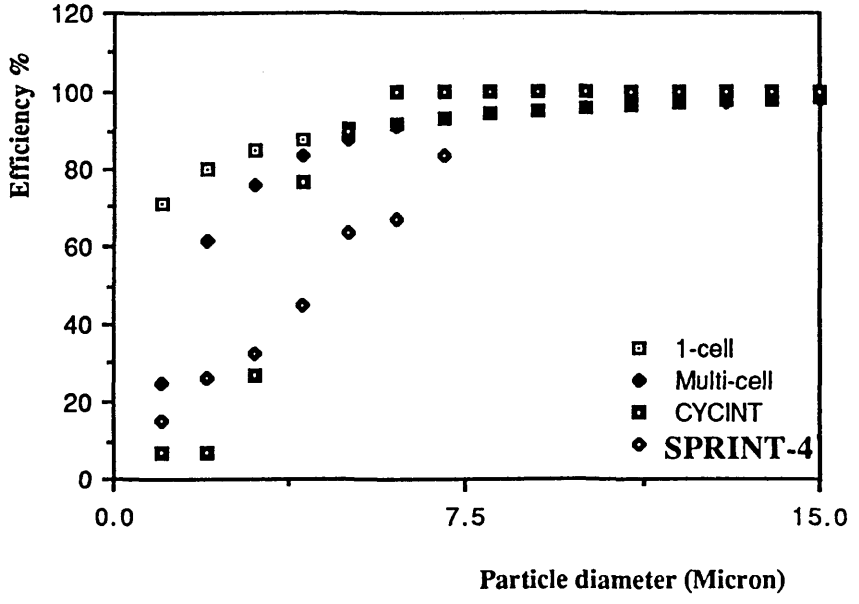

Fig. 4.53 One & Multicell Cyclone grade efficiency with Syenex 40

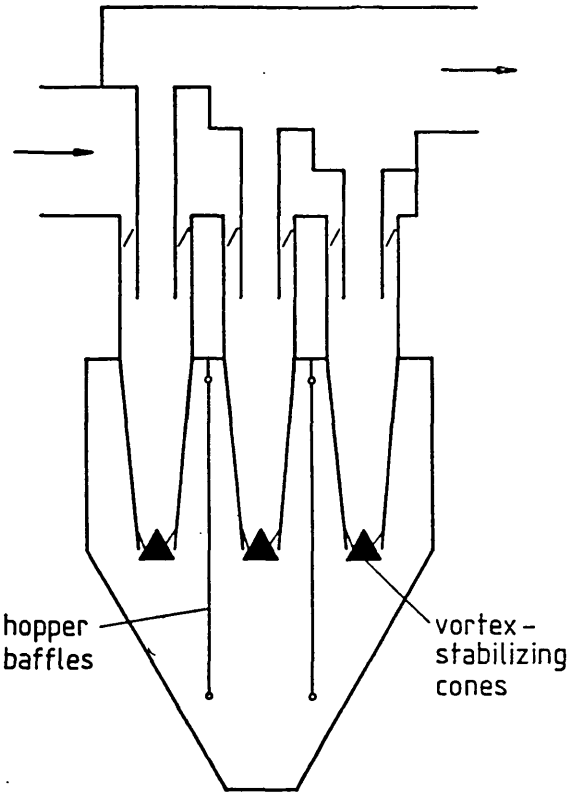

Fig. 4.54 Locations of vortex-stabilizing cones and hopper baffles (not used simultaneously)

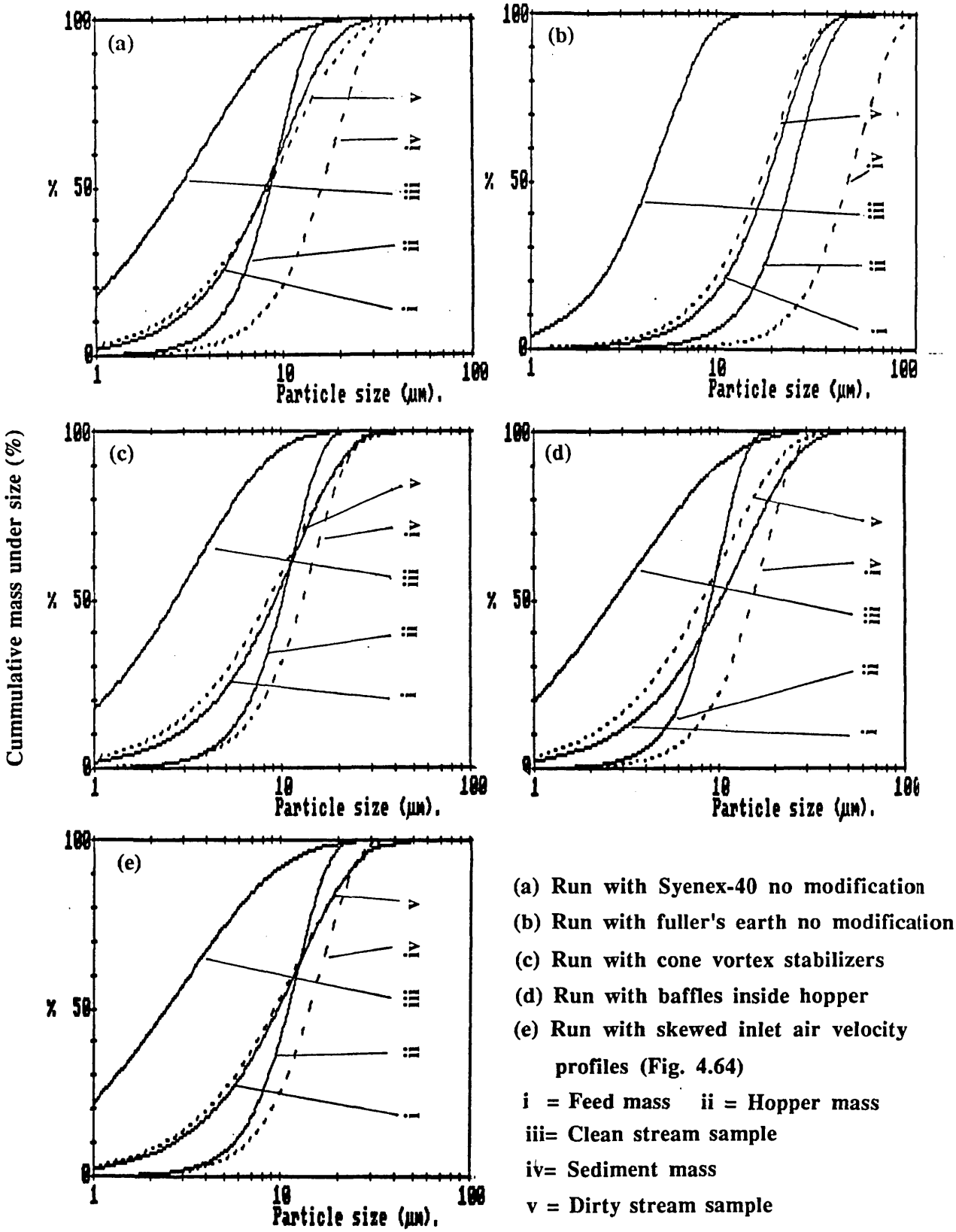

(a) Run with Syenex-40 no modification
(b) Run with fuller's earth no modification
(c) Run with cone vortex stabilizers
(d) Run with baffles inside hopper
(e) Run with skewed inlet air velocity profiles (Fig. 4.64)

i = Feed mass ii = Hopper mass
iii= Clean stream sample
iv= Sediment mass
v = Dirty stream sample

Fig. 4.55 Size distributions of feed mass, hopper mass, clean and dirty gas samples and sediment mass in multicell cyclone efficiency tests

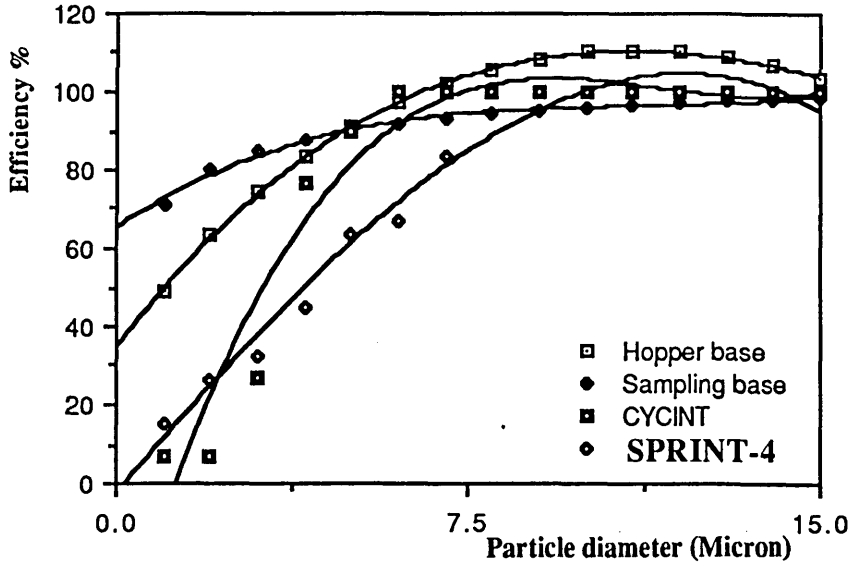

Fig. 4.56 One-cell Cyclone grade efficiency with Syenex-40

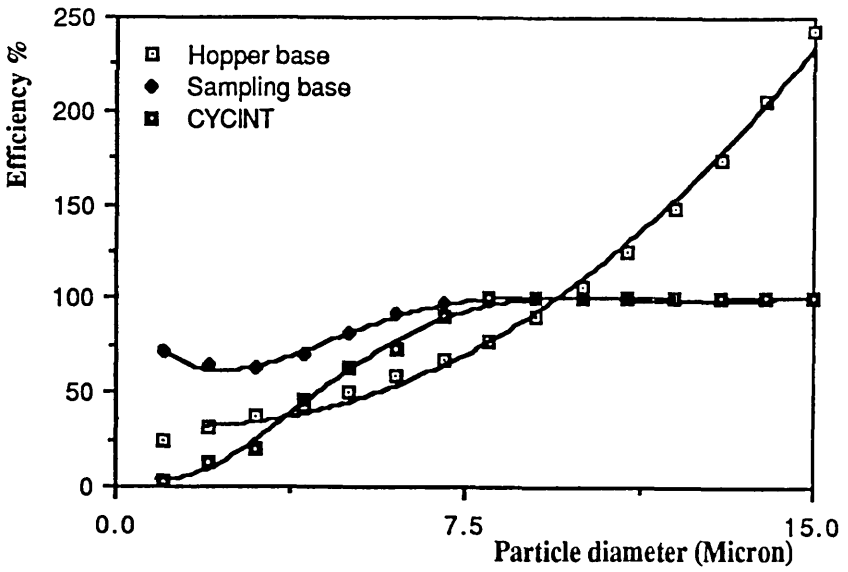

Fig. 4.57 One-cell Cyclone grade efficiency with pozzolan

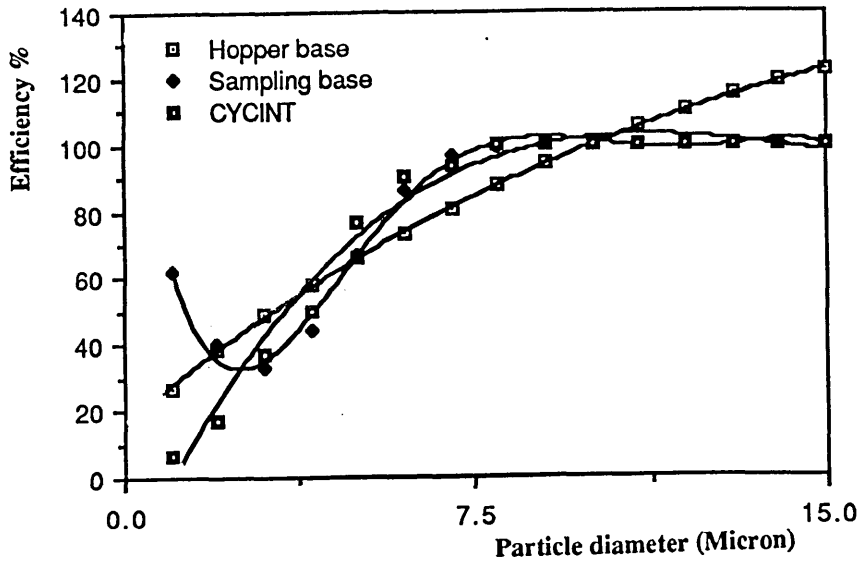

Fig. 4.58 One-cell Cyclone grade efficiency with fuller's earth

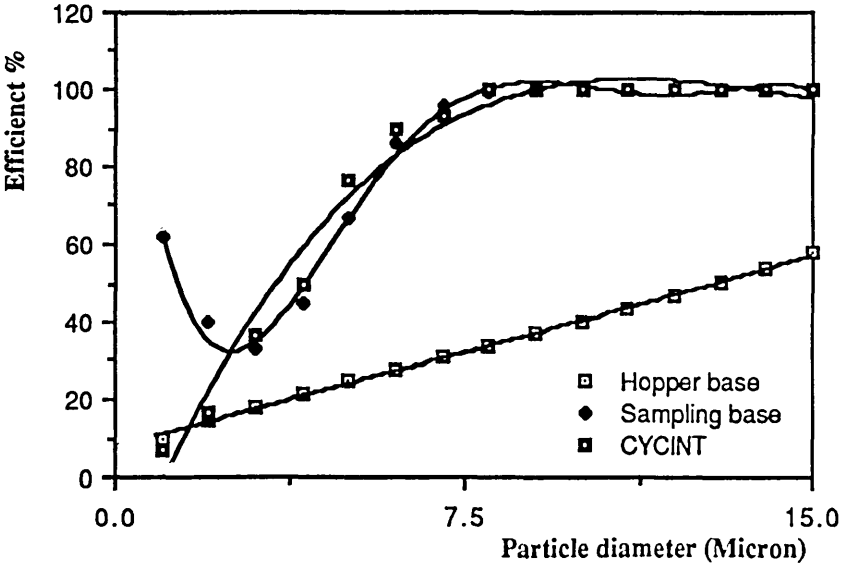

Fig. 4.59 Multicell Cyclone grade efficiency with fuller's earth

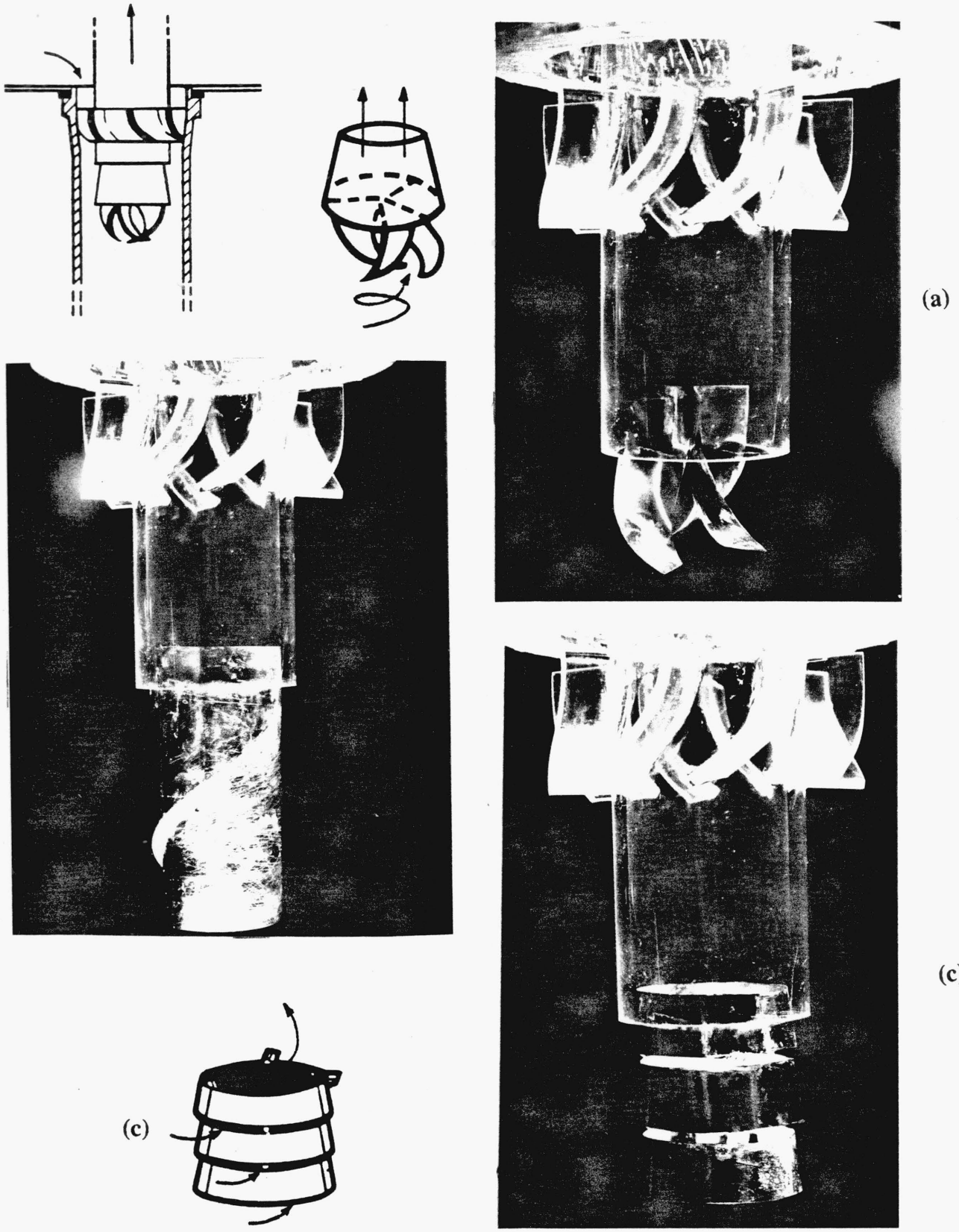

Fig. 4.60 Clean-gas outlet tube extension devices tested

(a) De-swirling vanes

(b) Spiral-slotted extension

(c) Triple cone

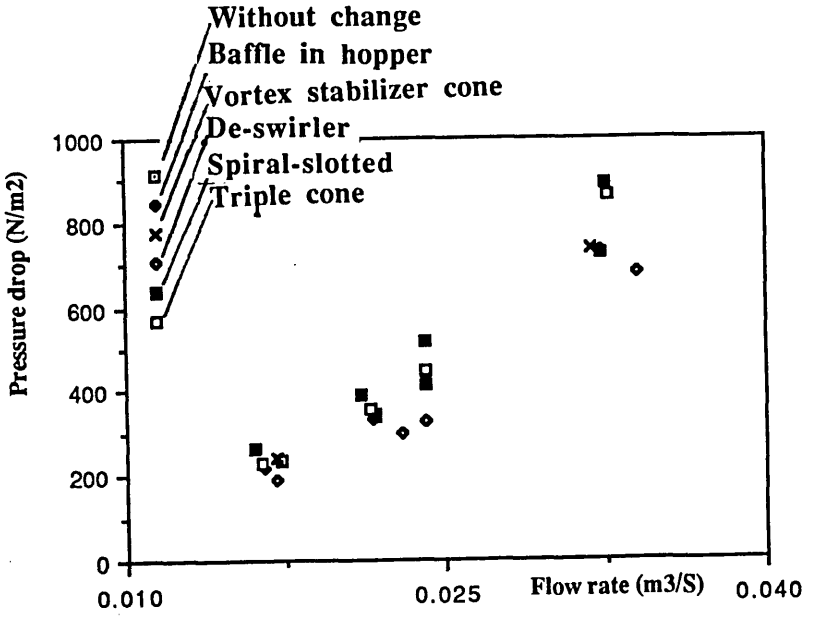

Fig. 4.61 One-cell pressure drop with various modifications

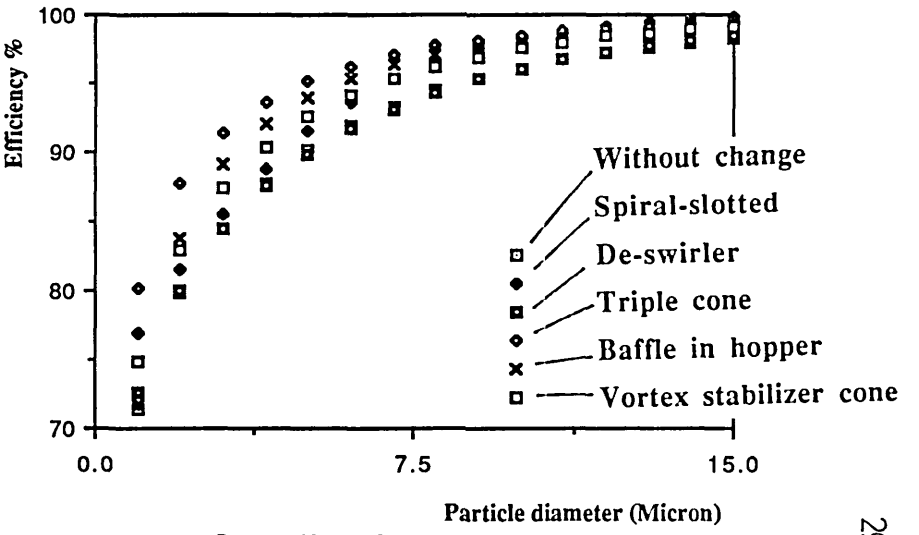

Fig. 4.62 One-cell cyclone grade efficiency with various modifications

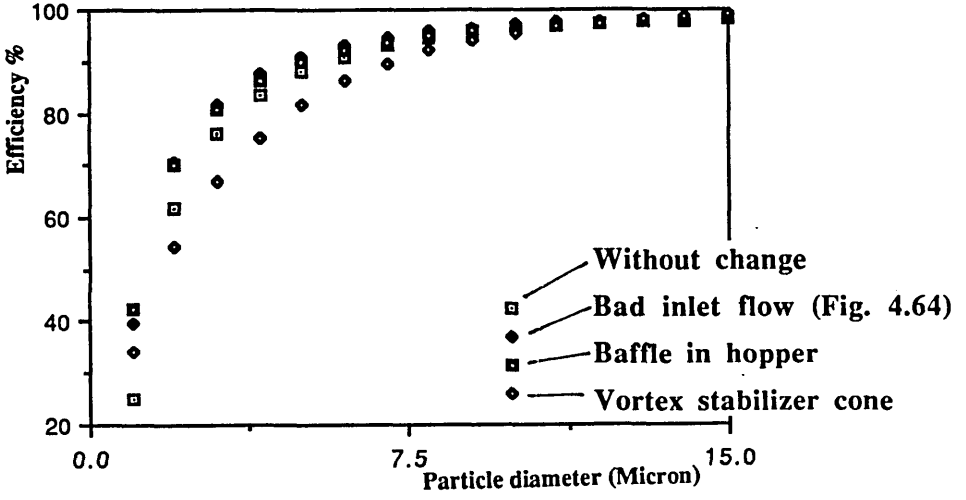

Fig. 4.63 Multicell cyclone grade efficiency with various modifications

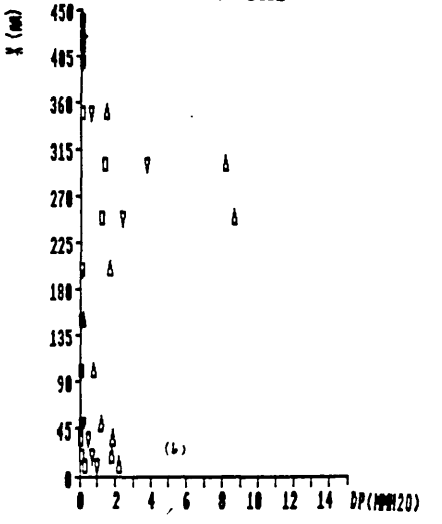

(bad inlet flow)

Fig. 4.64 Pressure profile at cyclone entrance

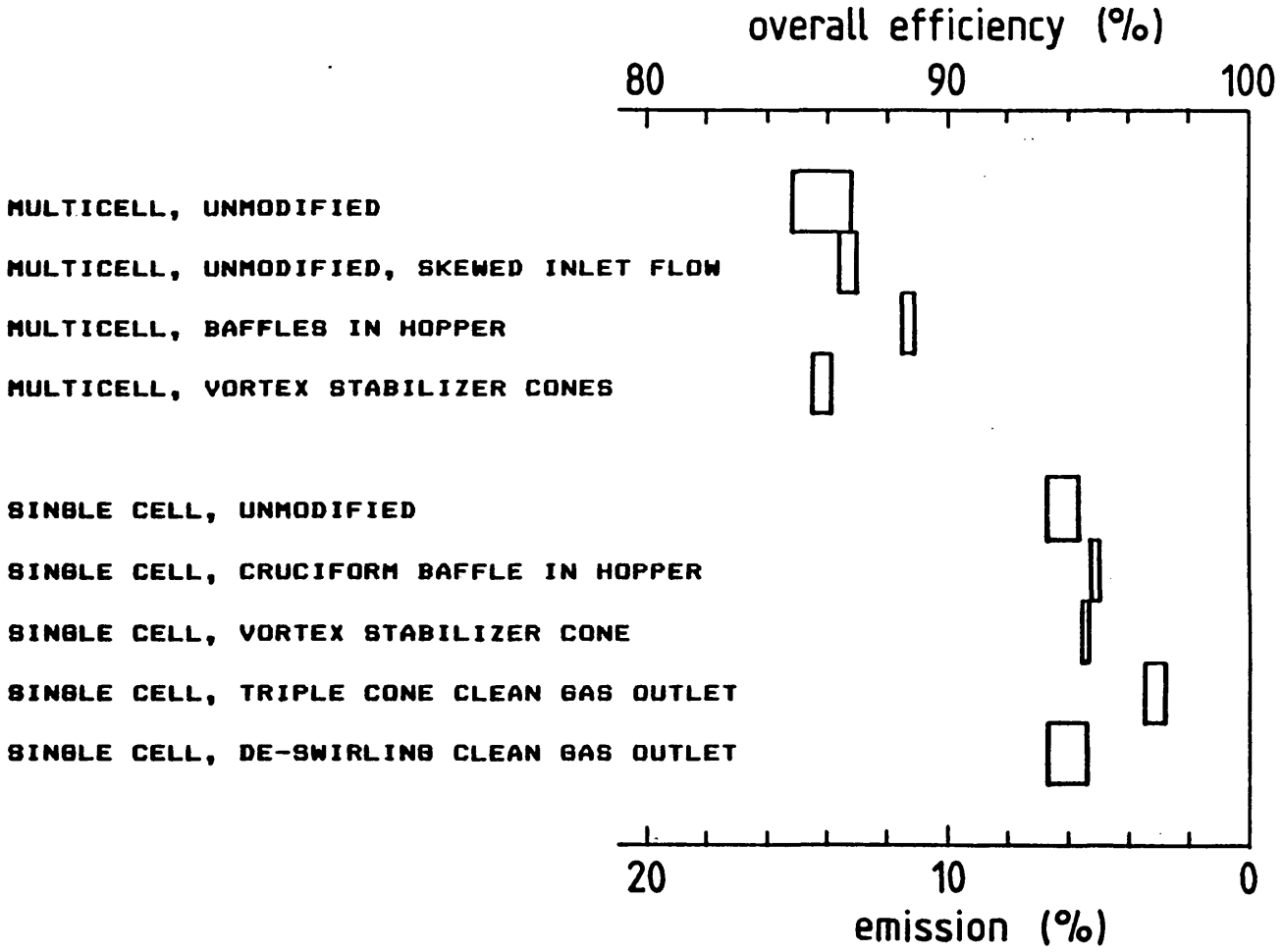

Fig. 4.65 Overall mass collection efficiencies of multicell and single-cell cyclones (various configurations), based on feed mass (corrected for sedimentation in low-velocity region of upstream ducting) and clean-stream sample mass

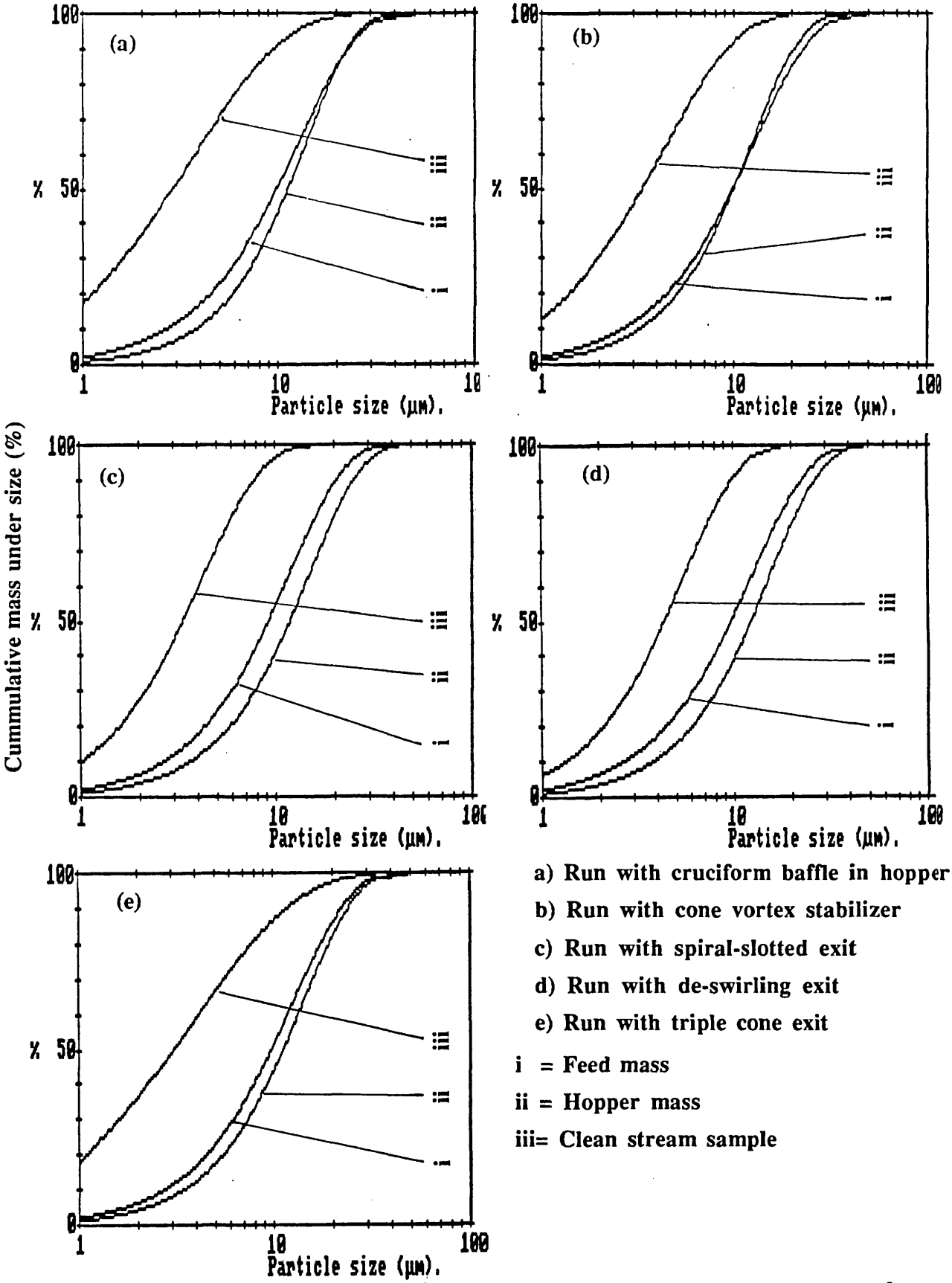

a) Run with cruciform baffle in hopper

b) Run with cone vortex stabilizer

c) Run with spiral-slotted exit

d) Run with de-swirling exit

e) Run with triple cone exit

i = Feed mass

ii = Hopper mass

iii= Clean stream sample

Fig. 4.66 Size distributions of feed mass, hopper mass, clean-gas sample for modified one-cell cyclone efficiency tests (Syenex-40)

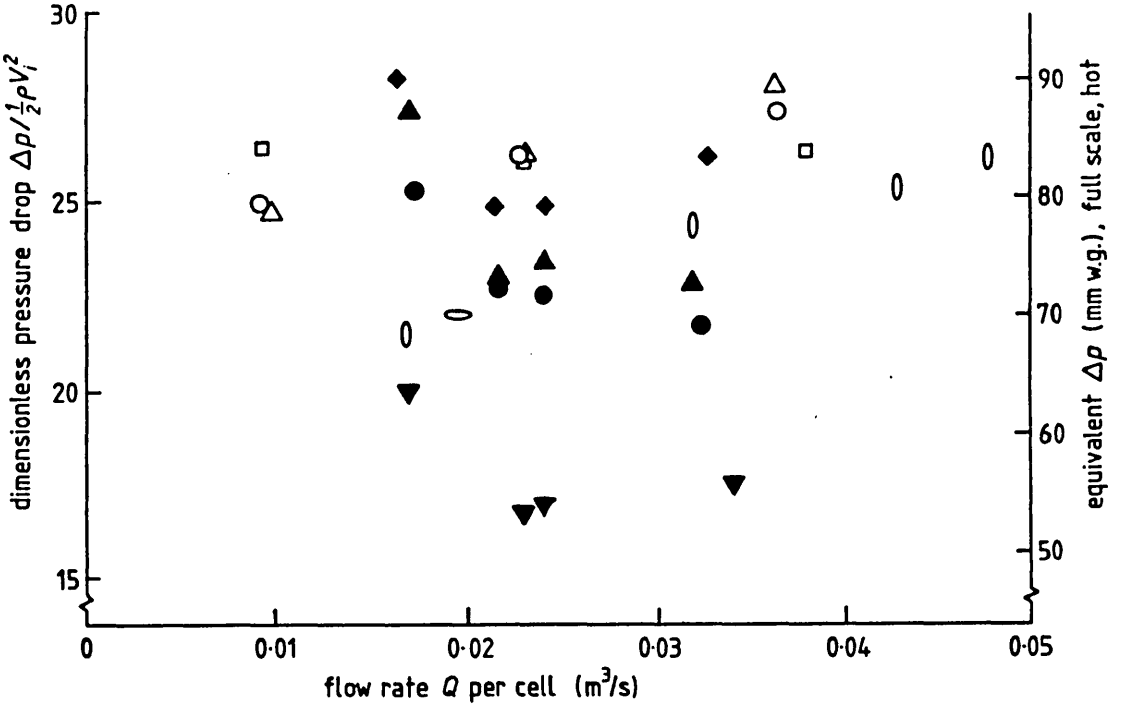

Multicell:

- ○ unmodified, configured for dust measurements
- ⬭ unmodified, skewed inlet flow
- 0 unmodified, configured for aerodynamic measurements (flow straighteners in clean gas outlets, no sediment dispersal jets)
- □ baffles in hopper
- △ vortex stabilizer cones

Single cell (corrected for flow area change):

- ● unmodified
- ▲ vortex stabilizer cone
- ◆ triple cone clean gas outlet
- ▼ de-swirling clean gas outlet

Fig. 4.67 Pressure drop across multicell and single-cell cyclones (Single-cell exit pressure adjusted on basis of loss-free diffusion to same bulk mean velocity as at inlet pressure measurement point)

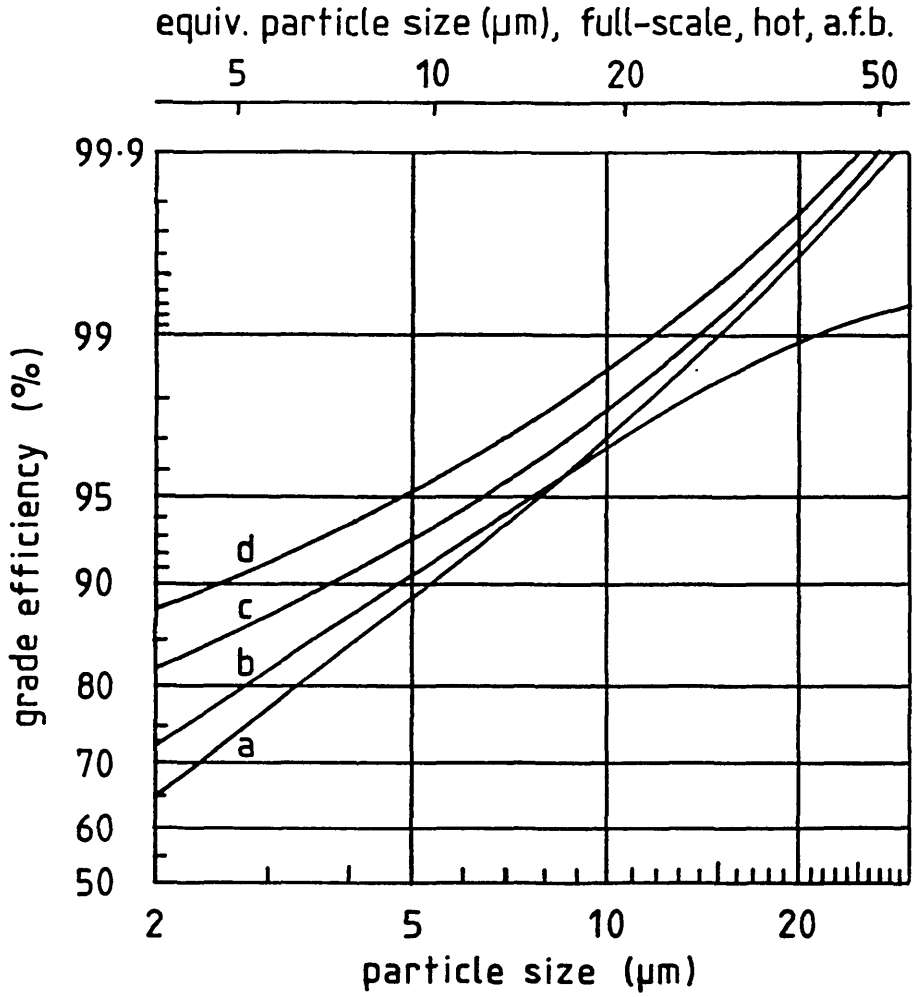

a — multicell, unmodified
b — multicell, baffles in hopper
c — single cell, unmodified
d — single cell, triple cone entry to clean gas outlet tube

Fig. 4.68 Typical grade efficiencies of multicell and single-cell cyclone configurations

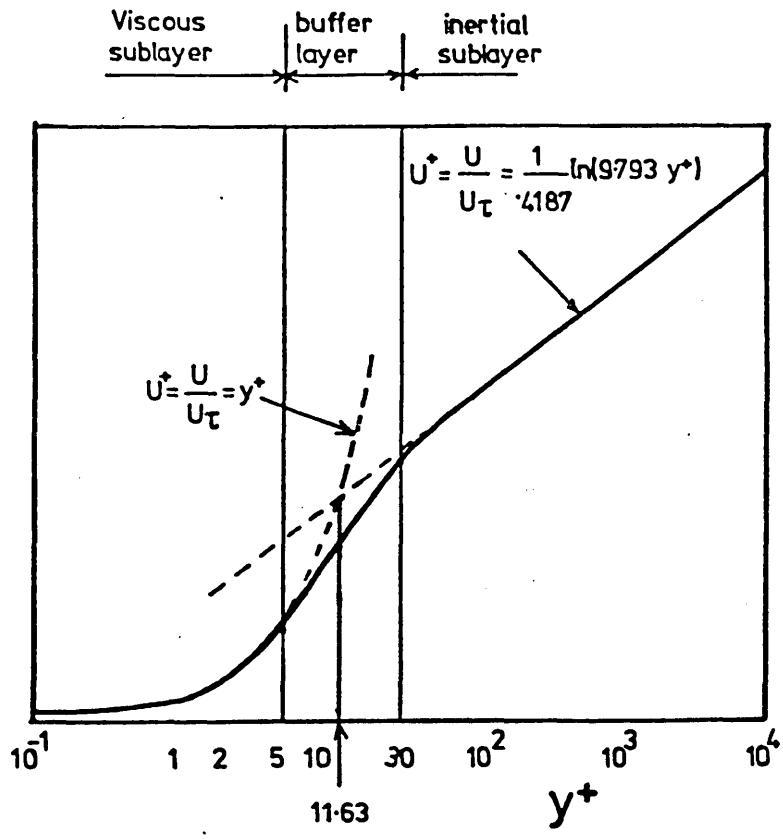

Fig. 5.1 The law of the wall

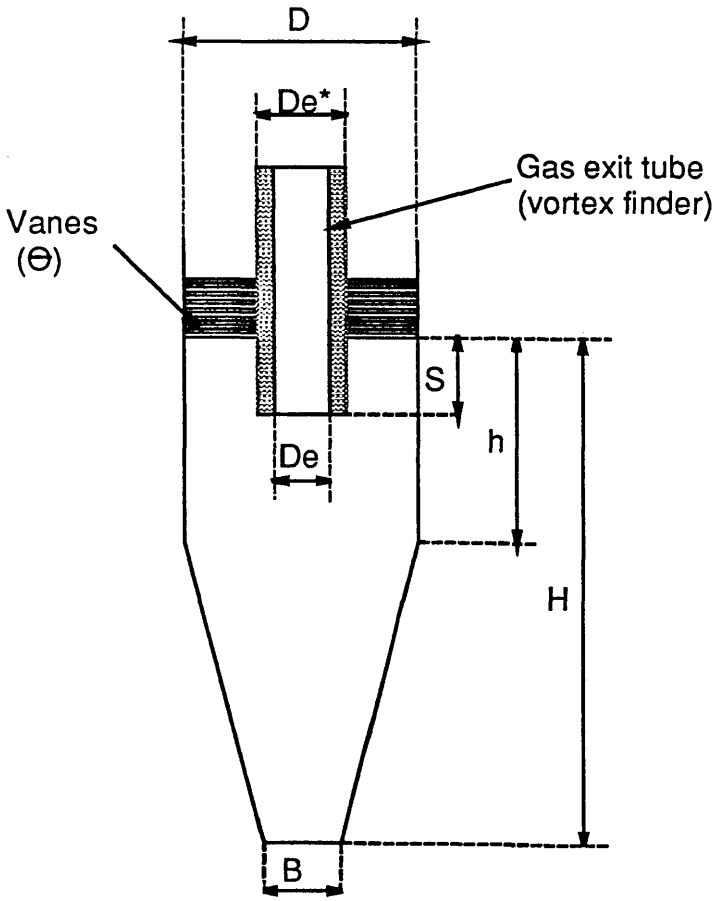

Fig. 5.2 Notation for cyclone geometry

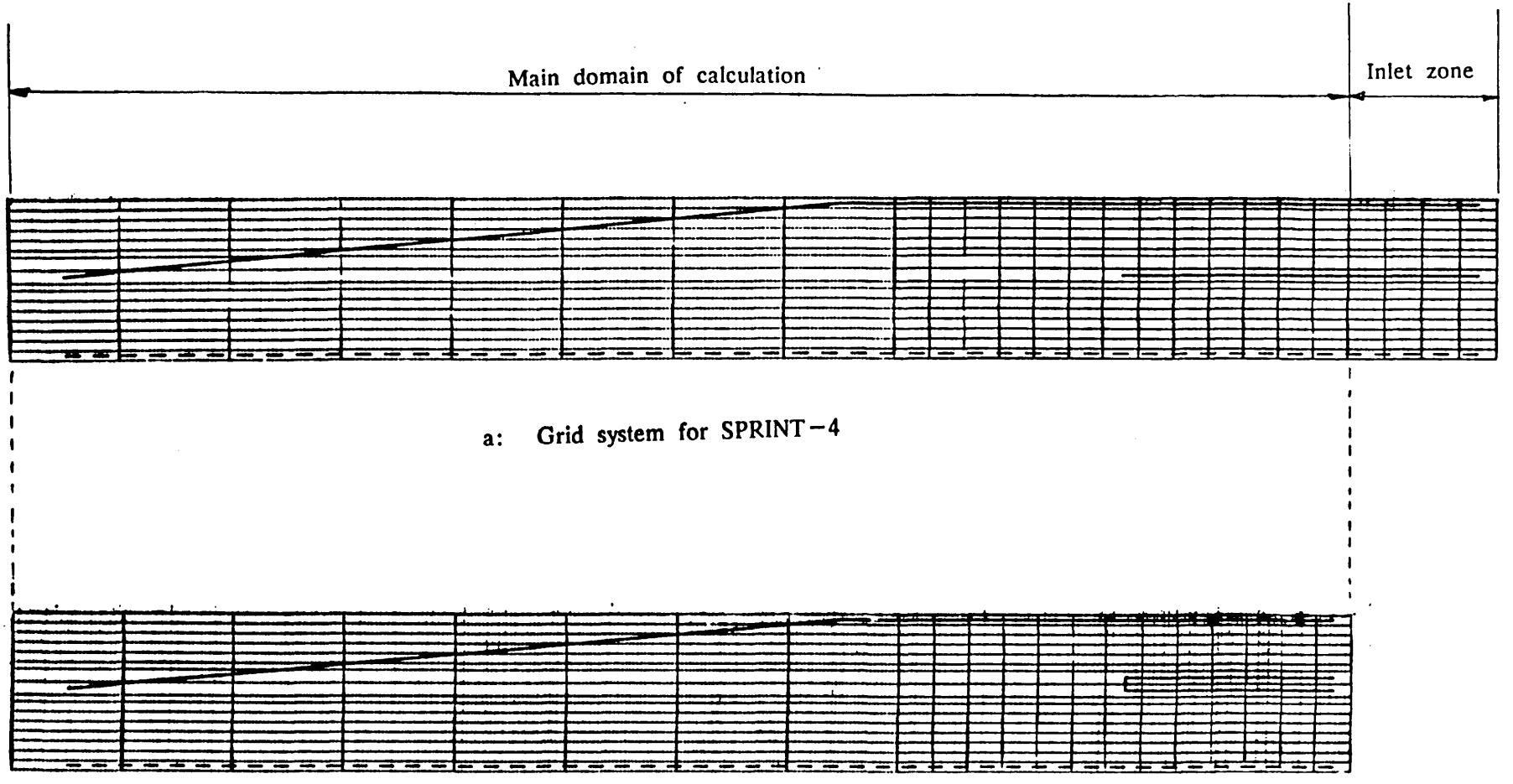

a: Grid system for SPRINT−4

b: Grid system for CYCINT

Fig. 5.3 Grid systems for SPRINT-4 and CYCINT-1 computer programs

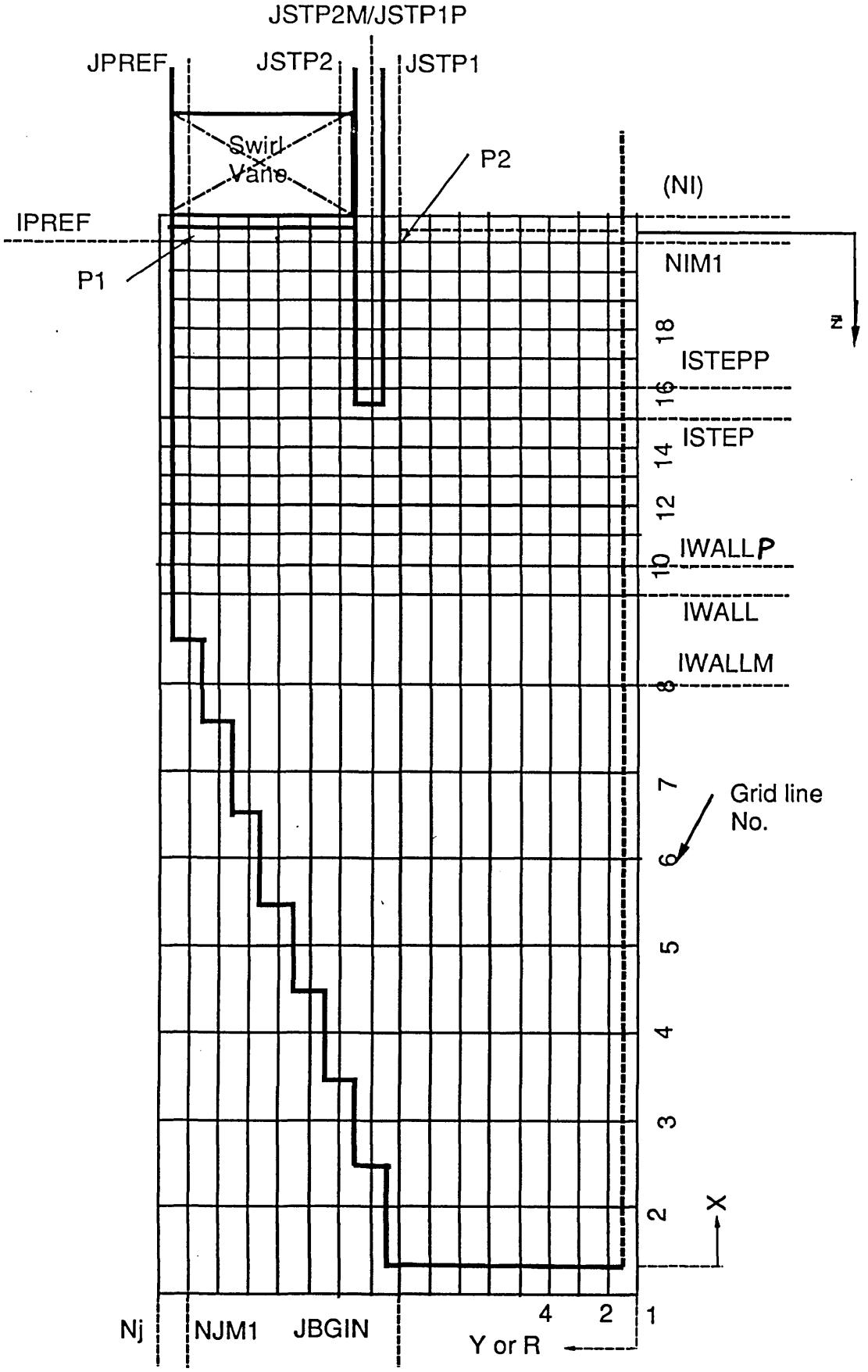

Fig. 5.4 Detail of CYCINT-1 grid system

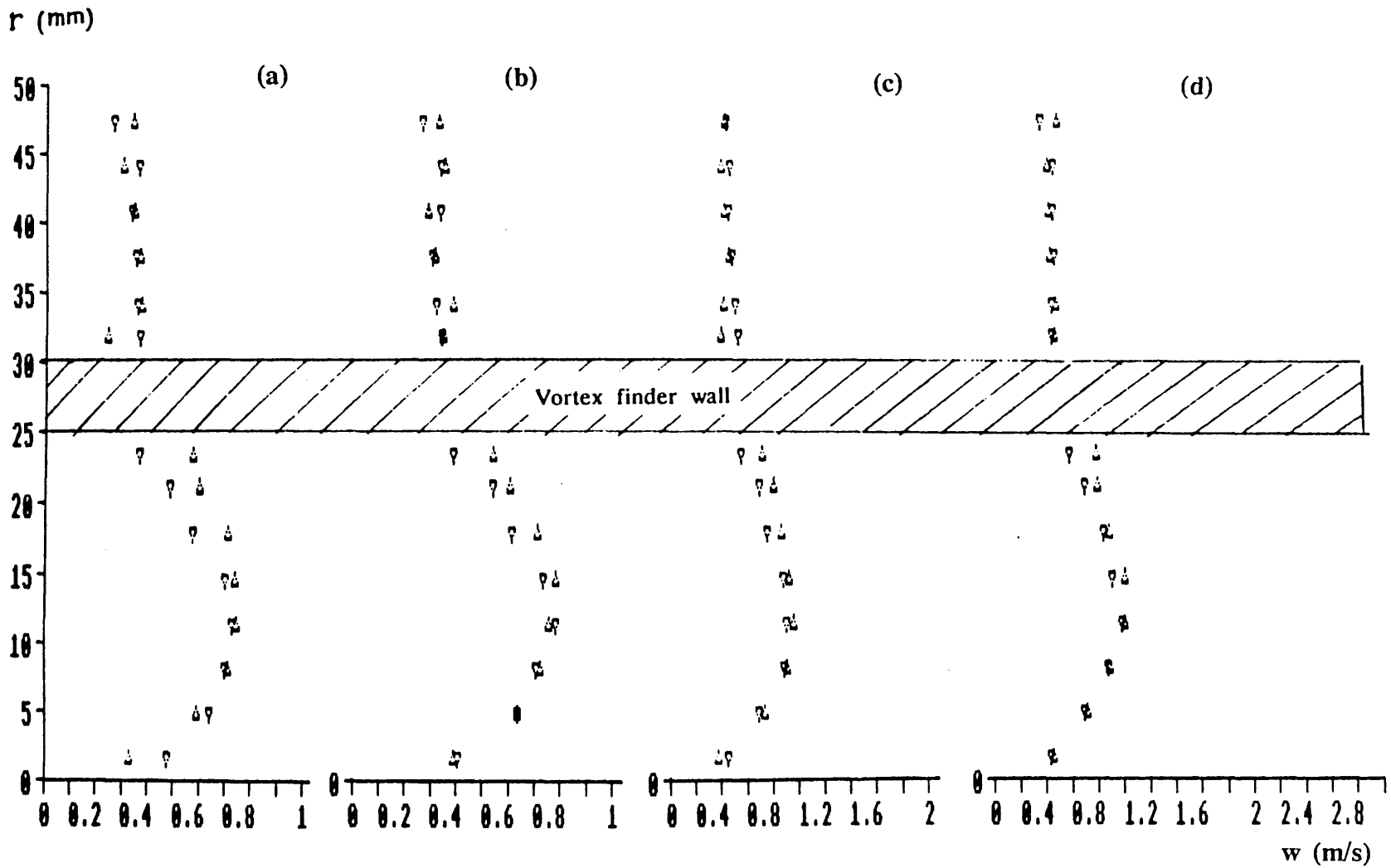

a: Flow rate 70 ℓ/min, z = 5·8 mm

b: Flow rate 70 ℓ/min, z = 17·44 mm

c: Flow rate 100 ℓ/min, z = 5·8 mm

d: Flow rate 100 ℓ/min, z = 17·44 mm

Fig. 5.5 Swirl velocity profile below vane position (Experimental results)

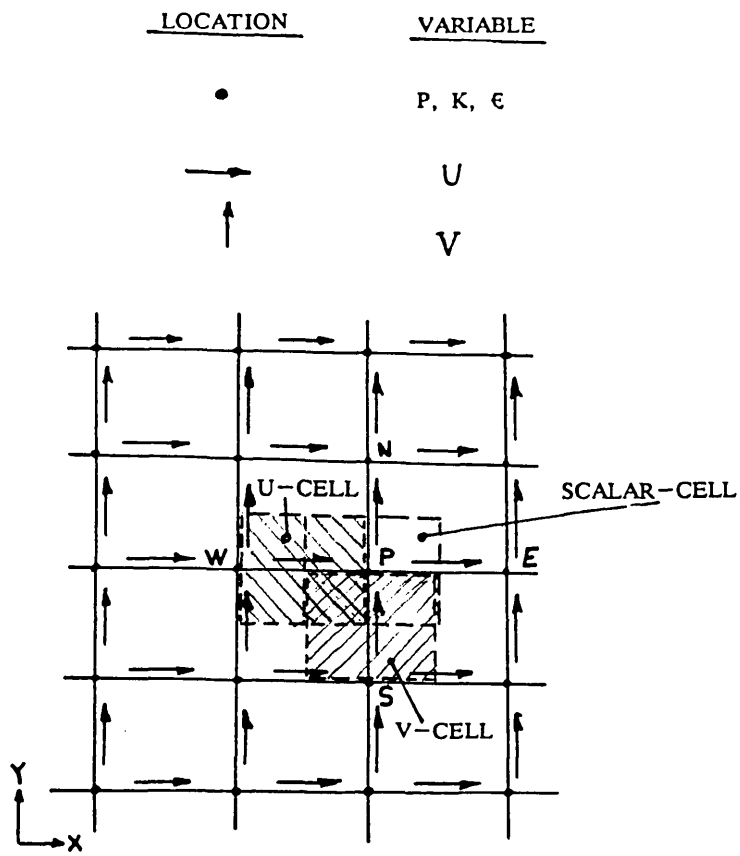

Fig. 5.6 Backward staggered grid

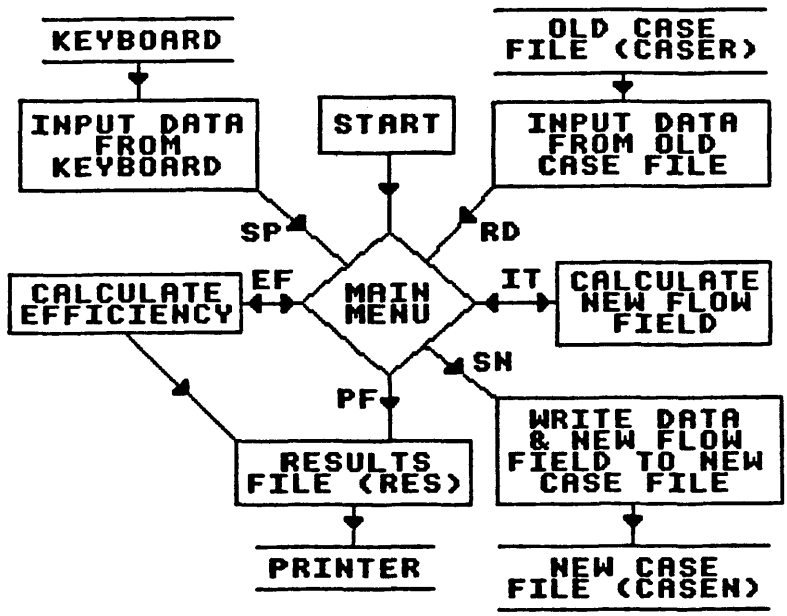

Fig. 5.7 Structure of CYCINT-1

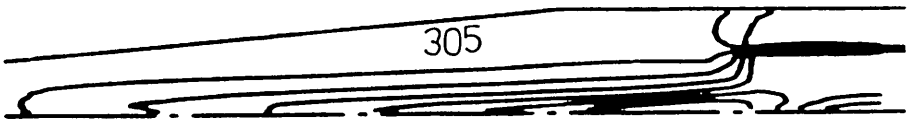

a- Contours of u-velocity (MAX. = 0.278E 02 , MIN. =-0.130E 02)

b- Contours of u-velocity (MAX. = 0.324E 02 , MIN. =-0.139E 02)

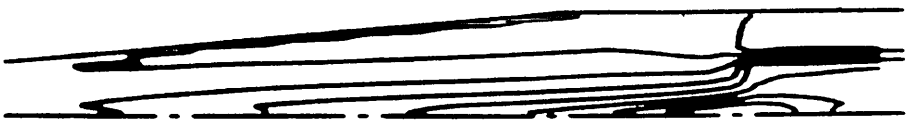

c- Contours of u-velocity (MAX. = 0.202E 02 , MIN. =-0.676E 01)

a- Contours of v-velocity (MAX. = 0.117E 01 , MIN. =-0.105E 02)

b- Contours of v-velocity (MAX. = 0.145E 01 , MIN. =-0.123E 02)

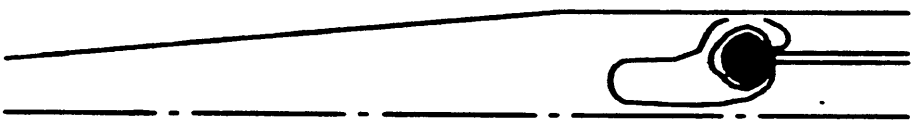

c- Contours of v-velocity (MAX. = 0.409E 00 , MIN. =-0.588E 01)

a- Contours of w-velocity (MAX. = 0.277E 02 , MIN. = 0.000E 00)

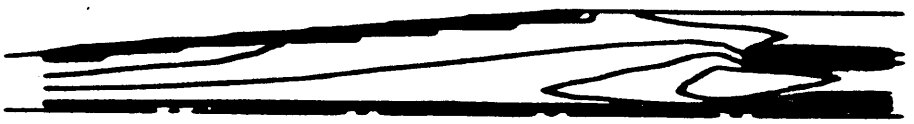

b- Contours of w-velocity (MAX. = 0.325E 02 , MIN. = 0.000E 00)

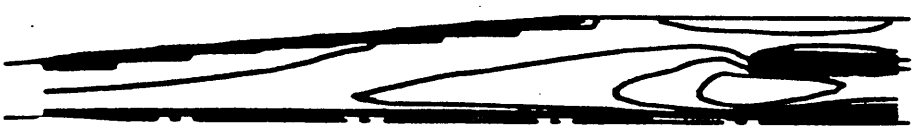

c- Contours of w-velocity (MAX. = 0.155E 02 , MIN. = 0.000E 00)

(a) Full scale cyclone

(b) Experimental cyclone (Re=67400, for Re matching)

(c) Experimental cyclone (Re=32600, for St matching)

Fig. 5.8 Comparison of velocity contours of full scale cyclone and experimental cyclone

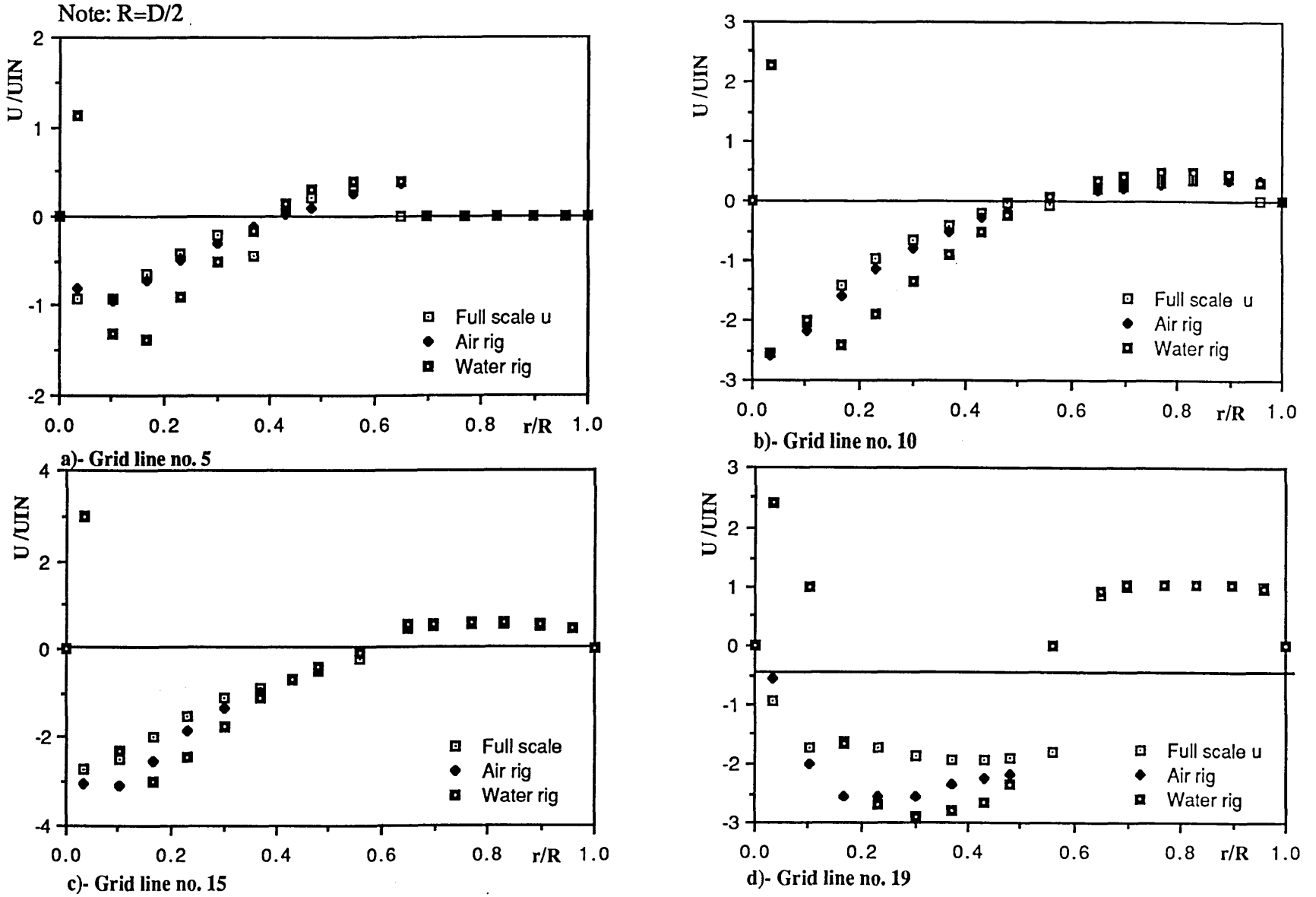

Fig. 5.9 Non dimensional axial velocity profile at Re=67400

Note: R=D/2

v_{ave} is defined as the average of radial velocity below vane trailing edge along grid line NIM1 (Fig. 5.4) and $v_{ave} = 5.8 * 10^{-3} u_{in}$

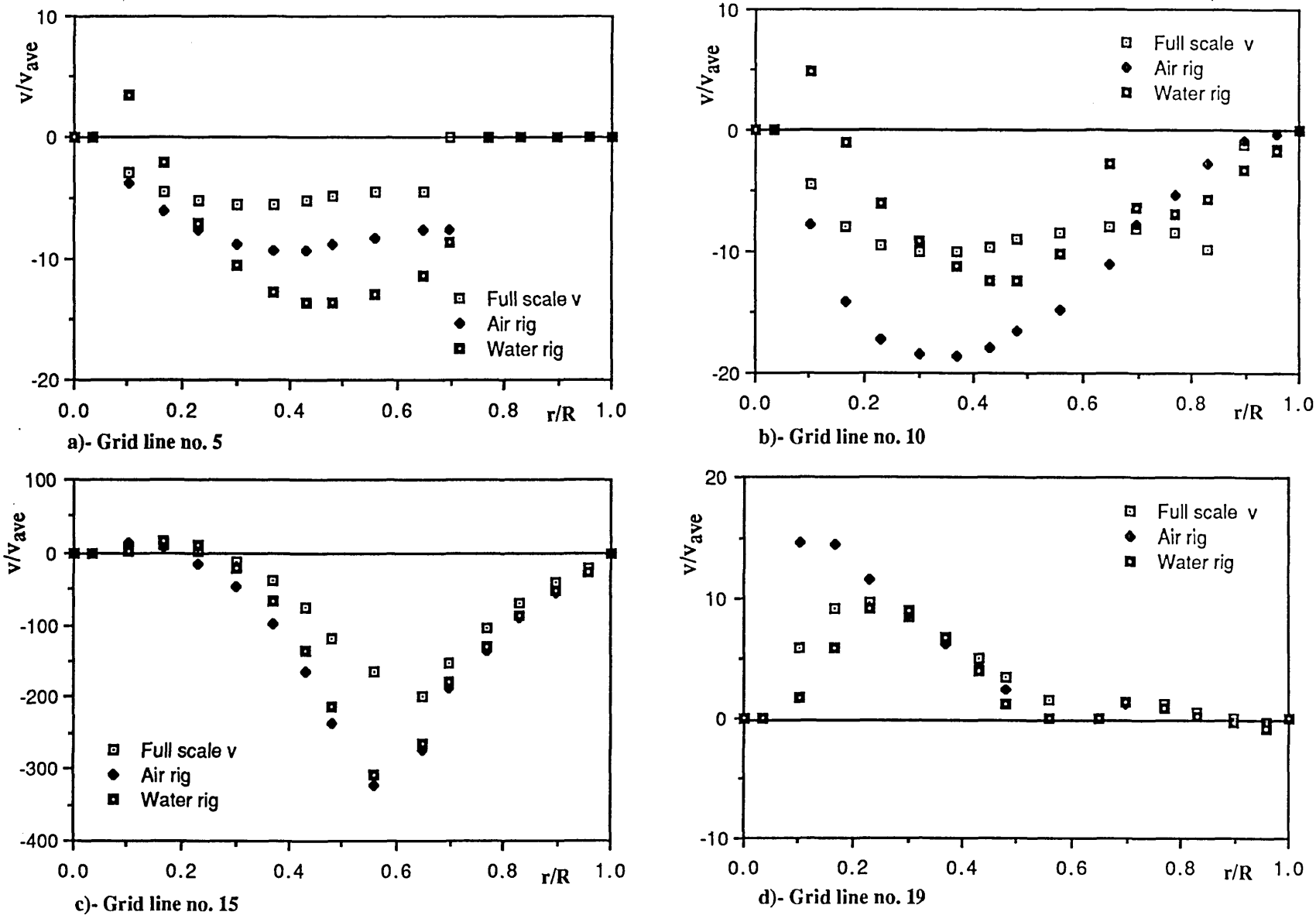

Fig. 5.10 Non dimensional radial velocity profile at Re=67400

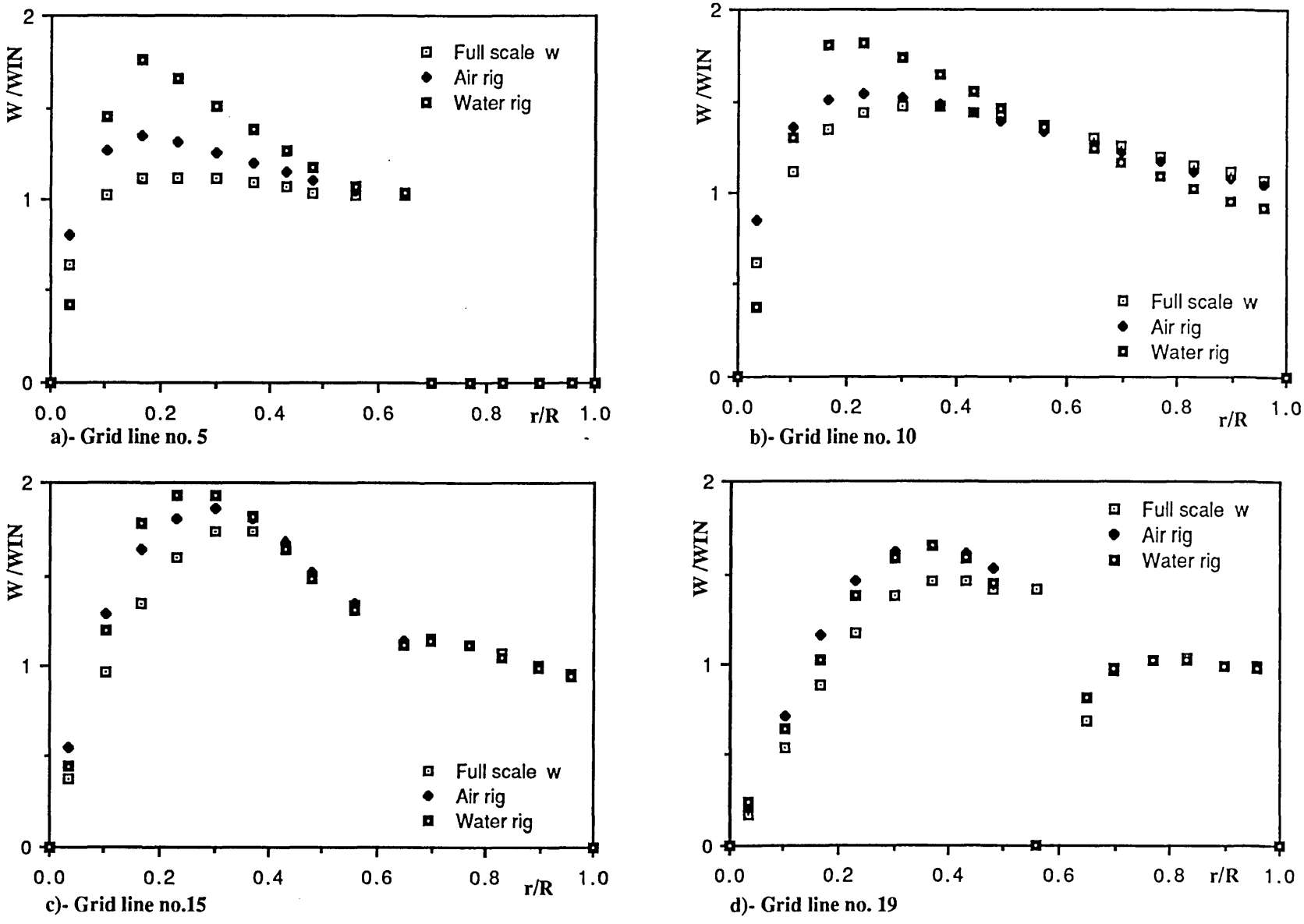

Fig. 5.11 Non dimensional tangential velocity profile at Re=67400

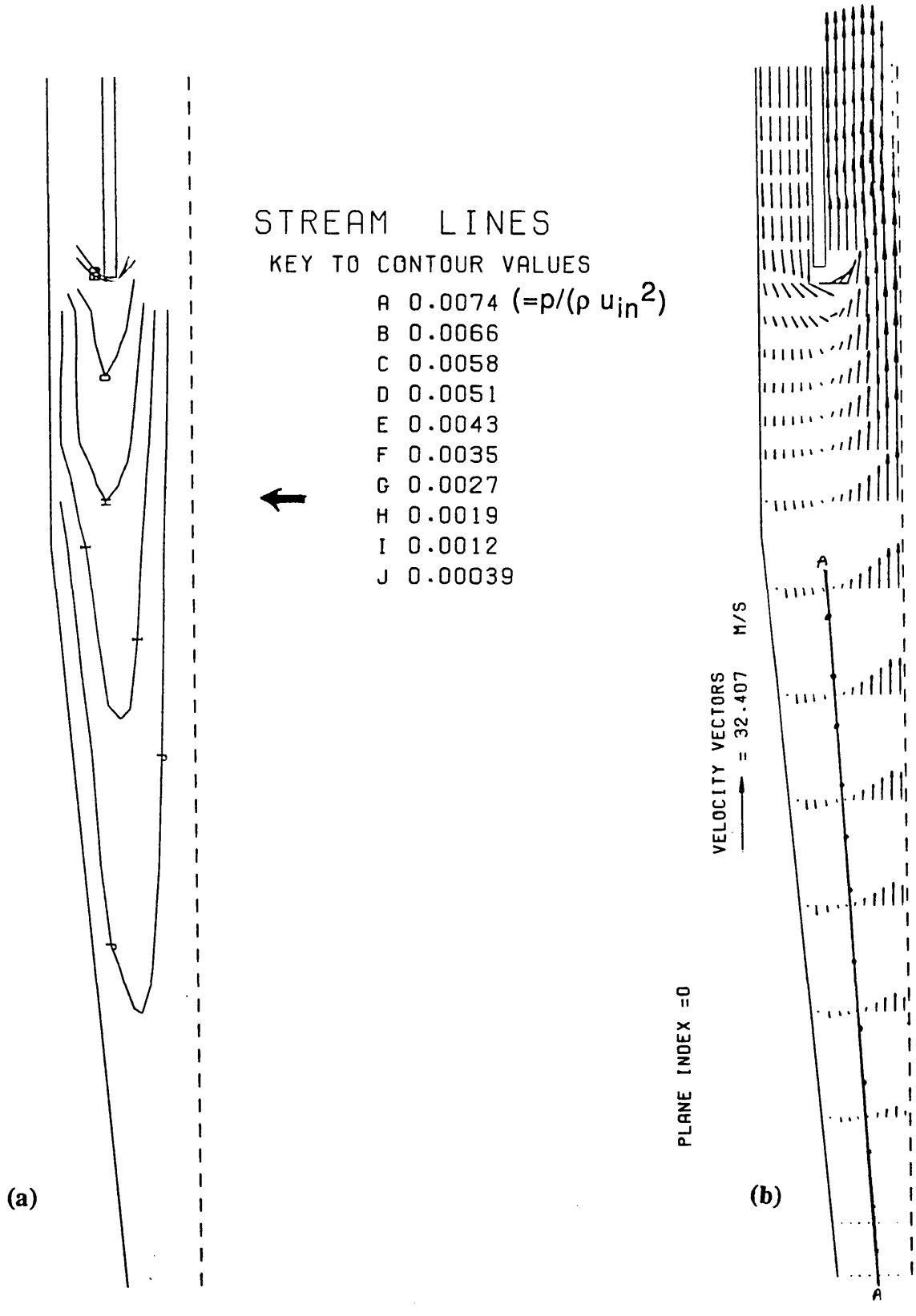

Fig. 5.12 Stream lines (a) and velocity vectors (b) for experimental cyclone at Re=67400

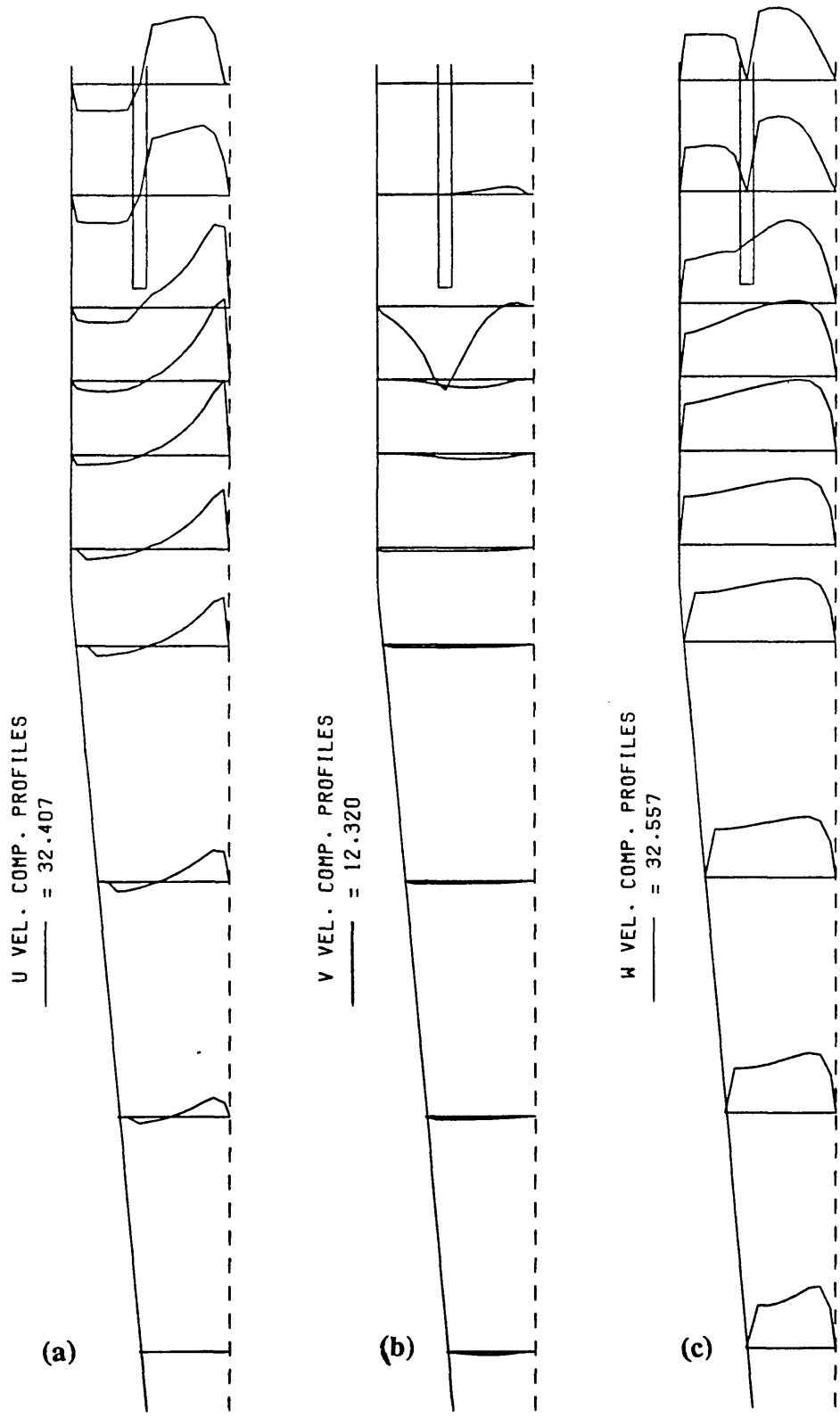

Fig. 5.13 Velocity profiles inside experimental cyclone at Re=67400

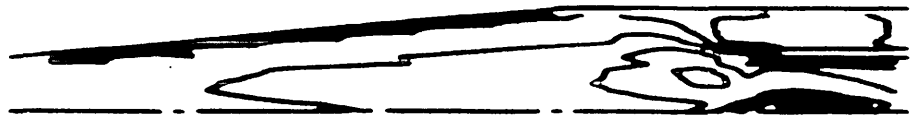

Contours of fluctuation of u (MAX. = 0.125E 02 , MIN. = 0.000E 00)

Contours of fluctuation of v (MAX. = 0.101E 02 , MIN. = 0.000E 00)

Contours of fluctuation of w (MAX. = 0.683E 01 , MIN. = 0.000E 00)

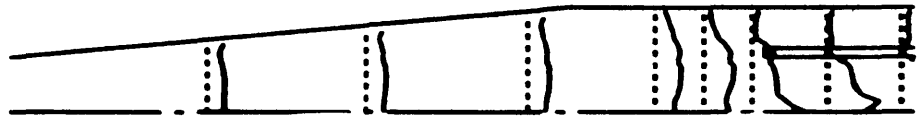

Profiles of fluctuation of u (MAX. = 0.125E 02 MIN. = 0.000E 00)

Profiles of fluctuation of v (MAX. = 0.101E 02 MIN. = 0.000E 00)

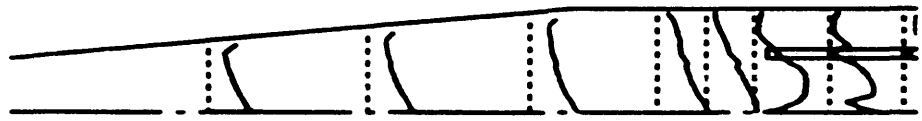

Profiles of fluctuation of w (MAX. = 0.683E 01 MIN. = 0.000E 00)

Contours of k (MAX. = 0.906E 02 , MIN. = 0.000E 00)

Fig. 5.14 Turbulence predictions for experimental cyclone at Re=67400

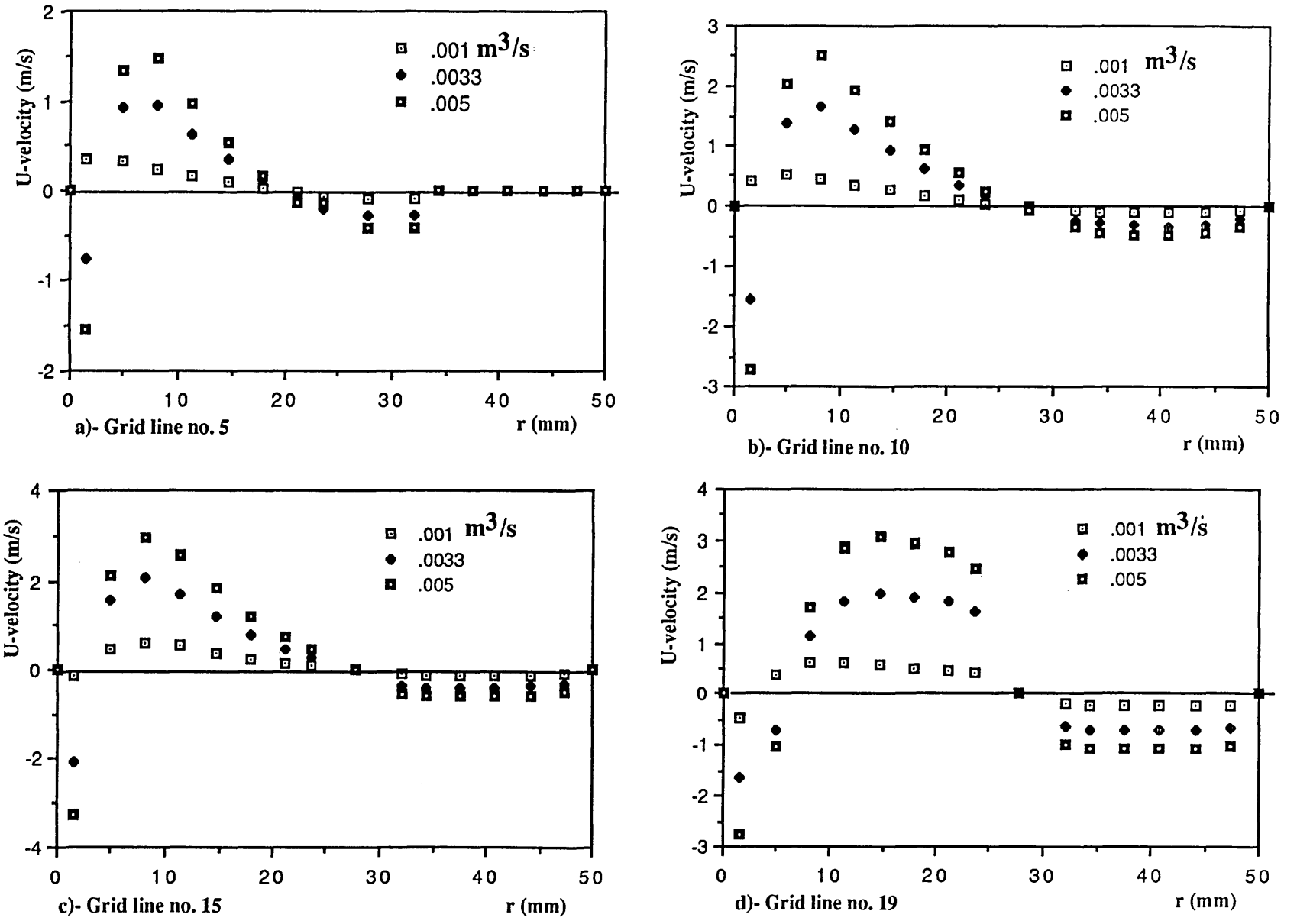

Fig. 5.15 Axial velocity profiles at three flow rates (water rig)

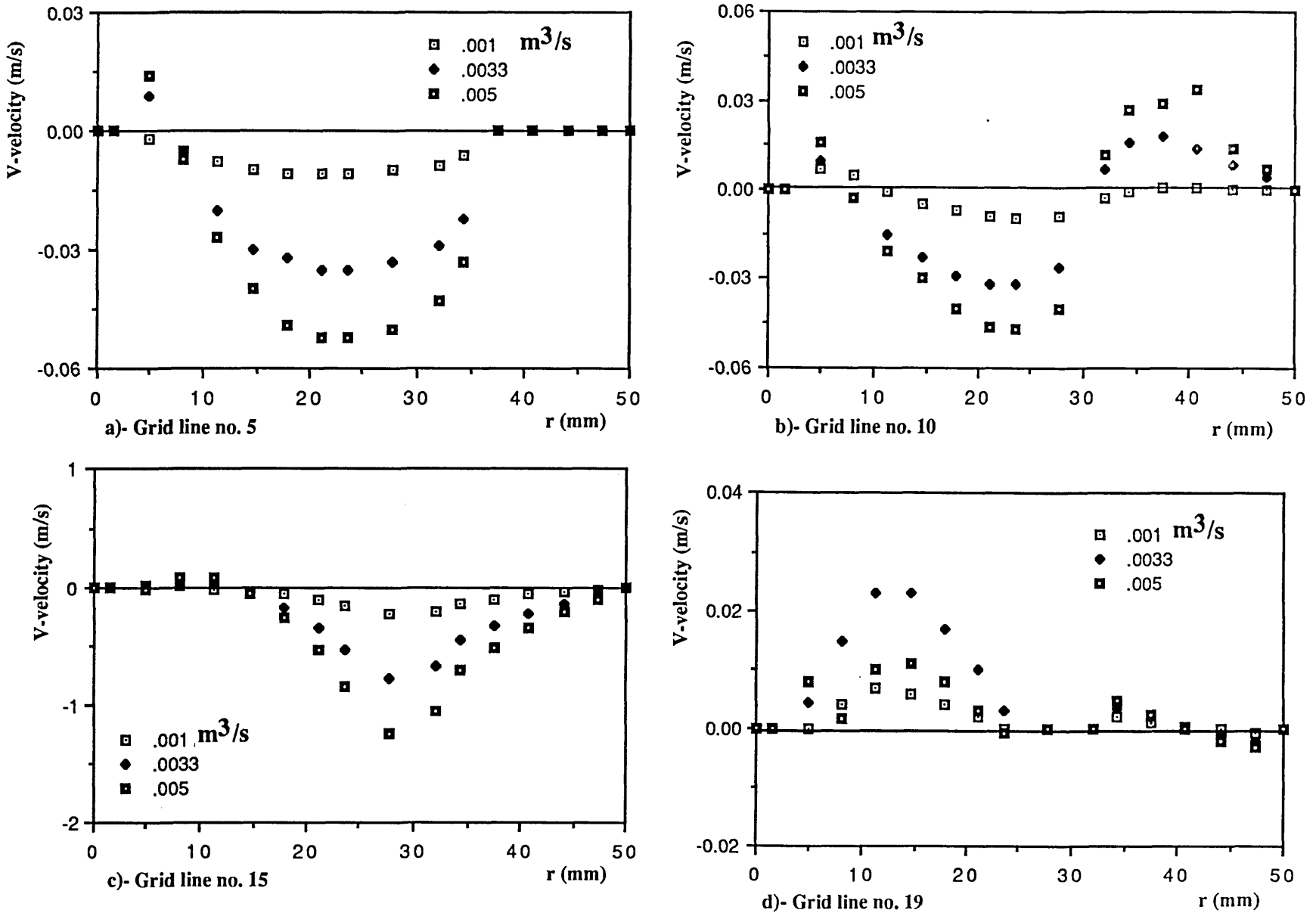

Fig. 5.16 Radial velocity profiles at three flow rates (water rig)

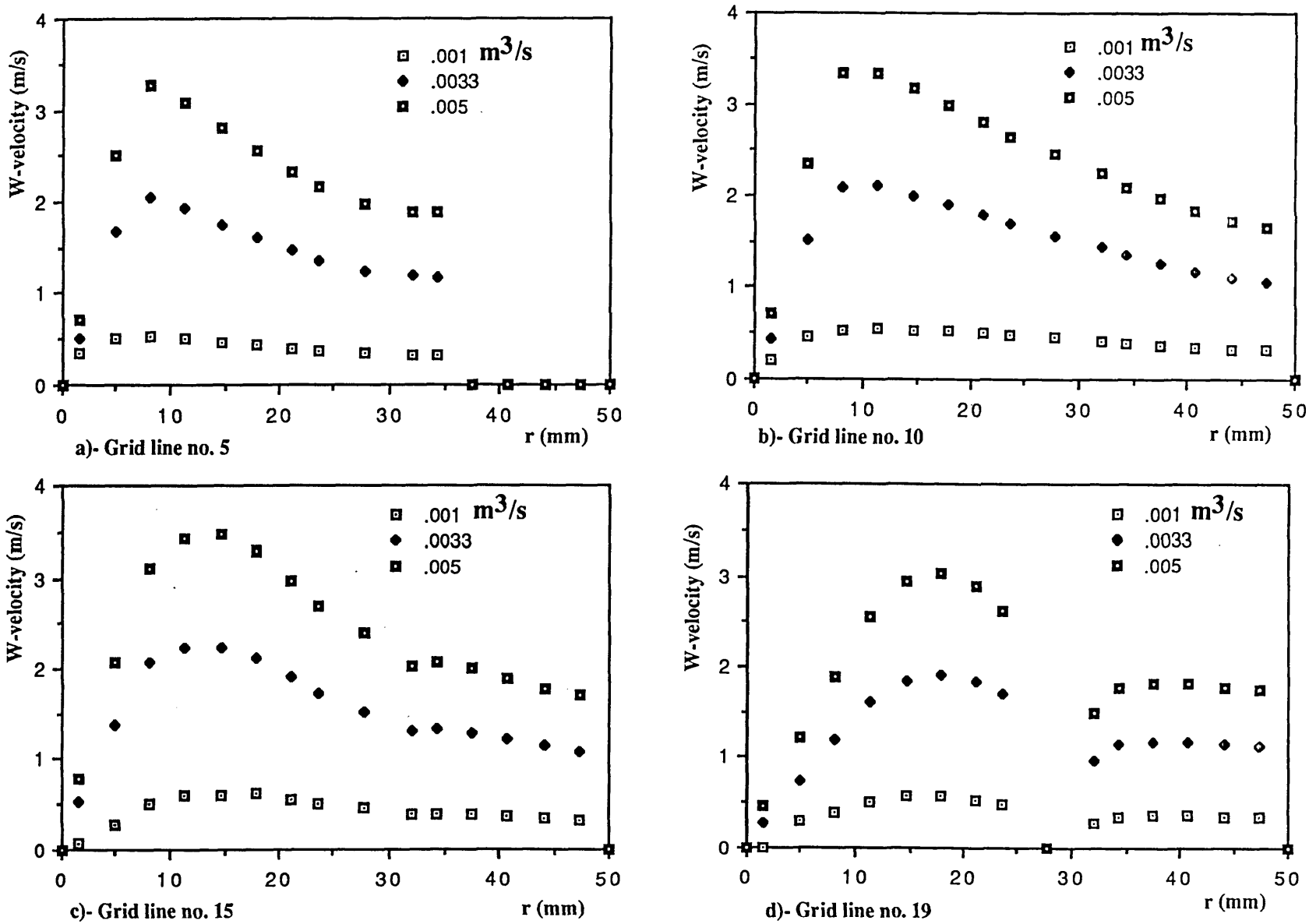

Fig. 5.17 Tangential velocity profiles at three flow rates (water rig)

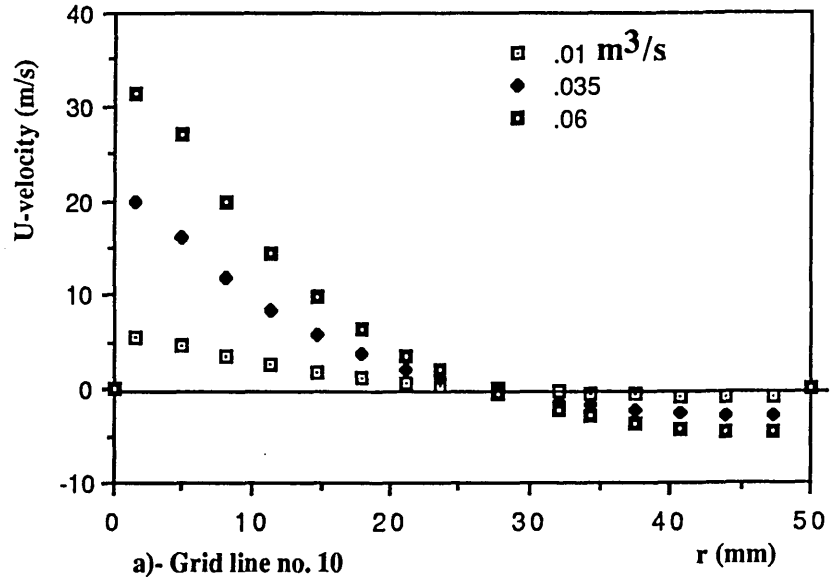

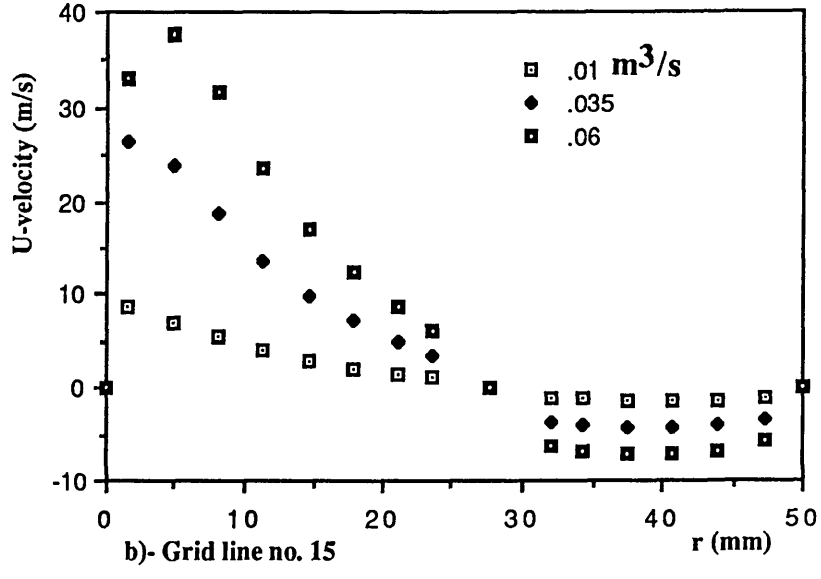

Fig. 5.18 Axial velocity profiles at three flow rates (air rig)

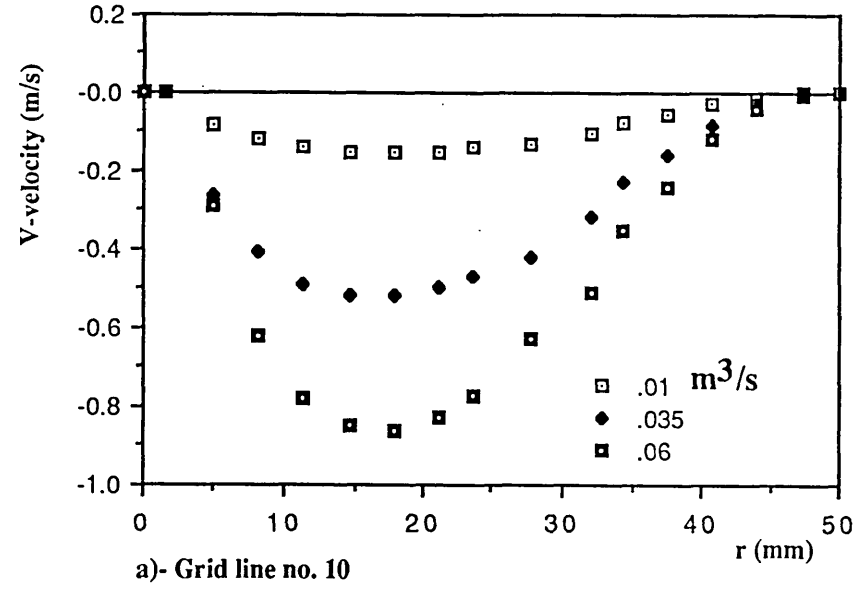

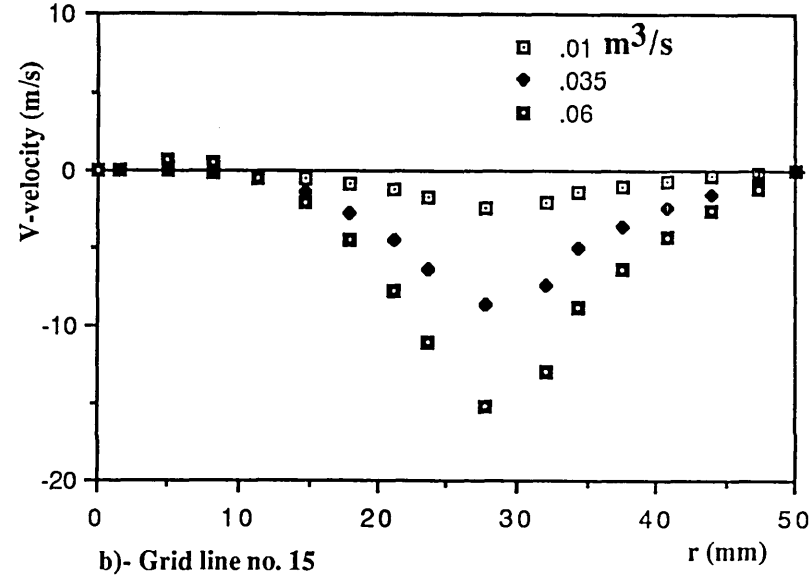

Fig. 5.19 Radial velocity profiles at three flow rates (air rig)

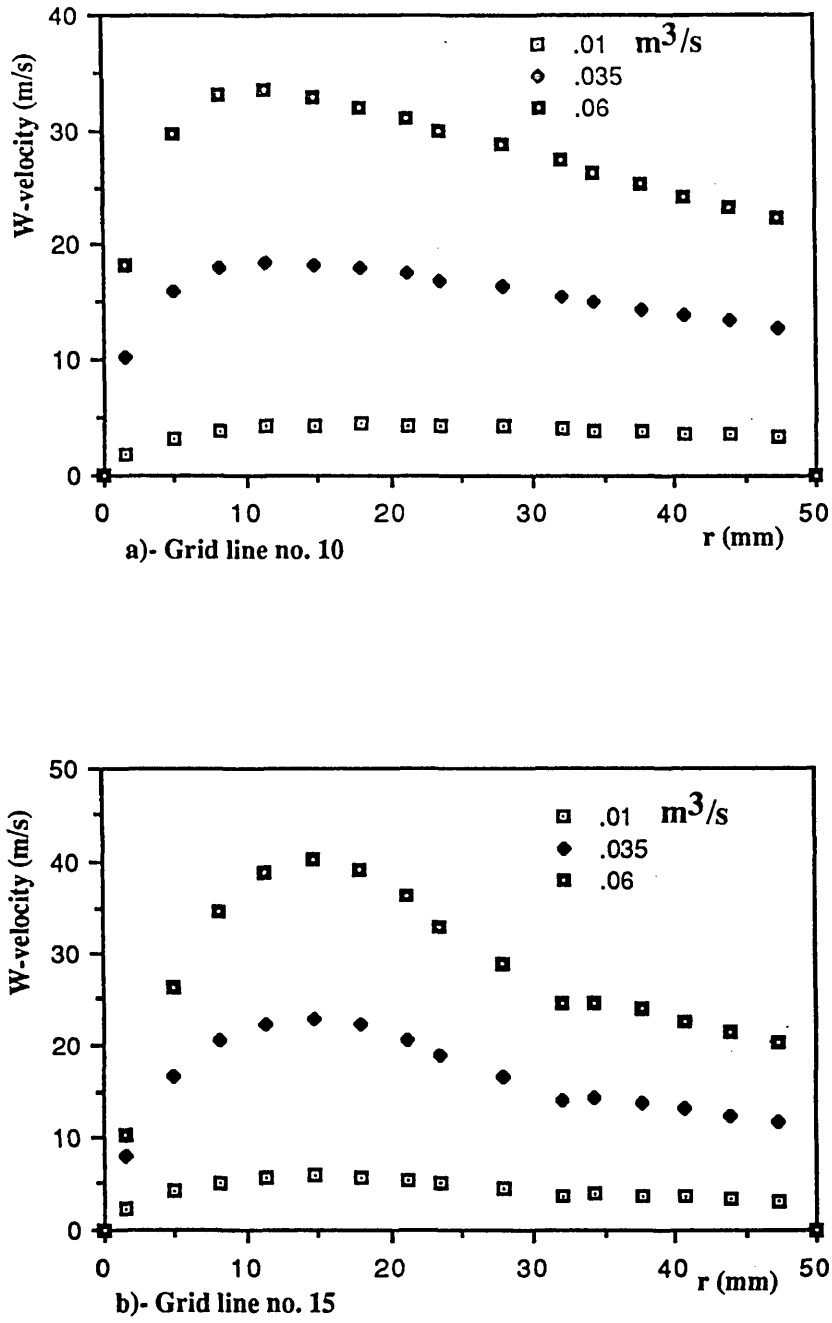

Fig. 5.20 Tangential velocity profiles at three flow rates (air rig)

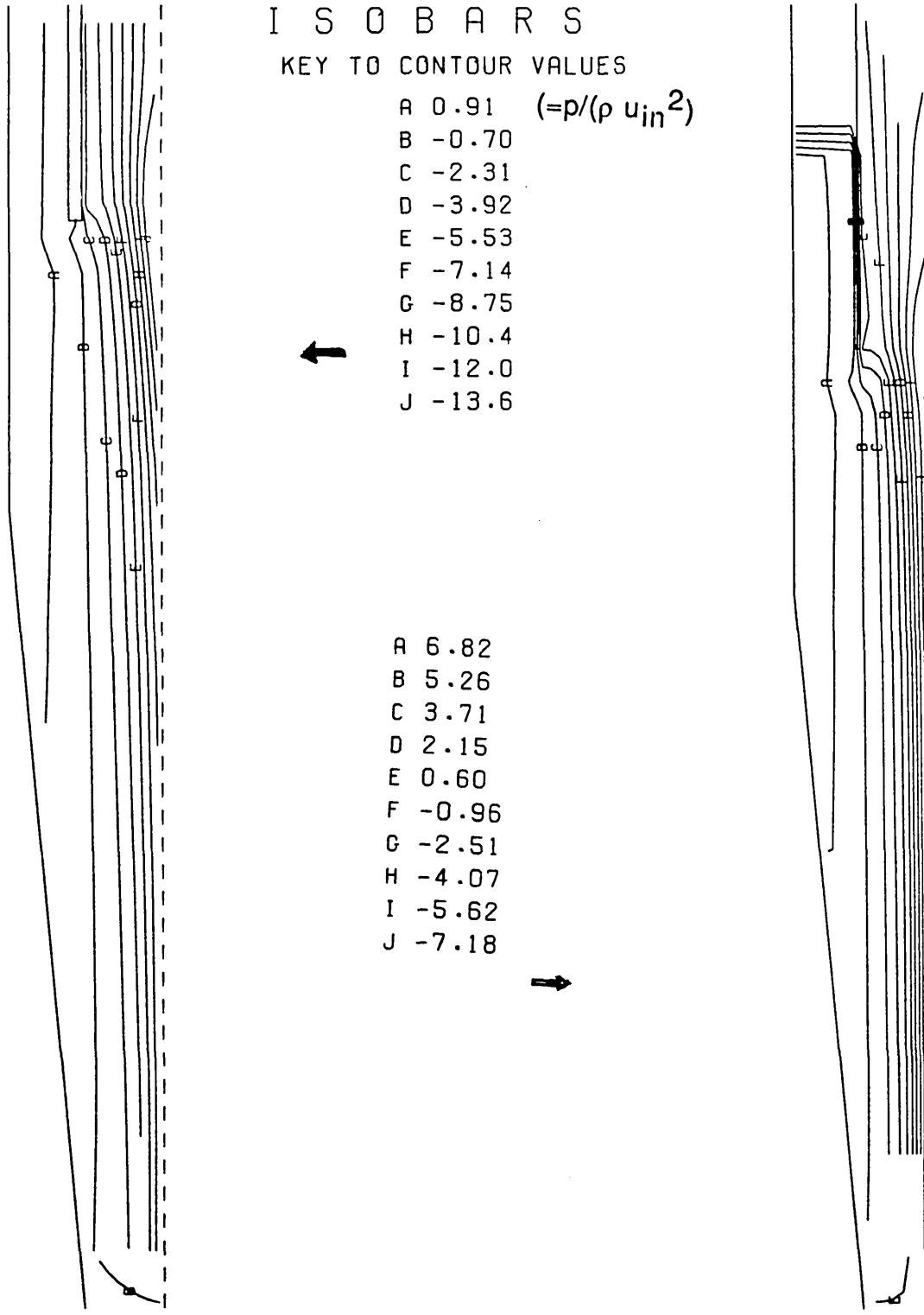

(a) CYCINT-1 Prediction **(b) SPRINT-4 prediction**

Fig. 5.21 Pressure contours predicted by CYCINT-1 and SPRINT-4 for experimental cyclone (St No. matching flow rate)

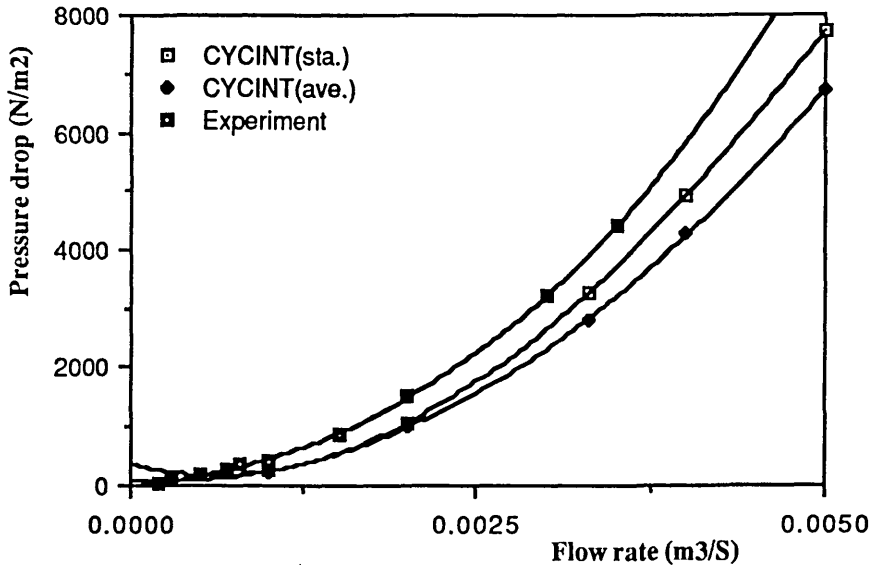

Fig. 5.22 Cyclone pressure drop in water rig

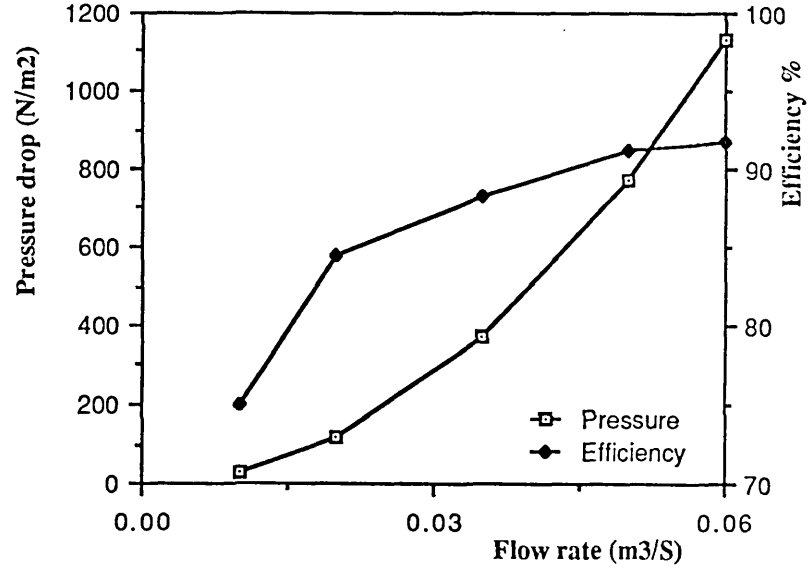

Fig. 5.23 Cyclone pressure drop and mass efficiency versus flow rate for experimental cyclone (CYCINT-1)

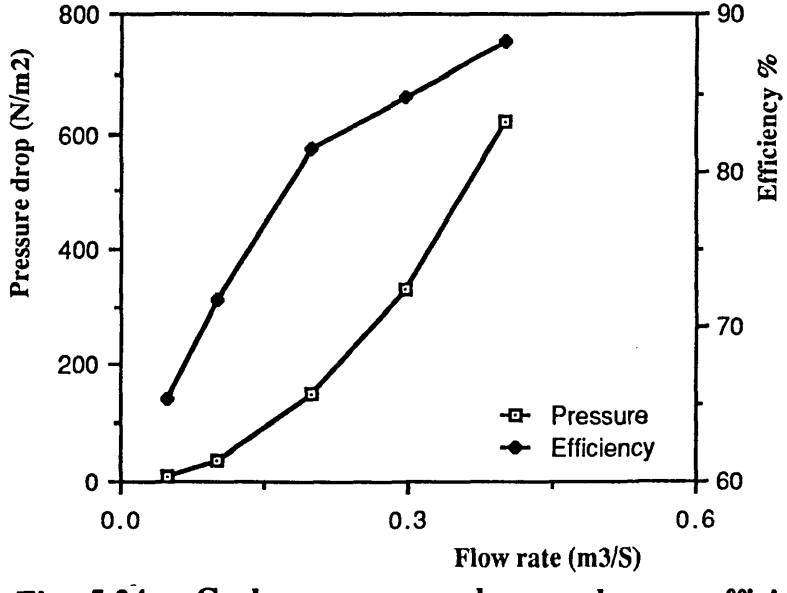

Fig. 5.24 Cyclone pressure drop and mass efficiency versus flow rate for full-scale cyclone (CYCINT-1)

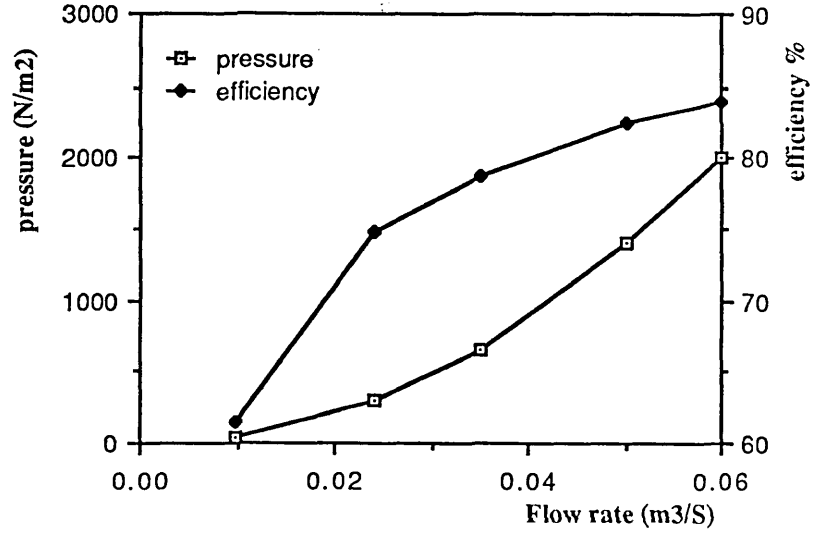

Fig. 5.25 Cyclone pressure drop and mass efficiency predicted by SPRINT-4 (experimental cyclone)

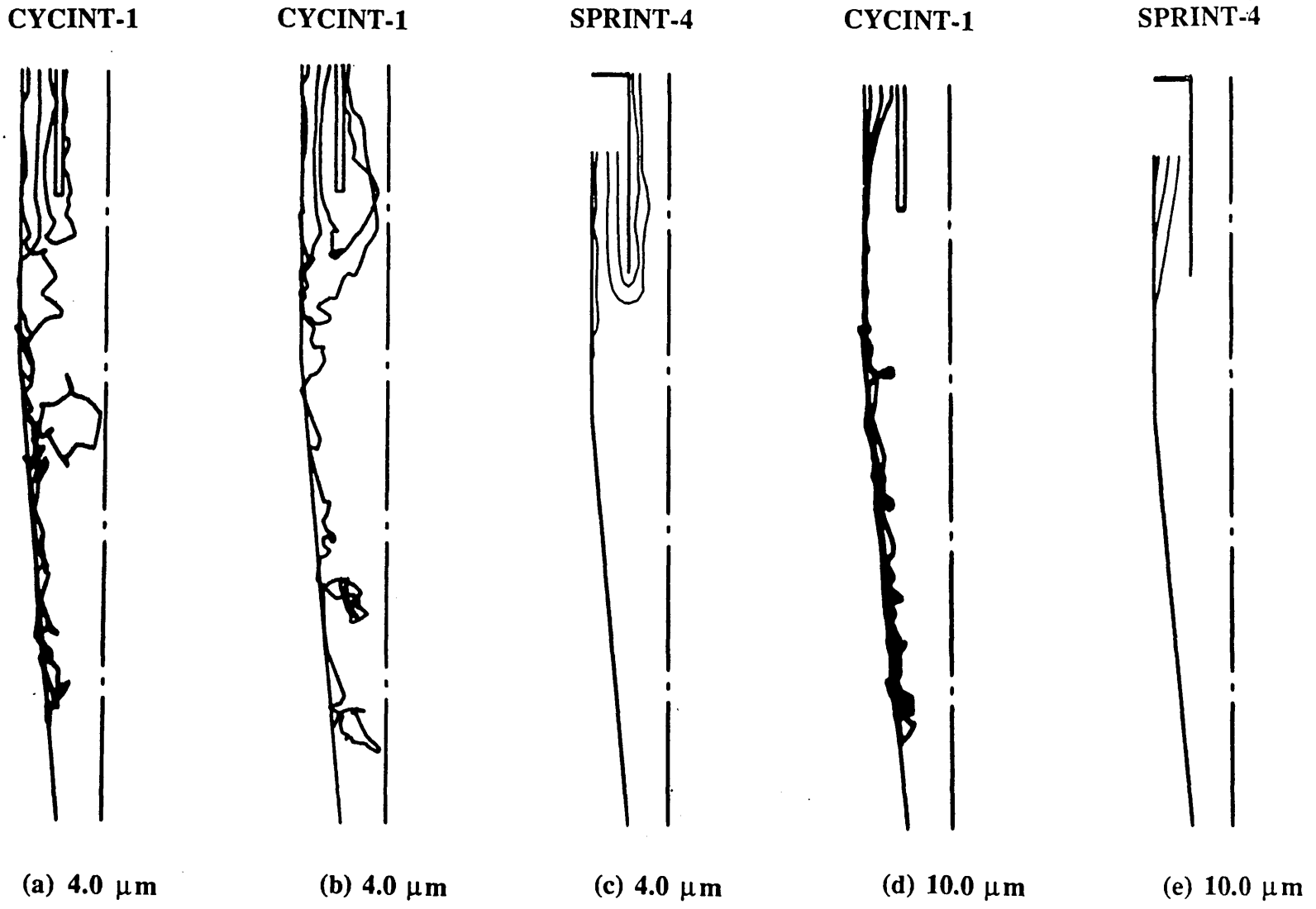

Fig. 5.26 Particle trajectory predictions by CYCINT-1 and SPRINT-4 (4 & 10 μm)

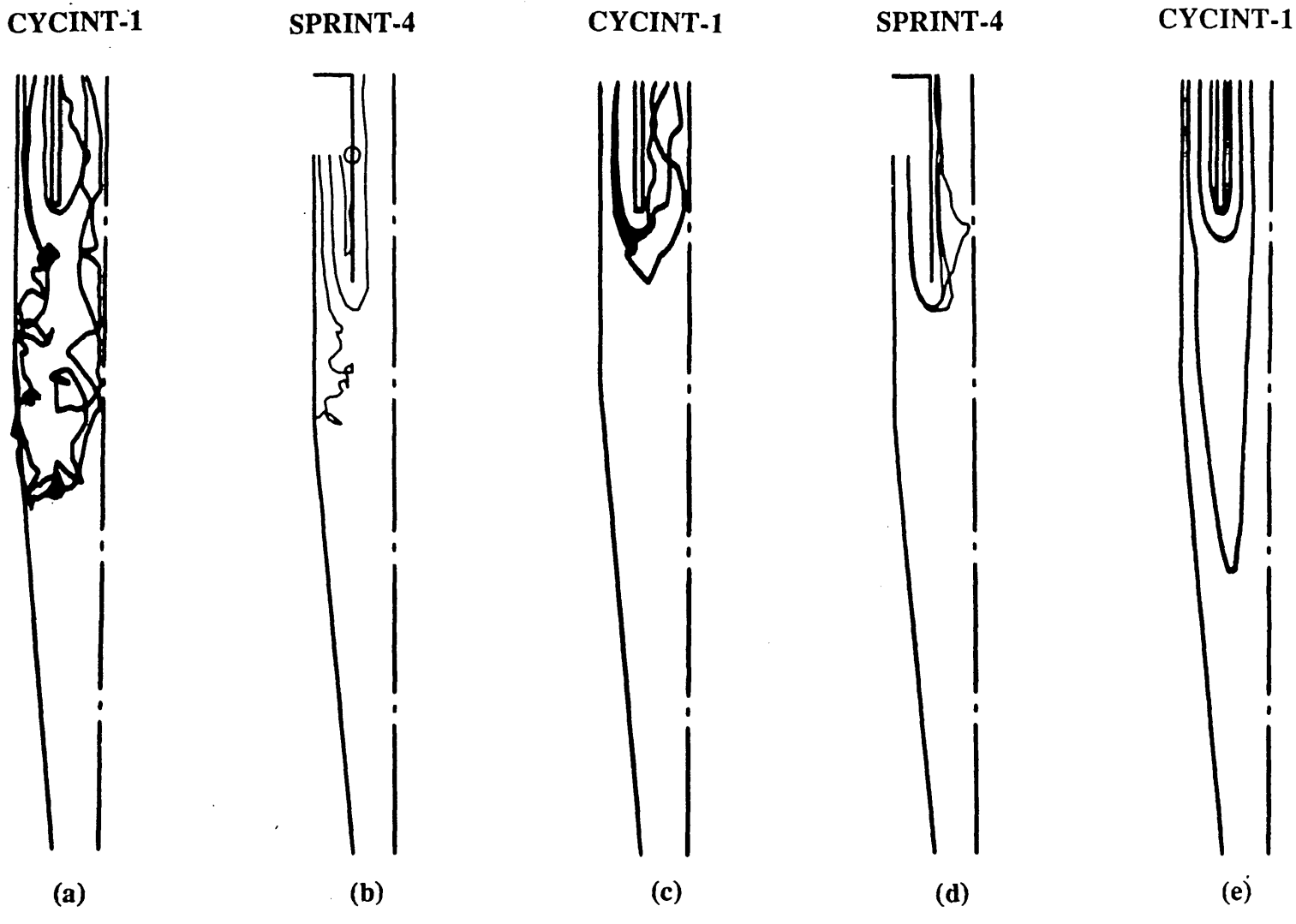

Fig. 5.27 Particle trajectory predictions by CYCINT-1 and SPRINT-4 (1 μm)

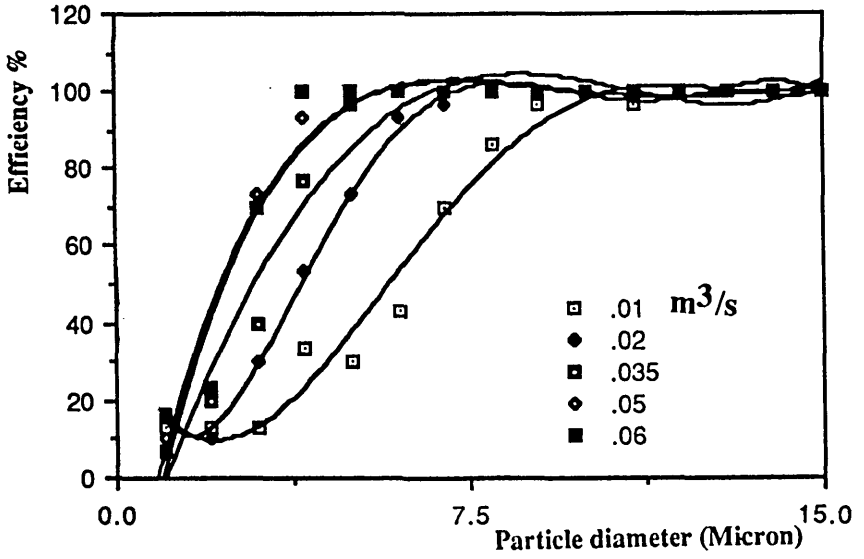

Fig. 5.28 Grade efficiency curve for one-cell cyclone (predicted by CYCINT-1)

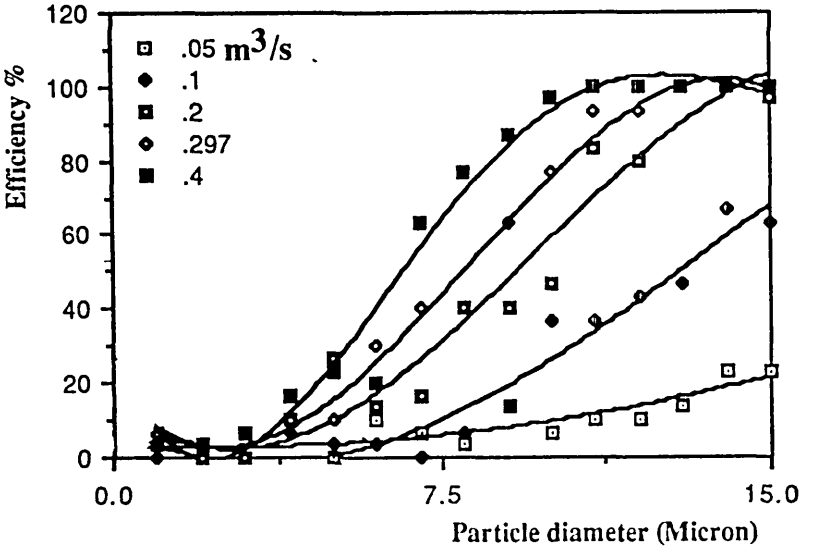

Fig. 5.29 Grade efficiency curve for full scale cyclone (prediction by CYCINT-1)

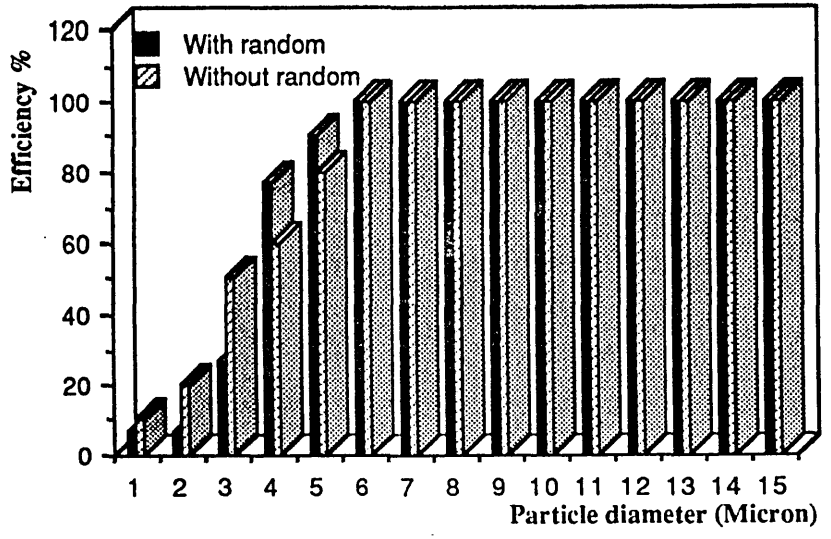

Fig. 5.30 Grade efficiency prediction with and without effect of turbulence

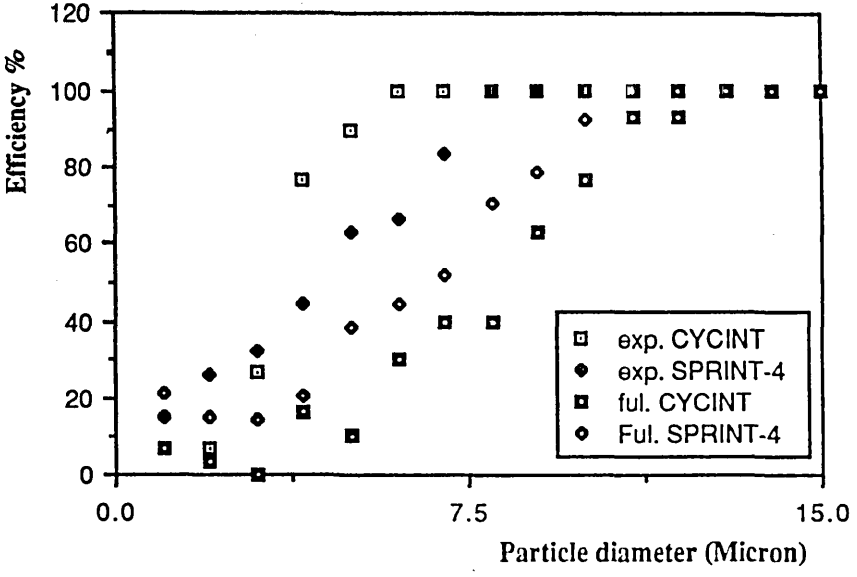

Fig. 5.31 Grade efficiency curve for full and experimental scale (Stokes No. matching)

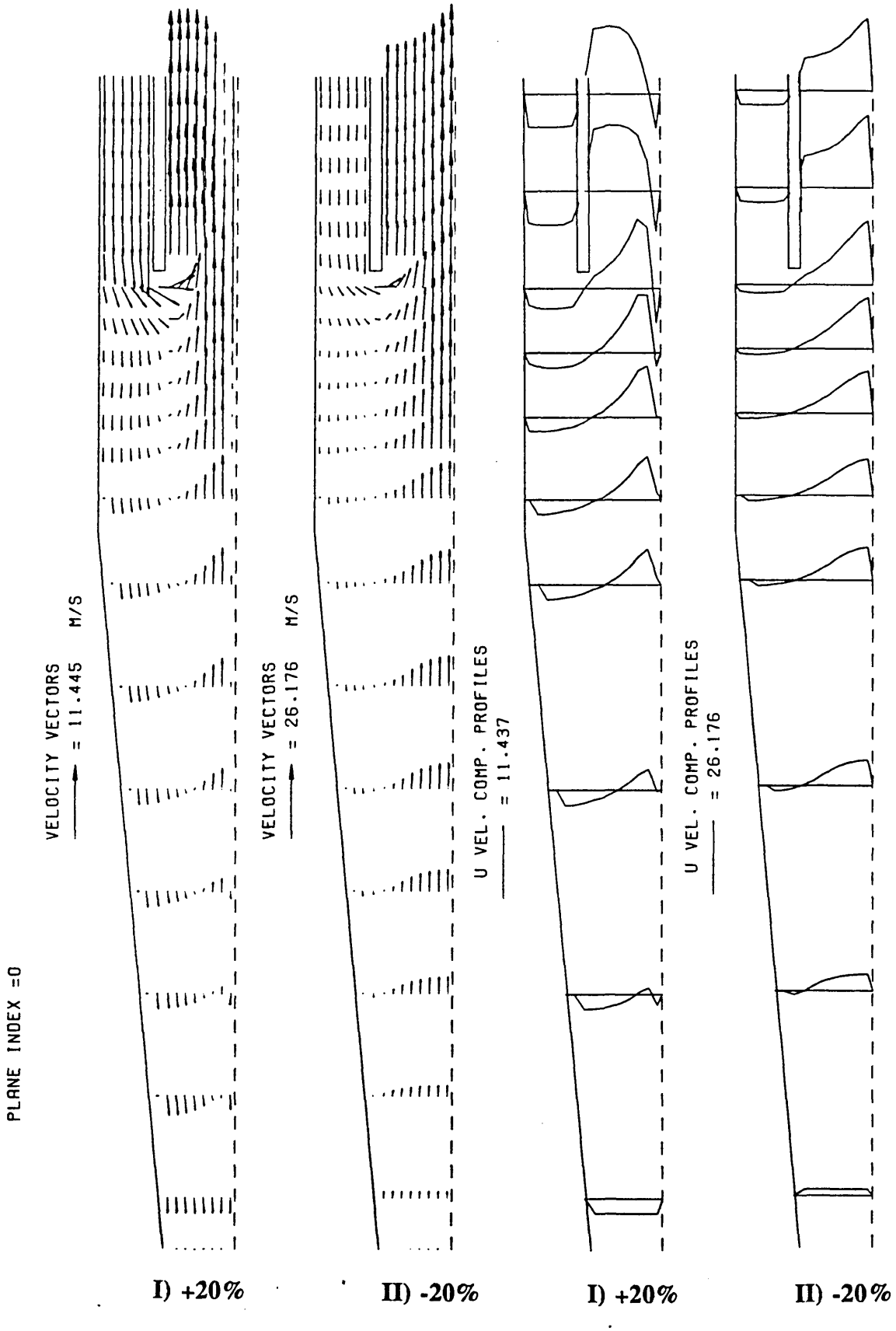

Fig. 5.32a Effect of underflow on flow field for experimental cyclone ($Q=0.0242\ m^3/s$)

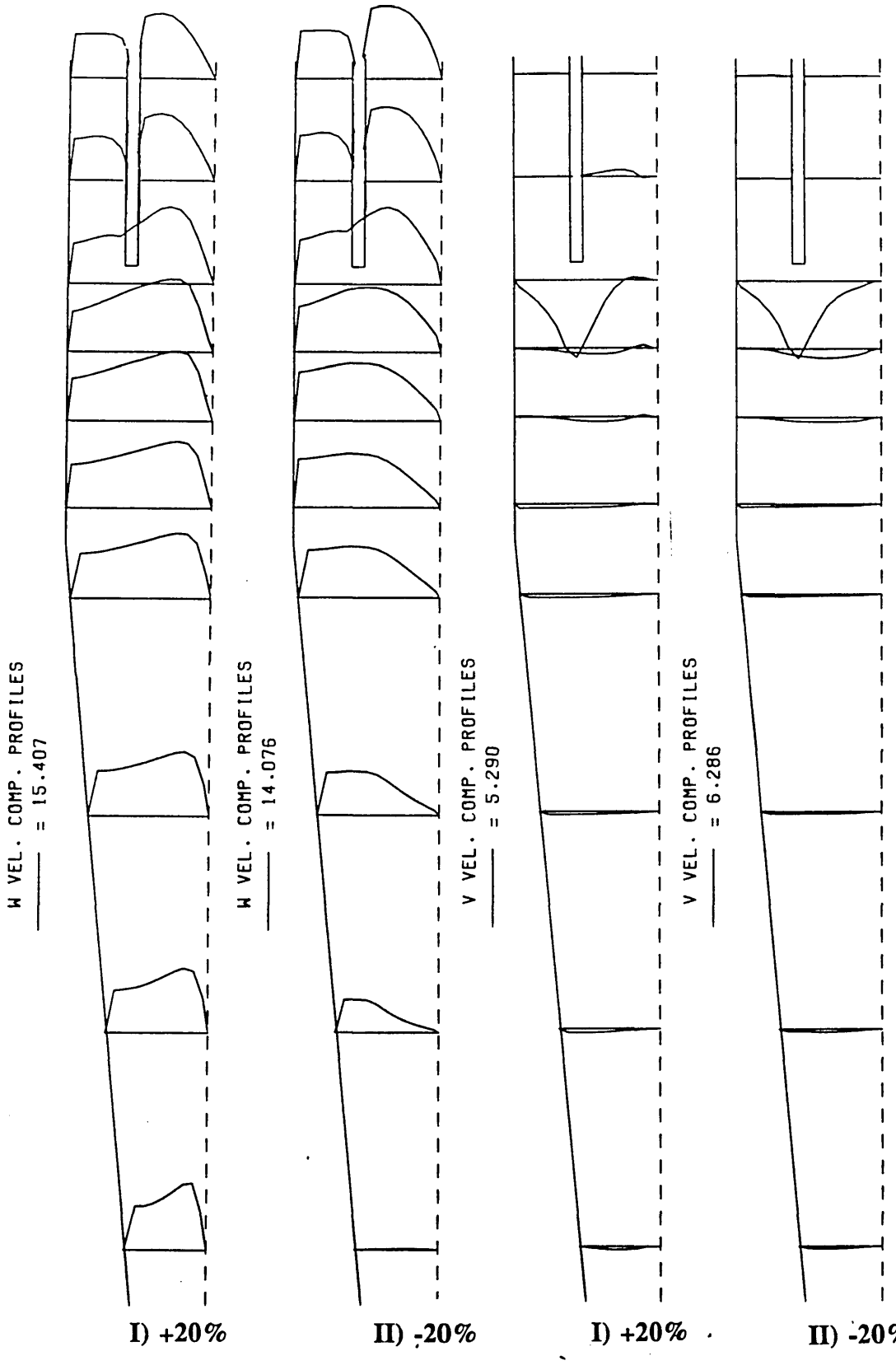

Fig. 5.32b Effect of underflow on flow field for experimental cyclone (Q=0.0242 m^3/s)

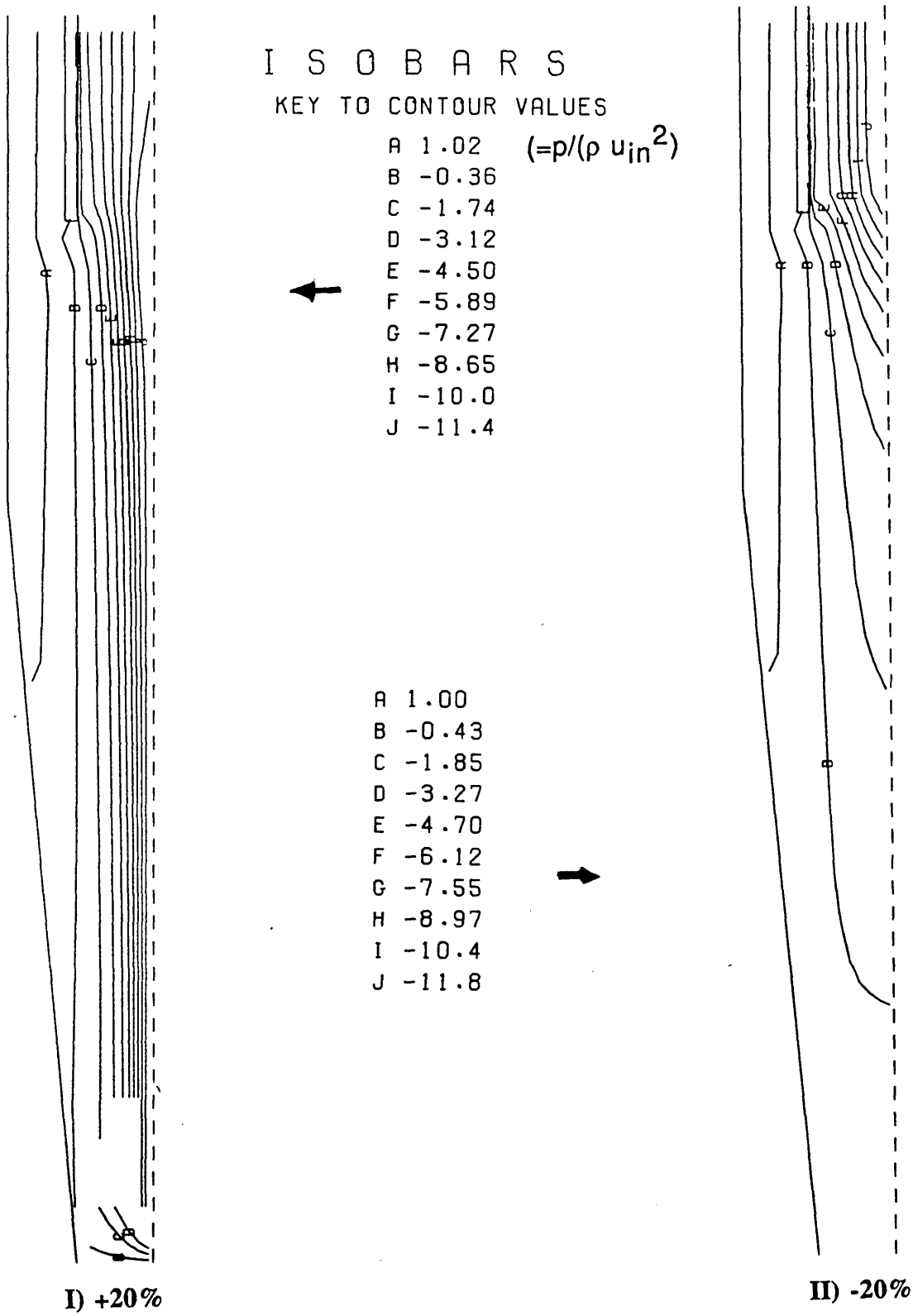

Fig. 5.32c Effect of underflow on flow field for experimental cyclone (Q=0.0242 m^3/s)

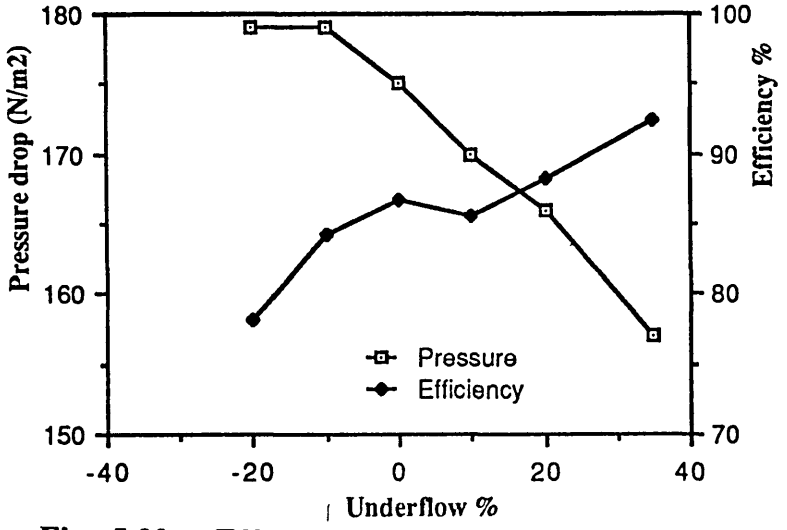

Fig. 5.33 Effect of bottom bleed on cyclone pressure drop and mass efficiency (CYCINT-1)

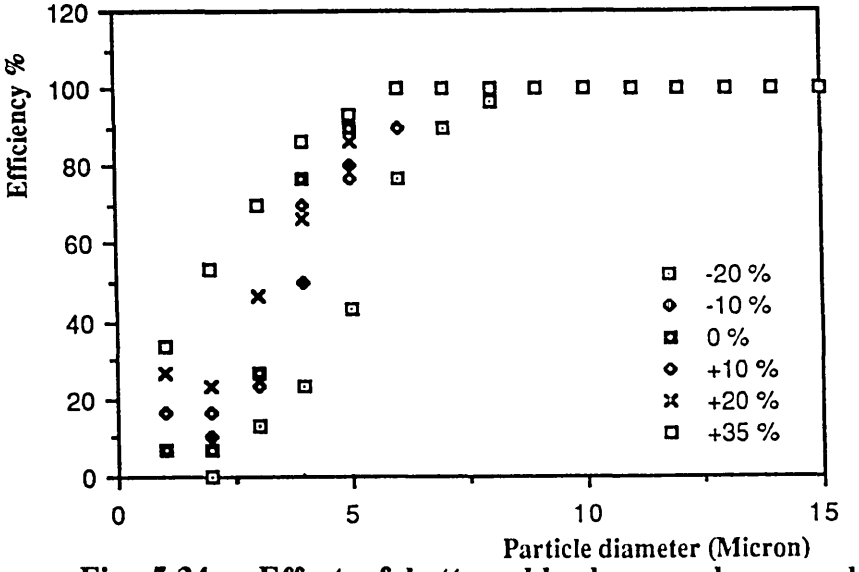

Fig. 5.34 Effect of bottom bleed on cyclone grade efficiency (CYCINT- 1)

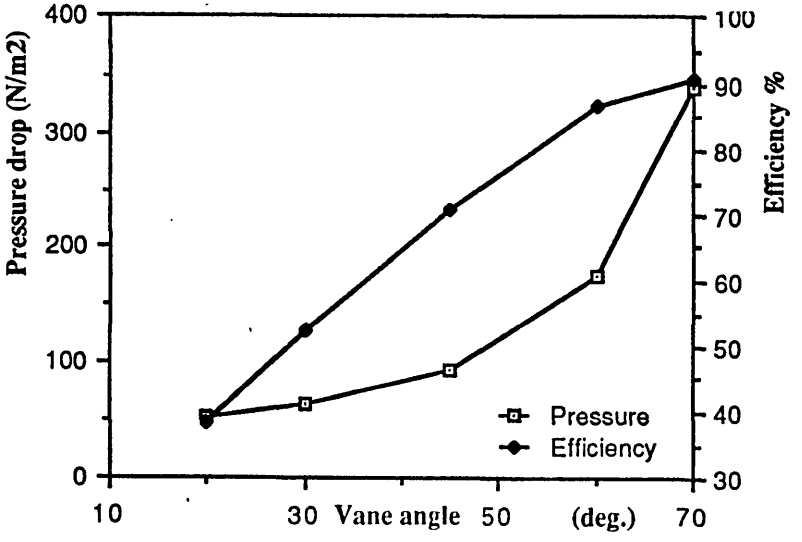

Fig. 5.35 Effect of vane angle on cyclone pressure drop and mass efficiency (CYCINT-1)

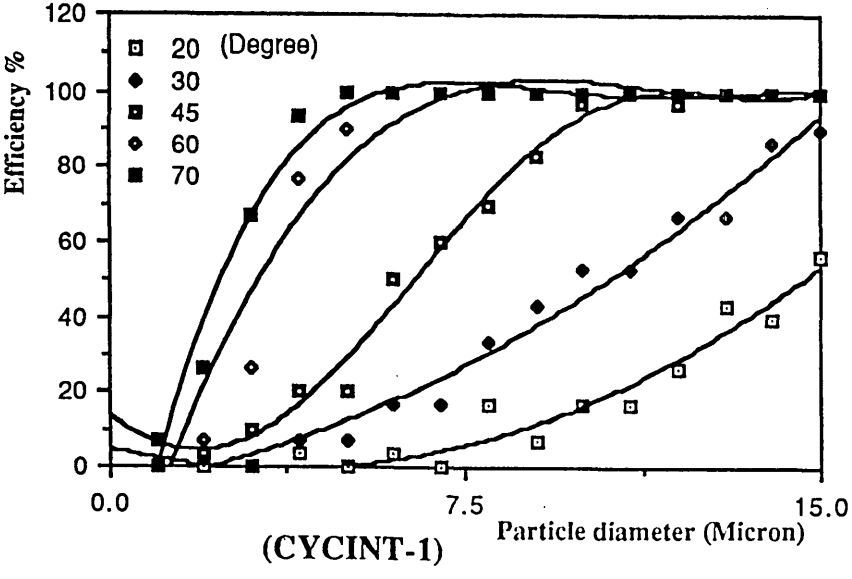

(CYCINT-1)

Fig. 5.36 Effect of vane angle on cyclone grade efficiency

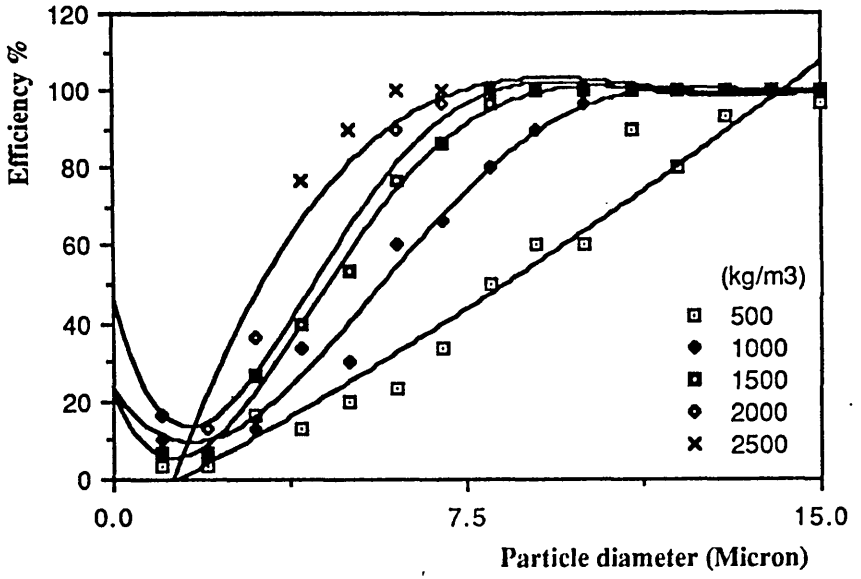

Fig. 5.37 Effect of particle material density on cyclone grade efficiency (CYCINT-1)

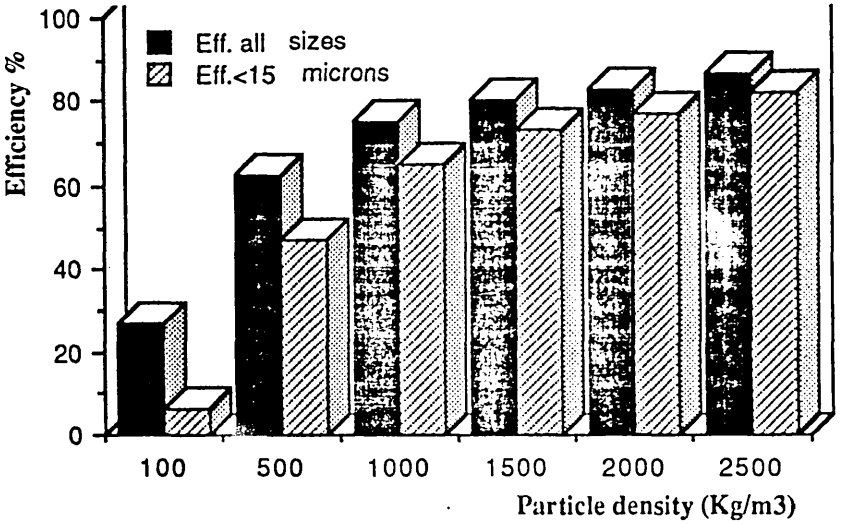

Fig. 5.38 Effect of particle material density on mass efficiency of fine and coarse dust (CYCINT-1)

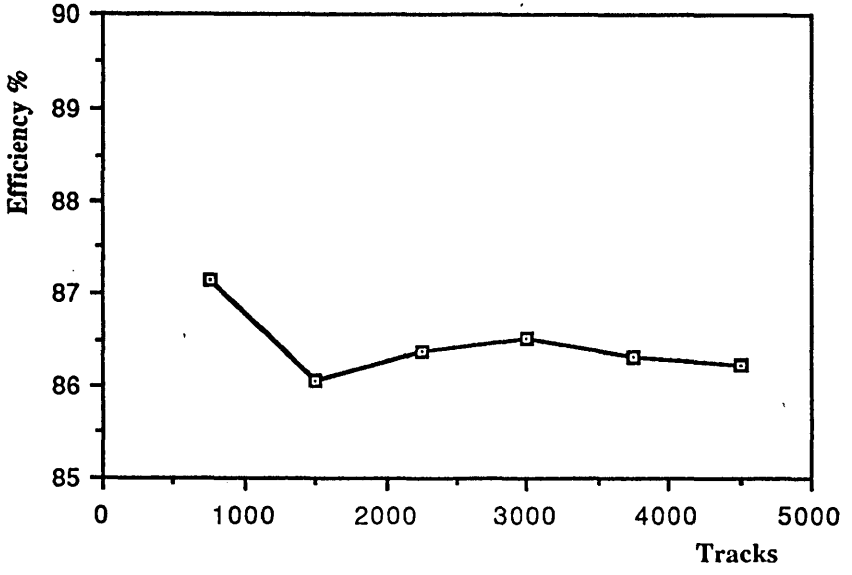

Fig. 5.39 Effect of number of tracks on mass efficiency

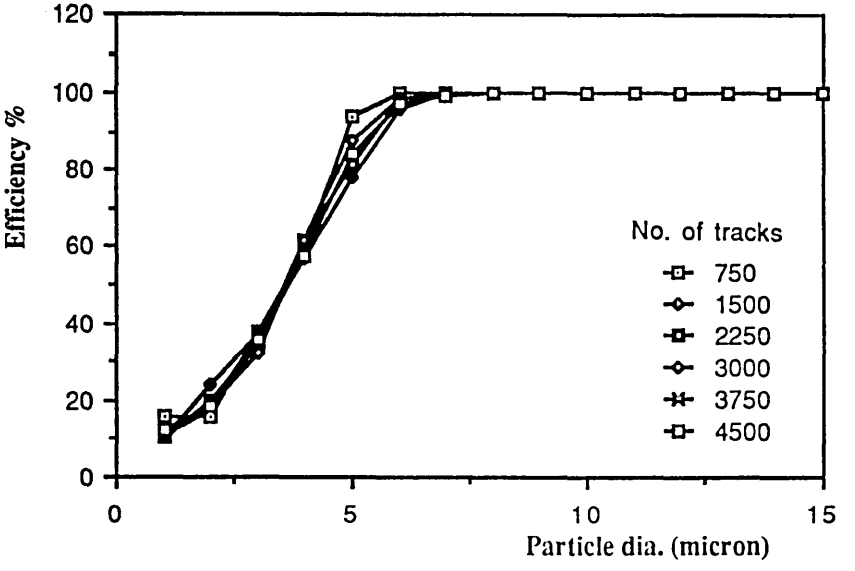

Fig. 5.40 Effect of number tracks on grade efficiency

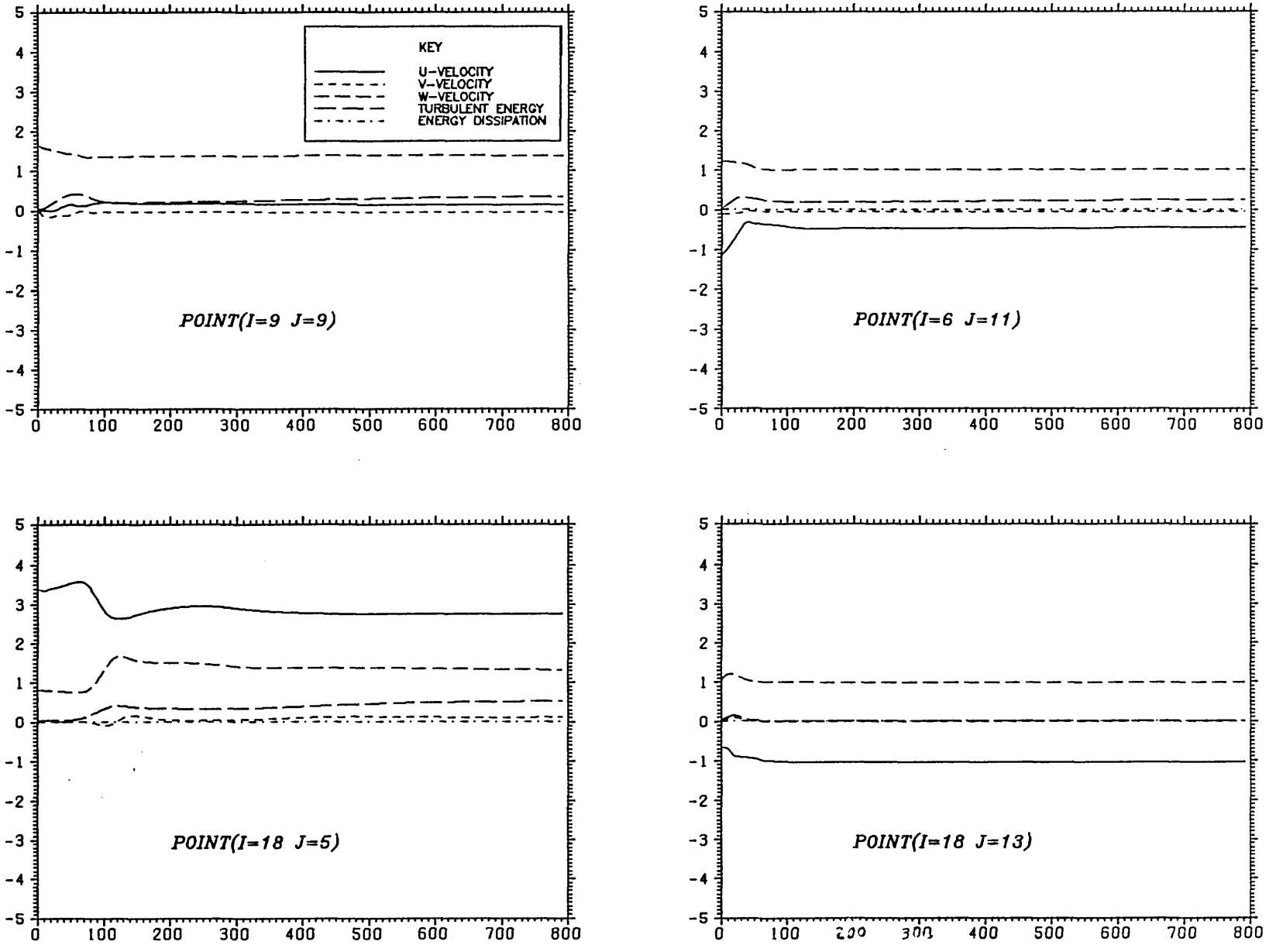

Fig. 5.41 Effect of No. of iterations on dimensionless flow parameters u/u_{in}, w/w_{in}, v/u_{in}, k/k_{in}, and $\varepsilon/\varepsilon_{in}$ (water, Re=67400)

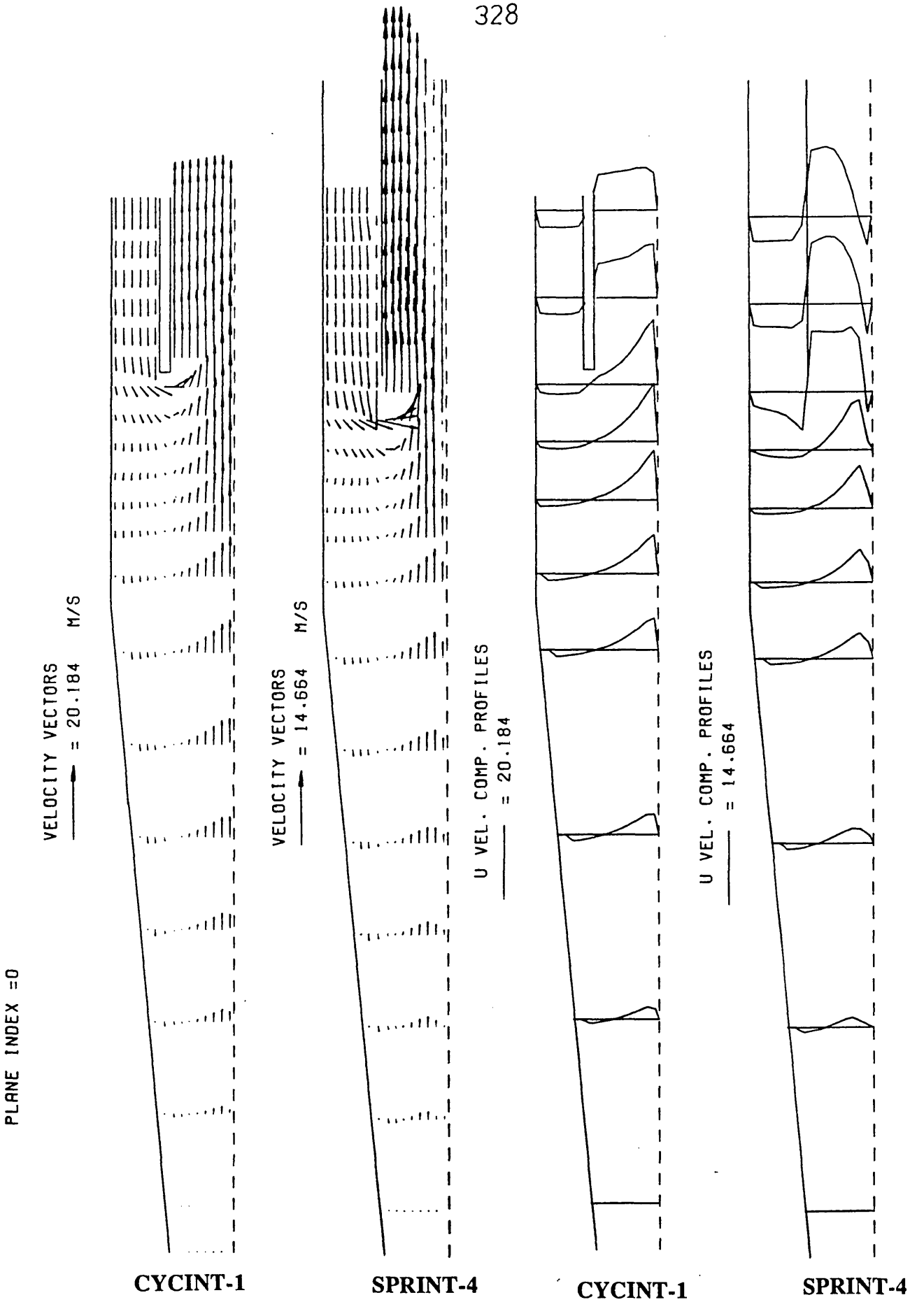

Fig. 5.42a Cyclone flow field prediction by CYCINT-1 & SPRINT-4 for experimental cyclone (Q= 0.024 m^3/s)

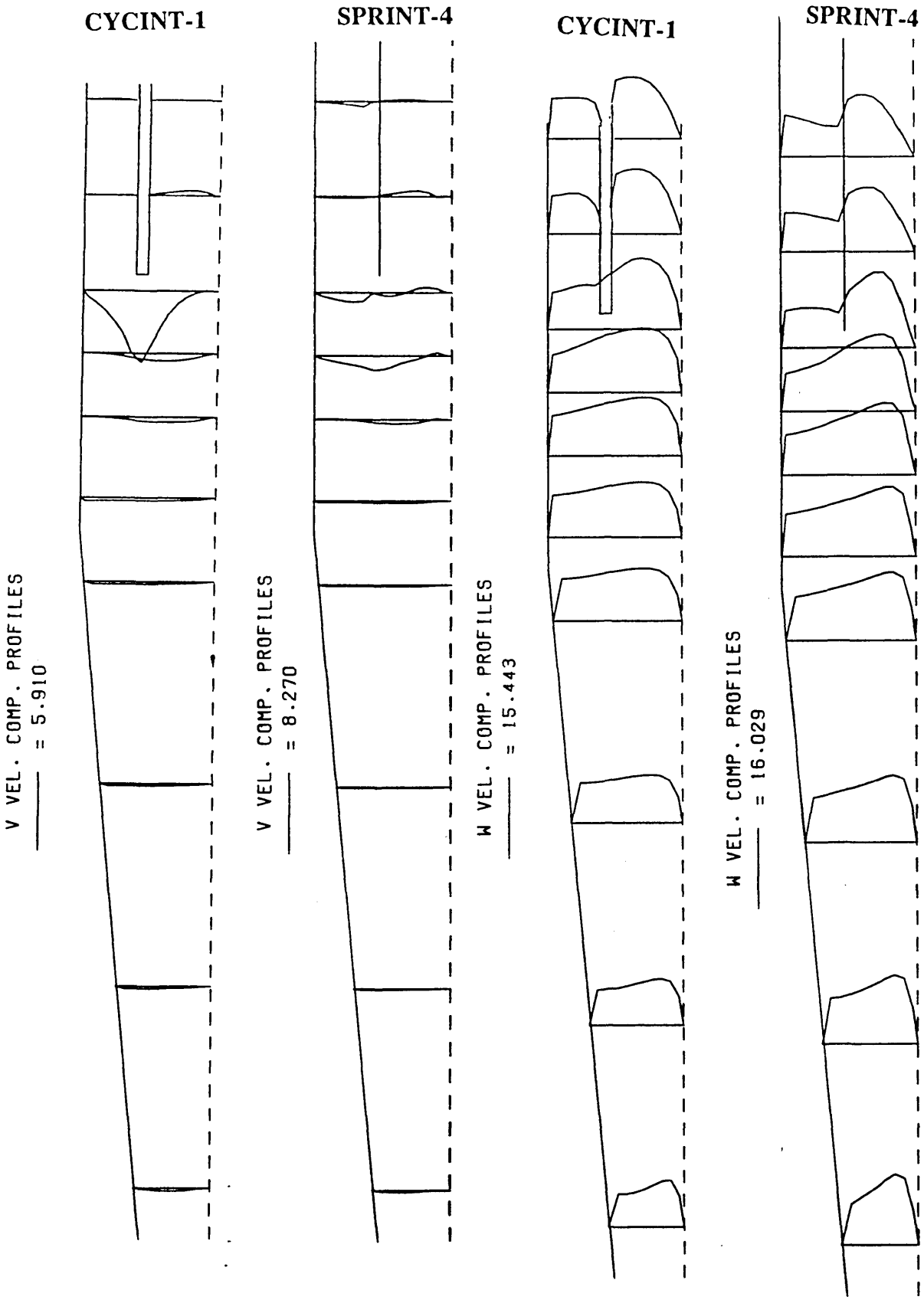

Fig. 5.42b Cyclone flow field prediction by CYCINT-1 & SPRINT-4 for experimental cyclone (Q= 0.024 m^3/s)

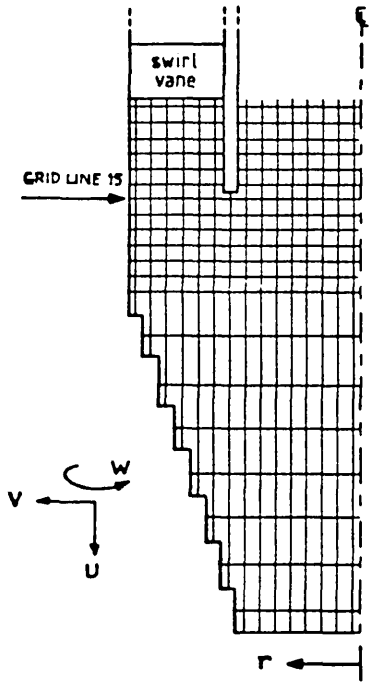

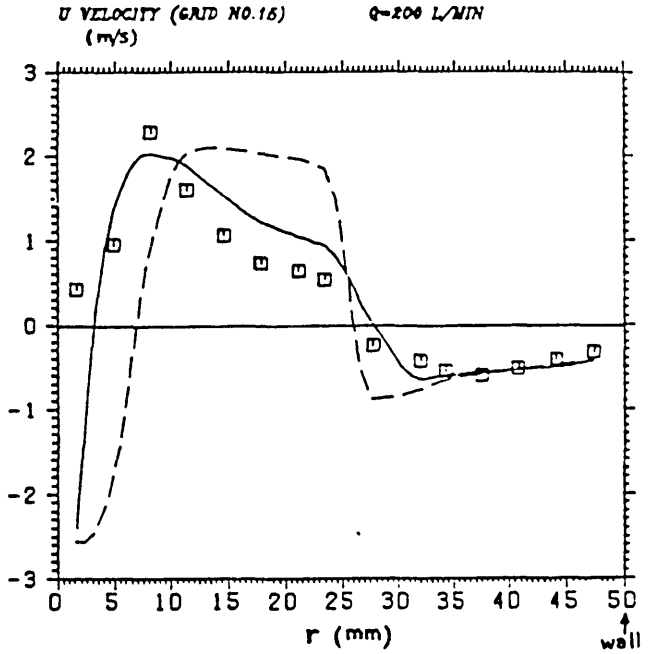

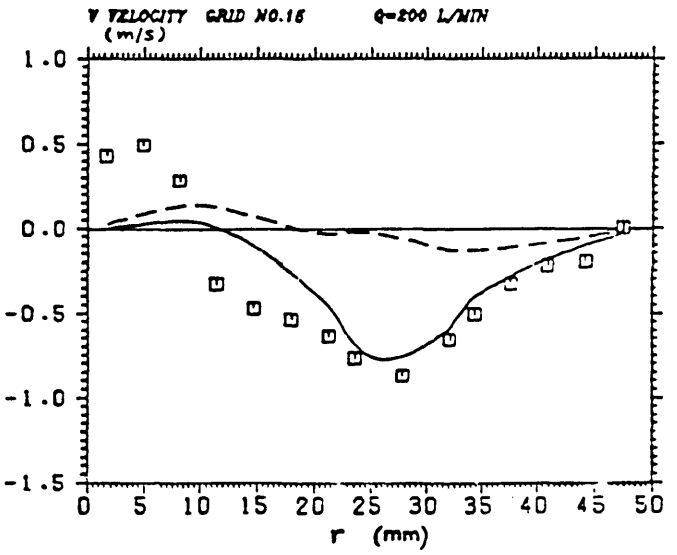

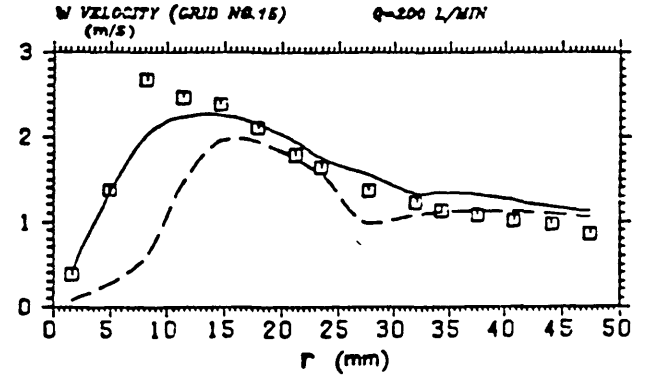

□ Measured (by laser Doppler in single−cell rig) at full−scale Re. No.

------ Computed by original Sheffield University SPRINT4 program

——— Computed by CYCINT

Fig. 5.43 Comparison between velocity measurements and prediction of CYCINT-1 & SPRINT-4

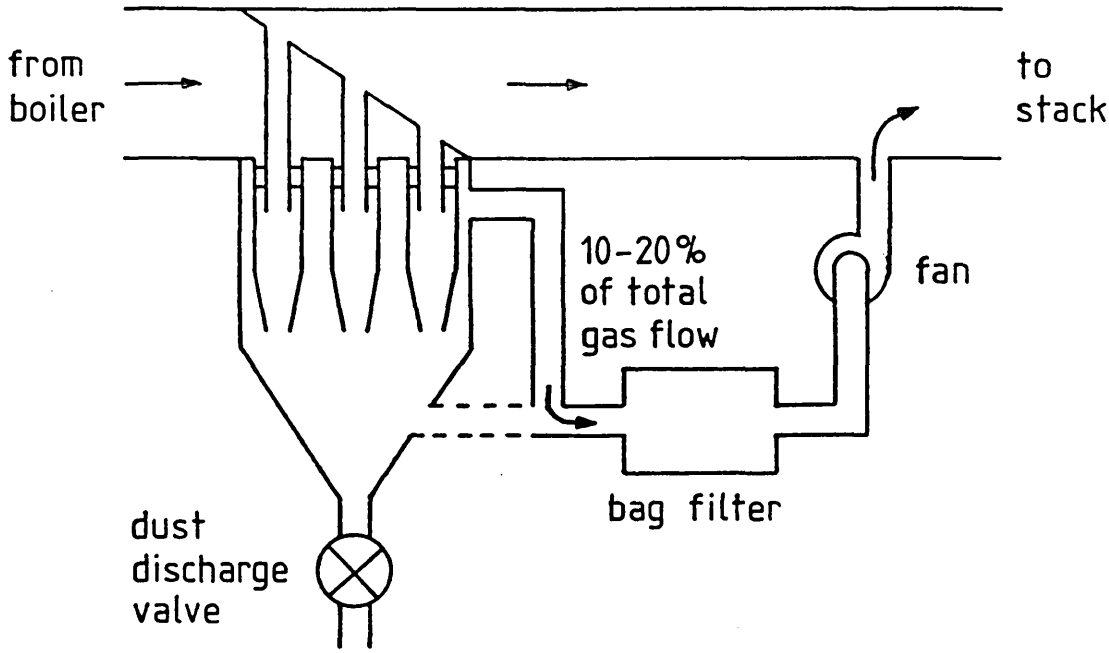

Fig. 6.1 Principle of a multicell sidestream separator

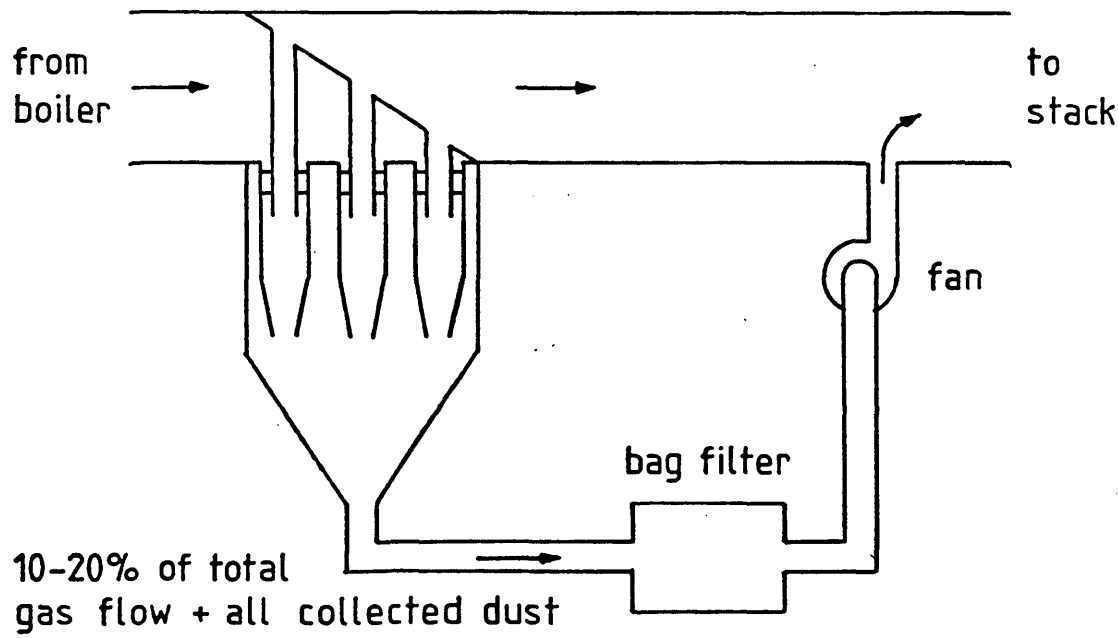

Fig. 6.2 Principle of a multicell concentrator

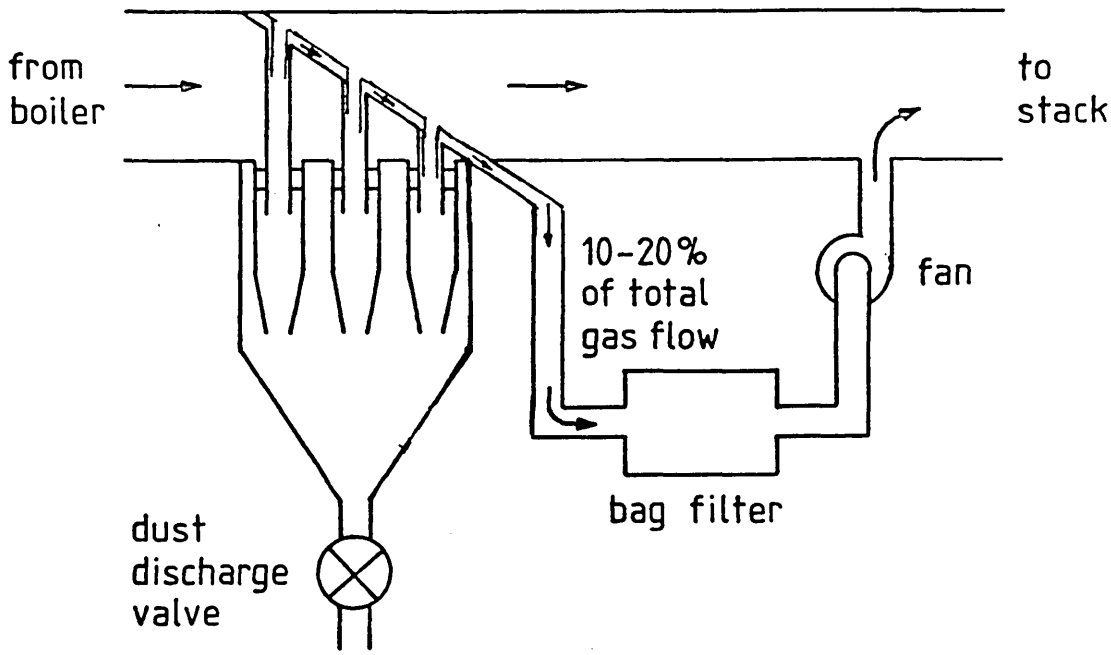

Fig. 6.3 Principle of a multicell separator with gas exit scavenging

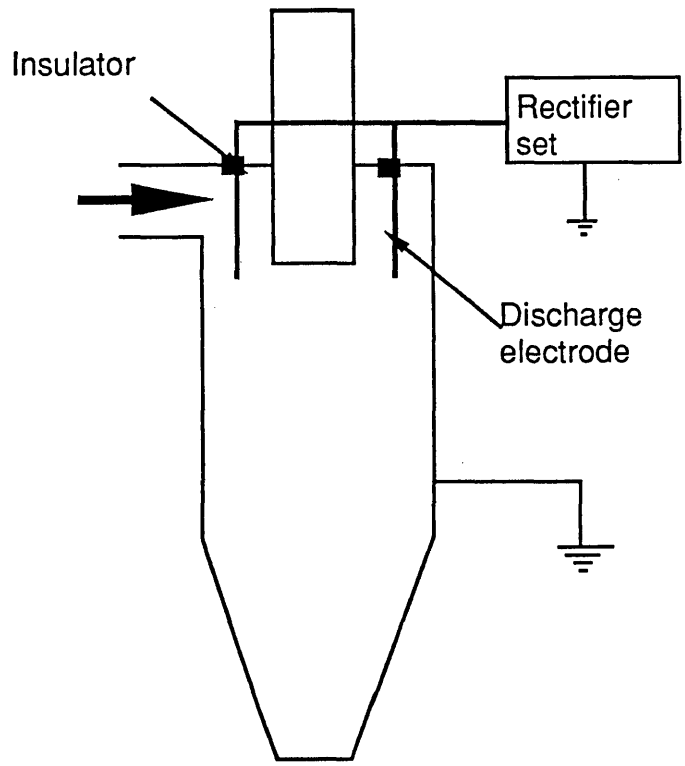

Fig. 6.4 Combination of cyclone and electrostatic precipitator

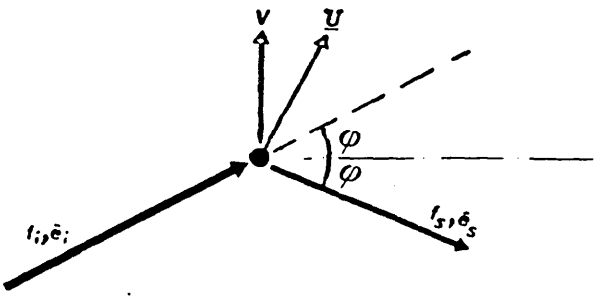

Fig. A.1 Principle of laser Doppler anemometry

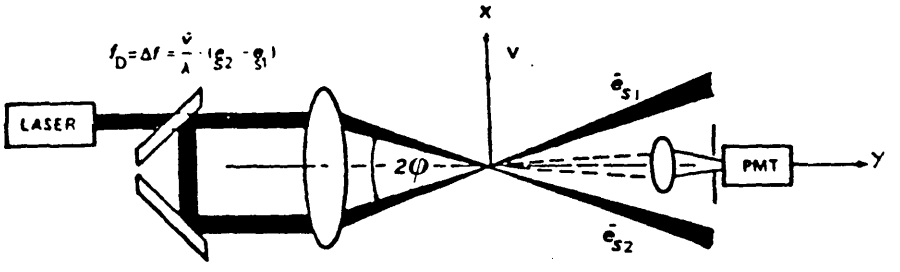

Fig. A.2 Differential Doppler mode (or fringe mode) principle

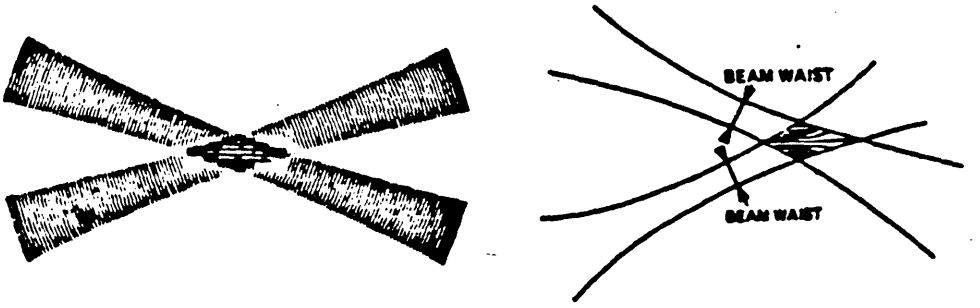

(a) Correct (b) Skewed

Fig. A.3 Fringe patterns caused by laser beam crossing

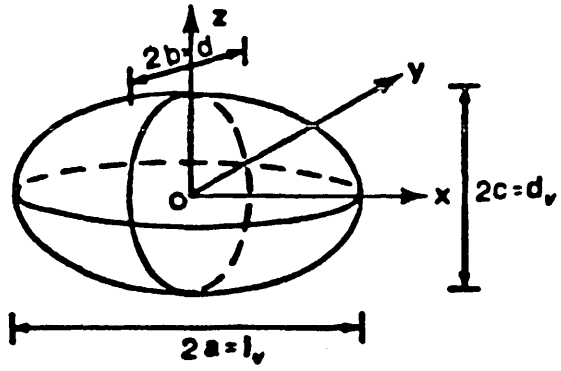

Fig. A.4 Intersection volume (schematic view)

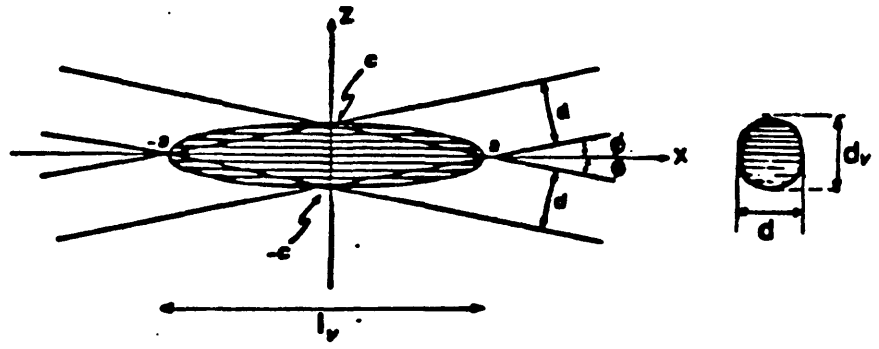

Fig. A.5 Intersection volume geometry

Signal from photodetector

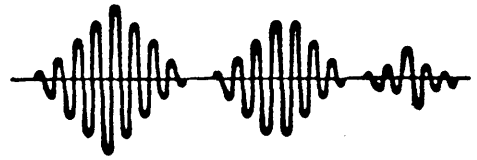

After high-pass filter

Fig. A.6 Photomultiplier output signal

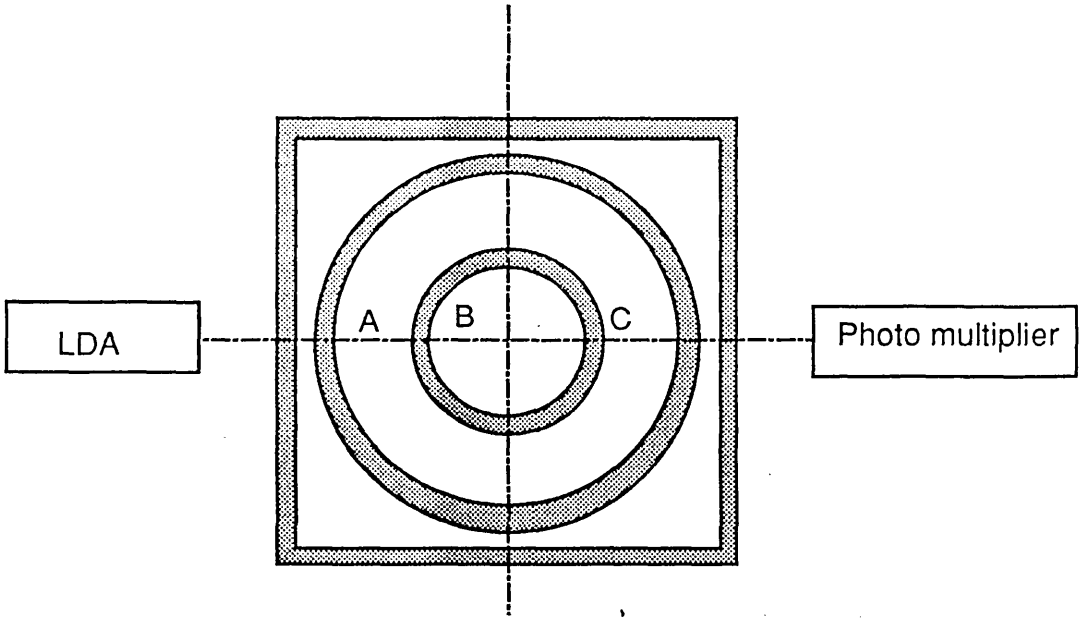

Fig. B.1 One-cell cyclone cross-section (near vanes), showing three measurement locations requiring different refraction corrections)

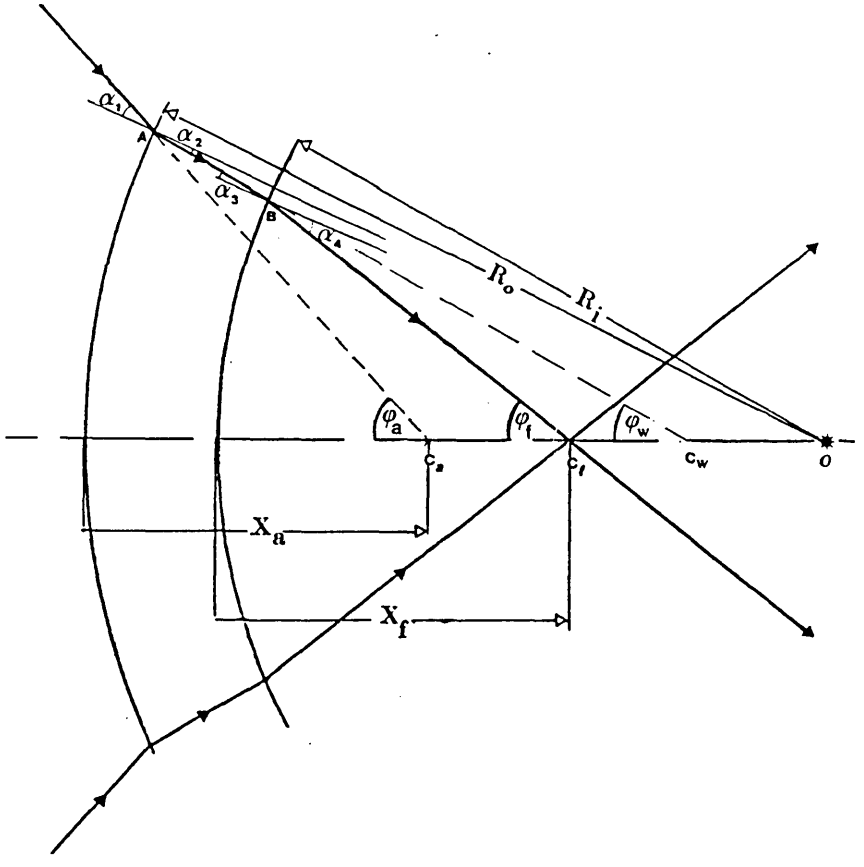

Fig. B.2 Refraction of laser beams for one circular parallel boundary

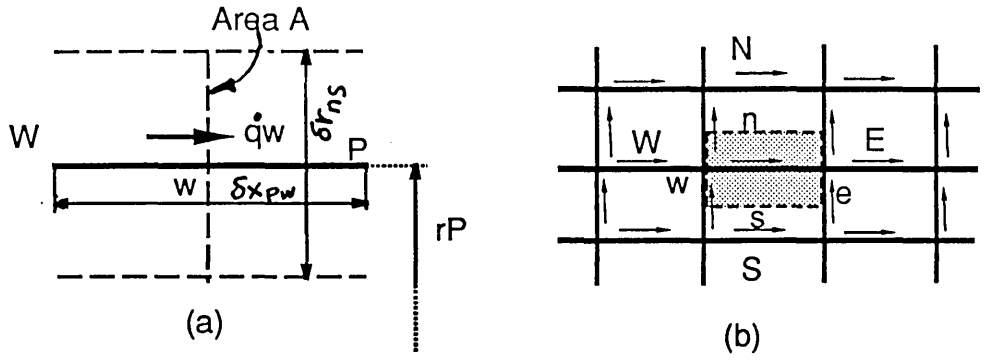

Fig. D.1 Explanation of transport fluxes through cell walls

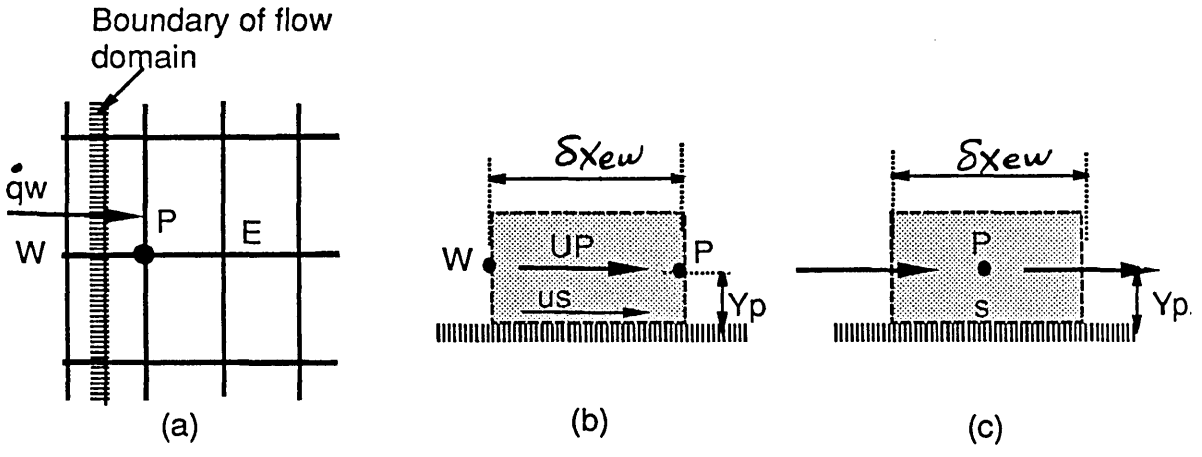

Fig. D.2 Insertion of boundary condition for finite difference method

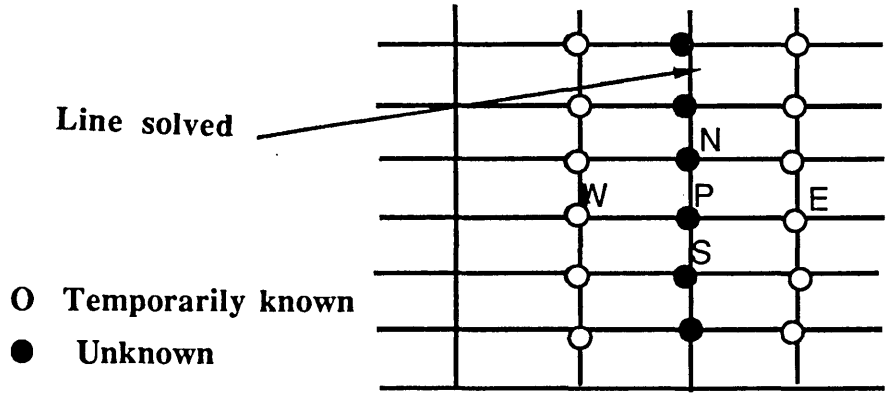

Fig. D.3 Explanation of line-by-line method